JWES-AE-2601(E)



JWES
The Japan Welding Engineering Society

Final Report

Subcommittee on Constraint based Assessment on Fracture in ductile-brittle transition temperature region

September 2026

The Japan Welding Engineering Society
Atomic Energy Research Committee
Subcommittee on Constraint based Assessment on Fracture in ductile-brittle transition temperature region

Copyright © 2026 The Japan Welding Engineering Society, All Rights Reserved.

The following statement shall be included when citing this document:

Final Report (September 2026)

The Japan Welding Engineering Society

Atomic Energy Research Committee

Subcommittee on Constraint based Assessment on

Fracture in ductile-brittle transition temperature region

Copyright © 2026 The Japan Welding Engineering Society, All Rights Reserved.

Table of Contents

1. Introduction....1
2. Organizational structure and activity period....3
3. Investigation of fracture evaluation methods considering plastic constraint effects....4
3.1 Investigation of fracture evaluation methods....4
3.1.1 Investigation by the CAF subcommittee....4
3.1.2 Investigation by the CAF-II subcommittee....5
3.2 Proposal of fracture evaluation methods....10
4. Verification of applicability of fracture evaluation methods employing plastic constraint effects....15
4.1 Fracture tests on specimens with varied plastic constraint levels....15
4.1.1 Objectives....15
4.1.2 Test matrix....15
4.1.3 Test results....27
4.2 Fracture evaluation method....125
4.2.1 Overview....125
4.2.2 Analysis conditions....125
4.2.3 Benchmark analysis....133
4.3 Verification results....163
4.3.1 Calculation of Weibull parameters....163
4.3.2 Calculation of GTN model parameters....165
4.3.3 Fracture prediction of flat plate specimens....167
5. Development of fracture evaluation methods for reactor pressure vessels....177
5.1 Evaluation of plastic constraint for reactor pressure vessels....177
5.1.1 Plastic constraint correction factor χ....177
5.1.2 Plastic constraint effects during PTS events....179
5.1.3 Verification of no ductile crack initiation during PTS events....198

Copyright © 2026 The Japan Welding Engineering Society, All Rights Reserved.

5.2 Examination of simplified evaluation method accounting for plastic constraint effects 202
5.2.1 Model for calculating plastic constraint correction factor χ 202
5.2.2 Construction of database for χ formulation 213
5.2.3 Formulation of χ 229
5.2.4 Setting method for material properties used in χ calculation 237
5.2.5 Application examples of plastic constraint correction 259
6. Study towards standardization 265
7. Summary 266

Appendix 1 Committee Member List 270
Appendix 2 Draft Code for Simplified Evaluation Method: "Correction Method for PTS Transient Curve Considering Plastic Constraint Effects" 275
Appendix 3 Draft Standard for Simplified and Detailed Evaluation Methods: "Method of Constraint Loss Correction for Fracture Driving Force in PTS Transient of Reactor Pressure Vessel" 286
Appendix 4 Fundamental Study of Fracture Analysis by Benchmark Analysis 307

Copyright © 2026 The Japan Welding Engineering Society, All Rights Reserved.

1. Introduction

Current fracture mechanics evaluation methods assess the structural integrity using fracture toughness as material properties obtained from laboratory specimens with high plastic constraint such as three-point bending specimens or compact tension specimens. However, flaws actually observed in structures are often detected in the form of small surface flaws, and the stress field is often dominated by tensile loading. When tensile loading is dominant, the plastic constraint on the flaw is lower than that of fracture toughness specimens under bending load, and significantly higher fracture resistance is sometimes observed. This dependence of fracture resistance on plastic constraint is widely known among the experts. The international standard, ISO 27306, which specifies a correction method for plastic constraint effects in fracture evaluation for brittle fracture, was published in 2009 and revised in 2016, and it is partially incorporated into WES2808, a Welding Engineering Standard by the Japan Welding Engineering Society (JWES), , which is a fracture evaluation method for brittle fracture of steel structures under cyclic loading. These standards consider plastic constraint effects to eliminate excessive conservatism of conventional methods and appropriately evaluate fracture safety of structures.

The CAF Subcommittee has developed a fracture evaluation method considering plastic constraint effects for fracture modes involving cleavage fracture accompanied by ductile crack propagation in the ductile-brittle transition temperature (DBTT) region, which is important for the integrity evaluation of actual structures, aiming at improvement of integrity evaluation for aged plants after long term operation. As fracture evaluation methods considering plastic constraint effects, there are stochastic models such as the Beremin model for brittle fracture and damage mechanics models such as the Gurson model for ductile fracture. Although discussions on their applicability are still continuing in the world, verification of the models, establishment of analysis methods for application to actual structures, and standardization of the above models have not been sufficiently conducted. From fiscal year 2018 to 2022, the CAF Subcommittee investigated the latest knowledge, conducted numerical analyses for fracture tests with different plastic constraint levels for confirmation of their applicability, and produced a draft guideline for application to actual structures. The CAF-II Subcommittee, aiming at social implementation of this guideline, focused on the Pressurized Thermal Shock (PTS) evaluation method in the Japan Electric Association codes JEAC4206 "Method for Confirmation of Fracture Toughness during

Copyright © 2026 The Japan Welding Engineering Society, All Rights Reserved.

Service Period for Reactor Pressure Vessel," and formulated a draft standard.

This document summarizes the results obtained by the CAF Subcommittee and the CAF-II Subcommittee.

Copyright © 2026 The Japan Welding Engineering Society, All Rights Reserved.

2. Organizational structure and activity period

This investigation was initiated through the two subcommittees under the Atomic Energy Research Committee of the Japan Welding Engineering Society: the "Subcommittee for Establishing Fracture Assessment Criteria Considering Plastic Constraint Effect" (CAF Subcommittee*) and the "Subcommittee for Establishing Fracture Assessment Criteria Considering Plastic Constraint Effect (Part 2)" (CAF-II Subcommittee). The chairperson for both subcommittees was Professor Emeritus Fumiyoshi Minami of University of Osaka, with Professor Mitsuru Ohata of University of Osaka serving as the vice-chairperson.

The member lists of the CAF and CAF-II Subcommittees are provided in Appendix 1.

- CAF Subcommittee: Constraint based Assessment of Fracture in ductile-brittle transition temperature region

The CAF Subcommittee conducted its activities over a five-year period, from April 2018 to March 2023, while the CAF-II Subcommittee had been active for a two-year term spanning from April 2023 to March 2025.

Copyright © 2026 The Japan Welding Engineering Society, All Rights Reserved.

3. Investigation of fracture evaluation methods considering plastic constraint effects

3.1 Investigation of fracture evaluation methods

3.1.1 Investigation by the CAF subcommittee

A literature survey was conducted on the recent research, as well as application cases related to the Beremin Model for brittle fracture and damage mechanics models for ductile fracture. This survey aimed to summarize the modeling, evaluation accuracy, identification of technical challenges, and application scopes. The selected literature, categorized into brittle fracture, ductile fracture, and coupled fracture modes, is summarized in Tables 3.1.1-1 to 3.1.1-3.

Moreover, to support benchmark analyses and the development of a relevant guideline, a detailed investigation was performed classifying the literature by the items. The analysis items are as follows.

(1) Brittle fracture (including brittle fracture in coupled modes)

a) Definition of the stress-strain curve

b) Mesh size

c) Function of the Weibull distribution

d) Evaluation method of the effect of plastic strain

e) Evaluation method of the effect of ductile crack

f) Specimens and their amounts used for parameter definition, and specimens used for predictability verification

g) Temperature dependence of Weibull parameters

h) Values of Weibull parameters

i) Application examples to actual structures

j) Application examples to irradiated materials

k) Effect of biaxial loading

l) Material dependence of plastic constraint effect

(2) Ductile fracture (including ductile fracture in coupled modes)

a) Definition of the stress-strain curve

b) Mesh size

c) Element type

Copyright © 2026 The Japan Welding Engineering Society, All Rights Reserved.

d) Model of Damage mechanics

e) Consideration of secondary voids and rationale for their inclusion or exclusion

f) Specimens and their amounts used for parameter definition, and specimens used for predictability verification

g) Method of parameters determination

h) Temperature dependence of parameters

i) Parameters of damage mechanics

j) Application examples to actual structures

3.1.2 Investigation by the CAF-II Subcommittee

At the WG on Flaw Evaluation of the ASME Sec. XI standards meeting held in May 2023, it was reported that an observer from Framatome introduced ongoing considerations in France regarding the adoption of fracture evaluation methods incorporating the plastic constraint effect. Discussions with regulatory authorities are included in the project timeline. To monitor the developments in France on this topic, a survey was conducted of the papers presented at the 2023 and 2024 ASME Pressure Vessels & Piping Conference (ASME PVP) as well as the SMiRT27 conference held in 2024. Additionally, presentations from Japan related to the plastic constraint effect at these conferences were reviewed. The surveyed literature is summarized in Tables 3.1.2-1 and 3.1.2-2.

In France, fracture evaluation approaches based on the pseudo J-Q method and the Beremin model are currently under consideration. With a view toward extending operational lifetimes beyond 60 years, electric utilities and regulators are engaged in discussions regarding the introduction of fracture evaluation methods that incorporate the plastic constraint effect. Given these developments, continuous monitoring of trends in France is essential when considering the integration of the plastic constraint effect into draft standards in Japan.

Copyright © 2026 The Japan Welding Engineering Society, All Rights Reserved.

Table 3.1.1-1 List of literature survey in CAF subcommittee (brittle fracture)

No.	Author	Issue	Title
C-1	F. M. Beremin	1983	A Local Criterion For Cleavage Fracture Of A Nuclear Pressure Vessel Steel
C-2	F. Mudry	1987	A Local Approach To Cleavage Fracture
C-3	C. Ruggieri	2016	A Probabilistic Model Including Constraint And Plastic Effects For Fracture Toughness Predictions In A pressure Vessel Steel
C-4	X. Gao, G. Zhang, T.S. Srivatsan	2005	Prediction Of Cleavage Fracture In Ferritic Steels: A Modified Weibull Stress Model
C-5	T.L. Anderson, B.D. Rose	?	A Modified Weibull Stress Model For Cleavage Fracture That Incorporates Threshold Toughness
C-6	X. Gao, R. H. Dodds Jr., R. L. Tregoning, J. A. Joyce, R. R. Link	1999	A Weibull Stress Model To Predict Cleavage Fracture In Plates Containing Surface Cracks
C-7	S.R. Bordet A, A.D. Karstensen A, D.M. Knowles B, C.S. Wiesner	2005	A New Statistical Local Criterion For Cleavage Fracture In Steel. Part I: Model Presentation
C-8	S.R. Bordet, A.D. Karstensen, D.M. Knowles, C.S. Wiesner	2005	A New Statistical Local Criterion For Cleavage Fracture In Steel. Part II: Application To An Offshore Structural Steel
C-9	J. P. Mathieu, K. Inal, S. Berveiller, O. Diard	2010	A Micromechanical Interpretation Of The Temperature Dependence Of Beremin Model Parameters For French RPV Steel
C-10	K. Rosahl, J. D. Booker, S. Lewis, D. J. Smith	2011	A Statistical Approach For Transferring Fracture Events Across Different Sample Shapes
C-11	C. Ruggieri, R. H. Dodds Jr.	2015	An Engineering Methodology For Constraint Corrections Of Elastic-Plastic Fracture Toughness – Part I: A Review On Probabilistic Models And Exploration Of Plastic Strain Effects
C-12	C. Ruggieri, R. G. Savioli, R. H. Dodds Jr.	2015	An Engineering Methodology For For Constraint Corrections Of Elastic-Plastic Fracture Toughness –Part II: Effects Of Specimen Geometry And Plastic Strain On Cleavage Fracture Predictions
C-13	C. Ruggieri, R. H. Dodds Jr.	2016	A Modified Weibull Stress Approach To Predict Specimen Geometry Effects In A Pressure Vessel Steel
C-14	X. Gao, C. Ruggieri, R. H. Dodds. Jr.	1998	Calibration of Weibull Stress Parameters Using Fracture Toughness Data
C-15	A. H. Sherry, M. A. Wilkes, D. W. Beardsmore, D. P. G. Lidbury	2005	Material constraint parameters for the assessment of shallow defects in structural components – Part I: Parameter solutions
C-16	A. H. Sherry, D. G. Hooton, D. W. Beardsmore, D. P. G. Lidbury	2005	Material constraint parameters for the assessment of shallow defects in structural components – Part II: Constraint-based assessment of shallow defects
C-17	D. P. G. Lidbury, A. H. Sherry, B. R. Bass, P. Gilles, D. Connors, U. Eisele, E. Keim, H. Keinanen, K. Wallin, D. Lauerova, S. Marie, G. Nagel, K. Nilsson, D. Siegele, Y. Wadier	2006	Validation of constraint-based methodology in structural integrity of ferritic steels for nuclear reactore pressure vessels
C-19	Mitsuru Ohata, Yasuhito Takashima, Fumiyoshi Minami	2016	WES 2808 for Brittle Fracture Assessment of Steel Components under Seismic Conditions – Part V: Equivalent CTOD ratio for correction of constraint loss in beam-to-colum connections
C-21	D. Moinereau, A. Dahl, S. Chapuliot, D. Lidbury	2006	SMILE Project The Effect Of Warm Pre-Stress In RPV Assessment : Synthesis Of Experimental Results And Analyses
C-22	D. Lauerova, N. Taylor, V. Pistora, P. Minnebo, E. Paffumi	2009	Benchmark Analyses for Fracture Mechanics Methods for Assessing Sub-Clad Flaws NESC-VI Final Report
C-23	D. Moinereau, S. Chapuliot, S. Marie, P. Gilles	2012	Nesc VII : A European Project For Application Of WPS In RPV Assessment Including Biaxial Loading
C-25	J. P. Petti, R. H. Dodds, Jr.	2005	Calibration of The Weibull Stress Scale Parameter, σ_u, Using The Master Curve
C-26	B. Wasiluk, J. P. Petti, R. H. Dodds Jr.	2006	Temperature Dependence Of Weibull Stress Parameters Studies Using The Euro-material
C-27	G. Qian, M. Niffenegger	2015	Investigation On Constraint Effect Of A Reactor Pressure Vessel Subjected To Pressurized Thermal Shocks
C-28	M. Shimodaira, T. Tobita, Y. Nagoshi, K. Lu, J. Katsuyama	2021	Effect Of Plastic Constraint And Cladding On Semi-Elliptical Shasped Crack In Fracture Toughness Evaluation For A Reactor Pressure Vessel Steel
C-29	M. Shimodaira, T. Tobita, H. Takamizawa, J. Katsuyama, S. Hanawa	2020	Constraint Effect On Fracture Mechanics Evaluation For An Under-clad Crack In A Reactore Pressure Vessel Steel
C-30	K. Wallin, S. X. Zu	2022	A Review Of Constraint Effects On Fracture Toughness For Structural Integrity Assessment In Fitness-For-Service Codes

Copyright © 2026 The Japan Welding Engineering Society, All Rights Reserved.

Table 3.1.1-2 List of literature survey in CAF subcommittee (ductile fracture)

No.	Author	Issue	Title
D-1	H.Y. Tu, S. Schmauder, U. Weber, Y. Rudnik, V. Ploshikhin	2012	Simulation Of The Damage Behaviour Of Electron Beam Welded Joints With The Rousselier Model
D-2	M.P. Valeta ,C. Poussard, F. Zydownik C. Sainte Catherine	?	Micro-Mechanical Modelling Of Ductile Tearing Resulting From A Thermo-Mechanical Loading
D-3	C. Poussard, D. Miannay And C. Sainte Catherine	?	Finite Element Modelling Of A Smooth Tensile Specimen And A Compact Tension Specimen With The Gurson-Tveergard-Needleman And Rousselier Micromechanical Models
D-4	A. L. Gurson	1977	Continuum theory of ductile rupture by void nucleation and growth : Part I – Yield criteria and flow rules for porous ductile media
D-5	U. Prahl, S. Bourgeois, T. Pandorf, M. Aboutayeb, O. Debordes, D. Weichert	2002	Damage Parameter Identification By A Periodic Homogenization Approach
D-6	M. Seidenfuss, E. Roos	2004	Lissac – Size And Geometry Effects On The Failure Behaviour Of Notched Specimens
D-7	S. Gehrlicher, X. Schuler, M. Seidenfuss, J. Mahlke	2013	Damage Modelling Of The Load-Bearing Capacity Of Degraded Steam
D-8	B.K. Dutta, S. Guin, M.K. Sahu, M.K. Samal	2008	A phenomenological form of the q2 parameter in the Gurson model
D-9	Geralf Hütter, Lutz Zybell, Meinhard Kuna	2014	Size effects due to secondary voids during ductile crack propagation
D-10	Diego F.B. Sarzosa, Matthias Verstraete, Stijn Hertelé, Rudi Denys, Claudio Ruggieri	2016	Numerical simulation of ductile crack growth in medium wide plate specimens using 3-D computational cells
D-11	Xian-Kui Zhu	2016	Review of fracture toughness test methods for ductile materials in low-constraint conditions
D-12	M. Daly, T.L. Burnett, E.J. Pickering, O.C.G. Tuck, F. L eonard, R. Kelley, P.J. Withers, A.H. Sherry	2017	A multi-scale correlative investigation of ductile fracture
D-13	Z.L. Zhang, C. Thaulow, J. Oé degard	2000	A complete Gurson model approach for ductile fracture
D-14	J. Xu, Z.L. Zhang, E Ostby, B. Nyhus, and D. B.Sun	2010	Constraint effect on the ductile crack growth resistance of circumferentially cracked pipes
D-15	H. Nakamura, K. Arai, M. Kikuchi	2021	Study on local failure conditions of nuclear containment steels (Limit characteristics in liner steel in triaxial stress state)
D-16	K. Arai, H. Nakamura, M. Kikuchi	2021	Study on local failure conditions of nuclear containment steels (Tensile tests for notched round-bar specimens of welds and plate specimens of base metals)
D-17	T. Nicak, R. Alexey	2021	Post-Test Analysis Of A Large Scale Mock-up Test Performed In The European Project Atlas+
D-18	J. Beswick, P. James, J. Sharples	2020	Implementation Of Ductile Damage Models To Determine Constraint Parameters For Ductile Materials: Phase 1 – Generic Constraint Conditions
D-19	Z. Yinhui, J. Shuai	2020	The Effects Of Material Properties On Crack Tip Constraint and CTOD Fracture Toughness For Commonly Used Pipelines Steel
D-20	T. Yamada, M. Ohata	2019	Proposal Of Ductile Damage Model Based On Unit Cell Analysis For Prediction Of Ductile Crack Growth Resistance Of Cracked Component
D-21	G. Thorwald, K. Bagnoli	2019	Adjusted J-R Toughness Curve For Pipes Using J-A2 Crack Constraint Of CT Specimens And 3D Crack Meshes
D-22	Y. Hioe , S. Kalyanam , G. Wilkowski, S. Pothana, J. Martin	2017	Fracture Toughness Variation With Flaw Depth In Various Specimen Geometries And Role Of Constraint In Material Fracture Resistance
D-23	G. Wilkowski, S. Kalyanam, Y. Hioe, F. W. Brust, S. Pothana, M. Uddin, F. Orth	2019	Constraint Efects Of Surface Crack Depth On Toughness – Experimental And Numerical Assessments
D-24	S. Kalyanam, L.T. Hill, G. Wilkowski, Y. Hioe, F. W. Brust	2021	Strain Based Damage Model Predictions Of Ductile Crack Growth In Multiple Fracture Specimen Geometries

Copyright © 2026 The Japan Welding Engineering Society, All Rights Reserved.

Table 3.1.1-3 List of literature survey in CAF subcommittee

(brittle fracture after ductile crack initiation)

No.	Author	Issue	Title
CD-1	K. Hojo, N. Ogawa, T. Hirota, K. Yoshimoto, Y. Nagoshi, S. Kawabata	2016	Application of Coupled Damage and Beremin Model to Ductile – Brittle Transition Temperature Region Considering Constraint Effect
CD-2	M. Moattari, I. Sattari-Far, I. Persechino, N. Bonora	2016	Prediction Of Frature Toughness In Ductile-To-Brittle Transition Region Using Combined Cdm And Beremin Models
CD-3	A. Pineau	2007	Development Of The Local Approach To Fracture Over The Past 25 Years : Theory And Applications
CD-4	M. K. Samal, M. Seidenfuss, E. Roos, B. K. Dutta, H. S. Kushwaha	2008	Experimental and Numerical Investigation of Ductile-to-brittle Transition In A Pressure Vessel Steel
CD-5	B. Tanguy, A. Parrot, F. Cl ´ Emendot, G. Chas	2011	Assessment Of Pressure Vessel Steel Irradiation Embrittlement Up To 40 Years Using Local Approach To Fracture Modelling. Application To The French Surveillance Program
CD-6	A. Pineau	2003	Comprehensive Structural Integiry 7.05 Practical Application of Loca Approach Methods
CD-7	A. Pineau, T. Pardoen	2007	Comprehensive Structural Integiry 2.06 Failure of Metals
CD-8	J. C. Sobotka, R. H. Dodds Jr.	2014	Effects of steady ductile crack growth on clevage fracture from three-dimensional, small-scale yielding simulations
CD-9	Avinash Gopalan, M.K. Samal, J.K. Chakravartty	2015	Fracture toughness evaluation of 20MnMoNi55 pressure vessel steel in the ductile to brittle transition regime: Experiment & numerical simulations
CD-10	A. H. Sherry, D. W. Bearsmore, D. P. G. Lidbury. M. A. Sheikh. I. C. Howard	1998	The application of local approach to predict the outcome of the NESC Experiment
CD-11	Luca Esposito, Domenico Gentile, Nicola Bonora	2007	Investigation On The Weibull Parameters Identification For Local Approach Application In The Ductile To Brittle Transition Regime
CD-12	Fumiyoshi Minami, Mitsuru Ohata, Daisuke Watanabe, Satoshi Igi, Takahiro Kubo, Nobuhisa Suzuki	2010	Crack geometry effect on stress – strain fields for crack under biaxial loading
CD-13	Fumiyoshi Minami, Takanori Katou and Hongyang Jing	2001	Application of the Local Approach to Fracture in the Brittle-to-Ductile Transition Region of Mismatched Welds

Copyright © 2026 The Japan Welding Engineering Society, All Rights Reserved.

Table 3.1.2-1 List of literature survey in CAF-II subcommittee (ASME PVP)

Author	Title	Note
O. Ancelet, S. Marie, S. Chapuliot, and A. Parrot	Application of the J-Q Methodology to Consider the Geometrical Effect on Fracture for Large Steam-Generator Tube-Sheet	PVP2023-106269
M. Shimodaira, Y. Yamaguchi, K. Iwata, J. Katsuyama, and Y. Chimi	Biaxial Constraint Effect on Fracture Toughness Evaluation of Reactor Pressure Vessel under Pressurized Thermal Shock Events	PVP2024-123136
J. Louerat, O. Ancelet, S. Marie, and A. Dahl	Consideration of Constraint Effect in Fracture Mechanics Assessment for a Vessel Low Alloy Steel	PVP2024-123672
O. Ancelet, S. Marie, S. Chapuliot, A. Parrot	Fracture Mechanics Assessment of the Steam Generator Tube-Sheet Plate through a Modified Global Approach to Consider the Geometrical Effect on Fracture	PVP2024-123456
K. Hojo, T. Hirota, Y. Nagoshi, T. Fukahori, K. Shimizu, M. Shimodaira, T. Ogawa, K. Yashirodai, M. Ohata and F. Minami	Plastic Constraint Correction Factor χ for WES Standard on Brittle Fracture in Ductile-Brittle Transition Temperature Region	PVP2024-123140

Table 3.1.2-2 List of literature survey in CAF-II subcommittee (SMiRT27)

Author	Title	Note
A. Parrot, S. Chapuliot, O. Ancelet, S. Marie	Fracture Mechanics Assessment of the Steam-Generator Tube-Sheet plate through a J-Q approach for consideration of the constraint loss	
Panel Discussion	Enabling Safe and Efficient Long-Term Nuclear Plant Operation	

Copyright © 2026 The Japan Welding Engineering Society, All Rights Reserved.

3.2 Proposal of fracture evaluation methods

As a result of the literature survey conducted in Section 3.1, the Beremin model for brittle fracture and the GTN model for ductile fracture have been relatively extensively studied as fracture evaluation methods capable of accounting for the plastic constraint effect. Since these are currently regarded as the most effective evaluation methods for brittle fracture and brittle fracture following ductile crack propagation, the following fracture evaluation models will be employed in the studies from Chapter 4 onward.

(1) Beremin model

As a model for brittle fracture, the Beremin Model, which enables evaluation of fracture probability, is utilized. Weibull stress analysis based on the Beremin Model is conducted using stress-strain data for Finite Element (FE) analysis. The fracture probability based on Weibull stress and the Weibull stress itself are expressed by the following equations:

$$P_f = 1 - \exp\left(-\left(\frac{\sigma_w}{\sigma_u}\right)^m\right) \tag{3.2-1}$$

$$\sigma_w = \left(\frac{1}{V_0}\int_{V_0}(\sigma_1)^m dV\right)^{\frac{1}{m}} \tag{3.2-2}$$

where P_f is the cumulative fracture probability, σ_1 is the principal stress, V_0 is the reference fracture volume containing a single brittle microcrack, σ_w is the Weibull stress, and σ_u and m are the scale and shape parameters of the Weibull distribution, respectively.

Since the shape parameter, m, appears in both equations, an initial value of m is assumed. The maximum principal stress σ_1 at fracture is obtained from FE Analysis, and the Weibull stress is calculated for each specimen according to equation (3.2-2). The cumulative fracture probability for each specimen is then computed using equation (3.2-1) and plotted on Weibull probability paper. The value of m is iteratively adjusted, and equations (3.2-2) and (3.2-1) are recalculated until the slope derived by the maximum likelihood estimation method converges with the assumed m.

The workflow of the Weibull stress analysis is shown in Figure 3.2-1. Because the number of specimens is finite and the calculated cumulative fracture probabilities are subjected to statistical

Copyright © 2026 The Japan Welding Engineering Society, All Rights Reserved.

errors, bias correction is applied using equations (3.2-3) and (3.2-4). The shape parameter, m, obtained by the maximum likelihood estimation method is denoted m_t, and corrected by B_n, a function of the number of specimens n.

$$m = B_n m_t \tag{3.2-3}$$

$$B_n = (2.04\, n^{-1.1} + 1)^{-1} \qquad (n \leq 120) \tag{3.2-4}$$

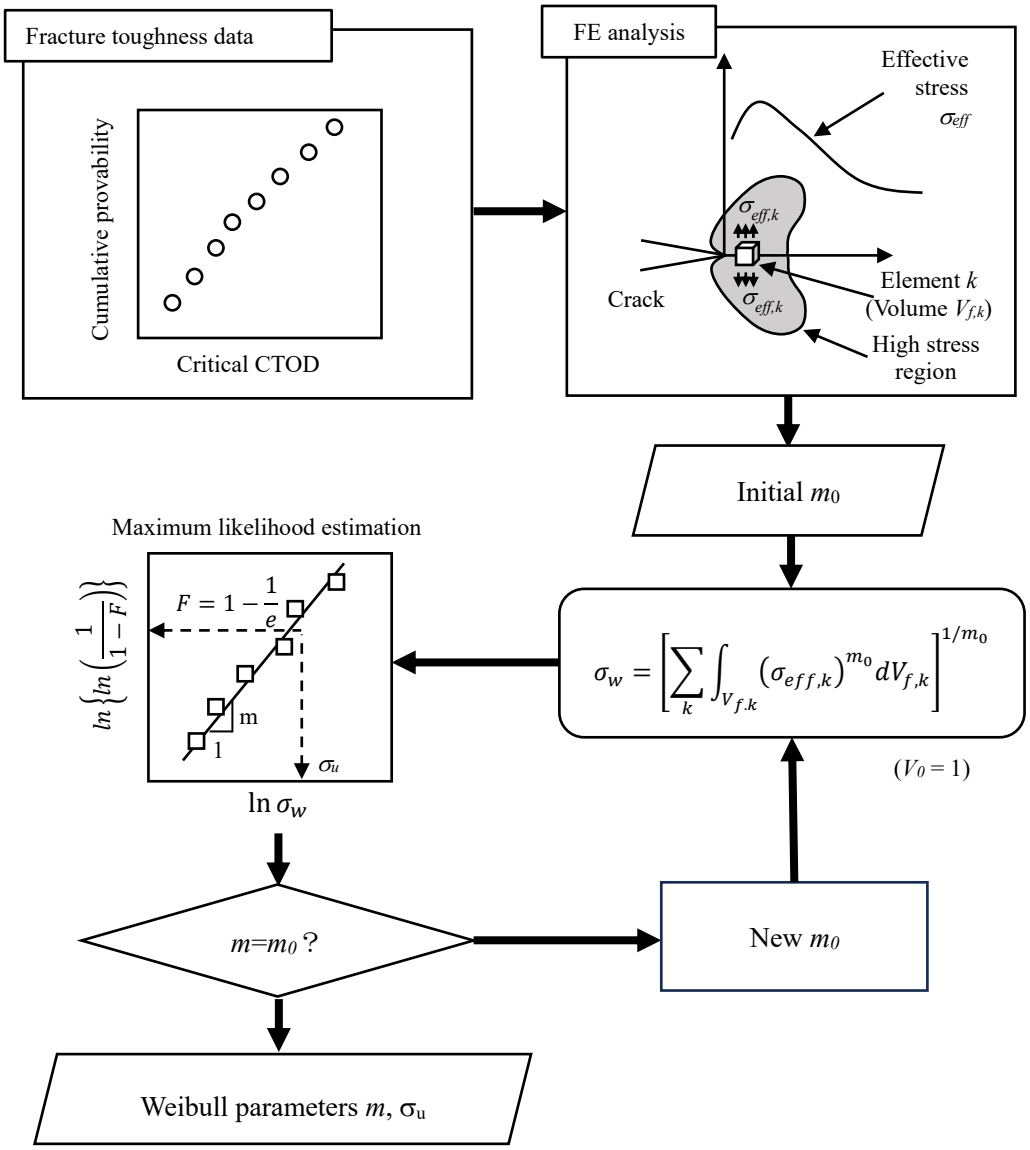


Fig. 3.2-1 Workflow of determination of Weibull stress parameters

In the calculation of the Weibull parameter m, when the available test data are limited and the

Copyright © 2026 The Japan Welding Engineering Society, All Rights Reserved.

accuracy of m may be comprised, Gao et al. proposed a method that utilizes fracture data from two different specimen configurations (Reference C-14). This approach converts the J-integral at fracture of specimens that do not satisfy the small scale yielding (SSY) condition into an equivalent SSY-based J-integral via the Weibull stress. It leverages the fact that the shape parameter of the Weibull distribution for the J-integral of specimens satisfying SSY is 2, thereby ensuring that the J-integral corresponding to a cumulative fracture probability of 63.2% is equivalent for both specimen types , which allows determination of the value of m. When one specimen type satisfies SSY, the procedure is as follows:

1) Obtain fracture test data for two specimen types: specimen A, which satisfies SSY condition, and specimen B, which undergoes large scale yielding (LSY).
2) Assume an initial value of m and establish the relationship between the Weibull stress σ_w and the J-integral for specimens A and B,
3) Convert the J-integral at fracture of specimen B to the equivalent SSY J-integral $J_{(i)SSY}$ via the Weibull stress (see Figure 3.2-2).

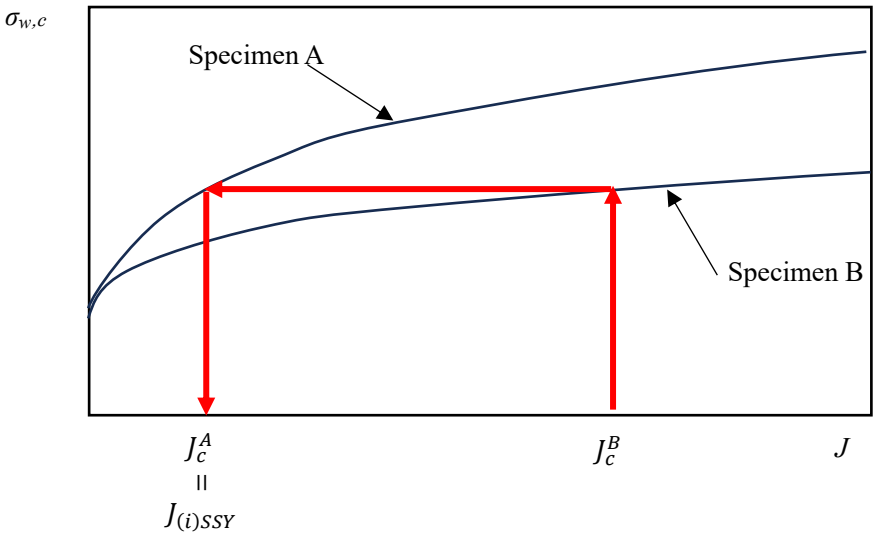


Fig. 3.2-2 Conversion of J-integral between test specimen configurations A and B.

4) Using the known Weibull shape factor of 2 for the SSY condition, determine the J-integrals β_A and β_B corresponding to the cumulative fracture probability of 63.2% for specimens A and B, respectively.

Copyright © 2026 The Japan Welding Engineering Society, All Rights Reserved.

5) Repeat steps 2) to 4) adjusting m iteratively until β_A and β_B converge, thereby determining the optimal m.

The overall workflow for determining the Weibull shape parameter is shown in Figure 3.2-3. Henceforth, this approach will be referred to as the "two-specimens method."

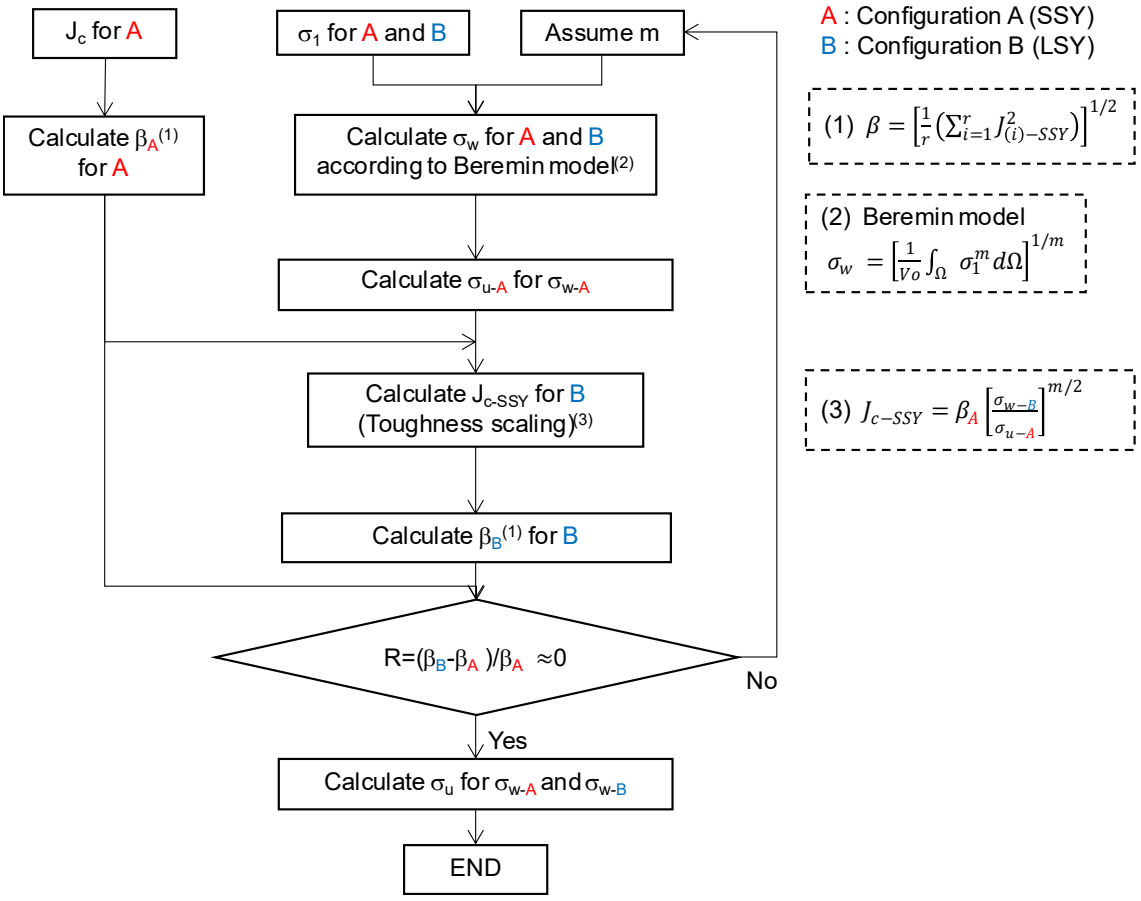


Fig. 3.2-3 Determination procedure of Weibull parameters by two-configuration test method

Copyright © 2026 The Japan Welding Engineering Society, All Rights Reserved.

(2) GTN model

As a damage mechanics model for ductile fracture, the GTN Model is employed, which utilizes the following yield function incorporating the nucleation, growth, and coalescence behavior of voids. In the context, f denotes the void volume fraction, f^* the effective void volume fraction, f_c critical void volume fraction, f_F the fracture void volume fraction, q_1 to q_3 are model constants, σ_0 is the yield stress, and σ_m is the hydrostatic stress. ductile crack propagation is assumed to be initiated when f^*reaches f_F.

$$\Phi = \left(\frac{\sigma_{eq}}{\sigma_0}\right) + 2fq_1 \cosh\left(\frac{3}{2}\frac{q_2\sigma_m}{\sigma_0}\right) - \left(1 + q_3 f^2\right) \qquad (3.2\text{-}5)$$

where,

$$f^* = \begin{matrix} f & \text{for} & f \le f_c \\ f_c + K(f - f_c) & \text{for} & f > f_c \end{matrix} \qquad (3.2\text{-}6)$$

$$K = \frac{1/q_1 - f_c}{f_F - f_c} \qquad (3.2\text{-}7)$$

By iteratively adjusting the parameters of the GTN model, FE analyses are performed for specimens exhibiting ductile crack propagation. The parameters of the GTN model are calibrated to achieve agreement between the computed and experimentally obtained load-displacement curves.

(3) Coupled model

For fracture evaluation of brittle fracture occurring subsequent to ductile crack propagation, FE analysis employing the GTN model is first conducted. Subsequently, the Weibull stress is calculated based on the stress distribution at the crack tip obtained from this FE analysis, following the Beremin model framework, to evaluate fracture behavior.

Copyright © 2026 The Japan Welding Engineering Society, All Rights Reserved.

4. Verification of applicability of fracture evaluation methods employing plastic constraint effects

Chapter 3 provided a review of fracture evaluation methods that incorporate the plastic constraint effect, focusing on both brittle and ductile fracture modes. Based on this review, Chapter 4 presents fracture tests conducted on specimens with varying levels of plastic constraint, aimed at validating the applicability of the candidate fracture evaluation methods.

It should be noted that the material procurement, test execution, and experimental data discussed herein are derived from the research project titled "Establishment of Fracture Assessment Criteria for Reactor Vessels Considering Constraint Effect (Step 1–3)" performed by the Japanese PWR five electric power companies joint research group. The results have been referenced and analyzed by the CAF Subcommittee of the Japan Welding Engineering Society with permission from the participating Japanese PWR electric utilities.

4.1 Fracture tests on specimens with varied plastic constraint levels

4.1.1 Objectives

The fracture evaluation methods under consideration include the Beremin model for brittle fracture, the GTN model for ductile fracture, and a Coupled model addressing brittle fracture accompanied by a limited ductile crack growth. This study aims to experimentally validate these models through targeted fracture tests.

4.1.2 Test matrix

4.1.2.1 Materials

Specimens were taken from two low-alloy steels (designated SQV2A), utilized as reactor pressure vessel steel plates, with dimensions of approximately 1000 mm (rolling direction) × 2500 mm (transverse direction) × 245 mm (thickness). These steels, labeled A-1 and A-2, originate from the same steel plate and exhibit comparable tensile properties and fracture toughness. Their chemical compositions are summarized in Table 4.1.2-1. Hereafter, these steels are collectively referred to as low-alloy steel B.

4.1.2.2 Test matrix

Table 4.1.2-2 outlines the performed tests and their respective objectives including:

Copyright © 2026 The Japan Welding Engineering Society, All Rights Reserved.

- Material characterization (cross-sectional microstructure observation, hardness measurement, chemical composition analysis)
- Tensile tests
- Charpy impact tests
- Fracture tests using C(T) specimens
- Fracture tests using SE(B) specimens
- Fracture tests on flat plate specimens with a surface flaw

The fracture test matrix and specimen sampling locations are detailed in Tables 4.1.2-3 through 4.1.2-7 and Figure 4.1.2-1, respectively. Test temperatures T_1, T_2, and T_3 correspond to conditions targeting brittle fracture, brittle fracture following ductile crack growth, and ductile fracture, respectively.

Tensile tests were performed at six temperatures spanning the lower to upper shelf regions, with two specimens per temperature to ensure repeatability. Charpy impact tests similarly covered six temperature points with 2–3 specimens each.

Fracture tests employed three specimen types: standard C(T) specimens, two variants of SE(B) specimens with different flaw depths to change the plastic constraint level, and surface-flawed plate specimens subjected to tensile and bending loads. To capture variability, approximately eight specimens were tested at brittle fracture and brittle fracture post-ductile crack growth temperatures. At ductile fracture temperatures, only C(T) specimens were tested (two specimens per temperature), given their established testing standards and expected low variability.

The master curve reference temperature (T_0) was determined using both C(T) and SE(B) specimens, facilitating parameter calibration for the fracture evaluation models. Flat plate specimens with a surface flaw were employed to further validate these fracture evaluation models. Although these tests involve larger-scale specimens and fewer repetitions, the number of tests at brittle fracture and brittle fracture post-ductile crack growth temperatures was increased to 4–6 specimens each. At room temperature, fracture under bending load was not anticipated; therefore, only a single tensile load specimen was tested.

Copyright © 2026 The Japan Welding Engineering Society, All Rights Reserved.

4.1.2.3 Requirements on specimen's geometry and size

Surface-flawed plate specimens were designed to represent low plastic constraint levels, adhering to the following criteria:

- Simulate plastic constraint levels equivalent to assumed flaws in RPV integrity evaluations.
- Induce the targeted fracture modes (brittle fracture, ductile fracture, brittle fracture following ductile crack growth) prior to full cross-sectional yielding.
- Employ semi-elliptical flaw geometries to maximize stress intensity factor, K, at the deepest point of the flaw.
- Conform to ASTM E2899-15[4-1] specimen shape requirements as closely as possible.
- Limit flaw aspect ratio, a/c, to a maximum of 0.4 to facilitate fatigue pre-crack introduction.
- Ensure test machine load capacity does not exceed 1000 tons at plastic collapse, which should satisfy the specimens' size.

Specimen and flaw dimensions were established through the following procedure:

(1) Preliminary dimension setting

Using T-stress and K_I formulations from ASTM E2899-15, plastic constraint levels were evaluated, and load at full cross-section yielding along with K_I were calculated. Dimensions satisfying the above constraints were tentatively defined.

(2) Elastic-plastic FE analysis (damage mechanics analysis)

FE analyses using the Beremin model and damage mechanics model were performed on the preliminary specimen configurations to calculate K_J values and predict fracture behavior under brittle, ductile, and mixed modes. These analyses validated the specimen and flaw dimensions as well as the selected test temperatures.

The finalized specimen and flaw dimensions, determined according to this methodology, are summarized in Table 4.1.2-8. The flaw aspect ratio, a/c, was fixed at 0.4, specimen width and length conform to ASTM E2899-15, and flaw depth, a, was varied, assuming a nominal plate thickness of 45 mm (later adjusted to 50.8 mm). Figure 4.1.2-2 presents elastic K_I and normalized T-stress values at loads corresponding to plastic collapse. Yield stress values used for plastic collapse evaluation correspond to temperatures near T_0.

Results indicate that smaller flaw depths, particularly under tensile loading, reduce K_I at plastic

Copyright © 2026 The Japan Welding Engineering Society, All Rights Reserved.

collapse, but also lower T-stress, which facilitates fatigue pre-crack introduction. Consequently, a flaw depth of 5 mm was selected.

To maintain dimensional correlation between fracture toughness specimens and surface-flawed plate specimens, the following criteria were adopted:

- Width W and thickness B of C(T) and SE(B) specimens are matched as closely as possible.
- Width W_{SE} of SE(B) specimens and thickness B_{FP} of surface-flawed plate specimens are made as the same as possible.
- Thickness B_{SE} of SE(B) specimens and surface flaw length $2c$ of surface-flawed plate specimens are approximately equal.

The resulting specimen dimensions are detailed in Table 4.1.2-9. C(T) and SE(B) specimens are of 1T size, while surface-flawed plate specimens have a thickness of 50.8 mm, matching the SE(B) specimen width. Plate specimen length was set to 500 mm to optimize specimen yield from the steel material. For tensile testing, approximately 2-meter-long tabs were welded to ensure secure gripping, with an 80 mm thickened shoulder region at the weld to prevent fracture initiation. The test section length was fixed at 300 mm.

Copyright © 2026 The Japan Welding Engineering Society, All Rights Reserved.

Table 4.1.2-1 Chemical composition of test material (ladle analysis)

Material	Chemical composition（mass%）							
	C	Si	Mn	P	S	Ni	Cr	Mo
Low alloy steel B	0.18	0.25	1.43	0.002	<0.001	0.66	0.15	0.52
JIS G3120:2003 SQV2A	≦0.25	0.15-0.40	1.15-1.50	≦0.030	≦0.030	0.40-0.70	≦0.30	0.45-0.60

Table 4.1.2-2 Test items and objective

Test Item	Objective
Material confirmation tests (cross-sectional microstructure observation, hardness test, chemical composition analysis)	・ Confirm the homogeneity of the material.
Tensile test	・ Obtain stress-strain curves in the temperature range where fracture tests are performed, for use in fracture model analysis. ・ Estimate true stress-true strain in the high strain region.
Charpy impact test	・ Acquire Charpy transition curves to understand the lower shelf temperature region, ductile-to-brittle transition temperature region, and upper shelf temperature region, as a reference for selecting fracture test temperatures.
Fracture toughness test using C(T) specimen	・ Determine the reference temperature To of the Master curve. ・ Obtain test data for setting fracture evaluation parameters.
Fracture toughness test using SE(B) specimen	・ Determine the reference temperature To of the Master curve. ・ Obtain test data for setting fracture evaluation parameters. ・ Confirm the influence of plastic constraint on fracture characteristics using two types of SE(B) specimens with deep flaws (a/W =0.5) and shallow flaws (a/W =0.1).
Fracture test using flat plate specimen with surface flaw	・ Conduct fracture tests using flat plate specimens with semi-elliptical surface flaws and low plastic constraint, and verify the fracture evaluation model.

Copyright © 2026 The Japan Welding Engineering Society, All Rights Reserved.

Table 4.1.2-3 Tensile test matrix

Specimen	Orientation	Temperature (°C)	Number
ϕ10 mm tensile specimen with circumferential knife edge	T	RT	2※1
		-20	2※1
		-50	2※1
		-80	2※1
		-100	2※1
		-120	2※1
	L	RT	1
	S	RT	1
JIS Z2241 No.10 tensile specimen	T	RT	1

※1：In two tensile tests, one specimen is tested until fracture, and the other specimen is stopped just before fracture.

Table 4.1.2-4 Charpy impact test matrix

Specimen	Orientation	Temperature (°C)	Number
V-notch standard size Chary impact test specimen	T-S	70	3
		RT	3
		-10	3
		-30	3
		-50	3
		-80	2

Copyright © 2026 The Japan Welding Engineering Society, All Rights Reserved.

Copyright © 2026 The Japan Welding Engineering Society, All Rights Reserved.

Table 4.1.2-5 Fracture toughness test matrix (C(T) specimen)

Specimen	Test temperature*(°C)							Note
	Brittle fracture (T_1)			Brittle fracture after ductile crack growth (T_2)			Ductile fracture (T_3)	
	-110	-80	-50	-20	-15	-10	RT	
1T C(T)	1	7	1	2	2	5	2	Total 20

* Test temperatures were determined based on the results of the Charpy impact tests.

Table 4.1.2-6 Fracture toughness test matrix (SE(B) specimen)

Specimen		Test temperature*(°C)							Note
		Brittle fracture (T_1)	Brittle fracture after ductile crack growth (T_2)					Ductile fracture (T_3)	
		-80	-50	-30	-20	-15	-10	RT	
1T SE(B)	Deep flaw (a/W: approx. 0.5)	7	—	—	7	1	1	—	Total 16
	Shallow flaw (a/W: approx. 0.5)	10	1	1	7	—	—	—	Total 19

* Test temperatures were determined based on the results of fracture toughness tests using 1T C(T) specimens.

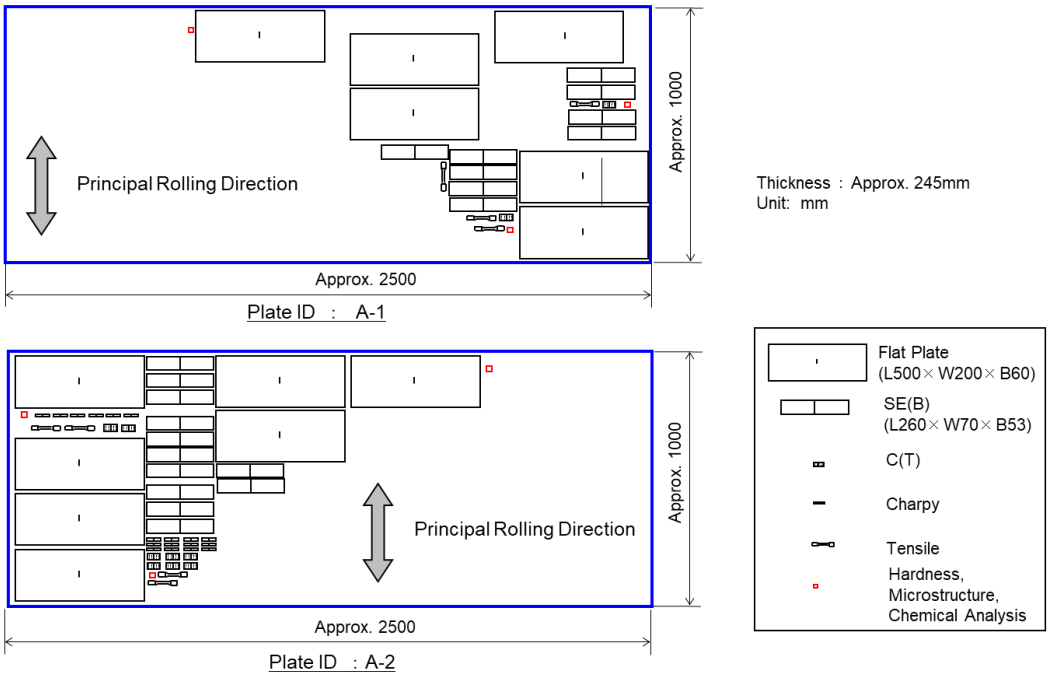
a : flaw depth, W : specimen width

Copyright © 2026 The Japan Welding Engineering Society, All Rights Reserved.

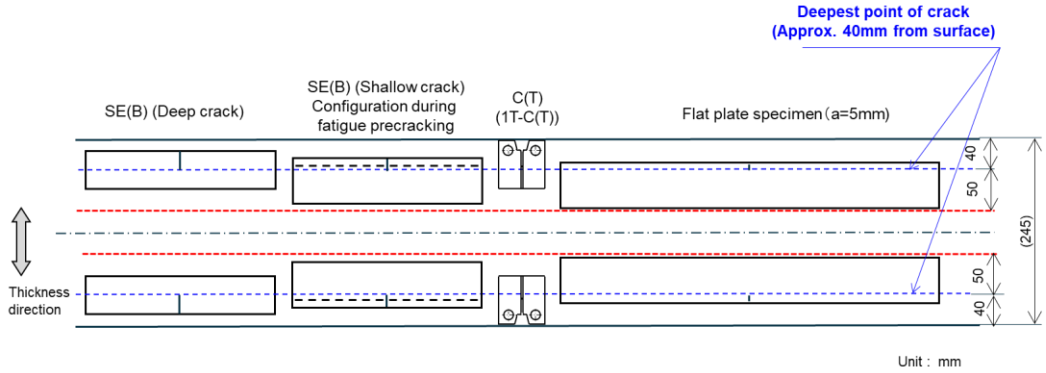
Table 4.1.2-7 Flat plate fracture test matrix

Test item		Test temperature*(°C)				Note
		Brittle fracture (T_1)	Brittle fracture after ductile crack growth (T_2)		Ductile fracture (T_3)	
		-120°C	-100°C	-80°C	RT	
Flat plate specimen with surface flaw (a/B : approx.0.1)	Bending (Preliminary test)	—	1	1	—	Total 2
	Tensile (Preliminary tests)	—	1	1	—	Total 2
	Bending (Main tests)	4	—	6	—	Total 10
	Tensile (Main tests)	6	—	5	1	Total 12

a : flaw depth, B : specimen thickness



(a) Width direction



(b) Thickness direction

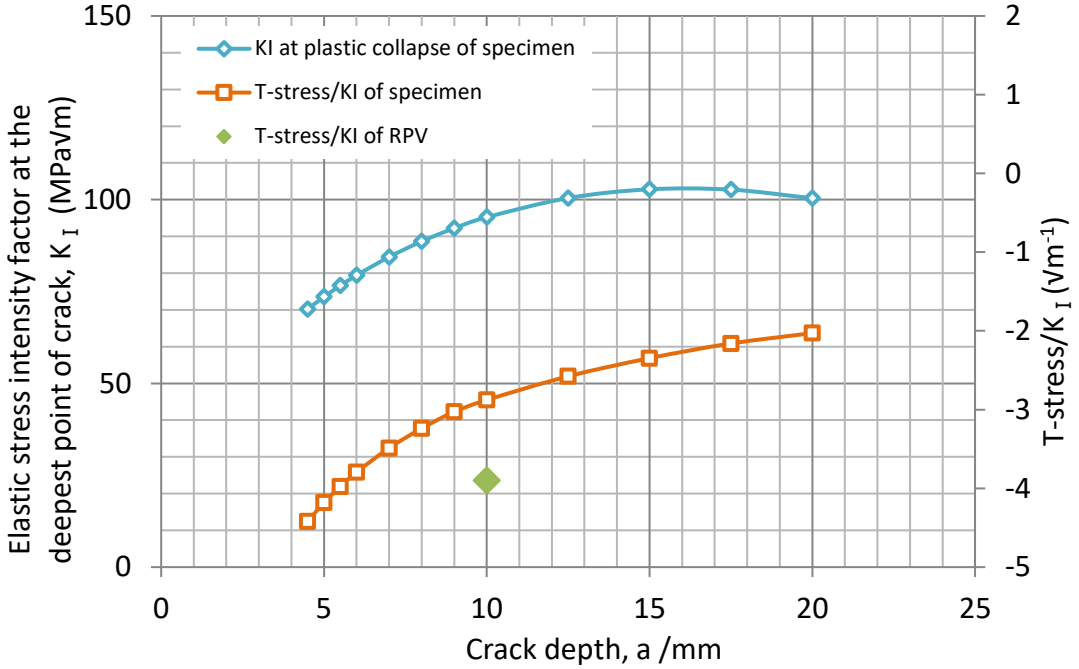
Fig. 4.1.2-1 Sampling location of test specimens

Copyright © 2026 The Japan Welding Engineering Society, All Rights Reserved.

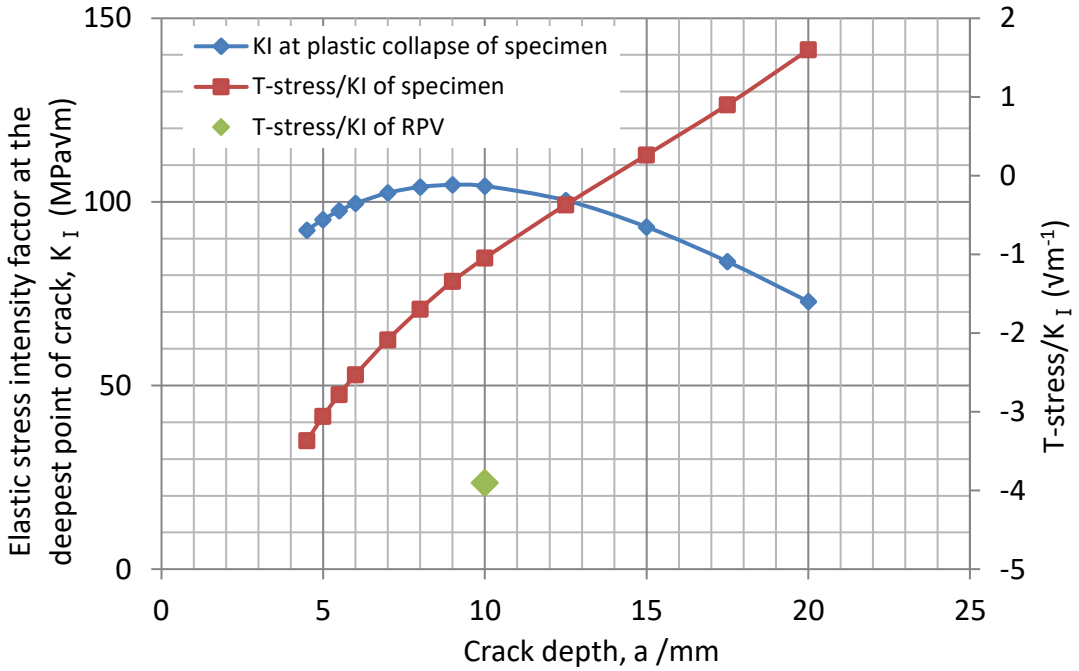
Table 4.1.2-8 Geometry of flat plate specimen with surface flaw

Item		Tensile	Bending
Flaw geometry	Flaw depth, a	5	5
	Flaw length, $2c$	25	25
	a/c	0.4	0.4
	a/B	0.1	0.1
Specimen geometry	Thickness, B	50.8	50.8
	Length, L	300	500
	Width, W	200	200

Copyright © 2026 The Japan Welding Engineering Society, All Rights Reserved.



(a) Tensile



(b) Bending

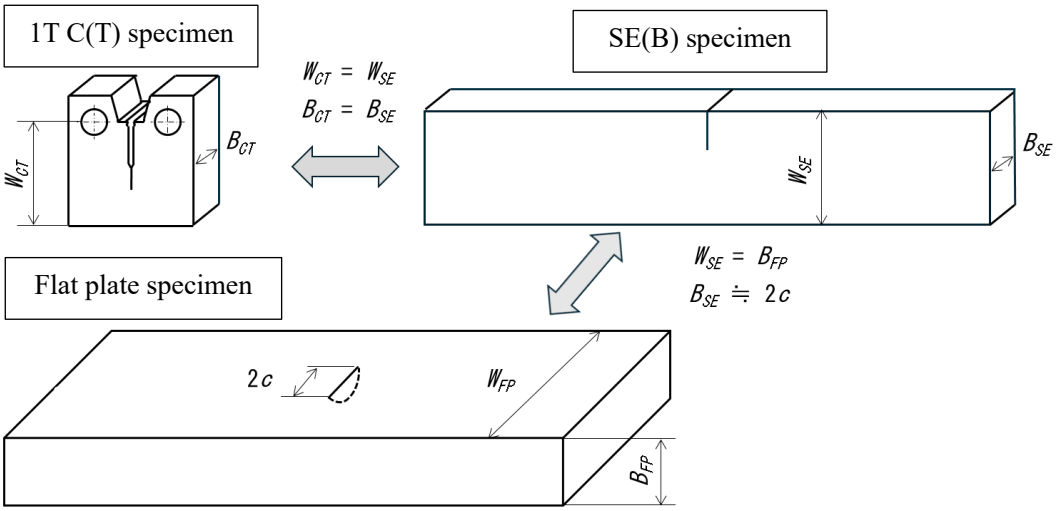
Fig. 4.1.2-2 K_I and T-stress/K_I of flat plate specimen with surface flaw at plastic collapse

(Thickness=45mm, a/c=0.4)

Copyright © 2026 The Japan Welding Engineering Society, All Rights Reserved.

Table 4.1.2-9 Relationship between fracture toughness test specimen and flat plate specimen with surface flaw

Specimen	Specimen dimension
C(T)	1T C(T) specimen (W_{CT}=50.8mm, B_{CT}=25.4mm)
SE(B)	1T SE(B) specimen (W_{SE}=50.8mm, B_{SE}=25.4mm)
Flat plate specimen with surface flaw	Thickness 50.8mm (W_{FP}=200mm, B_{FP}＝50.8mm)
Note	・ The width, W_{SE} of the SE(B) specimen was matched with the thickness, B_{FP} of the flat plate specimen with surface flaw. ・ The thickness B_{SE} of the SE(B) specimen was matched with the thickness B_{CT} of the C(T) specimen. ・ The thickness B_{SE} of the SE(B) specimen was matched with the surface flaw length 2c of the flat plate specimen with surface flaw.



Copyright © 2026 The Japan Welding Engineering Society, All Rights Reserved.

4.1.3 Test results

4.1.3.1 Material characterization

To verify the homogeneity of the test material, chemical composition, microstructure, and hardness distribution were evaluated at representative locations within the steel plate. The chemical composition analysis results are summarized in Table 4.1.3.1-1. Figure 4.1.3.1-1 presents the microstructure and hardness distribution across the cross section at a typical location. Although the influence of the steel plate edge (side surface) was found to be minimal, the test plan ensured that the test sections were positioned at least approximately 40 mm away from the plate edges.

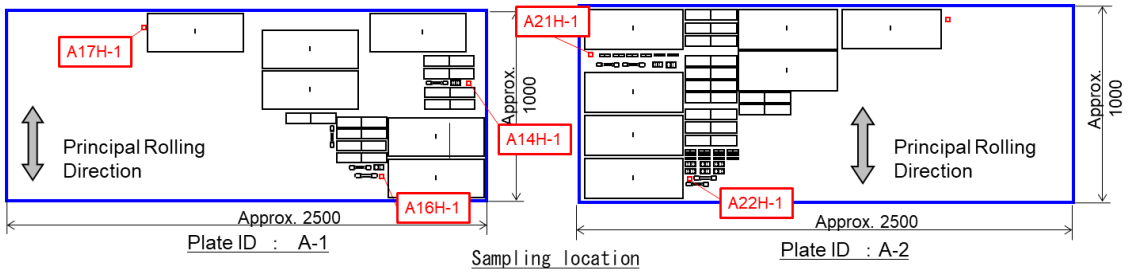
Copyright © 2026 The Japan Welding Engineering Society, All Rights Reserved.

Table 4.1.3.1-1 Chemical composition of test material

供試材		Chemical Composition（Mass%）						
		C*1	Si*2	Mn*2	P*2	S*1	Ni*2	Mo*2
Sample ID	A14H-1	0.18	0.27	1.43	<0.005	<0.001	0.66	0.52
	A16H-1	0.18	0.27	1.43	<0.005	<0.001	0.66	0.51
	A17H-1	0.18	0.27	1.43	<0.005	<0.001	0.67	0.51
	A21H-1	0.18	0.27	1.43	<0.005	<0.001	0.66	0.51
	A22H-1	0.18	0.27	1.43	<0.005	<0.001	0.66	0.51
Ladle analysis		0.18	0.25	1.43	0.002	＜0.001	0.66	0.52
JIS G 3120:2003 SQV2A		≦0.25	0.15～0.40	1.15～1.50	≦0.030	≦0.030	0.40～0.70	0.45～0.60

*1： Combustion-Infrared Absorption Method

*2：ICP-OES (Inductively Coupled Plasma Optical Emission Spectrometry)



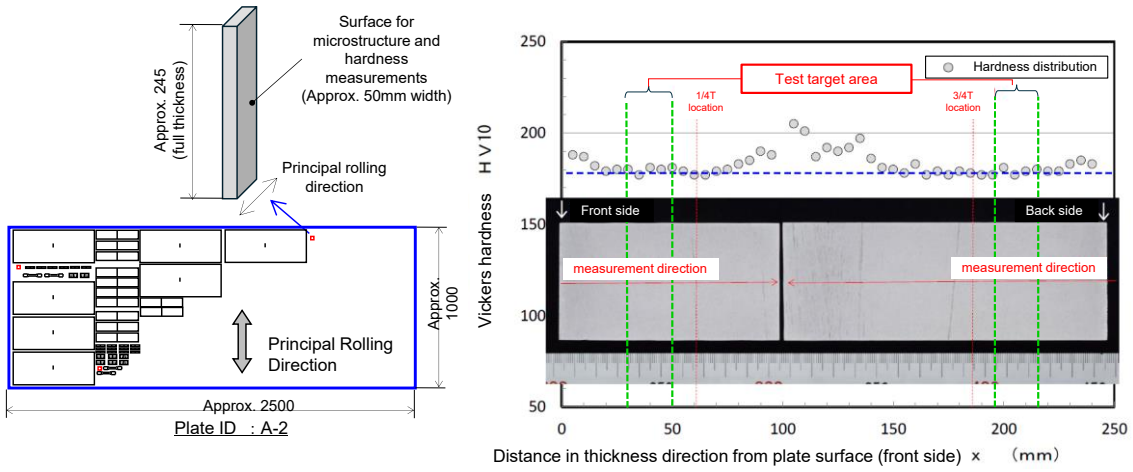


Fig. 4.1.3.1-1 Structure and hardness distribution in the cross section

Copyright © 2026 The Japan Welding Engineering Society, All Rights Reserved.

4.1.3.2 Tensile test

Tensile tests were performed to characterize the tensile properties of low alloy steel B and their temperature dependence, to obtain stress-strain data for subsequent analyses, to assess the presence of anisotropy in the material's tensile behavior, and to evaluate the influence of specimen geometry.

(1) Specimens

The following tensile specimens were taken from low alloy steel B: 10 mm diameter specimens with collars (annular knife-edge ridges), as shown in Figure 4.1.3.2-1, and standard JIS No. 10 specimens. To measure elongation up to fracture, the 10 mm diameter specimens with collars were primarily used. To evaluate the effect of specimen dimensions, standard JIS No. 10 specimens without collars were also employed. The sampling locations and orientations for the tensile specimens are as follows:

- Sampling location: approximately one-quarter thickness position
- Sampling orientation: transverse (T), longitudinal (L), and short transverse (S) directions

(2) Test method

The tests were performed in accordance with JIS Z 2241-2011 [4-2]. A constant strain rate corresponding to a stress increase of 15 MPa/s was maintained from the start to the end of the test, and stress-strain data were recorded continuously until specimen fracture. Strain was measured using an extensometer throughout the entire test duration.

Since the JIS No. 10 specimen lack collars and thus do not allow elongation measurement up to fracture, elongation was recorded to the maximum extent possible.

For the T-direction tests on the 10 mm diameter specimens with collars, interrupted testing was performed in high strain region following the maximum load point (necking onset) to investigate the stress-strain behavior At each interruption, the load P, neck diameter a, and neck curvature radius R were measured.

(3) Test results

The test results are summarized in Table 4.1.3.2-1. The nominal stress-strain curves and the true stress-true strain curves obtained from the tensile tests are shown in Figs. 4.1.3.2-2 and 4.1.3.2-3, respectively. As shown in the table, the 10 mm diameter specimens with collars (A16UT-1) and the JIS No. 10 specimens (A22UT-2X) exhibited nearly identical same tensile properties. At all test

Copyright © 2026 The Japan Welding Engineering Society, All Rights Reserved.

temperatures, yielding was observed following elastic deformation, and the yield point, 0.2% proof stress, and tensile strength decreased monotonically with increasing test temperature. Additionally, the yield strain (strain range over the yield plateau) increased as the test temperature decreased.

Fig. 4.1.3.2-4 shows the temperature dependence of each characteristic obtained from the tensile test. A typical low alloy steel trend was observed: with decreasing temperature, 0.2% proof stress, tensile strength, and elongation increased, while reduction of area decreased.

Fig. 4.1.3.2-5 shows the tensile properties at room temperature in the transverse (T, perpendicular to the main rolling direction), longitudinal (L, main rolling direction), and short transverse (S, thickness direction) orientations. Although elongation in the S direction was slightly lower compared to the other directions, no significant differences attributable to sampling orientation were observed.

Fig. 4.1.3.2-6 shows examples of specimen appearance after tensile tests. For specimens subjected interrupted testing (e.g., Fig. 4.1.3.2-6(b)), the neck radius and curvature were measured and the results are summarized in Table 4.1.3.2-3. The curvature radius was measured within ±1 mm axially from the most necked section.

(4) Evaluation

Using the data obtained from the interrupted tensile tests, the true stress σ_t and true strain ε beyond the onset of local necking were estimated by applying Bridgman's correction formulas, as expressed Equations (4.1.3.2-1) and (4.1.3.2-2).

$$\sigma_t = \frac{\sigma}{\left(1+\frac{2R}{a}\right)\ln\left(1+\frac{a}{2R}\right)} \quad (4.1.3.2\text{-}1)$$

$$\varepsilon = 2\ln\frac{a_0}{a} \quad (4.1.3.2\text{-}2)$$

Here, $\sigma = P/\pi a^2$, where P is the load at interruption, R is the curvature radius of the neck, a is the radius of the necked cross-section, and a_0 is the initial neck radius.

Estimated values of true stress and true strain are presented in Table 4.1.3.2-4. It should be noted that the test performed at -20°C resulted in fracture during the intended interruption; therefore, evaluations were performed at -120, -100, -80, -50, and 23°C. Considering these data, the true stress-true strain relationship in the high strain region used for FE analysis was derived and is shown in Fig. 4.1.3.2-7.

Copyright © 2026 The Japan Welding Engineering Society, All Rights Reserved.

To assess the temperature dependence of the yield stress σ_Y (strength corresponding to 0.2% plastic strain, i.e., 0.2% proof stress), the experimentally obtained values were compared with the temperature-dependent equations from BS7910:2013+A1:2015 (Equation (4.1.3.2-3)) and WES1108-2016 for steels with tensile strengths in 400–590 MPa range (Equation (4.1.3.2-4)).

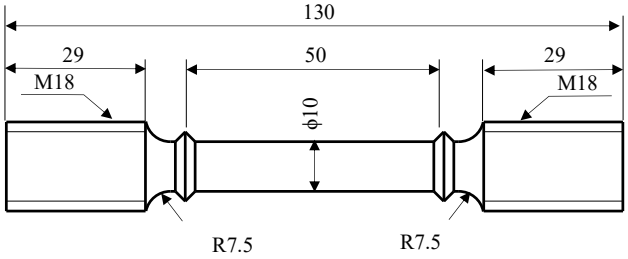
$$\sigma_{YS(T)} = \sigma_{YS(RT)} + \frac{10^5}{491 + 1.8T} - 189 \quad (4.1.3.2\text{-}3)$$

$$\sigma_{YS(T)} = \sigma_{YS(RT)} \exp\left(0.234\left(\frac{\sigma_{YS(RT)}}{E}\right)^{-1.5}\left(\frac{1}{27.6(T+273)} - \frac{1}{27.6 \times 293}\right)\right) \quad (4.1.3.2\text{-}4)$$

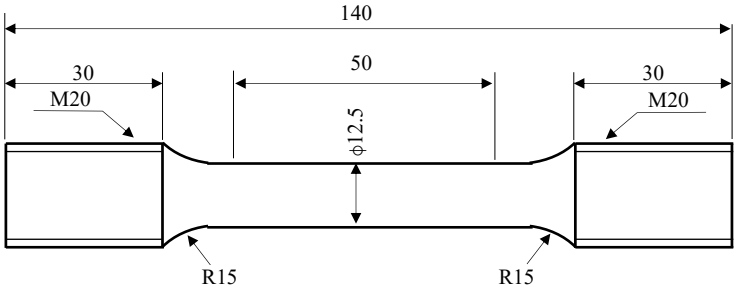
Here, $\sigma_Y(T)$ is the 0.2% proof stress at temperature T (MPa), $\sigma_Y(RT)$ is σ_Y at room temperature (MPa), E is Young's modulus (GPa), and T is temperature (°C).

Fig. 4.1.3.2-4(a) presents the curves represented by the BS7910 equation (4.1.3.2-3) and the WES1108 equation (4.1.3.2-4). From room temperature to -50°C, the WES1108 equation shows good agreements with the test results of low alloy steel B, whereas below -80°C, the BS7910 equation provides a better fit. The applicable range of the WES equation is from room temperature down to -100°C. Considering the primary temperature range for data acquisition in this study, which is below -80°C, the temperature-dependent σ_Y calculated from the BS7910 equation (4.1.3.2-3) will be used to determine $K_{Jc(limit)}$ values necessary for evaluating the validity of fracture toughness data.

Copyright © 2026 The Japan Welding Engineering Society, All Rights Reserved.



(a) Tensile specimen (ϕ10 mm with collar)



(b) Tensile specimen (JIS No. 10)

Unit: mm

Fig. 4.1.3.2-1 Geometry of tensile specimen

Copyright © 2026 The Japan Welding Engineering Society, All Rights Reserved.

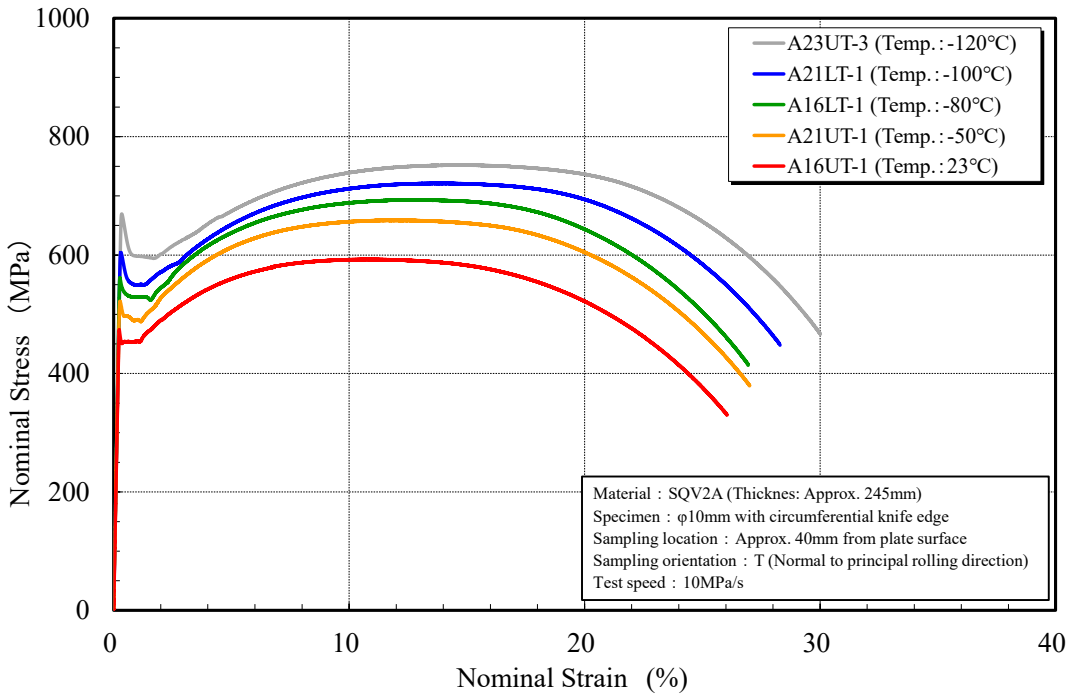
Copyright © 2026 The Japan Welding Engineering Society, All Rights Reserved.

Table 4.1.3.2-1 Tensile test results

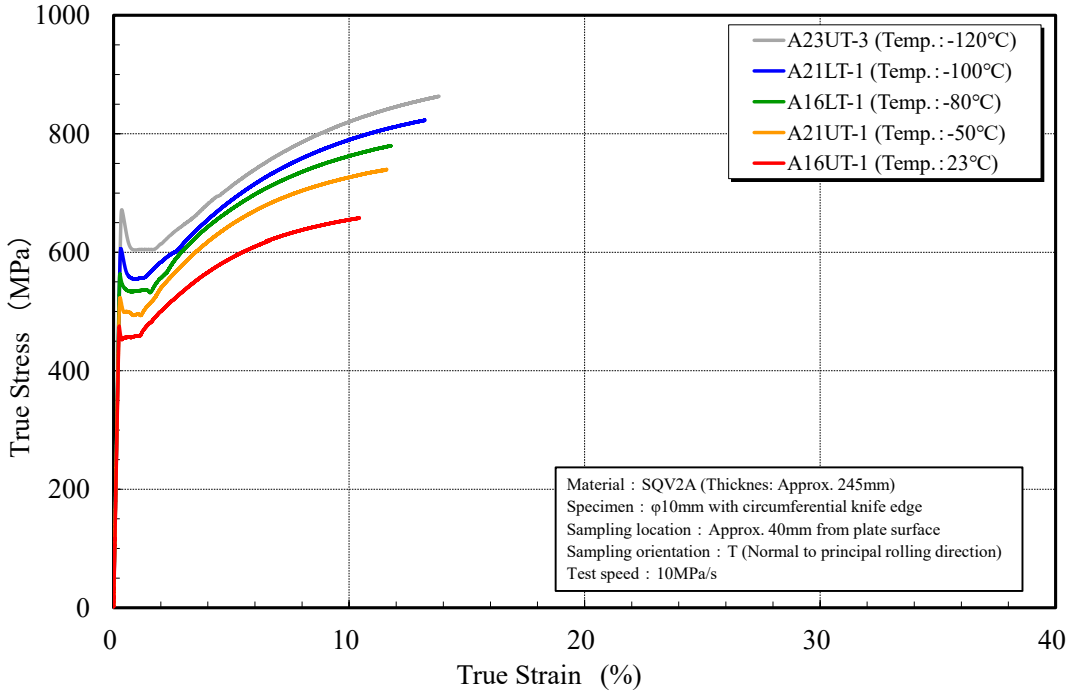
Temperature (°C)	Specimen ID*1	Orientation	Upper yield point (MPa)	Lower yield point (MPa)	0.2% yield strength (MPa)	Tensile strength (MPa)	Elongation after fracture (%)	Uniform elongation (%)	Reduction of area (%)	Fracture location	Note
-120	A22UT-3	T	669	594	640	752	29.8	14.5	67.6	A	Fracture
-120	A22UT-4	T	667	601	638	756	—	14.4	—	—	Interruption
-100	A21LT-1	T	604	549	576	721	28.6	13.7	67.8	A	Fracture
-100	A21LT-2	T	599	546	572	718	—	13.4	—	—	Interruption
-80	A16LT-1	T	562	524	538	693	27.6	12.7	69.9	A	Fracture
-80	A16LT-2	T	562	522	536	693	—	12.5	—	—	Interruption
-50	A21UT-1	T	522	488	497	659	27.8	12.0	72.5	A	Fracture
-50	A21UT-2	T	514	484	488	653	—	11.9	—	—	Interruption
-20	A22LT-1	T	492	466	474	626	27.2	11.5	72.9	A	Fracture
-20	A22LT-2	T	486	475	475	629	25.9	11.3	72.9	A	Fracture
23	A16UT-1*2	T	474	453	453	593	26.6	10.7	75.4	A	Fracture
23	A16UT-2	T	476	451	453	592	—	10.7	—	—	Interruption
23	A16UL-1	L	481	451	453	596	26.2	10.5	75.2	A	Fracture
23	A16LS-1	S	471	454	454	597	24.0	9.9	71.8	A	Fracture
23	A22UT-2X	T	472	451	453	592	29.8	—	75.0	A	Fracture

*1 The ϕ 10 mm specimens with collars were used, except for A22UT-2X, which was a JIS No. 10 specimen.

*2 It was confirmed that the tensile properties of the collard specimens are nearly identical to those of A22UT-2X.



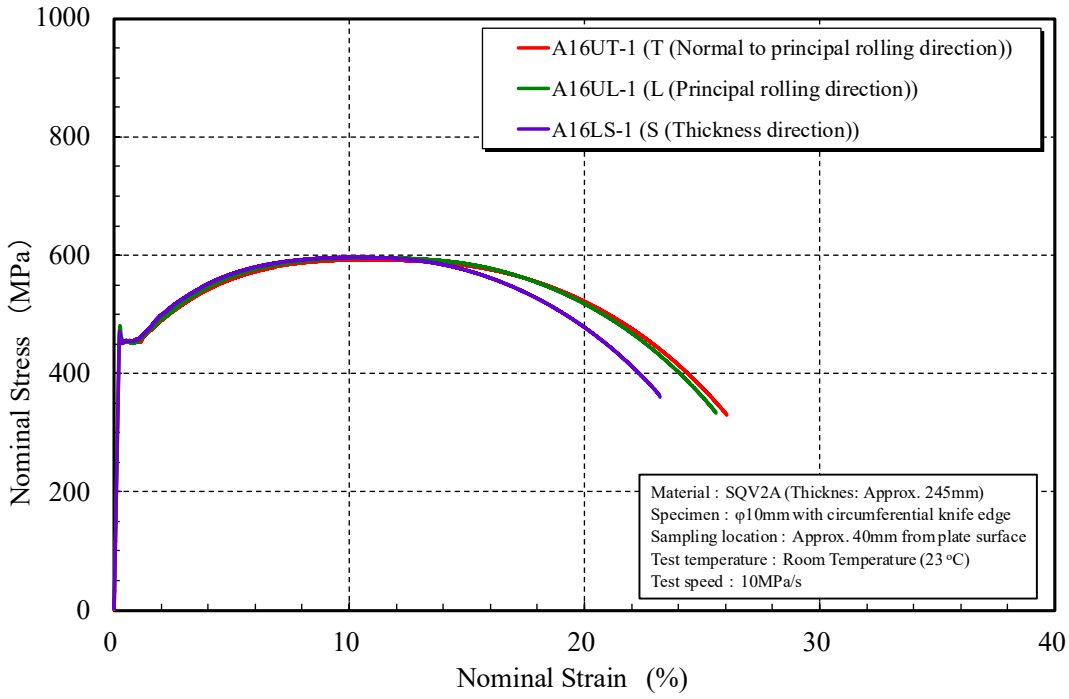
(a) Nominal stress-strain



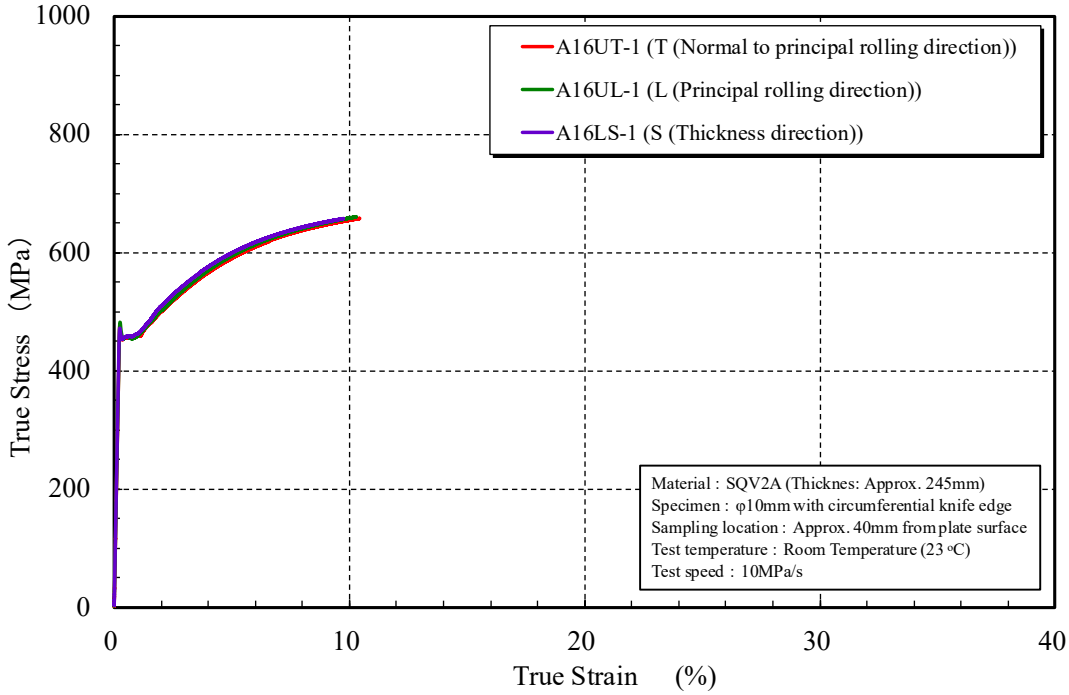
(b) True stress– true strain

Fig. 4.1.3.2-2 Stress – strain curve at test temperature

Copyright © 2026 The Japan Welding Engineering Society, All Rights Reserved.



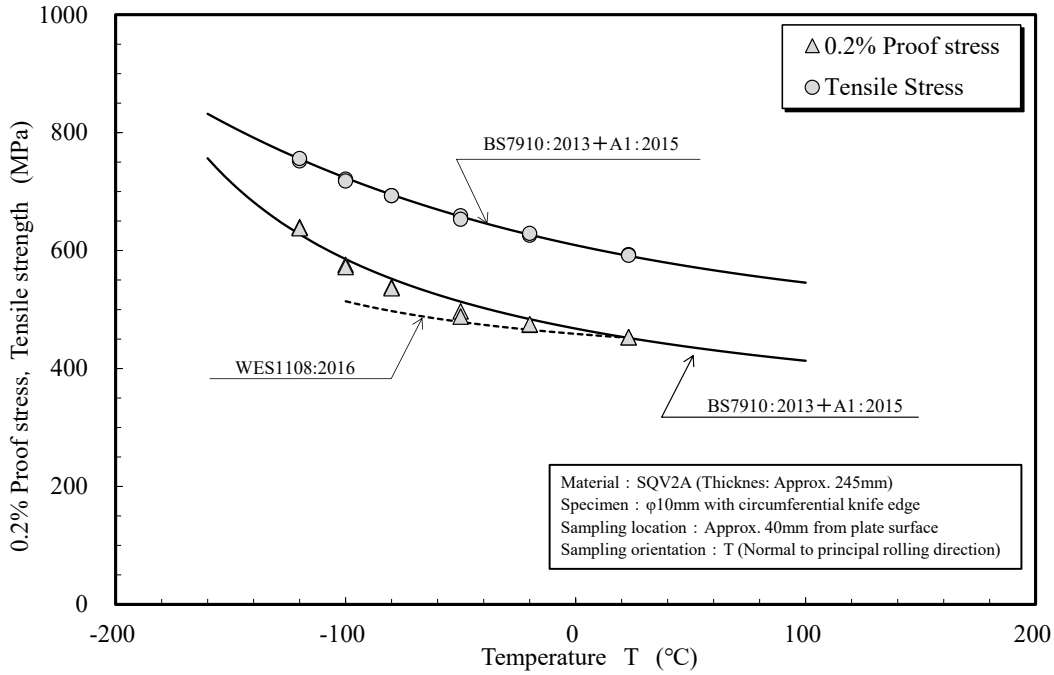
(a) Engineering stress – engineering strain



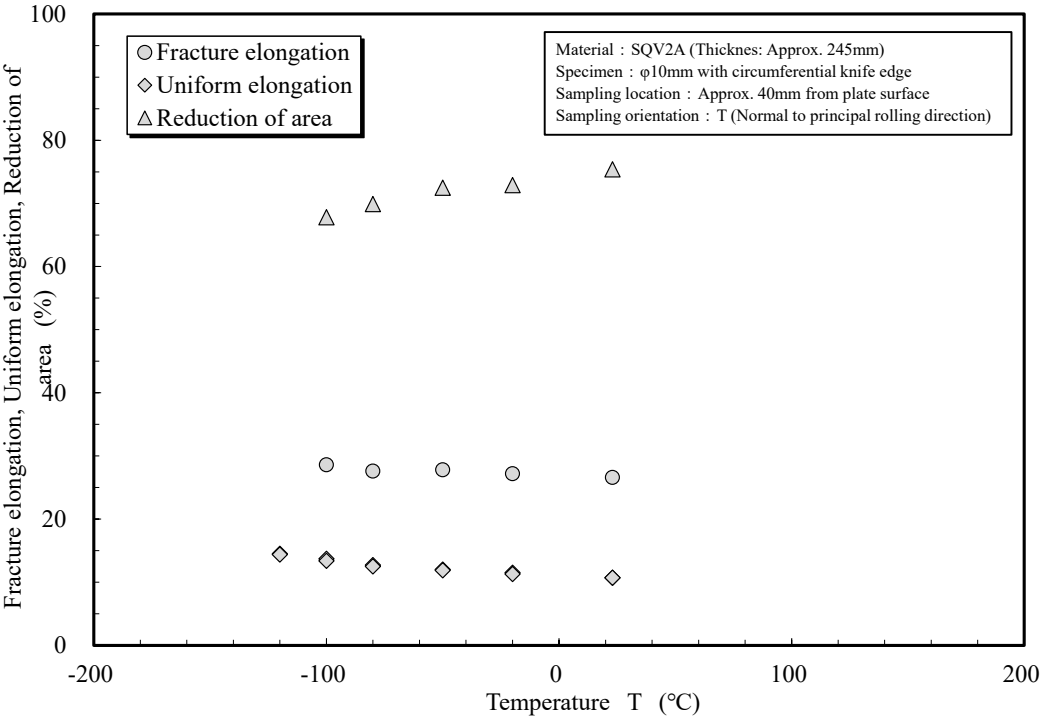
(b) True stress – true strain

Fig. 4.1.3.2-3 Stress – strain curve from different specimen direction

Copyright © 2026 The Japan Welding Engineering Society, All Rights Reserved.



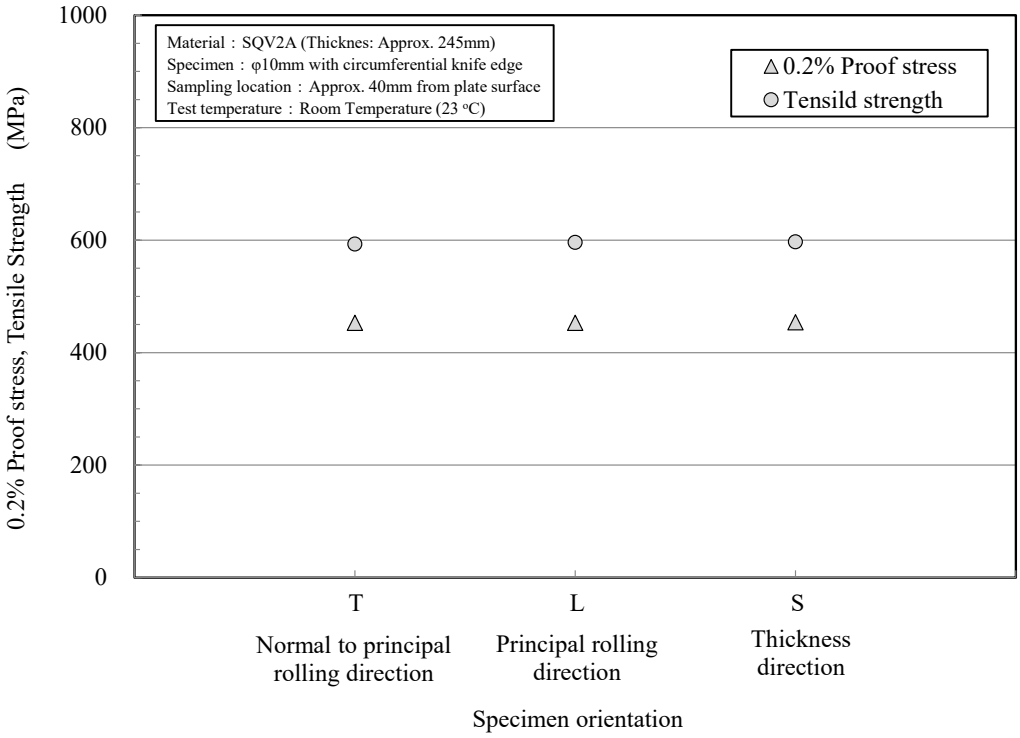
(a) 0.2% proof strength, tensile strength



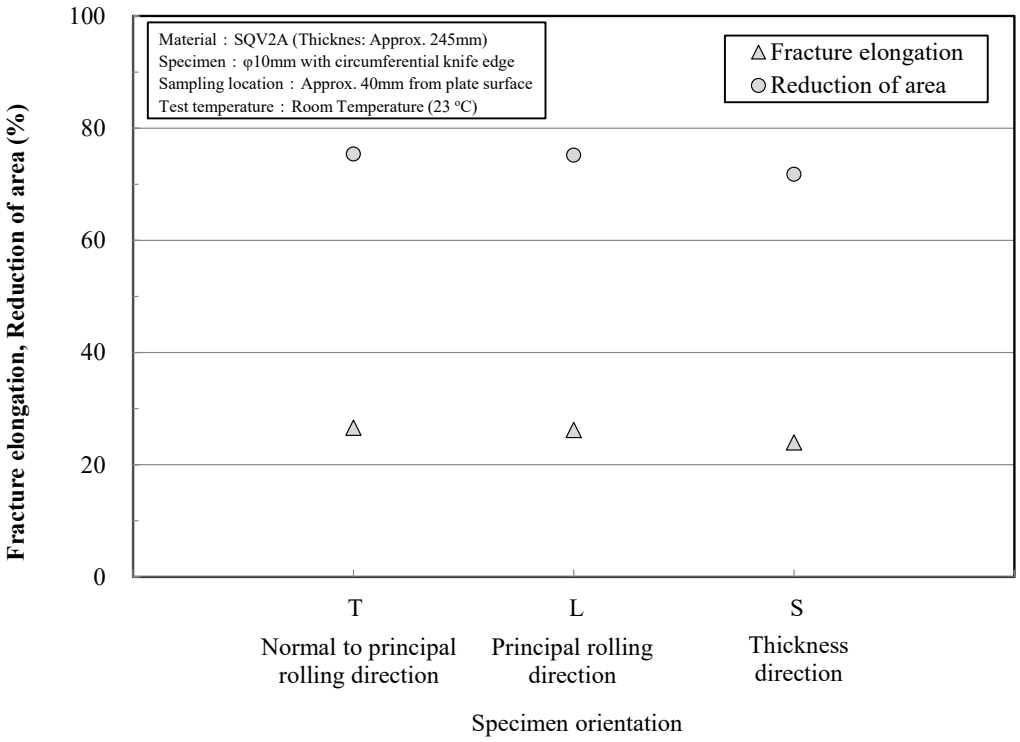
(b) Elongation at fracture, uniform elongation, reduction of area

Fig. 4.1.3.2-4 Temperature dependence of tensile properties

Copyright © 2026 The Japan Welding Engineering Society, All Rights Reserved.



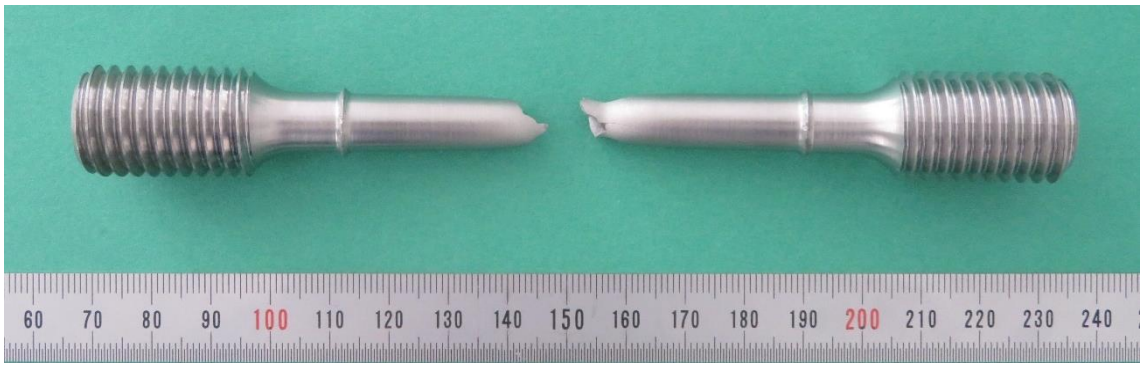
(a) 0.2% proof strength, tensile strength



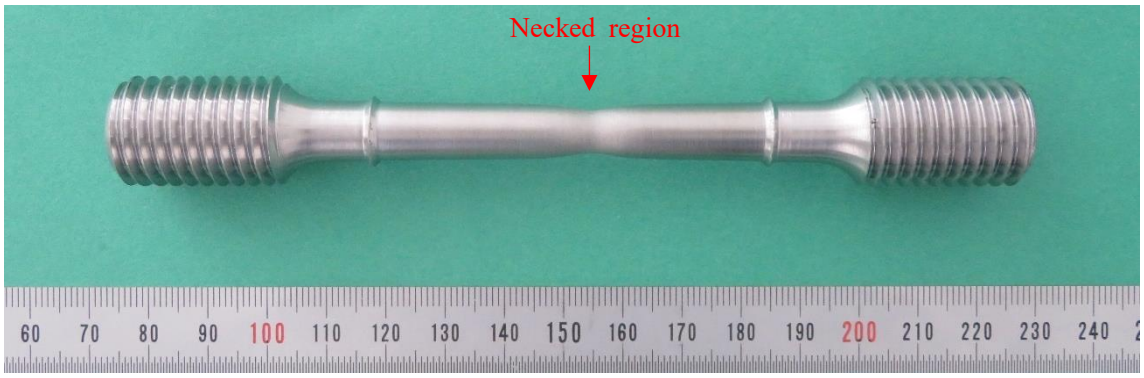
(b) Elongation at fracture, uniform elongation, reduction of area

Fig. 4.1.3.2-5 Comparison of tensile properties for specimen direction

Copyright © 2026 The Japan Welding Engineering Society, All Rights Reserved.



(a) Fractured specimen (test temperature: -120°C, specimen ID: A22UT-3）



(b) Interrupted test specimen (test temperature: -120°C, specimen ID: A22UT-4）

Fig. 4.1.3.2-6 Appearance example after tensile tests

Copyright © 2026 The Japan Welding Engineering Society, All Rights Reserved.

Table 4.1.3.2-3 Curvature measurements of the necked region after interrupted testing

Test temperature (°C)	Specimen ID	Initial radius of neck, a_0 (mm)	Radius of neck, a (mm)	Curvature radius of neck, R (mm)
-120	A22UT-4	5.01	3.45	8.42
-100	A21LT-2	5.00	3.19	5.85
-80	A16LT-2	5.00	3.17	5.42
-50	A21UT-2	5.00	2.91	4.22
23	A16UT-2	5.01	2.77	3.63

Table 4.1.3.2-4 True stress and true strain obtained from interrupted test results

Test temperature (°C)	Specimen ID	Interrupted load, P (N)	True strain, ε_t (-)	True stress, σ_t (MPa)
-120	A22UT-4	46,588	0.75	1,250
-100	A21LT-2	41,428	0.90	1,150
-80	A16LT-2	39,136	0.91	1,097
-50	A21UT-2	33,413	1.09	1,091
23	A16UT-2	28,697	1.18	1,015

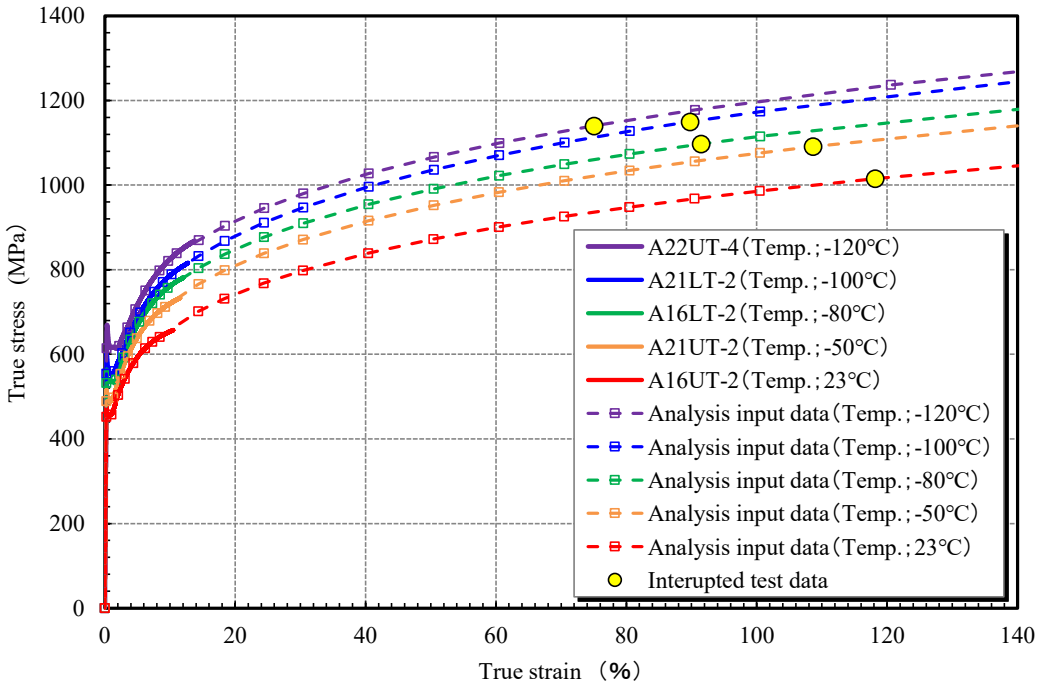


Fig. 4.1.3.2-7 True stress - true strain curves used for FE analysis

Copyright © 2026 The Japan Welding Engineering Society, All Rights Reserved.

4.1.3.3 Charpy impact test

Charpy impact tests were performed to characterize the toughness (impact properties) of low alloy steel B and to obtain reference data for selecting test temperatures for fracture toughness tests.

(1) Specimens

The sampling location and orientation of the Charpy impact specimens are as follows:

- Sampling location : Position where the V-notch tip is approximately 40 mm from the steel plate surface
- Sampling orientation : T-S direction (with the notch face parallel to the rolling direction and the notch direction aligned with the thickness direction)

The shape and dimensions of the Charpy impact specimens are shown in Fig. 4.1.3.3-1. The specimens conformed to the V-notch specimen specification defined JIS Z 2242-2018 [4-3].

(2) Test Method

Test temperatures were determined sequentially based on the results of preceding tests. The initial test was performed at room temperature, followed by the tests at -80°C, -50°C, -30°C, -10°C, and 70°C in that order. The test matrix is shown in Table 4.1.2-4.

All tests were performed in accordance with JIS Z 2242-2018. Measurements of absorbed energy, shear fracture appearance, and lateral expansion were also carried out following the procedures specified in the same standard.

(3) Test Results

Table 4.1.3.3-1 summarizes the absorbed energy, shear fracture appearance, and lateral expansion obtained from the Charpy impact tests at each temperature. The relationships between temperature and these parameters are illustrated in Fig. 4.1.3.3-2. Absorbed energy, shear fracture appearance, and lateral expansion all increased with rising temperature, exhibiting typical brittle-to-ductile transition behavior, and tended to saturate at high temperatures. At 70°C, the shear fracture appearance reached 100% for all three specimens was, confirming that this temperature corresponds to the upper shelf temperature.

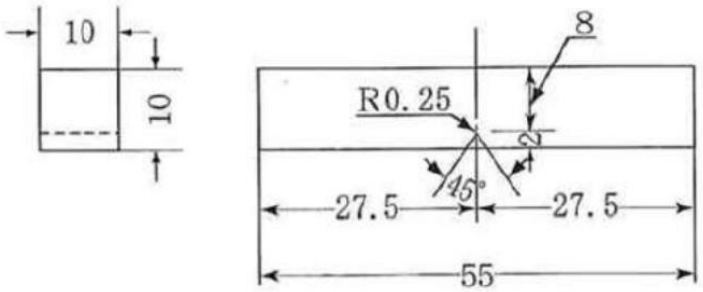
(4) Evaluation

The Charpy impact properties evaluated based on the test data are summarized in Table 4.1.3.3-2. Using the obtained T_{r30} = -55°C as reference, the test temperatures for fracture toughness tests with

Copyright © 2026 The Japan Welding Engineering Society, All Rights Reserved.

C(T) specimens were established. Specifically, according to JEAC4216-2015 [4-4] Appendix B, the reference temperature was set at -80°C from $T = T_{r30} - 24$°C (i.e, -79°C). To verify temperature dependence around this reference, fracture toughness tests were performed at three temperatures: -110°C, -80°C, and -50°C with one specimen each temperature. Subsequent fracture toughness test temperatures were to be determined based on the results of these initial tests.

Copyright © 2026 The Japan Welding Engineering Society, All Rights Reserved.



Unit：mm

Fig. 4.1.3.3-1 Geometry of Charpy impact specimen (V notch standard size)

Table 4.1.3.3-1 Charpy impact test results

Specimen ID	Test temperature (°C)	Absorbed Energy (J)	Lateral expansion (mm)	Shear Fracture Appearance (%)
A22UCV-05	70	260	2.38	100
A22UCV-06	70	238	2.37	100
A21UCV-03	70	237	2.51	100
A22UCV-01	22	227	2.29	90
A22UCV-02	22	196	2.36	80
A21UCV-01	22	216	2.42	90
A22UCV-11	-10	178	2.17	60
A22UCV-12	-10	169	2.43	60
A21UCV-06	-10	145	1.97	50
A21UCV-05	-30	136	1.88	35
A22UCV-10	-30	119	1.70	30
A22UCV-09	-30	107	1.55	30
A22UCV-03	-50	45	0.69	10
A21UCV-02	-50	22	0.41	10
A22UCV-04	-50	29	0.53	5
A21UCV-04	-80	15	0.29	0
A22UCV-08	-80	6	0.17	0

Copyright © 2026 The Japan Welding Engineering Society, All Rights Reserved.

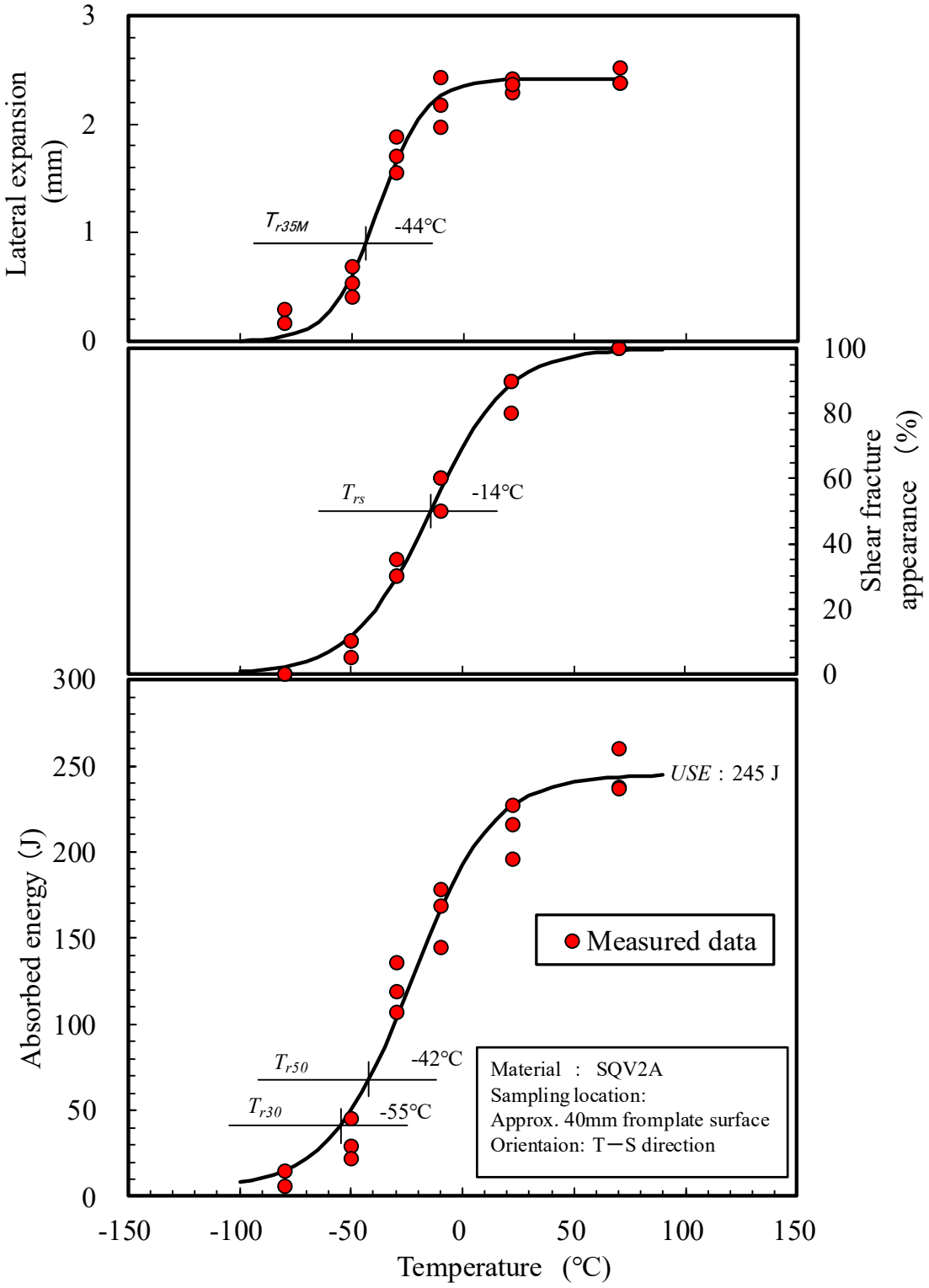


Fig. 4.1.3.3-2 Charpy impact test results

Copyright © 2026 The Japan Welding Engineering Society, All Rights Reserved.

Table 4.1.3.3-2 Charpy impact characteristics

Orientation	Sampling location	T_{r30} (°C)	T_{r50} (°C)	T_{r35M} (°C)	T_{rs} (°C)	*USE* (J)
T-S	Approx. 40mm from surface	-55	-42	-44	-14	245

T_{r30} : Transition temperature indicating an absorbed energy of 41 J

T_{r50} : Transition temperature indicating an absorbed energy of 68 J

T_{r35M} : Transition temperature showing an lateral expansion of 0.90 mm

T_{rs} : Transition temperatureat which the shear fracture appearance is 50%

USE : Average absorbed energy of all specimens measured at the temperature where the ductile fracture ratio is 100%

Copyright © 2026 The Japan Welding Engineering Society, All Rights Reserved.

4.1.3.4 Fracture toughness test (C(T) specimens)

Fracture toughness tests were performed using 1TC(T) specimens over a temperature range encompassing both brittle fracture and ductile fracture (ductile crack growth) to determine the master curve reference temperature T_0 and establish fracture evaluation parameters.

(1) Specimens

C(T) specimens were taken from low alloy steel B such that the fatigue pre-crack tip was located approximately 40 mm from the surface in the thickness direction. The specimen geometry is shown in Fig. 4.1.3.4-1.

To introduce a fatigue pre-crack approximately 2 mm in length, specimens were taken from a position where the notch tip was about 38 mm from the pate surface of the steel (corresponding to a fatigue pre-crack tip position roughly 40 mm from the surface). After machining, fatigue pre-cracks were introduced at room temperature, followed by side groove machining with a depth of 10% of the specimen thickness (10%B) on one side.

(2) Test method

Fracture toughness tests were performed in accordance with the following standards at temperatures near the master curve reference temperature T_0. Test temperatures were determined based on the Charpy impact tests results (Section 4.1.3.3) and fracture toughness test outcomes. The test matrix is summarized in Table 4.1.2-5.

- Standards: JEAC4216-2015 and ASTM E1820-2018 [4-5]
- Test temperatures: Room temperature, -10°C, -15°C, -20°C, -50°C, -80°C, and -110°C
- Loading rate: dK/dt = 0.1 to 2 (MPa$\sqrt{}$m/s) in the initial elastic region
- Material properties

  Elastic modulus: E = 202100 – 62.6 T (MPa)

  T: Test temperature (°C)

  (per JEAC4216-2015, MCT-1300, material group A)

  Poisson's ratio: ν = 0.3

  0.2% proof stress at room temperature: approx.. 460 (MPa)

  Tensile strength at room temperature: approx. 600 (MPa)

During fracture toughness testing, load (via load cell output) and load-line displacement (measured by a clip gauge) were continuously recorded. The clip gauges were calibrated over the

Copyright © 2026 The Japan Welding Engineering Society, All Rights Reserved.

applicable temperature range covering all test temperatures.

Based on the fracture toughness data obtained, the master curve reference temperature T_0 was evaluated following JEAC4216-2015.

(3) Test Results

A summary of the fracture toughness test results obtained from C(T) tests is provided in Table 4.1.3.4-1, Representative load P – load-line displacement δ_L curves are shown in Fig. 4.1.3.4-2. The curves from the specimens tested at the same test temperature exhibited good agreement.

Applying the master curve method to data within the transition temperature range (Fig. 4.1.3.4-3) yielded a T_0 of approximately -88°C. All data obtained within the applicable master curve temperature range ($T_0 \pm 50$°C) fell within the cumulative failure probability bounds of 5% to 95%.

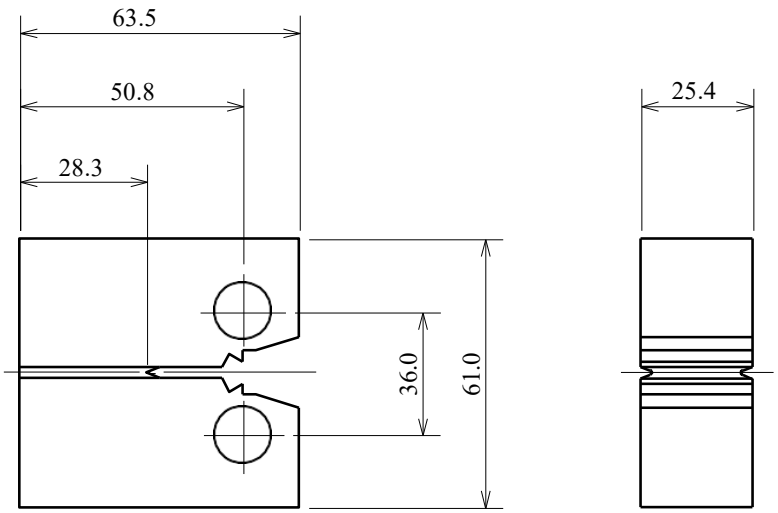
Furthermore, Additionally, a Weibull plot of seven data points obtained at -80°C (Fig. 4.1.3.4-4) revealed a slope parameter $b = 8.7$, indicating small data scatter.

At room temperature, fracture toughness tests using the unloading compliance method produced J-Δa curves and relationships between Δa and δ_L with minimal variation among specimens, as shown in Figs. 4.1.3.4-5 and 4.1.3.4-6, respectively,

Fig. 4.1.3.4-7 presents the thickness-direction distribution of ductile crack growth -80°C.

Fracture surface appearances are shown in Fig. 4.1.3.4-8. At the candidate temperature T_1 of -110°C and -80°C, no ductile crack growth was observed. In contrast, at the candidate temperature T_2 of -10°C, ductile crack growth exhibited significant variability with some specimens showing growth exceeding 9 mm.

Copyright © 2026 The Japan Welding Engineering Society, All Rights Reserved.



Unit：mm

Fig. 4.1.3.4-1 Geometry of C(T) specimen

Copyright © 2026 The Japan Welding Engineering Society, All Rights Reserved.

Copyright © 2026 The Japan Welding Engineering Society, All Rights Reserved.

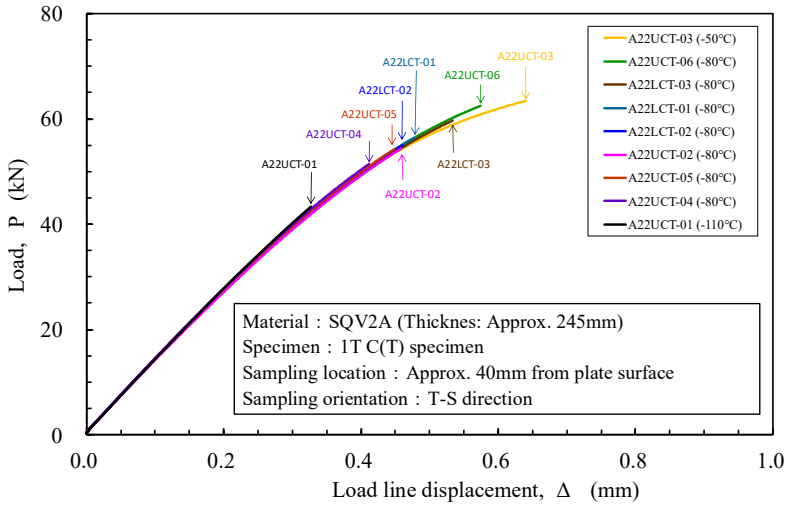
Table 4.1.3.4-1 Fracture toughness test results of C(T) specimen

Material	Specimen ID	Temp. T (℃)	Specimen dimension(mm) Width W	Thickness B	Net thickness B_N	Crack size a_0	Ductile crack growth Δa_p (mm) Average	Max	Fracture load P (kN)	Elastic J J_e (kJ/m^2)	Plastic J J_p (kJ/m^2)	Fracture toughness J_c (kJ/m^2)	K_{Jc} (MPa$\sqrt{}$m)	$K_{Jc(limit)}$ (MPa$\sqrt{}$m)	Validity for $K_{Jc(limit)}$	Validity for ductile crack growth
Low Alloy Steel B	A22UCT-01	-110	50.80	25.42	20.51	25.35	0.00	0.00	43.4	28.7	2.28	31.0	84.3	343	valid	valid
	A22UCT-06	-80	50.80	25.44	20.52	25.38	0.03	0.05	62.6	60.4	26.6	86.9	141	326	valid	valid
	A22LCT-03	-80	50.80	25.44	20.53	25.53	0.02	0.04	59.7	56.0	19.7	75.7	131	325	valid	valid
	A22LCT-01	-80	50.79	25.45	20.53	25.26	0.01	0.04	56.5	48.5	13.3	61.8	119	327	valid	valid
	A22LCT-02	-80	50.79	25.44	20.54	25.38	0.01	0.02	55.1	46.8	11.5	58.3	115	326	valid	valid
	A22UCT-02	-80	50.79	25.44	20.50	25.40	0.00	0.02	54.4	45.9	10.8	56.6	114	326	valid	valid
	A22UCT-05	-80	50.78	25.44	20.54	25.33	0.02	0.04	54.3	45.2	10.6	55.8	113	326	valid	valid
	A22UCT-04	-80	50.78	25.45	20.54	25.20	0.01	0.04	51.5	40.0	7.35	47.4	104	327	valid	valid
	A22UCT-03	-50	50.78	25.42	20.50	25.30	0.04	0.07	63.4	62.2	42.1	104	153	313	valid	valid
	A22LCT-04	-20	50.80	25.45	20.61	25.34	0.40	0.58	73.1	83.0	496	579	360	303	invalid	valid
	A22LCT-05	-20	50.81	25.44	20.63	25.45	0.27	0.57	69.8	76.8	301	377	290	302	valid	valid
	A21UCT-02	-15	50.80	25.45	20.63	25.46	0.36	0.64	71.6	81.0	471	552	351	300	invalid	valid
	A21UCT-01	-15	50.80	25.45	20.63	25.43	0.21	0.36	69.3	75.5	287	362	284	300	valid	valid
	A16UCT-01	-10	50.80	25.45	20.60	25.52	7.66	9.11	49.9	39.7	3864	3904	933	298	invalid	invalid
	A16LCT-01	-10	50.79	25.45	20.62	25.50	4.39	5.98	64.9	67.1	2833	2900	804	298	invalid	invalid
	A21LCT-02	-10	50.79	25.44	20.64	25.53	1.64	3.37	74.2	87.9	1666	1754	625	298	invalid	invalid
	A22LCT-06	-10	50.78	25.45	20.64	25.46	7.72	9.63	76.1	91.7	1433	1524	583	299	invalid	invalid
	A21LCT-01	-10	50.80	25.47	20.65	25.38	0.20	0.28	67.8	72.0	266	338	274	299	valid	valid
	A14LCT-01	24	50.81	25.46	20.63	25.55	3.86	4.39	72.3	-	-	1161	506	289	invalid	invalid
	A14UCT-01	24	50.79	25.46	20.62	25.44	3.92	4.90	73.1	-	-	1104	493	290	invalid	invalid

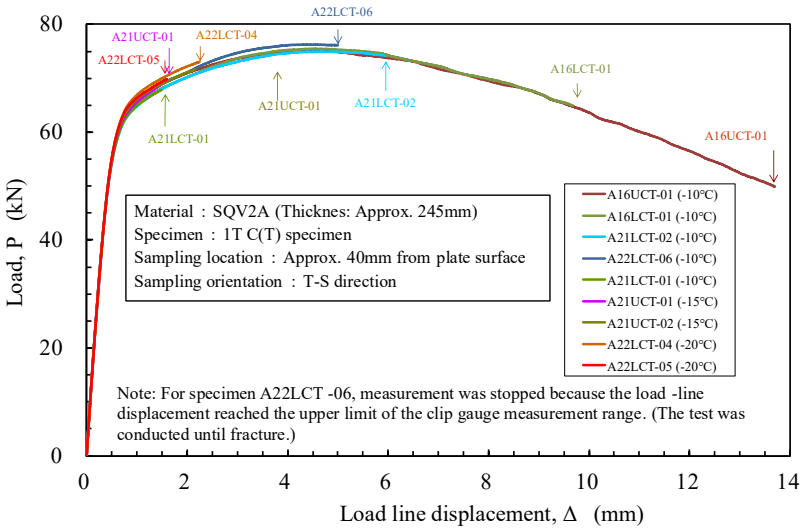
Note 1: Young's modulus is based on the temperature-dependent formula for material group A in JEAC4216-2015 (E(T)=202,100－62.6T (MPa)).

Note 2: Yield stress uses the temperature-dependent formula from BS7910:2013 + A1:2015(σ_Y (T)= $\sigma_{Y(RT)}$ ＋ 10^5 / (491+1.8T)-189 (MPa)), where $\sigma_{Y(RT)}$ is the experimentally measured yield stress at room temperature, 453 MPa.

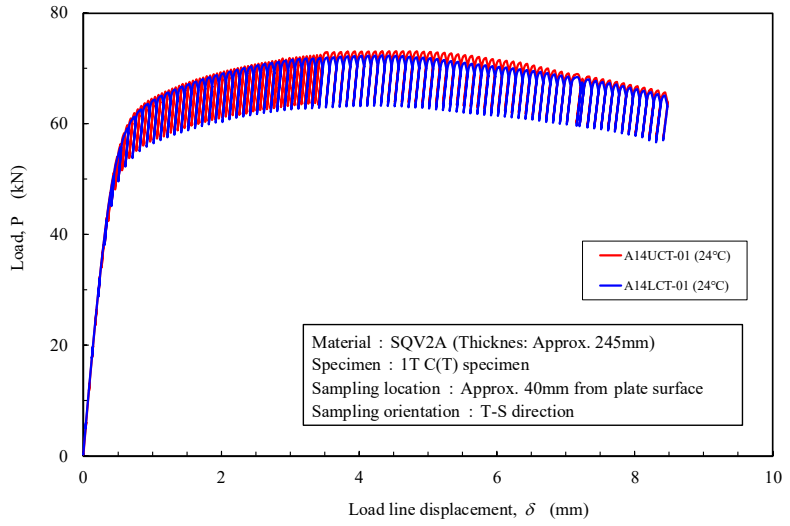
Note 3: At the test temperature of 24°C, since testing was performed using the unloading compliance method, J_e and J_p are indicated as "—". Also, the column for J_c shows the value of J_{Ic}.



(a) T_1 candidate temperature (-110°C～-50°C)



(b) T_2 candidate temperature(-20°C～-10°C)



(c) T_3 candidate temperature (room temperature)

Fig. 4.1.3.4-2 Load P -load line displacement δ_L curve (C(T))

Copyright © 2026 The Japan Welding Engineering Society, All Rights Reserved.

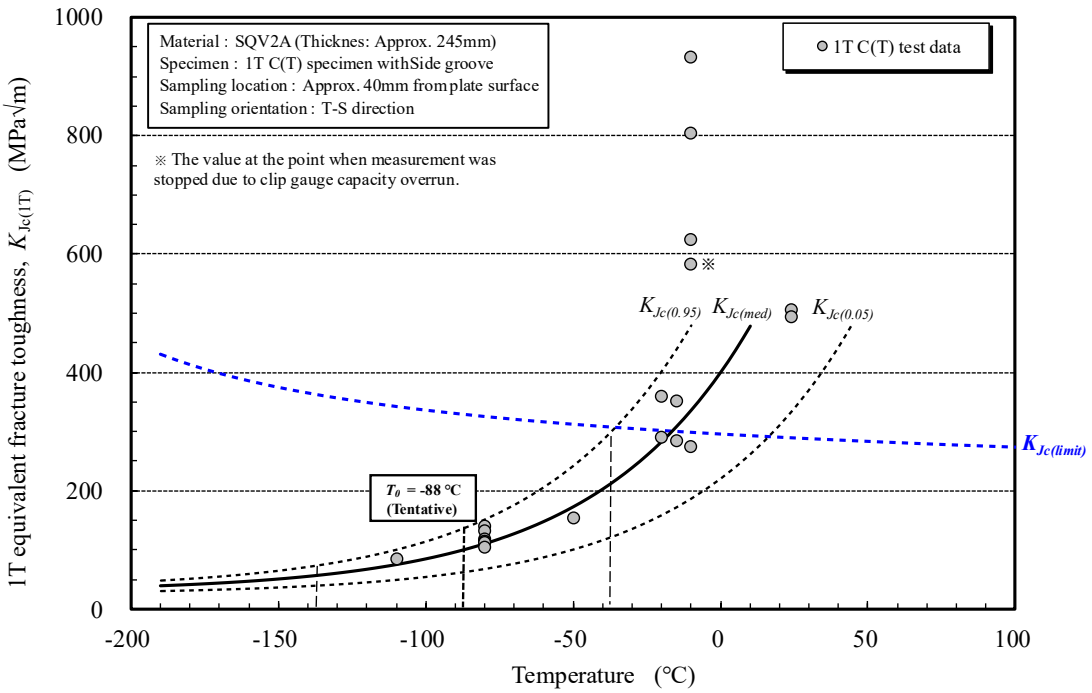


Fig. 4.1.3.4-3 Temperature dependence of K_{Jc} of C(T) specimen

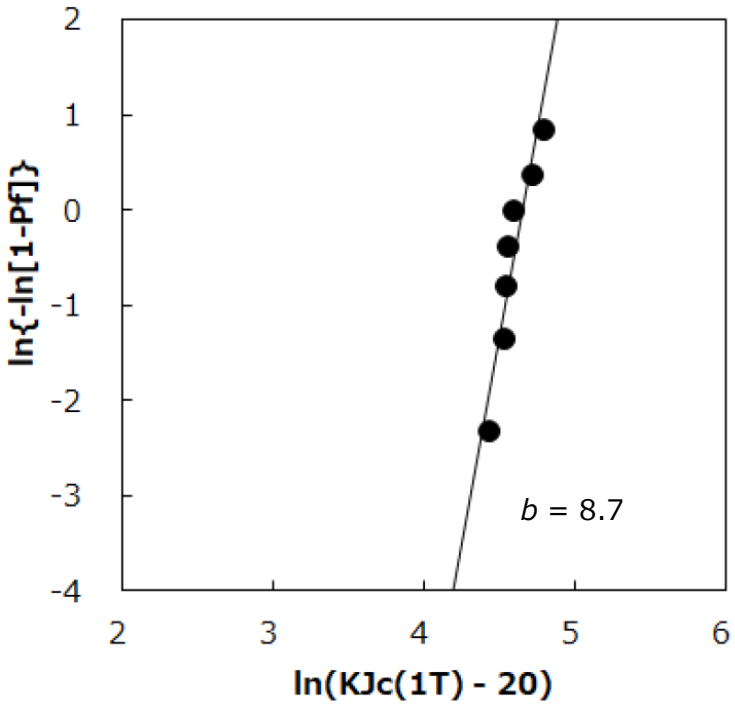


Fig. 4.1.3.4-4 Weibull distribution of K_{Jc} (-80°C) (C(T))

Copyright © 2026 The Japan Welding Engineering Society, All Rights Reserved.

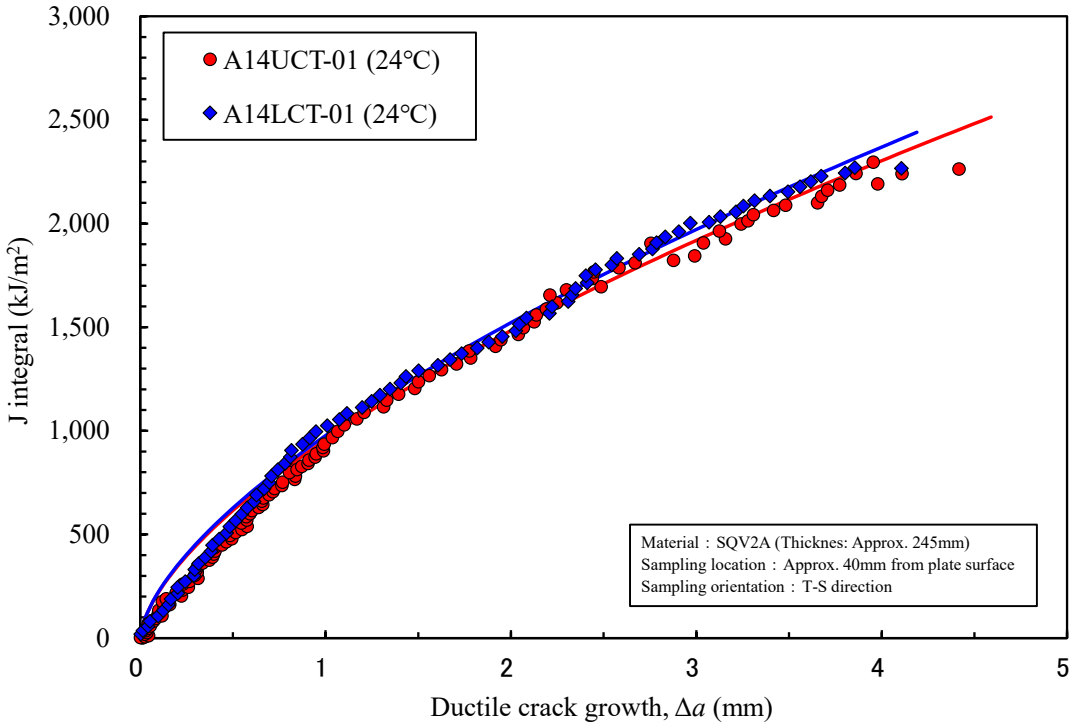


Fig. 4.1.3.4-5 *J*-Δ*a* curve (C(T), RT)

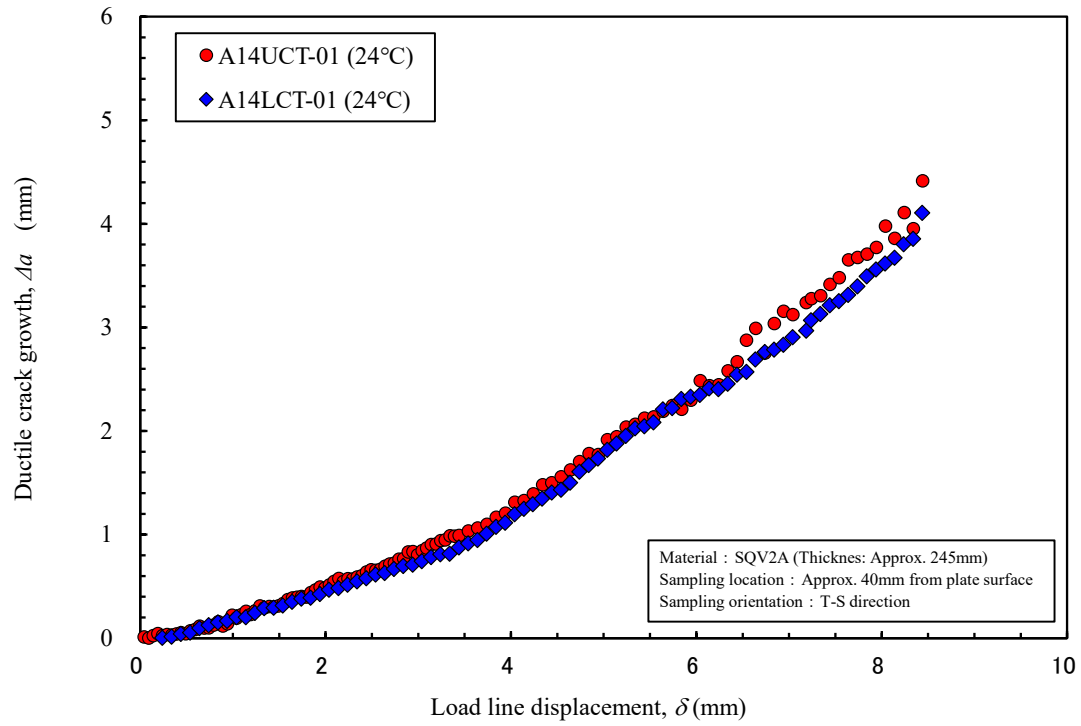


Fig. 4.1.3.4-6 Ductile crack growth amount Δ*a* and load line displacement δ_L curve (C(T), RT)

Copyright © 2026 The Japan Welding Engineering Society, All Rights Reserved.

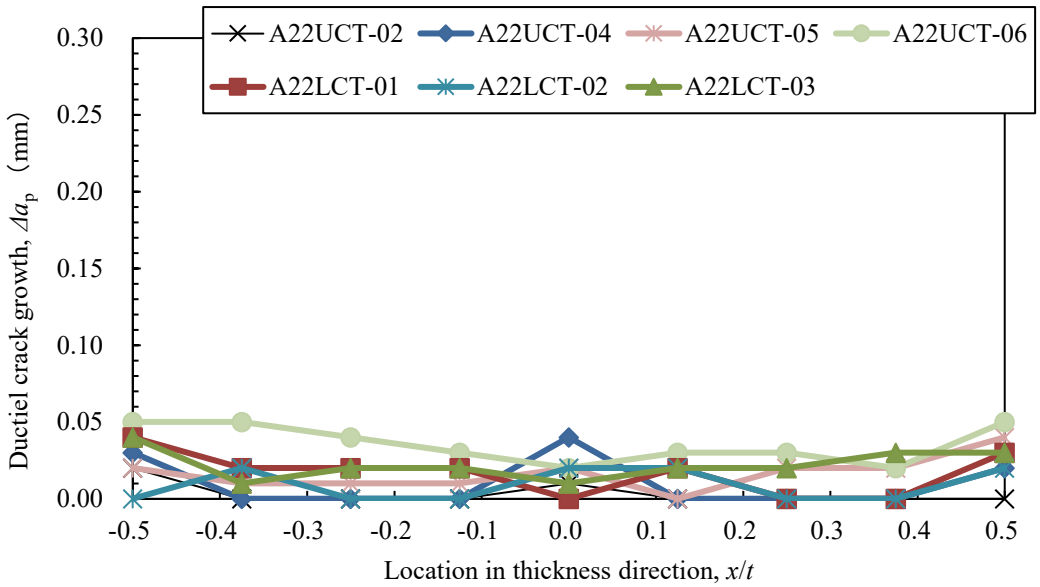
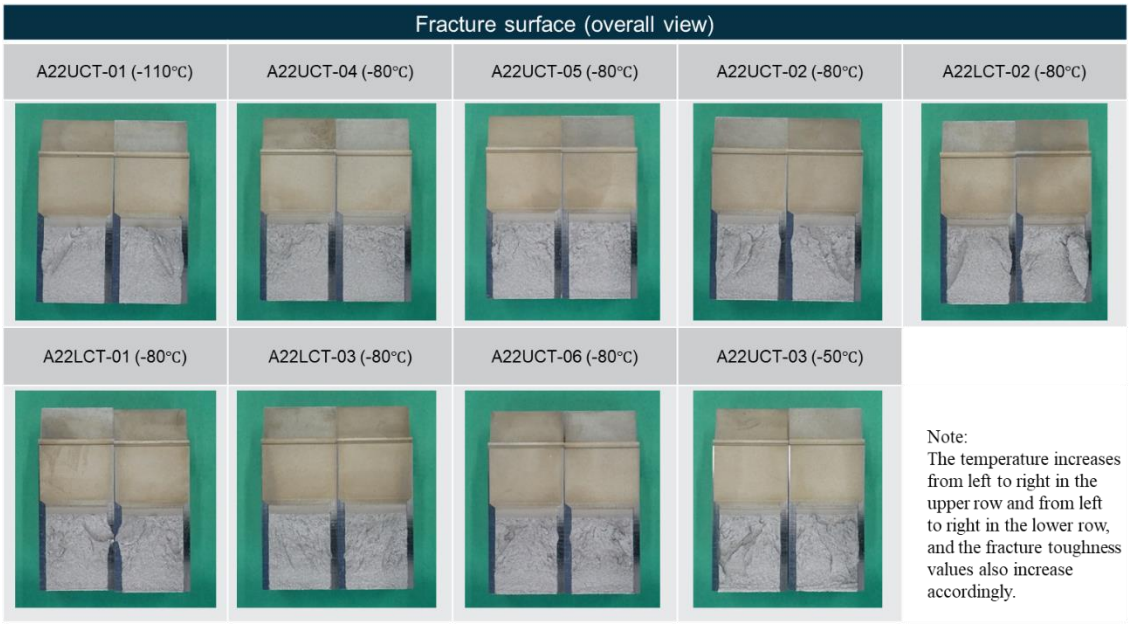
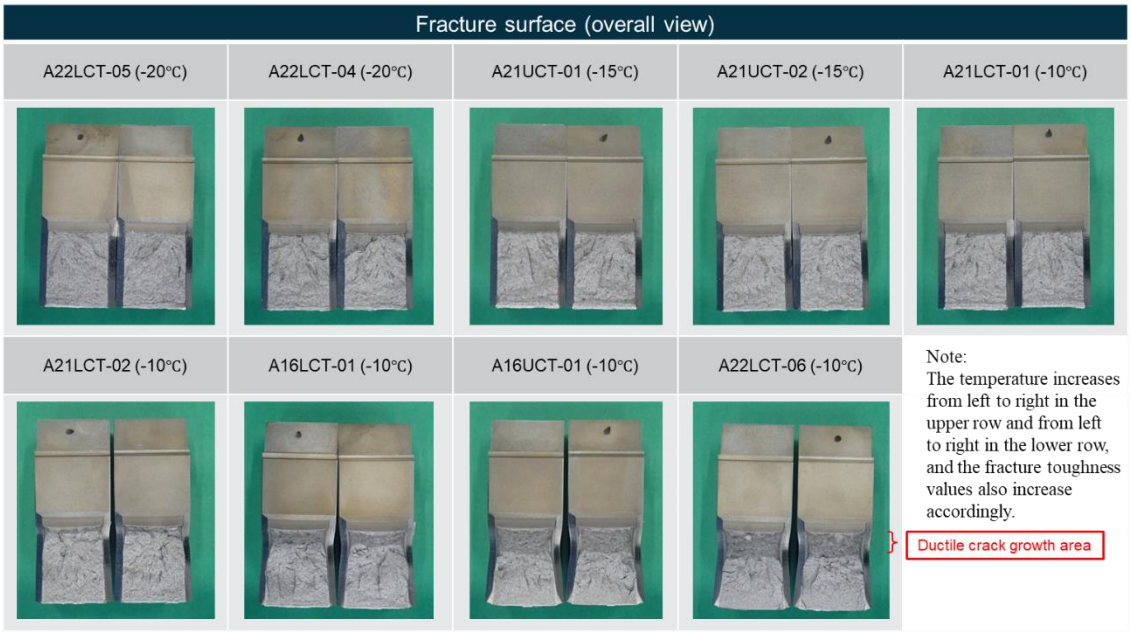


Fig. 4.1.3.4-7 Ductile crack growth profiles over specimen thickness (C(T) at -80°C)

Copyright © 2026 The Japan Welding Engineering Society, All Rights Reserved.



(a) T_1 candidate temperature



(b) T_2 candidate temperature

Fig. 4.1.3.4-8 Fracture surface (C(T))

Copyright © 2026 The Japan Welding Engineering Society, All Rights Reserved.

4.1.3.5 Fracture toughness test (SE(B) specimens)

To set parameters for the fracture evaluation model that accounts for the plastic constraint effect, fracture test data were obtained using 1TSE(B) specimens over the temperature range where brittle fracture and brittle fracture following ductile crack growth occur. Additionally, two types of SE(B) specimens with deep flaws (a/W = 0.5) and shallow flaws (a/W = 0.1) were employed to investigate the influence of plastic constraint on fracture characteristics.

(1) Specimens

Figs. 4.1.3.5-1 and 4.1.3.5-2 show the specimen geometries of SE(B) specimens with a/W = 0.5 and a/W = 0.1, respectively, at introducing fatigue pre-crack (primary machining). After specimen fabrication, fatigue pre-cracks were introduced at room temperature by cyclic three-point bending loads. Side grooves were not machined.

Following fatigue pre-cracking, the 53 mm thick SE(B) specimens (primary machined) were cut at 18 mm from the side surface, and the cut surface was used as a reference to produce specimens with a thickness of 25.4 mm. For the a/W = 0.1 SE(B) specimens (primary machined), finishing was performed so that W = 50.8 mm, using the rear surface as a reference. The final dimensions of SE(B) specimens with a/W = 0.5 and a/W = 0.1 are shown in Figs. 4.1.3.5-3 and 4.1.3.5-4, respectively.

(2) Test method

Fracture tests on SE(B) specimens were performed under three-point bending with a span of 203.2 mm, as shown in Fig. 4.1.3.5-5. Load and displacement were measured using instruments attached to the testing machine, with simultaneous recording of load-line displacement and crack mouth opening displacement (CMOD). The CMOD was measured by the double clip gauge method, attaching two sets of knife edges at different heights, as shown in Fig. 4.1.3.5-6. The loading rate during testing was controlled as dK/dt = 0.1 to 2 MPa$\sqrt{\text{m}}$/s in the initial elastic region. The test matrix is shown in Table 4.1.2-6.

(3) Test Results

Fracture toughness test results for SE(B) specimens (a/W = 0.5) are shown in Table 4.1.3.5-1, and those for SE(B) specimens (a/W = 0.1) are shown in Table 4.1.3.5-2. Some specimens exhibiting non-uniform fatigue pre-cracks, failing to meet homogeneity criteria, were excluded from evaluation.

Load versus load line displacement and load versus CMOD for SE(B) specimens (a/W = 0.5) are shown in Fig. 4.1.3.5-7, and those for SE(B) specimens (a/W = 0.1) are shown in Fig. 4.1.3.5-8. At -

Copyright © 2026 The Japan Welding Engineering Society, All Rights Reserved.

20°C, specimens with shallow flaws exhibited exceptionally large displacement up to final fracture, sometimes exceeding the measurement ranges of the clip gauges (maximum 10 mm for load-line displacement and maximum 15 mm for CMOD). The load-line displacement values showed large scatter and were estimated to be influenced by deformation at the contact points between specimen and jig during three-point bending. Therefore, CMOD was used for fracture toughness evaluation.

CMOD was measured by the double clip gauge on SE(B) specimens and converted to crack mouth opening displacement on the specimen surface using Equation (4.1.3.5-1). Here, V_1 and V_2 are displacements of displacement gauges 1 and 2, and z_1 and z_2 are the heights of the knife edges, respectively. In this test, z_1 = 1.6 mm and z_2 = 11.6 mm.

$$CMOD = V_1 - \frac{z_1}{z_2 - z_1}(V_2 - V_1) \qquad (4.1.3.5\text{-}1)$$

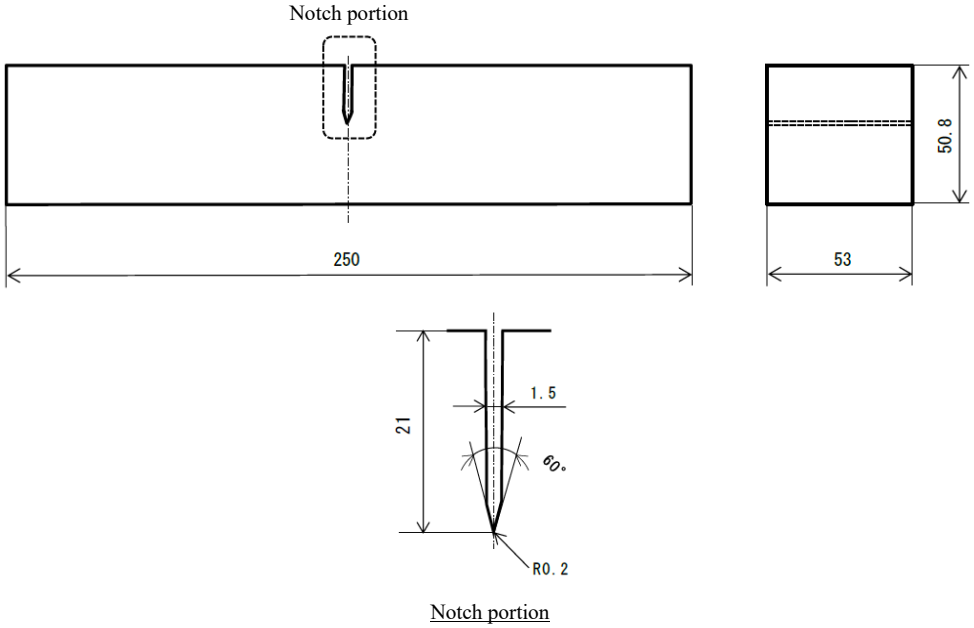
Fig. 4.1.3.5-9 shows K_{Jc} evaluated based on the crack mouth opening displacement for SE(B) specimens and the master curve evaluations, including data obtained from C(T) specimens. The T_0 for SE(B) specimens (a/W = 0.5) was -101°C, close to the result from C(T) specimens (T_0 = -88°C). However, K_{Jc} values for SE(B) specimens (a/W = 0.1) were significantly larger, resulting in T_0 = -142°C, indicating a pronounced plastic constraint effect due to the shallow flaw geometry.

Fig. 4.1.3.5-10 presents a comparison between *J-Δa* curves obtained by the unload compliance method at room temperature for C(T) specimens and J-integral versus ductile crack growth for C(T) and SE(B) specimens that fractured in brittle manner below 10°C. The *J-Δa* curve for SE(B) specimens with a/W = 0.1 lies above those of SE(B) specimens with a/W = 0.5 and C(T) specimens at the same test temperature, indicating higher ductile fracture resistance.

Fig. 4.1.3.5-11 shows the thickness direction distribution of ductile crack growth at -80°C. The ductile crack growth of a/W = 0.1 specimens was larger than that of a/W = 0.5 specimens. This is attributed to the fact that while a/W = 0.1 specimens exhibit higher ductile resistance, cleavage fracture occurs before ductile crack growth in a/W = 0.5 specimens.

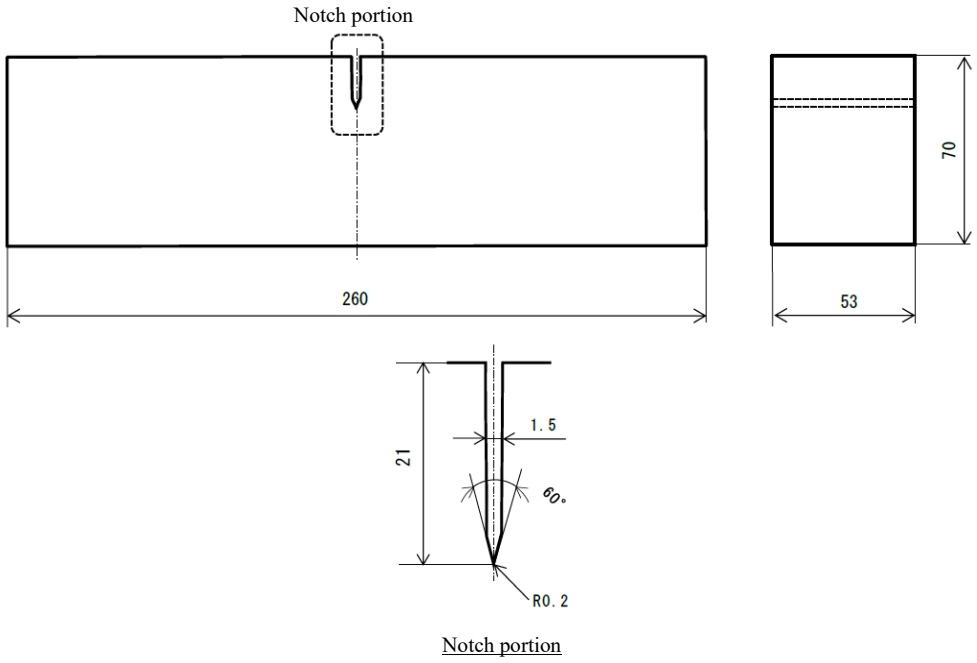
Fracture surface photographs of both types of SE(B) specimens are shown in Figs. 4.1.3.5-12 and 4.1.3.5-13. Some specimens with non-uniform fatigue pre-cracks were excluded from evaluation due to failure to meet homogeneity criteria. At the candidate temperature T_1, no ductile crack growth was observed on the fracture surfaces, confirming complete cleavage fracture. At the candidate temperature T_2, dimples were observed at the fatigue pre-crack tip, followed by cleavage fracture.

Copyright © 2026 The Japan Welding Engineering Society, All Rights Reserved.



Unit: mm

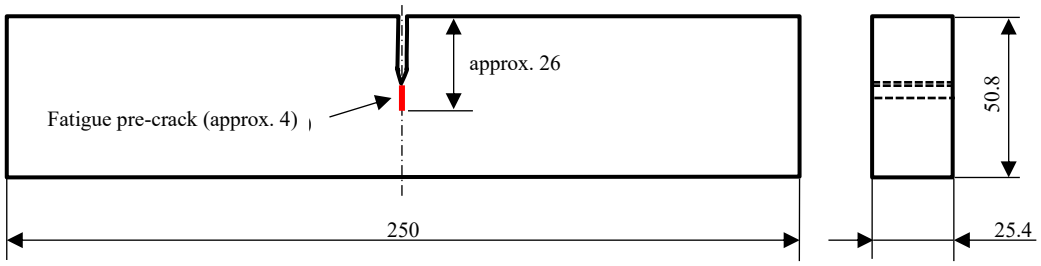
Fig. 4.1.3.5-1 Pre-processing geometry of SE(B) specimen (a/W=0.5)



Unit: mm

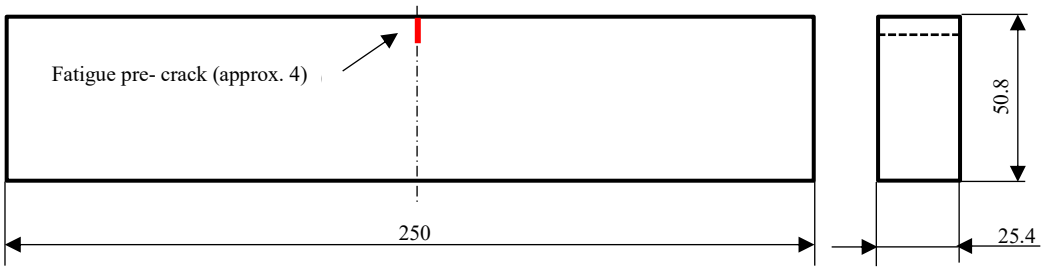
Fig. 4.1.3.5-2 Pre-processing geometry of SE(B) specimen (a/W=0.1)

Copyright © 2026 The Japan Welding Engineering Society, All Rights Reserved.



Unit: mm

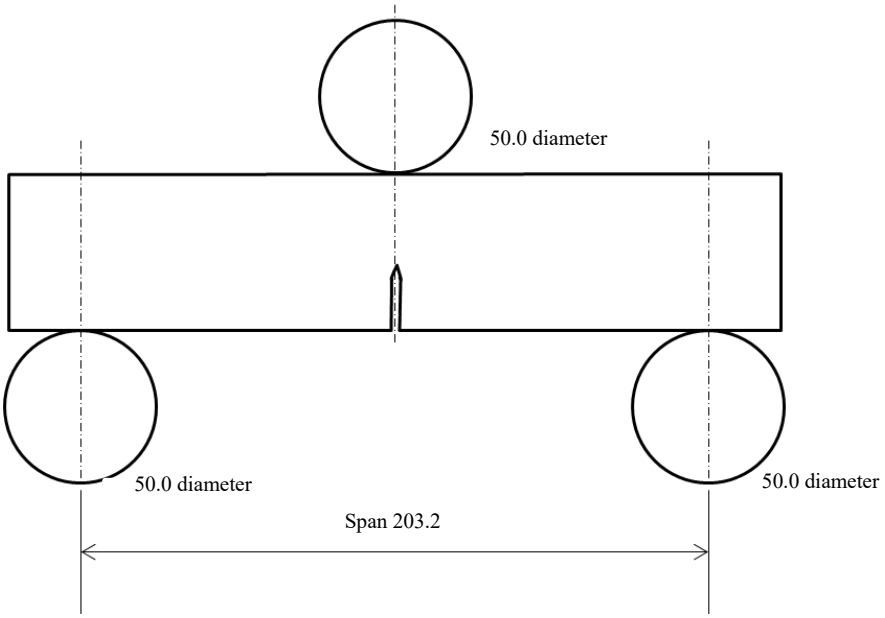
Fig. 4.1.3.5-3 Geometry of SE(B) specimen (a/W=0.5)



Unit: mm

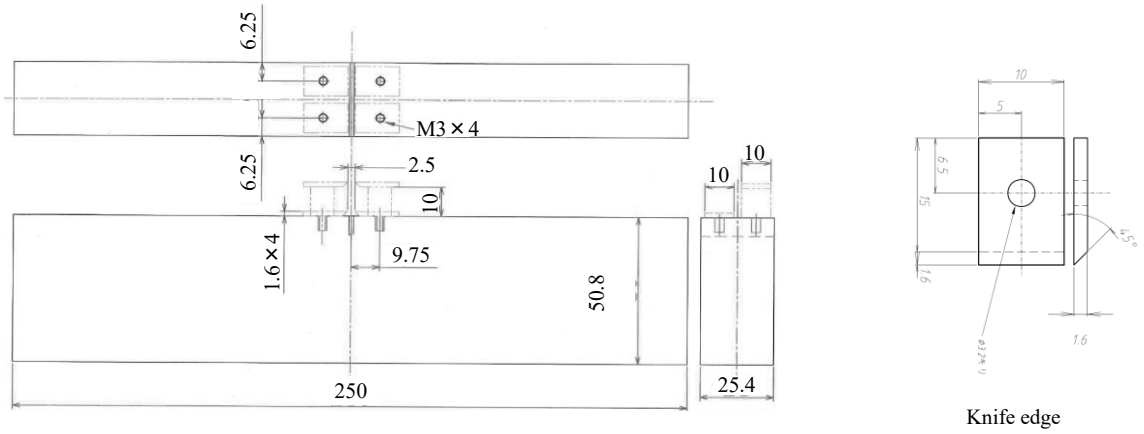
Fig. 4.1.3.5-4 Geometry of SE(B) specimen (a/W=0.1)

Copyright © 2026 The Japan Welding Engineering Society, All Rights Reserved.



Unit: mm

Fig. 4.1.3.5-5 Setup of fracture toughness test using SE(B) specimen (a/W=0.5 and 0.1)



Unit: mm

Fig. 4.1.3.5-6 Installation of knife edges on SE(B) specimen (a/W=0.5 and 0.1)

Copyright © 2026 The Japan Welding Engineering Society, All Rights Reserved.

Copyright © 2026 The Japan Welding Engineering Society, All Rights Reserved.

Table 4.1.3.5-1 Fracture toughness test results of SE(B) specimen (a/W=0.5)

Material	Specimen ID	Temp. T (℃)	Specimen dimension: Width W (mm)	Thickness B (mm)	Net thickness $B_{N(mm)}$	Crack size $a_{0(mm)}$	Span S (mm)	a_0/W	Fracture load P_c (kN)	Elastic J J_e (kJ/m^2)	Plastic J J_p (kJ/m^2) LLD	Plastic J J_p (kJ/m^2) CMOD	Fracture toughness J_c (kJ/m^2) LLD	Fracture toughness J_c (kJ/m^2) CMOD	Fracture toughness K_{Jc} (MPa$\sqrt{}$m) LLD	Fracture toughness K_{Jc} (MPa$\sqrt{}$m) CMOD	$K_{Jc(limit)}$ (MPa$\sqrt{}$m)	Validity for $K_{Jc(limit)}$	Validity for ductile crack growth	Fracture displacement (mm) LLD	Fracture displacement (mm) CMOD	Ductile crack growth Δa_p (mm) Average	Ductile crack growth Δa_p (mm) Max
Low alloy steel B	A14U-SEBD-01	-80	50.78	25.38	25.38	23.73	203.2	0.467	69.5	60.1	96.5	98.2	157	158	189	190	336	Valid	Valid	1.23	0.80	0.05	0.09
	A16L-SEBD-01	-80	50.80	25.40	25.40	26.44	203.2	0.520	53.8	50.2	27.3	31.7	77.5	81.9	133	137	319	Valid	Valid	0.89	0.56	0.01	0.01
	A22U-SEBD-01	-80	50.77	25.39	25.39	26.36	203.2	0.519	52.9	48.3	27.7	22.8	76.0	71.1	132	127	319	Valid	Valid	0.73	0.50	0.00	0.00
	A14L-SEBD-01	-80	50.80	25.40	25.40	26.17	203.2	0.515	52.9	46.9	20.9	22.9	67.9	69.9	124	126	321	Valid	Valid	0.81	0.49	0.00	0.01
	A22U-SEBD-02	-80	50.79	25.36	25.36	25.94	203.2	0.511	52.0	44.1	12.7	15.1	56.8	59.3	114	116	322	Valid	Valid	0.66	0.42	0.00	0.00
	A16U-SEBD-01	-80	50.80	25.40	25.40	26.33	203.2	0.518	50.2	43.0	11.3	13.4	54.4	56.5	111	113	320	Valid	Valid	0.74	0.46	0.00	0.00
	A22L-SEBD-01	-80	50.82	25.36	25.36	26.20	203.2	0.516	49.6	41.4	10.4	13.3	51.7	54.6	108	112	321	Valid	Valid	0.63	0.41	0.00	0.00
	A16L-SEBD-02	-20	50.78	25.39	25.39	26.61	203.2	0.524	61.1	67.7	-	-	-	-	-	-	295	—	—	—	—	4.62	6.28
	A22U-SEBD-05	-20	50.78	25.40	25.40	26.21	203.2	0.516	68.6	80.9	-	2889	-	2970	-	815	297	Invalid	—	—	10.9	2.56	4.06
	A22L-SEBD-02	-20	50.78	25.40	25.40	25.91	203.2	0.510	71.2	83.9	1485	1600	1569	1684	592	613	299	Invalid	Invalid	8.50	6.52	1.38	2.21
	A16U-SEBD-03	-20	50.80	25.39	25.39	26.31	203.2	0.518	62.8	68.5	571	598	640	667	378	386	297	Invalid	Valid	4.03	2.91	0.35	0.56
	A14L-SEBD-02	-20	50.81	25.40	25.40	26.36	203.2	0.519	60.4	63.7	452	471	516	535	339	346	297	Invalid	Valid	3.36	2.46	0.31	0.46
	A22L-SEBD-04	-20	50.78	25.36	25.36	26.31	203.2	0.518	57.2	57.3	337	328	394	385	297	293	297	Valid	Valid	2.76	1.89	0.27	0.42
	A22L-SEBD-05	-20	50.78	25.39	25.39	26.38	203.2	0.519	52.8	49.1	124	123	173	172	197	196	296	Valid	Valid	1.71	1.46	0.08	0.14
	A22U-SEBD-04	-15	50.78	25.39	25.39	26.37	203.2	0.519	66.4	77.5	-	3011	-	3089	-	830	295	Invalid	—	—	11.48	2.79	4.10
	A14U-SEBD-02	-10	50.81	25.39	25.39	26.42	203.2	0.520	65.6	76.0	-	3020	-	3096	-	830	293	Invalid	—	—	11.5	2.87	4.64

Note 1: Young's modulus is based on the temperature-dependent formula for material group A in JEAC4216-2015 (E(T)=202,100－62.6T (MPa)).

Note 2: Yield stress uses the temperature-dependent formula from BS7910:2013 + A1:2015(σ_Y (T)= $\sigma_{Y(RT)}$ + 10^5 / (491+1.8T)-189 (MPa)), where $\sigma_{Y(RT)}$ is the experimentally measured yield stress at room temperature, 453 MPa.

Note 3: For specimens A16L-SEBD-02, A22U-SEBD-05, A22U-SEBD-04, and A14U-SEBD-02, fracture occurred outside the clip gauge measurement range for load-line displacement, therefore the fracture toughness values for LLD are indicated as "—".

Note 4: For specimen A16L-SEBD-02, fracture occurred outside the clip gauge measurement range for crack mouth opening displacement (CMOD), therefore the fracture toughness value for CMOD is indicated as "—".

Note 5: Specimen A14U-SEBD-01 is excluded from evaluation because the fatigue pre-crack length is invalid.

Note 6: LLD refers to load-line displacement, and CMOD refers to crack mouth opening displacement.

.

Copyright © 2026 The Japan Welding Engineering Society, All Rights Reserved.

Table 4.1.3.5-2 Fracture toughness test results of SE(B) specimen (a/W=0.1)

Material	Specimen ID	Temp. T (℃)	Specimen dimension: Width W (mm)	Thickness B (mm)	Net thickness $B_{N(mm)}$	Crack size $a_{0(mm)}$	Span S (mm)	a_0/W	Fracture load P_c (kN)	Elastic J J_e (kJ/m^2)	Plastic J J_p (kJ/m^2) LLD	Plastic J J_p (kJ/m^2) CMOD	Fracture toughness J_c (kJ/m^2) LLD	Fracture toughness J_c (kJ/m^2) CMOD	Fracture toughness K_{Jc} (MPa√m) LLD	Fracture toughness K_{Jc} (MPa√m) CMOD	$K_{Jc(limit)}$ (MPa√m)	Validity for $K_{Jc(limit)}$	Validity for ductile crack growth	Fracture displacement (mm) LLD	Fracture displacement (mm) CMOD	Ductile crack growth Δa_p (mm) Average	Ductile crack growth Δa_p (mm) Max
Low alloy steel B	A14U-SEBS-01	-80	50.80	25.40	25.40	4.10	203.2	0.081	207	54.6	470	542	525	597	346	369	442	Valid	Valid	3.69	1.14	0.19	0.27
	A22L-SEBS-01	-80	50.78	25.35	25.35	4.06	203.2	0.080	199	50.3	313	404	363	454	288	321	442	Valid	Valid	2.89	0.87	0.19	0.26
	A14L-SEBS-01	-80	50.77	25.36	25.36	4.15	203.2	0.082	197	50.2	314	382	364	432	288	314	442	Valid	Valid	2.76	0.87	0.13	0.18
	A16U-SEBS-01	-80	50.79	25.38	25.38	3.37	203.2	0.066	195	41.2	207	326	249	367	238	289	445	Valid	Valid	2.11	0.73	0.09	0.14
	A22U-SEBS-03	-80	50.76	25.40	25.40	4.00	203.2	0.079	188	44.3	231	273	276	317	250	269	442	Valid	Valid	2.71	0.67	0.08	0.13
	A22U-SEBS-02	-80	50.78	25.40	25.40	4.07	203.2	0.080	187	44.6	232	241	277	285	251	255	442	Valid	Valid	2.45	0.59	0.10	0.14
	A16L-SEBS-02	-80	50.83	25.37	25.37	4.00	203.2	0.079	174	37.8	100	145	138	183	177	204	443	Valid	Valid	1.84	0.35	0.02	0.03
	A22L-SEBS-03	-80	50.72	25.36	25.36	4.06	203.2	0.080	175	39.1	137	124	176	164	200	193	442	Valid	Valid	2.32	0.39	0.04	0.06
	A16L-SEBS-01	-80	50.76	25.39	25.39	4.13	203.2	0.081	175	39.5	53.5	85.4	93.0	125	145	169	442	Valid	Valid	1.38	0.29	0.00	0.00
	A22U-SEBS-01	-80	50.81	25.38	25.38	3.83	203.2	0.075	175	36.7	53.9	84.1	90.6	121	144	166	443	Valid	Valid	1.21	0.29	0.00	0.00
	A14L-SEBS-02	-50	50.78	25.34	25.34	2.29	203.2	0.045	268	55.8	-	3001	-	3056	-	830	432	Invalid	Invalid	-	4.79	0.98	1.42
	A22U-SEBS-04	-30	50.78	25.39	25.39	3.80	203.2	0.075	243	71.7	-	6154	-	6226	-	1181	416	Invalid	Invalid	-	9.22	5.78	6.36
	A22U-SEBS-05	-20	50.76	25.40	25.40	3.71	203.2	0.073	212	53.6	-	7780	-	7834	-	1323	411	Invalid	Invalid	-	11.68	8.29	12.46
	A16L-SEBS-03	-20	50.78	25.38	25.38	3.51	203.2	0.069	238	64.5	-	6882	-	6947	-	1246	412	Invalid	Invalid	-	10.12	5.76	8.81
	A22L-SEBS-05	-20	50.77	25.38	25.38	3.72	203.2	0.073	227	61.7	-	6735	-	6797	-	1232	411	Invalid	Invalid	-	10.13	6.26	9.56
	A14U-SEBS-02	-20	50.78	25.39	25.39	3.74	203.2	0.074	235	66.4	-	6624	-	6691	-	1223	411	Invalid	Invalid	-	9.92	6.50	8.81
	A22L-SEBS-02	-20	50.77	25.38	25.38	3.89	203.2	0.077	209	54.4	-	5993	-	6047	-	1162	411	Invalid	Invalid	-	9.56	5.16	8.13
	A22L-SEBS-04	-20	50.77	25.40	25.40	3.76	203.2	0.074	238	68.4	-	5820	-	5888	-	1147	411	Invalid	Invalid	-	8.89	4.13	6.82
	A16U-SEBS-02	-20	50.78	25.38	25.38	3.85	203.2	0.076	244	73.5	-	5561	-	5635	-	1122	411	Invalid	Invalid	-	8.76	4.13	5.13

Note 1: Young's modulus is based on the temperature-dependent formula for material group A in JEAC4216-2015 (E(T)=202,100－62.6T (MPa)).

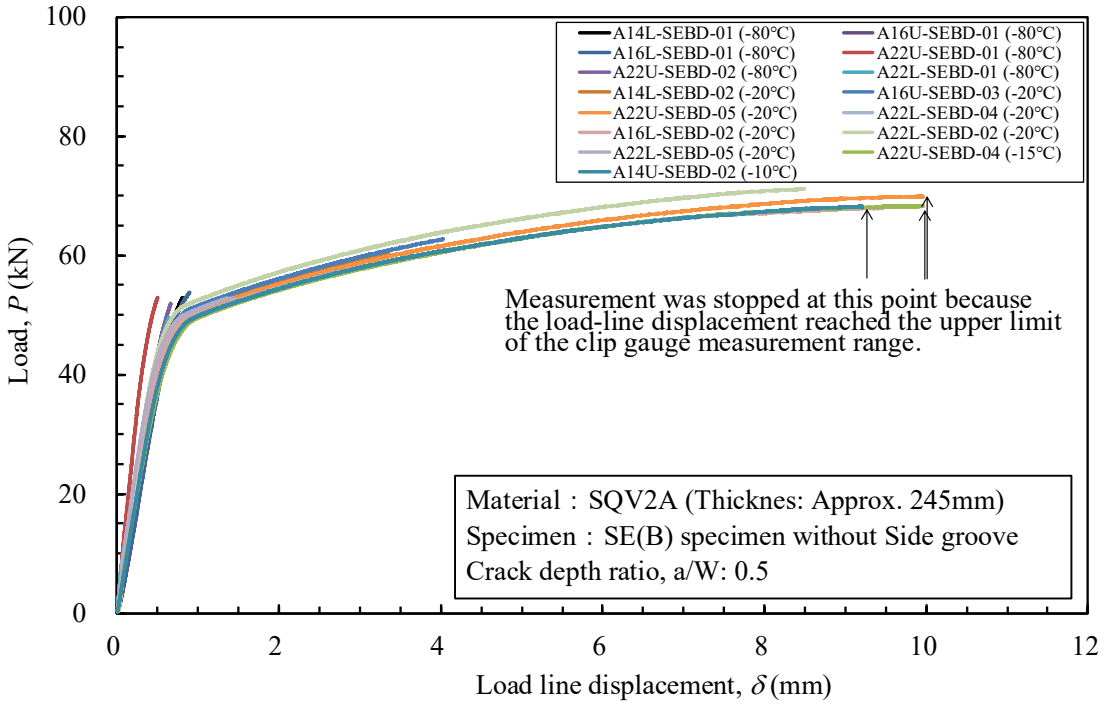
Note 2: Yield stress uses the temperature-dependent formula from BS7910:2013 + A1:2015($\sigma_Y(T)=\sigma_{Y(RT)}+10^5/(491+1.8T)-189$ (MPa)), where $\sigma_{Y(RT)}$ is the experimentally measured yield stress at room temperature, 453 MPa.

Note 3: At test temperatures of -50°C, -30°C, and -20°C, fracture occurred outside the clip gauge measurement range for load-line displacement; therefore, fracture toughness values for LLD are indicated as "—".

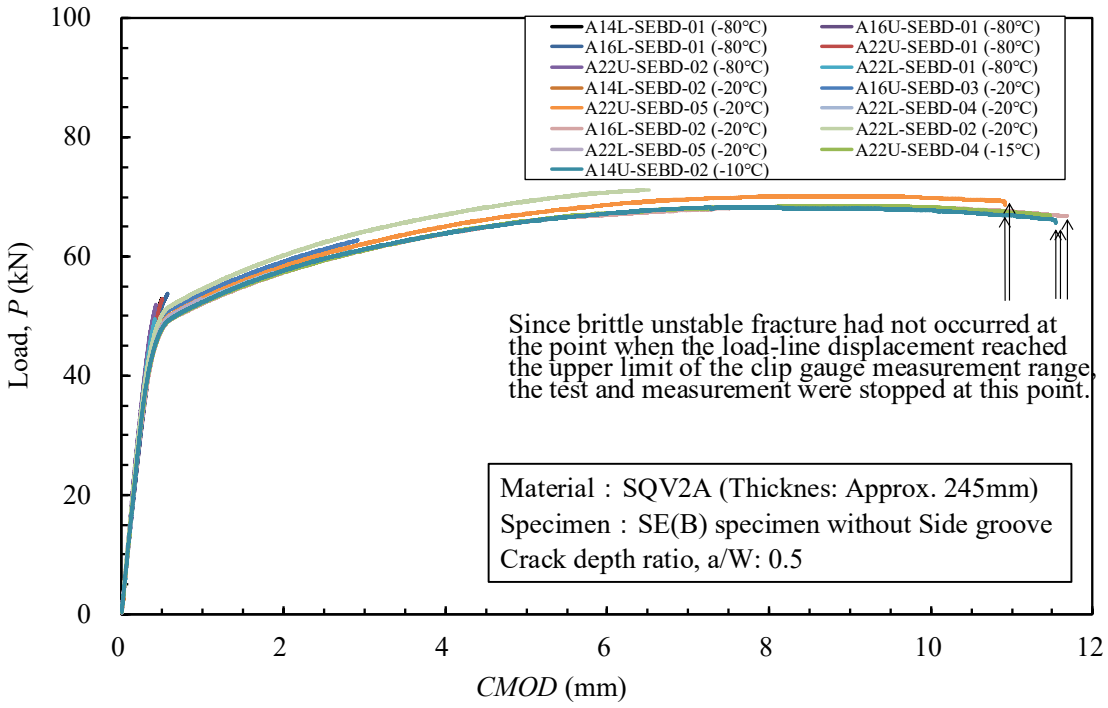
Note 4: Specimen A14L-SEBS-02 is excluded from evaluation because the fatigue pre-crack length is invalid.

Note 5: LLD refers to load-line displacement, and CMOD refers to crack mouth opening displacement.

.



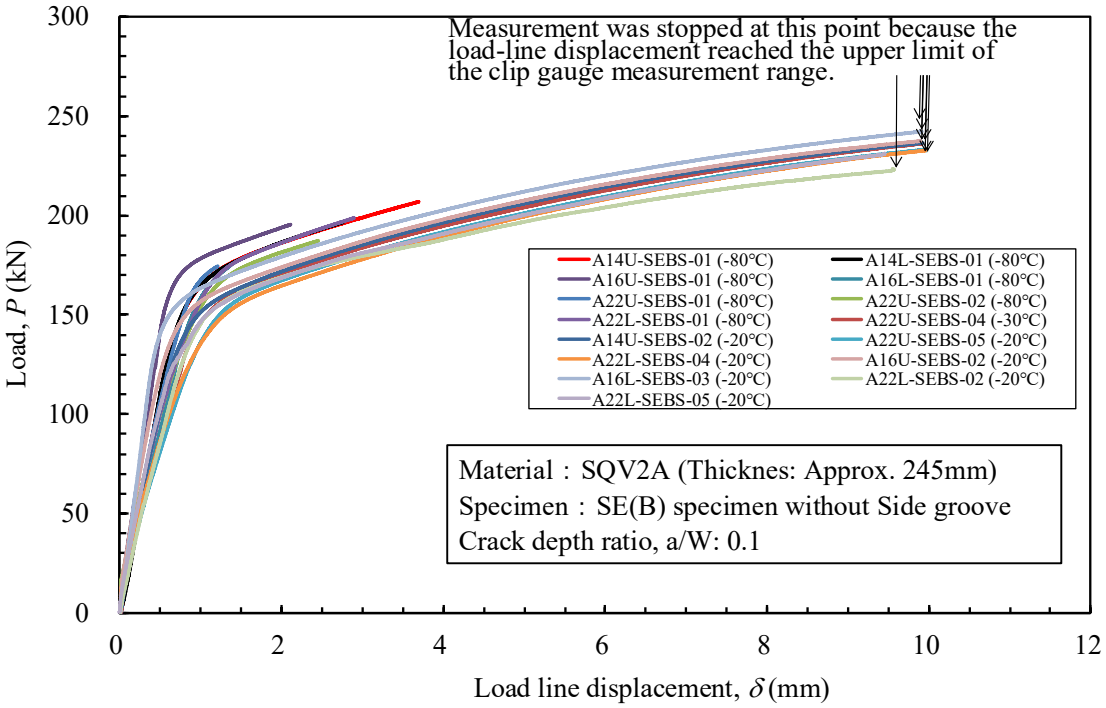
(a) Load – Load line displacement



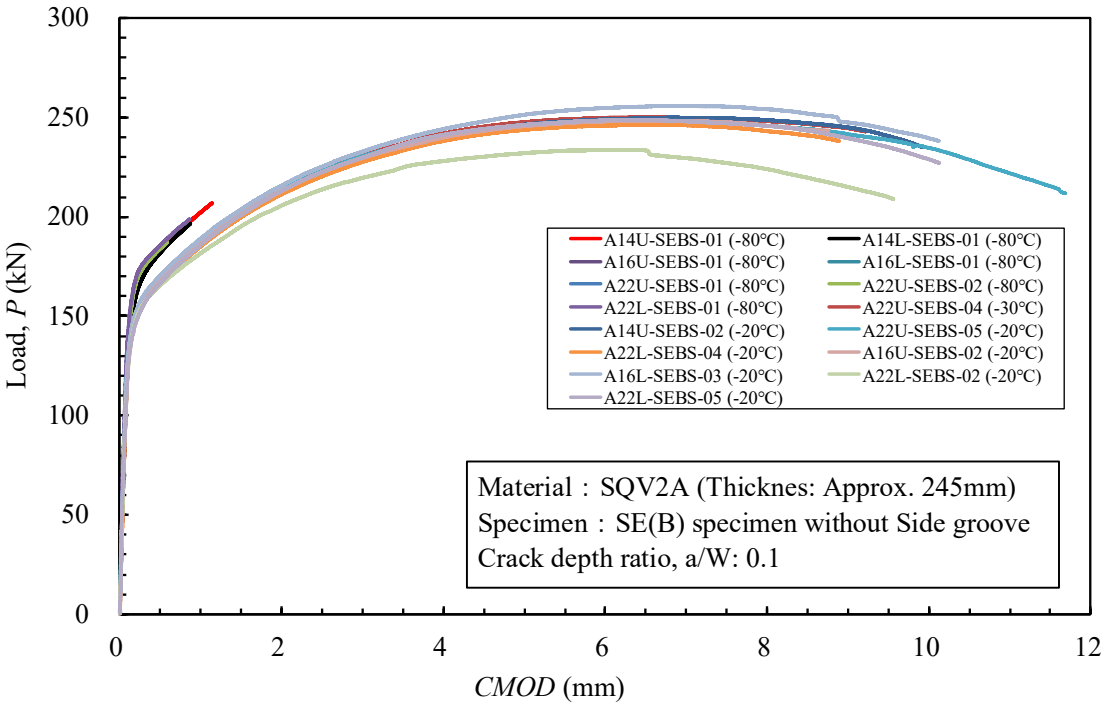
(b) Load - CMOD

Fig. 4.1.3.5-7 Load - displacement curve (SE(B), a/W=0.5)

Copyright © 2026 The Japan Welding Engineering Society, All Rights Reserved.



(a) Load – Load line displacement



(b) Load - CMOD

Fig. 4.1.3.5-8 Load - displacement curve (SE(B), a/W=0.1)

Copyright © 2026 The Japan Welding Engineering Society, All Rights Reserved.

Copyright © 2026 The Japan Welding Engineering Society, All Rights Reserved.

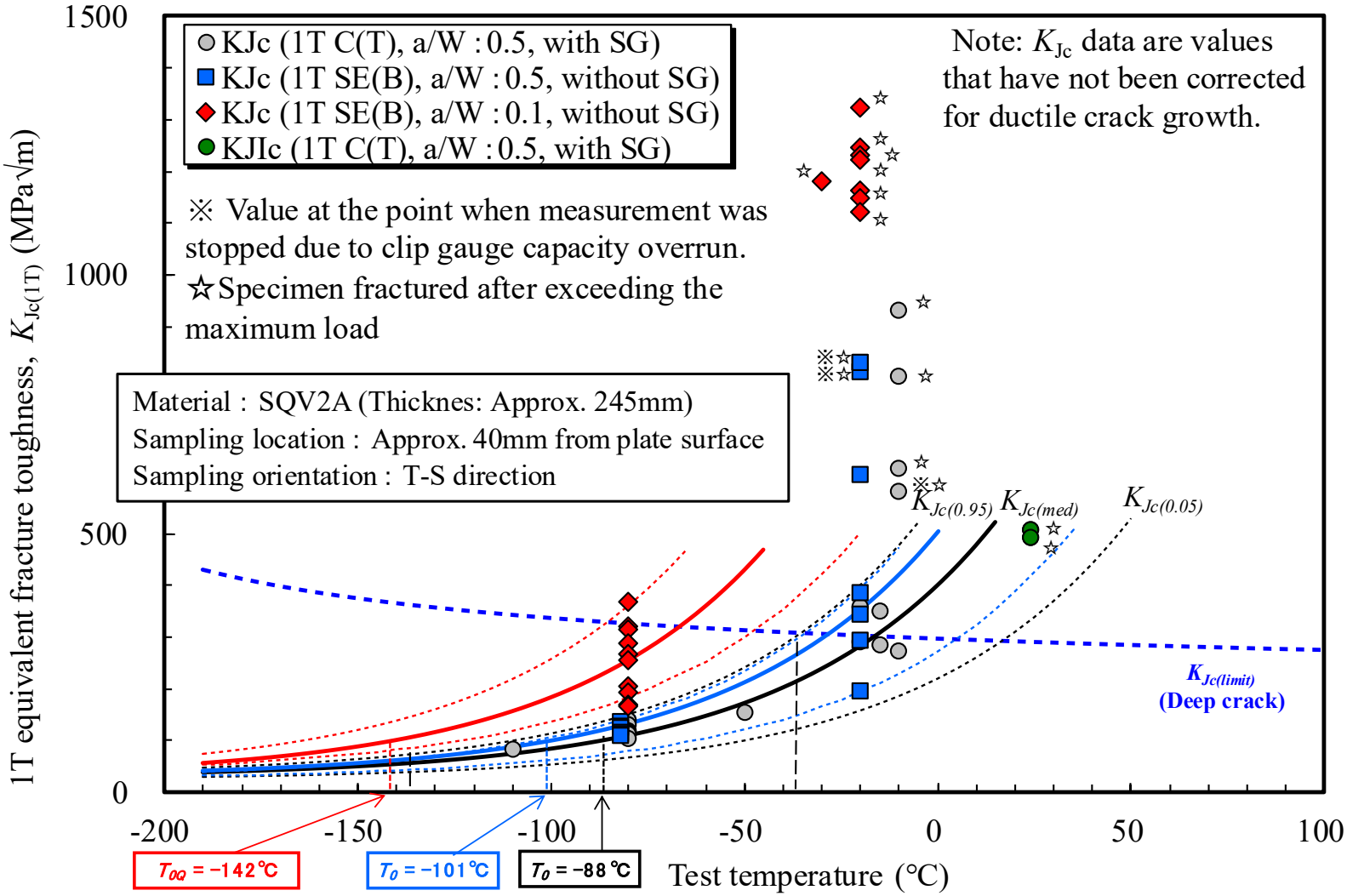
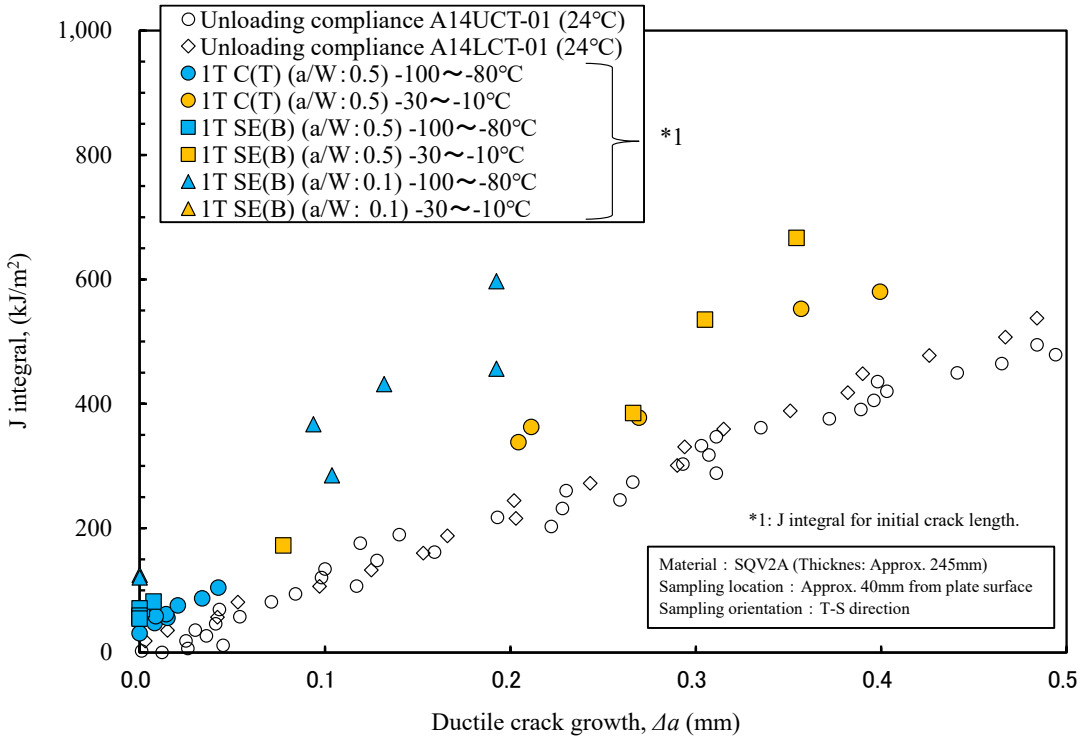
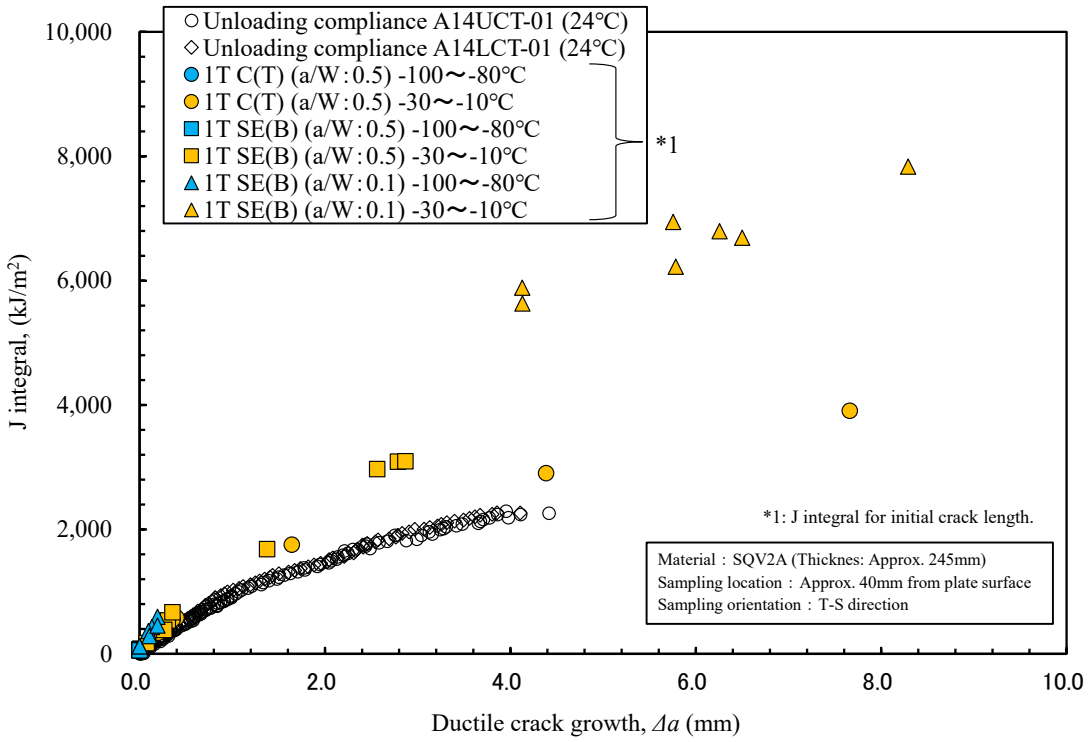


Fig. 4.1.3.5-9 Temperature dependence of K_{Jc} of SE(B) specimen



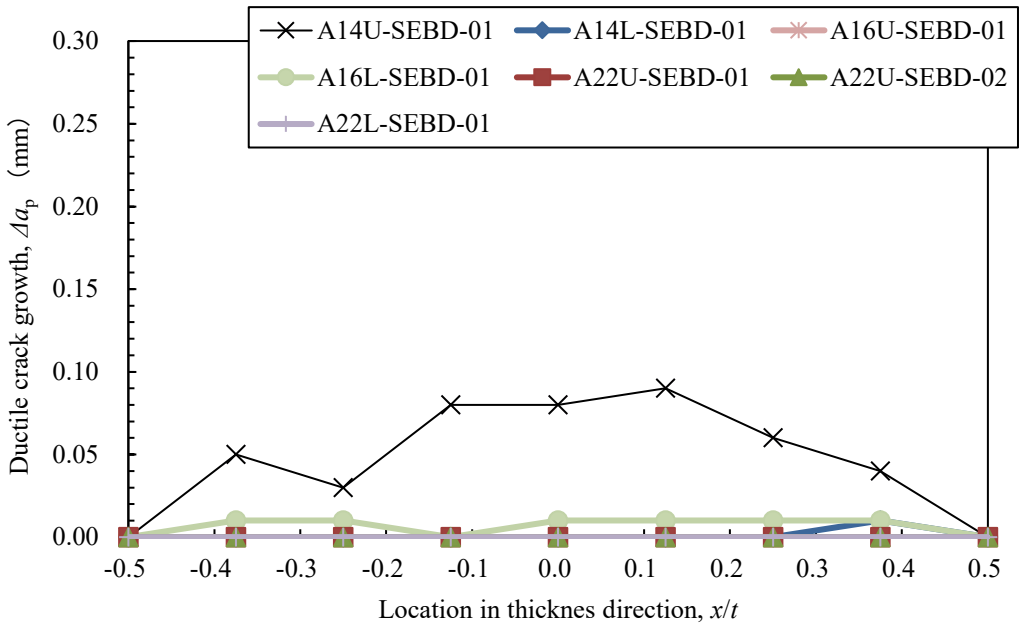
(a) Small Δ*a* region



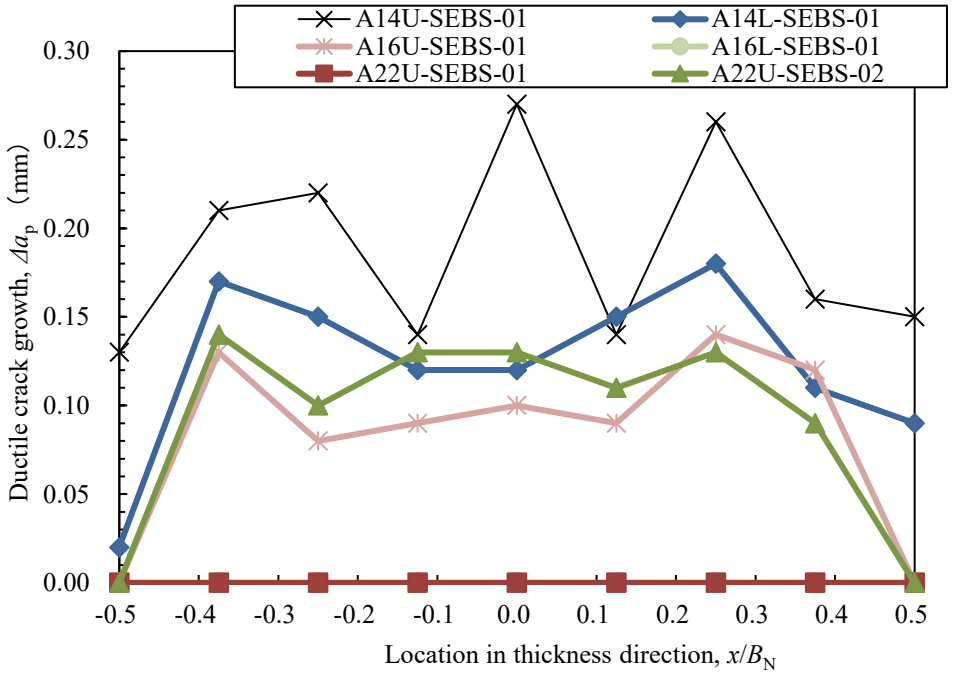
(b) Large Δ*a* region

Fig. 4.1.3.5-10 Comparison of *J*-Δ*a* curve between C(T) and SE(B) specimens

Copyright © 2026 The Japan Welding Engineering Society, All Rights Reserved.



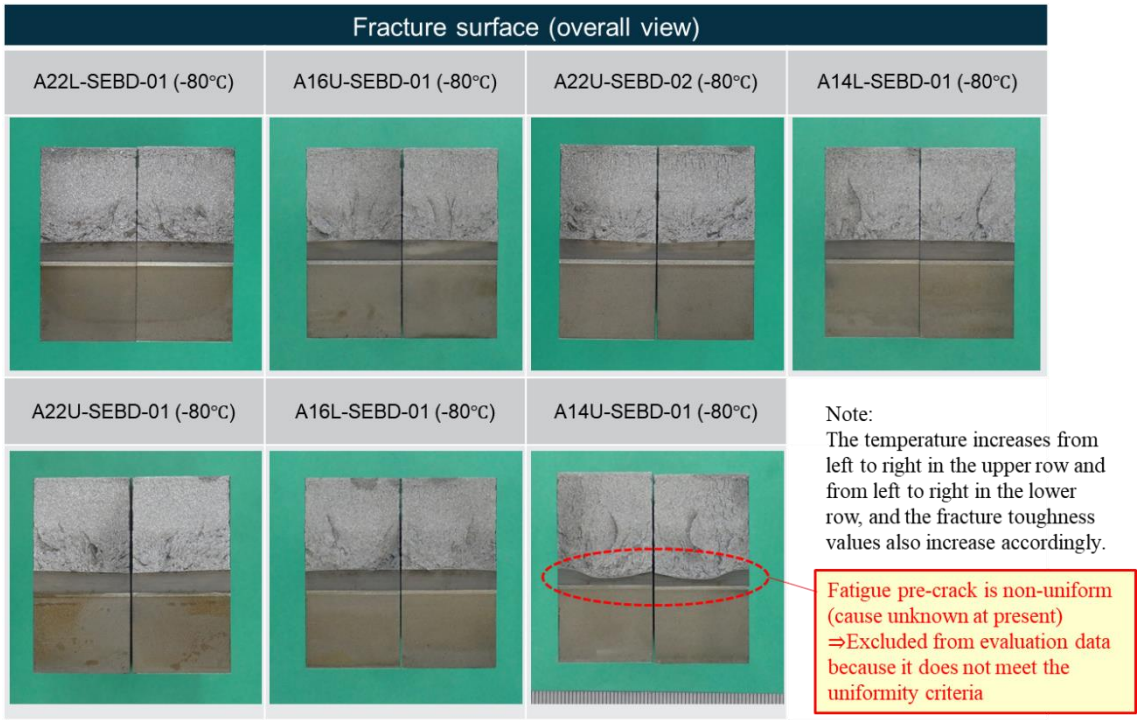
(a) a/W=0.5



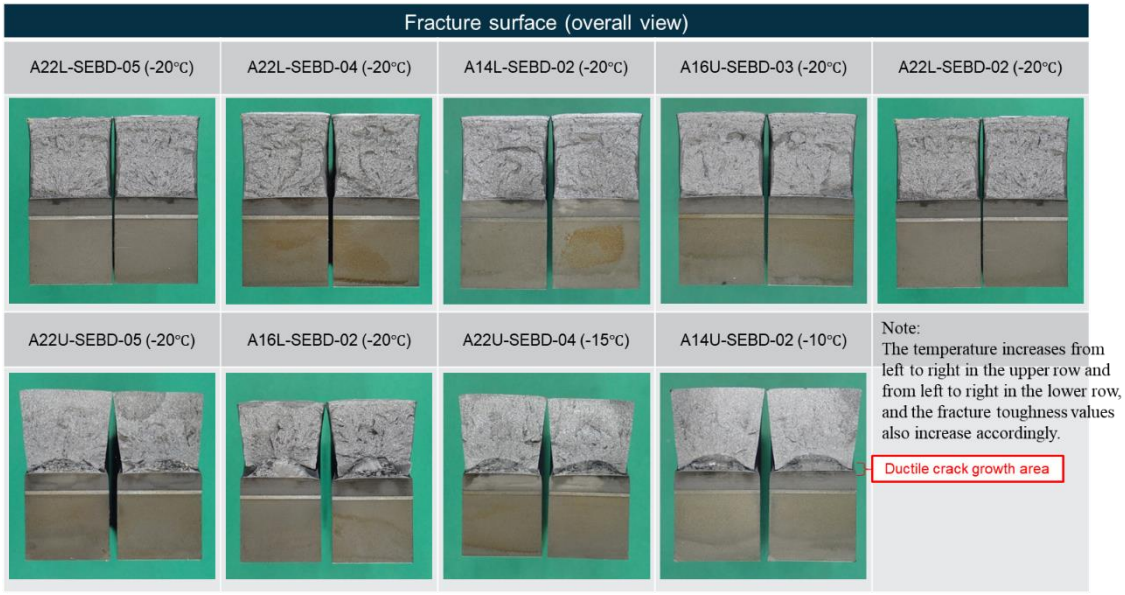
(b) a/W=0.1

Fig. 4.1.3.5-11 Ductile crack growth profiles over specimen thickness (SE(B) at -80°C)

Copyright © 2026 The Japan Welding Engineering Society, All Rights Reserved.



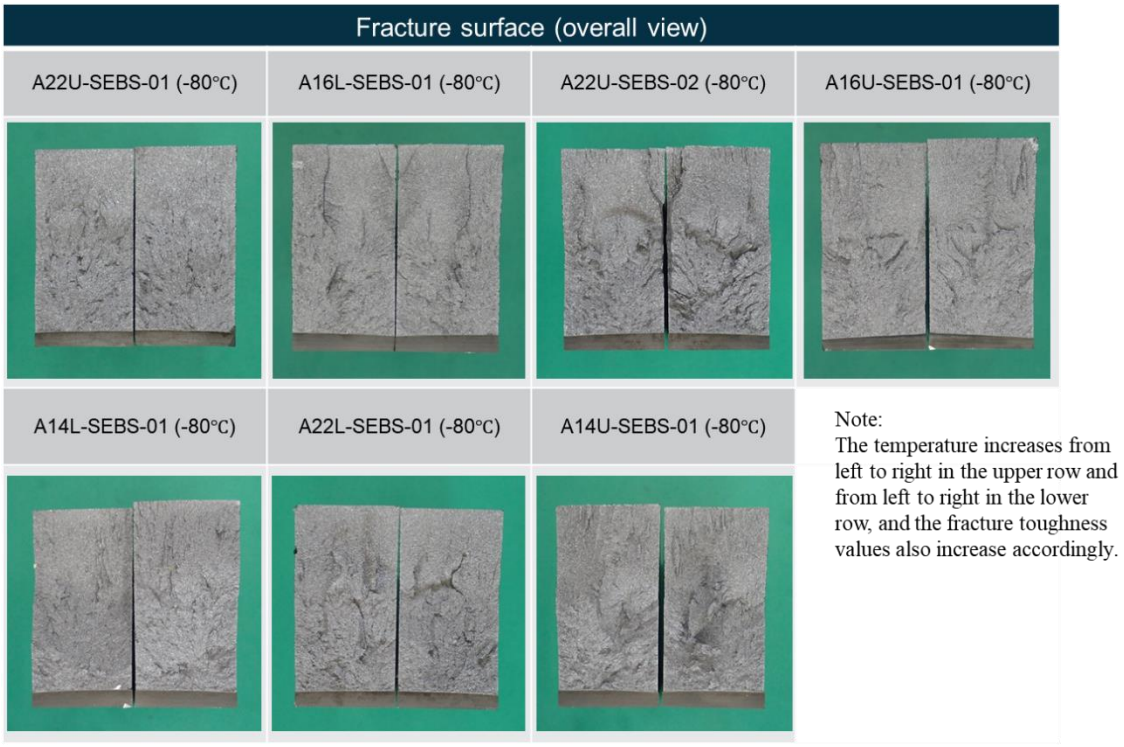
(a) T_1 candidate temperature (-80ºC)



(b) T_2 candidate temperature (-20～-10ºC)

Fig. 4.1.3.5-12 Fracture surface (SE(B), a/W=0.5)

Copyright © 2026 The Japan Welding Engineering Society, All Rights Reserved.



(a) T_1 candidate temperature (-80°C)



(b) T_2 candidate temperature (-50～-20°C)

Fig. 4.1.3.5-13 Fracture surface (SE(B), a/W=0.1)

Copyright © 2026 The Japan Welding Engineering Society, All Rights Reserved.

4.1.3.6 Preliminary and main tests of Surface-flawed flat plate tensile specimen

Fracture tests were performed using surface flawed plate specimens (tensile loading) with low plastic constraint to obtain fracture test data for validating fracture evaluation models considering the plastic constraint effect.

(1) Test specimens

The specimens were taken from low alloy steel B with approximate dimensions of 1000 mm (rolling direction) × 2500 mm (transverse rolling direction) × 245 mm (plate thickness).

During fatigue pre-crack introduction, the specimen thickness at the test section was machined to approximately 60 mm. Fatigue pre-cracks were propagated from an EDM slits by repeated bending loads. Subsequently, both specimen surfaces were machined by approximately 5 mm to achieve a fatigue pre-crack depth of 5 mm and a net section thickness (parallel section) of 50.8 mm. The procedure for fatigue pre-cracking is shown in Fig. 4.1.3.6-1. This procedure is common with the plate bending test described later in section 4.1.3.7.

To ensure sufficient gripping length, the overall specimen length was approximately 3,000 mm. K-shaped grooves were provided at both ends of the test section, and tab plates were welded to secure gripping allowance. The manufacturing procedure for the flat plate specimens (tensile loading) is shown in Fig. 4.1.3.6-2. The tab plate material was fabricated from 100 mm thick, 330 mm wide, and 1190 mm ling welded structural rolled steel (SM490). To prevent fracture initiation from the tab welds during the tests, the thickness at the tab weld region was increased to 80 mm, thicker than the test section thickness of approximately 50 mm.

Fig. 4.1.3.6-3 shows the final geometry of the surface-flawed plate tensile specimen. Three sets of tab plates were prepared and reused by detaching the welds after each test.

(2) Test method

A test machine with a maximum load capacity of 10 MN was used for the flat plate tensile test specimens. The test conditions are summarized as follows:

- Control method: displacement control (cylinder displacement rate 0.04 mm/sec)
- Holding time: at least 60 minutes after the test specimen surface temperature reached the test temperature
- Test standard: ASTM E2899-15 (complied with as much as possible)

Copyright © 2026 The Japan Welding Engineering Society, All Rights Reserved.

The test speed was controlled so that the loading rate at the deepest crack tip dK/dt in the elastic region was comparable to that of C(T) and SE(B) specimens, i.e., approximately 0.1 to 2 MPa√m/s.

For cooling the test specimen, a cooling box enclosing the general section of the flat plate specimen was fabricated, and temperature was controlled by liquid nitrogen spray. To avoid fracture initiation at the weld, the tab welds were positioned outside the cooling box. Preliminary cooling tests confirmed that the specimen surface temperature could be maintained within ±3°C of the target temperature.

For crack opening displacement measurement, the double clip gauge method was applied using two clip gauges at different distances from the test specimen surface, as shown in Fig. 4.1.3.6-4. The knife edge geometry used is shown in Fig. 4.1.3.6-5. Crack opening displacement was measured at 5 mm and 25 mm from the test specimen surface.

For strain measurement, elastic strain gauges for low temperatures were used to measure strain at 11 locations: four on the crack surface, two on the specimen side, and five on the side opposite to the flaw. The strain gauge locations are shown in Fig. 4.1.3.6-6, which also indicates thermocouple locations. Thermocouples were installed-each one on the specimen surface introduced the crack and the opposite specimen surface- to monitor temperature during the test.

Prior to tensile load, alignment of the testing machine and jig was adjusted at room temperature, and after specimen installation, a preload of 1500–2000 kN, sufficiently below the expected fracture load, was applied. It was confirmed that the strain gauge output was within about 10% variation before proceeding with loading to fracture at a constant displacement rate.

Fig. 4.1.3.6-7 shows the appearance of the flat plate tensile specimen before testing, and Fig. 4.1.3.6-8 shows the test setup during the fracture test. In addition to crack opening displacement, stroke displacement (crosshead displacement) was also measured.

(3) Test results

Based on the test matrix shown in Table 4.1.2-7, two preliminary tests and twelve main tests were performed.

a. Preliminary tests

To determine the test temperature for the main test, preliminary tensile tests on surface- flawed flat plate specimens were performed at -100°C and -80°C. A summary of preliminary test results is

Copyright © 2026 The Japan Welding Engineering Society, All Rights Reserved.

shown in Table 4.1.3.6-1. The load P versus crack opening displacement COD and load P versus stroke displacement δ_s obtained in the tests are shown in Figs. 4.1.3.6-9 and 4.1.3.6-10, respectively. Both specimens fractured after the overall plastic deformation. The fracture loads were 5,836 kN at -100°C and 5,328 kN at -80°C. The P-δ_s curves exhibited a load drop prior to fracture in both cases.

Fracture surface photographs and SEM observation are shown in Figs. 4.1.3.6-11 and 4.1.3.6-12, respectively. Due to the fatigue pre-cracking procedure, the surface flaw shape was arc-shaped rather than semi-elliptical.

At -100°C, no significant plastic deformation was observed on the specimen surface. The flawed cross section decreased by 2–3%. SEM observations confirmed cleavage fracture occurred after formation of a micro stretch zone.

At -80°C, similarly, no significant plastic deformation was observed on the specimen surface, and the area reduction of the flawed cross section was about 3%, comparable to -100°C. However, about 50 μm of ductile crack growth was confirmed at -80°C, followed by cleavage fracture.

From SE(B) test results, the initial estimate was that the T_1 temperature for the surface flawed flat plate test was -80°C. However, since slight ductile crack growth was confirmed in the preliminary test at -80°C and a micro stretch zone was also present at -100°C, the test temperature for T_1 shifted to the lower temperature of -120°C.

Also, in the preliminary test at -80°C, brittle fracture after slight ductile crack growth was confirmed, so -80°C was selected as the T_2 temperature.

b. Main tests

Based on the preliminary test results, the main test temperatures were set at -80°C as the test temperature for brittle fracture after ductile crack growth and at -120°C as the brittle fracture test temperature. Additionally room temperature was included as the ductile fracture temperature, resulting in three test temperatures.

A summary of the test results is shown in Table 4.1.3.6-2. Twelve fracture tests were performed: one at room temperature (15°C), five at -80°C, and six at -120°C. Of the six tests at -120°C, two specimens (IDs: A24UFP-B11 and A24LFP-T11) were performed performed additionally to acquire detailed data on displacement and temperature distribution of the test specimen during the test.

Load versus crack opening displacement is shown in Fig. 4.1.3.6-13, and load versus stroke displacement is shown in Fig. 4.1.3.6-14. Fracture surface photographs after the test are shown in Fig.

Copyright © 2026 The Japan Welding Engineering Society, All Rights Reserved.

4.1.3.6-15.

At room temperature, crack opening displacement exceeded the upper limit of the clip gauge of 7 mm, and as shown in Fig. 4.1.3.6-15 (1/12), ductile fracture occurred from the flawed section after significant necking.

At -80°C, one of five specimens (A15LFP-T4) fractured by ductile fracture from a location other than the flaw, as shown in Fig. 4.1.3.6-15 (2/12). For this specimen, the flaw vicinity was extracted post-test, subjected to thermal etching, cooled by liquid nitrogen, and the fracture surface was opened for detailed observation of ductile crack growth. The other four specimens fractured brittle from the flaw, as shown in Figs. 4.1.3.6-15 (3/10) to (6/12).

At -120°C, all six specimens fractured in brittle manner from the flaw, as shown in Figs. 4.1.3.6-15 (7/12) to (12/12).

Representative SEM fracture surface observation are shown in Fig. 4.1.3.6-16. At -80°C, ductile crack growth was confirmed to varying degrees among the specimen. At -120°C, fatigue pre-crack and cleavage fracture surfaces were adjacent with no ductile crack growth observed. These results confirmed that the target fracture mode were successfully achieved.

Fig. 4.1.3.6-17 shows the relationship between test temperature and K_{Jc}. The figure also shows K_{Jc} obtained from C(T) specimens and SE(B) specimens (a/W = 0.5 and 0.1). K_{Jc} obtained from the flat plate tensile test was larger than those from C(T) and SE(B) specimens (a/W = 0.5), confirming the effect of smaller plastic constraint at the crack tip.

Copyright © 2026 The Japan Welding Engineering Society, All Rights Reserved.

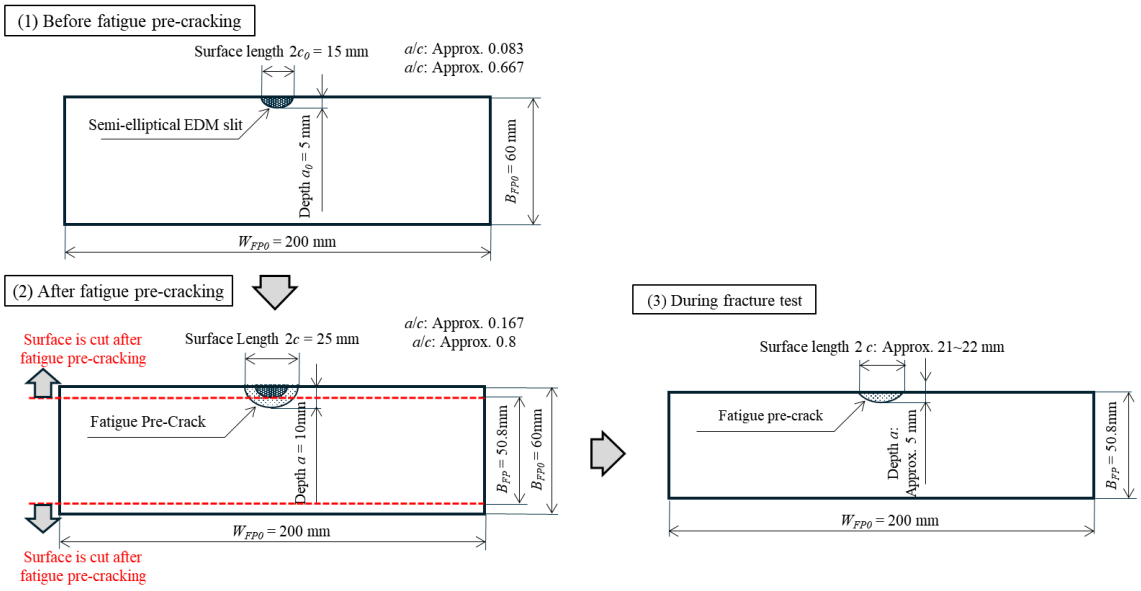


Fig. 4.1.3.6-1 Fatigue pre-crack introduction procedure for flat plate specimen

(tensile load and bending load)

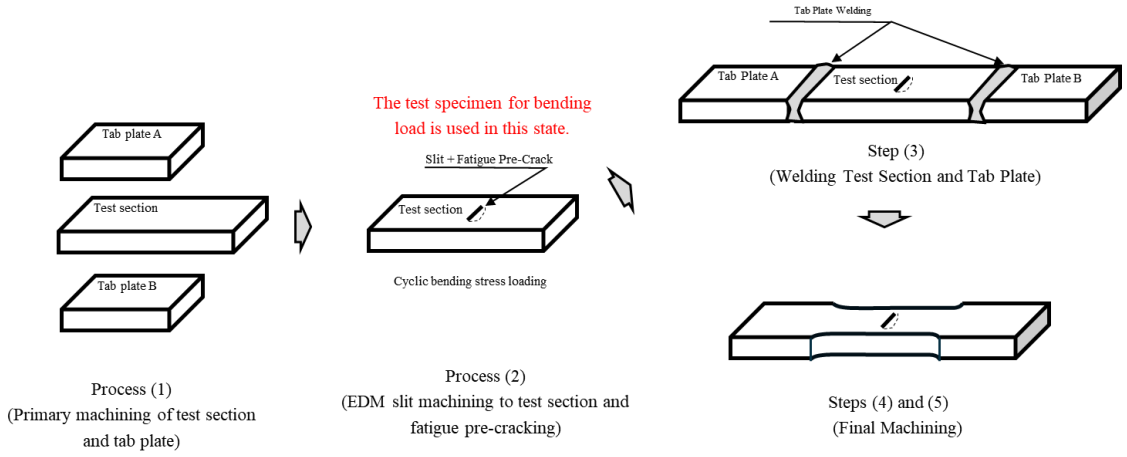
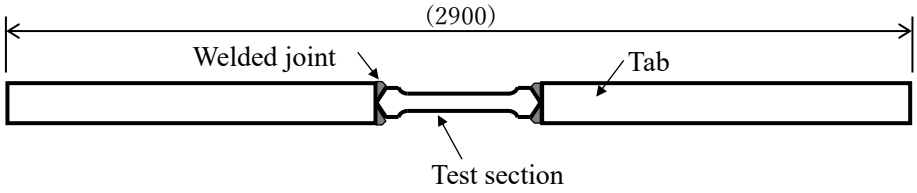
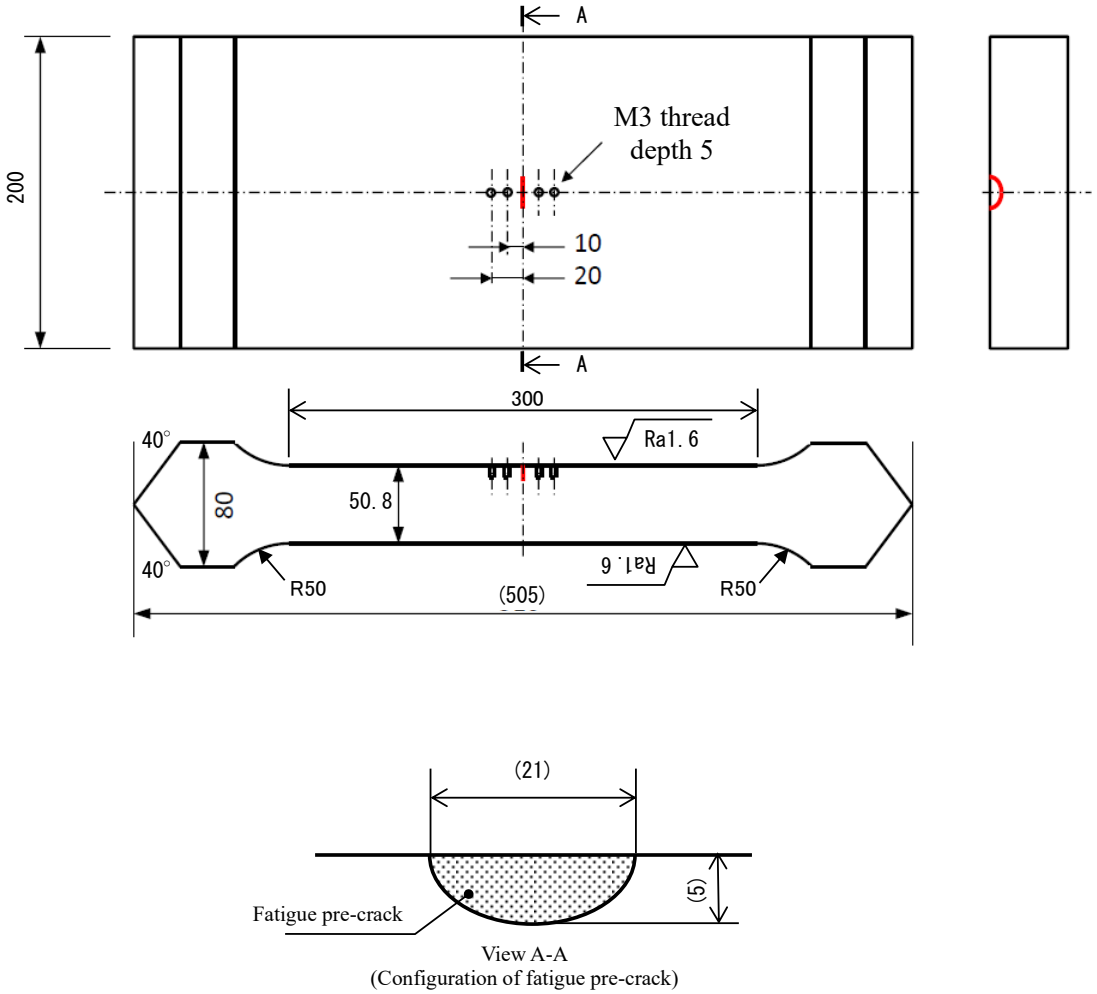


Fig. 4.1.3.6-2 Production procedure for flat plate specimen with surface flaw under tensile load

Copyright © 2026 The Japan Welding Engineering Society, All Rights Reserved.



(a) Overall configuration including tab



(b) Detail around test section

Unit: mm

Fig. 4.1.3.6-3 Geometry of flat plate specimen with surface flaw under tensile load

Copyright © 2026 The Japan Welding Engineering Society, All Rights Reserved.

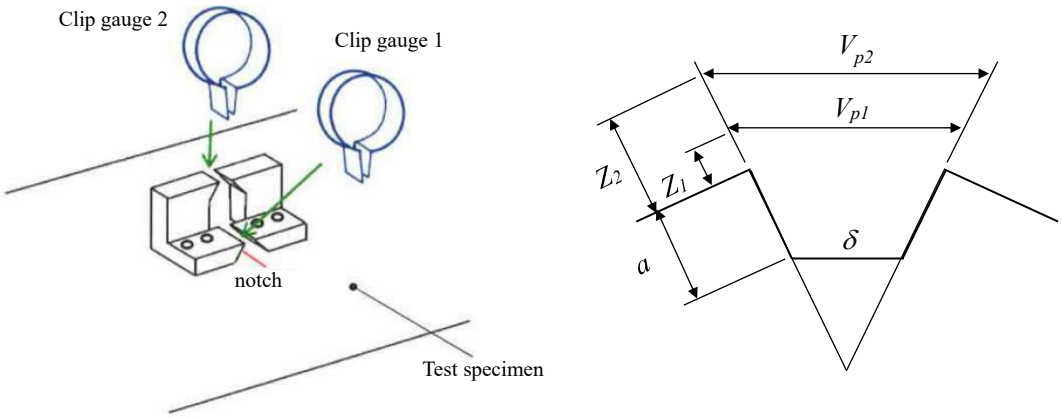
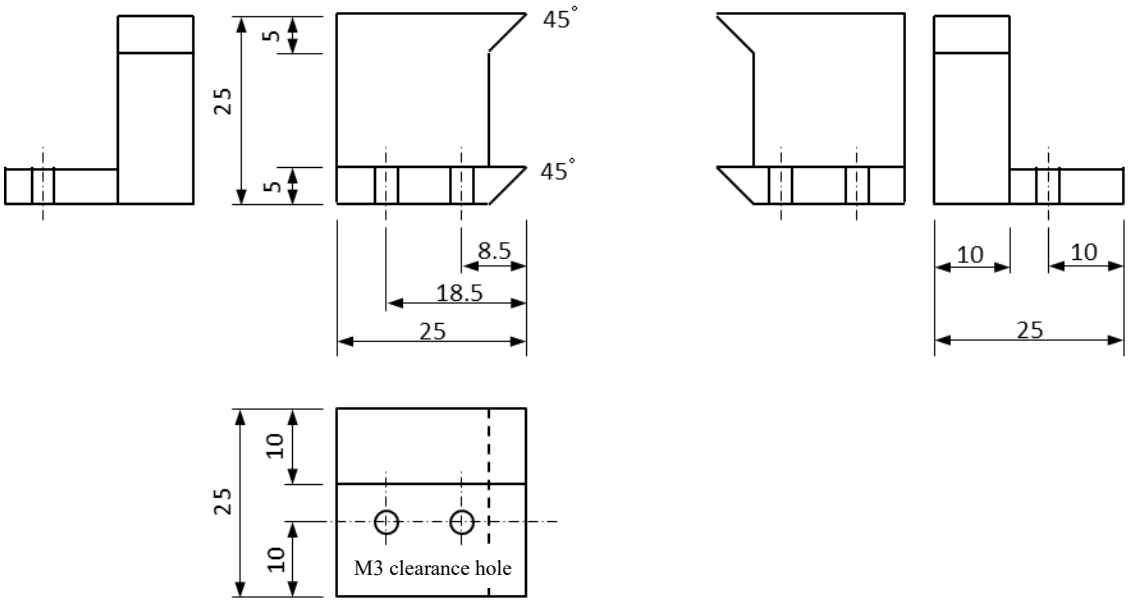


Fig. 4.1.3.6-4 Measurement image of crack opening displacement by double clip gauge method



Unit: mm

Fig. 4.1.3.6-5 Geometry of knife edge (tensile load and bending load)

Copyright © 2026 The Japan Welding Engineering Society, All Rights Reserved.

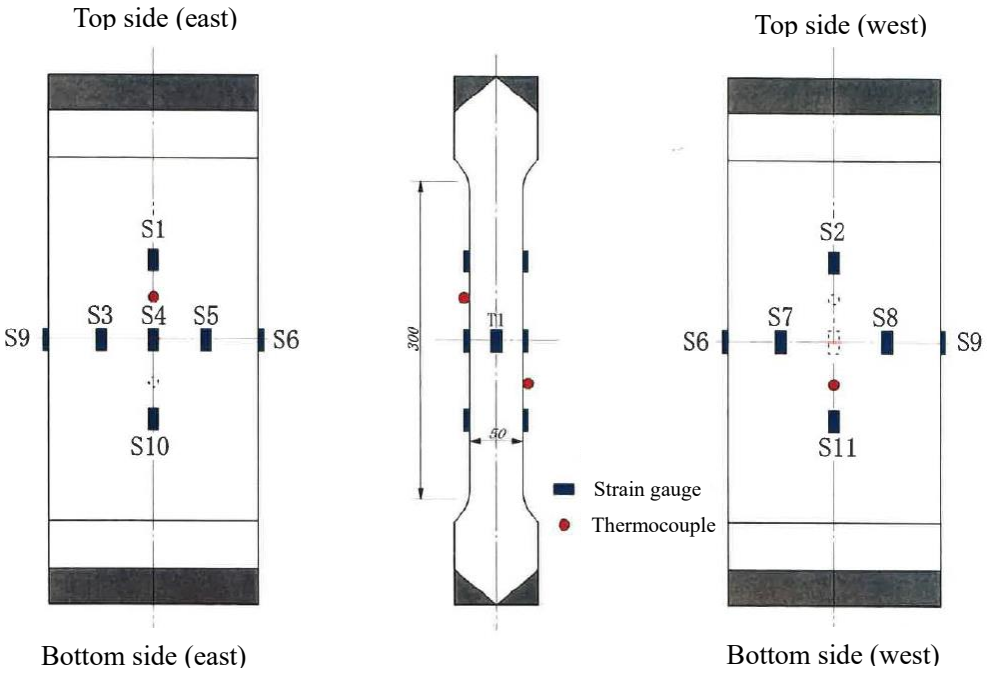


Fig. 4.1.3.6-6 Location of thermocouples and strain gauges

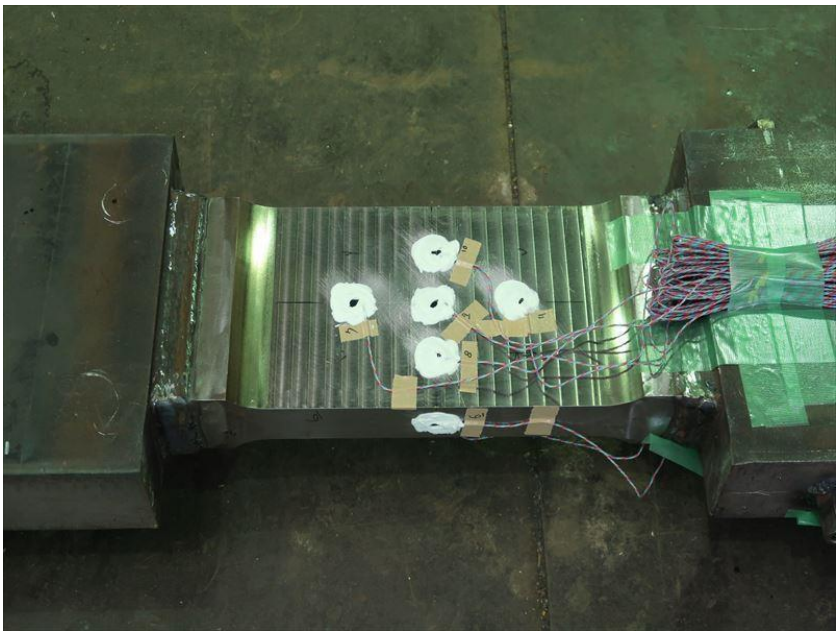
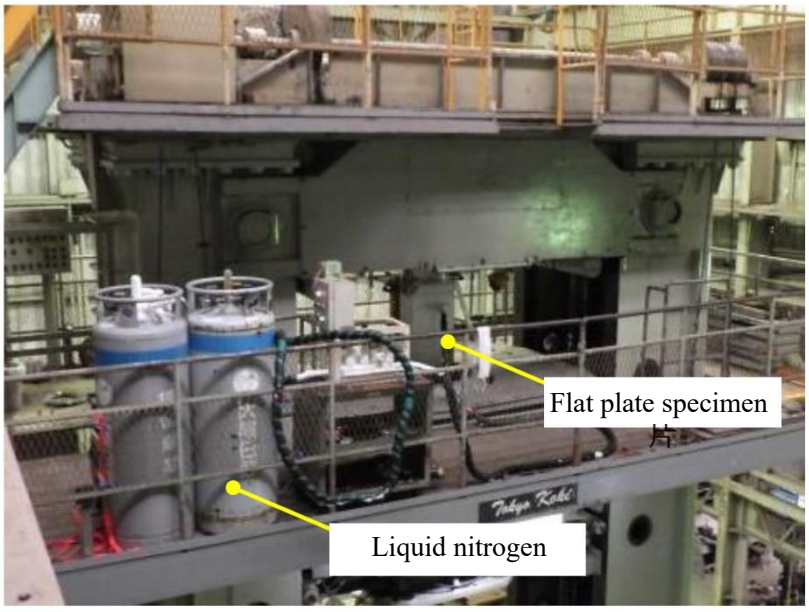


Fig. 4.1.3.6-7 Appearance of flat plate specimen with surface flaw under tensile load

Copyright © 2026 The Japan Welding Engineering Society, All Rights Reserved.



(a) Overall view of test machine



(b) Enlargement of test section

Fig. 4.1.3.6-8 Setup of flat plate specimen with surface flaw subjected by tensile load

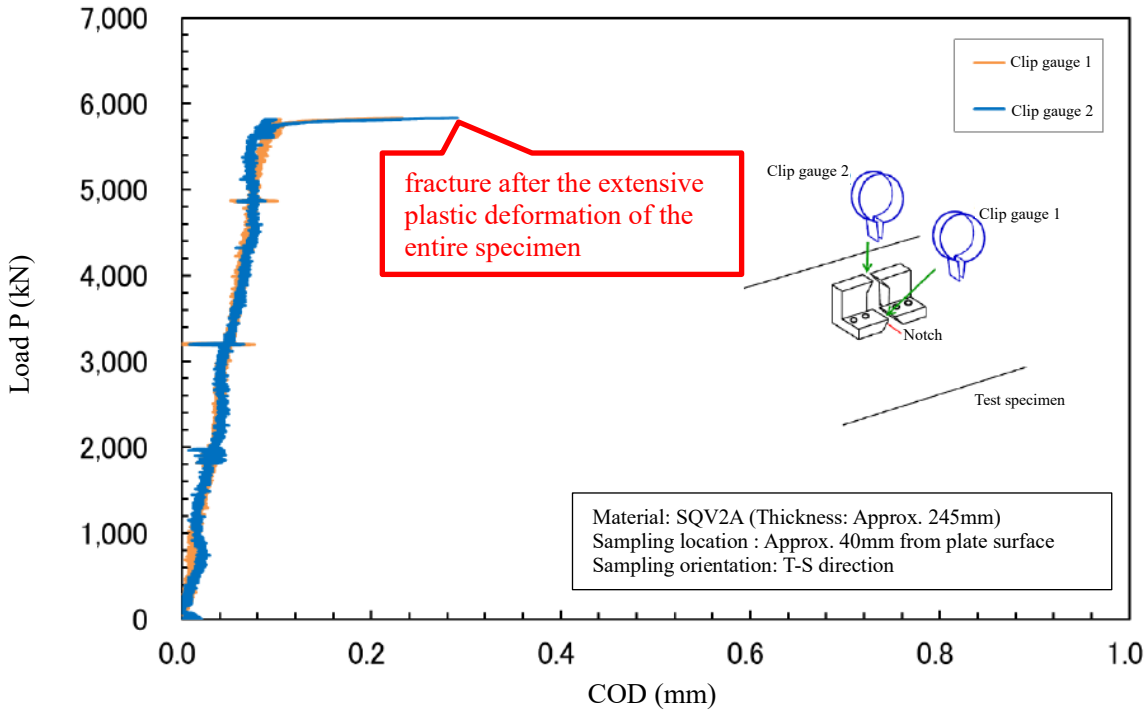
Copyright © 2026 The Japan Welding Engineering Society, All Rights Reserved.

Table 4.1.3.6-1 Preliminary test result of flat plate specimen with surface flaw under tensile load

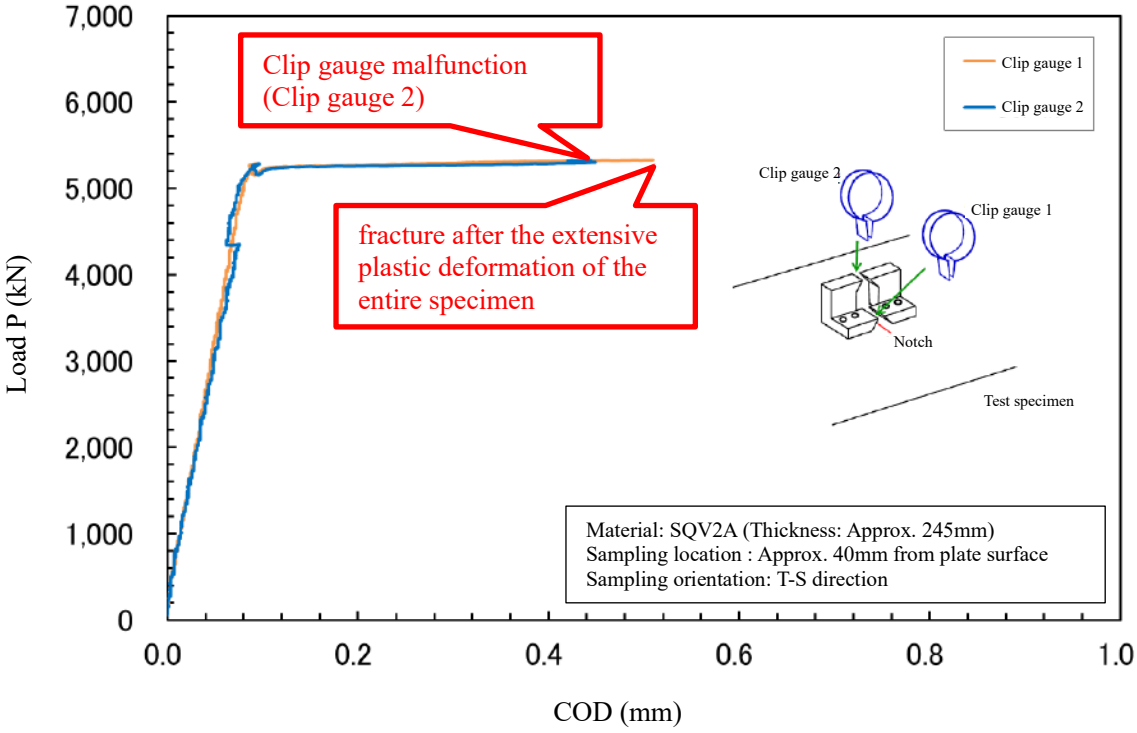
Specimen ID	Test temperature (°C)	Fracture mode *1	Plate width W (mm)	Plate thickness B (mm)	Precrack depth a_0 (mm)	Precrack surface length $2c$ (mm)	Ductile crack growth (mm)	Fracture load (kN)	COD1 at fracture (mm)	COD2 at fracture (mm)	Stroke displacement at fracture (mm)	Test temperature at fracture (°C)
A11LFP-T-1	-80	DB	200	50.8	5.18	21.4	0.05	5328	0.50	0.44	13.19	-81.5
A11UFP-T-1	-100	B	200	50.8	5.23	21.2	0.00	5836	0.23	0.28	16.90	-102.4

*1 DB: brittle fracture after ductile crack growth, B: brittle fracture

Copyright © 2026 The Japan Welding Engineering Society, All Rights Reserved.



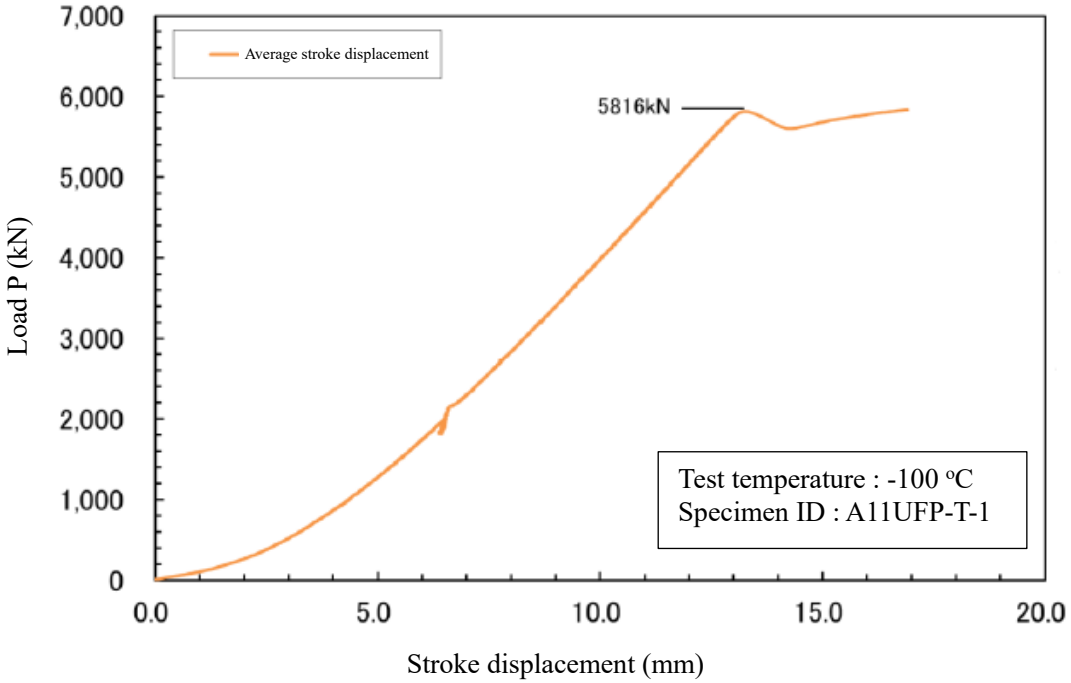
(a) -100°C



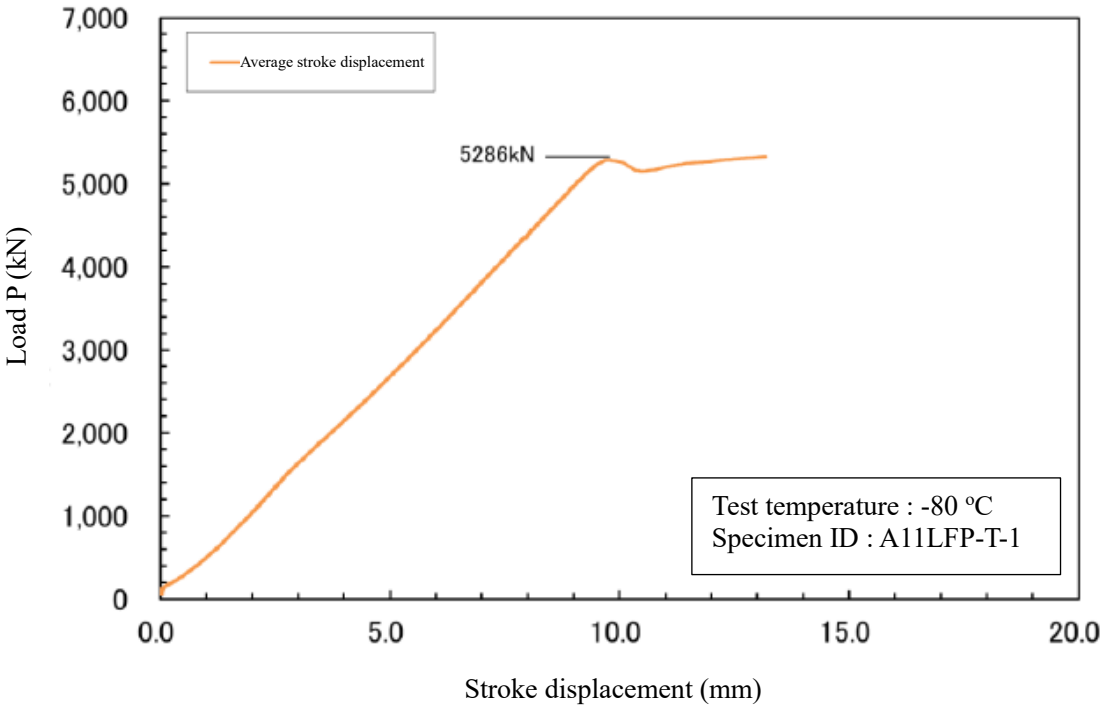
(b) -80°C

Fig. 4.1.3.6-9 Load *P- COD* curve (flat plate specimen under tensile load by pretest)

Copyright © 2026 The Japan Welding Engineering Society, All Rights Reserved.



(a) -100ºC



(b) -80ºC

Fig. 4.1.3.6-10 Load P - stroke displacement δ_s curve

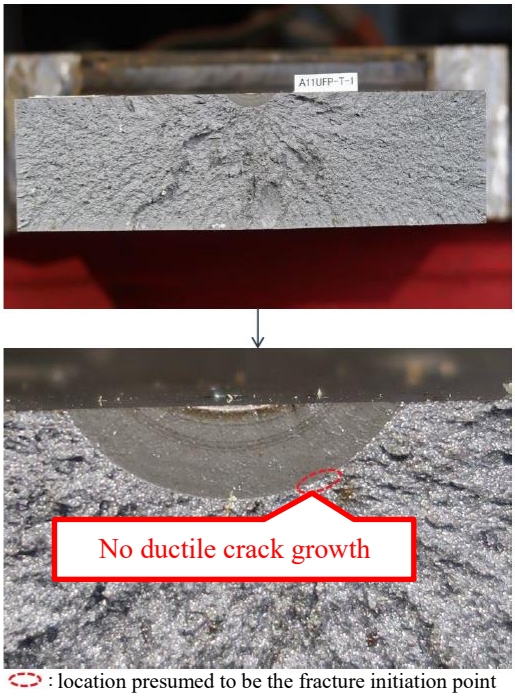
(flat plate specimen under tensile load by pretest)

Copyright © 2026 The Japan Welding Engineering Society, All Rights Reserved.

Specimen appearance



Fracture surface appearance



: location presumed to be the fracture initiation point

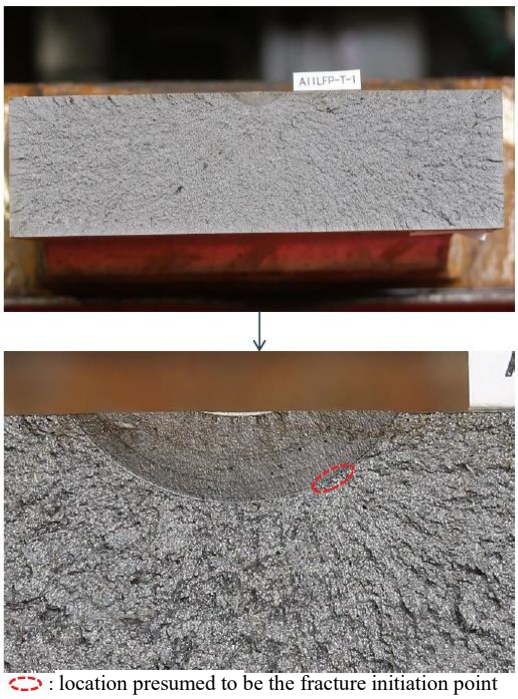
- No significant plastic deformation was observed.
- The cross-sectional area of the fracture surface had decreased by 2 to 3%.
- No ductile crack growth was observed at the front edge of the pre-crack.

(a) -100ºC

Specimen appearance



Fracture surface appearance



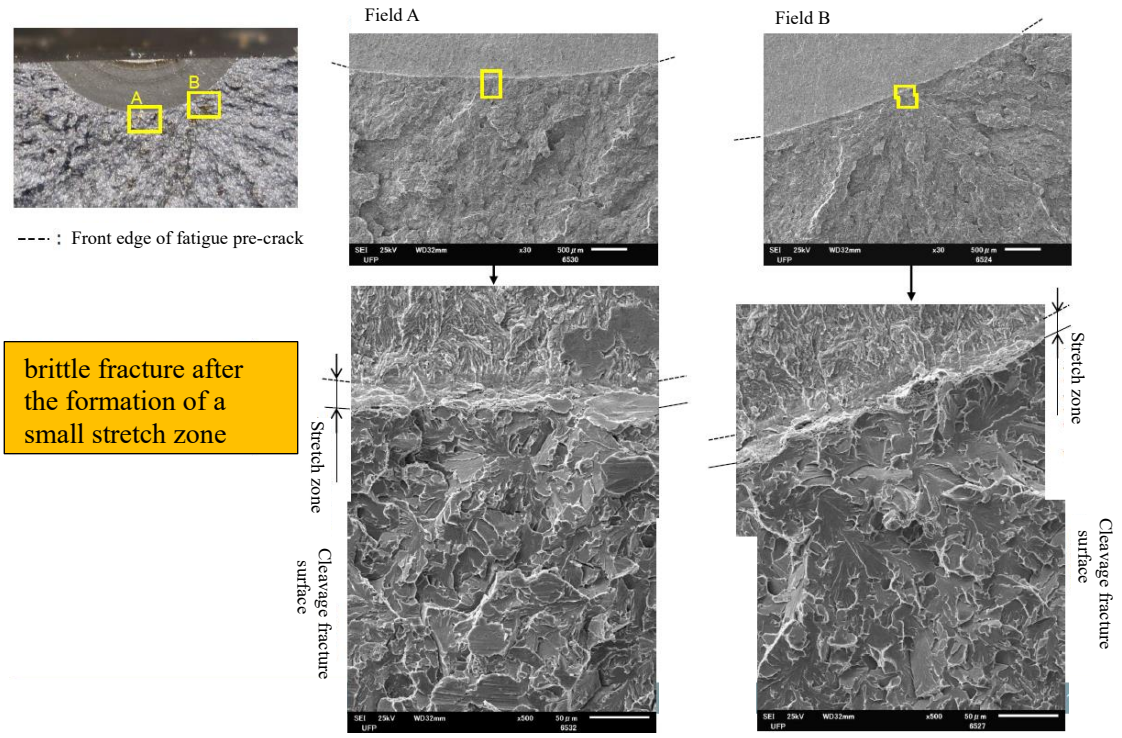
: location presumed to be the fracture initiation point

- No significant plastic deformation was observed.
- The cross-sectional area of the fracture surface had decreased by 3%.
- A small area suspected to be ductile crack growth was observed at the front edge of the pre-crack.

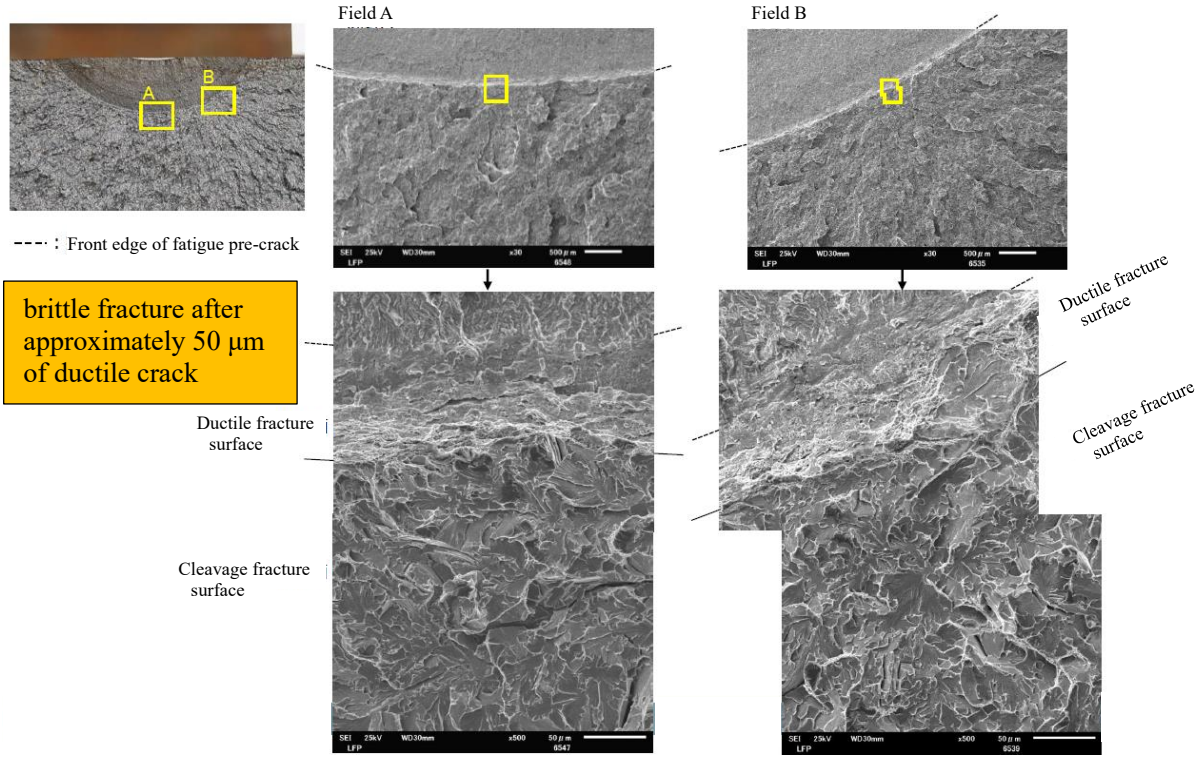
(b) -80ºC

Fig. 4.1.3.6-11 Fracture surface of flat plate specimen under tensile load by pretest

Copyright © 2026 The Japan Welding Engineering Society, All Rights Reserved.



(a) -100°C



(b) -80°C

Fig. 4.1.3.6-12 SEM observation of fracture surface of flat plate specimen under tensile load by pretest

Copyright © 2026 The Japan Welding Engineering Society, All Rights Reserved.

Copyright © 2026 The Japan Welding Engineering Society, All Rights Reserved.

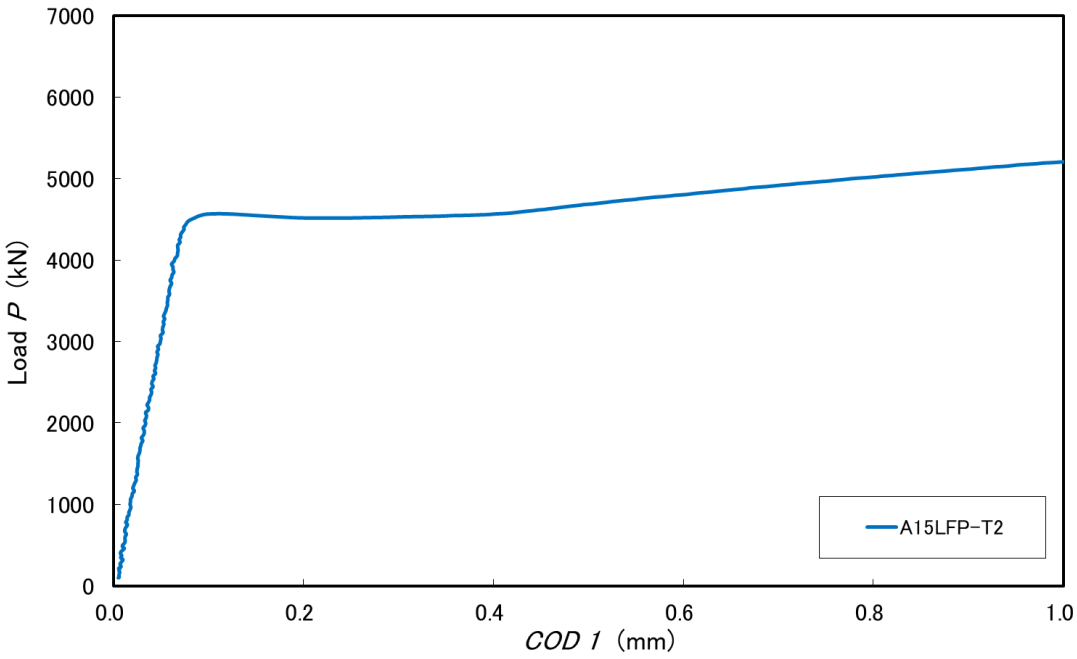
Table 4.1.3.6-2 Result of flat plate specimen with surface flaw under tensile load

Specimen ID	Test temperature (℃)	Fracture mode *1	Plate width W (mm)	Plate thickness B (mm)	Precrack depth a_0 (mm)	Precrack surface length $2c$ (mm)	Ductile crack growth (mm)	Fracture load (kN)	COD1 at fracture (mm)	COD2 at fracture (mm)	Stroke displacement at fracture (mm)	Test temperature at fracture (℃)	K_{Jc} (MP$\sqrt{}$m)
A15LFP-T2	Room Temperature	D	200	50.8	4.83	18.2	(Not Measurable)	5147	(Not Measurable)	(Not Measurable)	(Not Measurable)	15	(Not Measurable)
A15LFP-T4*2	-80	(Not fractured)	200	50.8	5.32	19.3	2.59	5158	(Not Measurable)	(Not Measurable)	(Not Measurable)	(Not fractured)	(Not fractured)
A15UFP-T3	-80	DB	200	50.8	4.72	21.3	0.13	5515	0.77	0.82	15.62	-82.5	229
A21UFP-T5	-80	DB	200	50.8	5.10	21.5	0.07	5178	0.44	0.46	12.43	-77.4	188
A21UFP-T7	-80	DB	200	50.8	4.85	20.9	0.08	5393	0.64	0.65	14.15	-92.3	212
A23UFP-T9	-80	DB	200	50.8	5.04	21.2	0.04	5385	0.31	0.60	12.16	-86.5	169
A15UFP-T1	-120	B	200	50.8	4.54	20.6	0.00	6001	0.29	0.35	15.70	-123.2	196
A21LFP-T6	-120	B	200	50.8	4.84	20.8	0.00	6112	0.18	0.25	14.18	-121.9	115
A21LFP-T8	-120	B	200	50.8	4.68	20.7	0.00	6090	0.30	0.46	14.51	-126.8	135
A23LFP-T10	-120	B	200	50.8	5.25	21.4	0.00	6173	0.15	0.23	14.25	-128.7	135
A24UFP-B11※3	-120	B	200	50.8	4.67	21.7	0.00	6032	0.24	0.47	17.36	-120.6	149
A24LFP-T11※3	-120	B	200	50.8	4.32	21.8	0.00	6043	0.25	-	14.56	-120.3	131

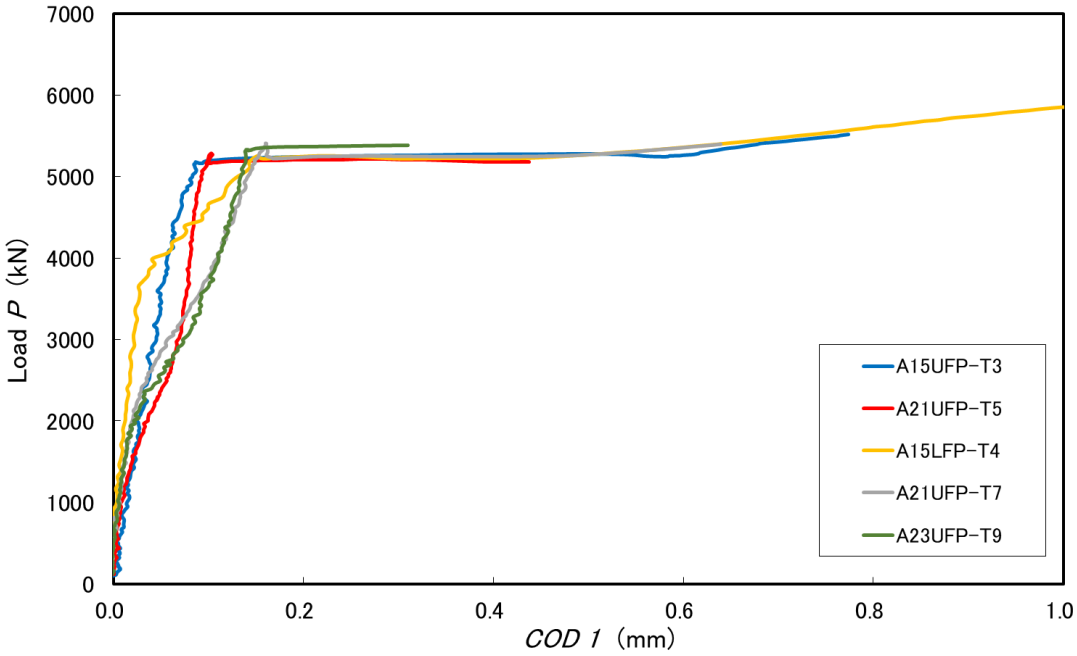
*1 D: Ductile fracture, DB: Brittle fracture after ductile crack propagation, B: Brittle fracture

*2 Fracture from areas other than cracks

*3 Additional tests



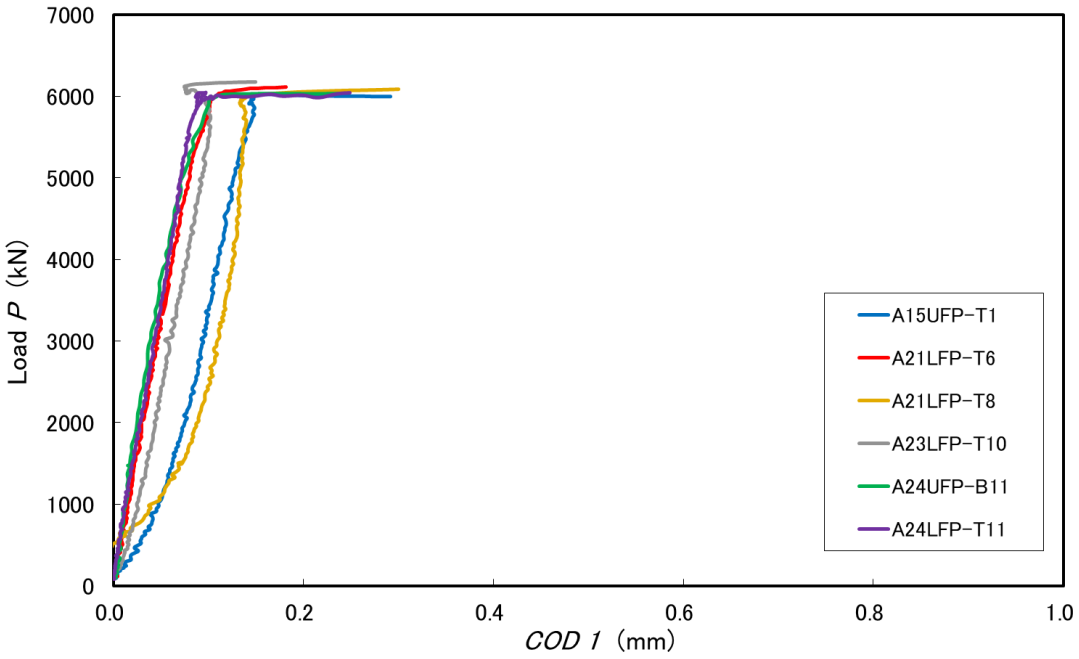
(a) Room temperature



(b) -80ºC

Fig. 4.1.3.6-13 *P-COD* curve of flat plate specimen with surface flaw under tensile load (1/2)

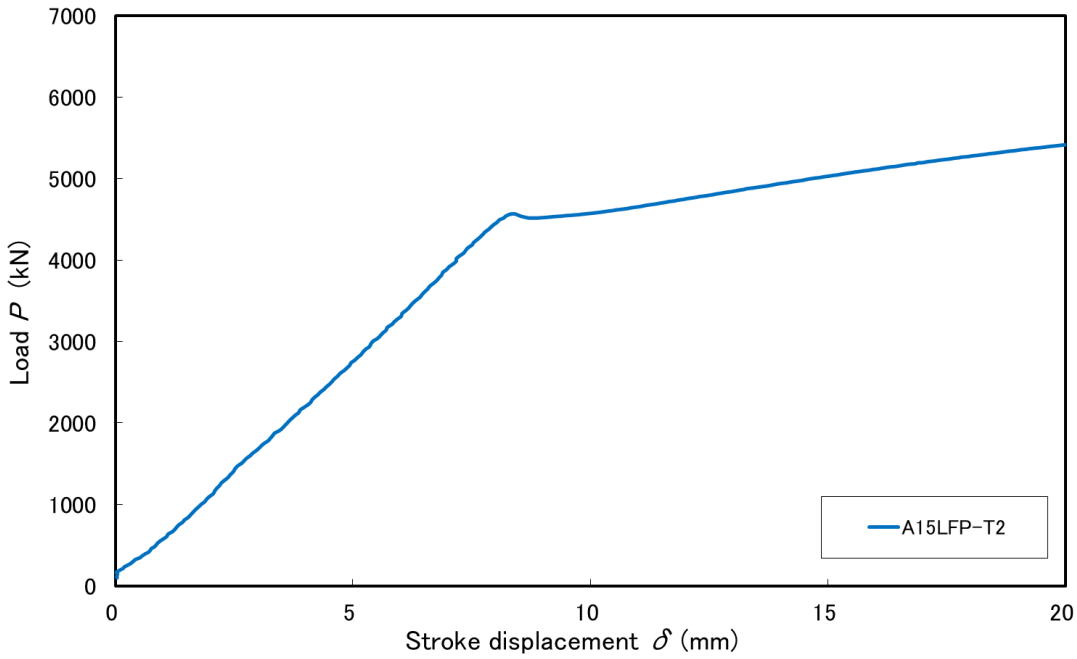
Copyright © 2026 The Japan Welding Engineering Society, All Rights Reserved.



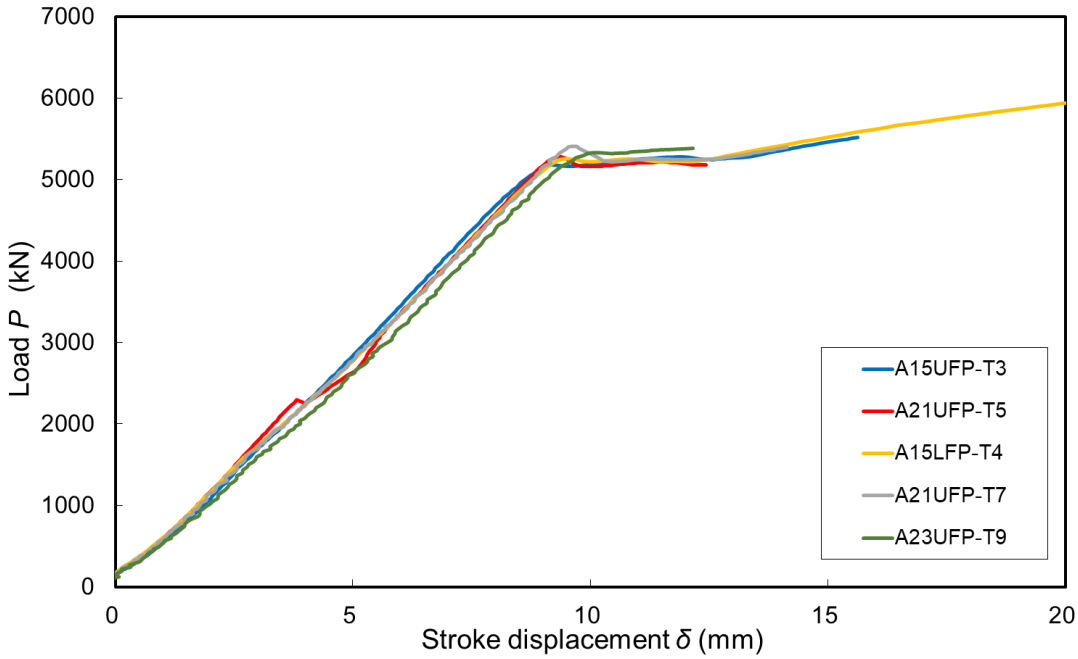
(c) -120°C

Fig. 4.1.3.6-13 *P-COD* curve of flat plate specimen with surface flaw under tensile load (2/2)

Copyright © 2026 The Japan Welding Engineering Society, All Rights Reserved.



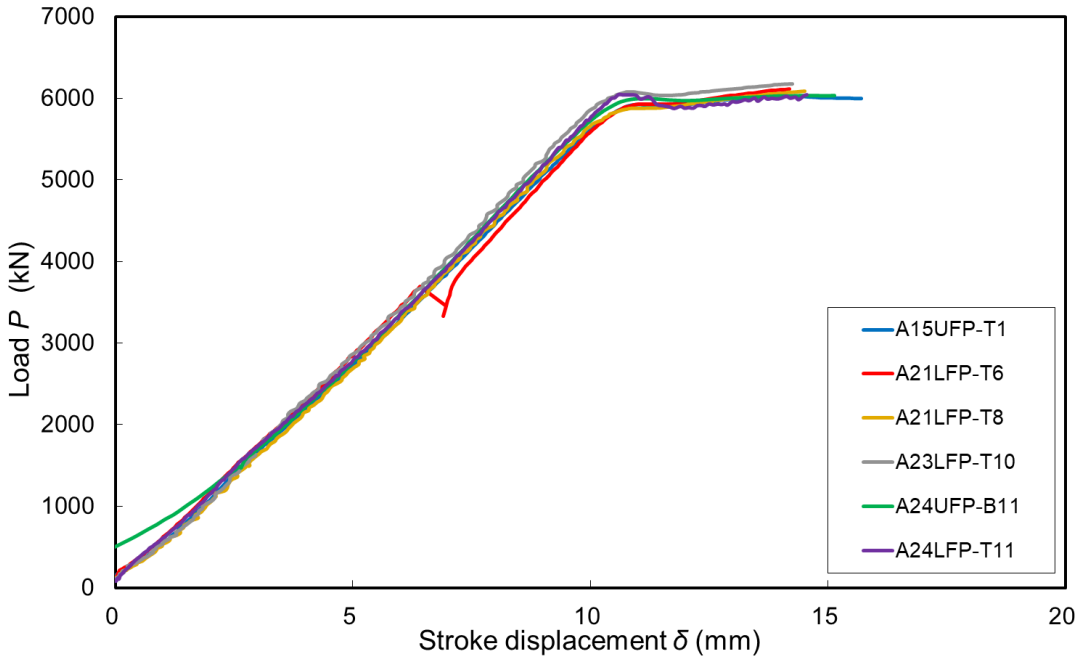
(a) Room temperature



(b) -80ºC

Fig. 4.1.3.6-14 *P*-Stroke displacement curve of flat plate specimen with surface flaw under tensile load (1/2)

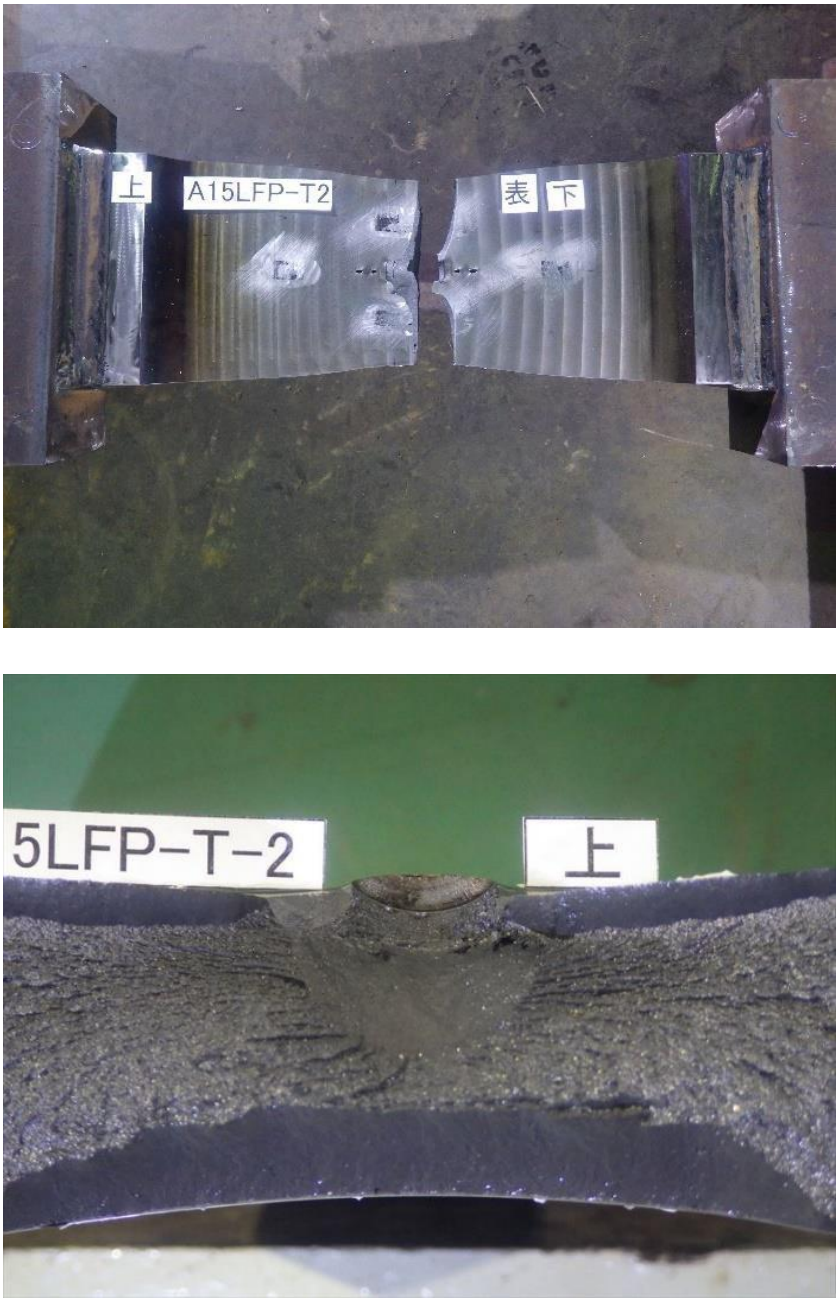
Copyright © 2026 The Japan Welding Engineering Society, All Rights Reserved.



(c) -120°C

Fig. 4.1.3.6-14 *P*-Stroke displacement curve of flat plate specimen with surface flaw under tensile load (2/2)

Copyright © 2026 The Japan Welding Engineering Society, All Rights Reserved.

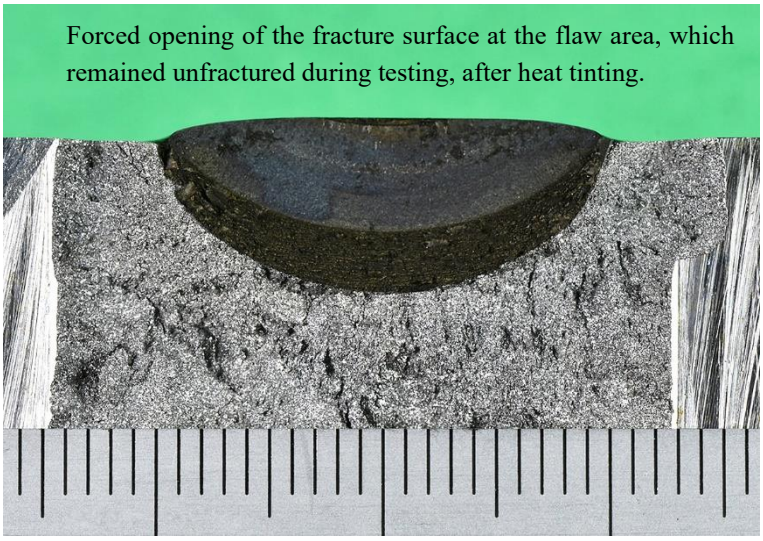


(a) Room temperature (A15LFP-T2)

Fig. 4.1.3.6-15 Fracture surface of flat plate specimen with surface flaw under tensile load (1/12)

Copyright © 2026 The Japan Welding Engineering Society, All Rights Reserved.

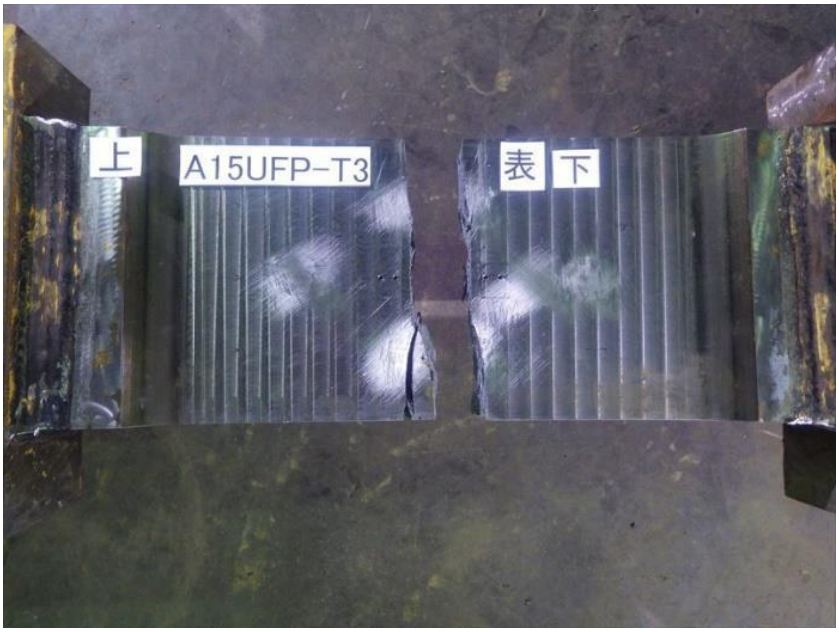


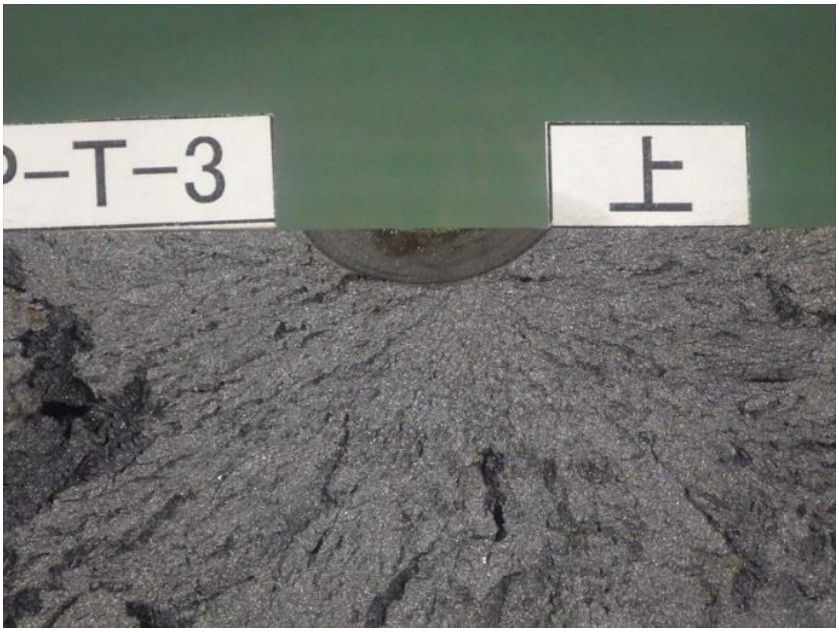


(b) -80°C (A15LFP-T4) (fracture occurred from a part other than flaw plane)

Fig. 4.1.3.6-15 Fracture surface of flat plate specimen with surface flaw under tensile load (2/12)

Copyright © 2026 The Japan Welding Engineering Society, All Rights Reserved.





(c) -80°C (A15UFP-T3)

Fig. 4.1.3.6-15 Fracture surface of flat plate specimen with surface flaw under tensile load (3/12)

Copyright © 2026 The Japan Welding Engineering Society, All Rights Reserved.





(d) -80ºC (A21UFP-T5)

Fig. 4.1.3.6-15 Fracture surface of flat plate specimen with surface flaw under tensile load (4/12)

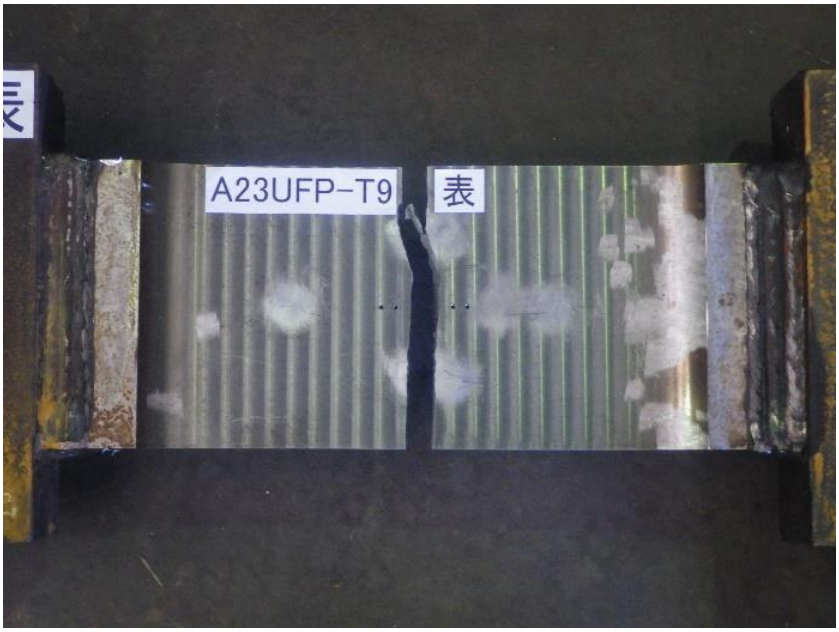
Copyright © 2026 The Japan Welding Engineering Society, All Rights Reserved.



(e) -80ºC (A21UFP-T7)

Fig. 4.1.3.6-15 Fracture surface of flat plate specimen with surface flaw under tensile load (5/12)

Copyright © 2026 The Japan Welding Engineering Society, All Rights Reserved.

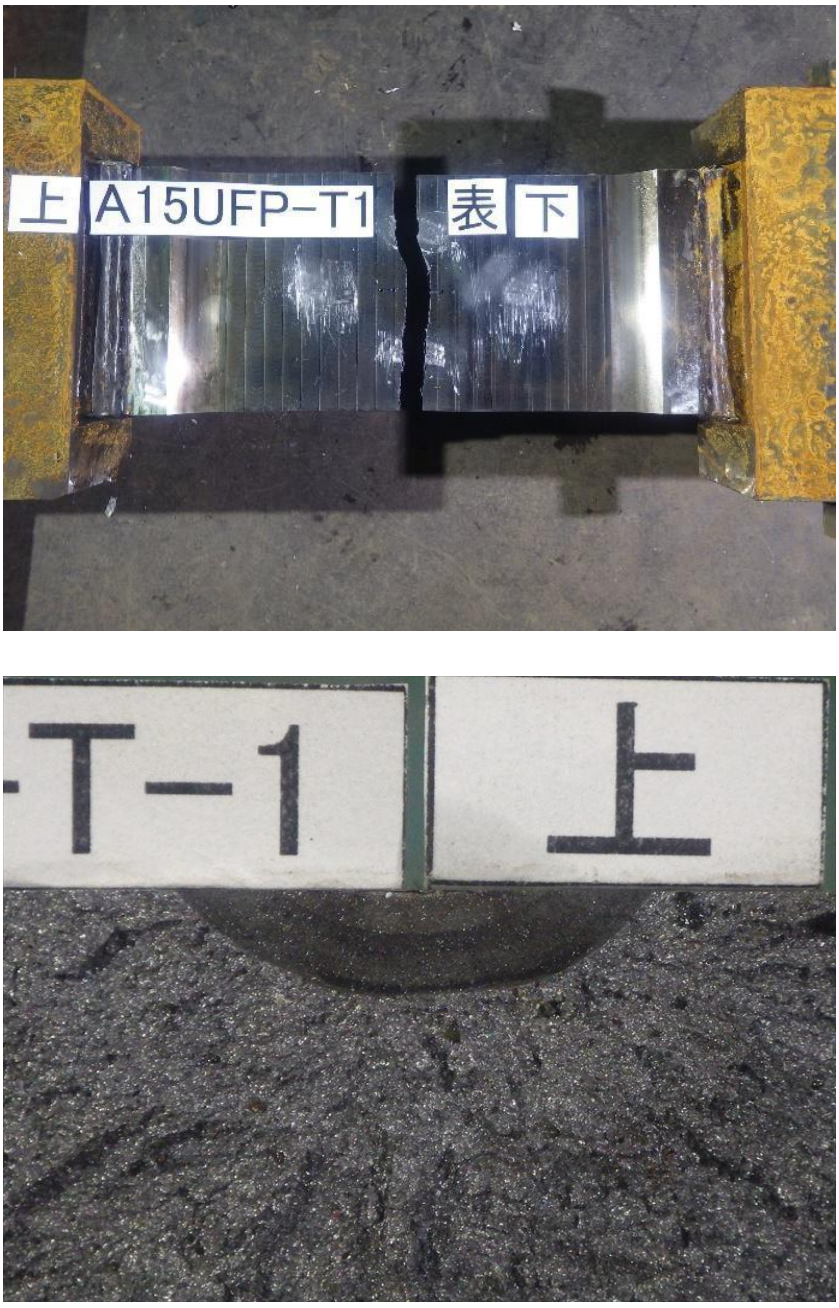




(f) -80°C (A23UFP-T9)

Fig. 4.1.3.6-15 Fracture surface of flat plate specimen with surface flaw under tensile load (6/12)

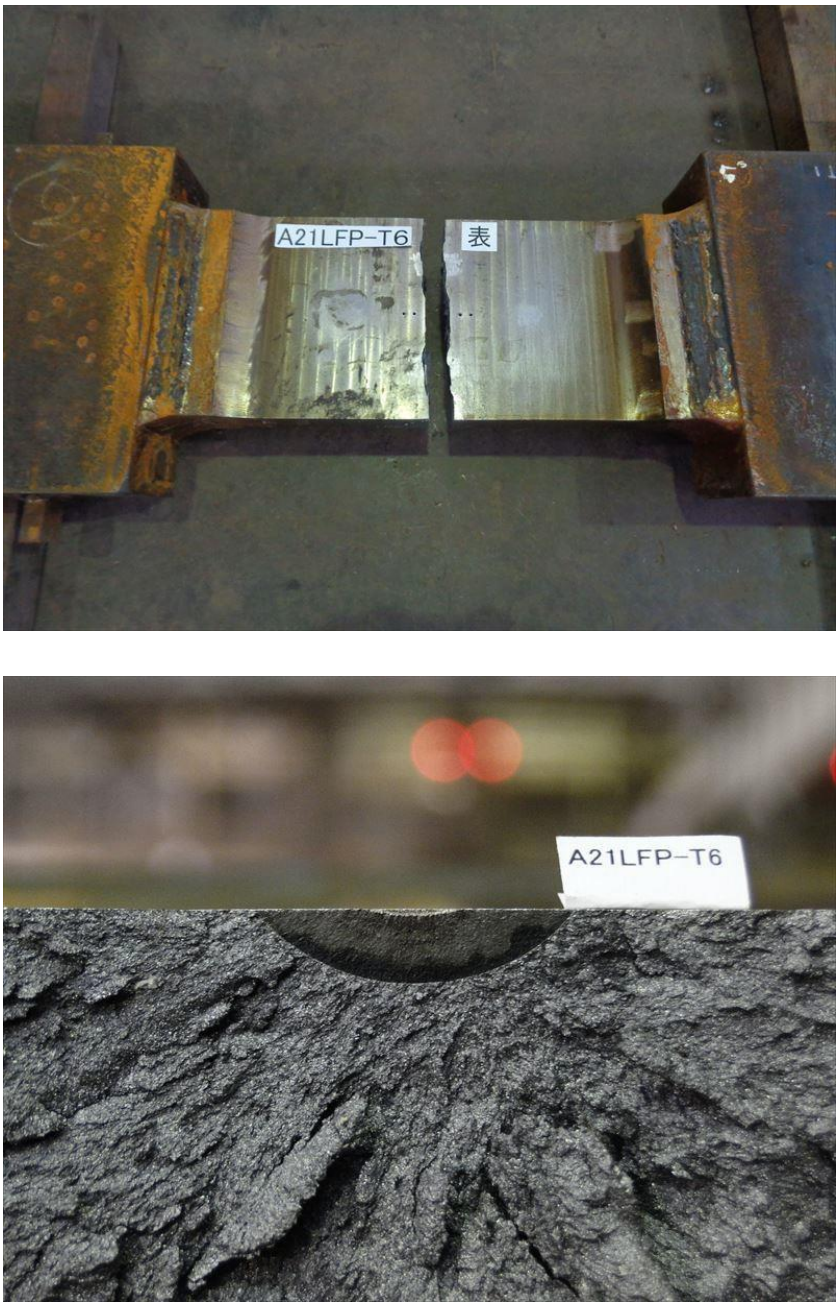
Copyright © 2026 The Japan Welding Engineering Society, All Rights Reserved.



(g) -120°C (A15UFP-T1)

Fig. 4.1.3.6-15 Fracture surface of flat plate specimen with surface flaw under tensile load (7/12)

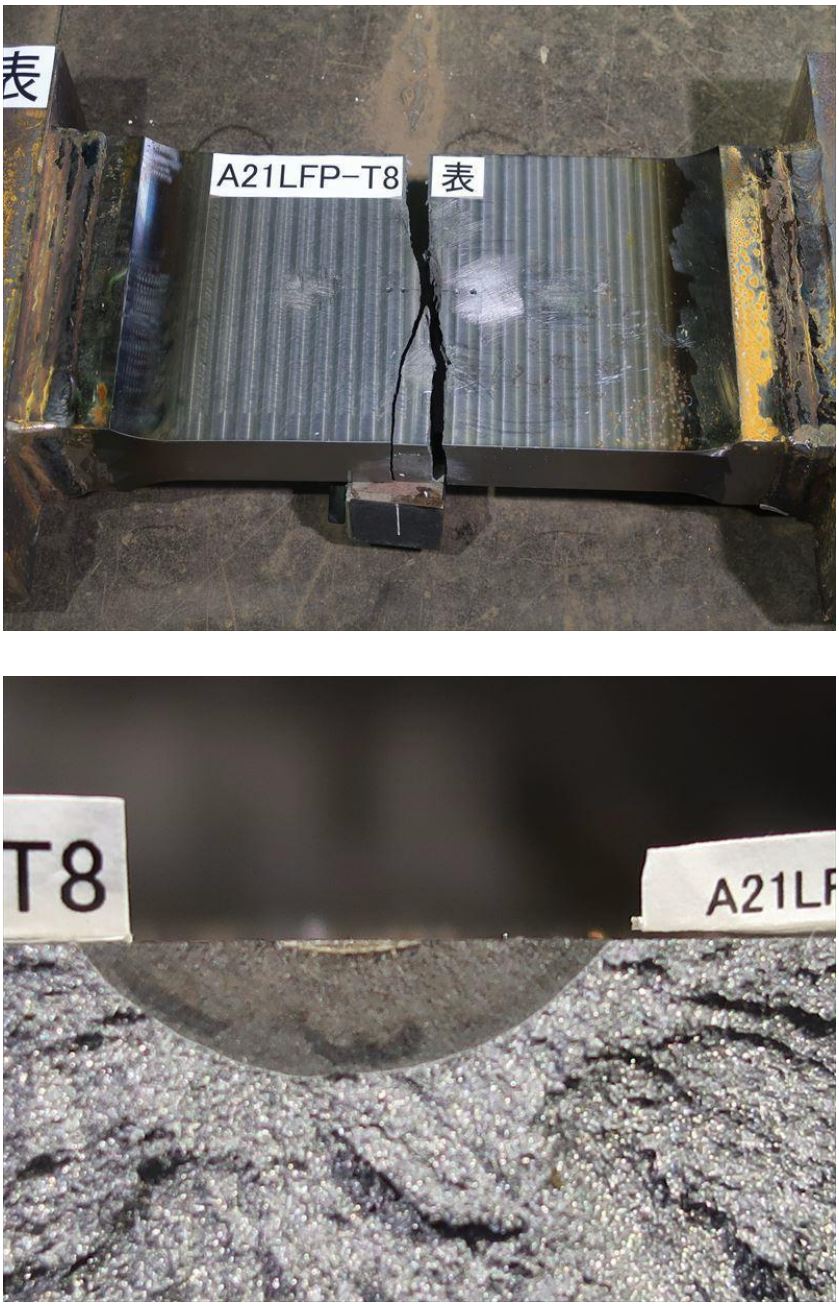
Copyright © 2026 The Japan Welding Engineering Society, All Rights Reserved.



(h) -120°C (A21LFP-T6)

Fig. 4.1.3.6-15 Fracture surface of flat plate specimen with surface flaw under tensile load (8/12)

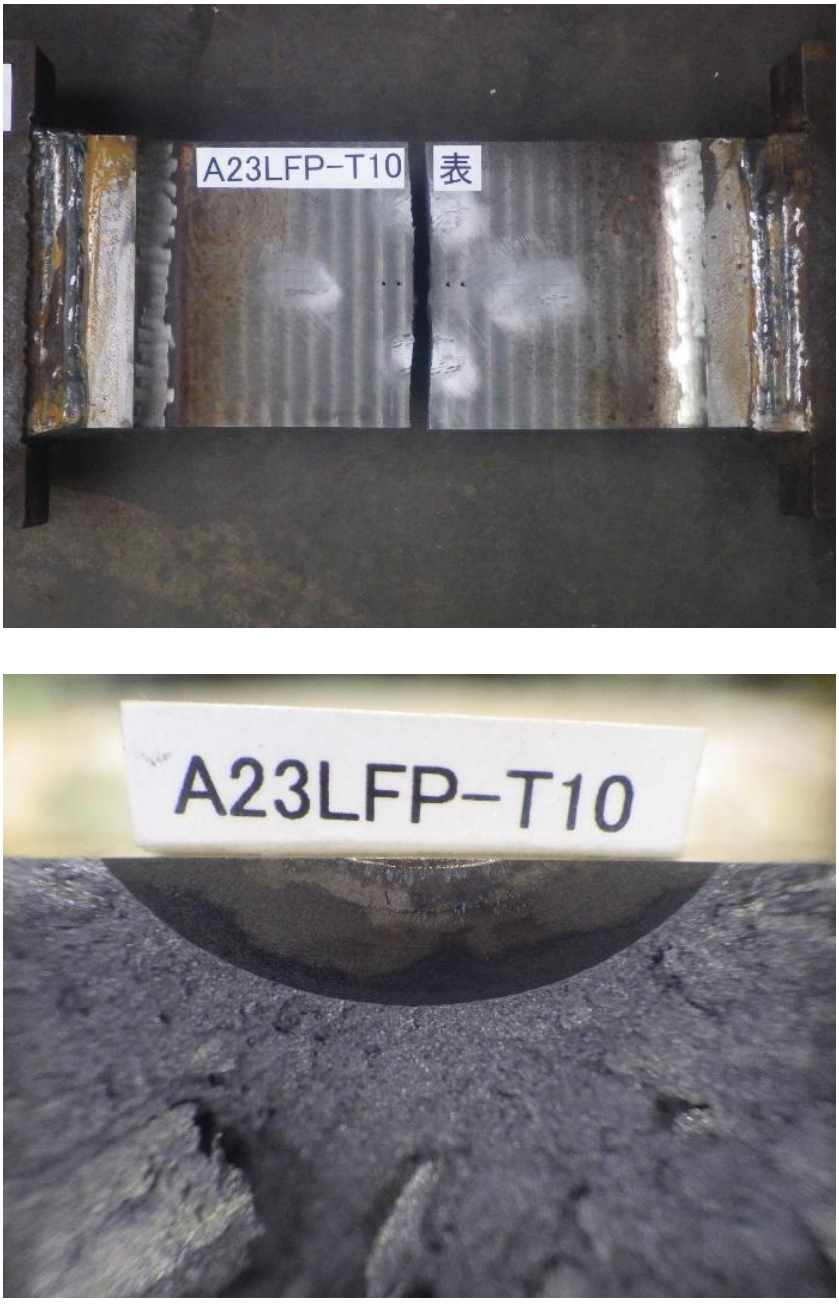
Copyright © 2026 The Japan Welding Engineering Society, All Rights Reserved.



(i) -120°C (A21LFP-T8)

Fig. 4.1.3.6-15 Fracture surface of flat plate specimen with surface flaw under tensile load (9/12)

Copyright © 2026 The Japan Welding Engineering Society, All Rights Reserved.



(j) -120°C (A23LFP-T10)

Fig. 4.1.3.6-15 Fracture surface of flat plate specimen with surface flaw under tensile load (10/12)

Copyright © 2026 The Japan Welding Engineering Society, All Rights Reserved.





Top side of fracture surface

Bottom side of fracture surface

(k) -120°C (A24UFP-B11)

Fig. 4.1.3.6-15 Fracture surface of flat plate specimen with surface flaw under tensile load (11/12)

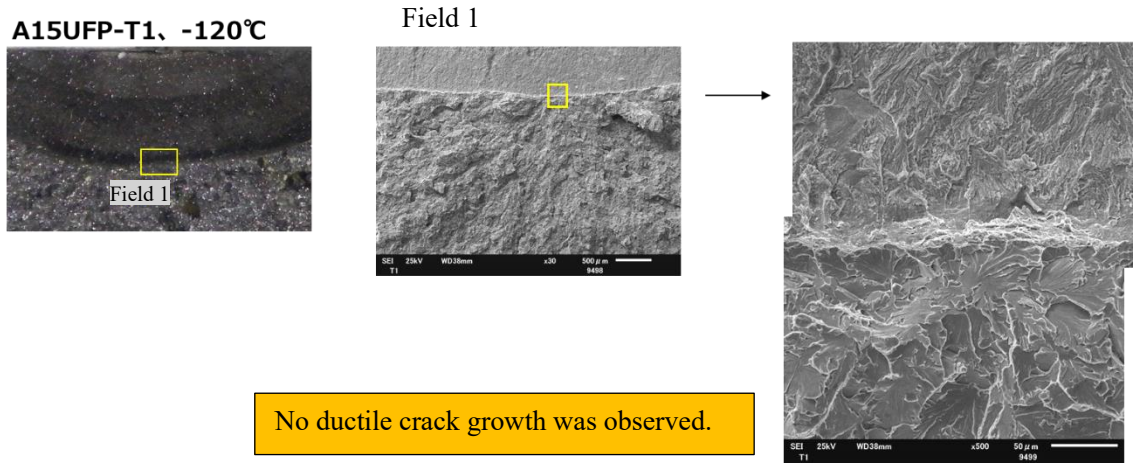
Copyright © 2026 The Japan Welding Engineering Society, All Rights Reserved.



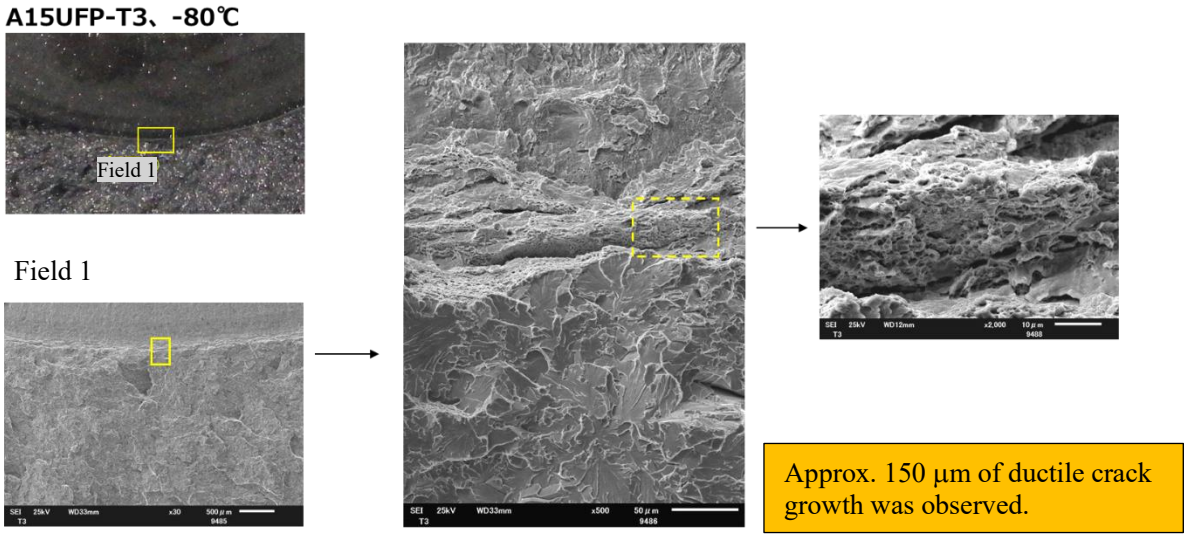
(l) -120ºC (A24LFP-T11)

Fig. 4.1.3.6-15 Fracture surface of flat plate specimen with surface flaw under tensile load (12/12)

Copyright © 2026 The Japan Welding Engineering Society, All Rights Reserved.



(a) -120°C



(b) -80°C

Fig. 4.1.3.6-16 SEM observation of fracture surface of flat plate specimen with surface flaw under tensile load

Copyright © 2026 The Japan Welding Engineering Society, All Rights Reserved.

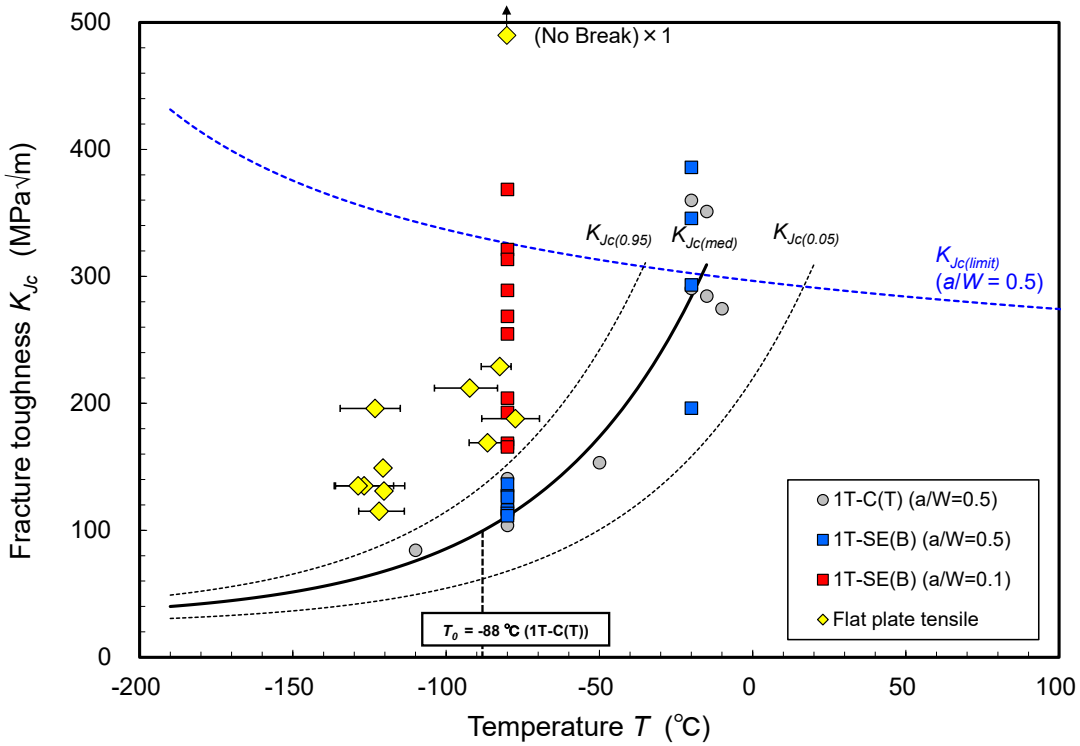


Fig. 4.1.3.6-17 Temperature dependence of K_{Jc} of flat plate specimen with surface flaw under tensile load and fracture toughness test specimens

Copyright © 2026 The Japan Welding Engineering Society, All Rights Reserved.

4.1.3.7 Preliminary and main test surface-flawed flat late bending specimens

Similar to the surface-flawed flat plate tensile specimens, fracture tests were performed using surface-flawed flat plate specimens subjected to bending loads with low plastic constraint.

(1) Test specimens

The test specimens were taken from the same low alloy steel B as the tensile specimens. An EDM slit approximately 5 mm deep was introduced into 60 mm thick base material, and a fatigue pre-crack of about 5 mm was propagated. Subsequently, the specimen surface was machined so that only a fatigue pre-crack with an approximate surface length of 21 mm and a depth of 5 mm remained.

Fig. 4.1.3.7-1 shows the final shape of the surface flawed plate bending test specimen. The specimens were taken from both the back and front surfaces of the steel plate so that the crack tip was located approximately 40 mm from the steel surface.

(2) Test method

Fracture tests were performed by applying four-point bending loads to flat specimens of 200 mm width, thickness 50.8 mm, with a shallow fatigue flaw approximately 5 mm deep. The test conditions are as follows:

- Test method: four-point bending load
- Control method: displacement control
- Test speed: 0.01 mm/s
- Holding time: at least 30 minutes after reaching the test temperature
- Applicable standard: ASTM E2899-15 (complied with as much as possible)

The tests were performed under displacement control at a constant displacement rate and were terminated upon specimen fracture. Prior to testing, strain gauge outputs on the specimen were verified within the elastic region to ensure that the load was applied symmetrically on both sides of the flaw within 5%.

The test apparatus was an electro-hydraulic servo fatigue testing system with a capacity of ±10 MN. During testing, the specimens and jigs were enclosed within a thermostatic chamber and cooled to the target test temperature by liquid nitrogen spray. Figures 4.1.3.7-2 and 4.1.3.7-3 show the appearance of the testing machine, thermostatic chamber, and the specimen setup, respectively. Figure 4.1.3.7-4 shows the locations of strain gauges and thermocouples on the specimen. Six thermocouples

Copyright © 2026 The Japan Welding Engineering Society, All Rights Reserved.

were attached: four arranged circumferentially at a radius of 20 mm centered on the flaw, and two near the longitudinal ends of the specimen. Five strain gauges were attached: two on the flawed specimen surface three on the opposite surface.

Clip gauges were attached to the specimen to measure load-line displacement, acquiring the displacement difference of the loading jig. *COD* was measured at 5 mm and 25 mm from the specimen surface using knife-edges mounted on the specimen surface (refer to Fig. 4.1.3.6-5). Clip gauge installation is shown in Fig. 4.1.3.7-5. The position near the surface at 5 mm was designated as *COD*1, and the 25 mm position as *COD*2. In this study, *COD*1 was used as representative value for comparison with analysis results. The load-line displacement δ_L was measured by a clip gauge which was attached to a jig for measurement of load-line displacement.

(3) Test results

Based on the test matrix shown previously in Table 4.1.2-7, two preliminary tests and ten main tests were performed on plate specimens (bending load).

a. Preliminary Test Results

To determine the test temperature for the main test, preliminary bending tests on flat plate specimen with a surface flaw were performed at -100°C and -80°C. A summary of preliminary test results is shown in Table 4.1.3.7-1. The relationships between load *P* and *COD*, as well as load *P* and load-line displacement δ_L prior to fracture, are shown in Figs. 4.1.3.7-6 and 4.1.3.7-7, respectively. The displacement at -80°C was considerably larger than at -100°C. This is due to the large plastic deformation of the entire specimen at -80°C, as described later. The fracture loads were 895 kN at -100°C and 1,157 kN at -80°C.

Photographs of the fracture surface and SEM observation are shown in Figs. 4.1.3.7-8 and 4.1.3.7-9, respectively. At -100°C, no significant deformation of the specimen was observed, and fracture initiation was confirmed from the fatigue pre-crack. No ductile crack growth was observed at the fatigue crack tip. SEM observations revealed cleavage fracture following formation of a small stretch zone. In contrast, at -80°C, large plastic deformation was observed throughout the specimen. The fracture originated from the fatigue pre-crack, and about 1 mm of ductile crack growth was observed ahead of the pre-crack tip.

b. Main Test Results

Based on the preliminary test results, the main test temperatures were selected as T_1: -120°C and

Copyright © 2026 The Japan Welding Engineering Society, All Rights Reserved.

T_2: -80°C, and tests were performed on four specimens at -120°C and six specimens at -80°C, totaling ten tests. The test results are shown in Table 4.1.3.7-2.

Load P – COD curves at -120°C and -80°C are shown in Fig. 4.1.3.7-10, and load P – load line-displacement δ_L curves are shown in Fig. 4.1.3.7-11. Fracture loads ranged from approximately 907 to 973 kN at -120°C and from approximately 830 to 988 kN at -80°C. Some specimens at -80°C did not fracture.

Photographs of the tested specimens are shown in Fig. 4.1.3.7-12, and representative SEM fracture surface observation are shown in Fig. 4.1.3.7-13. Specimens tested at -120°C exhibited minimal plastic deformation, with cleavage fracture initiating from the fatigue pre-crack and no ductile crack growth observed at the pre-crack tip. At -80°C, although fracture also initiated from the fatigue pre-crack, slight plastic deformation was observed, and small region suggestive of ductile crack growth near the pre-crack tip were identified.

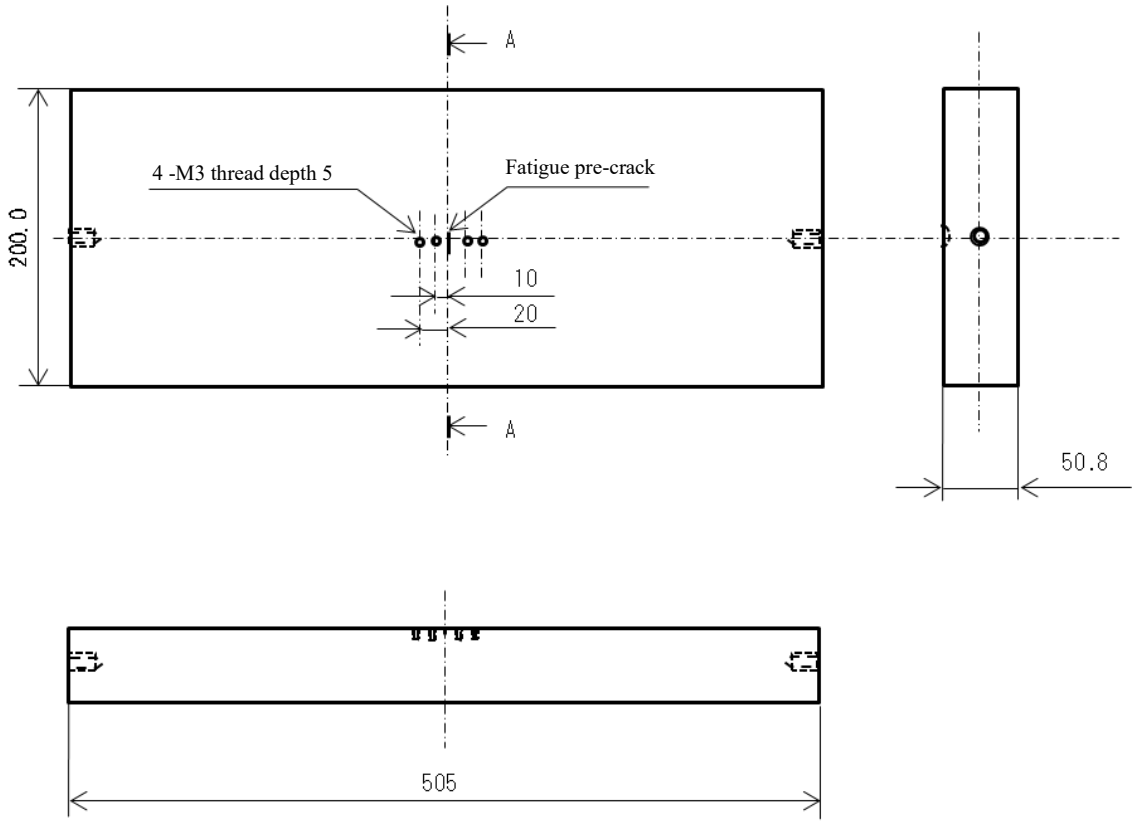
(4) Fracture toughness evaluation

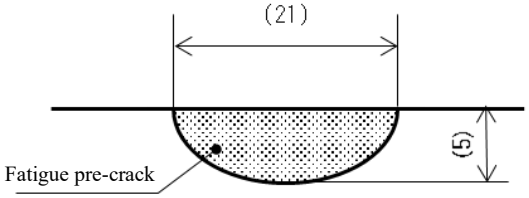
FE analyses were performed under the prescribed conditions to obtain the relationship between COD_1 and K_{Jc}. The K_{Jc} values calculated from COD_1 at fracture for each specimen are listed in Table 4.1.3.7-2. Details of the FE analysis are described in Section 4.3.

Figure 4.1.3.7-14 compares the temperature dependence of K_{Jc} for surface-flawed flat plate bending specimens with C(T) specimens, SE(B) specimens (a/W = 0.5 and 0.1), and surface-flawed flat plate tensile specimens. At the test temperature of -80°C, the data segregate into two groups: one comprising C(T) specimens and SE(B) specimens with a/W = 0.5, and the other including SE(B) specimens with a/W = 0.1, surface-flawed flat plate bending specimens, and flat plate tensile specimens. The lower bound K_{Jc} values of the latter group are nearly equivalent and clearly larger than those of the former group. The latter group is characterized by a small ratio of flaw depth to thickness, a/W = 0.1, resulting in reduced plastic constraint at the crack tip. This trend is also observed at -120°C (comparison with the master curve obtained from 1T C(T) specimens).

Comparing surface-flawed flat plate bending specimens with flat plate tensile specimens, the lower bound K_{Jc} values at -80°C and -120°C are nearly identical, varying within about twice the lower bound K_{Jc}. Additionally, some specimens at -80°C did not fracture from the crack region. These observations suggest that for flat plate specimens with surface flaws of around a/W = 0.1, the difference in fracture toughness values between bending and tensile load condition is not significant.

Copyright © 2026 The Japan Welding Engineering Society, All Rights Reserved.





View A-A
(Configuration of fatigue pre-crack)

Unit: mm

Fig. 4.1.3.7-1 Geometry of flat plate specimen with surface flaw under bending load

Copyright © 2026 The Japan Welding Engineering Society, All Rights Reserved.



(a) Overall view of test machine



(b) Constant temperature chamber

Fig. 4.1.3.7-2 Setup of flat plate specimen with surface flaw under bending load

Copyright © 2026 The Japan Welding Engineering Society, All Rights Reserved.

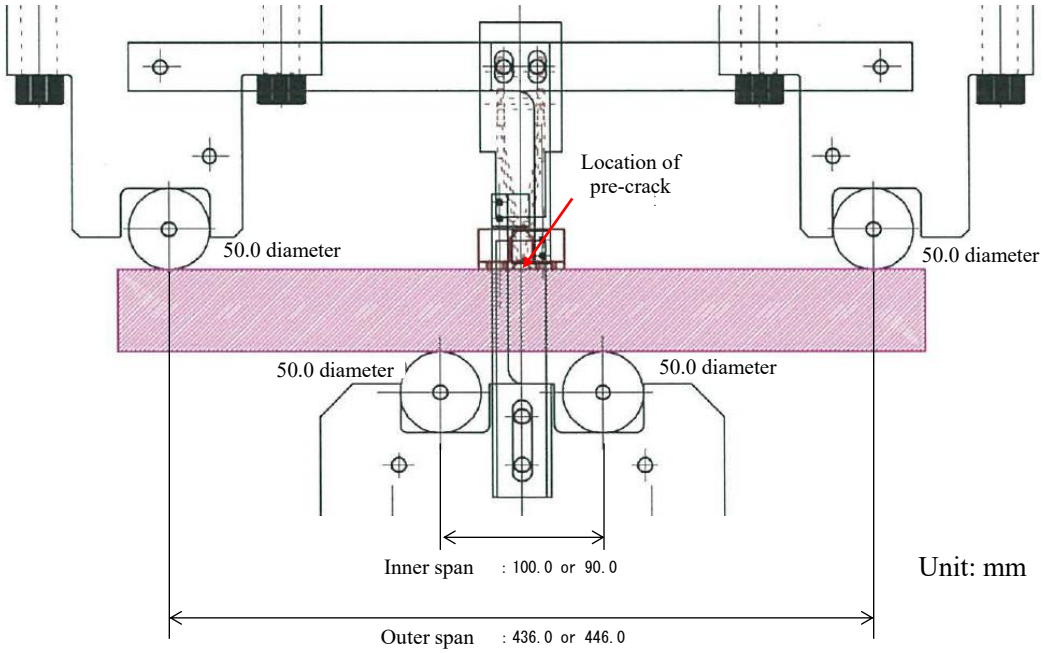


Fig. 4.1.3.7-3 Setup of flat plate specimen with surface flaw under bending load

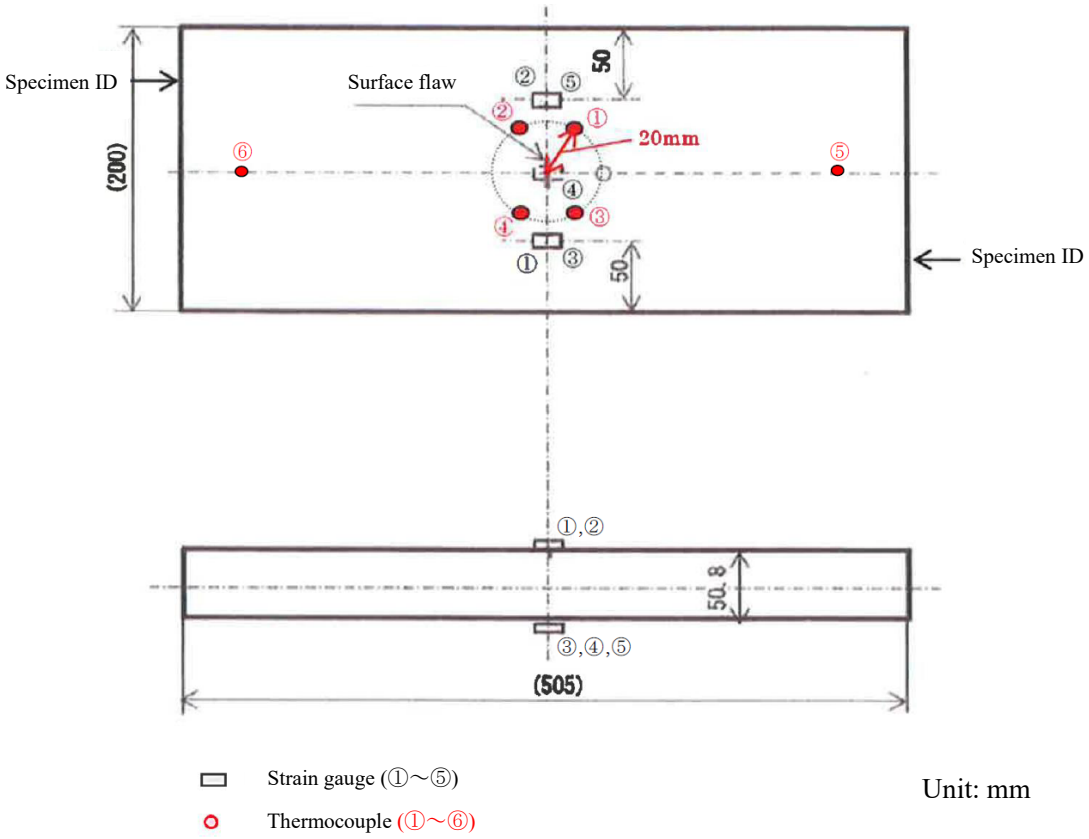


Fig. 4.1.3.7-4 Installation points of strain gauges and thermocouples

Copyright © 2026 The Japan Welding Engineering Society, All Rights Reserved.

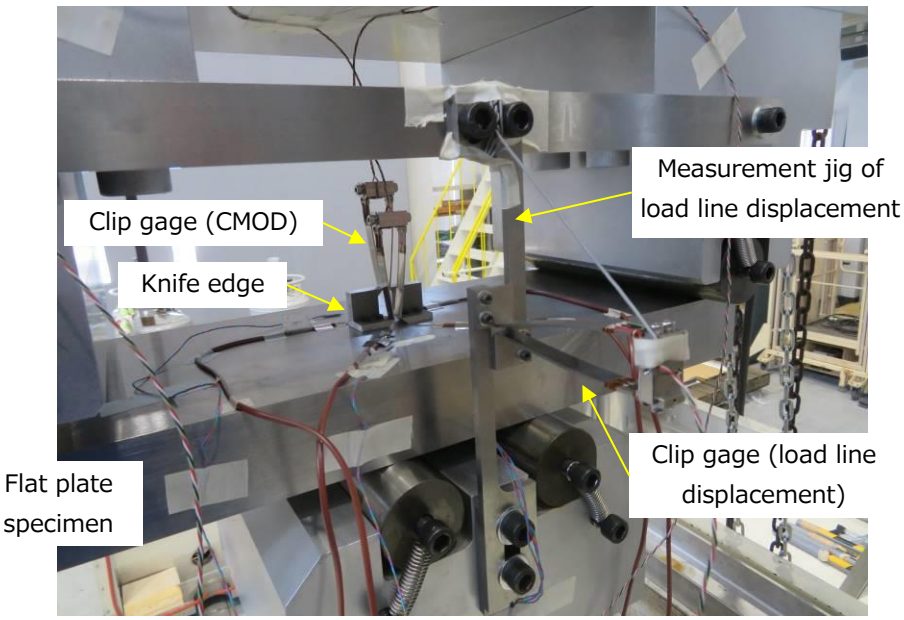


Fig. 4.1.3.7-5 Setting of clip gauges

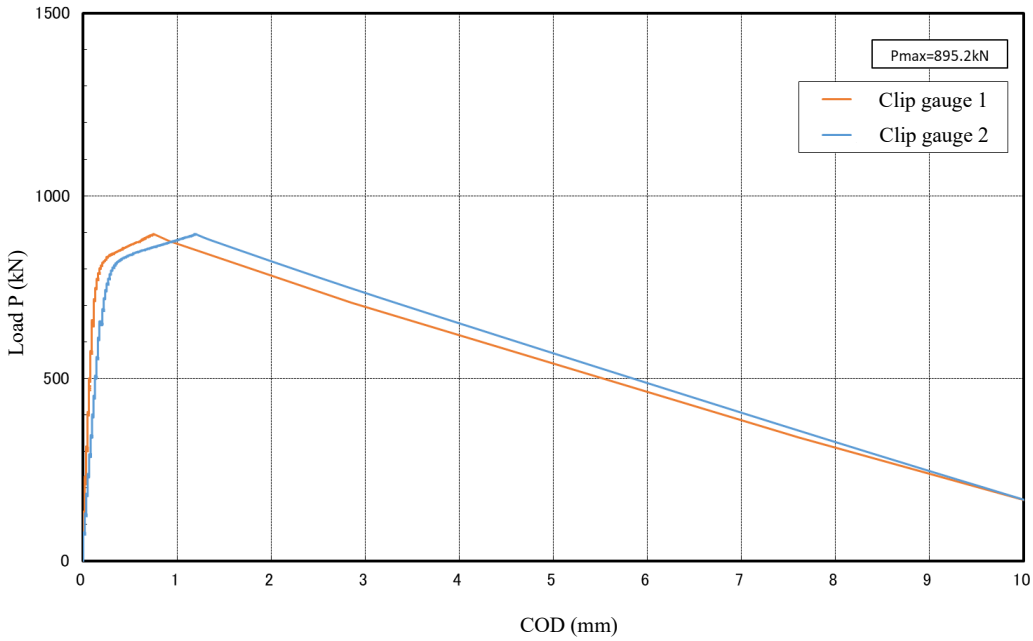
Copyright © 2026 The Japan Welding Engineering Society, All Rights Reserved.

Copyright © 2026 The Japan Welding Engineering Society, All Rights Reserved.

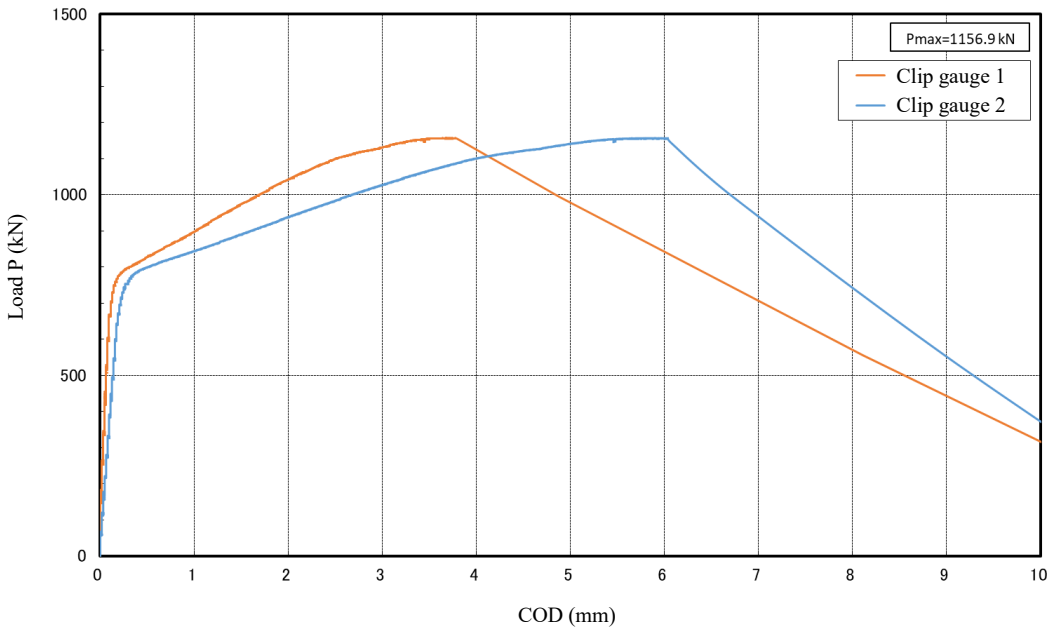
Table 4.1.3.7-1 Pretest result of flat plate specimen with surface flaw under bending load

Specimen ID	Test temperature (℃)	Fracture mode *1	Plate width W (mm)	Plate thickness B (mm)	Precrack depth a_0 (mm)	Precrack surface length $2c$ (mm)	Ductile crack growth (mm)	Fracture load (kN)	COD1 at fracture (mm)
A13UFP-01	-80	DB	200	50.8	4.50	20.2	0.62	1157	3.79
A13LFP-01	-100	B	200	50.8	4.38	20.3	0.00	895.2	0.74

*1 DB: brittle fracture after ductile crack propagation, B: brittle fracture



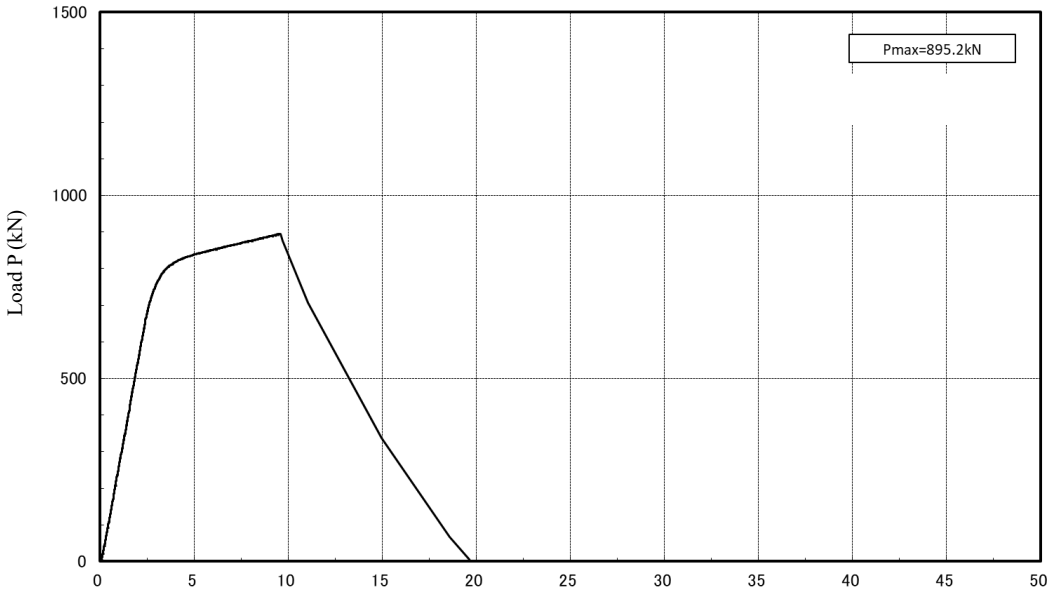
(a) -100°C (A13LFP-01)



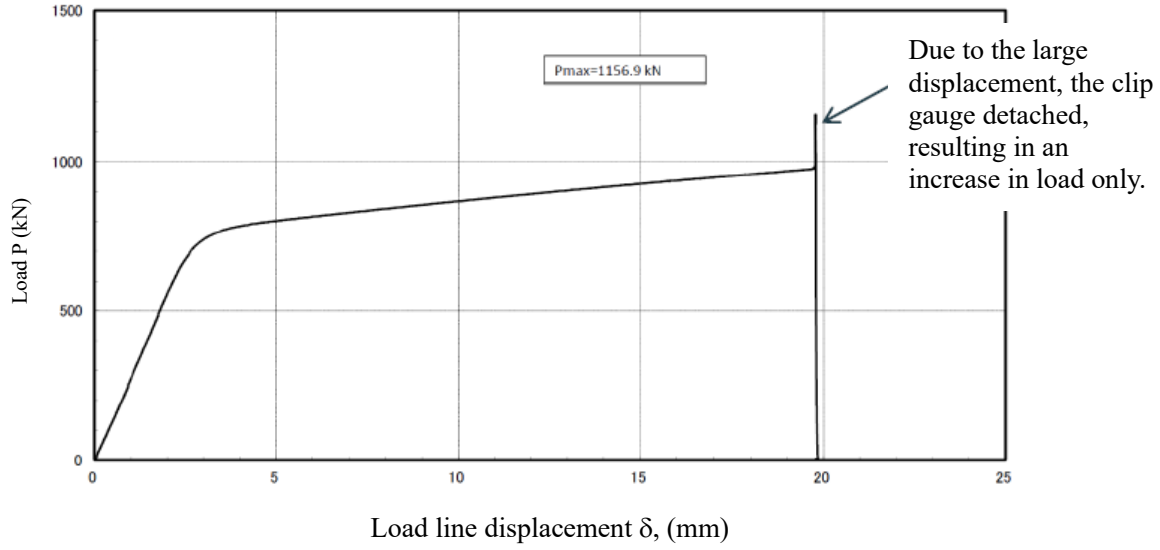
(b) -80°C (A13UFP-01)

Fig. 4.1.3.7-6 Load *P- COD* curve (pretest of flat plate specimen under bending load)

Copyright © 2026 The Japan Welding Engineering Society, All Rights Reserved.



(a) -100ºC (A13LFP-01)

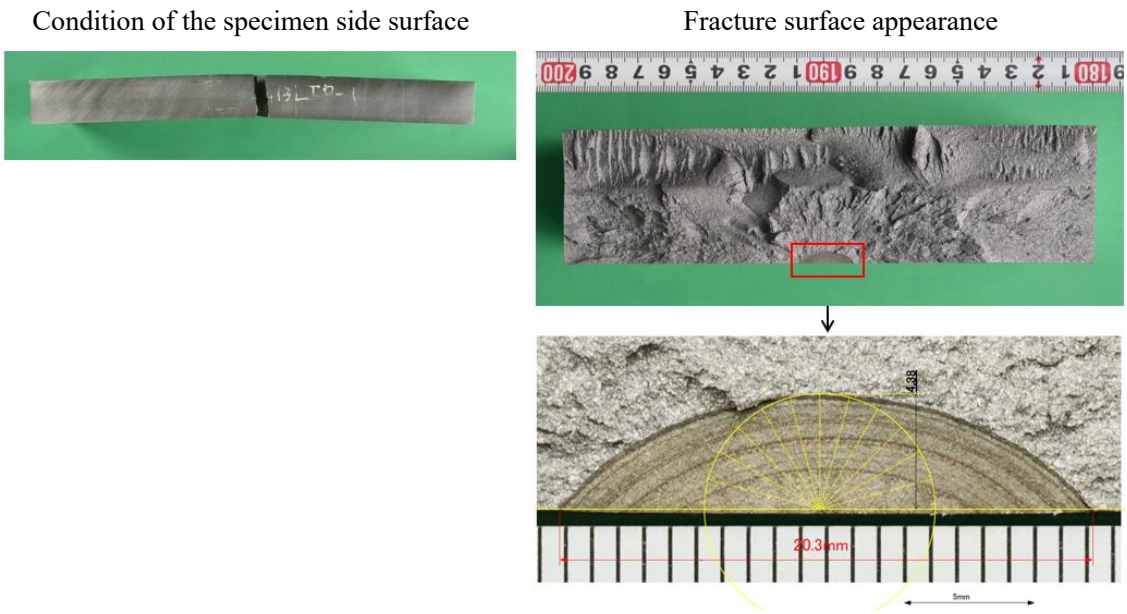


(b) -80ºC (A13UFP-01)

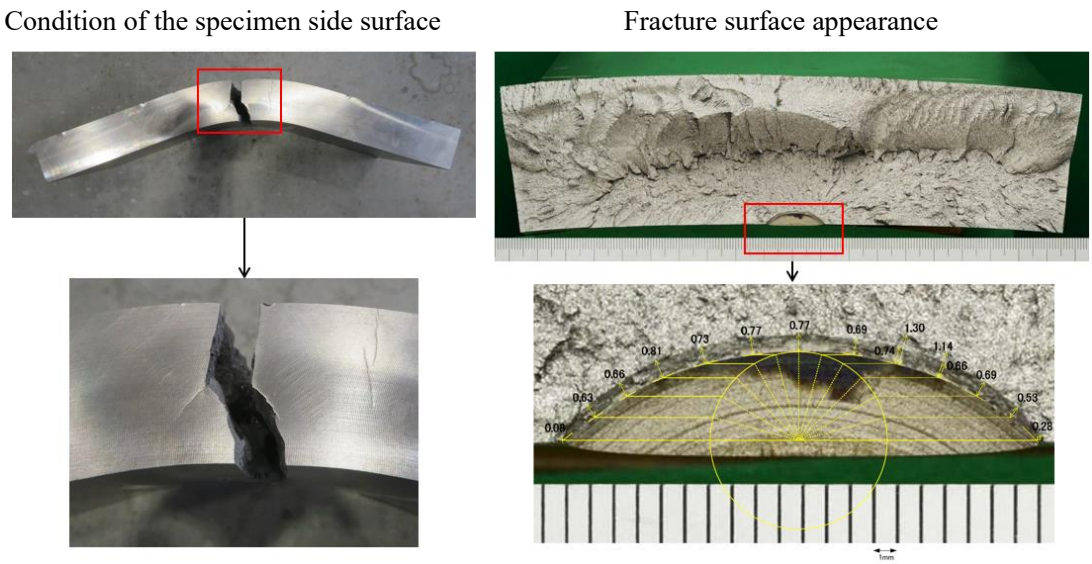
Fig. 4.1.3.7-7 Load *P*-load line displacement δ_L curve

(pretest of flat plate specimen under bending load)

Copyright © 2026 The Japan Welding Engineering Society, All Rights Reserved.



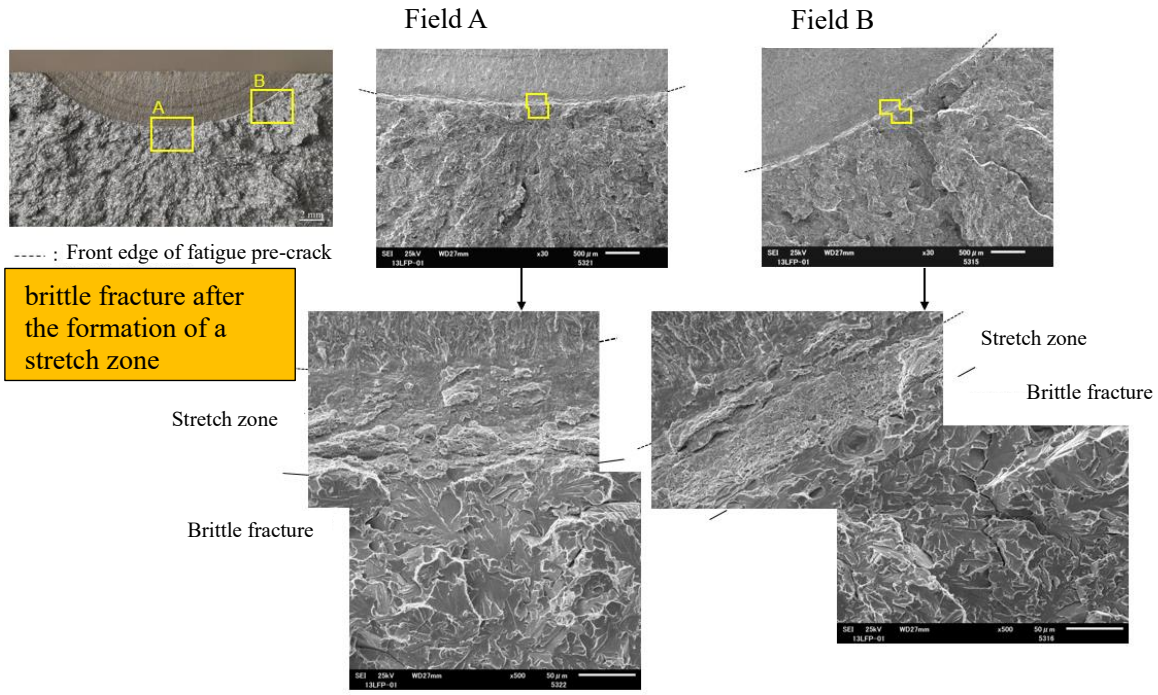
(a) -100°C (A13LFP-01)



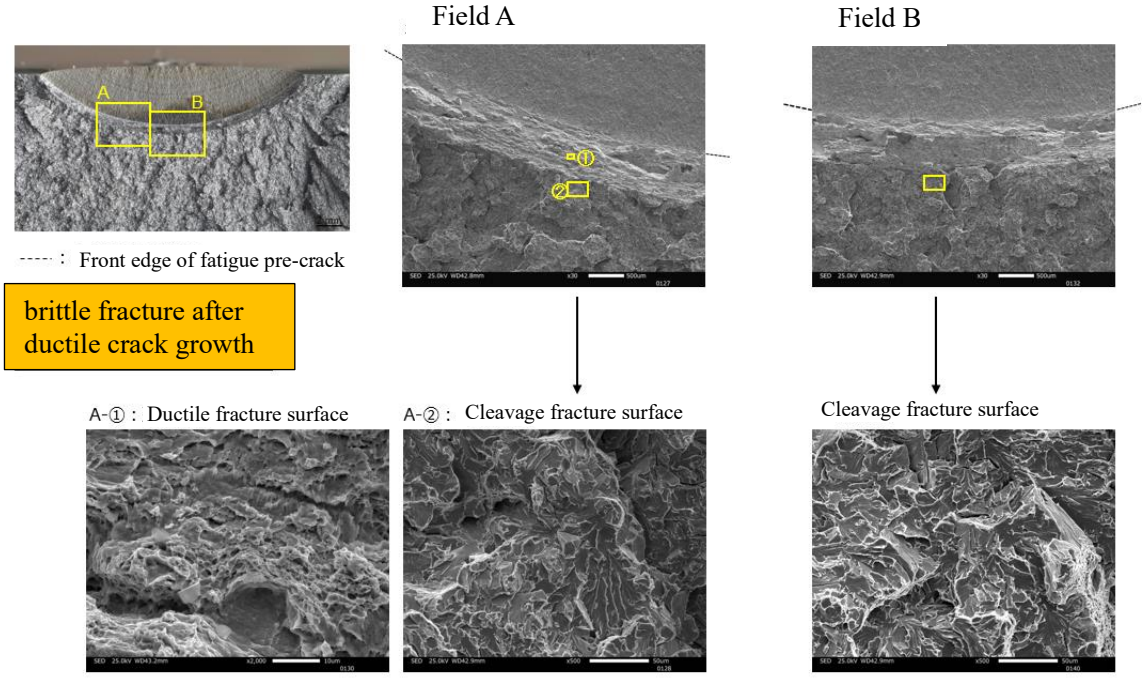
(b) -80°C (A13UFP-01)

Fig. 4.1.3.7-8 Fracture surface of flat plate specimen under bending load (pretest)

Copyright © 2026 The Japan Welding Engineering Society, All Rights Reserved.



(a) -100°C (A13LFP-01)



(b) -80°C (A13UFP-01)

Fig. 4.1.3.7-9 SEM observation of fracture surface of flat plate specimen under bending load (pretest)

Copyright © 2026 The Japan Welding Engineering Society, All Rights Reserved.

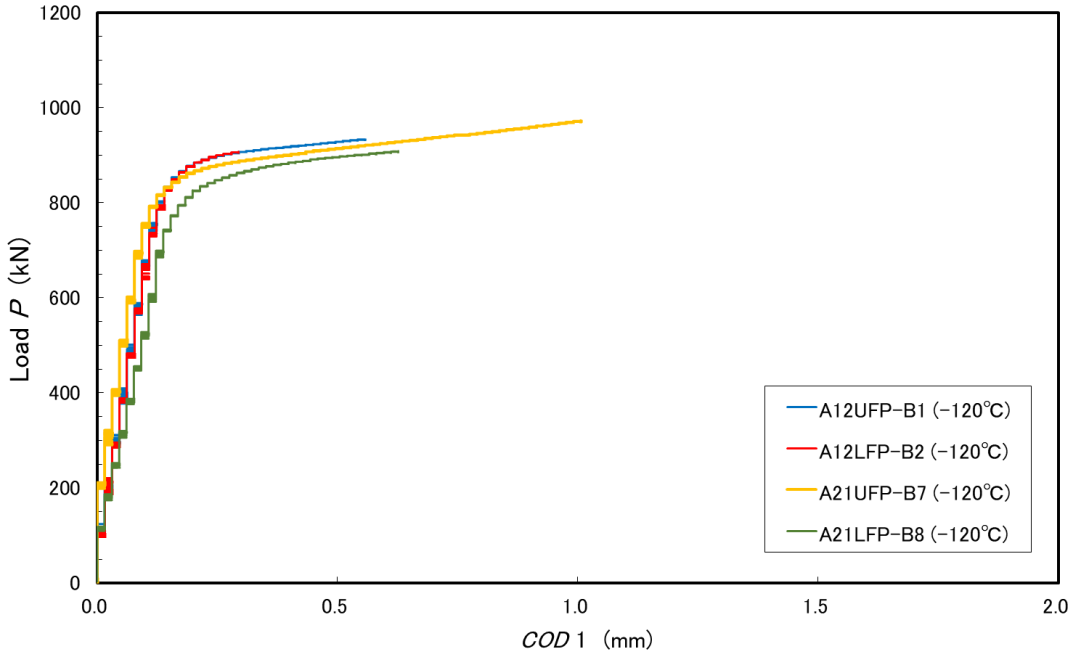
Copyright © 2026 The Japan Welding Engineering Society, All Rights Reserved.

Table 4.1.3.7-2 Test result of flat plate specimen with surface flaw under bending load

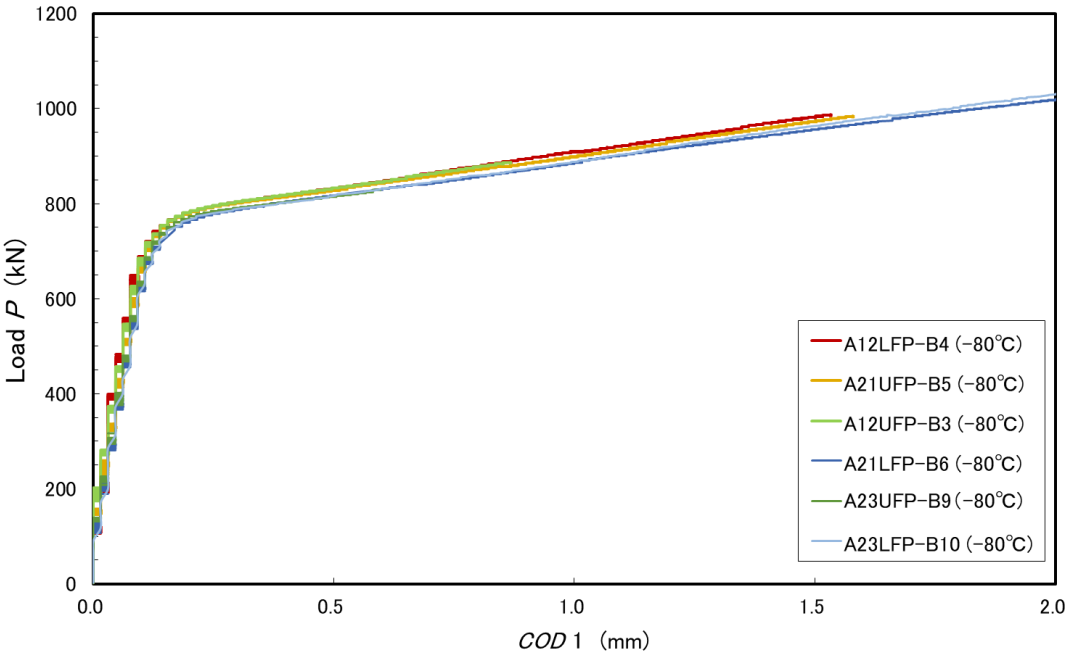
Specimen ID	Test temperature (℃)	Fracture mode *1	Plate width W (mm)	Plate thickness B (mm)	Precrack depth a_0 (mm)	Precrack surface length $2c$ (mm)	Ductile crack growth (mm)	Fracture load (kN)	COD1 at fracture (mm)	COD2 at fracture (mm)	K_{Jc} (MP$\sqrt{}$m)
A23LFP-B10	-80	(Not fractured)	200	50.8	4.05	19.4	1.01	(Not fractured)	(Not fractured)	(Not fractured)	(Not fractured)
A21LFP-B6	-80	(Not fractured)	200	50.8	4.25	19.6	0.76	(Not fractured)	(Not fractured)	(Not fractured)	(Not fractured)
A21UFP-B5	-80	DB	200	50.8	5.46	20.7	0.23	984.7	1.58	2.51	292
A12LFP-B4	-80	DB	200	50.8	4.57	20.5	0.16	988.2	1.53	2.56	287
A12UFP-B3	-80	DB	200	50.8	4.35	20.0	0.10	887.2	0.87	1.43	208
A23UFP-B9	-80	DB	200	50.8	4.42	20.5	0.03	829.6	0.60	0.99	174
A21UFP-B7	-120	B	200	50.8	4.06	18.8	0.00	972.7	1.01	1.66	242
A21LFP-B8	-120	B	200	50.8	3.98	19.7	0.00	908.7	0.63	1.02	192
A12UFP-B1	-120	B	200	50.8	3.77	19.8	0.00	933.2	0.56	0.91	181
A12LFP-B2	-120	B	200	50.8	3.59	20.1	0.00	907.2	0.29	0.45	129

*1 DB: brittle fracture after ductile crack propagation, B: brittle fracture

.



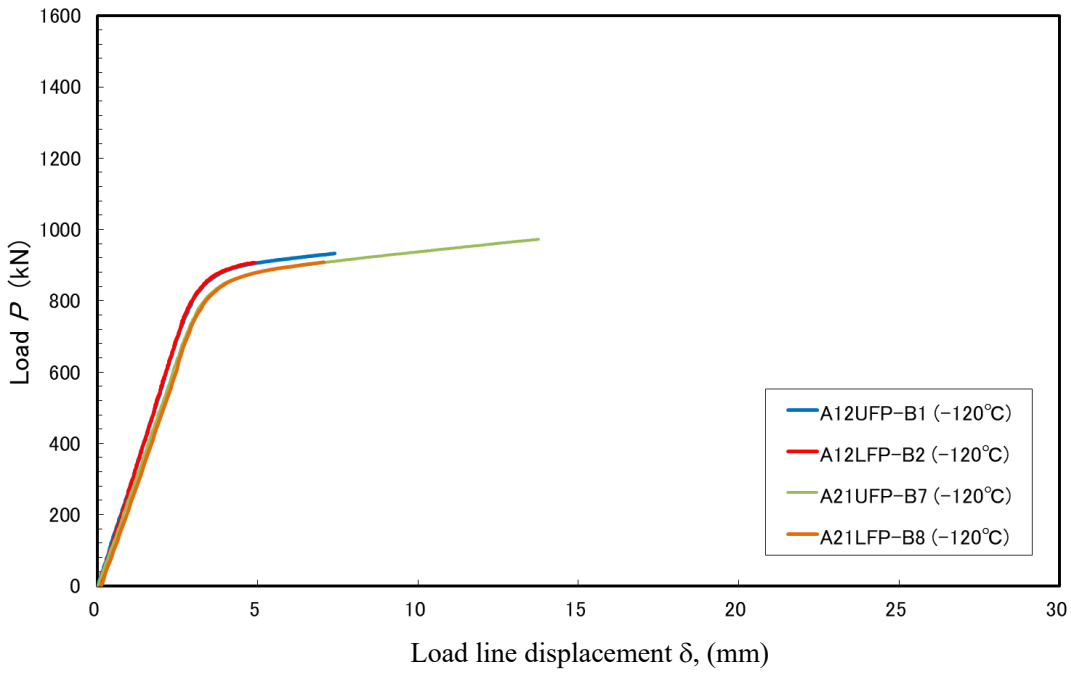
(a) -120ºC



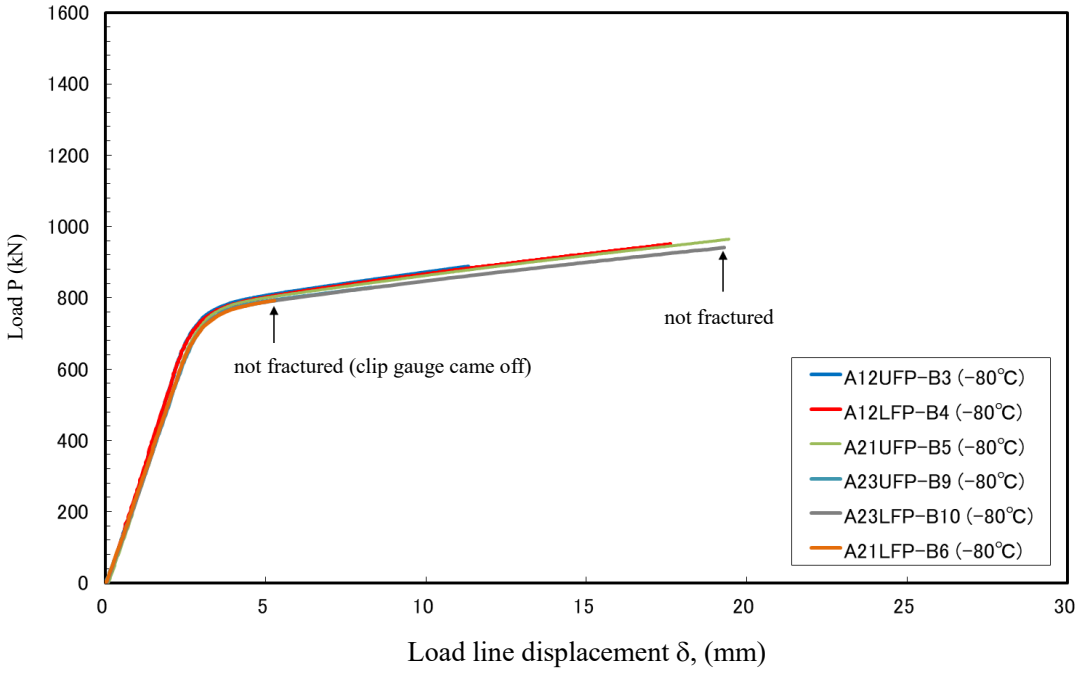
(b) -80ºC

Fig. 4.1.3.7-10 Load *P*- *COD* curve (flat plate specimen under bending load)

Copyright © 2026 The Japan Welding Engineering Society, All Rights Reserved.



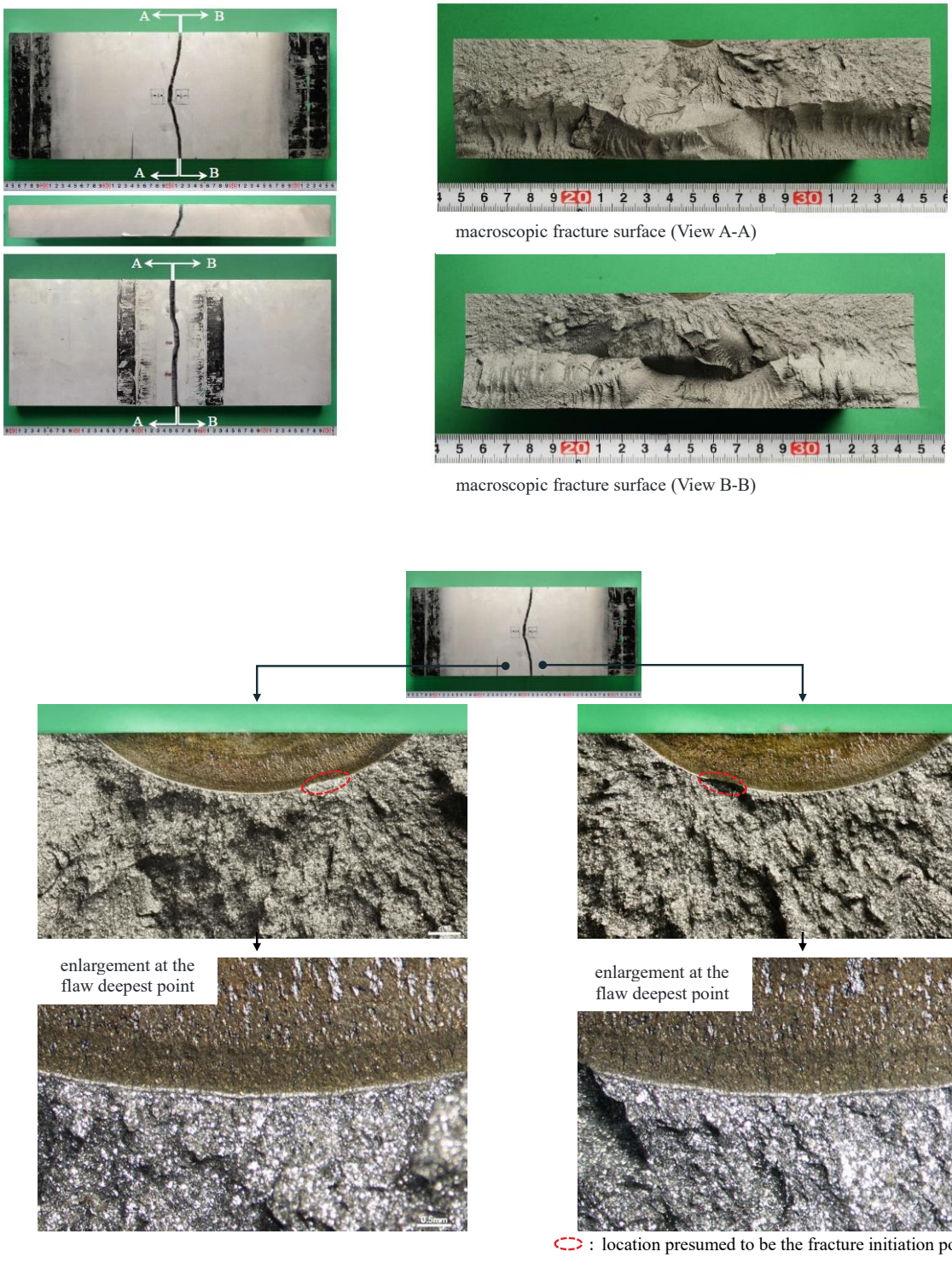
(a) -120°C



(b) -80°C

Fig. 4.1.3.7-11 Load P-load line displacement δ_L curve (flat plate specimen under bending load)

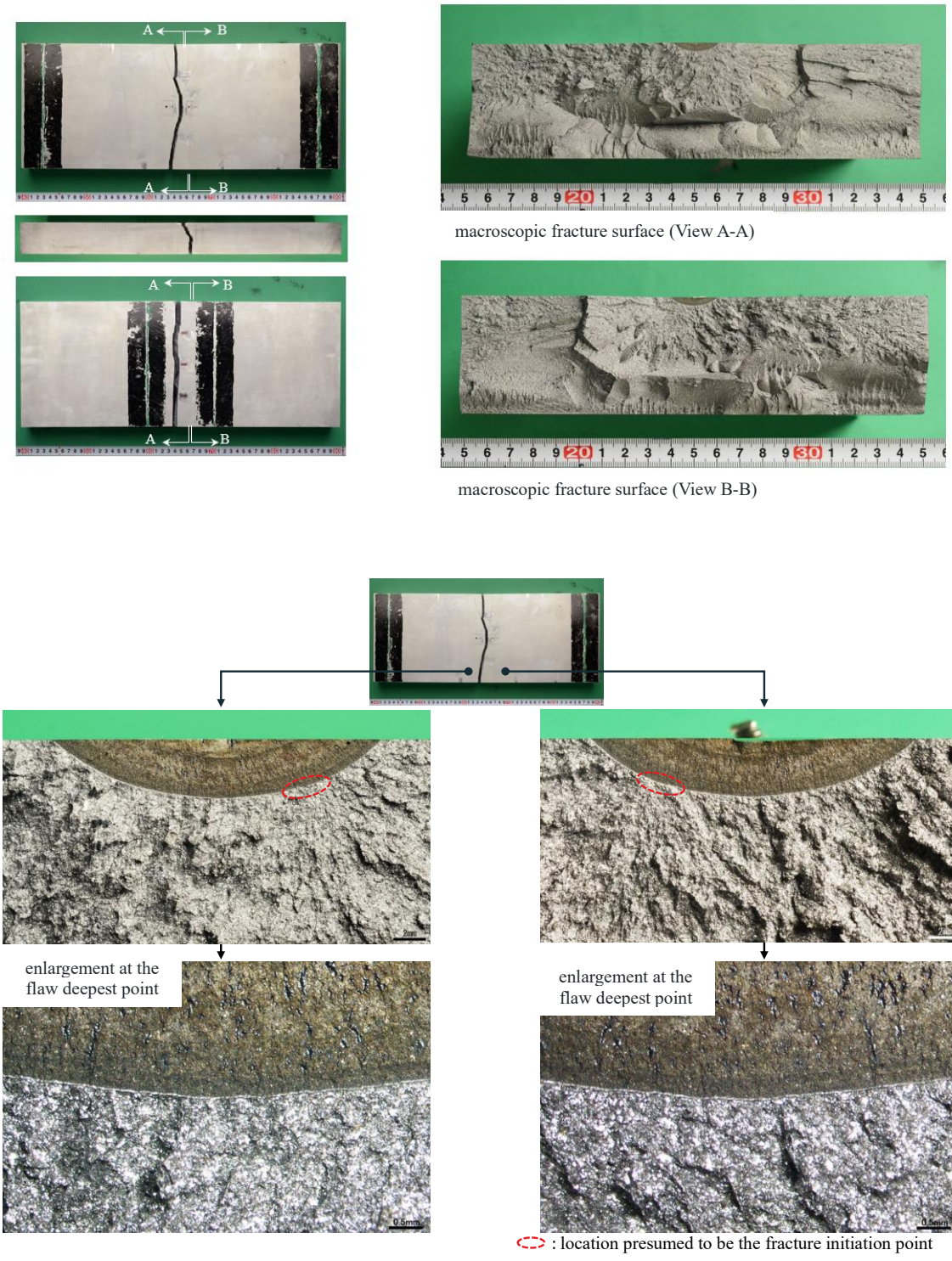
Copyright © 2026 The Japan Welding Engineering Society, All Rights Reserved.



(a) -120ºC (A12UFP-B1)

Fig. 4.1.3.7-12 Fracture surface of flat plate specimen under bending load (1/10)

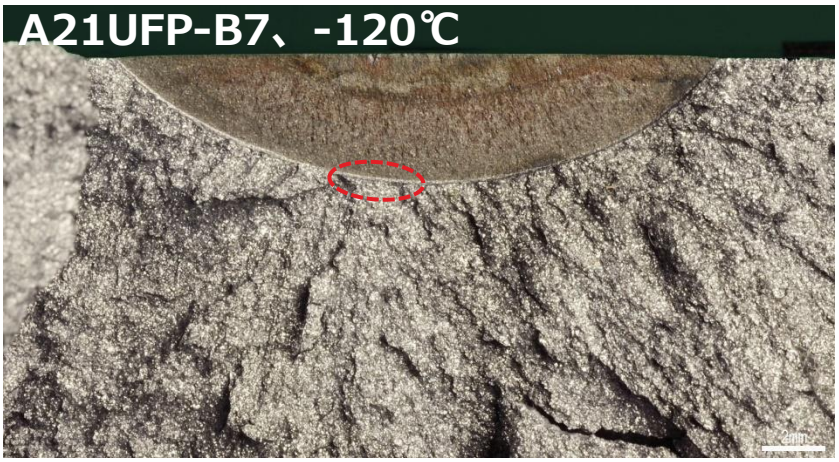
Copyright © 2026 The Japan Welding Engineering Society, All Rights Reserved.



(b) -120ºC (A12LFP-B2)

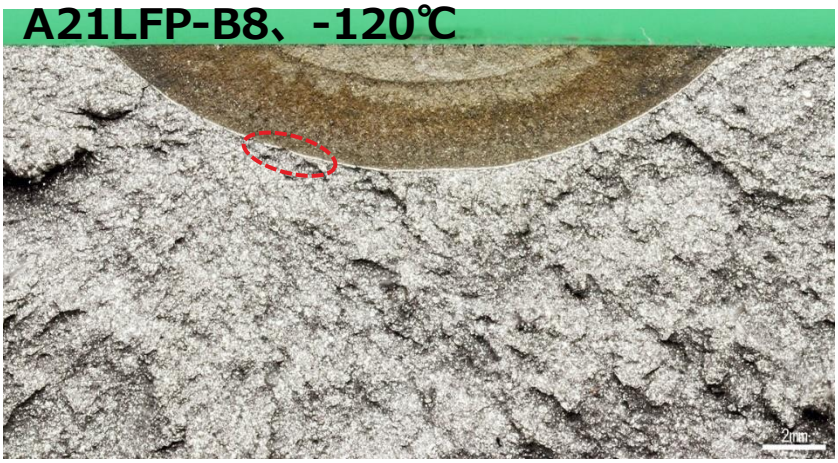
Fig. 4.1.3.7-12 Fracture surface of flat plate specimen under bending load (2/10)

Copyright © 2026 The Japan Welding Engineering Society, All Rights Reserved.



(c) -120°C (A21UFP-B7

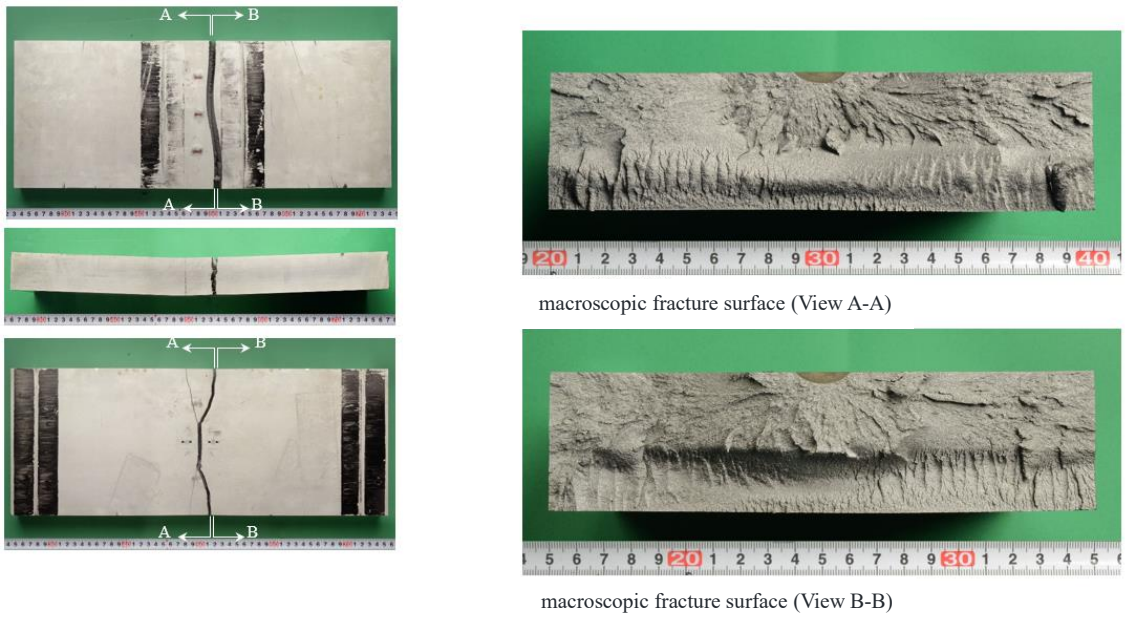
Fig. 4.1.3.7-12 Fracture surface of flat plate specimen under bending load (3/10)

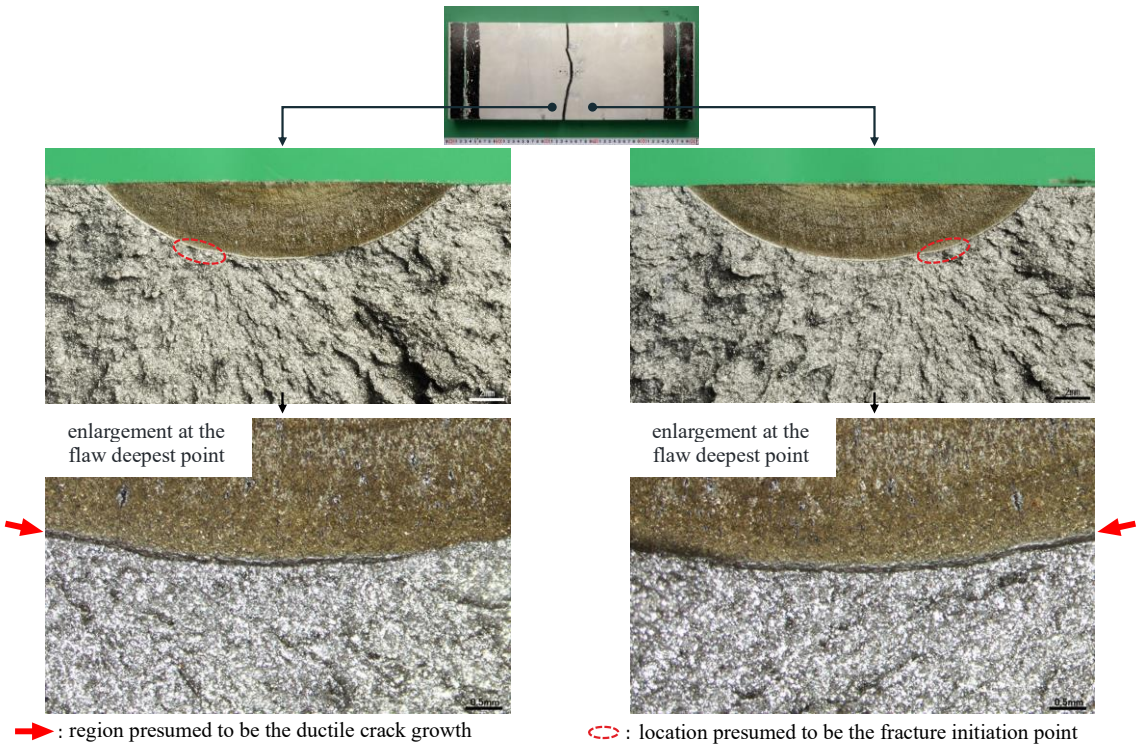


(d) -120°C (A21LFP-B8)

Fig. 4.1.3.7-12 Fracture surface of flat plate specimen under bending load (4/10)

Copyright © 2026 The Japan Welding Engineering Society, All Rights Reserved.

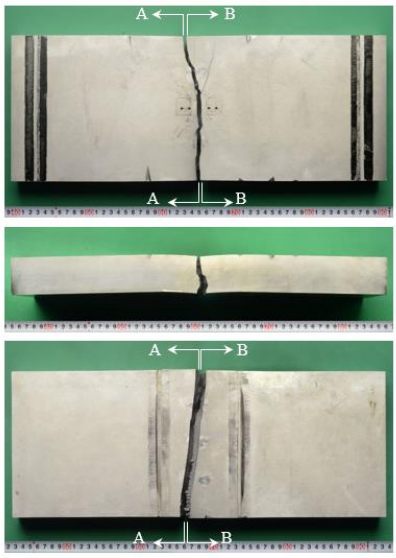




(e) -80ºC (A12UFP-B3)

Fig. 4.1.3.7-12 Fracture surface of flat plate specimen under bending load (5/10)

Copyright © 2026 The Japan Welding Engineering Society, All Rights Reserved.

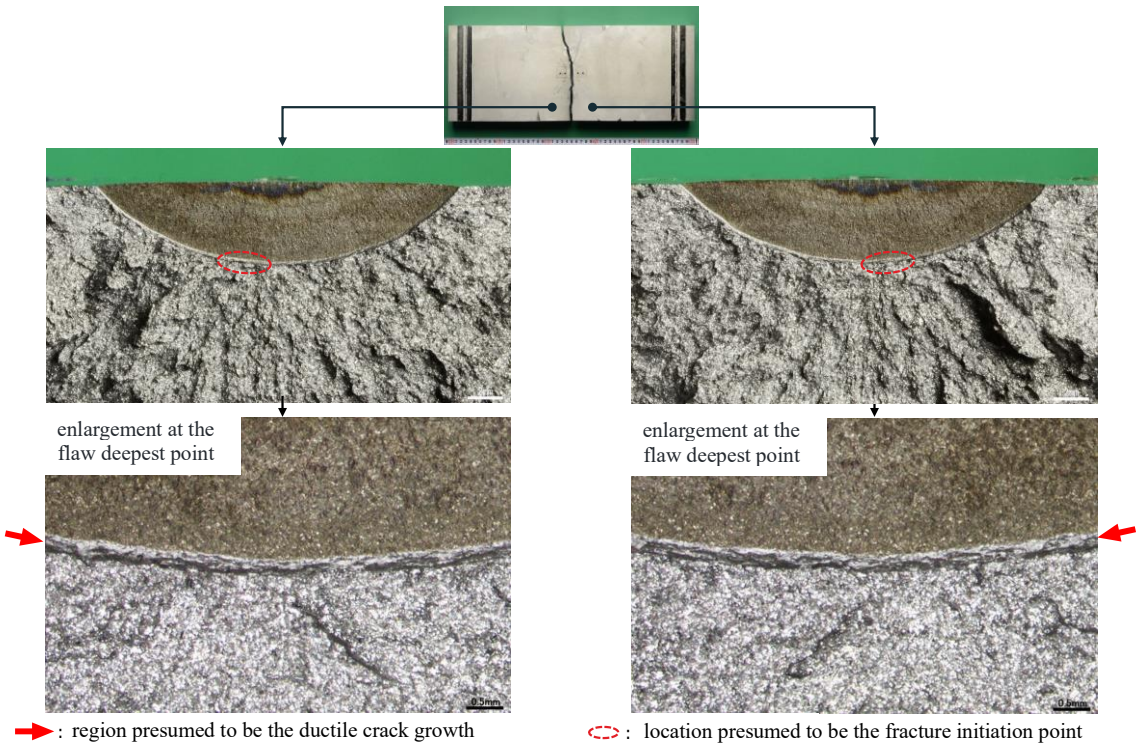




macroscopic fracture surface (View A-A)



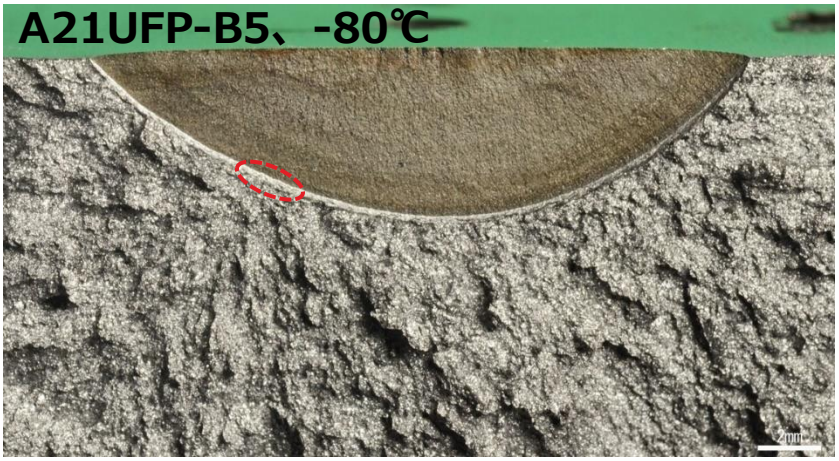
macroscopic fracture surface (View B-B)



(f) -80°C (A12LFP-B4)

Fig. 4.1.3.7-12 Fracture surface of flat plate specimen under bending load (6/10)

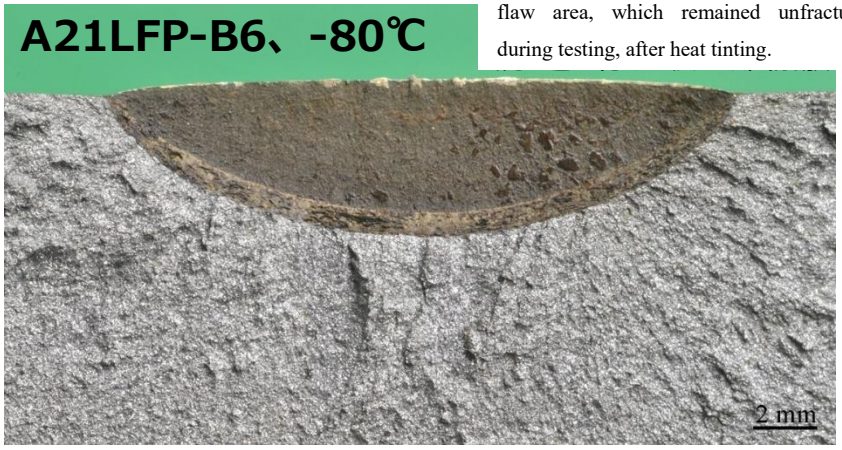
Copyright © 2026 The Japan Welding Engineering Society, All Rights Reserved.



(g) -80°C (A21UFP-B5)

Fig. 4.1.3.7-12 Fracture surface of flat plate specimen under bending load (7/10)

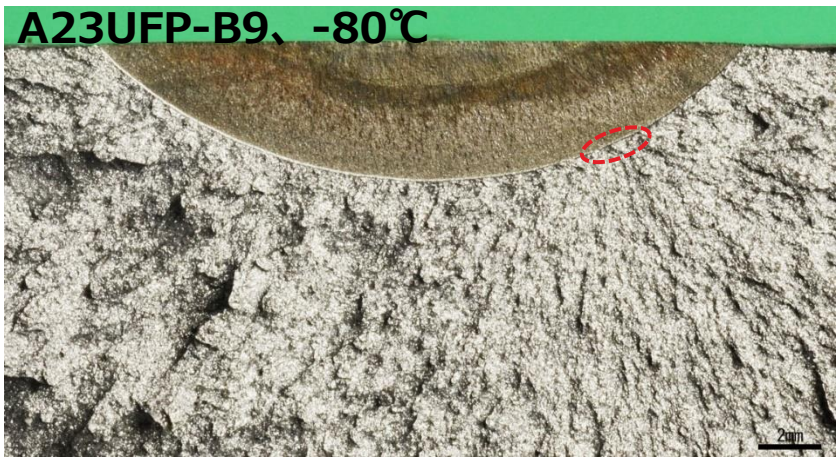
Forced opening of the fracture surface at the flaw area, which remained unfractured during testing, after heat tinting.



(h) -80°C (A21LFP-B6)

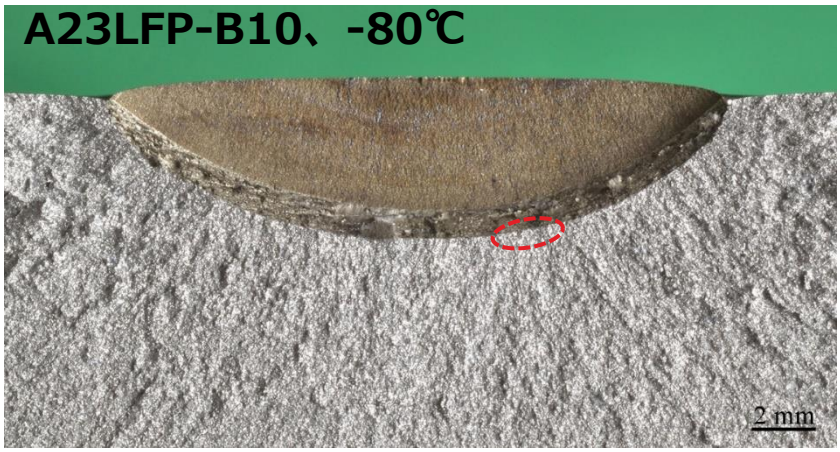
Fig. 4.1.3.7-12 Fracture surface of flat plate specimen under bending load (8/10)

Copyright © 2026 The Japan Welding Engineering Society, All Rights Reserved.



(i) -80°C (A23UFP-B9)

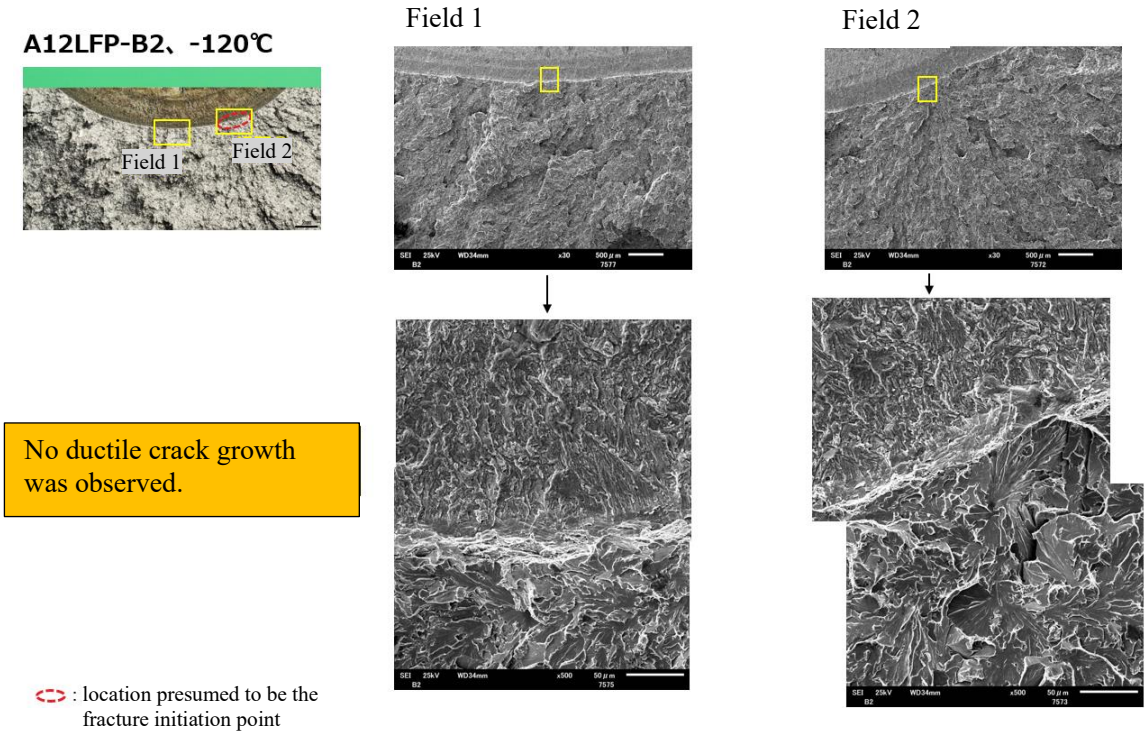
Fig. 4.1.3.7-12 Fracture surface of flat plate specimen under bending load (9/10)



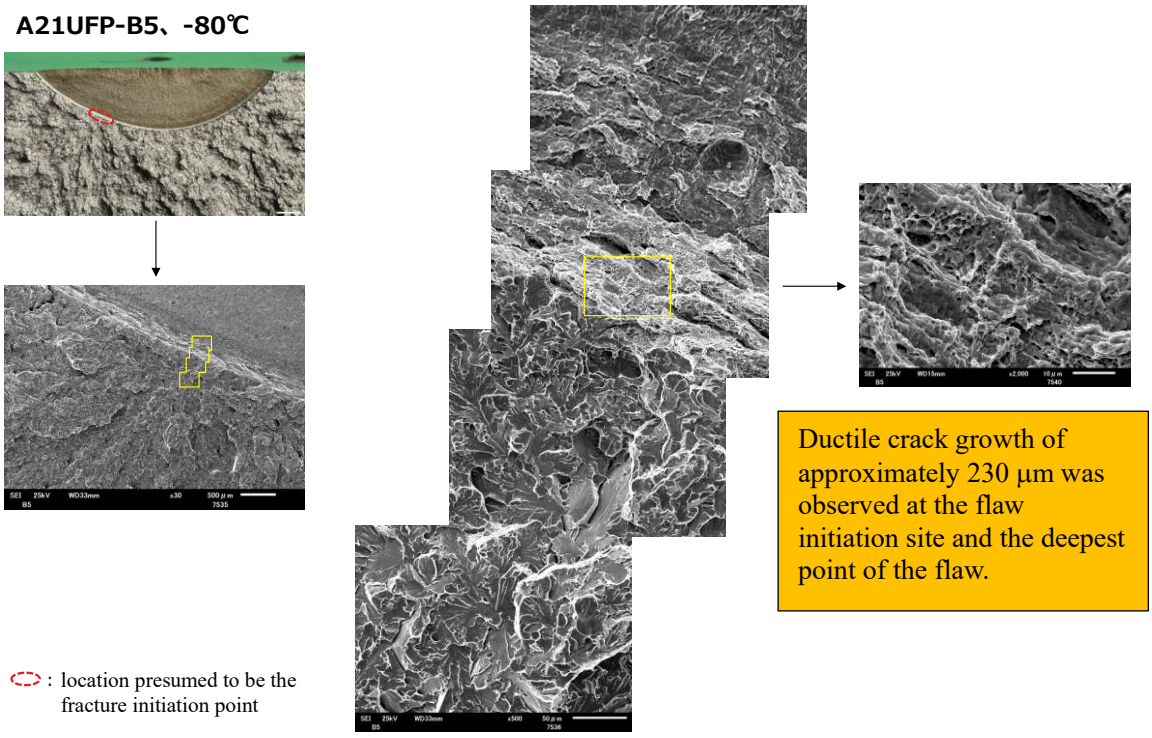
(j) -80°C (A23LFP-B10)

Fig. 4.1.3.7-12 Fracture surface of flat plate specimen under bending load (10/10)

Copyright © 2026 The Japan Welding Engineering Society, All Rights Reserved.



(a) -120°C



(b) -80°C

Fig. 4.1.3.7-13 SEM observation of fracture surface of flat plate specimen under bending

Copyright © 2026 The Japan Welding Engineering Society, All Rights Reserved.

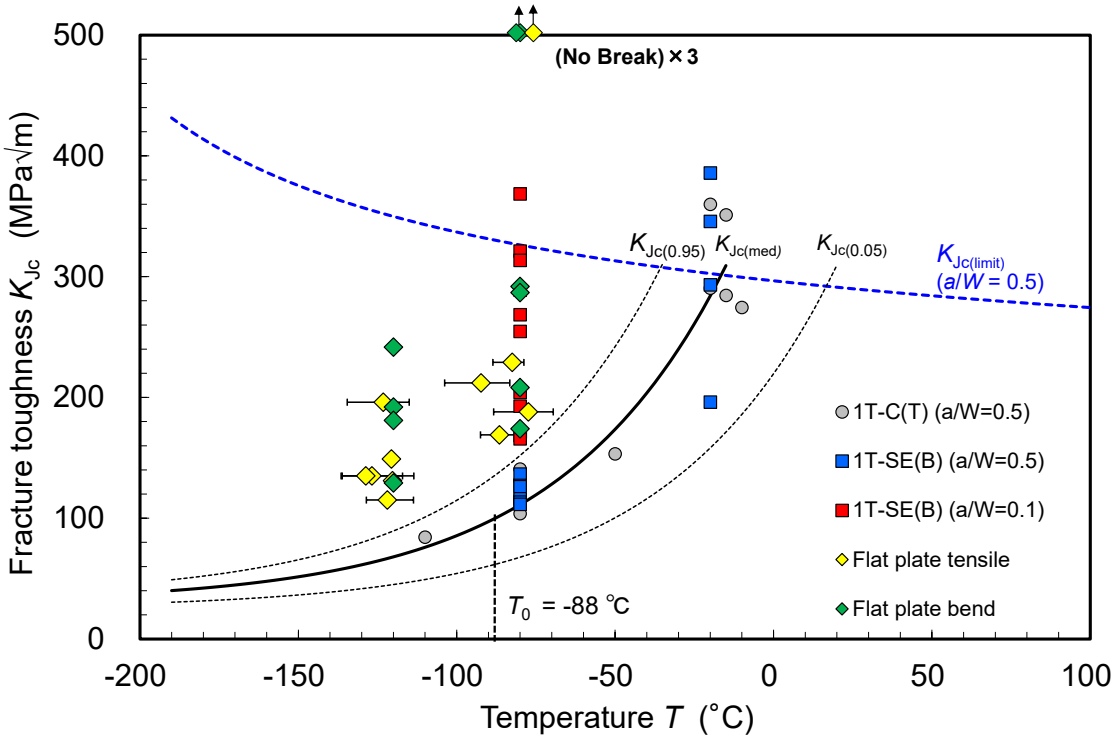


Fig. 4.1.3.7-14 Temperature dependence of K_{Jc} of flat plate specimen with surface flaw under bending or tensile load and fracture toughness test specimens

Copyright © 2026 The Japan Welding Engineering Society, All Rights Reserved.

4.2 Fracture evaluation method

4.2.1 Overview

In Section 4.1, fracture tests were performed using specimens with varying constraint levels to validate fracture evaluation methods considering the plastic constraint effect, thereby accumulating test data. In Section 4.2, the FE analysis conditions necessary to predict the fracture behavior of surface- flawed flat plate specimens with low plastic constraint are established based on fracture data of laboratory specimens with high plastic constraint. Additionally, benchmark analyses of the evaluation method are performed. Although the benchmark analysis described herein utilize low alloy steel B, preliminary basic studies of fracture analysis using benchmark method were also performed on low alloy steel A, which is of the same steel grade but froma different lot; these results are summarized in Appendix 4.

4.2.2 Analysis conditions

4.2.2.1 Material properties

The basic properties of low alloy steel B used in this analysis are as follows.

(1) Young’s modulus and Poisson’s ratio

The Young’s modulus and Poisson’s ratio employed are shown in Table 4.2.2-1.

(2) True stress – true strain curve

Based on the radius and curvature of the necked section in tensile and interrupted tensile tests of low alloy steel B, the true stress–true strain relationship in the high strain region was obtained using Bridgman’s equation. The true stress–true strain curves at each temperature were set as shown in Fig. 4.2.2-1.

Copyright © 2026 The Japan Welding Engineering Society, All Rights Reserved.

Table 4.2.2-1 Young's modulus and Poisson's ratio

Temperature (°C)	-120	-100	-80	-50	-20	23
Young's modulus (GPa)	210	208	207	205	203	201
Poisson's ratio	0.3					

Note) The Young's modulus E (MPa) was determined using the temperature-dependent equation described in JEAC4216-2015 (E = 210,584 - 62.6T, where T is the temperature in °C).

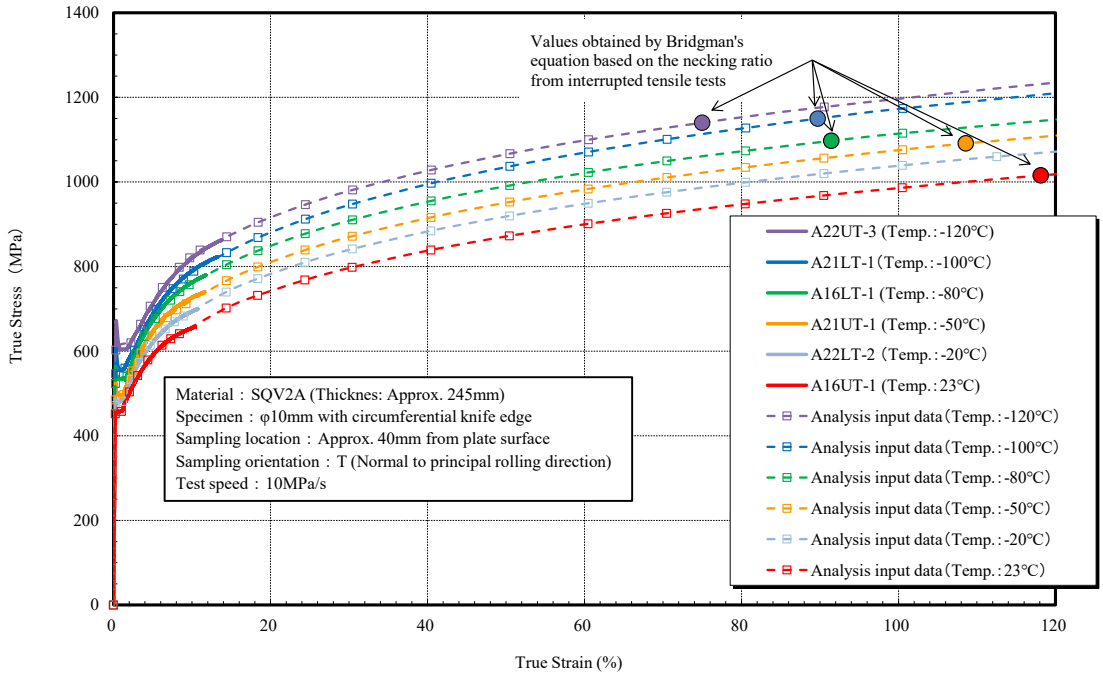


Fig. 4.2.2-1 True stress - True strain curve of low alloy steel B for fracture evaluation

Copyright © 2026 The Japan Welding Engineering Society, All Rights Reserved.

4.2.2.2 Applied fracture evaluation methods

To account for constraint effects in fracture evaluation, the Beremin model is applied for brittle fracture, the GTN model for ductile fracture, and the Coupled model combining both for brittle fracture accompanied by minor ductile crack growth. These model were introduced in Section 3.2.

4.2.2.3 FE analysis

(1) Beremin model

a. Laboratory specimens (C(T) and SE(B) specimens)

Since Weibull parameters of the Beremin model are determined by the two-specimens method, they were calculated from fracture data of two types of specimens with different constraint levels (SE(B) a/W=0.5 and SE(B) a/W =0.1 specimens). In addition, C(T) specimens were included in the benchmark analysis described later. For FE analyses for these three types of Beremin model, Abaqus Ver. 6.12 Abaqus Standard was used, employing 8-node reduced integration elements (C3D8). The analysis models are shown in Figs. 4.2.2.3-1 (a) to (c). Due to symmetry, quarter models were used.

For C(T) specimens, the element size at the crack tip was set to 0.03 mm × 0.03 mm × 0.03 mm. Side grooves and knife edges were modeled according to drawing dimensions. Plate thickness B and width W were set to drawing dimensions (B = 25.4 mm, W = 50.8 mm), and crack depth was set to the average pre-crack size of the -80°C test specimen, 25.35 mm. The pin was modeled in a quarter section and connected to the specimen. The pin was given about ten times the stiffness of the specimen (Young's modulus E = 2000 GPa). The load was applied as displacement in the X-direction at the center of the pin.

For SE(B) specimens, the element size at the crack tip was set to 0.03 mm × 0.03 mm × 0.3 mm. Since the stress distribution through the thickness relatively smooth, the thickness direction of the crack tip elements was divided into 40 layers (about 0.3 mm) to reduce calculation time. Plate thickness B, width W, and span were set to drawing dimensions (B = 25.4 mm, W = 50.8 mm, S = 203.2 mm), and crack depth was modeled as the average pre-crack length: 26.24 mm (a/W =0.5) and 3.96 mm (a/W =0.1). Knife edges were modeled as beam elements to output measured $CMOD$. The beam elements of the knife edges were modeled up to one layer of base material elements so that deformation was linked with the specimen. The rollers of the testing jig were modeled as rigid body elements, and displacement was applied under contact conditions. Friction was not considered at the contact surfaces.

Copyright © 2026 The Japan Welding Engineering Society, All Rights Reserved.

b. Surface-flawed flat plate specimens

The FE models of surface-flawed flat plate specimens are shown in Figs. 4.2.2.3-1 (d) and (e). Due to symmetry, quarter models were used. The flat plate bending specimens included rollers modeled the rollers as rigid body over a 180° arc and the knife edges modeled as beam elements. The element size at the crack tip was 0.03 mm × 0.03 mm × 0.1 mm. The initial flaw geometry was based on observations from preliminary tests, with the deepest crack depth a_0 of 4.38 mm and total crack length $2c_0$ of 20.3 mm. The number of J-integral region was set to 45.

The flat plate tensile specimens were modeled including the tab plates, and forced displacement was applied at the tab plate ends. The fracture prediction analysis model adopted the initially planned tab plate dimensions. Although the fracture test specimens had the tab plate with width of 330 mm and thickness of 100 mm, the analytical models employed dimensions of 200 mm and 80 mm, respectively. The connection between the tab plate and specimen is sufficiently distant from the flawed section, so differences in tab plate geometry between the models model and test specimens are not expected to affect the stress distribution near the crack tip. The element size at the crack tip was 0.03 mm × 0.03 mm × 0.1 mm. The initial flaw shape was based on observations from preliminary tests, with the deepest crack depth a_0 0f 5.2 mm and total crack length $2c_0$ of 21.3 mm. The number of J-integral regions was set to 55.

The FE code and element type used for the flat plate specimens were the same as those for laboratory specimens.

(2) GTN model

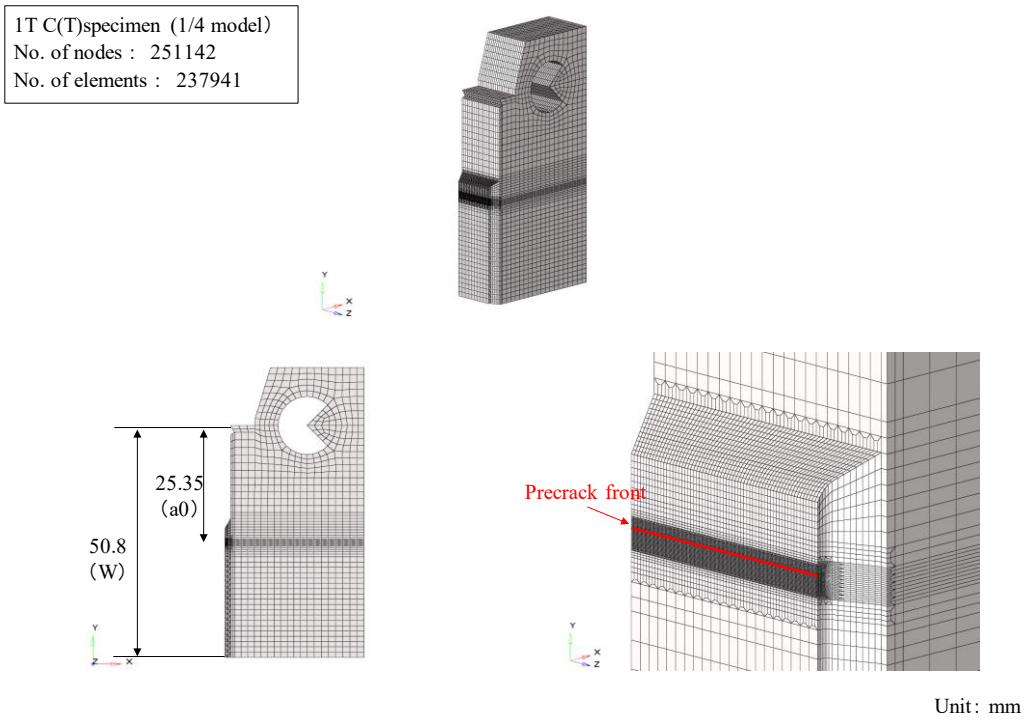
The GTN model parameters were calculated from results of C(T) specimens tested at room temperature. The analysis model used for FE analysis is shown in Fig. 4.2.2.3-2. The model included a 9.9 mm crack growth region. The element size at the crack tip was 0.03 mm × 0.03 mm × 0.06 mm.

Abaqus Explicit was used for GTN model analysis, with reduced integration elements (C3D8R).

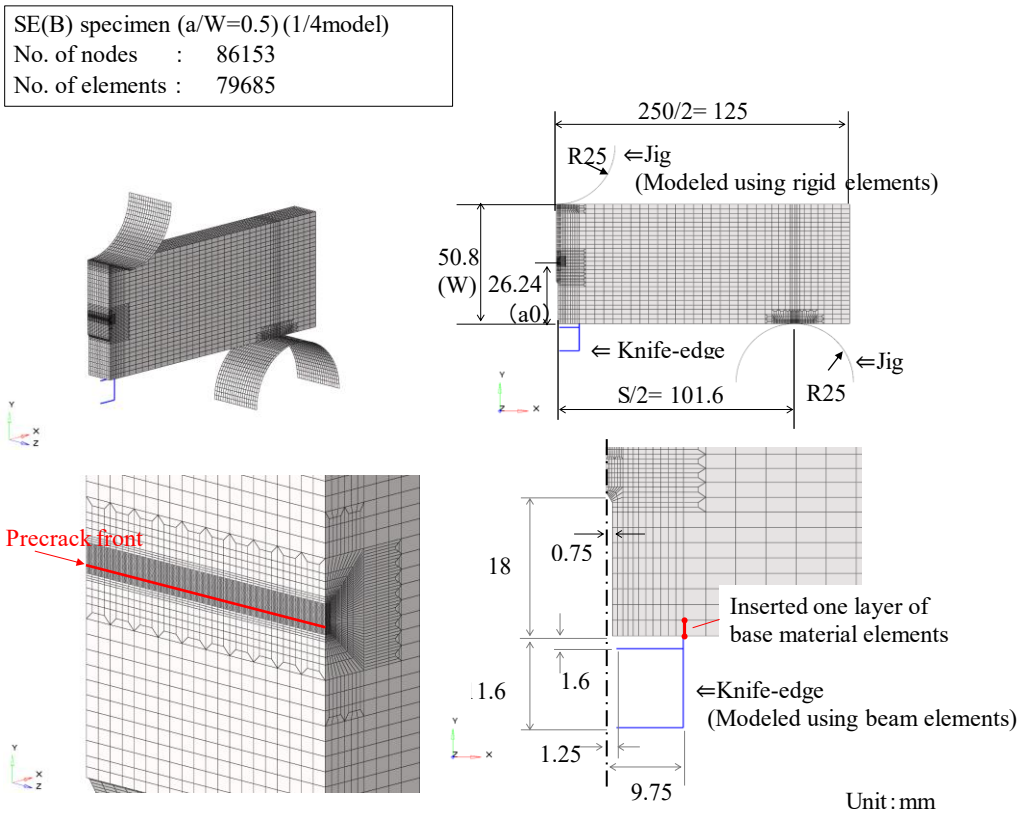
(3) Coupled model

The Coupled model was applied to the SE(B) specimen with a/W =0.1 at -80°C where minor ductile crack growth occurred, as well as to bending and tensile flat plate specimens. GTN model analysis was performed using Abaqus Explicit and reduced integration elements C3D8R. The FE models for these specimens were the same as those used in the Beremin model analyses.

Copyright © 2026 The Japan Welding Engineering Society, All Rights Reserved.



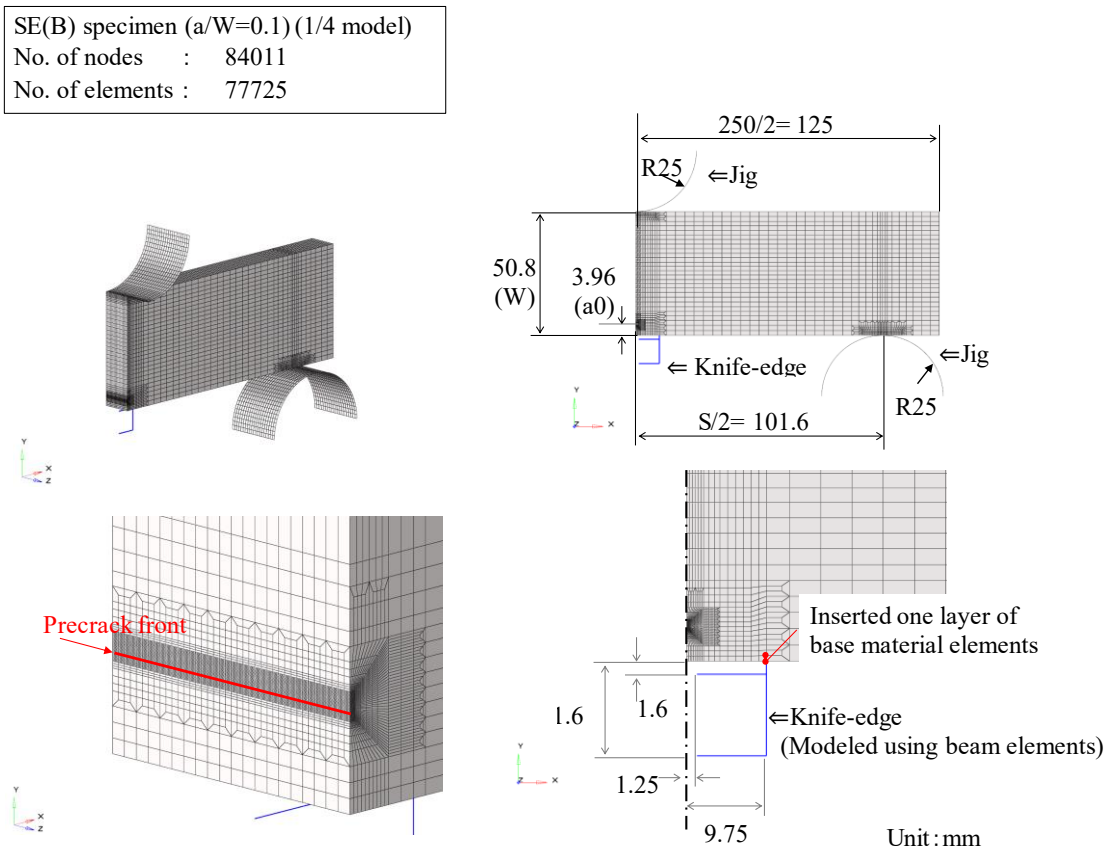
(a) 1T C(T) specimen



(b) SE(B) *a*/*W*=0.5 specimen

Fig. 4.2.2.3-1 FE model (1/3)

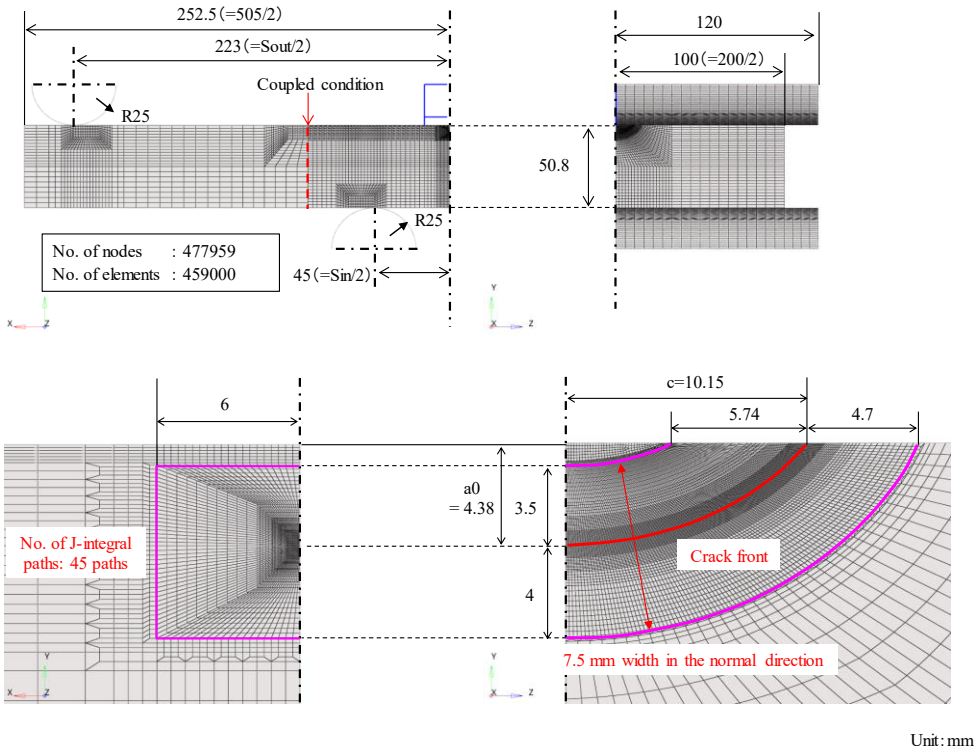
Copyright © 2026 The Japan Welding Engineering Society, All Rights Reserved.



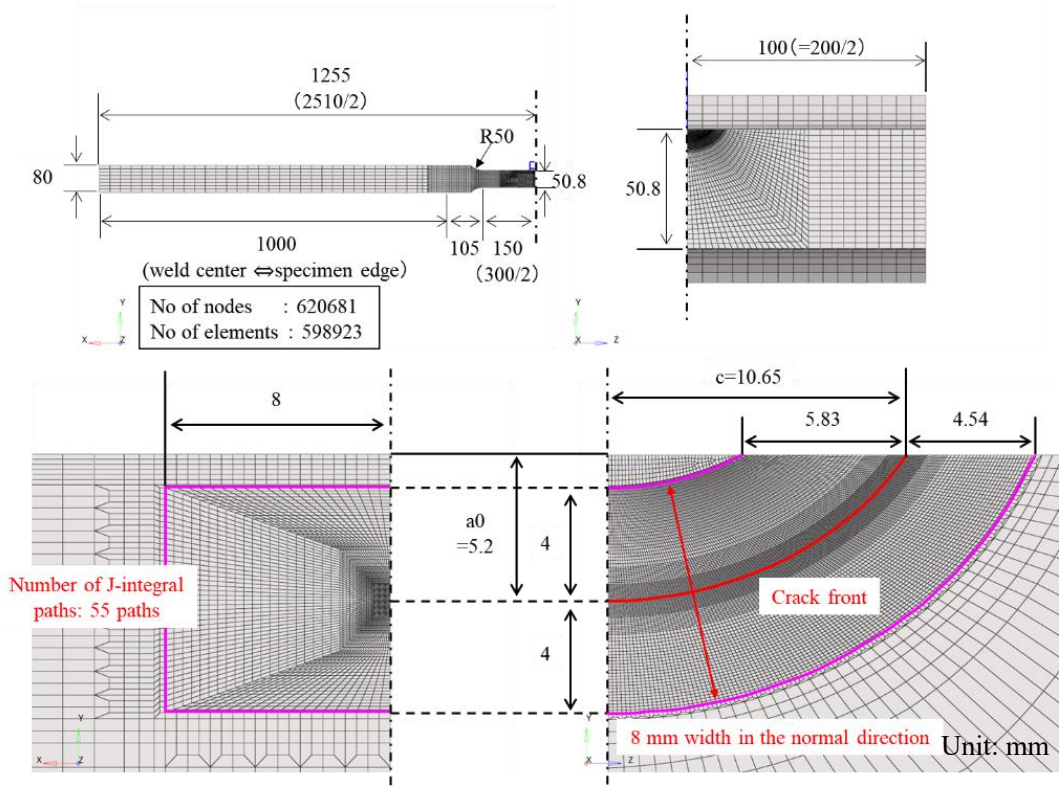
(c) SE(B) a/W=0.1 specimen

Fig. 4.2.2.3-1 FE model (2/3)

Copyright © 2026 The Japan Welding Engineering Society, All Rights Reserved.



(d) Flat plate bending specimen with surface flaw



(e) Flat plate tensile specimen with surface flaw

Fig. 4.2.2.3-1 FE model (3/3)

Copyright © 2026 The Japan Welding Engineering Society, All Rights Reserved.

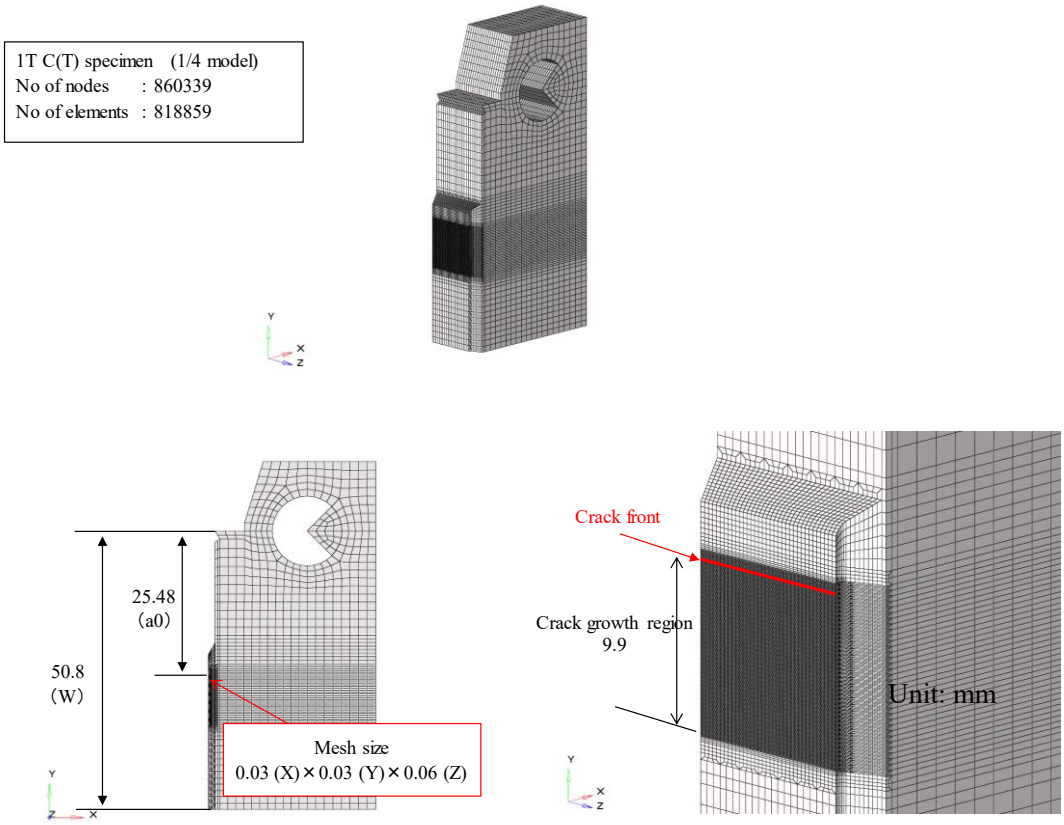


Fig. 4.2.2.3-2 FE model for determination of GTN model parameters

Copyright © 2026 The Japan Welding Engineering Society, All Rights Reserved.

4.2.3 Benchmark analysis

4.2.3.1 Necessity of benchmark analysis

To standardize fracture evaluation methods considering constraint effects in the future, it is essential to ensure that consistent results can be obtained regardless of the person under the same analysis conditions. Since fracture evaluation methods considering constraint effects are performed by numerical analysis, their results may vary depending on the numerical analysis code, analysis model in FE analysis, element type, and other factors. Differences in detailed evaluation methods of Weibull stress after FE analysis may also influence the outcomes. Therefore, it is necessary to understand how differences in numerical analysis codes, analysis models, element types, FE analysis methods, and Weibull stress evaluation methods after FE analysis affect fracture evaluation results. Accordingly, a benchmark problem was established using specimens of low alloy steel B with varying constraint levels, and fracture evaluation results from multiple organizations were compared to identify the factors influencing the fracture evaluation outcomes.

4.2.3.2 Analysis conditions

(1) Material properties

The material for the benchmark analysis is low alloy steel B with material properties identical to those described in Section 4.2.2.1.

(2) Applicable fracture evaluation methods

The fracture evaluation methods considering constraint effects are those described in Section 4.2.2.2 are used.

a. Beremin model

The flow of Weibull stress analysis for the Beremin model is the same as shown in 3.2(1). The two-specimens method was applied to determine the Weibull parameter m.

Table 4.2.3.2-1 shows the method of Weibull stress calculation in the benchmark analysis.

b. GTN model

GTN model parameters were adjusted through FE analyses of the specimens that fractured with ductile crack growth, to fit the load-displacement curves obtained experimentally. For this benchmark analysis, q_1, q_2, and q_3 were set to 1.5, 1, and 2.25, respectively.

c. Coupled model

For fracture evaluation of brittle fracture following ductile crack growth, FE analysis using the

Copyright © 2026 The Japan Welding Engineering Society, All Rights Reserved.

GTN model is first performed. The resulting stress distribution at the crack tip from this analysis is then used to calculate Weibull stress via the Beremin model to evaluate fracture.

d. Others

Additional conditions for the benchmark analysis are as follows:

1. The crack dimensions modeled shall match the initial crack dimensions of the MHI analysis model.
2. For calculating K_J in SE(B) specimens, the displacement at the node of the knife edge attachment is used.
3. The integration regions for J-integral is not needed the same, and shall be determined by each organization.
4. For flat plate specimens, clip gauges shall be modeled, and displacement at the clip gauge shall be compared with measured displacement values. If the clip gauge is not modeled, displacement at the midpoint of the clip gauge attachment positions, i.e., 15 mm from the flaw surface (midpoint between 10 mm and 20 mm), shall be output.

Copyright © 2026 The Japan Welding Engineering Society, All Rights Reserved.

Table 4.2.3.2-1 Weibull stress procedure in benchmark analyses.

Category	Item	Calculation condition (Basic Policy)	MHI's Condition (Reference)
Weibull stress calculation method	Stress component: σ_1	Maximum principal stress for each step	
	σ_1 output position	Integration point	8 integration points
	Volume	Element Volume	Element volume is calculated from initial coordinates.
	Reference volume: V_0	1 mm^3	
	Integration method	Gauss integral	
Integration volume	Target range	Exclude jig contact points, etc.	
	Stress limit	Plastic region (equivalent stress ≥ yield stress) and region where the stress is equal to or greater than the maximum value of the maximum principal stress at the time when the C (T) specimen reaches 20 MPa$\sqrt{}$m	
Analysis Output	Output step	Output in steps sufficient to smoothly reproduce the behavior of the load-displacement curve in the elastoplastic transient region (Approximately 50 steps)	C(T): Load Line Displacement =0.92 mm in 40 divisions SE (B) a/W=0.5: CMOD 0.8 mm in 46 divisions SE (B) a/W=0.1: CMOD 1.38 mm in 64 divisions
Calibration of Weibull parameters (Two-specimens method)	Test specimen	If it can be confirmed that K_{Jc}, which is the limit value of LSY corrected by Weibull stress based on SSY, is less than or equal to $K_{Jclimit}$, the Boundary Layer Model is not used. SSY: a/W0.5 Specimen (-80°C) LSY: a/W0.1 Specimens (-80°C) (see note) $K_{jclimit}=\sqrt{\frac{Eb_0\sigma_{YS}}{30(1-\nu^2)}}$	
	Formula for calculating β_A (scale parameter of SSY specimen)	Test results are entered as J values. $\beta=\left[\frac{1}{r}\left(\sum_{i=1}^{r}J_{(i)-SSY}^2\right)\right]^{1/2}$ Calculated as shape parameter 2	
	σ_w calculation formula	Beremin model $\sigma_w=\left[\frac{1}{Vo}\int_\Omega \sigma_1^m d\Omega\right]^{1/m}$	
	$\sigma_{u\text{-}A}$ equation (Shape parameter m is arbitrary.)	$\sigma_u=\left(\frac{1}{n}\sum_{i=1}^{n}{\sigma_{w(i)}}^m\right)^{1/m}$	
	$J_{c\text{-}SSY}$ (LSY specimen converted to SSY)	$J_{c-SSY}=\beta_A\left[\frac{\sigma_{w-B}}{\sigma_{u-A}}\right]^{m/2}$	
	Formula for calculating β_B (scale parameter after conversion of LSY specimen)	Test results are entered as J values. $\beta=\left[\frac{1}{r}\left(\sum_{i=1}^{r}J_{(i)-SSY}^2\right)\right]^{1/2}$ Calculated as shape parameter 2	
	Bias correction	None	
	Convergence criteria	$R=(\beta_B-\beta_A)/\beta_A<0.01$	
	σ_u calculation formula	$\sigma_u=\left(\frac{1}{n}\sum_{i=1}^{n}{\sigma_{w(i)}}^m\right)^{1/m}$ Use both $\sigma_{w\text{-}A}$ and $\sigma_{w\text{-}B}$	

[Note]
Conditions under which the Boundary Layer Model may not be used include:
1) All K_{Jc} of SSY must be less than or equal to $K_{Jclimit}$.
2) K_{Jc} obtained by correcting the limit value of LSY to SSY-based by Weibull stress must be less than or equal to $K_{Jclimit}$.
Here, since $K_{Jclimit}$=326 MPa・$m^{0.5}$ and the test data of SSY is 137 MPa・$m^{0.5}$ or less, 1) is satisfied.
(Note: -80 oC: Young's modulus 207 GPa, σ_{ys}=551.2MPa, b_0=25.4 (a/W=0.5), b_0=46.8 (a/W=0.1))

Copyright © 2026 The Japan Welding Engineering Society, All Rights Reserved.

4.2.3.3 Comparison of benchmark analysis results from participating organizations

The organizations participating in the benchmark analysis were Mitsubishi Heavy Industries (MHI), University of Osaka (UO), Tokyo University of Science (TUS), Central Research Institute of Electric Power Industry (CRIEPI), Hitachi and Hitachi-GE Nuclear Energy, Ltd. (Hitachi), Toshiba Energy Systems & Solutions Corporation (Toshiba), IHI Corporation (IHI), and Japan Atomic Energy Agency (JAEA).

The benchmark analysis for Weibull stress analysis of low alloy steel B was performed in two stages. In the first stage, recognizing that m value may vary among organizations, analyses were performed with m fixed at specified values. In the second stage, m was determined using the two-specimens method, and the fracture prediction performance for each specimen was evaluated. For the benchmark analysis of GTN model on low alloy steel B, differences in load–*COD* relationships and ductile crack growth–*J* relationships were evaluated using the same GTN model parameters.

(1) First stage Weibull stress analysis with fixed *m*

The Weibull stress analysis results with fixed m for each specimen are shown in Figs. 4.2.3.3-1 to 4.2.3.3-8. In the Weibull stress analysis, the integration range of Weibull stress was set to include the regions where the maximum principal stress of the specimen exceeds those corresponding to K_J = 20 MPa√m for the C(T) specimen. The maximum principal stresses used by each organization are shown in Table 4.2.3.3-1.

For the SE(B) specimen with a/W=0.1 at -80°C and the surface-flawed flat plate tensile specimens at -80°C and -120°C, the evaluation trends differed between m =10 and m=20 or 30. At m=10, TUS's σ_w was slightly larger than others, but at m=20 and 30, results from all organizations were nearly identical. For other specimens, results from all organizations were nearly consistent under all m values of 10, 20, and 30. Some discrepancies in σ_w for K_J below 20 MPa√m among organizations are attributed to differences in whether this stress range was included in the integration domain.

(2) Second stage Weibull stress evaluation using *m* from two configuration test method

Weibull stress evaluations using m calculated by the two-specimens method were performed for each specimen to evaluate fracture prediction accuracy. The m values obtained for each specimen are shown in Table 4.2.3.3-2, and the Weibull stress evaluation results using those m values are shown in

Copyright © 2026 The Japan Welding Engineering Society, All Rights Reserved.

Figs. 4.2.3.3-9 to 4.2.3.3-16.

As shown in Table 4.2.3.3-2, although some variation exists among organizations, m ranged from 9 to 27 when calculated by the two-specimens method.

As shown in Figs. 4.2.3.3-9 to 4.2.3.3-16, for SE(B) specimens, surface-flawed flat plate specimens under bending or tensile load, σ_w was slightly lower in the cases with small m (e.g., Toshiba and IHI with m=9 and 8.2), but σ_w–K_J relationships were nearly consistent among organizations for each specimen. Furthermore, the relationships between cumulative failure probability and K_J for each specimen showed much better agreement among organizations than the σ_w –K_J relationships. Figure 4.2.3.3-16 summarizes the cumulative failure probability–K_J relationships for surface-flawed flat plate tensile and bending specimens at -80°C and -120°C, confirming small differences among participating organizations.

These results indicate that even if different m values are obtained from fracture tests on high-constraint laboratory specimens, the predicted fracture probabilities for low-constraint specimens or structures using those m values do not significantly differ among analysts. This suggests minimal influence of the specific Beremin model analysis tools employed by different analysts.

For reference, test results are also shown in the cumulative failure probability–K_J relation graphs. In the flat plate specimens, fracture test results and fracture predictions under bending load agree well, whereas under tensile load, fracture probability predictions at high K_J tend to be lower than test results.

(3) Ductile crack growth prediction by GTN model

In the transition temperature region, where ductile crack growth is assumed, evaluation must consider this failure mode. Therefore, benchmark analyses using GTN model were performed. The GTN model parameters used are shown in Table 4.2.3.3-3.

GTN model analysis results for C(T) specimens (room temperature), SE(B) specimens (-20°C, a/W=0.5), and SE(B) specimens (-80°C, a/W=0.1) are shown in Figs. 4.2.3.3-17 through 4.2.3.3-19, respectively.

Regarding load–opening displacement relations, JAEA's load predictions for SE(B) specimens (-20°C, a/W=0.5) was slightly higher, but other results were in close agreement. Similarly, the ductile crack growth–J relations corresponded with the load–*COD* trends, with JAEA's predicting higher ductile crack growth resistance for SE(B) specimens (-20°C, a/W=0.5), but others were nearly consistent.

Copyright © 2026 The Japan Welding Engineering Society, All Rights Reserved.

(4) Weibull stress evaluation using coupled model

For fracture evaluation of brittle fracture following ductile crack growth, FE analysis using the GTN model was performed. Subsequently, Weibull stress was calculated using the stress distribution near the crack tip from the FE analysis via the Beremin model for fracture evaluation.

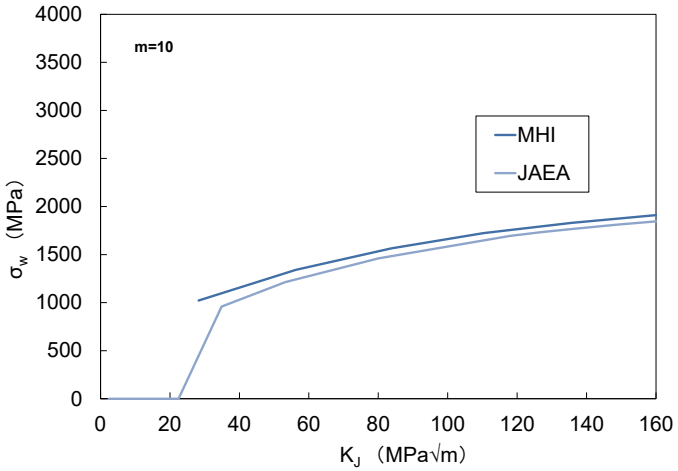
Figure 4.2.3.3-20 shows fracture prediction of SE(B) specimens (a/W=0.1) at -80°C using the coupled model. Figure 4.2.3.3-11 shows the relationship between K_J and cumulative failure probability for the same specimens and temperature using the Beremin model alone. Comparing these figures, it can be seen that UO's cumulative failure probability by the coupled model rises more steeply than MHI's at the same K_J. This is estimated to be because the J resistance of the SE(B) specimen (-80°C, a/W=0.1) in Fig. 4.2.3.3-19 was predicted lower by UO than MHI, making conditions closer to higher constraint specimens, resulting in higher cumulative failure probability at the same K_J than MHI.

Copyright © 2026 The Japan Welding Engineering Society, All Rights Reserved.

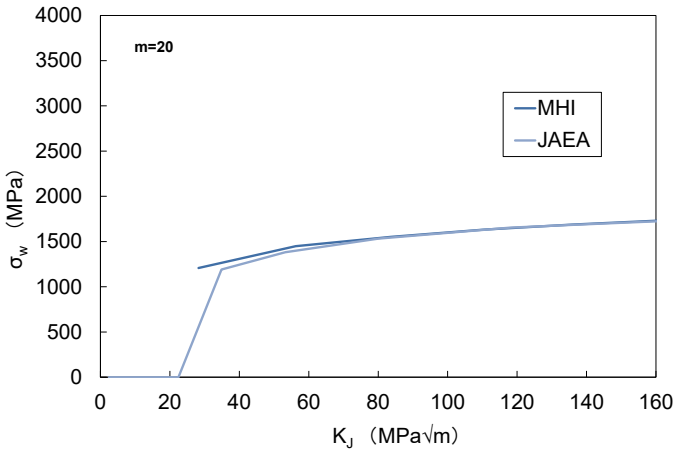
Table 4.2.3.3-1 Reference value of the maximum principal stress used for the integration range

	MHI	UO	CRIEPI	Hitachi	Toshima	IHI	JAEA
maximum principal stress (MPa)	1430	1328	1501	1440	1445	1452	1453

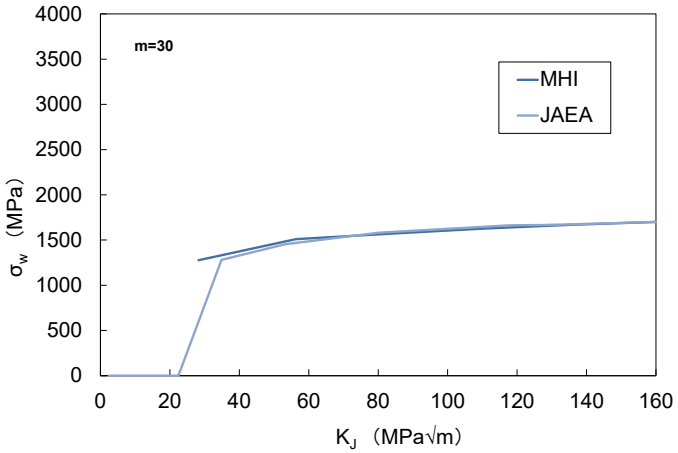
Copyright © 2026 The Japan Welding Engineering Society, All Rights Reserved.



(a) m=10



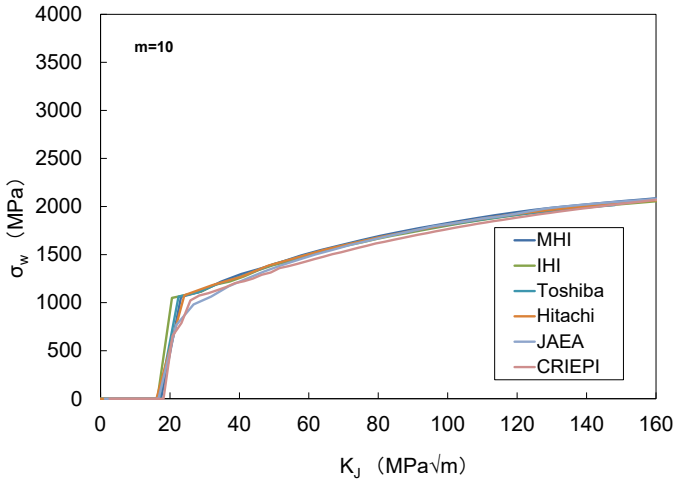
(b) m=20



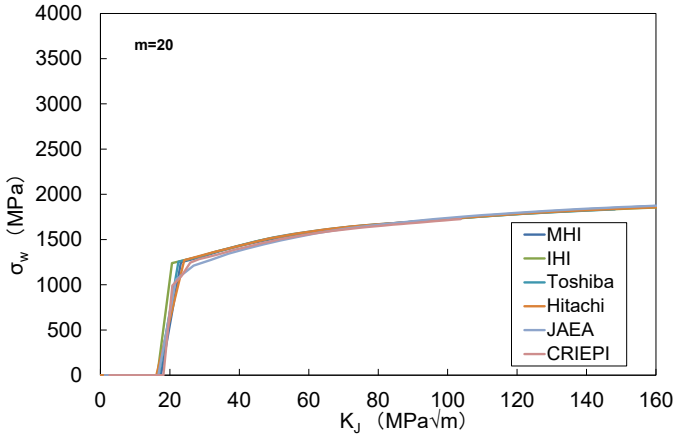
(c) m=30

Fig. 4.2.3.3-1 σ_w using fixed m for C(T) specimen (-10°C)

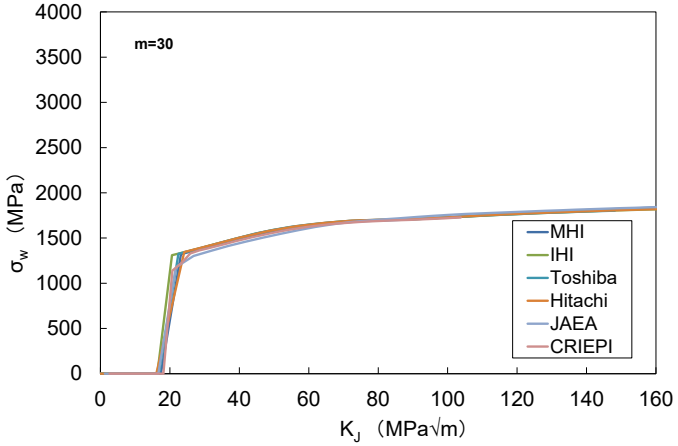
Copyright © 2026 The Japan Welding Engineering Society, All Rights Reserved.



(a) m=10



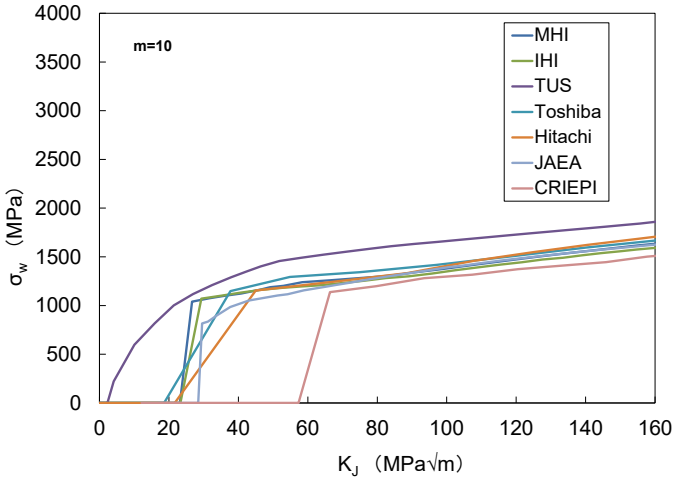
(b) m=20



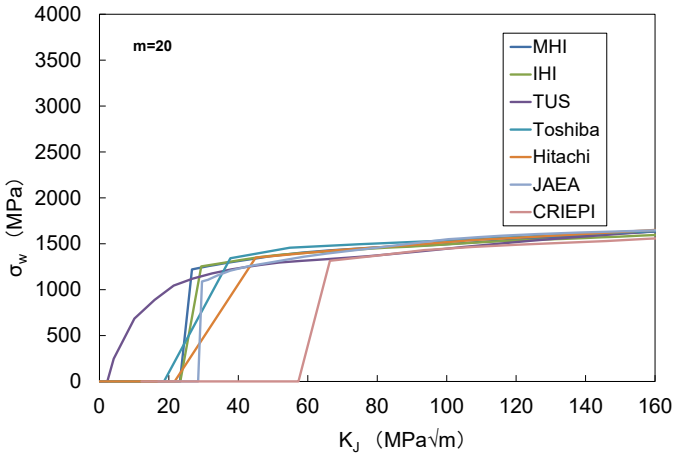
(c) m=30

Fig. 4.2.3.3-2 σ_w using fixed m for C(T) specimen (-80°C)

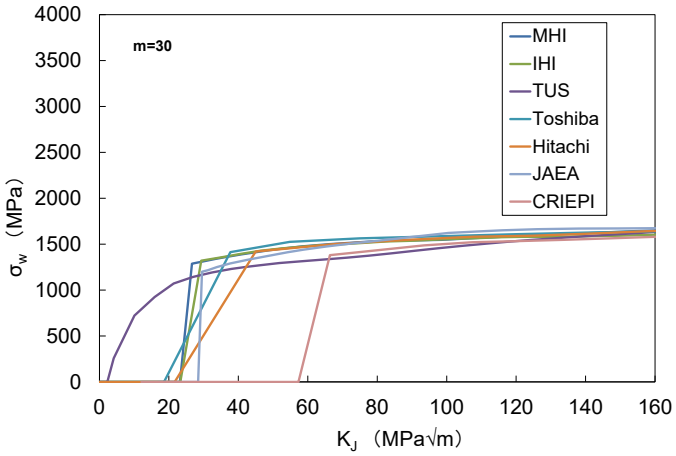
Copyright © 2026 The Japan Welding Engineering Society, All Rights Reserved.



(a) m=10



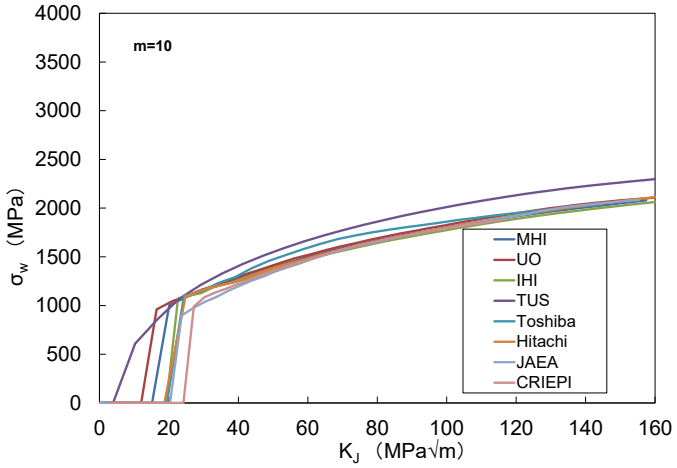
(b) m=20



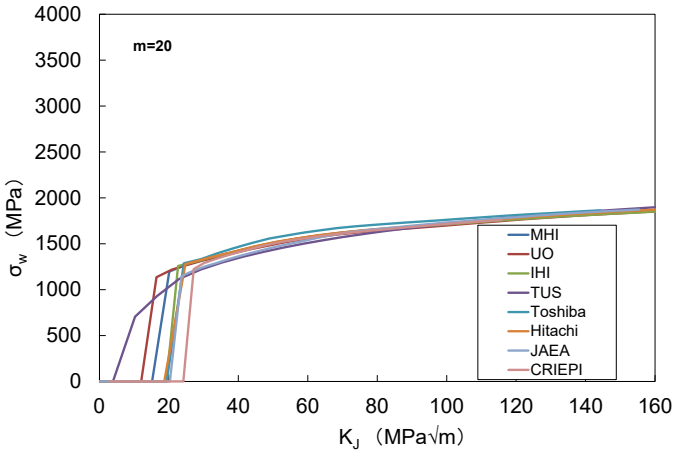
(c) m=30

Fig. 4.2.3.3-3 σ_w using fixed m for SE(B) specimen (-80°C, a/W=0.1)

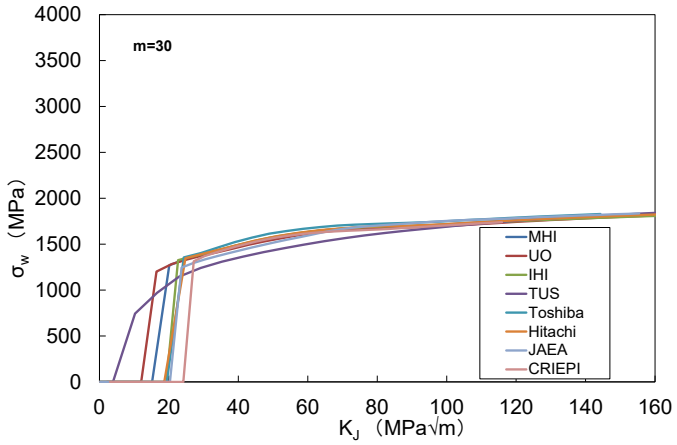
Copyright © 2026 The Japan Welding Engineering Society, All Rights Reserved.



(a) m=10



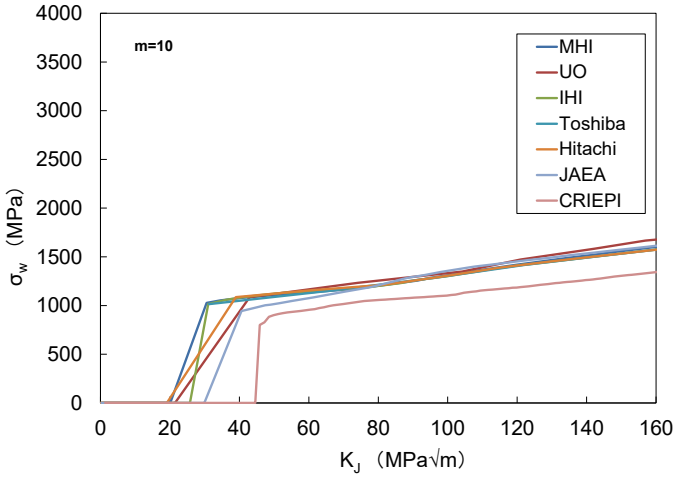
(b) m=20



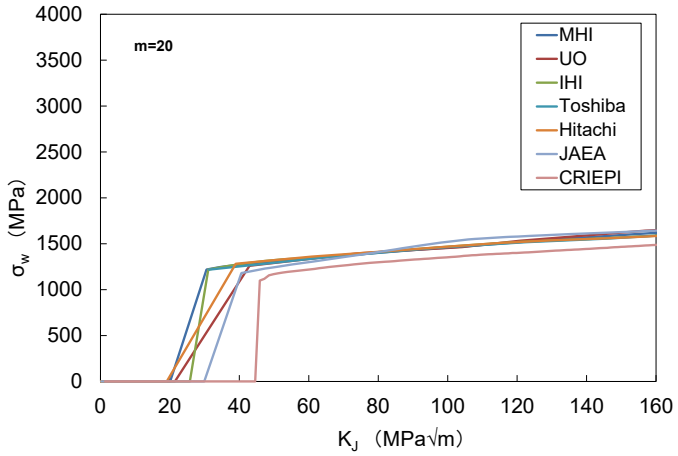
(c) m=30

Fig. 4.2.3.3-4 σ_w using fixed m for SE(B) specimen (-80°C, a/W=0.5)

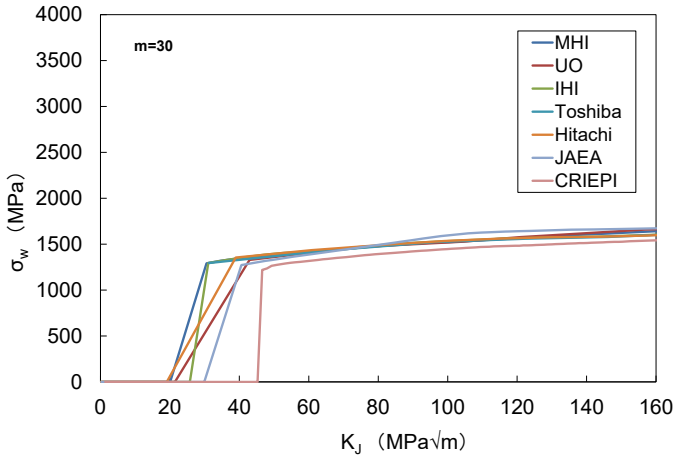
Copyright © 2026 The Japan Welding Engineering Society, All Rights Reserved.



(a) *m*=10



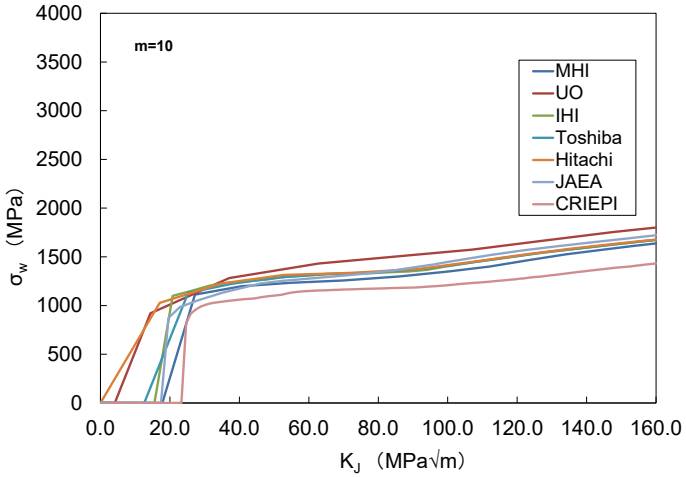
(b) *m*=20



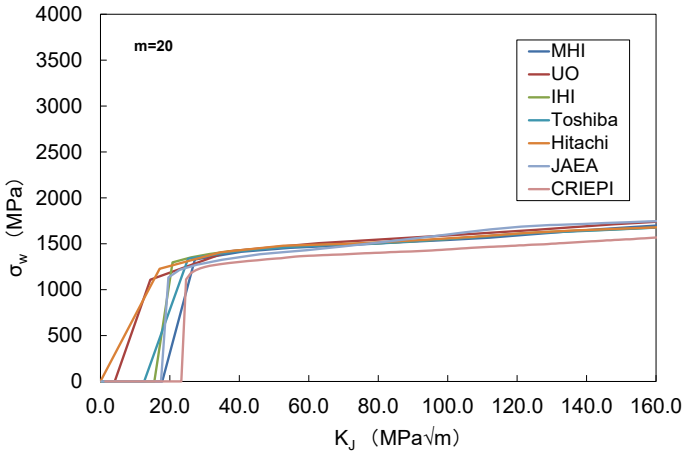
(c) *m*=30

Fig. 4.2.3.3-5 σ_w using fixed *m* for flat plate specimen with surface flaw under bending (-80°C)

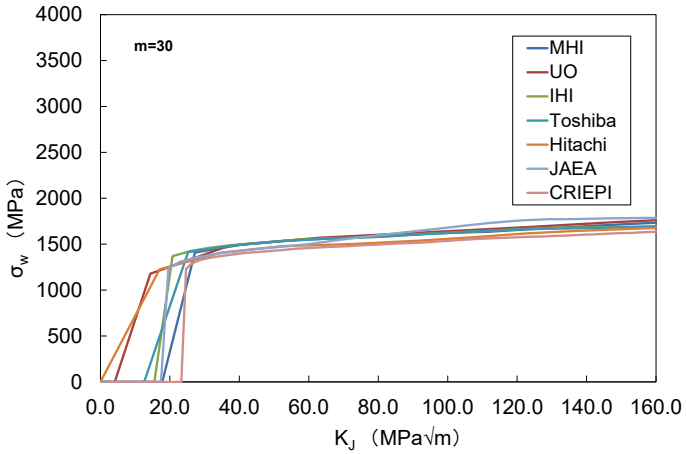
Copyright © 2026 The Japan Welding Engineering Society, All Rights Reserved.



(a) m=10



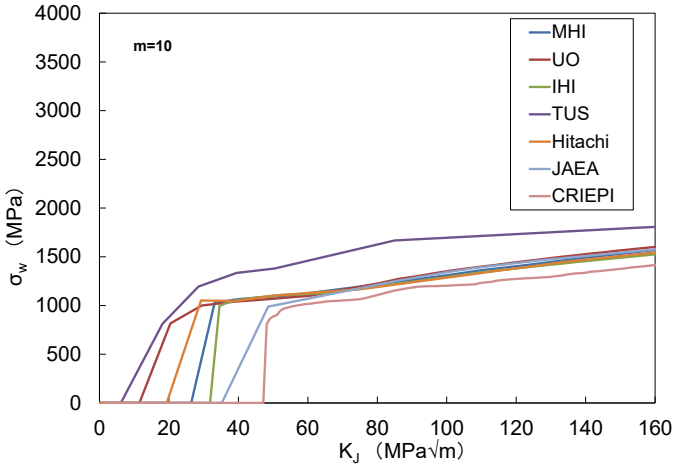
(b) m=20



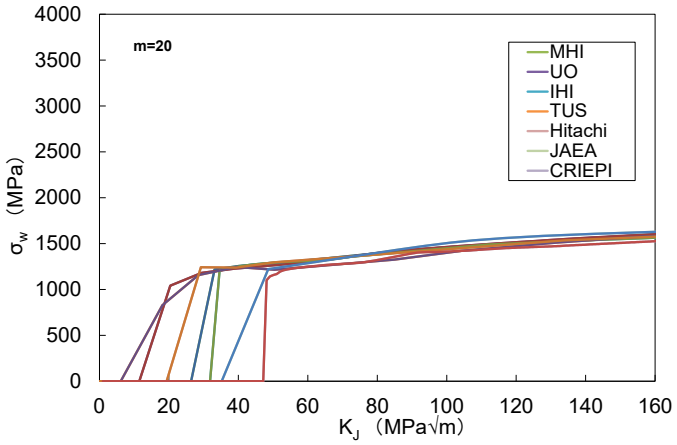
(c) m=30

Fig. 4.2.3.3-6 σ_w using fixed m for flat plate specimen with surface flaw under bending (-120°C)

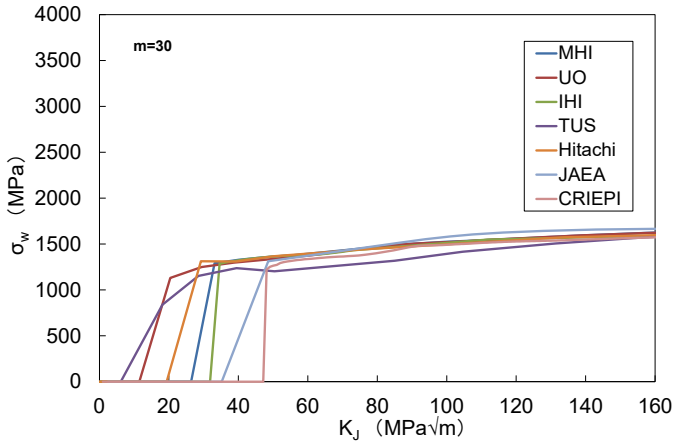
Copyright © 2026 The Japan Welding Engineering Society, All Rights Reserved.



(a) m=10



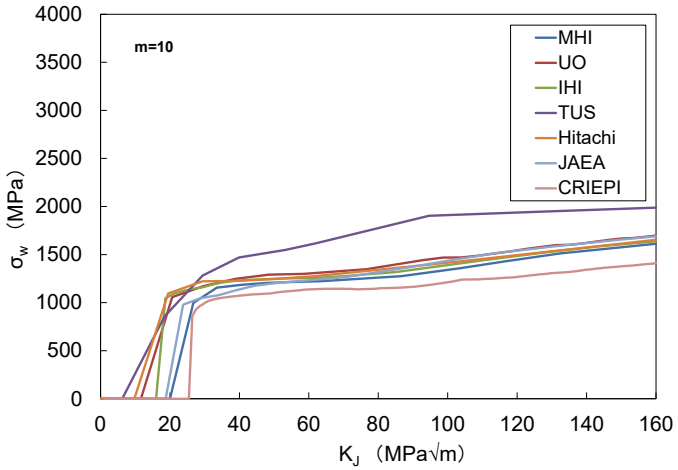
(b) m=20



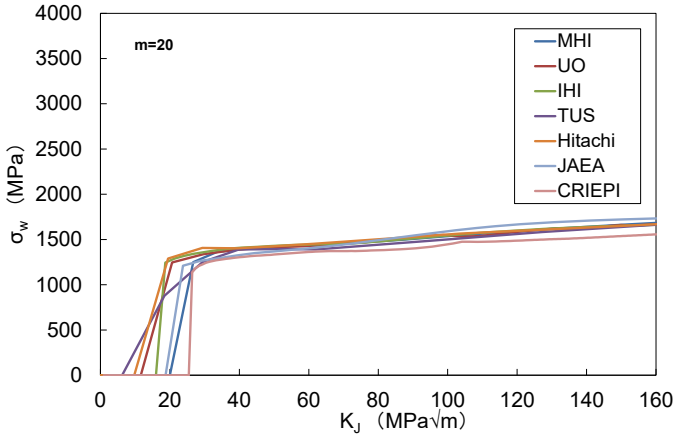
(c) m=30

Fig. 4.2.3.3-7 σ_w using fixed m for flat palate specimen with surface flaw under tensile (-80°C)

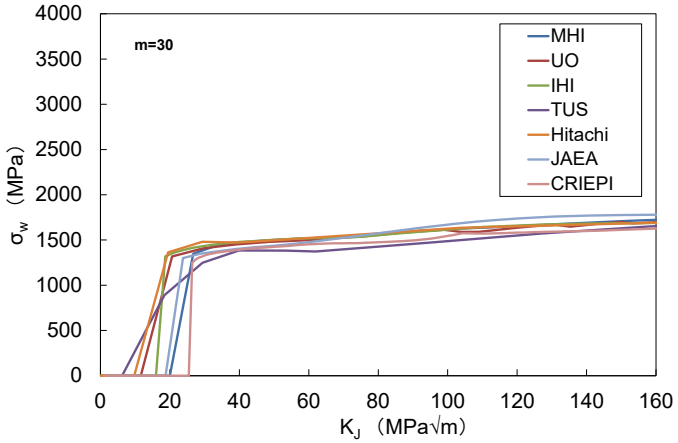
Copyright © 2026 The Japan Welding Engineering Society, All Rights Reserved.



(a) m=10



(b) m=20



(c) m=30

Fig. 4.2.3.3-8 σ_w using fixed m for flat palate specimen with surface flaw under tensile (-120°C)

Copyright © 2026 The Japan Welding Engineering Society, All Rights Reserved.

Table 4.2.3.3-2 *m* calculated by two configuration test method

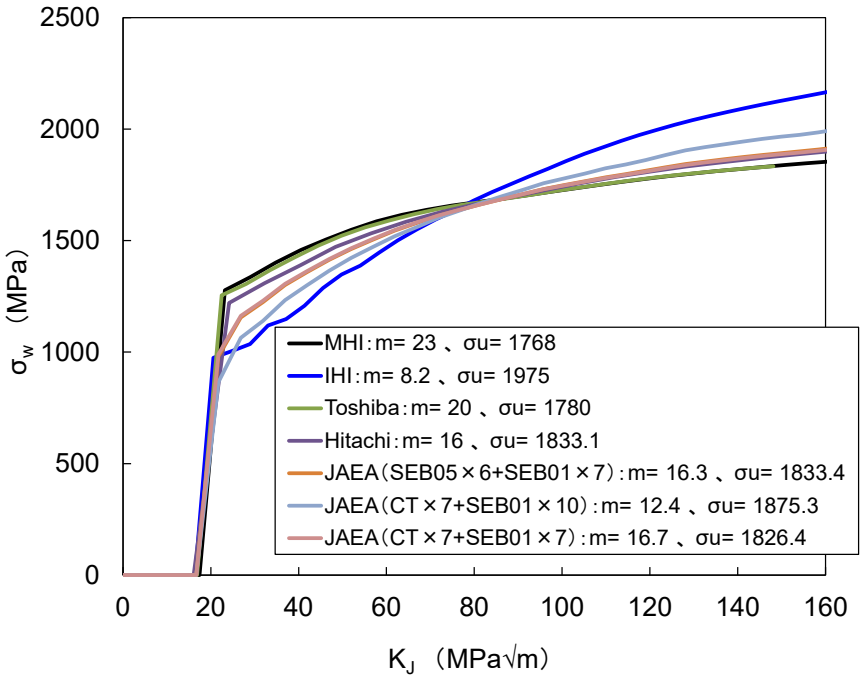
Combination of specimens used for determination of parameters	*m*						
	MHI	UO	IHI	Toshiba	Hitachi	TUS	JAEA
(1) SE(B)[*a*/*W*=0.5]×7 + SE(B)[*a*/*W*=0.1]×10	17	—	*1	*1	16	—	—
(2) SE(B)[*a*/*W*=0.5]×7 + SE(B)[*a*/*W*=0.1]×7	23	27	8.2	9	15*2	100*3	16
(3) C(T) ×7 + SE(B)[*a*/*W*=0.1]× 10	15	—	—	20	16	—	12
(4) C(T) ×7 + SE(B)[*a*/*W*=0.1]× 7	21	—	—	—	—	—	17

*1: Not converged

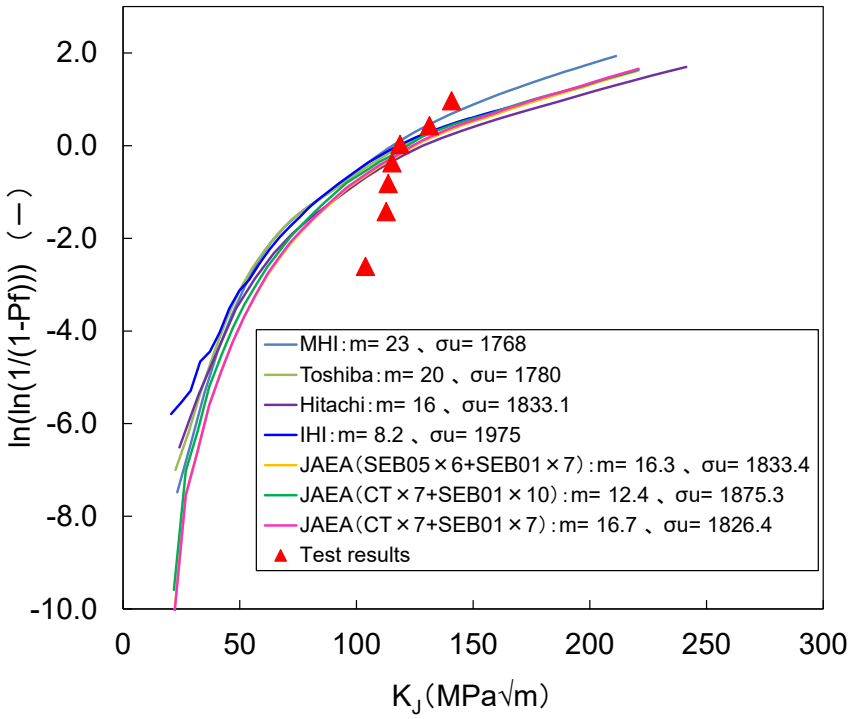
*2: The integration range of Weibull stress is not limited to be equal to or greater than the maximum principal stress of the C(T) specimen at K_J = 20 MPa√m.

*3: The provisional value was set because σ_w did not change between *m*=20 and *m*=200.

Copyright © 2026 The Japan Welding Engineering Society, All Rights Reserved.



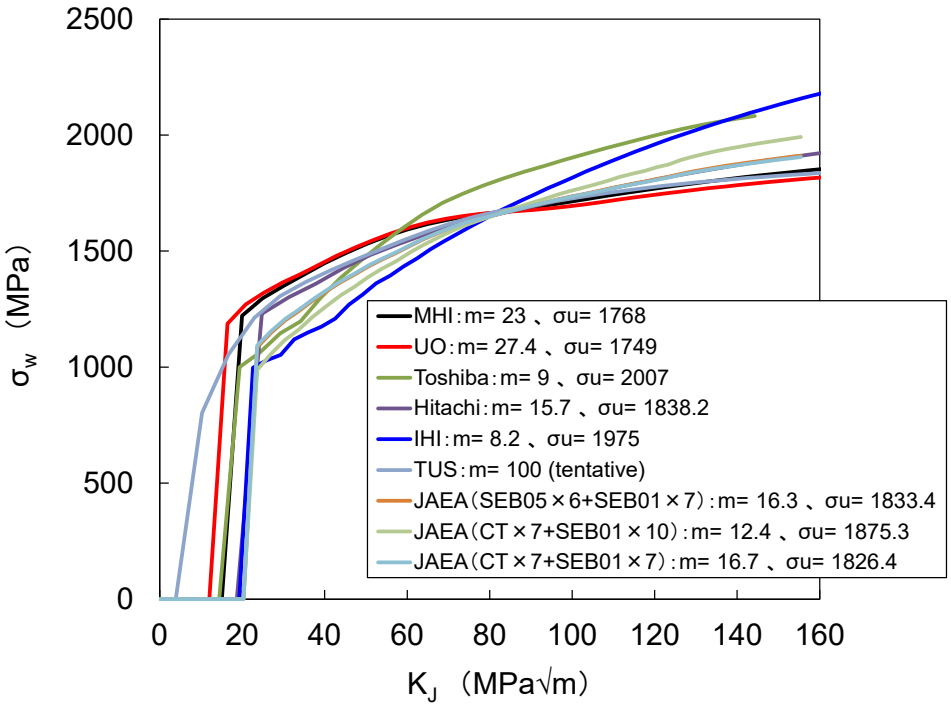
(a) Weibull stress



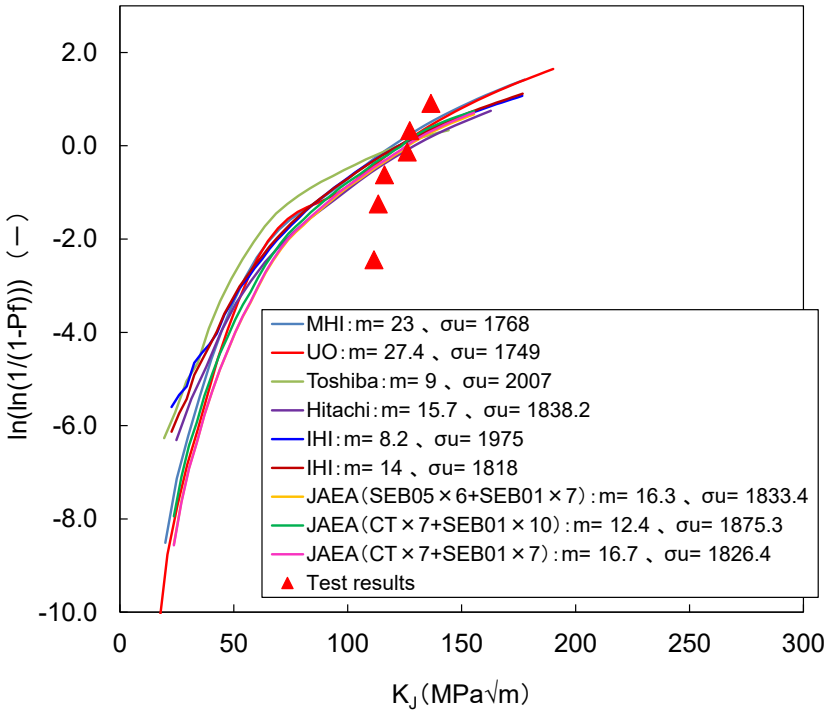
(b) Cumulative fracture probability

Fig. 4.2.3.3-9 Weibull stress and cumulative fracture probability for C(T) specimen (-80ºC) using *m* calibrated by two configuration test method

Copyright © 2026 The Japan Welding Engineering Society, All Rights Reserved.



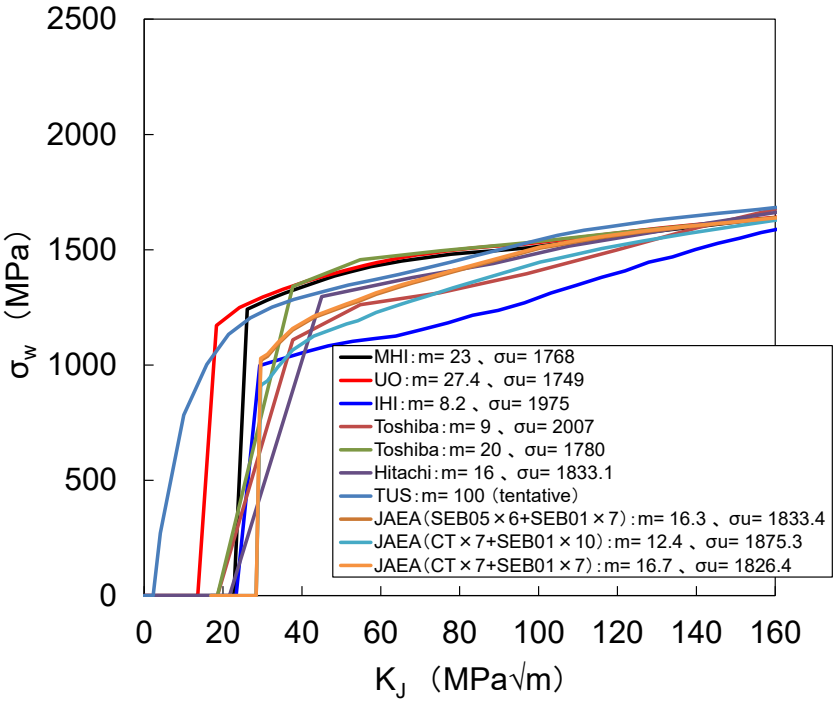
(a) Weibull stress



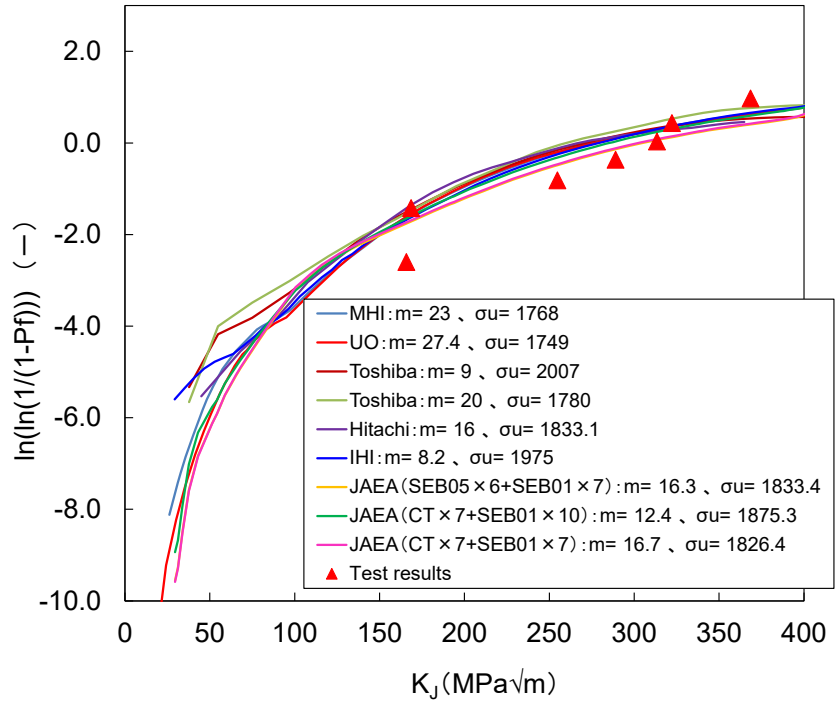
(b) Cumulative fracture probability

Fig. 4.2.3.3-10 Weibull stress and cumulative fracture probability for SE(B) specimen (-80°C, a/W=0.5) using m calibrated by two configuration test method

Copyright © 2026 The Japan Welding Engineering Society, All Rights Reserved.



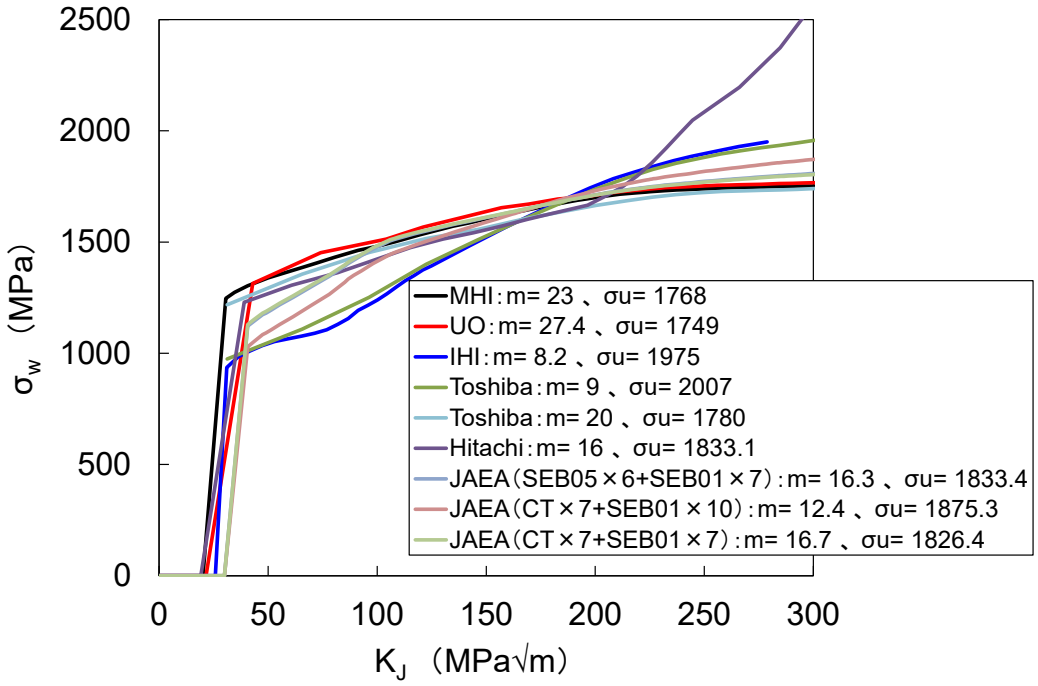
(a) Weibull stress



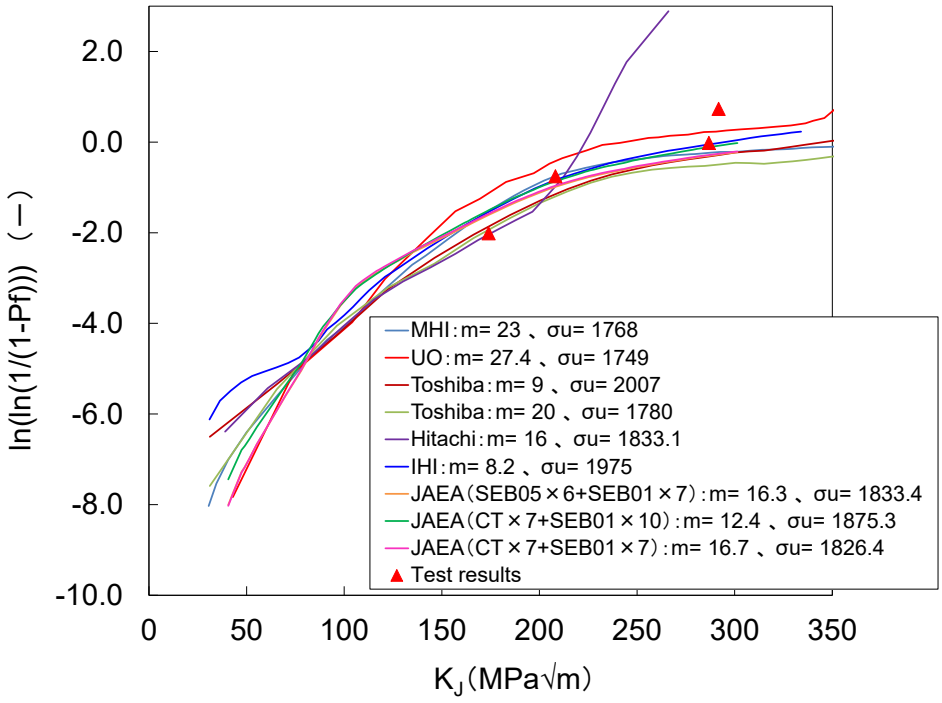
(b) Cumulative fracture probability

Fig. 4.2.3.3-11 Weibull stress and cumulative fracture probability for SE(B) specimen (-80°C, *a*/*W*=0.1) using *m* calibrated by two configuration test method

Copyright © 2026 The Japan Welding Engineering Society, All Rights Reserved.



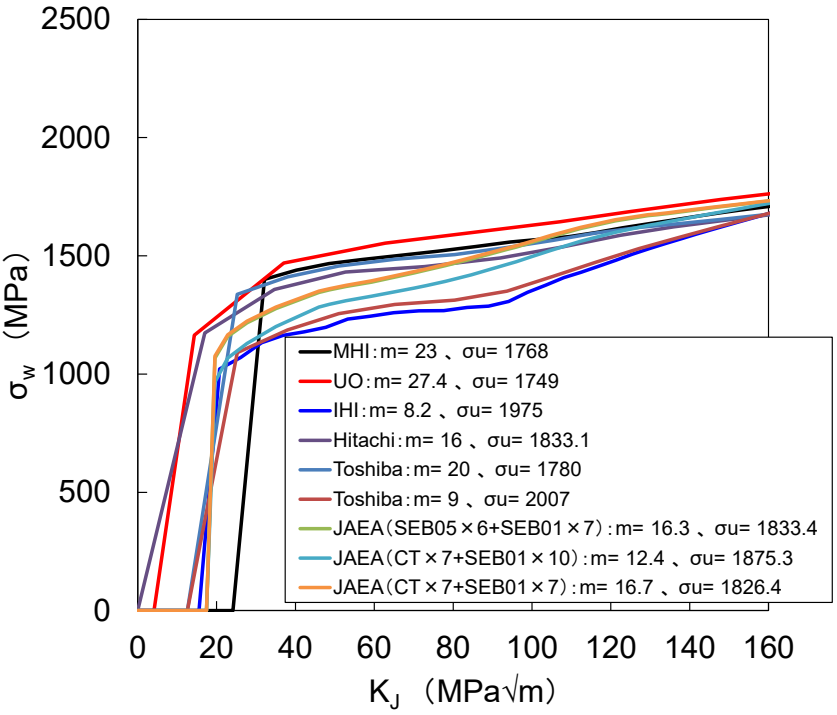
(a) Weibull stress



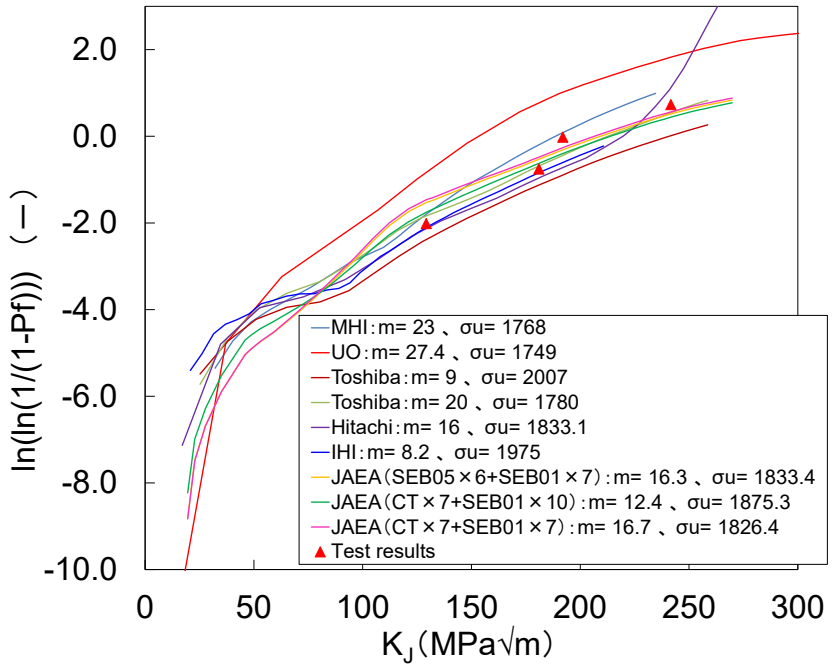
(b) Cumulative fracture probability

Fig. 4.2.3.3-12 Weibull stress and cumulative fracture probability for flat palate specimen with surface flaw under bending (-80ºC) using *m* calibrated by two configuration test method

Copyright © 2026 The Japan Welding Engineering Society, All Rights Reserved.



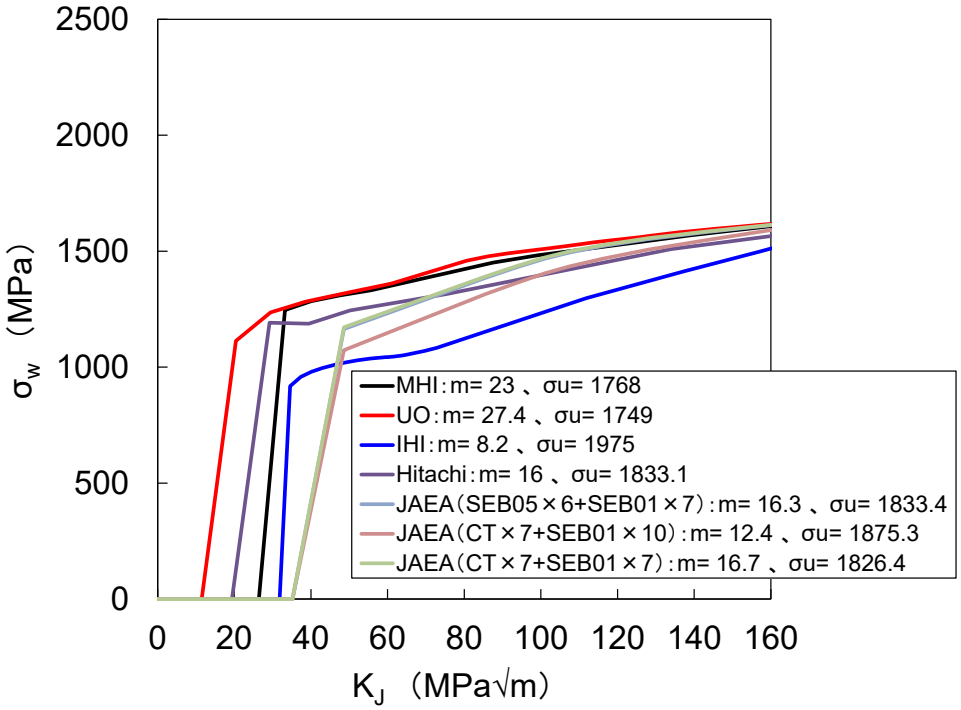
(a) Weibull stress



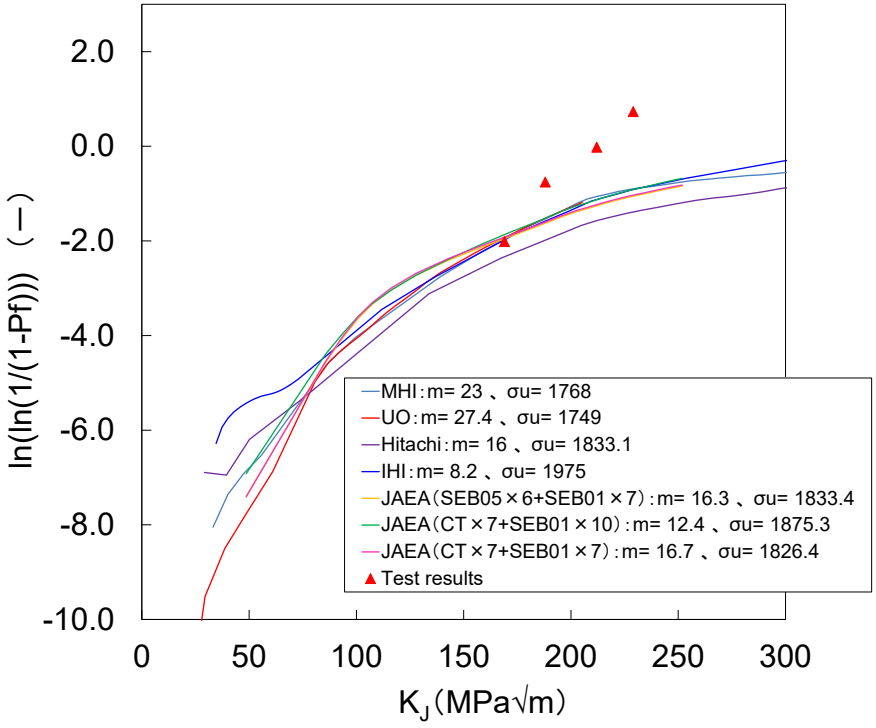
(b) Cumulative fracture probability

Fig. 4.2.3.3-13 Weibull stress and cumulative fracture probability for flat palate specimen with surface flaw under bending (-120°C) using *m* calibrated by two configuration test method

Copyright © 2026 The Japan Welding Engineering Society, All Rights Reserved.



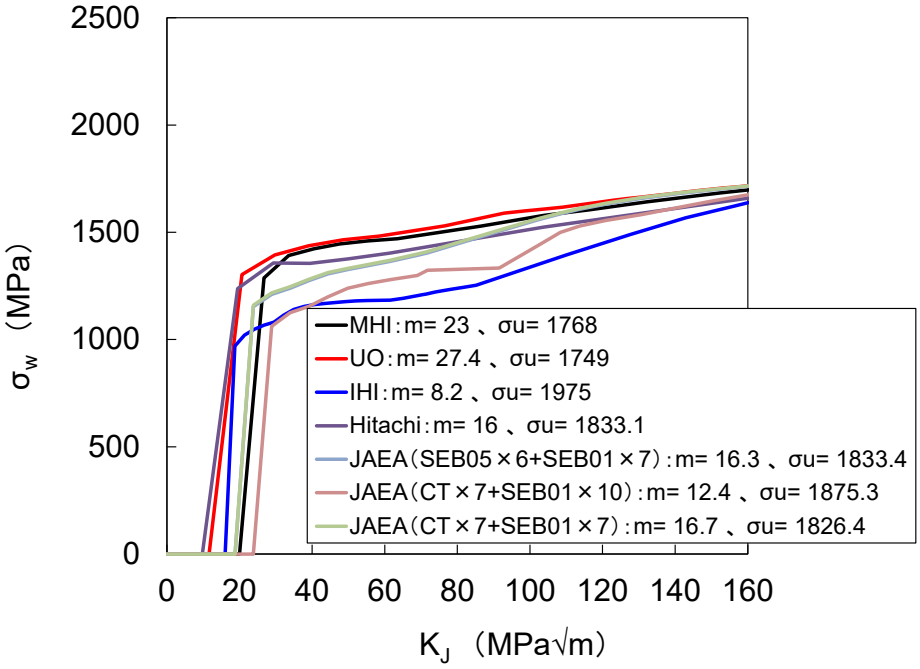
(a) Weibull stress



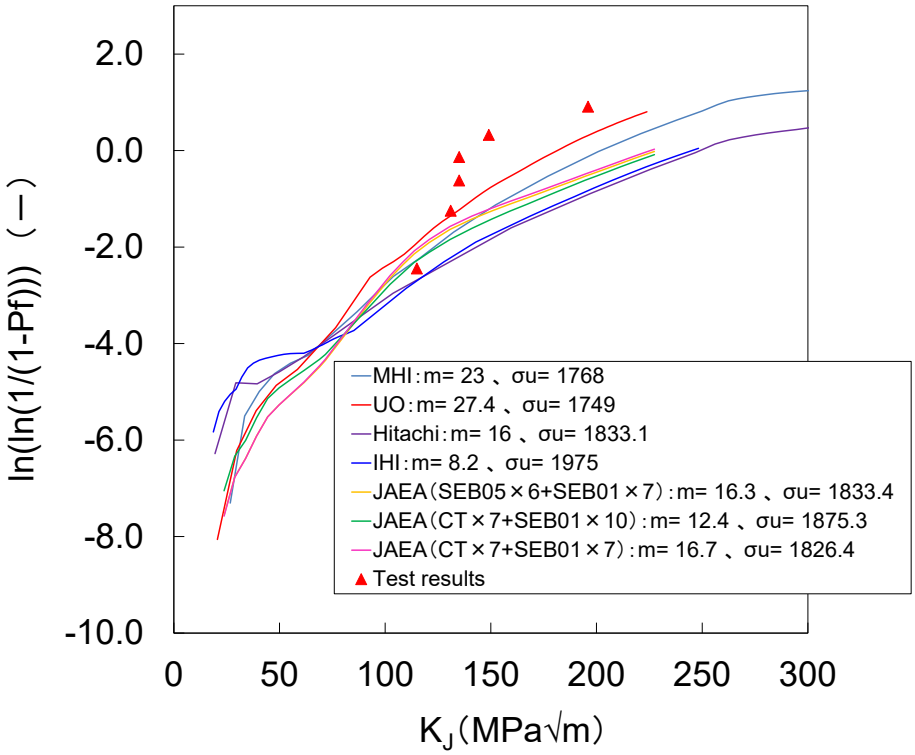
(b) Cumulative fracture probability

Fig. 4.2.3.3-14 Weibull stress and cumulative fracture probability for flat palate specimen with surface flaw under tensile (-80ºC) using *m* calibrated by two configuration test method

Copyright © 2026 The Japan Welding Engineering Society, All Rights Reserved.



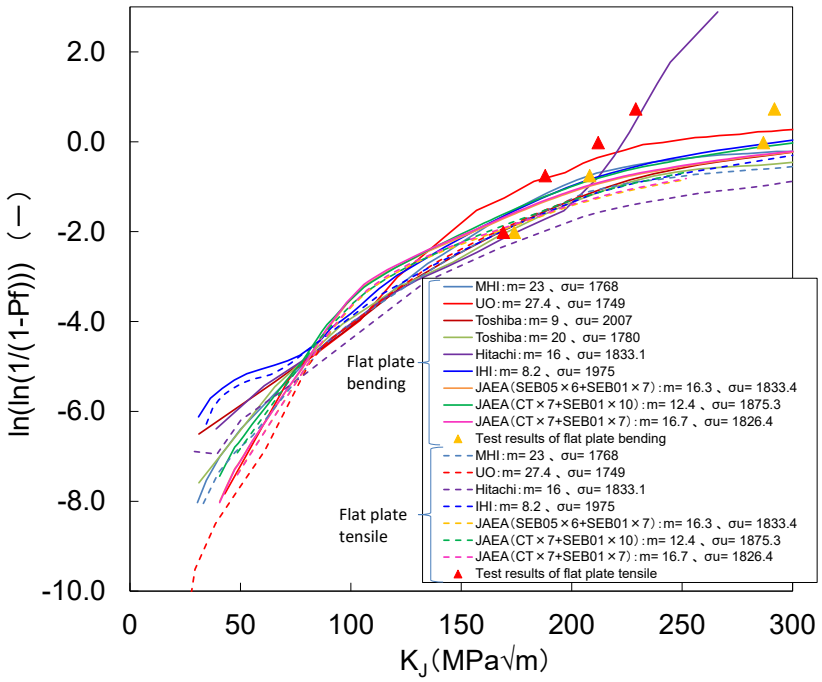
(a) Weibull stress



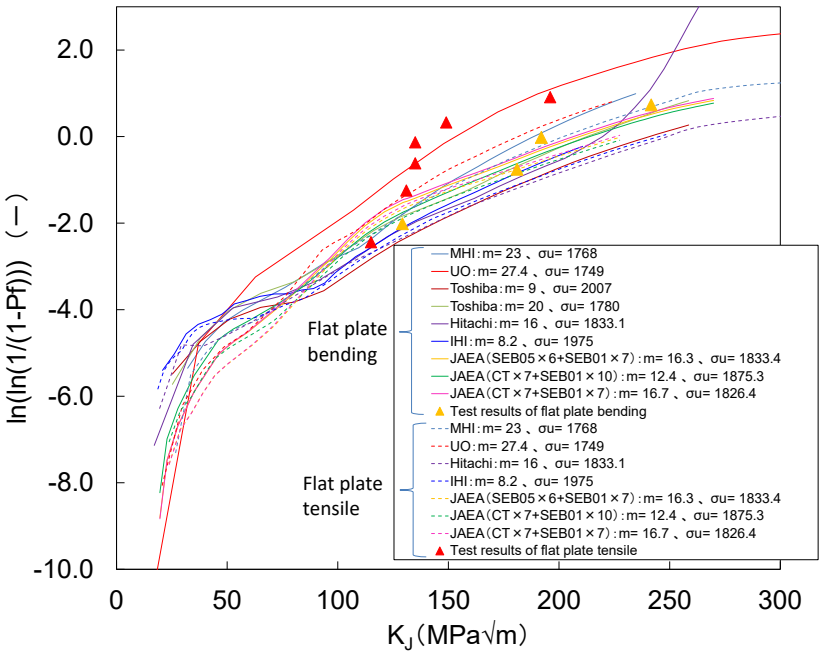
(b) Cumulative fracture probability

Fig. 4.2.3.3-15 Weibull stress and cumulative fracture probability for flat palate specimen with surface flaw under tensile (-120ºC) using *m* calibrated by two configuration test method

Copyright © 2026 The Japan Welding Engineering Society, All Rights Reserved.



(a) -80°C



(b) -120°C

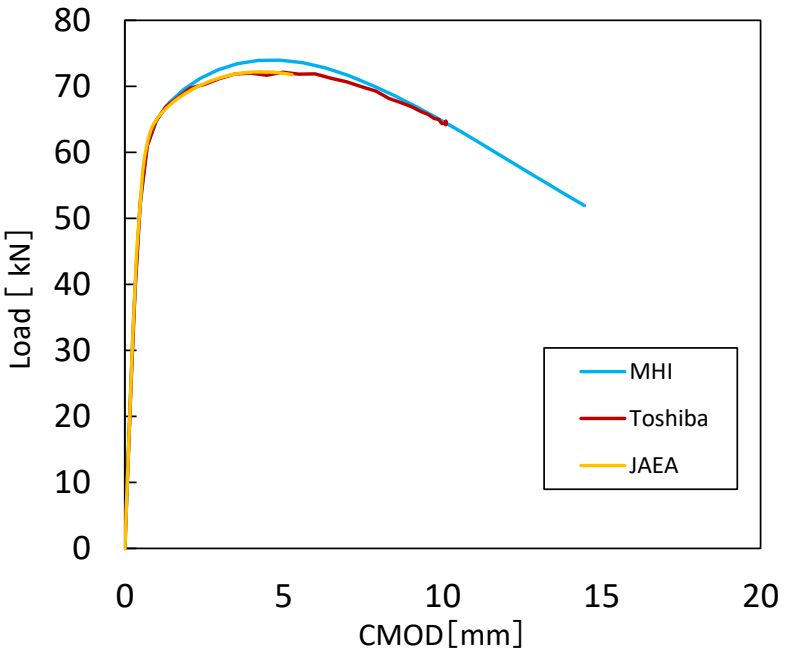
Fig. 4.2.3.3-16 Fracture prediction of flat plate specimens with surface flaw under bending and tensile

Copyright © 2026 The Japan Welding Engineering Society, All Rights Reserved.

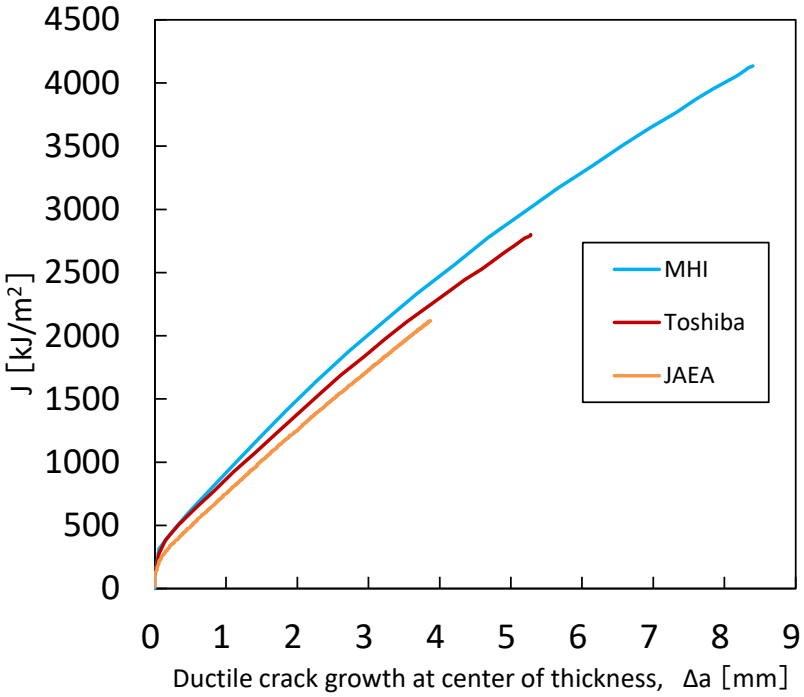
Table 4.2.3.3-3 GTN model's parameters

q_1	q_2	q_3	f_0	f_N	f_c	f_F	ε_N	S_N
1.5	1	2.25	1.00×10^{-5}	2.76×10^{-2}	7.00×10^{-2}	2.35×10^{-1}	6.62×10^{-1}	9.42×10^{-2}

Copyright © 2026 The Japan Welding Engineering Society, All Rights Reserved.



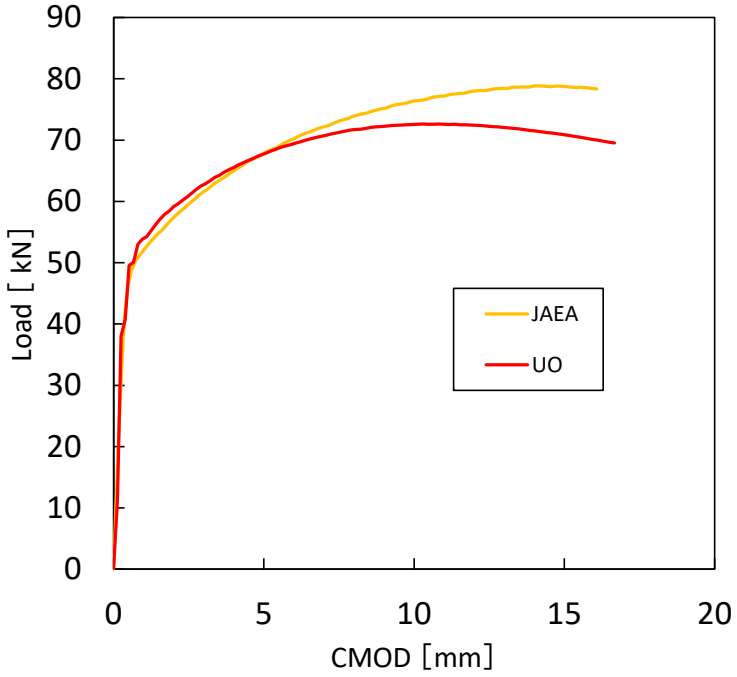
(a) Load - CMOD



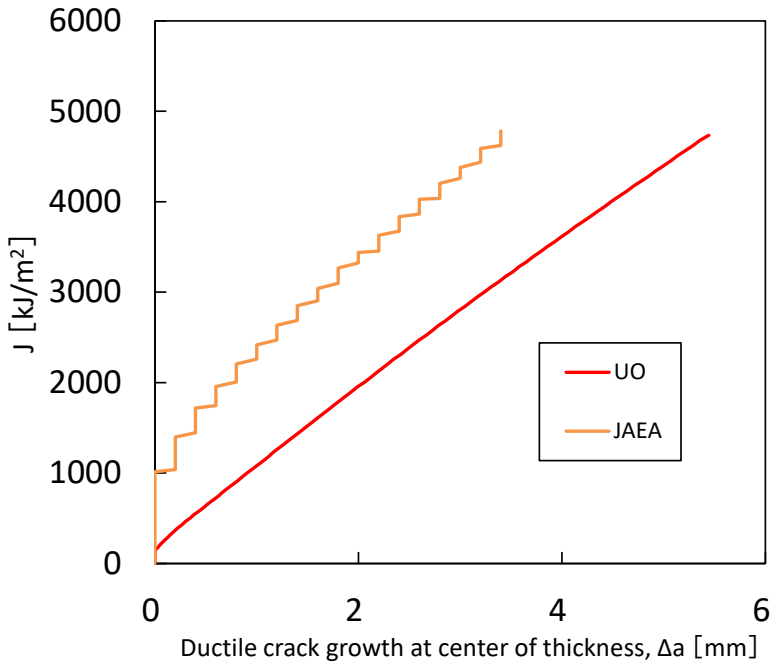
(b) J-integral – ductile crack growth

Fig. 4.2.3.3-17 GTN model Analysis Results for C(T) specimen (room temperature)

Copyright © 2026 The Japan Welding Engineering Society, All Rights Reserved.



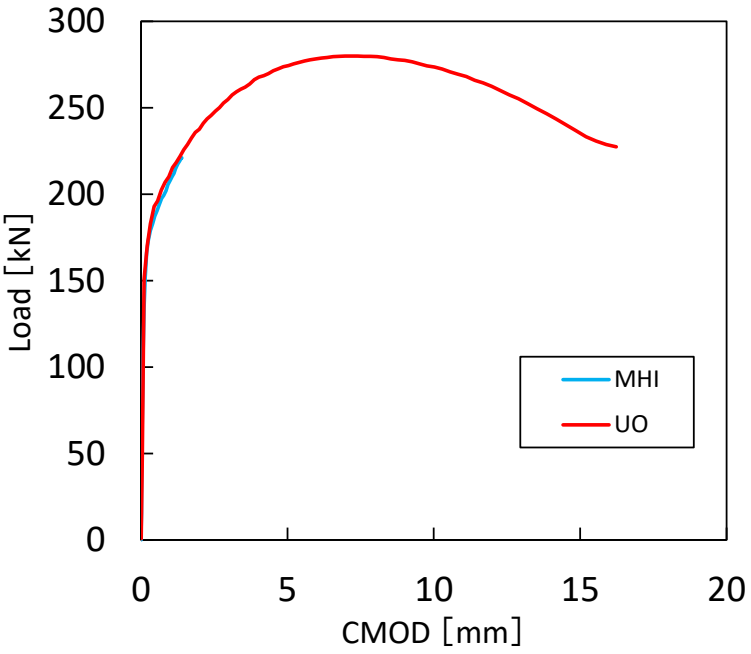
(a) Load - CMOD



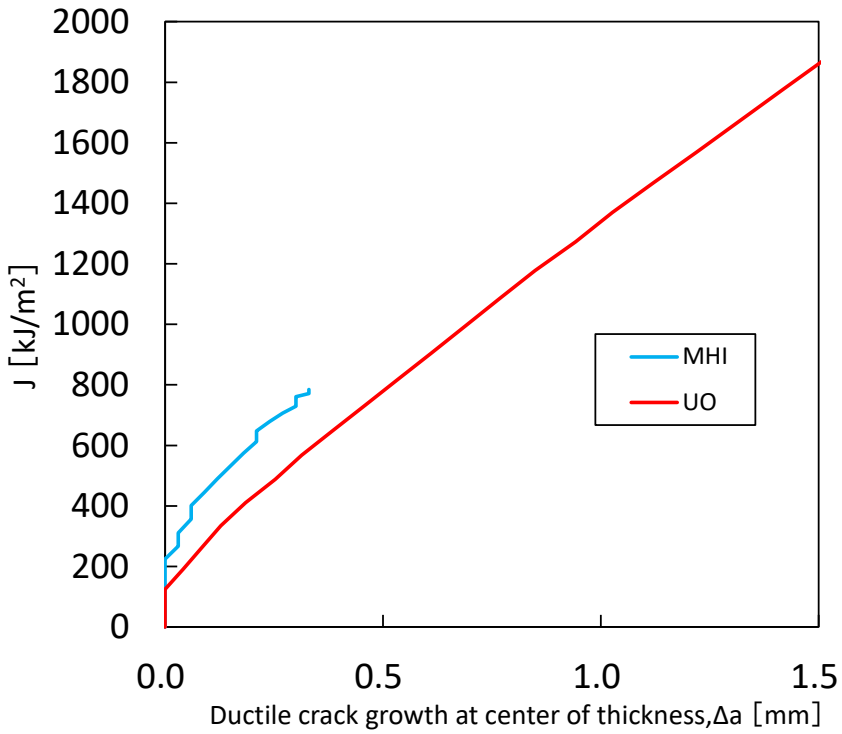
(b) J-integral – ductile crack growth

Fig. 4.2.3.3-18 GTN model Analysis Results for SE(B) specimen (-20°C, a/W=0.5)

Copyright © 2026 The Japan Welding Engineering Society, All Rights Reserved.



(a) Load - CMOD



(b) J-integral – ductile crack growth

Fig. 4.2.3.3-19 GTN Analysis Results for SE(B) specimen (-80°C, a/W=0.1)

Copyright © 2026 The Japan Welding Engineering Society, All Rights Reserved.

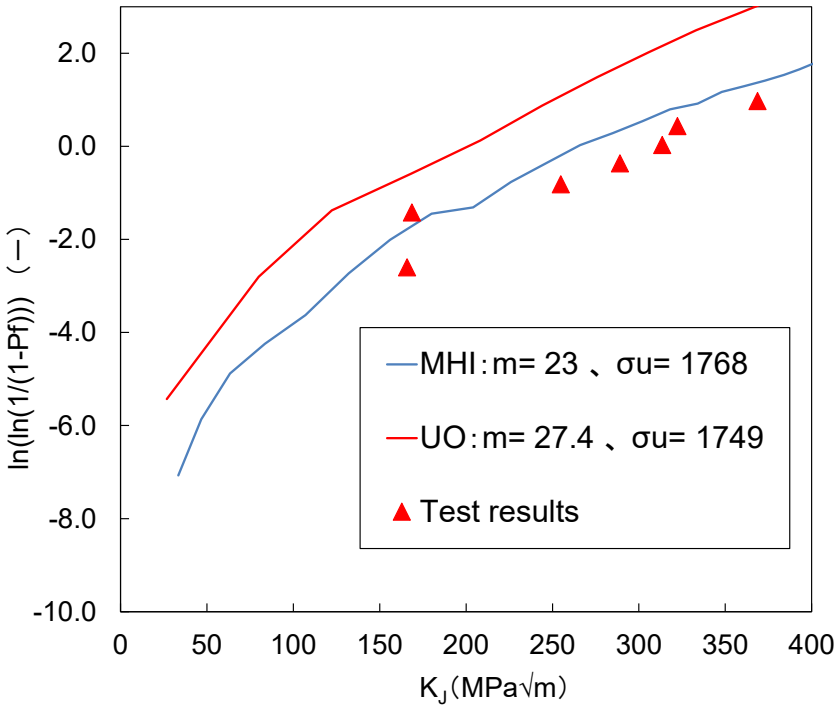


Fig. 4.2.3.3-20 Fracture prediction of SE(B) specimen (-80°C, a/W=0.1) using coupled model

Copyright © 2026 The Japan Welding Engineering Society, All Rights Reserved.

4.2.3.4 Summary

When the Weibull stress was calculated with the Weibull parameter m fixed for each specimen, nearly equivalent values of σ_w were obtained across all organizations. This verifies that, given an input m, the Weibull stress defined by Equation (3.2-2) is properly computed by the different organizations.

The m value determined by the two-specimens method varied depending on the combination of specimens used to determine the parameters, ranging from 9 to 27. When the converged m was small, σ_w tends to be slightly lower; however, the σ_w–K_J relationships for each specimen were nearly consistent among all organizations. The relationships between cumulative failure probability and K_J obtained using m values determined by each organization showed much smaller variation than the σ_w–K_J relationships among organizations.

These results indicate that even if different m values are derived from fracture test on high-constraint laboratory specimens by different analysts, the predicted fracture probabilities for low-constraint specimens or structures using those m values do not significantly differ. This demonstrate that the influence of the Beremin model analysis tools is minimal.

Regarding the GTN model analyses, the load–*COD* relationships and ductile crack growth–J relationships showed good agreement among organizations.

For the coupled model, a comparison was performed by two organizations for SE(B) specimens with a/W=0.1 at -80°C. Although there were some differences, these are estimated to be due to differences in J resistance curves derived from the GTN model.

Copyright © 2026 The Japan Welding Engineering Society, All Rights Reserved.

4.3 Verification results

4.3.1 Calculation of Weibull parameters

The Weibull parameters used for brittle fracture evaluation were calculated by applying the two-specimens method proposed in Section 3.2. Two types of SE(B) specimens with different crack depths and constraint levels were used for the calculation . The analysis model is shown in Fig. 4.2.2.3-1.

The two-specimens method yielded m = 23 and σ_u = 1768 MPa. Figure 4.3.1-1 shows the σ_W–J relationship for SE(B) specimens at m = 23. Figure 4.3.1-2 shows the Weibull plot of the limit Weibull stress of SE(B) specimens converged by the two-specimens method. Although the J_c value of SE(B) a/W=0.1 is larger than that of SE(B) a/W=0.5 due to different plastic constraint degrees, the critical Weibull stress almost coincides between the two by using m = 23.

Many literatures indicate that the Weibull parameter m for ferritic steel ranges from about 10 to 60, and the obtained value is within this range.

Copyright © 2026 The Japan Welding Engineering Society, All Rights Reserved.

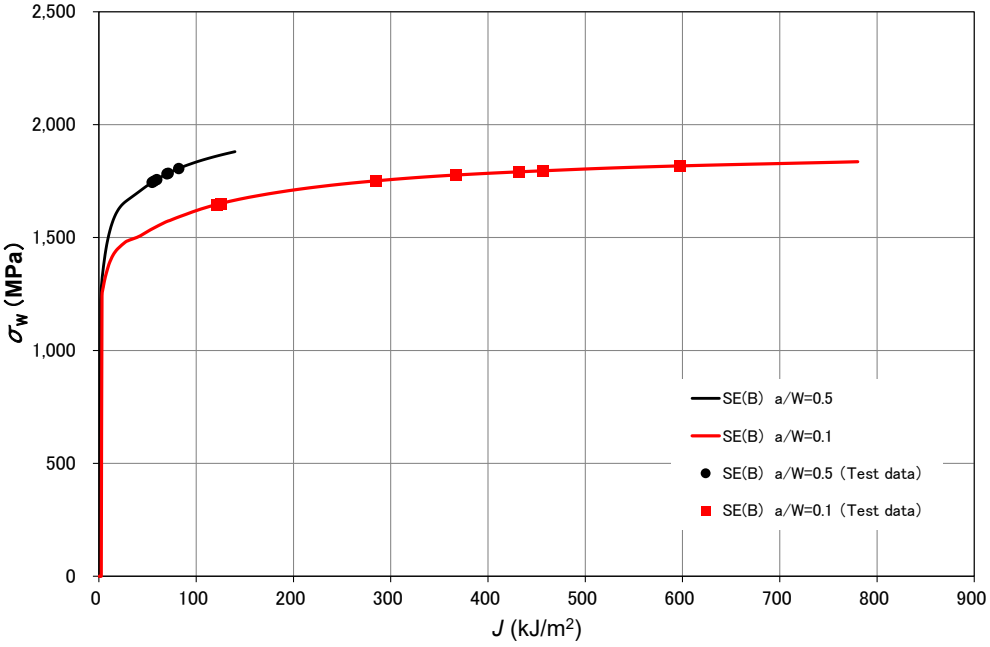


Fig. 4.3.1-1 σ_W – J relations of SE(B) specimen

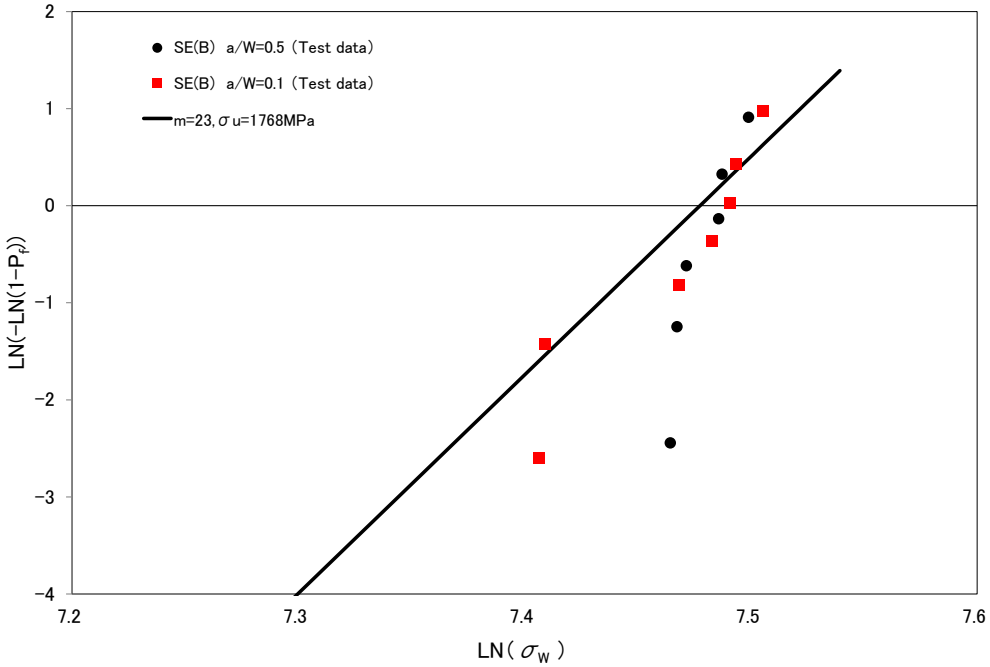


Fig. 4.3.1-2 Weibull plots of critical Weibull stress σ_{Wc} of SE(B)

Copyright © 2026 The Japan Welding Engineering Society, All Rights Reserved.

4.3.2 Calculation of GTN model parameters

As described in Section 4.2.2.3, the GTN model was used for the analysis of ductile crack growth. The GTN model parameters were calculated by fitting to the results of the room temperature C(T) test shown in Fig. 4.1.3.4-6. The number of GTN model parameters is nine: q_1, q_2, q_3, f_0, f_c, f_F, ε_N, f_N, and S_N. Referring to previous literature, q_1, q_2, and q_3 were fixed values ($q_1 = 1.5$, $q_2 = 1.0$, $q_3 = q_1^2$), and the other six parameters were fitting parameters. Each parameter was varied within a certain range and examined, and the values corresponding to the load–load line displacement and flaw shape were set as the optimal values.

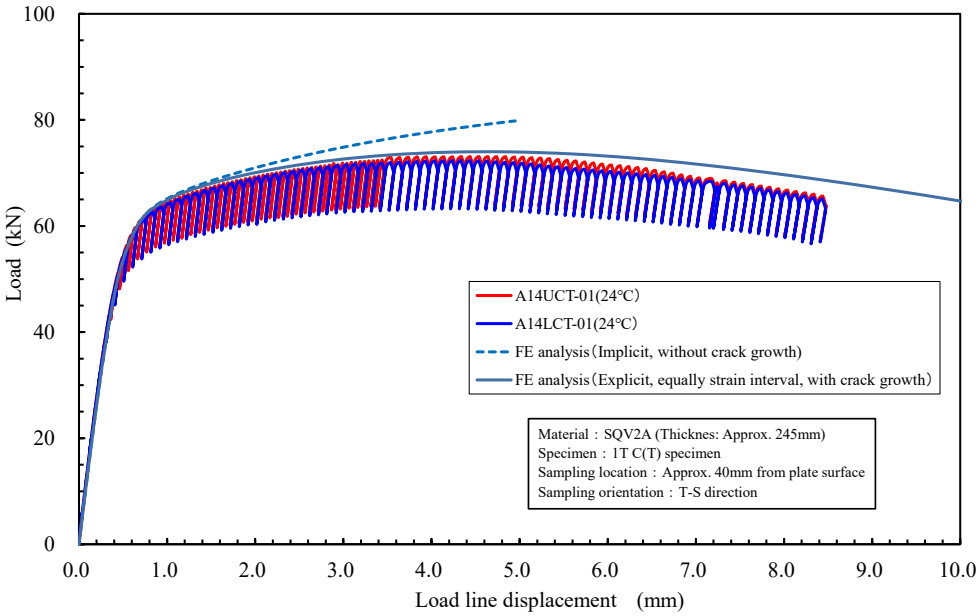
The analysis model used for FE analysis is shown in Fig. 4.2.2.3-2. The parameters obtained by fitting are shown in Table 4.3.2-1. Figure 4.3.2-1 compares the analysis results using these parameters with the test results. Considering crack growth by the GTN model, the load versus load-line displacement relationship agreed with the test results better than ordinary FE analysis without crack growth consideration. In addition, the thickness direction distribution of ductile crack growth obtained by fractography after the test almost coincided with the thickness direction distribution of crack growth by the GTN model. From these results, it is considered that the GTN parameter values shown in Table 4.3.2-1 are near-optimal solutions.

In general, ductile crack growth parameters, i.e., GTN model parameters, are considered temperature-independent constant. Therefore, the parameters obtained at room temperature are also applied to the analysis of flat plate specimens at -80°C.

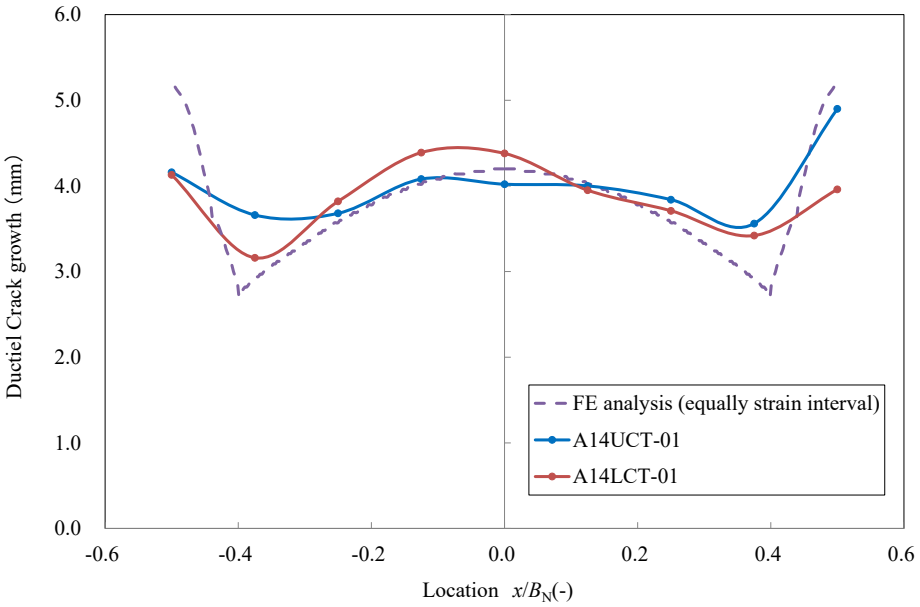
Table 4.3.2-1 GTN model parameters of low alloy steel B

f_0	f_N	f_c	f_F	ε_N	S_N
1.00×10^{-5}	2.76×10^{-2}	7.00×10^{-2}	2.35×10^{-1}	6.62×10^{-1}	9.42×10^{-2}

Copyright © 2026 The Japan Welding Engineering Society, All Rights Reserved.



(a) Load-Load line displacement



(b) Ductile crack growth distribution along thickness direction

Fig. 4.3.2-1 Reproduced analysis result of GTN model by using optimized parameters

Copyright © 2026 The Japan Welding Engineering Society, All Rights Reserved.

4.3.3 Fracture prediction of flat plate specimens

Using the model parameter values obtained from laboratory specimens in Sections 4.3.1 and 4.3.2, fracture predictions were performed for flat plate tensile and bending specimens. Since no ductile crack growth occurred in fracture tests at the test temperature of -120°C for both plate tensile and bending specimens, evaluations were performed without considering ductile crack growth. For specimens at -80°C, evaluations were performed using the coupled model, which considers ductile crack growth by employing the GTN model. Fracture evaluations compared the 5% and 95% cumulative failure probability K_J values estimated from the Weibull parameters m and σ_u with the K_{Jc} from test results to confirm whether they fell within the estimated range.

(1) Flat plate tensile specimens

The analysis model for fracture prediction of flat plate tensile specimens is shown in Fig. 4.2.2.3-1. The temperature condition for the analysis assumed a uniform test temperature distribution (-120°C or -80°C) for the entire model, including the tab plates. Although the actual temperature distribution in fracture tests differs from this condition, since fracture prediction is performed without test results, the test conditions were used directly as analysis conditions. The material properties of low alloy steel B shown in Fig. 4.2.2-1 were applied to the entire analysis model, including the tab plates.

Figure 4.3.3-1 compares the load–*COD* relationship from FE analysis at -120°C with measured values. The results agree closely, particularly with accurate prediction of yield load, confirming the appropriateness of the analysis. The load–*COD* relationship of T_6 specimen closely matches the analysis results. However, the elastic region behavior of the T_8 specimen and the yield region of the T_{10} specimen deviate significantly from the analysis, likely due to ambient temperature fluctuations caused by poor temperature control. Figure 4.3.3-2 shows the Weibull stress–K_J relationship for fracture limit evaluation.

Figure 4.3.3-3 compares the load–*COD* relationship from FE analysis at -80°C with measured ones. Similar to the -120°C case, the load–*COD* relationships agree well, indicating the validity of the analysis. Especially, the behavior of the non-fractured T_4 specimen closely corresponds to the analysis results, and the T_3 specimen also shows good agreement. However, some specimens (T_7 and T_9) at -80°C exhibit nonlinear load–*COD* relationships in the elastic region.

Figure 4.3.3-4 shows the Weibull stress–K_J relationships calculated using the stress-strain fields

Copyright © 2026 The Japan Welding Engineering Society, All Rights Reserved.

from conventional (implicit method, without GTN model) FE analysis and from GTN model analysis combined in the coupled model. The coupled model analysis uses the explicit method Abaqus Explicit, which lacks built-in J-integral calculation capability. Therefore, the K_J for the coupled model was interpolated from elastic-plastic FE analysis without the GTN model using the implicit solver. While the conventional elastic-plastic analysis show a plateau in the Weibull stress, the coupled model exhibits monotonically increasing Weibull stress with increasing load, appropriately reflecting the increase in fracture probability due to ductile crack growth.

(2) Flat plate bending specimens

Figure 4.3.3-5 and Fig. 4.3.3-6 compare FE analysis results with experimental data for the load–load-line displacement and load–COD_1 relationships at -120°C, respectively. The FE results closely match the test data. Figure 4.3.3-7 shows the calculated Weibull stress–K_J relationship. The fracture limits of -120°C specimens fall within the 5% to 95% cumulative failure probability range estimated from the critical Weibull stress, confirming the validity of the evaluation method.

Figure 4.3.3-8 and Fig. 4.3.3-9 compare the load–load-line displacement and load–COD_1 relationships at -80°C, respectively, again demonstrating good agreement between analysis and experiments supporting the FE model's validity.

Figure 4.3.3-10 compares Weibull stress from conventional elastic-plastic analysis without the GTN model with that from the coupled model combined with GTN analysis. K_J was calculated from conventional elastic-plastic FE analysis without the GTN model. The σ_w–K_J relationship from conventional FE analysis lacks plots beyond K_J = 330 MPa√m because of calculation errors caused by excessively large deformation and element distortion at the crack tip in the latter half of loading (beyond 400 MPa√m). In contrast, the coupled model shows monotonically increasing Weibull stress with increasing load, appropriately representing the increase in fracture probability due to ductile crack growth.

(3) Fracture prediction results

Figure 4.3.3-11 shows the relationship between fracture toughness K_J (K_{Jc}) obtained from fracture tests of flat plate specimens and standard laboratory specimens and test temperature. The figure also includes fracture toughness corresponding to 5% and 95% cumulative failure probabilities for flat

Copyright © 2026 The Japan Welding Engineering Society, All Rights Reserved.

plate tensile and bending specimens obtained from the above fracture prediction analyses.

Except for non-fractured data at -80°C, the K_{Jc} obtained from fracture tests fall within the predicted range, verifying that the fracture behavior of low-constraint surface-flawed flat plate specimens can be successfully predicted by the method proposed in Section 3.2.

The results discussed in this chapter have been published in references [4-6] to [4-8].

Copyright © 2026 The Japan Welding Engineering Society, All Rights Reserved.

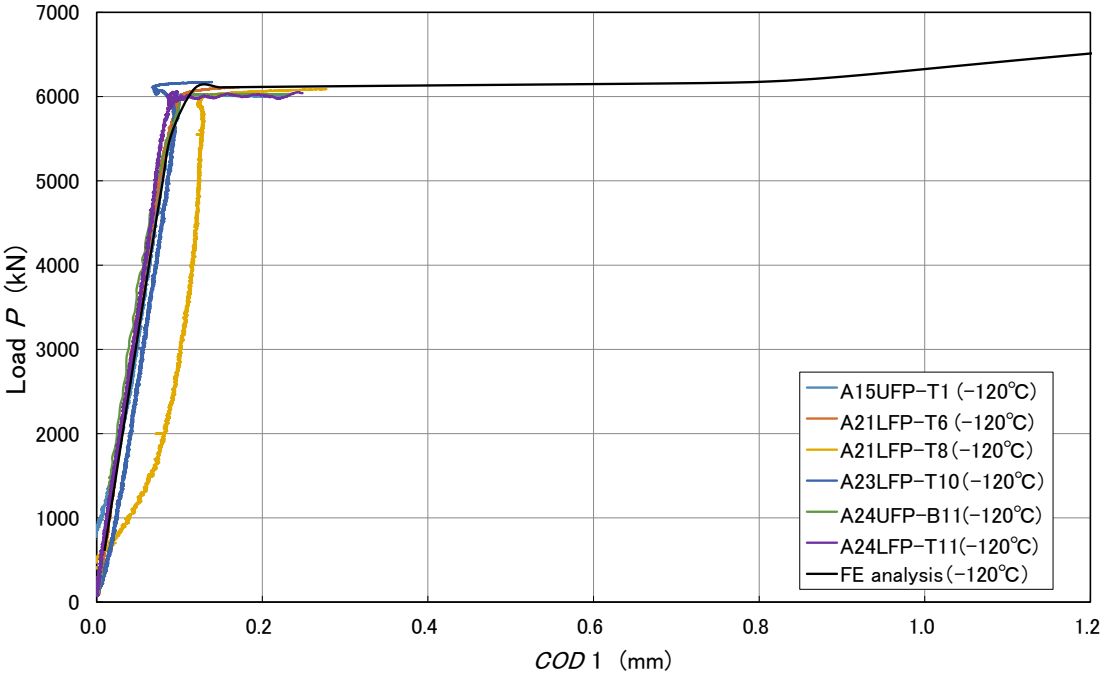


Fig. 4.3.3-1 Comparison of load – *COD* relation by FEA with those of fracture tests

(flat plate tensile specimen, -120 °C)

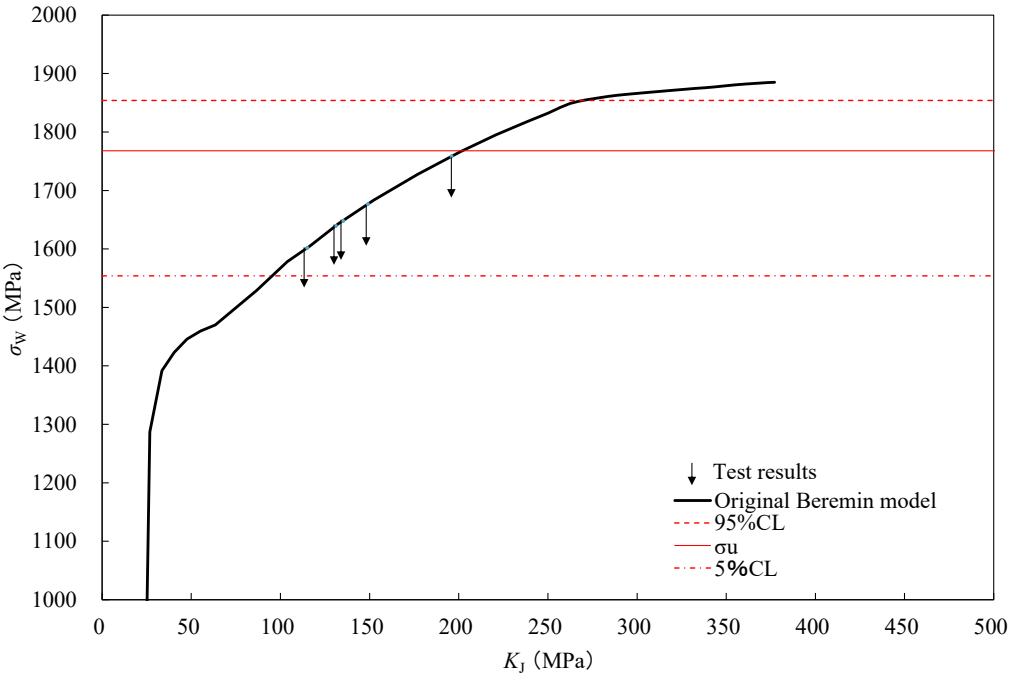


Fig. 4.3.3-2 σ_W-K_J relationship (flat plate tensile specimen, -120 °C)

Copyright © 2026 The Japan Welding Engineering Society, All Rights Reserved.

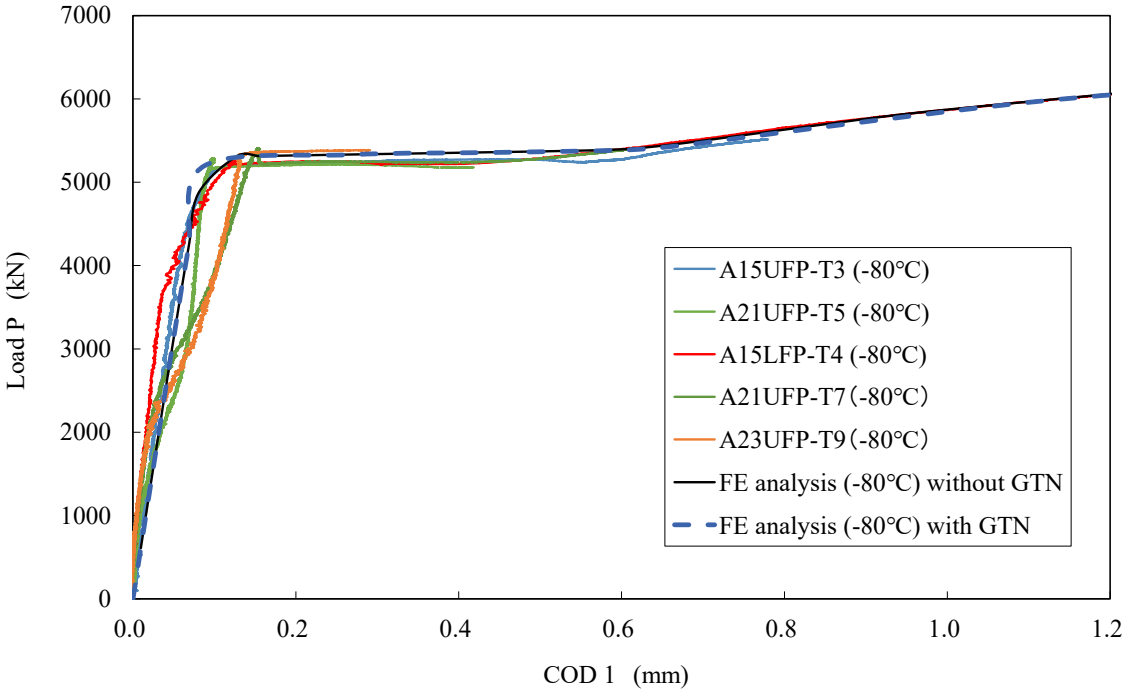


Fig. 4.3.3-3 Comparison of load – *COD* relation by FEA with those of fracture tests

(flat plate tensile specimen, -80 °C)

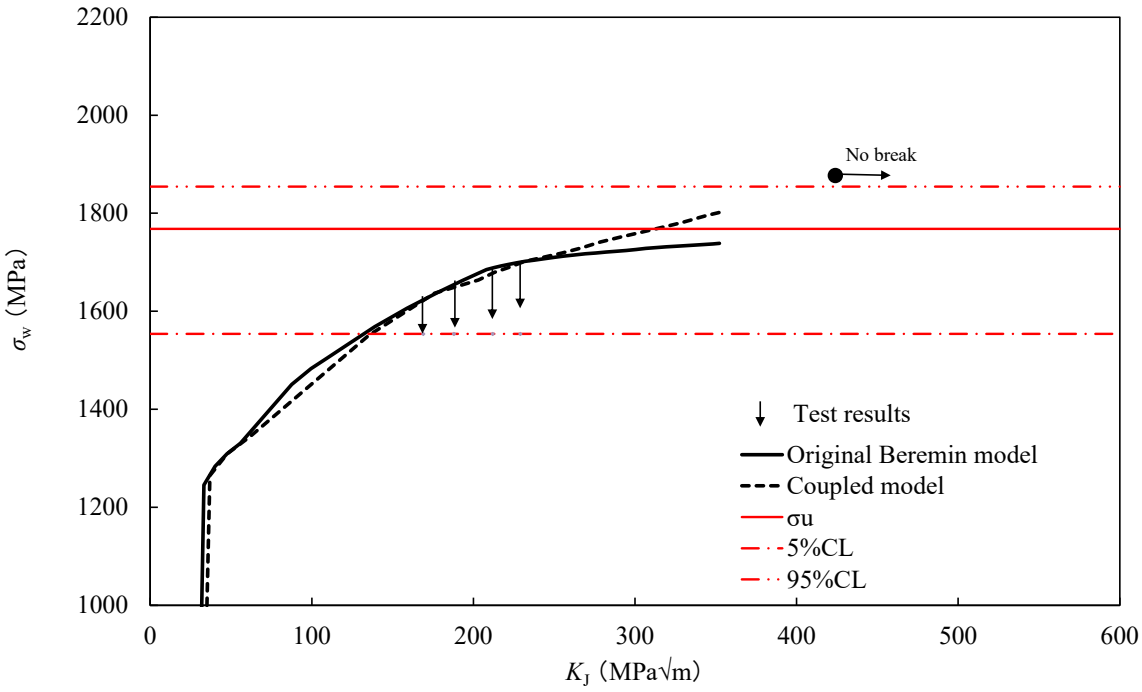


Fig. 4.3.3-4 σ_W-K_J relationship (flat plate tensile specimen, -80°C)

Copyright © 2026 The Japan Welding Engineering Society, All Rights Reserved.

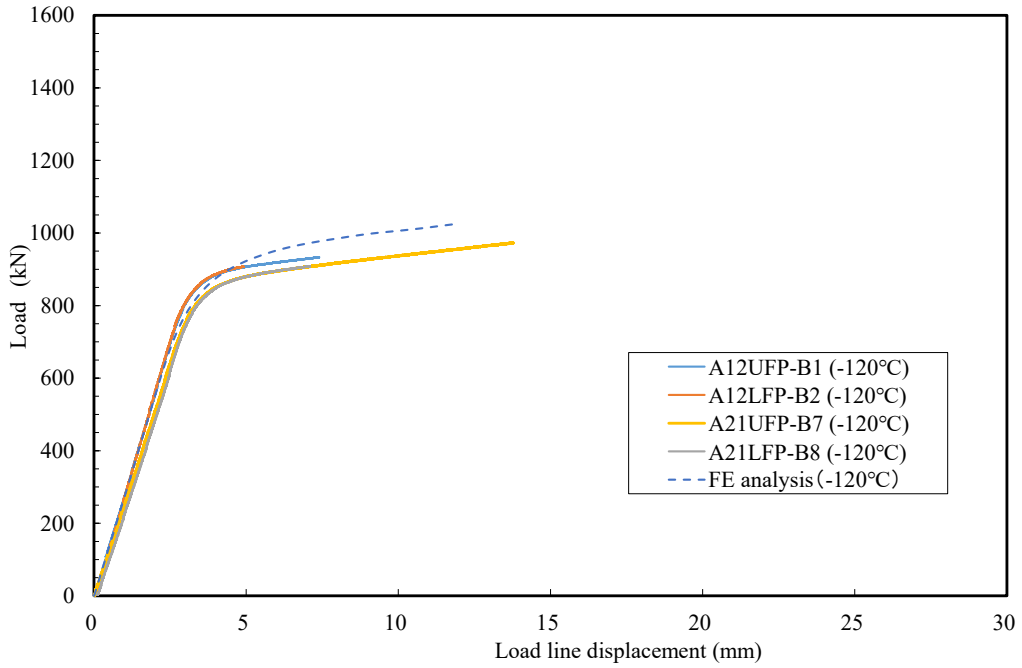


Fig. 4.3.3-5 Comparison of load – load line displacement relation by FEA with those of fracture tests (flat plate bending specimen, -120 °C)

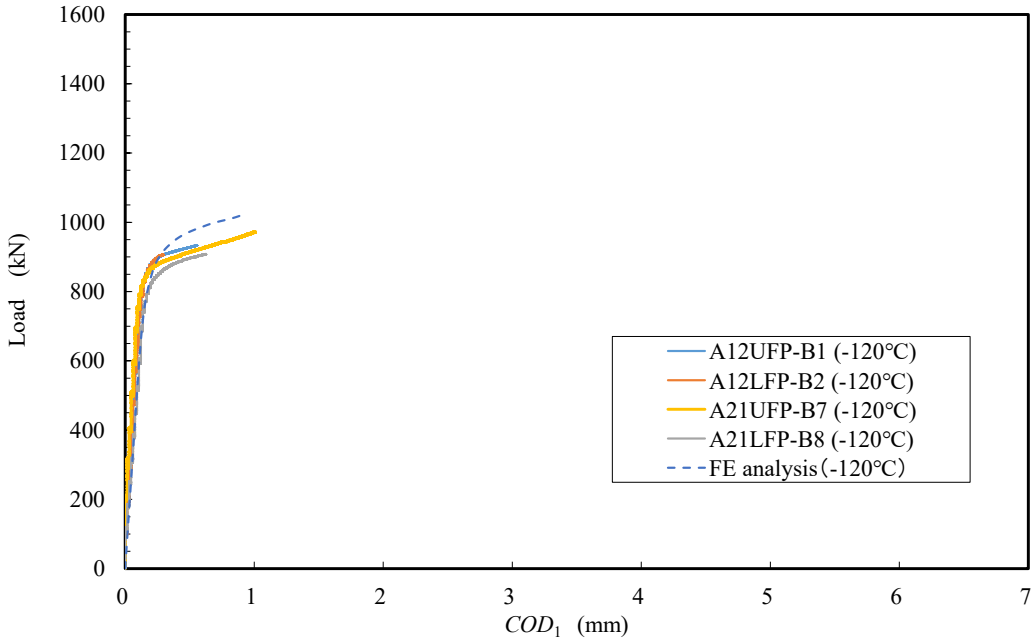


Fig. 4.3.3-6 Comparison of load – COD_1 relation by FEA with those of fracture tests (flat plate bending specimen, -120 °C)

Copyright © 2026 The Japan Welding Engineering Society, All Rights Reserved.

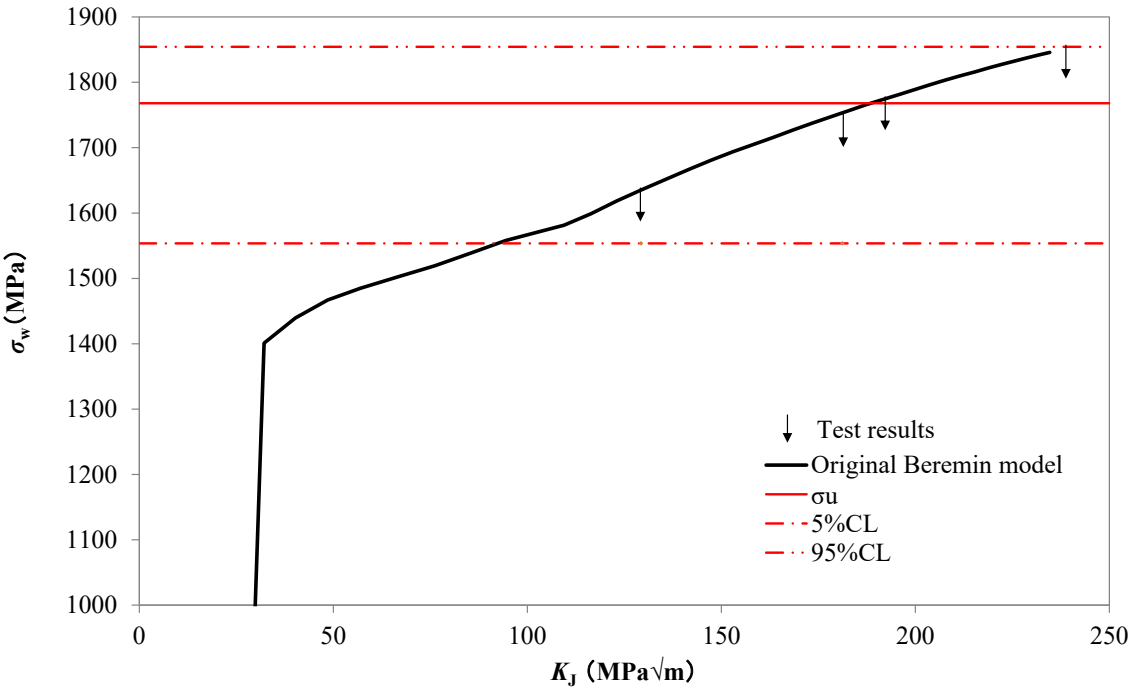


Fig. 4.3.3-7 σ_W-K_J relationship (flat plate bending specimen, -120°C)

Copyright © 2026 The Japan Welding Engineering Society, All Rights Reserved.

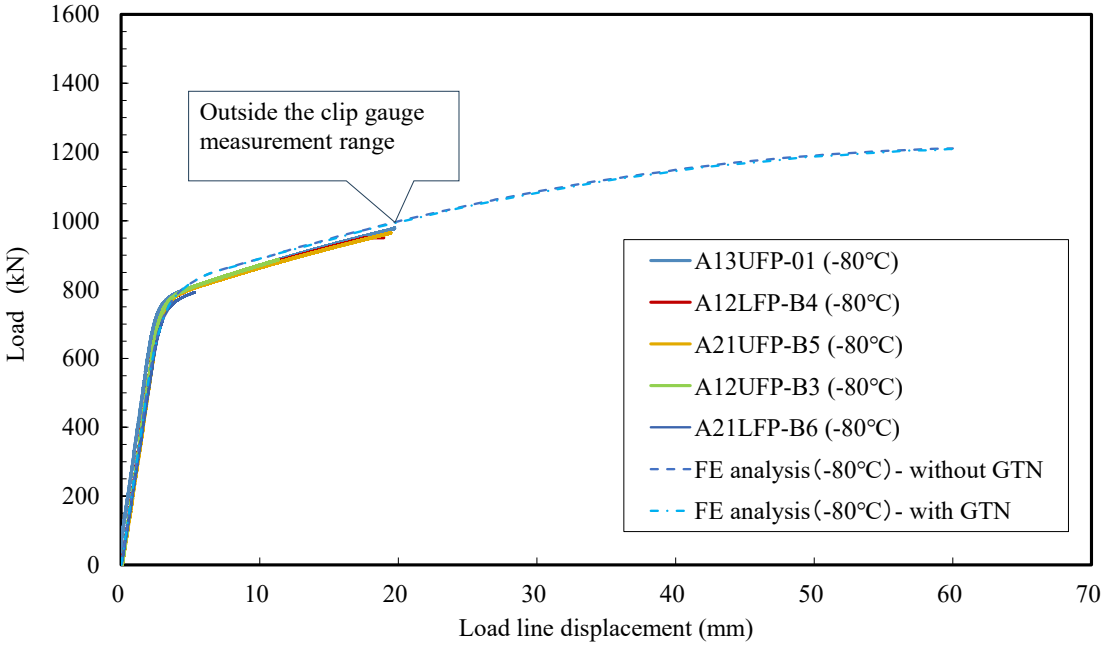


Fig. 4.3.3-8 Comparison of load – load line displacement relation by FEA with those of fracture tests

(flat plate bending specimen, -80 °C)

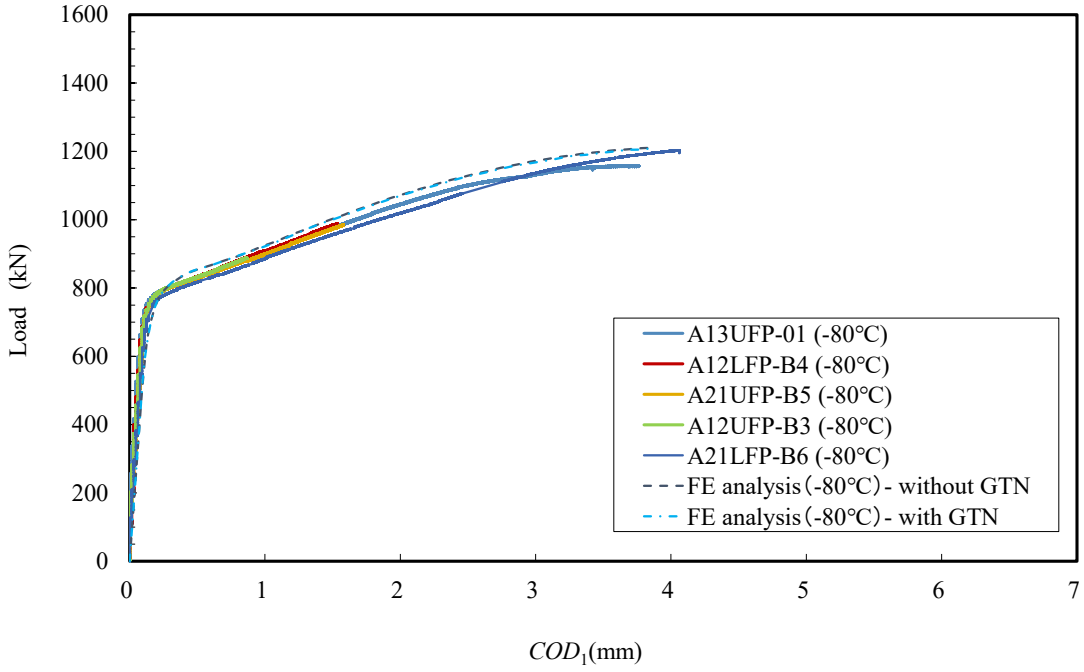


Fig. 4.3.3-9 Comparison of load – COD_1 relation by FEA with those of fracture tests

(flat plate bending specimen, -80 °C)

Copyright © 2026 The Japan Welding Engineering Society, All Rights Reserved.

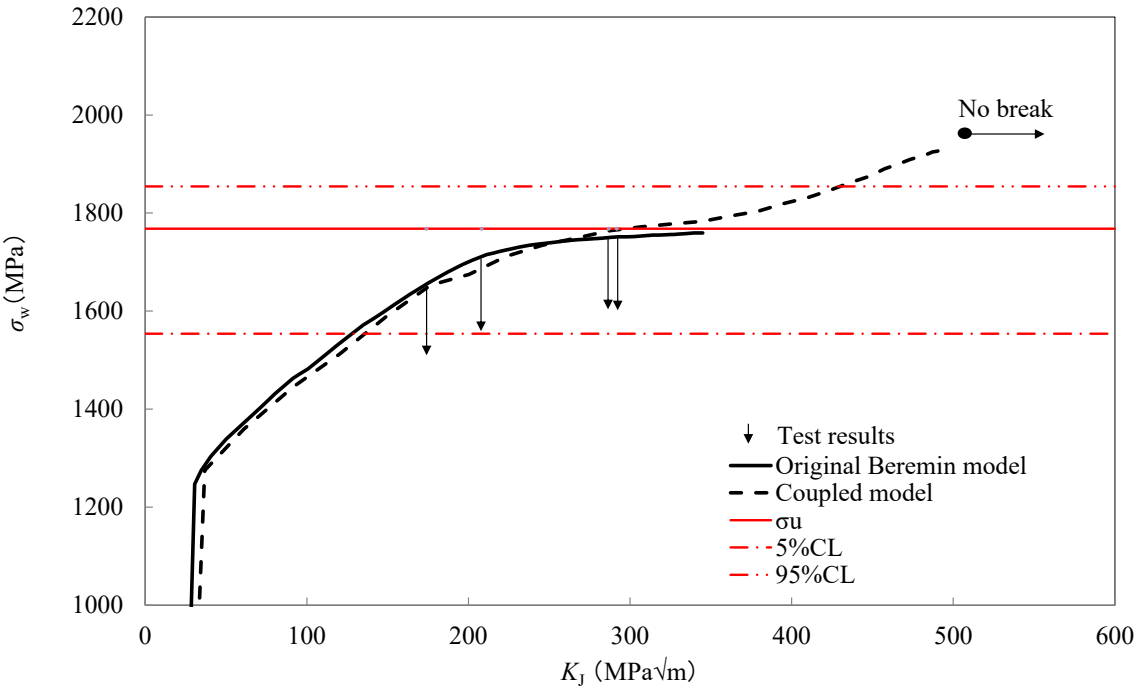


Fig. 4.3.3-10 σ_W-K_J relationship (flat plate bending specimen, -80 °C)

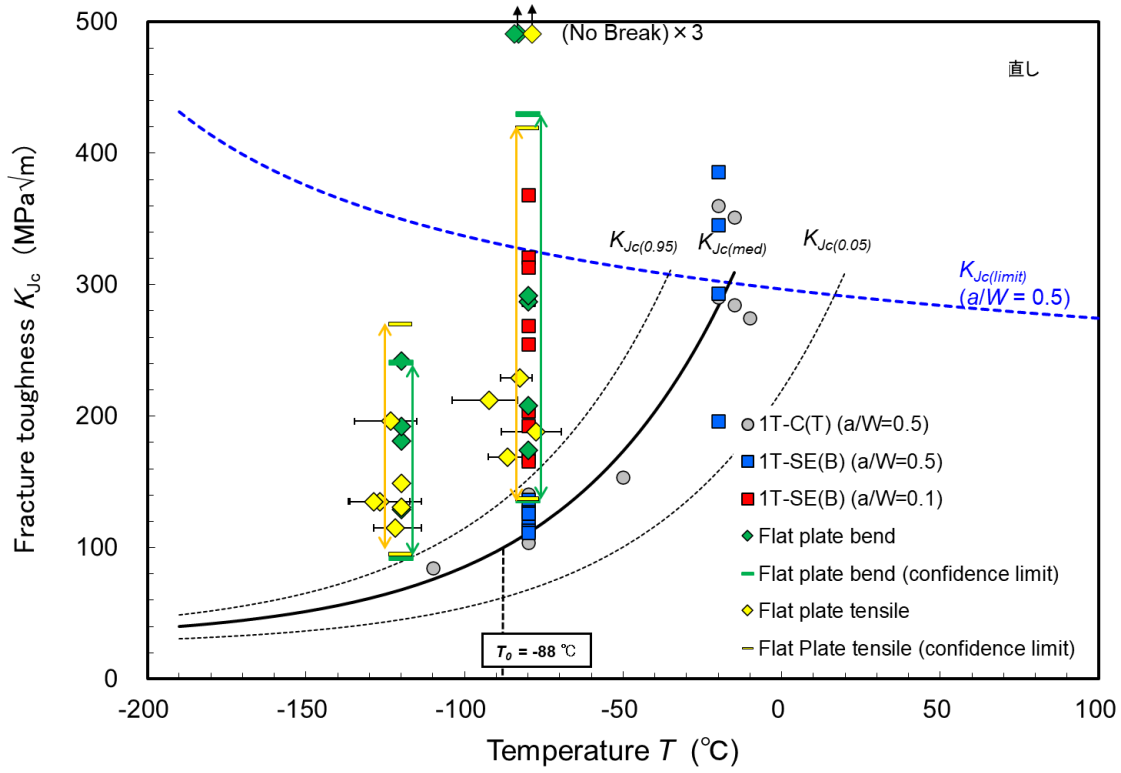


Fig. 4.3.3-11 K_{Jc}-Temperature relationship

Copyright © 2026 The Japan Welding Engineering Society, All Rights Reserved.

Reference

[4-1] ASTM, “Standard Test Method for Measurement of Initiation Toughness in Surface Flaws Under Tension and Bending”, ASTM E2899-15, (2015).

[4-2] Japanese Industrial Standard, “Metallic materials – Tensile testing – Method of test at room temperature”, JIS Z 2241-2011, (2011).

[4-3] Japanese Industrial Standard, “Method for Charpy pendulum impact test of metallic materials”, JIS Z 2242-2018, (2018).

[4-4] Japan Electric Association code, “Test Method for Determination of Reference Temperature, T_0, o Ferritic Steels”, JEAC4216-2015, (2015).

[4-5] ASTM, “Standard Test Method for Measurement of Fracture Toughness”, ASTM E1820-18, (2018).

[4-6] Hojo, K, Hirota, T, Nagoshi, Y, Fukahori, T, Sakima, K, Ohata, M, & Minami, F. "Constraint Effect on Fracture in Ductile-Brittle Transition Temperature Region." *Proceedings of the . Volume 1: Codes and Standards*. Virtual, Online. July 13–15, 2021. V001T01A055. ASME. https://doi.org/10.1115/PVP2021-61318

[4-7] Hojo, K, Hirota, T, Nagoshi, Y, Fukahori, T, Sakima, K, Ohata, M, & Minami, F. "Constraint Effect on Fracture in Ductile-Brittle Transition Temperature Region (Report 2)." *Proceedings of the . Volume 1: Codes and Standards*. Las Vegas, Nevada, USA. July 17–22, 2022. V001T01A003. ASME. https://doi.org/10.1115/PVP2022-84186

[4-8] Hojo, K, Hirota, T, Nagoshi, Y, Fukahori, T, Sakima, K, Ohata, M, & Minami, F. "Constraint Effect on Fracture in Ductile-Brittle Transition Temperature Region (Report 3)." *Proceedings of the .* Atlanta, Georgia, USA. July 16–21, 2023. V001T01A006. ASME. https://doi.org/10.1115/PVP2023-105965

Copyright © 2026 The Japan Welding Engineering Society, All Rights Reserved.

5. Development of fracture evaluation methods for reactor pressure vessels

5.1 Evaluation of plastic constraint for reactor pressure vessels

5.1.1 Plastic constraint correction factor χ

For brittle fracture evaluation of reactor pressure vessels (RPVs), neutron irradiation embrittlement shall be considered in service. The brittle fracture evaluation compares the fracture mechanics parameter (K_I or K_J) for assumed flaws in the RPV with fracture toughness (K_{Ic} or K_{Jc}) of the material obtained from fracture toughness test specimens (generally C(T) specimens). If the fracture mechanics parameter exceeds the fracture toughness value, there is a risk of brittle fracture.

However, as previously investigated, critical fracture toughness values for brittle fracture differ between fracture toughness specimens and specimens such as flat plates with a surface flaw, which is known as the effect of plastic constraint.

To consider the influence of plastic constraint of the structure and specimens, ISO27306[5-1] and BS7910[5-2] propose a plastic constraint correction factor. The plastic constraint correction factor is defined as the ratio of fracture mechanics parameters between the fracture toughness test specimens and the structural component models at equivalent Weibull stress level.

In this chapter, an evaluation methodology is assumed for pressurized thermal shock (PTS) events in RPVs, wherein the fracture toughness transition curve derived from test data is compared with the K_J values for the RPV (K_{JRV}) values obtained from FE analyses of the RPV model. The plastic constraint correction factor is established as illustrated in Figure 5.1.1-1.

First, the relationship between Weibull stress and K_J are calculated for both the RPV model and the fracture toughness test specimen (C(T) specimen). The plastic constraint correction factor χ is then defined by the ratio of K_J at equal Weibull stresses as expressed in Equation (5.1.1-1), where K_{JCT} denotes the K_J of the C(T) specimen.

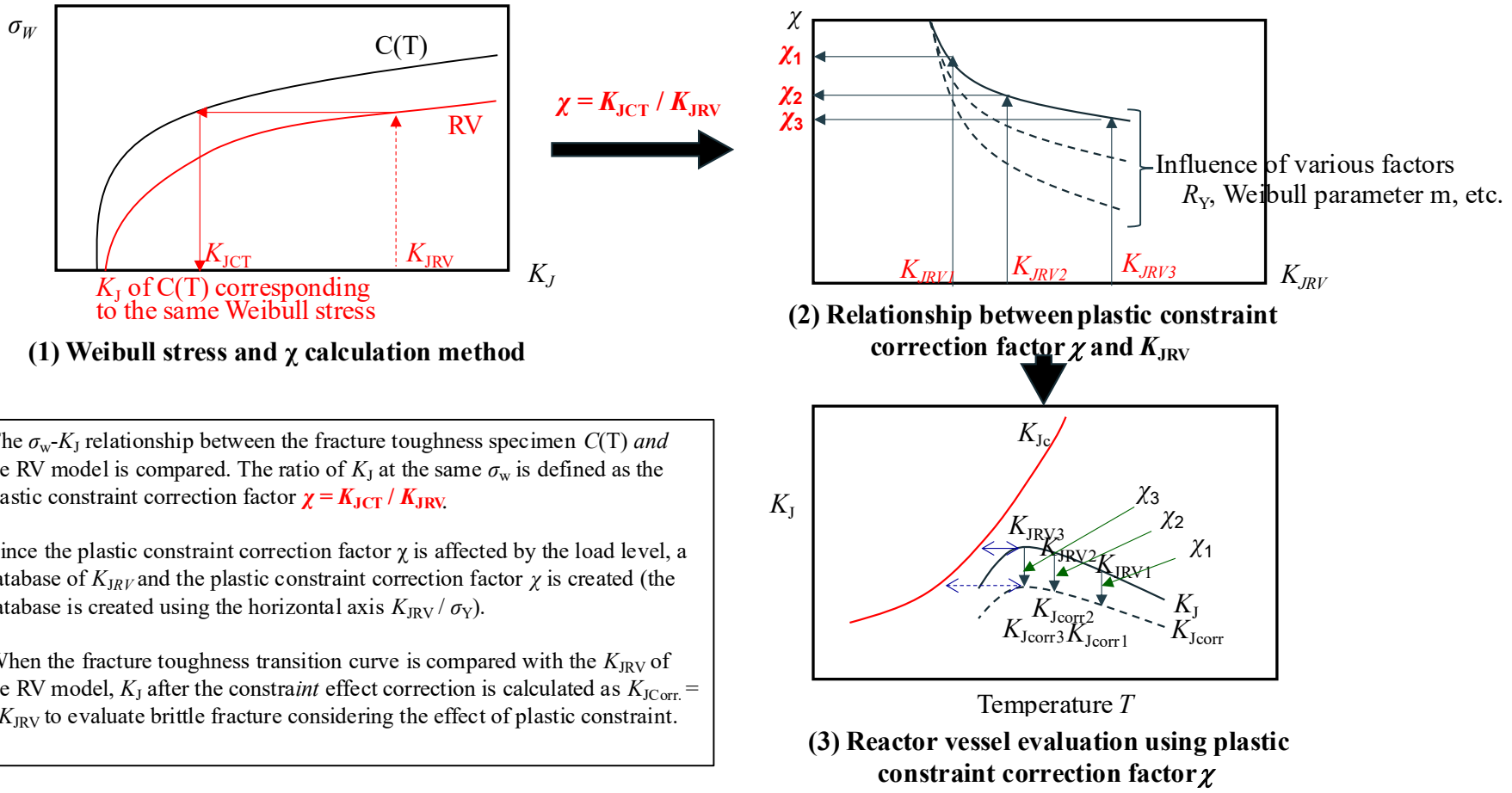
Since the plastic constraint correction factor is influenced by the loading level, a database correlating K_{JRV} and χ is developed to enable retrieval of χ values corresponding to various K_{JRV} levels. The calculated K_{JRV} of the RPV model is corrected by Equation (5.1.1-2) to obtain $K_{Jcorr.}$, which can then be directly compared with the fracture toughness transition curve.

$$\chi = K_{JCT} / K_{JRV} \quad (5.1.1\text{-}1)$$

$$K_{Jcorr.} = \chi K_{JRV} \quad (5.1.1\text{-}2)$$

Copyright © 2026 The Japan Welding Engineering Society, All Rights Reserved.

Copyright © 2026 The Japan Welding Engineering Society, All Rights Reserved.



(1) Weibull stress and χ calculation method

(2) Relationship between plastic constraint correction factor χ and K_{JRV}

(3) Reactor vessel evaluation using plastic constraint correction factor χ

(1) The σ_w-K_J relationship between the fracture toughness specimen *C*(T) *and* the RV model is compared. The ratio of K_J at the same σ_w is defined as the plastic constraint correction factor $\chi = K_{JCT} / K_{JRV}$.

(2) Since the plastic constraint correction factor χ is affected by the load level, a database of K_{JRV} and the plastic constraint correction factor χ is created (the database is created using the horizontal axis K_{JRV} / σ_Y).

(3) When the fracture toughness transition curve is compared with the K_{JRV} of the RV model, K_J after the constra*int* effect correction is calculated as $K_{JCorr.} = \chi K_{JRV}$ to evaluate brittle fracture considering the effect of plastic constraint.

Fig. 5.1.1-1 Application method of plastic constraint correction to reactor pressure vessel

5.1.2 Plastic constraint effects during PTS events

In loss-of-coolant accidents (LOCAs) or main steam pipe rupture accidents, which are assumed as service conditions C and D, the RPV is cooled by the operation of the emergency core cooling system. The resulting temperature gradient between the inner and outer surfaces of the RPV induces high tensile stress on the inner surface, which are further superimposed with membrane stresses due to internal pressure, thereby generating elevated tensile stresses on the vessel's inner surface. Such phenomena are referred to as Pressurized Thermal Shock (PTS) events.

The core region materials of RPVs are composed of low-alloy steels that exhibit superior mechanical properties and fracture toughness. Furthermore, non-destructive inspections during manufacturing and operation ensure the absence of detectable flaws. However, neutron irradiation during service elevates the ductile-to-brittle transition temperature and degrades fracture toughness. Under such embrittled conditions, the occurrence of a PTS event, combined with the presence of large flaws near the inner surface of the RPV, raises concerns regarding the potential for non-ductile fracture and catastrophic failure.

Therefore, JEAC4206[5-3] requires verification that the containment function of radioactive materials in the RPV, i.e., the retention function of the primary coolant, is sufficiently maintained during PTS events. This verification is performed through fracture mechanics evaluations of hypothetical flaws assumed near the RPV inner surface in service.

Table 5.1.2-1 summarizes the analysis conditions for PTS events considered in this chapter. Four transient scenarios were assumed: large-break LOCA (LBCOCA), medium-break LOCA (MBLOCA, small-break LOCA (SBLOCA), and safety valve sticking event (SOV). Among these, LBLOCA imposes the most sever thermal stresses. The temperature and internal pressure conditions for LBLOCA and SBLOCA correspond to those from Japanese PWR plants, while MBLOCA and SOV conditions are based on U.S. plant data. The assumed flaw follows the JEAC4206 PTS evaluation procedure: a semi-elliptical surface flaw with a depth of 10 mm and length of 60 mm, modeled immediately beneath the cladding on the inner surface of the RPV to provide the most severe evaluation from temperature and thermal stress conditions. The analysis described herein calculates the Weibull stress during PTS transients and evaluates plastic constraint levels as detailed in Table 5.1.2-2.

Copyright © 2026 The Japan Welding Engineering Society, All Rights Reserved.

(1) Analysis model and boundary conditions

FE analysis of the RPV was performed using a 1/12 symmetric sector model (60° circumferential angle, with the flaw surface as symmetry plane). The base metal thickness was set to 200 mm, with a 5.5 mm thick cladding layer. The flaw was modeled as a semi-elliptical axial flaw of 10 mm depth and 60 mm length beneath the cladding. The analysis model and boundary conditions are shown in Figs. 5.1.2-1 and 5.1.2-2. Radial sliding constraints were applied to circumferential end nodes, and axial thrust forces due to internal pressure were applied as axial loads at the axial ends opposite the crack. Internal pressure and thermal boundary conditions were applied to the vessel inner surface (cladding surface). To prevent element distortion or penetration due to crack closure from thermal deformation during transient analysis, rigid contact elements were introduced at the crack faces.

(2) Analysis code

Analysis was conducted using the commercial-based code Abaqus Ver. 6.12. The element type used was 8-node linear brick element (C3D8).

(3) Material Properties

Material properties were set as two types (unirradiated and irradiated) for the cladding, and three types (unirradiated, irradiated, and irradiated material with yield ratio of 0.6) for the base metal. Thermal conductivity and strength properties referred to standards and literature shown in Table 5.1.2-3. Except for plastic properties, unirradiated and irradiated materials had common properties.

For yield stress and tensile strength used to set stress-strain curves, submerged arc weld (SAW) data obtained before and after irradiation[5-4] were used for the cladding. The base metal unirradiated properties corresponded to low alloy steel A. For irradiated base metal, yield stress was set to 700 MPa and yield ratio R_Y (= yield stress / tensile strength) to 0.8, reflecting trends observed in surveillance test data. Regarding R_Y, it is noted that a smaller value leads to a larger plastic constraint correction factor according to ISO27306, resulting in a more conservative evaluation. To investigate the influence of R_Y, material properties were also defined with a fixed yield stress of 700 MPa but with a reduced yield ratio R_Y=0.6. For the unirradiated base metal, yield stress and tensile strength change little in the temperature range 100–200°C used for evaluation, so irradiated base metal was assumed to have no temperature dependence in the stress-strain curve.

The base metal stress-strain curve was approximated by the Ramberg-Osgood law using the yield

Copyright © 2026 The Japan Welding Engineering Society, All Rights Reserved.

stress and tensile strength with the WRC 413[5-5] formula. ASME Sec. VIII Div. 2[5-6] formula was used for the cladding stress-strain curve.

The equivalent stress–equivalent plastic strain relationships of the base metal and cladding before and after irradiation are shown in Figs. 5.1.2-3 and 5.1.2-4. The Ramberg-Osgood coefficient n is 8.9 for unirradiated at 150°C, 9.1 for irradiated, and 5.1 for irradiated with R_Y=0.6.

(4) Analysis procedure

The FE analysis proceeded through the following steps:

1. Thermal conduction analysis to calculate transient temperature distribution
2. Residual stress mapping
3. Stress analysis under operating temperature and pressure (initial state)
4. Stress analysis using temperature and pressure histories from step 1 to compute time histories of stress and K_J

Figure 5.1.2-5 shows the residual stress distribution considered in this analysis, derived from prior research[5-7] that accounted for cladding weld and post-weld heat treatment PWHT, showing three-axis stresses. Residual stresses within the cladding are significant, with biaxial tensile stresses in circumferential and axial directions, whereas the base metal is less affected.

Figure 5.1.2-6 shows the relationship between internal pressure and reactor coolant fluid temperature for each transient condition. LBLOCA condition exhibits rapid drops in pressure and temperature, causing thermal shock stress through the vessel wall thickness. The MBLOCA and SBLOCA conditions show more gradual decreases in pressure and temperature, with thermal stress developing as pressure decreases. SOV shows even more gradual decreases in temperature and internal pressure than SBLOCA, followed by a sudden increase in internal pressure.

(5) Analysis Results

Figure 5.1.2-7 shows the relationship between K_J and crack tip temperature for each transient, indicating higher K_J in the order of LBLOCA, MBLOCA, SBLOCA, and SOV, with LBLOCA being the most severe.

To evaluate brittle fracture potential, the Weibull stresses were calculated for both C(T) specimens and the RPV. The Weibull parameter used was m = 20, and the reference volume was 1 mm³. Figure 5.1.2-8 shows the Weibull stress–K_J relationship for C(T) specimens with unirradiated

Copyright © 2026 The Japan Welding Engineering Society, All Rights Reserved.

properties. Considering transient temperatures of the RPV, calculations were performed using material properties at 220°C, 150°C, and 100°C, yielding nearly identical results, indicating that temperature dependence of material properties can be neglected in the PTS transient region. Therefore, 150°C material properties are used for analysis of C(T) specimens including irradiated material.

To calculate the plastic constraint correction factor χ, Weibull stresses of C(T) specimens and the RPV were compared. The Weibull stress integral was performed for elements where stress exceeded the maximum principal stress near the crack tip at the mid-thickness of the plate, corresponding to K_J = 20 MPa√m, the lower bound of fracture toughness master curve method for C(T) specimens. Figure 5.1.2-9 shows the Weibull stress–K_J relationship for C(T) specimens and the RPV. For the RPV σ_w–K_J curve, unloading after maximum K_J was excluded considering high-temperature preloading (WPS effect). The Weibull stress of the RPV is lower than that of C(T) specimens at the same K_J. Weibull stress near the maximum K_J is nearly identical among the four transients. At low loads, LBCOCA Weibull stress is slightly higher than others.

Figure 5.1.2-10 shows the stress distribution near the crack tip at K_J = 20 MPa√m for each transient. LBCOCA shows higher stress than others. Figure 5.1.2-11 shows thickness direction stress distribution in the general section from elastic analysis. LBCOCA exhibits thermal shock stress distribution, with extremely high stress near the surface, indicating strong constraint and resulting in higher Weibull stress than other transients.

Figure 5.1.2-12 shows Q-factors calculated from crack tip stress fields for large and MBCOCA. The Q-factor for LBCOCA is high in the low load region, indicating high constraint. At K_J = 50–60 MPa√m, Q-factors for both are nearly equal, and at maximum load level, constraint degree is almost the same for all transients as reflected in Weibull stress trends.

From the Weibull stress–K_J relationship obtained, the plastic constraint correction factor χ was calculated. Figure 5.1.2-13 shows χ for each transient. For SOV, the maximum K_J value is small, and the plot does not show a monotonically decreasing trend as in other transients, but it is included within the range of large to SBCOCA. Near 20 MPa√m, LBLOCA χ approaches 1.0, indicating negligible plastic constraint effects; χ decreases with increasing load, reaching approximately 0.5 at maximum K_J. MBLOCA and SBCOCA show smaller χ values than LBCOCA in all regions, indicating that using LBCOCA's χ provides conservative evaluation for all transients.

Copyright © 2026 The Japan Welding Engineering Society, All Rights Reserved.

To clarify the effect of material properties on the plastic constraint correction factor χ, analyses were performed using irradiated material properties and R_Y = 0.6 properties for PTS-5 to PTS-7 shown in Table 5.1.2-2. Further analyses were performed using irradiated material properties for the base metal and unirradiated material properties for the cladding to confirm the influence of elastic-plastic properties of the cladding.

Figure 5.1.2-14 shows the Weibull stress–K_J relationships obtained from the analyses. From this figure, the following can be stated:

- Higher yield stress in irradiated materials leads to increased Weibull stresses compared to unirradiated materials.
- Using R_Y = 0.6, which corresponds to higher tensile strength, further increases Weibull stresses.
- When the base metal is irradiated, cladding property variations (irradiated vs. unirradiated) have minimal impact on Weibull stress–K_J curves.
- For irradiated base metal with R_Y = 0.6, the Weibull stress of the RPV –K_J curve approaches that of the C(T) specimen, indicating diminished plastic constraint effects.

Figure 5.1.2-15 shows the plastic constraint correction factor χ–K_J relationship obtained from Fig. 5.1.2-14. Similar to Fig. 5.1.2-14, the following can be stated:

- χ values using yield stress for irradiated base metal exceed those for unirradiated, reflecting conservative correction factors.
- Cladding property variations have negligible influence on χ when irradiated base metal properties are used.
- Using R_Y = 0.6 for irradiated base metal increases χ, consistent with ISO 27306 and BS 7910 findings that lower yield ratios reduce plastic constraint effects.

To exclude yield stress effects, Figure 5.1.2-16 normalizes K_J by yield stress σ_Y. The χ–normalized K_J curves for unirradiated material with R_Y=0.77 and irradiated material with R_Y=0.8, nearly coincide, demonstrating that χ can be represented by a single curve regardless of yield stress differences.

Based on these findings, m and yield ratio R_Y were selected as parameters for constructing a χ database, which will be developed in subsequent sections.

Copyright © 2026 The Japan Welding Engineering Society, All Rights Reserved.

Table 5.1.2-1 PTS transient analysis conditions

Item	Condition	
RPV Model	Japanese PWR model plant (Base metal thickness: 200mm, Cladding thickness: 5.5mm)	
Postulated flaw	Semi-elliptical flaw with 10 mm depth and 60 mm length beneath cladding (postulated flaw in the assessment procedure against PTS events in JEAC4206-2016)	
Transient	LBCOCA	The internal pressure drops instantaneously, but the stress due to thermal shock becomes most severe during the transient (transient defined in JEAC4206).
	MBCOCA	The stress from thermal shock and internal pressure during the transient lies between those of a LBCOCA and a SBCOCA (U.S. transient).
	SBCOCA	The stress due to thermal shock is smaller than that of a LBCOCA, but stress from internal pressure remains during the transient (transient defined in JEAC4206).
	SOV (Stuck Open Valve)	Due to sticking open of the pressurizer safety valve, the temperature decreases, and when the valve closes at the lowered temperature, the stress from pressure temporarily increases during the transient (U.S. transient).

Copyright © 2026 The Japan Welding Engineering Society, All Rights Reserved.

Table 5.1.2-2 FE analysis conditions for RPV models

Purpose	Case No.	Dimension		Material Properties				Min. mesh size (mm)	Load	Geometry of flaw (axial flaw)		Weibull Parameter	Note
		Base metal Inner radius Thickness (mm)	Cladding Thickness (mm)	Base metal	Base metal yield stress (MPa)	Base metal Yield Ratio	Cladding		Temperature Internal pressure	Depth (mm)	Length (mm)	m	
Weibull stress for each transient	PTS-1	2000 200	5.5	Elastic-Plastic Un-irradiated	450	0.77	Elastic-Plastic Un-irradiated	0.03	LBCOCA	10	60	20	
	PTS-2								Middle LOCA				
	PTS-3								SBCOCA				
	PTS-4								SOV				
Confirmation of the effect of material properties	PTS-5			Elastic - Plastic Irradiated	700	0.8	Elastic - Plastic Irradiated		LBCOCA				Irradiated condition
	PTS-6						Elastic - Plastic Un-irradiated						Effects of Cladding material properties
	PTS-7					0.6							Effects of yield ratio

Copyright © 2026 The Japan Welding Engineering Society, All Rights Reserved.

Table 5.1.2-3 References of material properties for FEA

Item		Cladding	Base metal
Thermal conductivity, Thermal diffusivity [ASME Sec. II Part D 2007～2009b Addenda]		Group J	Group C
Poisson's ratio		0.3	0.3
Thermal expansion coefficient [JSME Rules on Materials for Nuclear Facilities (JSME S NJ1-2012 including 2013 addenda)		Classification: TE6 Austenitic stainless steel	Classification: TE2 Carbon steel, Alloy steel
Young's modulus [JSME Rules on Materials for Nuclear Facilities (JSME S NJ1-2012 including 2013 addenda)		Classification: E1-9 Austenitic stainless steel	Classification: E1-3 Molybdenum steel
Yield stress Tensile stress	Un-irradiated	Refer to [5-4]	Data obtained from low alloy steel A
	Irradiated		σ_Y : 700MPa* R_Y : 0.8*

* Values set based on the trends observed in surveillance test data.

Copyright © 2026 The Japan Welding Engineering Society, All Rights Reserved.

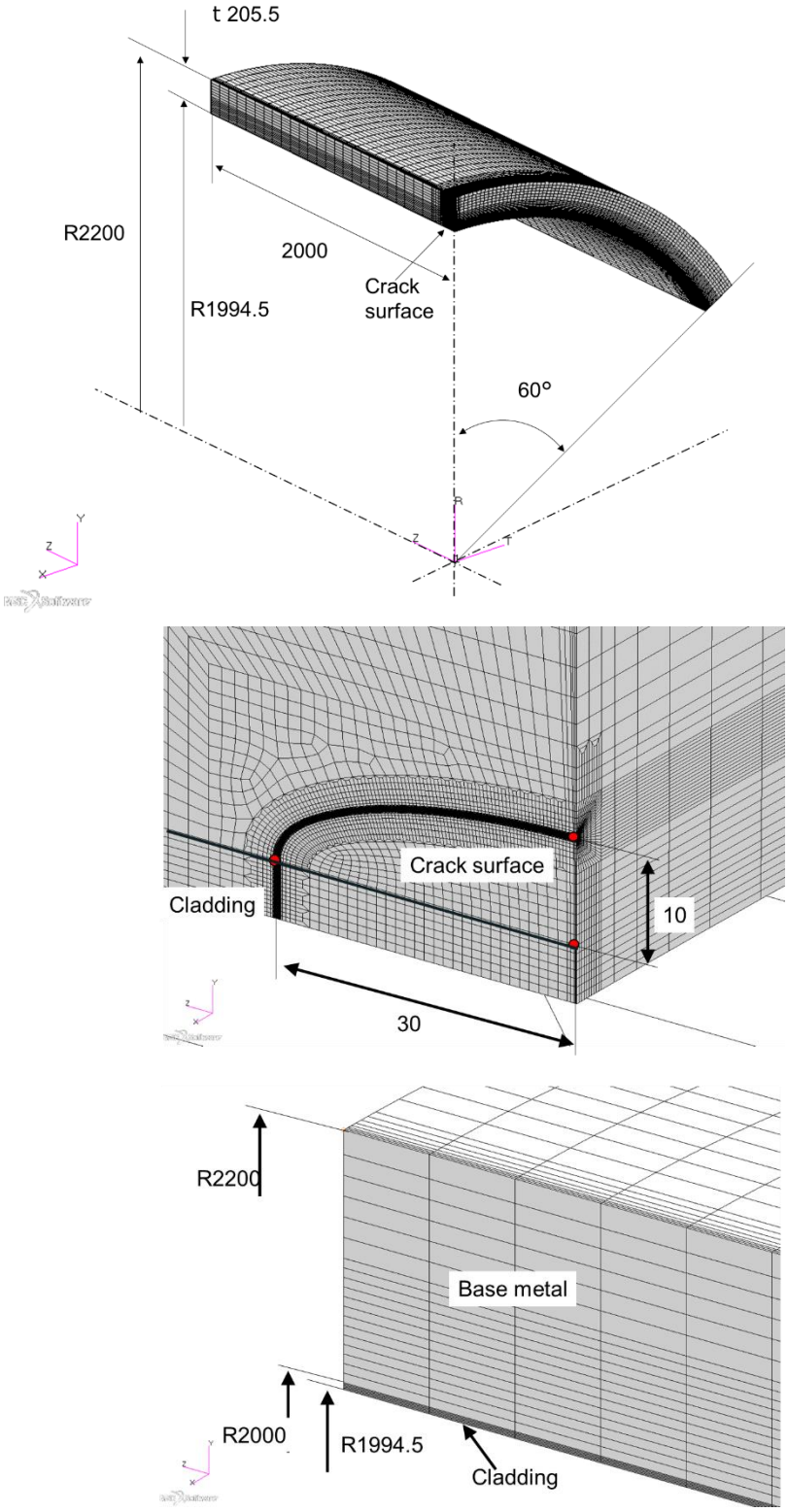
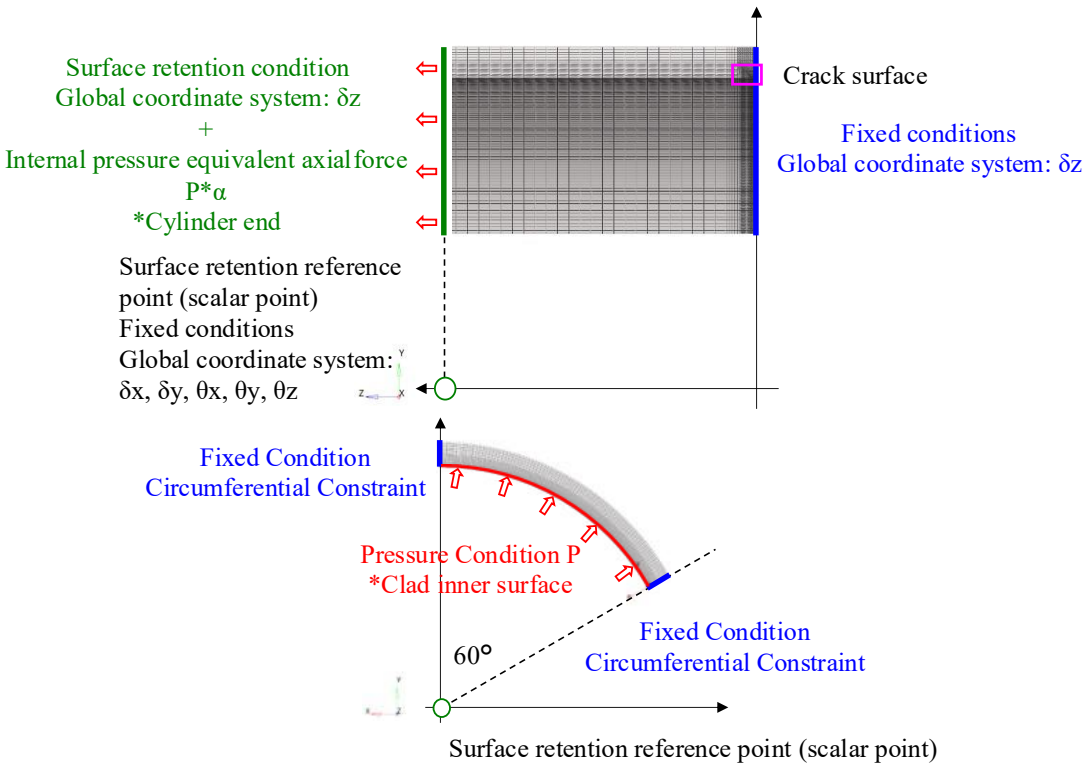


Fig.5.1.2-1 FE model of RPV

Copyright © 2026 The Japan Welding Engineering Society, All Rights Reserved.



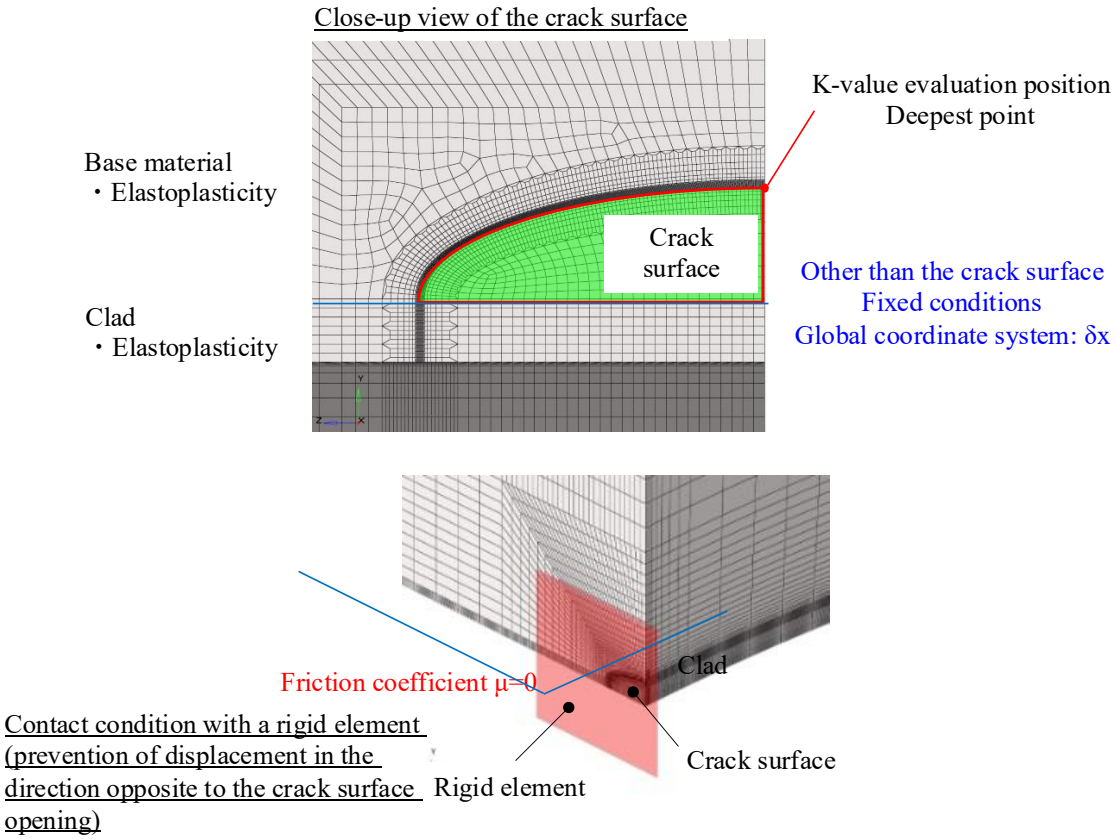
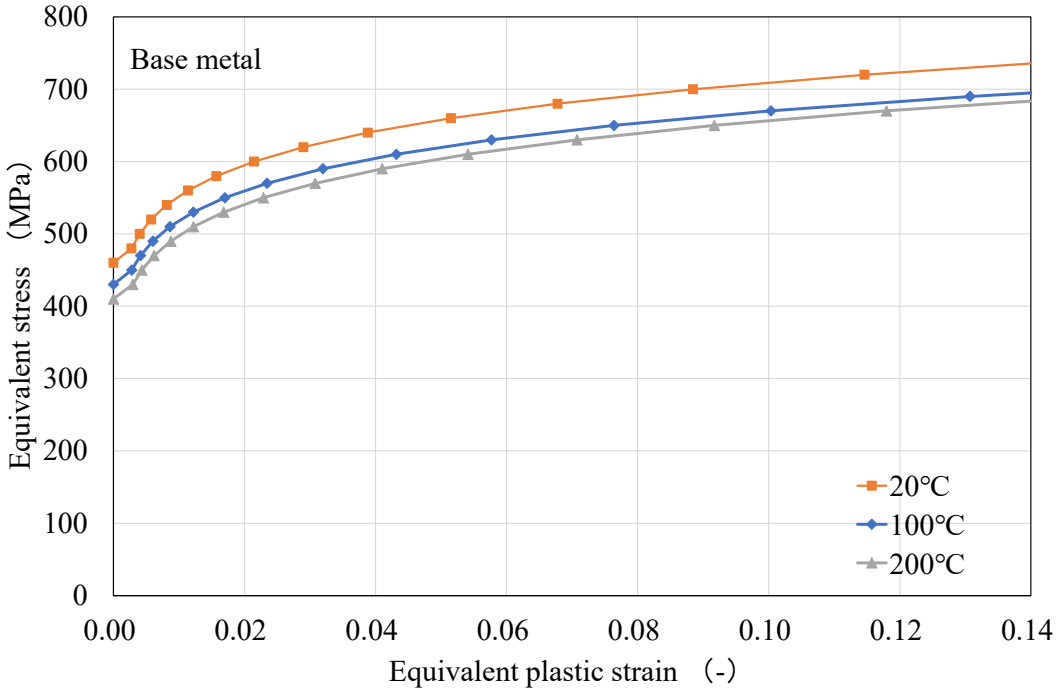


Fig.5.1.2-2 Boundary condition of FE model of RPV

Copyright © 2026 The Japan Welding Engineering Society, All Rights Reserved.



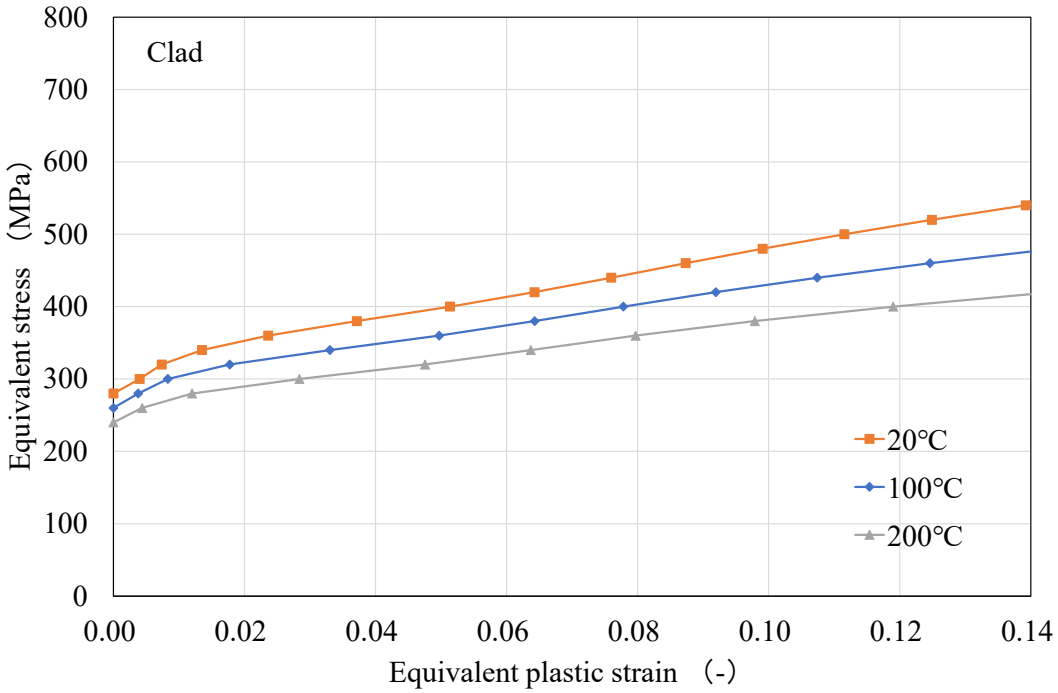
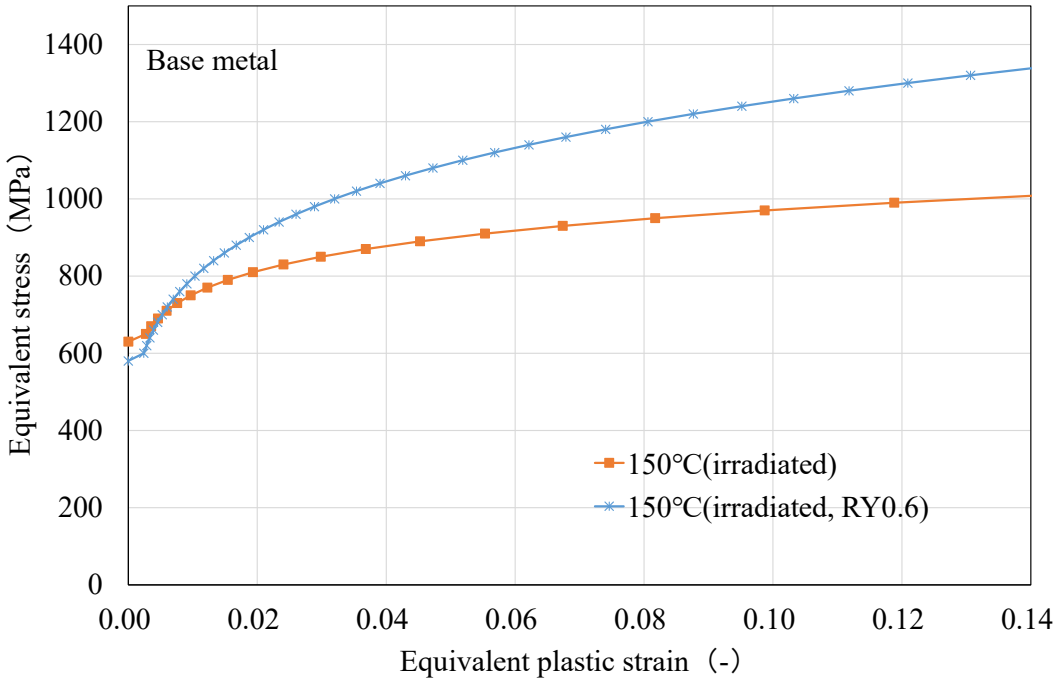


Fig. 5.1.2-3 Equivalent stress-equivalent plastic strain relationship (unirradiated)

Copyright © 2026 The Japan Welding Engineering Society, All Rights Reserved.



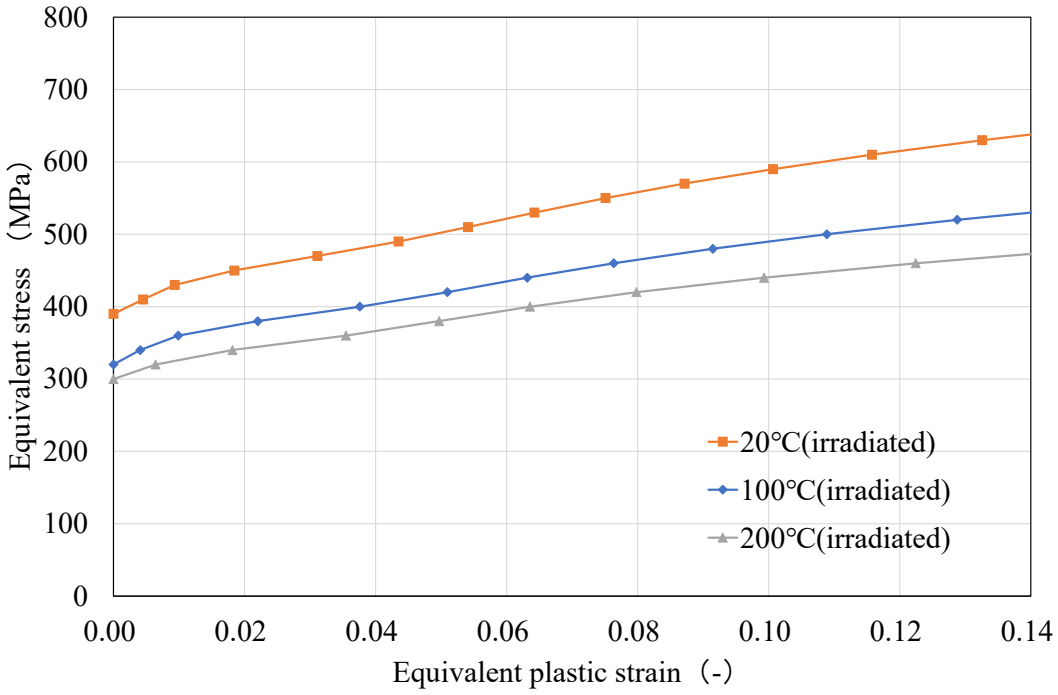


Fig. 5.1.2-4 Equivalent stress-equivalent plastic strain relation (irradiated)

Copyright © 2026 The Japan Welding Engineering Society, All Rights Reserved.

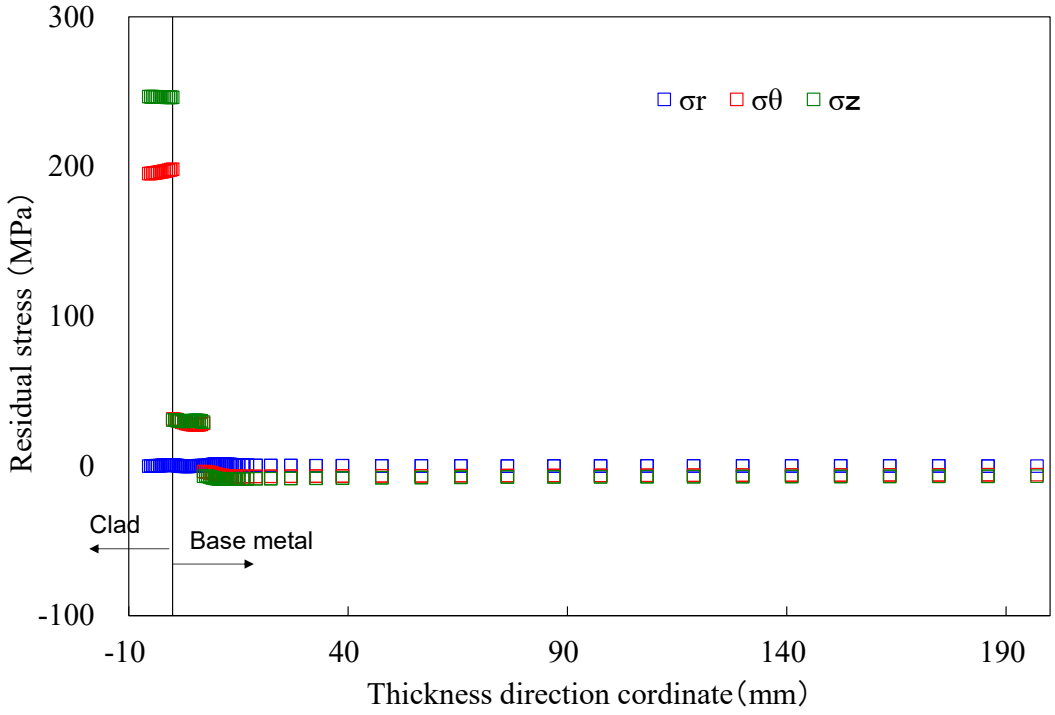
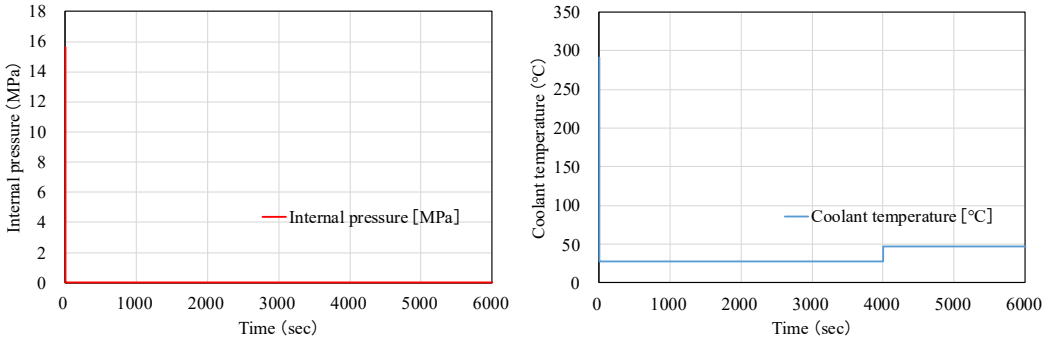
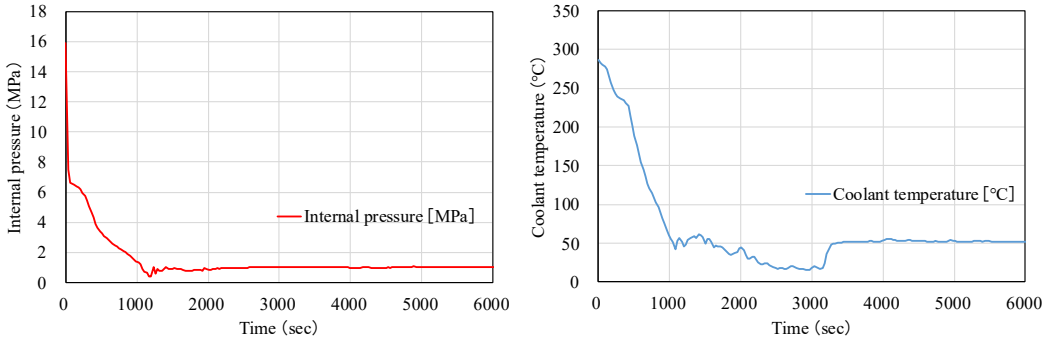


Fig. 5.1.2-5 Residual stress distribution induced by clad welding

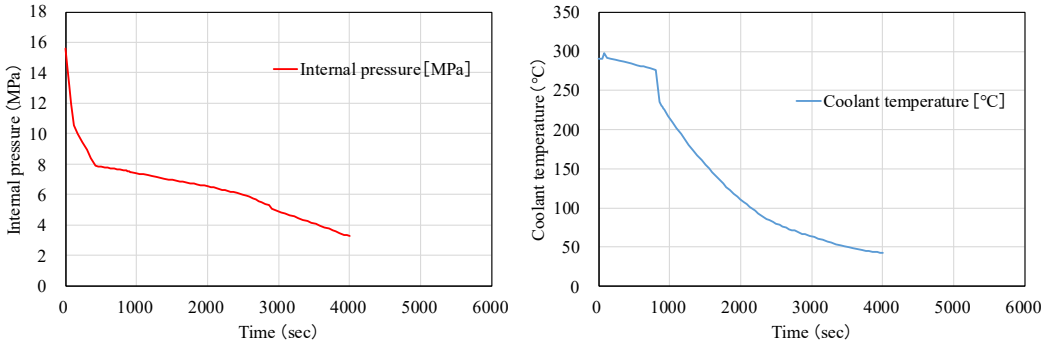
Copyright © 2026 The Japan Welding Engineering Society, All Rights Reserved.



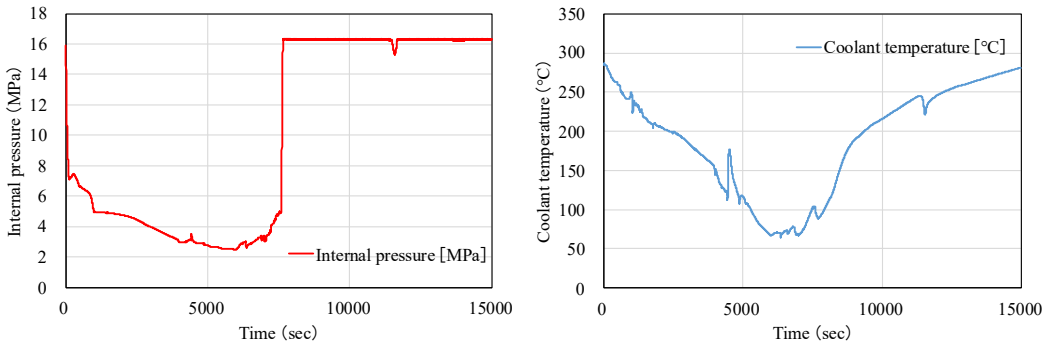
(a) LBCOCA



(b) MBCOCA



(c) SBCOCA



(d) SOV

Fig.5.1.2-6 Transient condition

Copyright © 2026 The Japan Welding Engineering Society, All Rights Reserved.

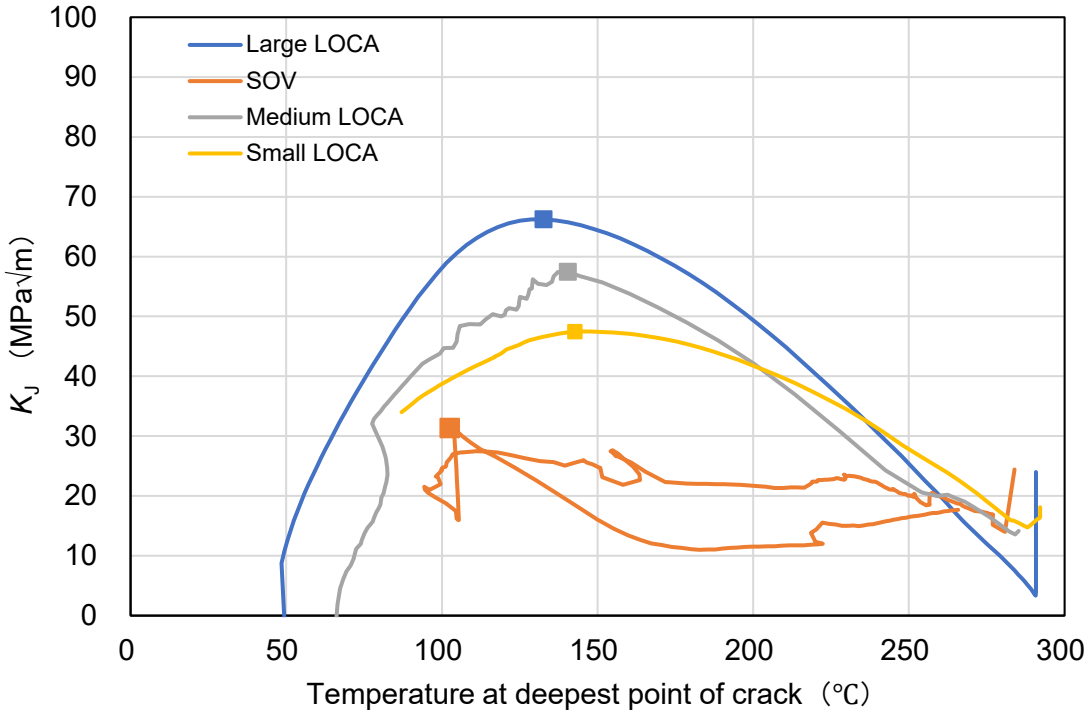


Fig.5.1.2-7 Relation of K_J – temperature at deepest point of flaw in PTS transient condition

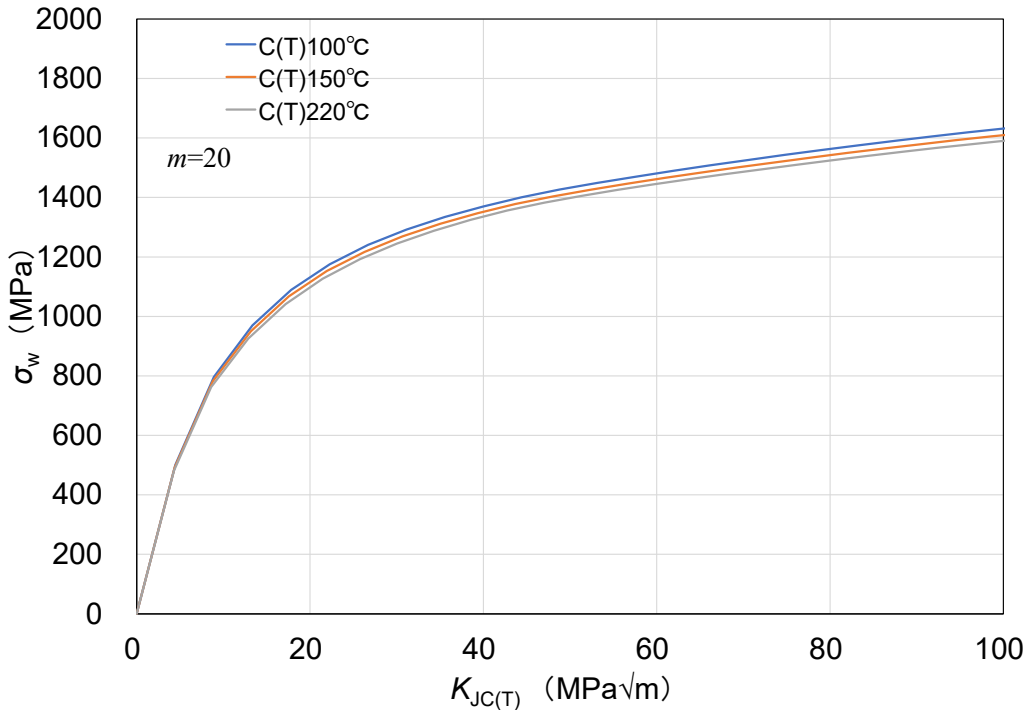


Fig.5.1.2-8 Temperature dependence of Weibull Stress-K_J relation of C(T) Specimens (unirradiated)

Copyright © 2026 The Japan Welding Engineering Society, All Rights Reserved.

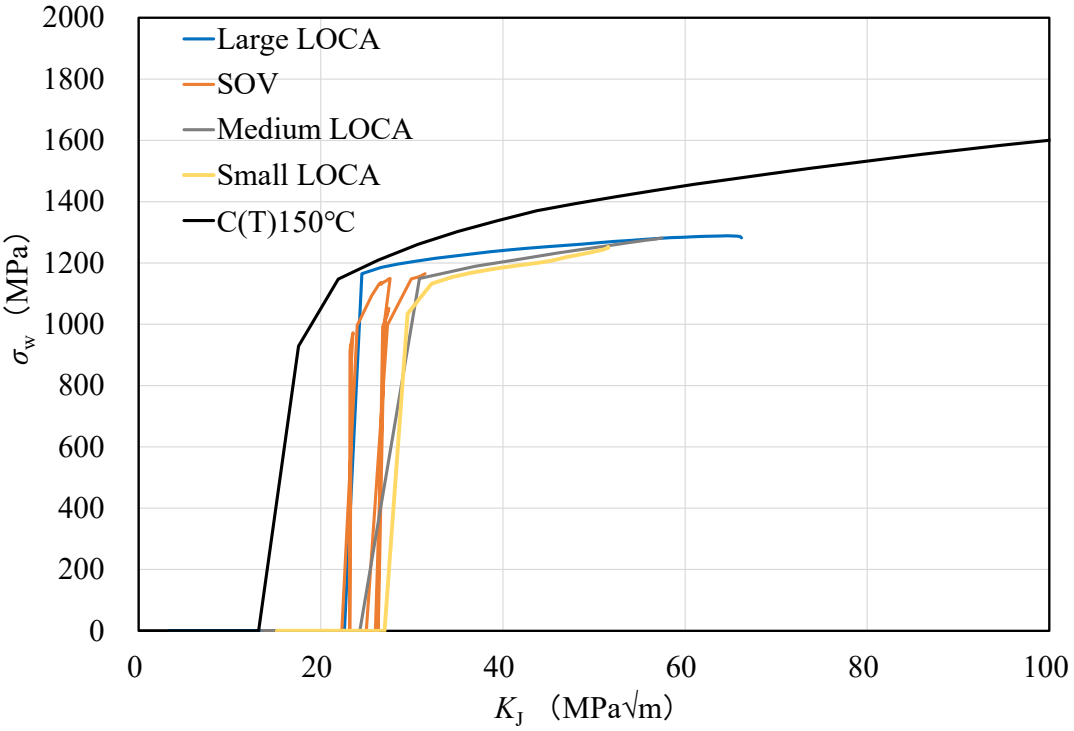


Fig. 5.1.2-9 Weibull stress - K_J relation in PTS transient condition

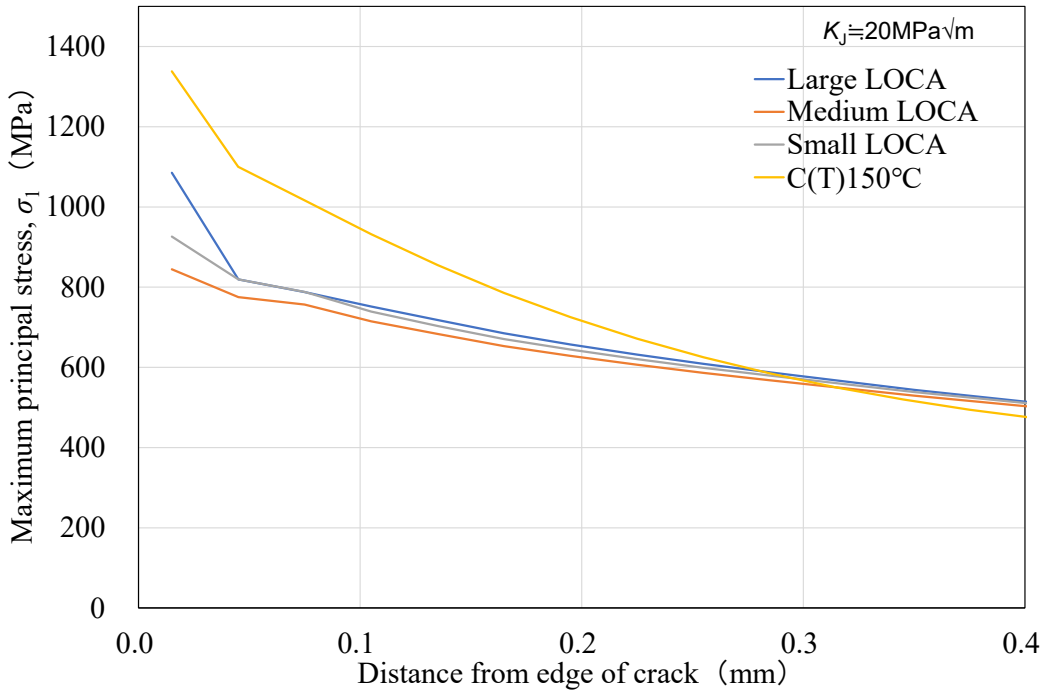


Fig. 5.1.2-10 Stress distribution near crack tip at K_J＝20MPa√m in PTS transient condition

(deepest point of flaw)

Copyright © 2026 The Japan Welding Engineering Society, All Rights Reserved.

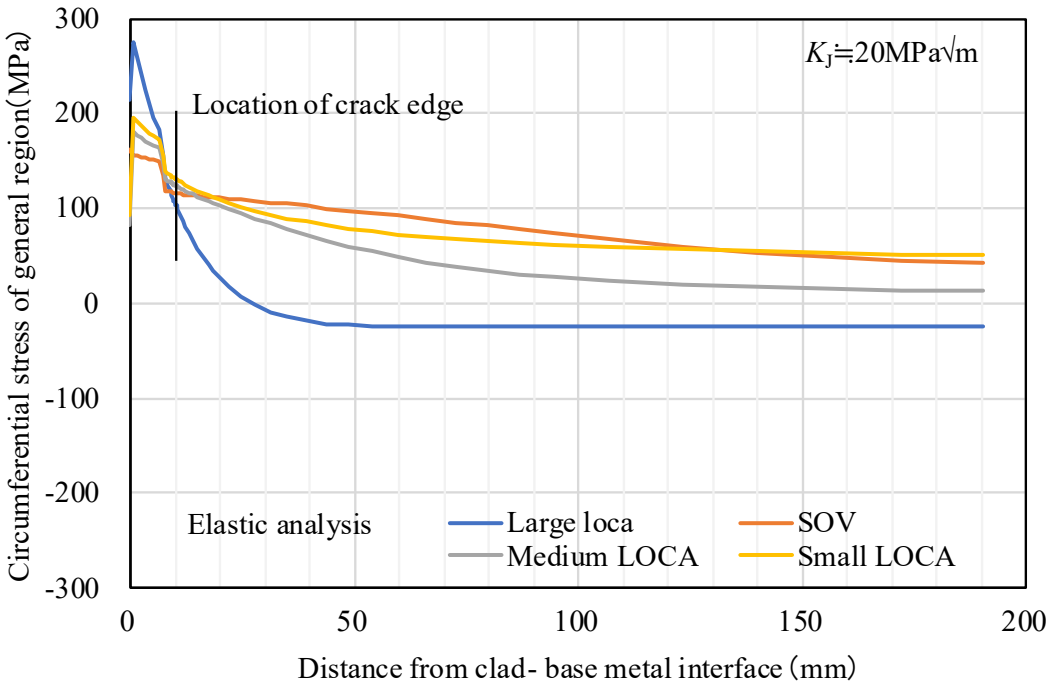


Fig. 5.1.2-11 Stress distribution in nominal cross section at K_J＝20MPa√m in PTS transient condition (Elastic analysis)

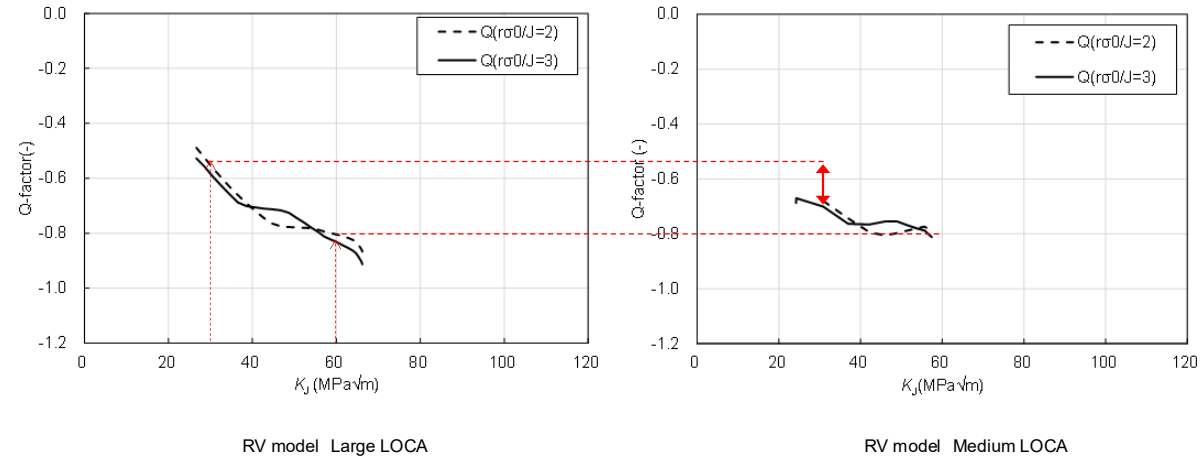


Fig. 5.1.2-12 Comparison of Q-factor

Copyright © 2026 The Japan Welding Engineering Society, All Rights Reserved.

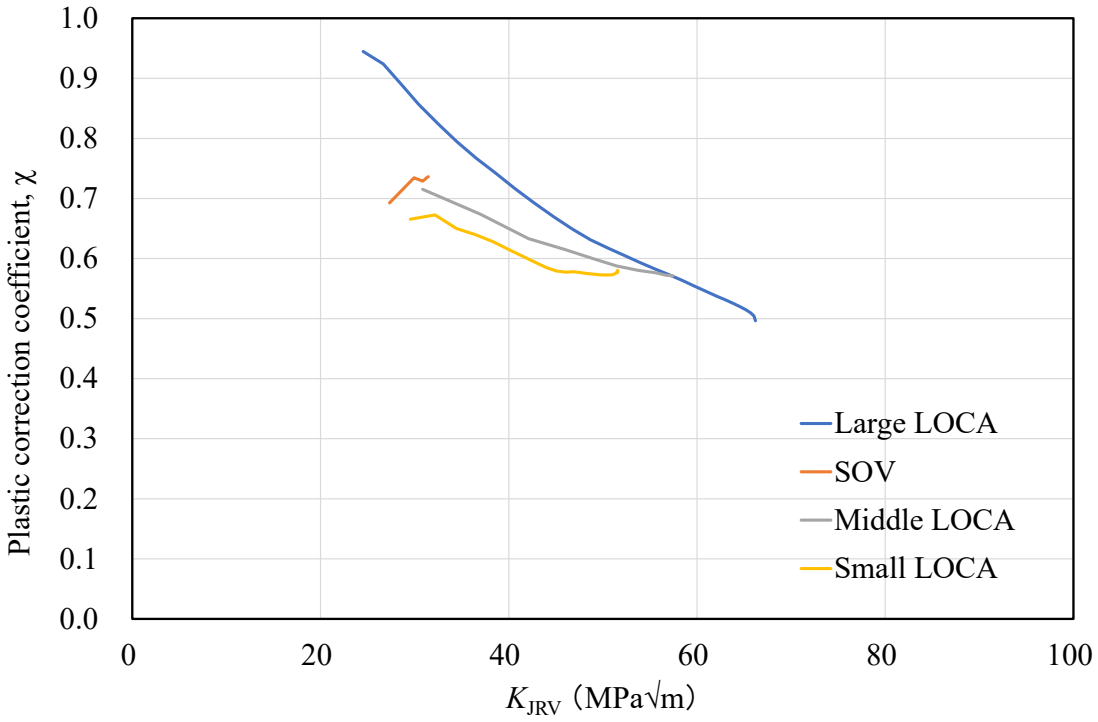


Fig.5.1.2-13 Relation of plastic constraint correction factor χ-K_J in PTS transient condition

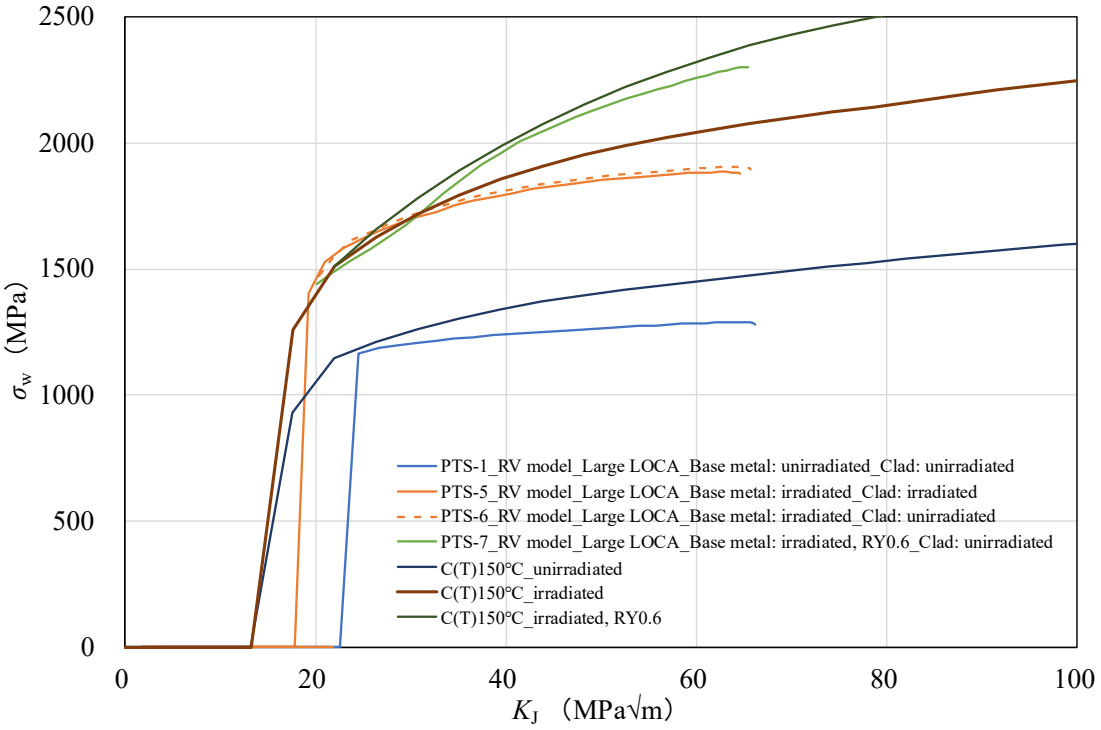


Fig. 5.1.2-14 Effect of stress-strain relation on σ_w-K_J relation

Copyright © 2026 The Japan Welding Engineering Society, All Rights Reserved.

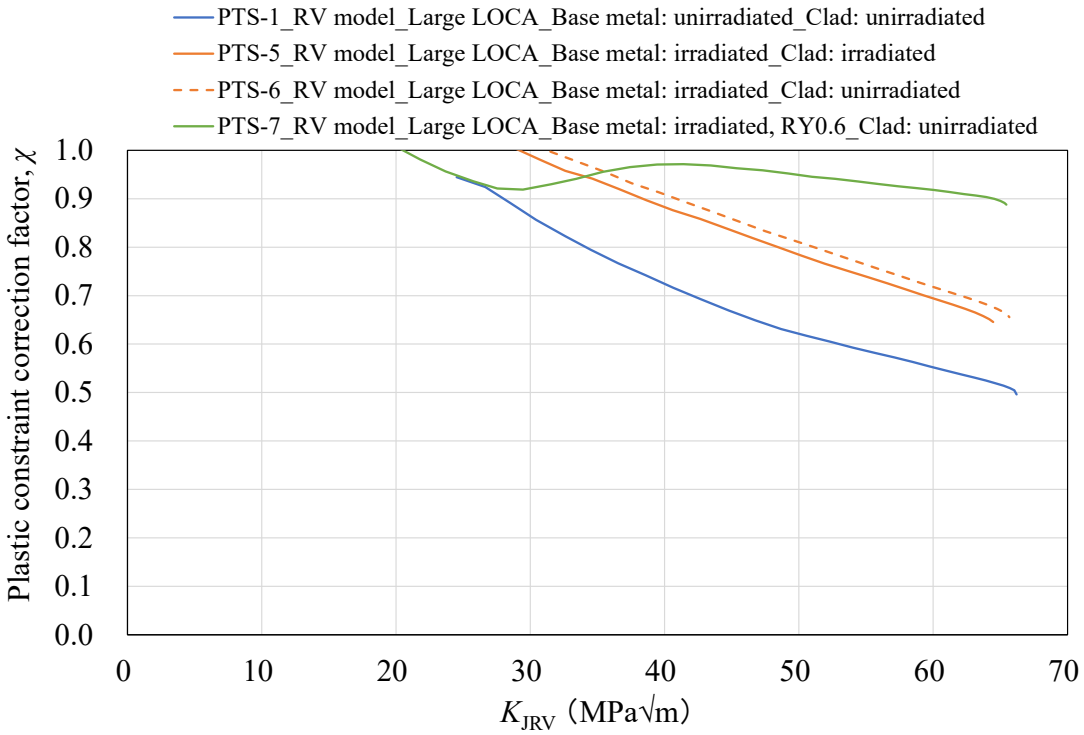


Fig.5.1.2-15 Effect of stress-strain relation on plastic constraint correction factor

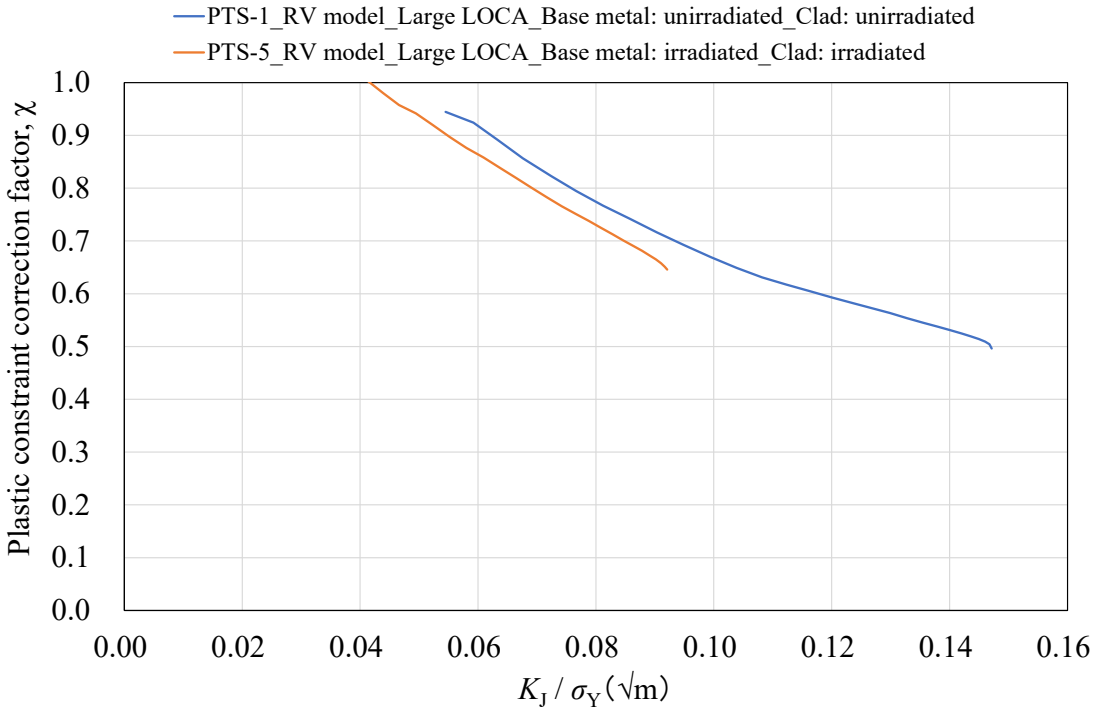


Fig.5.1.2-16 Effect of stress-strain relation on plastic constraint correction factor using K_J/σ_Y

Copyright © 2026 The Japan Welding Engineering Society, All Rights Reserved.

5.1.3 Verification of no ductile crack initiation during PTS events

In the preceding evaluation, the plastic constraint correction factor χ was calculated under the assumption that no ductile crack initiation occurs. In this section, no ductile crack initiation under PTS transient conditions is verified.

The ductile crack growth resistance (J-R curve) of RPV base metal, including the effect of neutron irradiation, were derived using the fracture toughness estimation formula (5.1.3-1) specified in JEAC4206, with a lower bound of *USE* of 60 J, which can be secured during long-term operation of PWR plants in Japan, and a representative operating temperature of 288°C for PWR plants. Here, M_j of 0.863, accounting for -2σ variability in service levels A, B, and C, as defined in JEAC4206, was applied.

$$J = M_j C_1 \Delta a^{c2} \qquad (5.1.3\text{-}1)$$

$$C_1 = exp(0.147 + 2.64log(USE) - 0.00087T)$$

$$C_2 = -0.549 + 0.383log(C_1)$$

$$M_j = 0.863$$

Figure 5.1.3-1 shows the J-R curve obtained by Equation (5.1.3-1) and the result of reproducing ductile crack growth behavior by the GTN analysis. The GTN model parameters were determined so that the ductile crack growth matched in the 1T C(T) specimen model. The analysis was conducted using Abaqus Explicit with reduced integration elements (C3D8R), employing a stress-strain curve with yield stress 700 MPa and R_Y = 0.8 as material properties. Young's modulus at 150°C, close to the maximum K_J temperature in PTS analysis, was used. Although it is preferable to determine the GTN parameters using crack growth data from the specimens with varying constraint conditions, such data were unavailable; therefore, calibration was performed solely with the 1T C(T) specimen model. The parameter calibration results are shown in Table 5.1.3-1.

Using the calibrated GTN model parameters, ductile crack growth analysis of the RPV model was performed. The analysis conditions and model geometry correspond to those shown in Figs. 5.1.2-1 and 5.1.2-2, respectively, and the simulation was performed using Abaqus Explicit and reduced integration elements (C3D8R). The stress-strain curve relationship shown in Fig. 5.1.2-4 was used. Figure 5.1.3-2 shows the results of ductile crack growth analysis by the GTN model. This figure presents calculations at three load levels: rated operation, K_J = 57.5 MPa√m, and K_J = 61.8 MPa√m (maximum K_J).

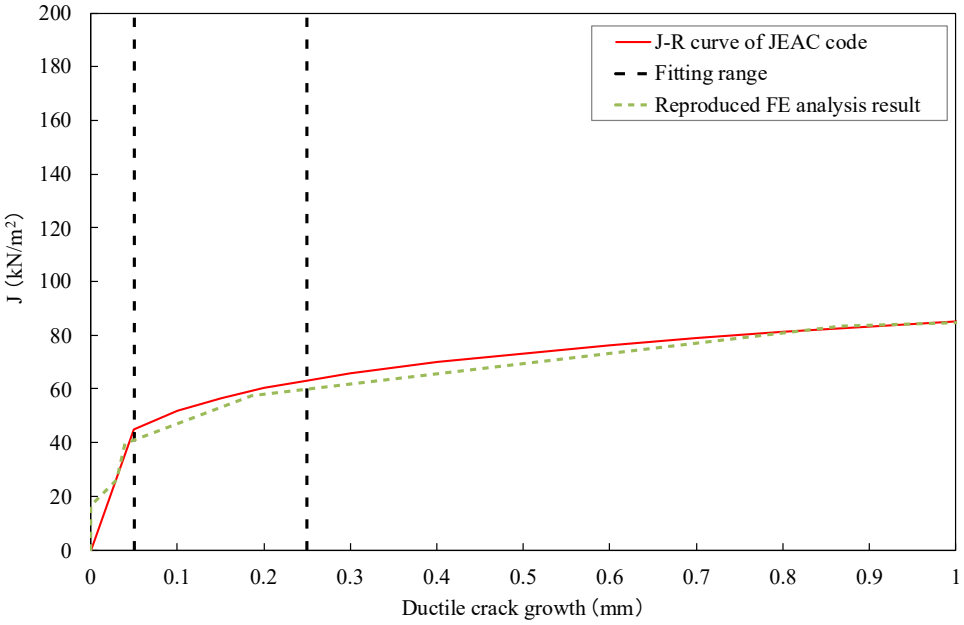
Copyright © 2026 The Japan Welding Engineering Society, All Rights Reserved.

At all load levels, no ductile crack growth was observed, confirming that χ is not affected by considering ductile crack growth. However, if ductile crack growth is anticipated at higher load levels, it is necessary to incorporate this behavior into the evaluation and adjust the plastic constraint effect correction accordingly.

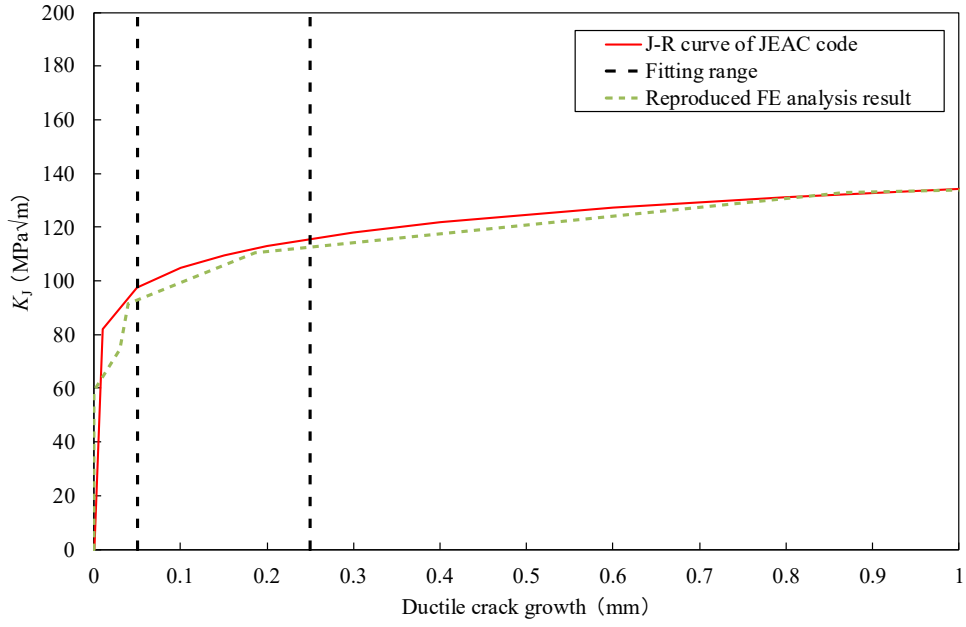
Copyright © 2026 The Japan Welding Engineering Society, All Rights Reserved.

Table 5.1.3-1 GTN model parameters of irradiated base metal (*USE* 60 J)

q_1	q_2	f_0	f_N	ε_N	S_N	f_c	f_F
1.5	1.0	6.49×10^{-3}	8.66×10^{-3}	2.81×10^{-1}	9.38×10^{-1}	2.37×10^{-2}	1.15×10^{-1}



(a) *J*-*Δa*



(b) K_J-*Δa*

Fig. 5.1.3-1 Resistance curve of irradiated base material

Copyright © 2026 The Japan Welding Engineering Society, All Rights Reserved.

Copyright © 2026 The Japan Welding Engineering Society, All Rights Reserved.

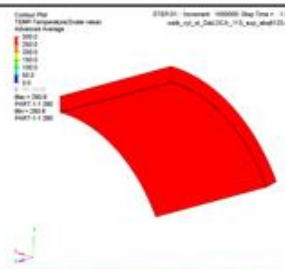
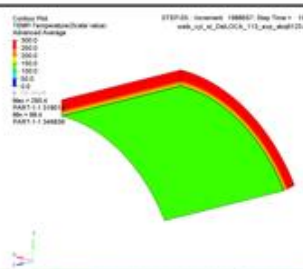
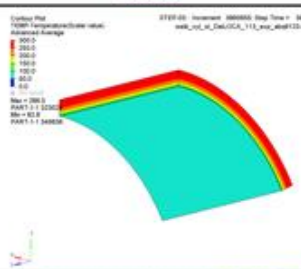
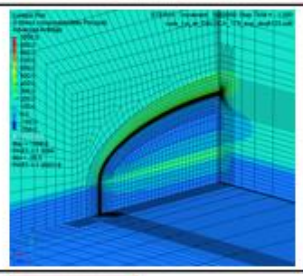
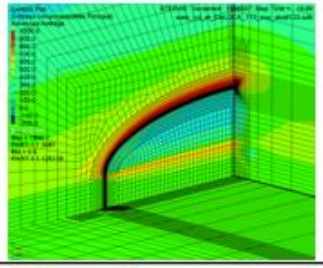
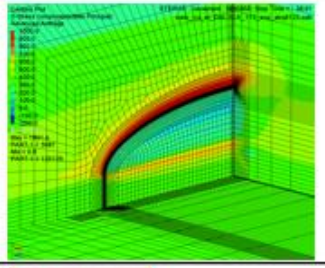
	Time step 1 (Rated operation)	Time step 2 (K_J = 57.5MPa$\sqrt{m}$)	Time step 3(K_{Jmax}=61.8MPa$\sqrt{m}$)
Temperature			
Maximum principal stress			
Ductile crack growth			

Fig. 5.1.3-2 Evaluation results of ductile crack growth

5.2 Examination of simplified evaluation method accounting for plastic constraint effects

5.2.1 Model for calculating plastic constraint correction factor χ

In the previous section, the plastic constraint correction factor χ was calculated under transient conditions of the RPV model. On the other hand, for performing fracture evaluations that incorporate χ in actual plants, it is preferable to represent the plastic constraint correction factor in the form of graphs, tables, or formulae, as exemplified by standards such as ISO 27306 or BS 7910. As mentioned earlier, χ is constructed based on two types of material parameters but also depends on load level, i.e., K_J, and flaw geometry and dimensions. While it is necessary to consider these factors when determining χ, analysis using the RPV model involves a large model and heavy computational load, and load levels cannot be freely controlled under PTS transient conditions with stress gradients in the thickness direction. Therefore, it was decided to use a flat plate model with a semi-elliptical flaw to database χ.

For the flat plate model, modeling methods and loading procedures were investigated to conservatively evaluate Weibull stress generated by PTS events. Table 5.2.1-1 shows the list of analysis conditions. Material properties of unirradiated material were used. The Weibull parameter m was set to 20. The purposes of each analysis case are as follows:

- Case Plate-1:

As a reference case, a model with cladding was used to simulate equi-biaxial bending loads generated by PTS transients, applying bending stresses to both end surfaces parallel and perpendicular to the flaw. No thermal or residual stresses were considered.

- Case Plate-2:

Using the same model conditions as Case Plate-1, membrane stresses were applied to both end surfaces to evaluate the influence of load stress distribution. No thermal or residual stresses were considered.

- Case Plate-3:

Using the same model conditions as Case Plate-1, only stress perpendicular to the flaw face was applied to evaluate the influence of multiaxial stress. No thermal or residual stresses were considered.

- Case Plate-4:

Using the same model conditions as Case Plate-1, residual stresses from cladding application and

Copyright © 2026 The Japan Welding Engineering Society, All Rights Reserved.

thermal stresses due to thermal expansion difference between cladding and base metal were considered. Residual stress distribution from Fig. 5.1.2-5 was input. Bending stresses were applied on both end faces.

- Case Plate-5:

A model without cladding was used, applying bending stress only in the flaw-perpendicular direction.

5.2.1.1 Analysis conditions

(1) Analysis model

Flat plate models with and without cladding are shown in Fig. 5.2.1-1. The flat plate model is a square with length $2L$ = 2000 mm, and plate thicknesses of 200 mm for the base metal and 5.5 mm for the cladding, the same as the RPV model. In the clad model, a semi-elliptical axial flaw 10 mm deep × 60 mm long was modeled beneath the clad. The analysis model was a quarter model for symmetry. Membrane or bending stresses were applied to the far ends from the flaw.

(2) Analysis code and element type

Abaqus Ver. 6.12 was used for analysis. Abaqus Standard was used for Weibull stress analysis with 8-node linear brick elements (C3D8). Abaqus Explicit was used for GTN model analysis with reduced integration elements (C3D8R).

(3) Material properties

Material properties of unirradiated material (yield stress 450 MPa, yield ratio 0.77) shown in Section 5.1 were used. The equivalent stress–equivalent plastic strain relationships of unirradiated material is shown in Fig. 5.1.2-3. The analysis temperature was 150°C, and Young's modulus at 150°C was used. Except for Case Plate-4, the stress-free temperature was set to 150°C to avoid thermal stress between cladding and base metal.

5.2.1.2 Results of investigation of χ calculation model

(1) Influence of load stress distribution

Figure 5.2.1-2(1) compares Weibull stress and K_J relationships when loaded by bending stress and membrane stress under equi-biaxial loading. Both results are nearly equal.

Figure 5.2.1-3 shows stress contour near the flaw for different load types. The maximum principal

Copyright © 2026 The Japan Welding Engineering Society, All Rights Reserved.

stress distribution shows nearly uniform stress distribution over the specimen for membrane stress loading, while bending stress loading causes high stress on the flaw face and stress gradients within the plate thickness. However, since the flaw depth a = 10 mm is very shallow relative to plate thickness t = 200 mm (a/t = 0.05), the maximum principal stress contours near the flaw are similar for bending and membrane loading with small stress gradients. Therefore, it is estimated that the difference in stress distribution form has no effect on Weibull stress.

(2) Influence of multiaxial loading

Figure 5.2.1-2(2) shows Weibull stress and K_J relationships for equi-biaxial bending loading and uniaxial bending loading (stress applied perpendicular to the flaw). As shown, both results coincide. From stress contour maps in Fig. 5.2.1-3, the stress fields near the flaw are equal in both cases, and due to the shallow flaw, no multiaxial effect appears. Similar results were confirmed in studies by Minami et al.[5-8], showing Weibull stress nearly equal for two-axial and uniaxial loading with shallow flaws. Thus, for the assumed shallow flaw, differences between uniaxial and biaxial loading need not be considered.

(3) Influence of Residual Stress

Figure 5.2.1-2(3) shows Weibull stress and K_J relationships for analyses considering residual stress and dissimilar metal thermal stress, and for those without these considerations. Residual stress considers thermal history of cladding welding and PWHT effects shown in Fig. 5.1.2-5, and thermal stress at 150°C relative to room temperature due to thermal expansion difference between stainless cladding and low alloy steel base metal. The figure shows that Weibull stress is slightly larger when residual stress is considered, but the difference is small.

(4) Influence of cladding

Figure 5.2.1-2(4) shows Weibull stress and K_J relationships for models with and without cladding under uniaxial loading perpendicular to the flaw. The model without cladding shows Weibull stress–K_J relationships shifted upward. Compared to the RPV model for LBCOCA, the unclad plate model's Weibull stress–K_J relationship is higher, i.e., conservative. Figure 5.2.1-4 shows stress distribution and plastic zone extent near the crack tip at the same K_J. Stress near the crack tip of C(T) specimens is also shown. The figure shows that stress is higher in the cladded condition than without cladding, and the plastic zone is larger with cladding, indicating looser plastic constraint.

Copyright © 2026 The Japan Welding Engineering Society, All Rights Reserved.

From these results, using an unclad flat plate model with uniaxial bending load and no residual stress for χ calculation allows conservative conditions compared to the RPV model. Figure 5.2.1-5 confirms this conservatism.

Copyright © 2026 The Japan Welding Engineering Society, All Rights Reserved.

Table 5.2.1-1 Analysis condition of flat plate model

Case No.	Dimension		Material Properties				Cladding residual stress, thermal stress of dissimilar material	Min. Mesh size (mm)	Load			Flaw geometry (semi-elliptical)		Weibull Parameter	Note
	Base metal width, thickness (mm)	Cladding thickness (mm)	Base metal	Base metal yield stress (MPa)	Base metal yield ratio	Clad			Temp. (°C)	Stress normal to flaw	Stress parallel to flaw	Depth (mm)	Length (mm)	m	
Plate-1	2000, 200	5.5	Elastic plastic, un-irradiated	450	0.77	Elastic plastic, un-irradiated	Not considered	0.03	150	Bending 500MPa	Bending 500MPa	10	60	20	
Plate-2										Membrane 500MPa	Membrane 500MPa				Effect of membrane /bending load
Plate-3										Bending 500MPa	—				Effect of multi-axial load
Plate-4							Considered			Bending 500MPa	Bending 500MPa				Effect of residual stress
Plate-5		—				—	Not considered			Bending 500MPa	—				Effect of cladding

Copyright © 2026 The Japan Welding Engineering Society, All Rights Reserved.

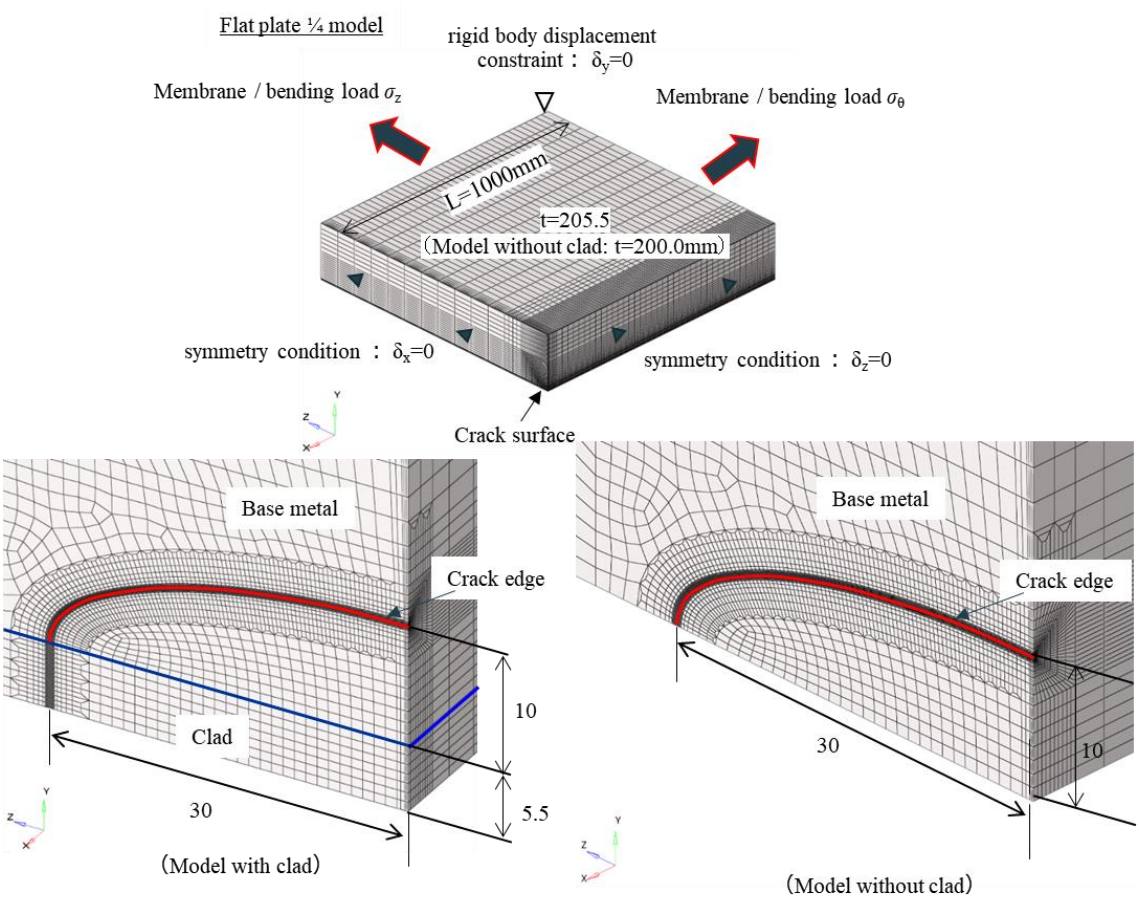
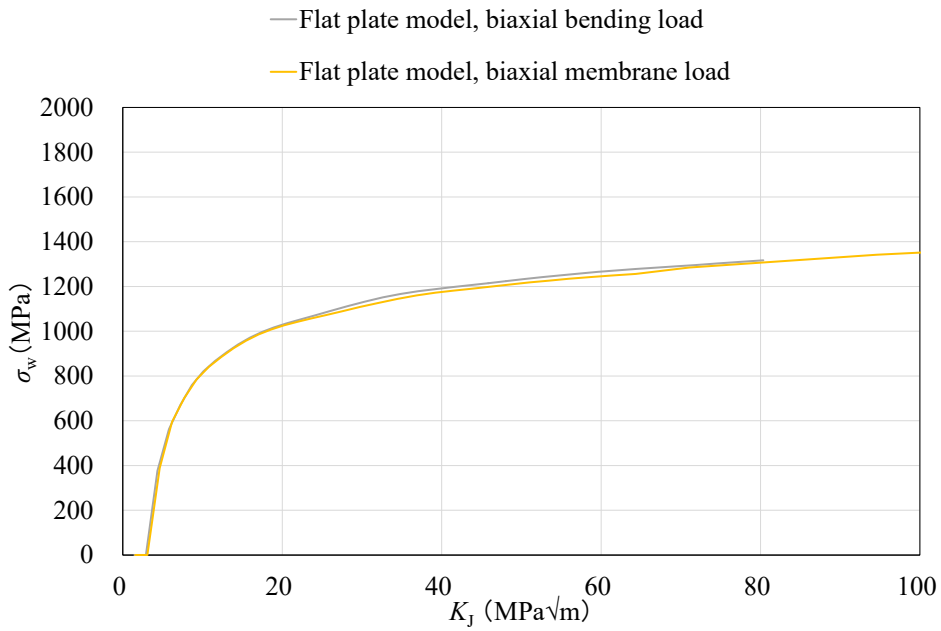
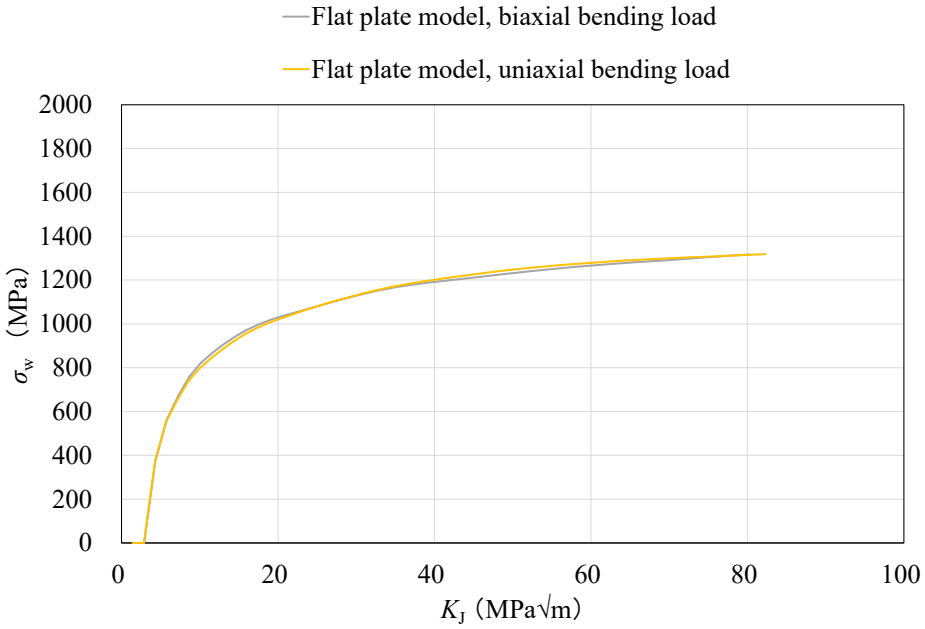


Fig. 5.2.1-1 Flat plate FE model

Copyright © 2026 The Japan Welding Engineering Society, All Rights Reserved.



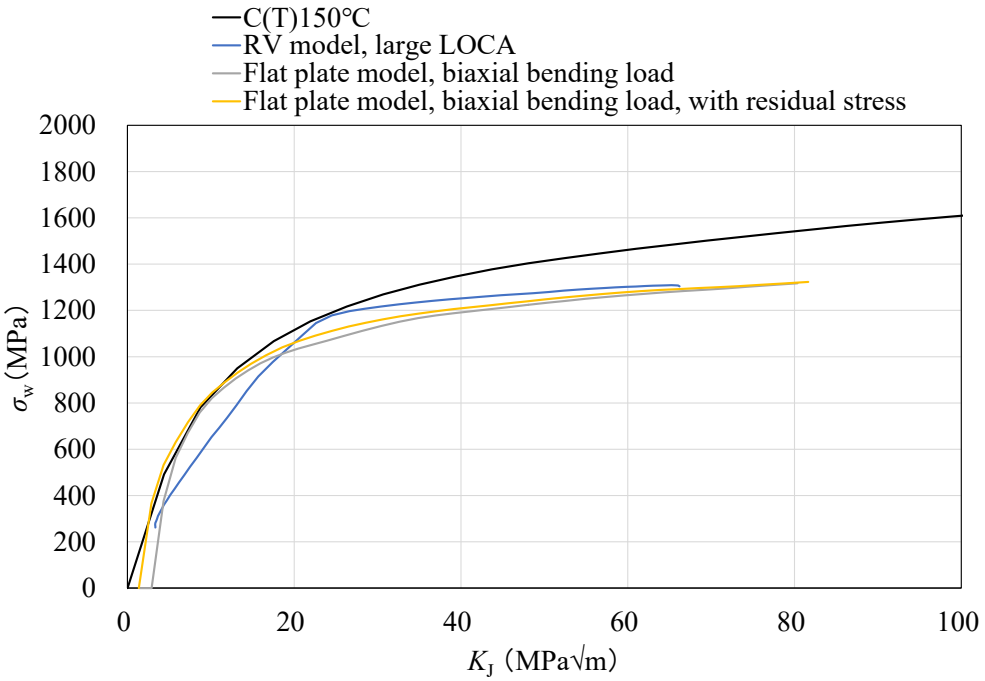
(1) Effect of loading type



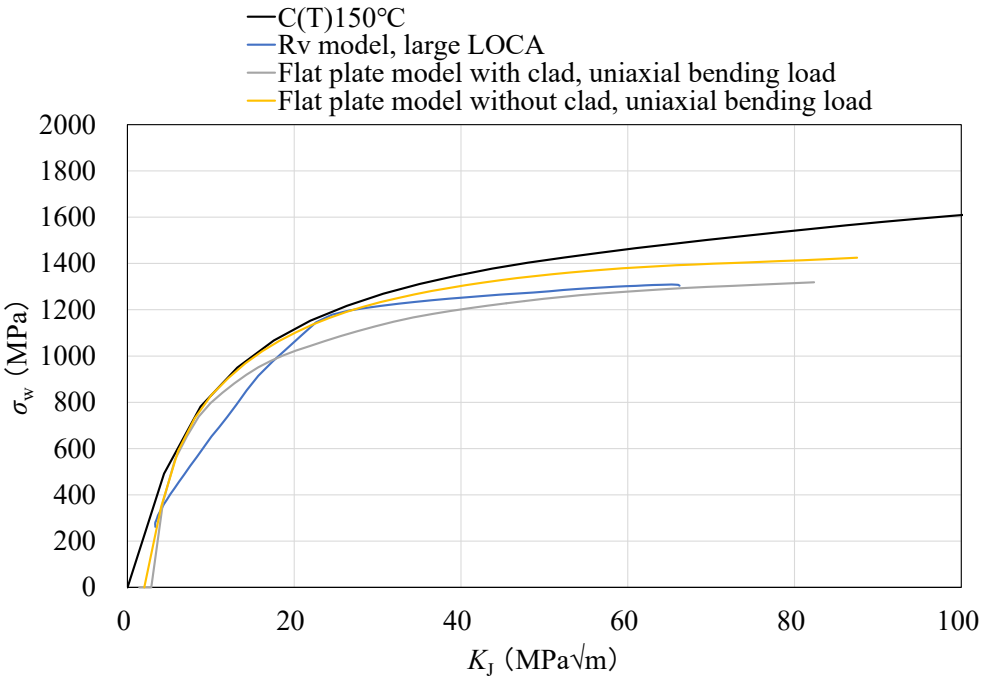
(2) Effect of multi-axial loading

Fig. 5.2.1-2 (1/2) Effect of each factor on σ_w-K_J relation

Copyright © 2026 The Japan Welding Engineering Society, All Rights Reserved.



(3) Effect of residual stress



(4) Effect of cladding

Fig. 5.2.1-2 (2/2) Effect of each factor on σ_w-K_J relation

Copyright © 2026 The Japan Welding Engineering Society, All Rights Reserved.

Copyright © 2026 The Japan Welding Engineering Society, All Rights Reserved.

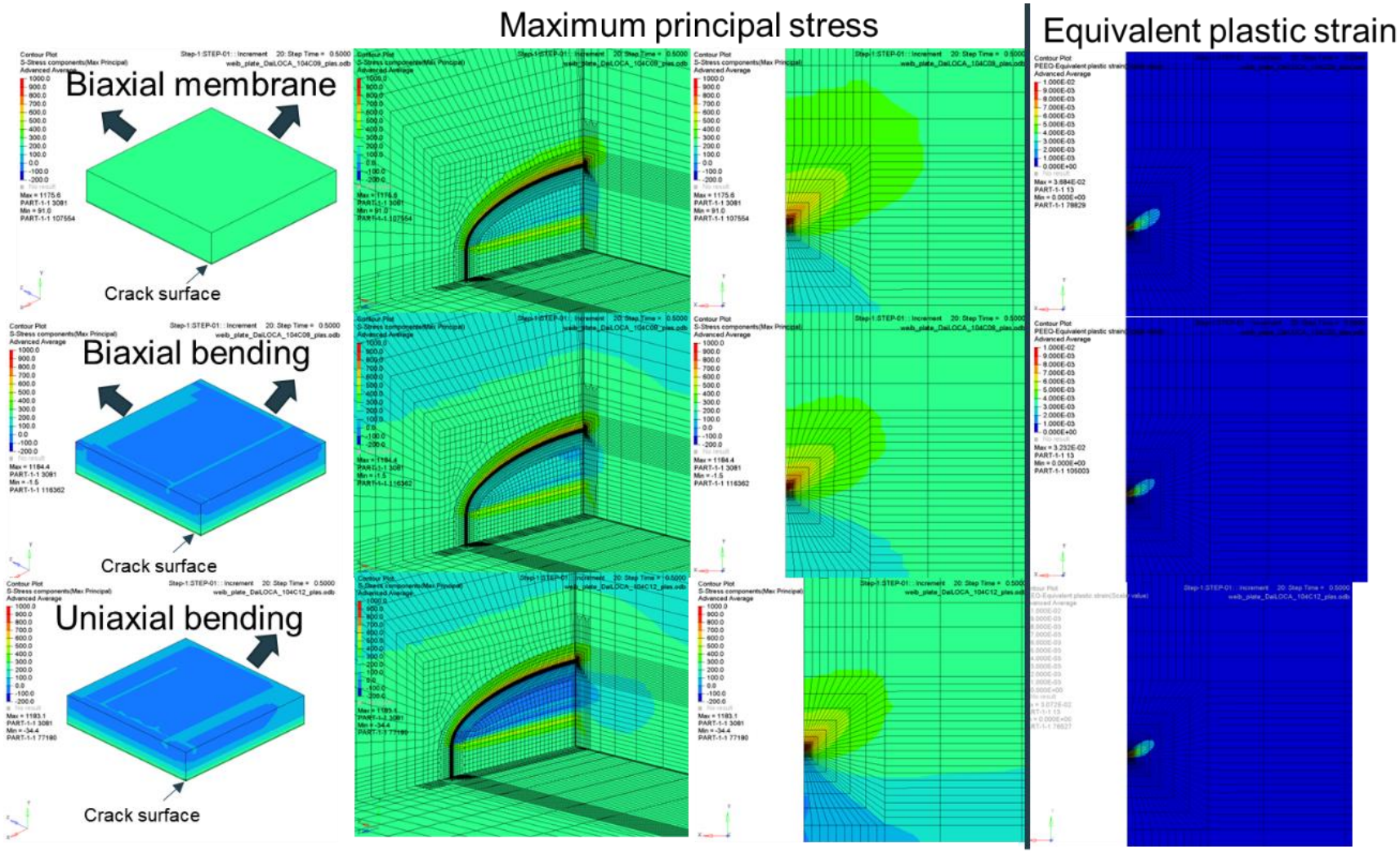
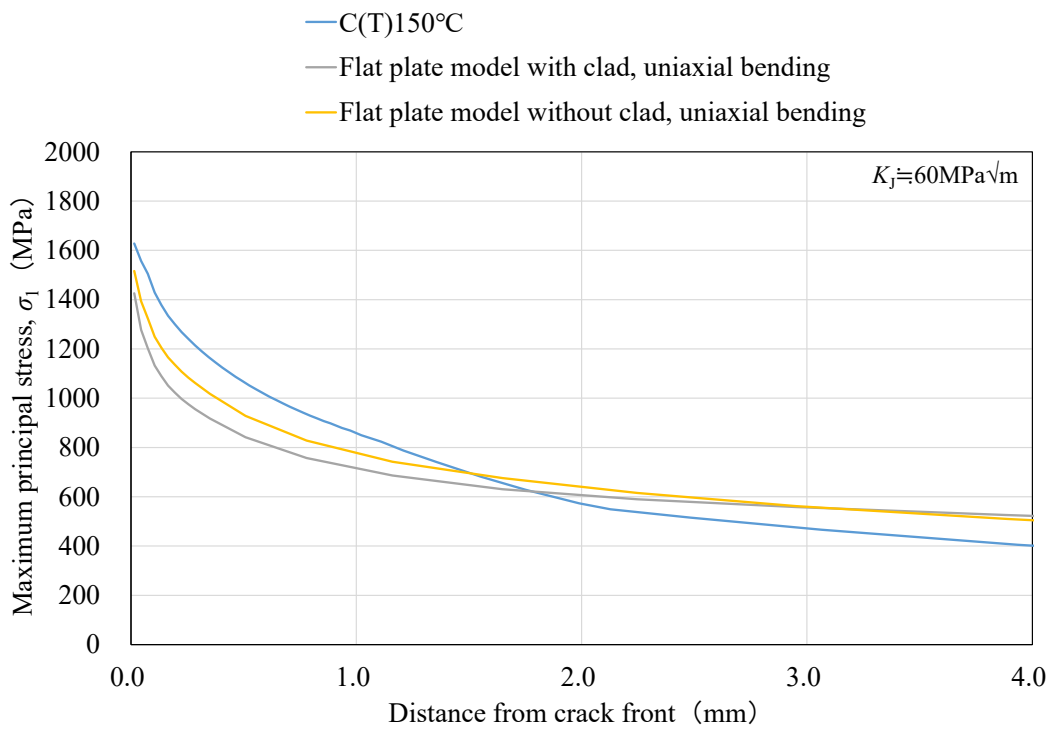


Fig.5.2.1-3 Comparison of stress distribution on flawed section under biaxial membrane / bending stress and uniaxial bending stress



Distribution of equivalent plastic strain near the deepest point of crack

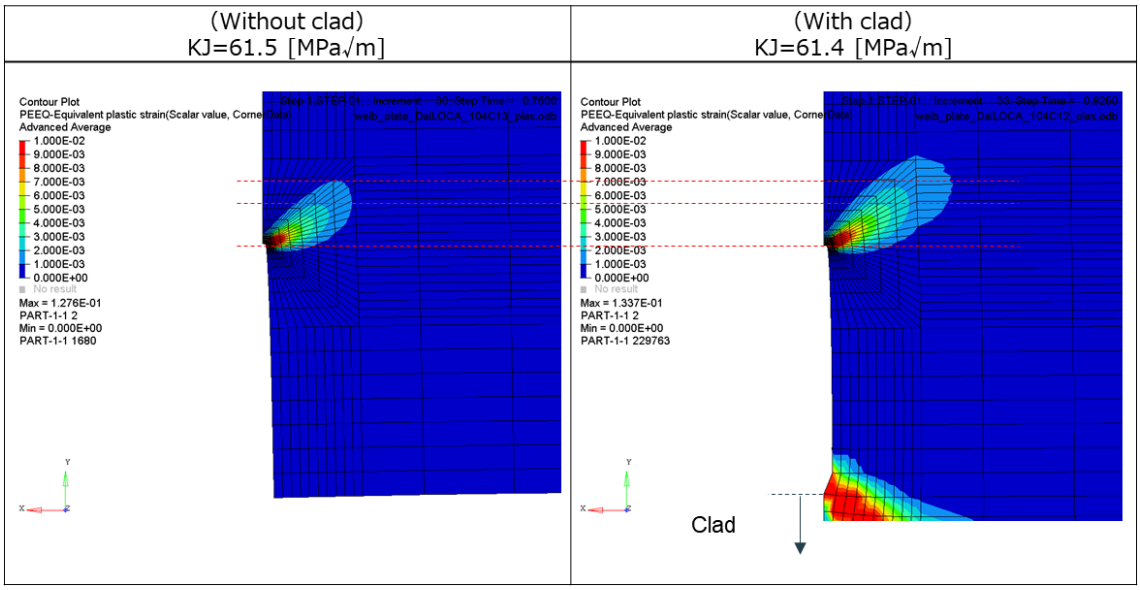


Fig.5.2.1-4 Comparison of stress distribution near crack tip with/without clad

Copyright © 2026 The Japan Welding Engineering Society, All Rights Reserved.

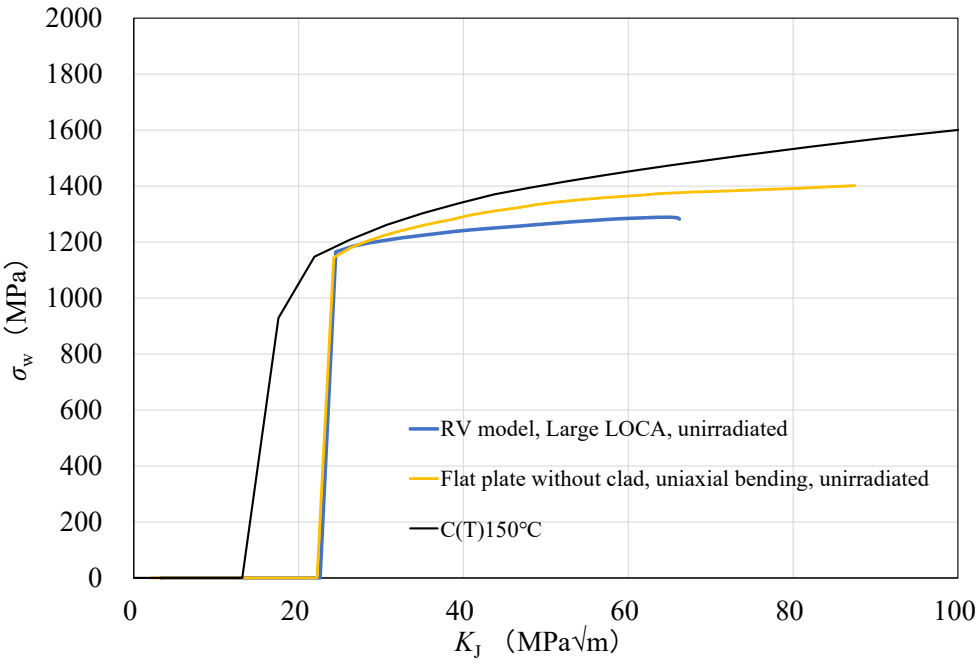


Fig. 5.2.1-5 σ_w-K_J relation of C(T) model, RPV model, and flat plate model without clad under bending

Copyright © 2026 The Japan Welding Engineering Society, All Rights Reserved.

5.2.2 Construction of database for χ formulation

5.2.2.1 Analysis using plate models

(1) Analysis Cases

Based on the results of Section 5.2.1, Weibull stress analyses were performed on plate models by varying plate thickness, flaw shape (flaw depth and length), tensile properties (yield stress, $\sigma_{Y,}$ and yield ratio, R_Y), and Weibull parameter m. The analysis cases using the plate models are shown in Table 5.2.2-1. For each analysis case, χ was calculated by comparing with the analysis results of C(T) specimens, and a database for χ formulation was constructed.

The plate thickness was set between 100 and 250 mm, covering the typical thickness range of BWR and PWR RPVs. Flaw depths were set to 10 mm, as assumed in JEAC4206 PTS evaluation, and also 5 mm and 7.5 mm, considering the possibility of evaluating smaller flaws in the future. Flaw lengths were set within a range of 1/6 to 1/3 aspect ratio (flaw depth / flaw half-length) for each flaw depth, based on the 1/6 aspect ratio assumed in JEAC4206 PTS evaluation.

For tensile properties, σ_Y was set to 450 MPa for unirradiated material and 700 MPa for irradiated material. In the analysis case with plate thickness 200 mm, flaw depth 10 mm, and flaw length 60 mm as a reference, the influence of R_Y, was confirmed by varying it to 0.6, 0.7, 0.8, 0.85, and 0.95 based on irradiated material properties. Additionally, to investigate the influence of σ_Y , R_Ys of 0.6 and 0.77 were set at 450 MPa σ_Ys. Weibull parameter m was calculated for three cases: 10, 20, and 30.

(2) Analysis Model

Based on the results of Section 5.2.1, an example of the plate model used for χ calculation (Analysis Model A: plate thickness 200 mm, flaw depth 10 mm, flaw length 60 mm) is shown in Fig. 5.2.2-1. The plate model is a uniaxial bending stress load model without cladding, and a quarter model was used considering symmetry. The element size near the crack tip was 0.03 mm × 0.03 mm. Load was applied as bending stress perpendicular to the flaw direction, and symmetry conditions were set on the flaw face. Since χ calculation requires analysis of specimens with high constraint, the FE model of the 1T C(T) specimen was also used.

(3) Material property settings

Material properties considered elastic-plastic behavior. Elastic properties were Young's modulus, E, 193 GPa (value at 150°C) and Poisson's ratio, ν, 0.3. The equivalent stress–equivalent plastic

Copyright © 2026 The Japan Welding Engineering Society, All Rights Reserved.

strain relationship after yielding was set by determining Ramberg-Osgood parameters using WRC 413 equations from tensile strength calculated from σ_Y and R_Y set in each analysis case. Examples of material properties and equivalent stress–equivalent plastic strain relationships used are shown in Fig. 5.2.2-2.

(4) FE Analysis

Analyses of 1T C(T) specimens and plate bending specimens were performed under the above conditions to obtain Weibull stress–K_J relationships. K_J for 1T C(T) was calculated from load–load line displacement relationships and JEAC4216 equations, and K_J for plate bending specimens was calculated by converting J-integral from Abaqus to K. Weibull stress used the maximum principal stress, σ_1, at integration points of each element as effective stress, with reference volume $V_0 = 1.0$ mm³. The lower limit of the integration stress region for Weibull stress calculation was set as σ_1, at the crack tip when $K_J = 20$ MPa√m in the 1T C(T) specimen analysis.

In the reference cases A-1 to A-8, analyses varying tensile properties showed that Weibull stress decreased with increasing K_J in relatively high K_J regions. This was attributed to the integration not including the maximum of σ_1 experienced by each element. Therefore, for cases A-1 to A-8 used for χ formulation and cases B to L, Weibull stress was calculated by integrating σ_1 peak experienced by each element. Generally, even if the stress peak decreases with load increase, the volume experiencing high stress moves forward of the flaw, increasing the volume effect of brittle fracture and thus the cumulative fracture probability. Therefore, it is considered more appropriate to consider the maximum principal stress experienced by each element as the integration target in Weibull stress analysis.

5.2.2.2 Influence of each factors on χ

Weibull stress analyses were performed on surface-flawed plate models under conditions varying plate thickness, flaw dimensions, yield ratio, Weibull parameter, and other parameters. The results examining the influence of each factor on the plastic constraint correction factor χ are presented below.

(1) Influence of plate thickness

Figures 5.2.2-3 and 5.2.2-4 show the results of investigating the effect of plate thickness on the correction factor χ for two crack sizes: 10 mm depth × 60 mm length and 5 mm depth × 30 mm length. In both cases, χ values were generally consistent, confirming that within the range of conditions considered in this study, plate thickness does not significantly affect χ.

Copyright © 2026 The Japan Welding Engineering Society, All Rights Reserved.

(2) Influence of flaw depth (constant flaw length)

Figs. 5.2.2-5 and 5.2.2-6 shows the influence of flaw depth on χ under constant flaw lengths of 30 mm and 45 mm. For both m=10 and m=20, shallower cracks correspond to smaller values of χ. Specifically, at a depth of 5 mm, χ tended to be approximately 10–20% smaller compared to a depth of 10 mm.

(3) Influence of flaw length

Figs. 5.2.2-7 and 5.2.2-8 show the influence of flaw length on χ for flaw depths of 10 mm and 7.5 mm. In both cases, smaller flaw lengths resulted in smaller χ values. For a flaw depth of 10 mm, a flaw half-length of 15 mm ($a/2c$ = 1/3) yielded about 10–20% smaller χ than 30 mm half-length ($a/2c$ = 1/6).

(4) Influence of yield stress σ_Y

Figs. 5.2.2-9 and 5.2.2-10 show the influence of yield stress on Weibull stress and. As shown in Fig. 5.2.2-9, lower σ_Y corresponds to lower Weibull stress. Furthermore, normalizing K_J by σ_Y demonstrated that the relationship between K_J and χ aligns more closely across different σ_Y.

(5) Influence of yield ratio R_Y

Figs. 5.2.2-11 and 5.2.2-12 show the influence of R_Y on χ for a flaw depth of 10 mm ($a/2c$ = 1/6). In the region of $K_J \geq 40$ MPa$\sqrt{}$m, larger R_Y corresponded to smaller χ, with differences up to about 40%. Since R_Y has a large influence on χ, setting an appropriate R_Y is particularly important for irradiated materials where strength increases and R_Y changes.

(6) Influence of Weibull parameter *m*

The effect of varying the Weibull parameter m from 10 to 30 was investigated for analysis cases A-1, A-5, B-1, B-2, and C-1, which were used in the formulation of χ. The results are shown in Figs. 5.2.2-13 and 5.2.2-14. As shown in Fig. 5.2.2-13, comparing results with the same flaw dimensions (the same case number), Weibull stress σ_W increases with increasing m in the low K_J region, whereas in the high K_J region, σ_W increases as m decreases. When m is small, large plastic zones at high K_J lead to larger σ_W due to volume effects. Since this trend is also observed in C(T) specimens, these effects tend to offset each other when calculating χ. Therefore, as shown in Figure 5.2.2-14, smaller m values correspond to larger χ values.

Copyright © 2026 The Japan Welding Engineering Society, All Rights Reserved.

Table 5.2.2-1 Analysis cases using flat plate models

Analysis model	Thickness t (mm)	Flaw depth a (mm)	Flaw length $2c$ (mm)	$a/(2c)$	σ_Y (MPa)	$R_Y = \sigma_Y/\sigma_B$	m	Analysis No.	Participant
A	200	10	60	1/6	700	0.95	10, 20, 30	A-1	MHI
						0.85		A-2	
						0.8		A-3	
						0.7		A-4	
						0.6		A-5	
					600	0.95		A-6	
					450	0.77		A-7	
						0.6		A-8	
B			30	1/3	700	0.95		B-1	
						0.60		B-2	
C		5		1/6		0.95		C-1	UO
						0.60		C-2	JAEA
D	100	10	60			0.95		D	UO
E	150							E-1	Toshiba
						0.6		E-2	
F	250					0.95		F	UO
G	100	5	30					G	Hitachi
H	250							H	
I	200	10	45	1/4.5				I	
J		7.5		1/6				J	
K			30	1/4				K	UO
L		5	15	1/3				L-1	JAEA
						0.6		L-2	

Analysis model A : Base case, effect of tensile property

Analysis model B : Effect of flaw length, yield ratio, capability of interpolation

Analysis model C : Effect of flaw depth, yield ratio

Analysis model D～F : Effect of thickness, yield ratio

Analysis model G, H : Effect of thickness in case of flaw depth of 5mm

Analysis model I～K : Capability of interpolation by flaw depth and length

Analysis model L : Additional analysis for formulation of χ

(The formulation of χ is planned to be set based on the analysis results of a 200 mm plate thickness, considering four cases: a = 5 mm, 10 mm, and $a/(2c)$ = 1/3, 1/6.)

Copyright © 2026 The Japan Welding Engineering Society, All Rights Reserved.

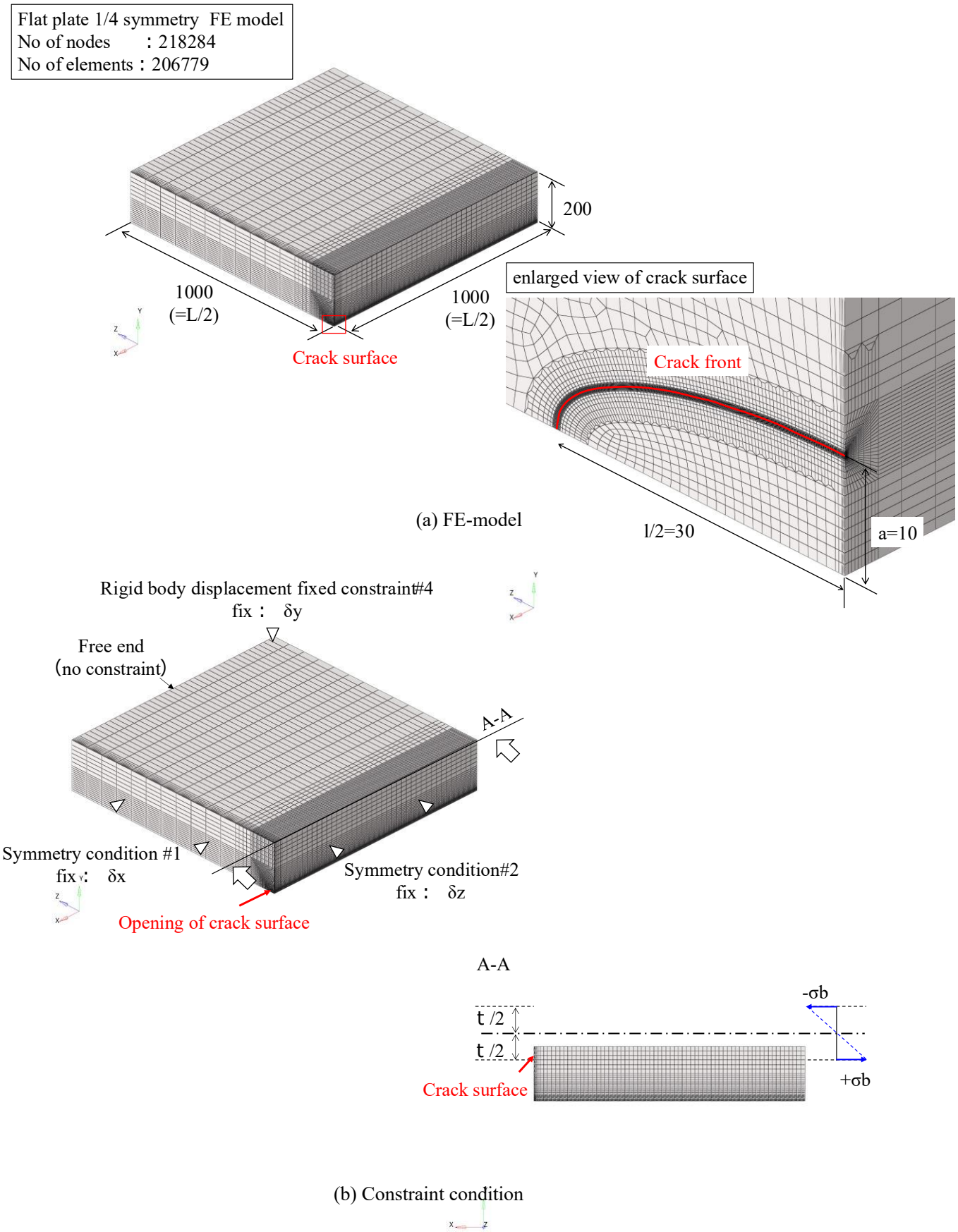


Fig.5.2.2-1 FE-model and constraint condition (example of Model A)

Copyright © 2026 The Japan Welding Engineering Society, All Rights Reserved.

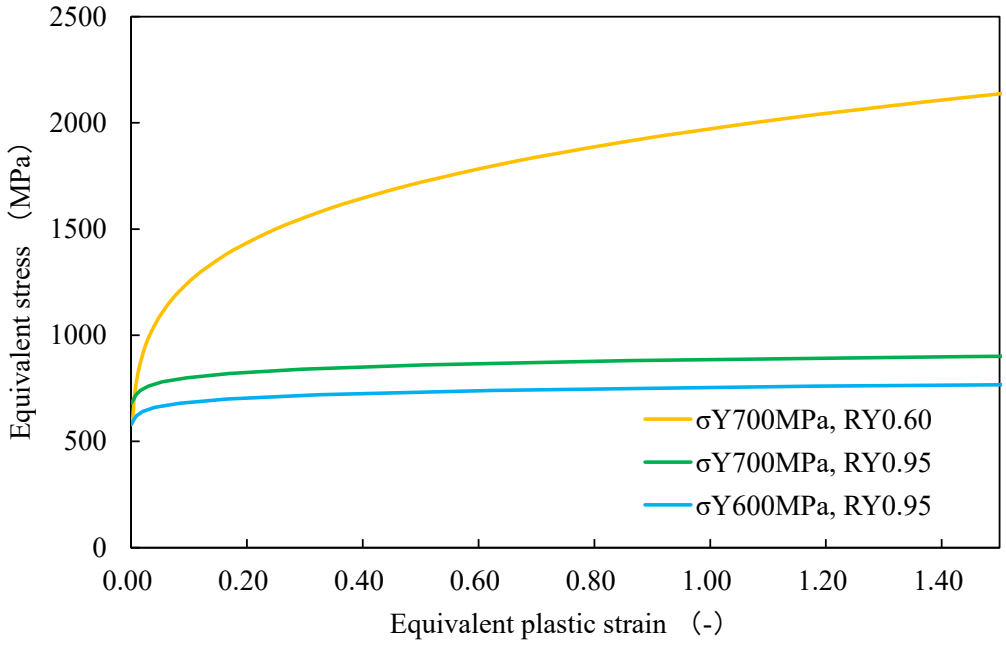
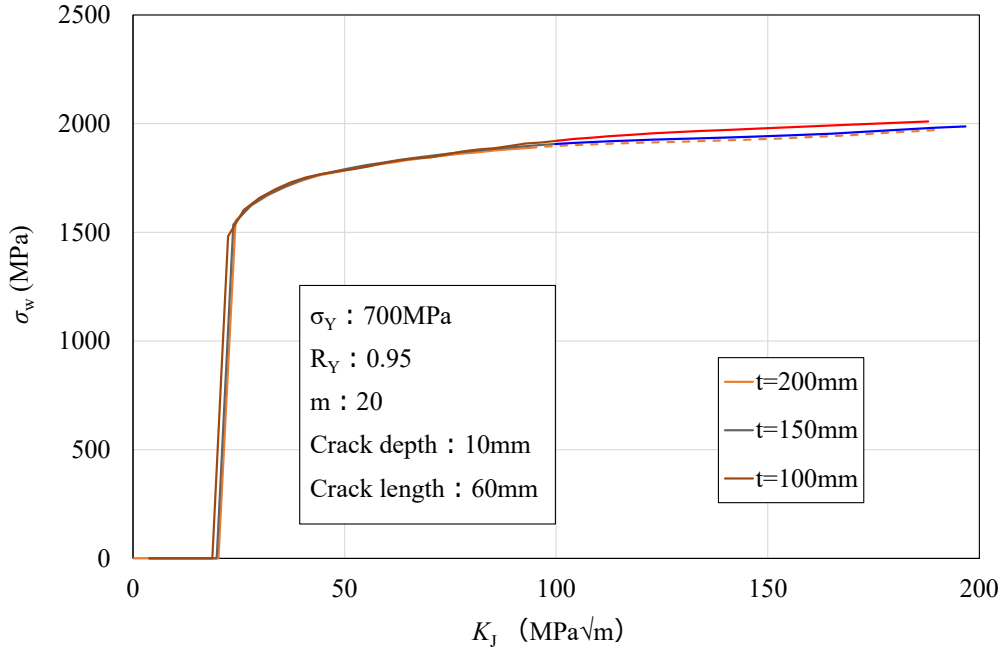
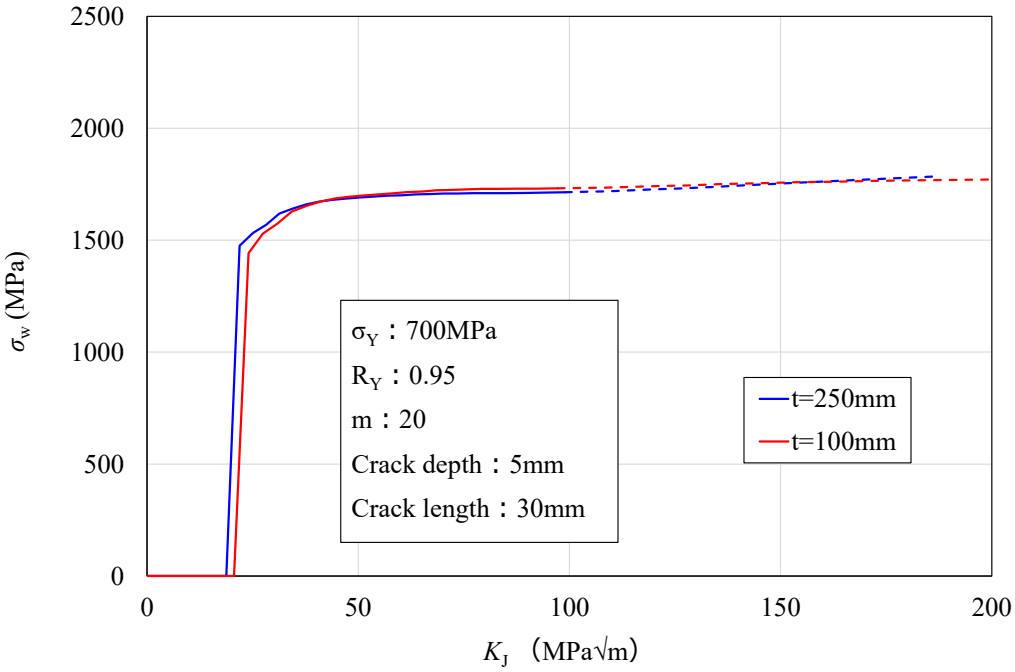


Fig.5.2.2-2　Equivalent stress – equivalent plastic strain curves

Copyright © 2026 The Japan Welding Engineering Society, All Rights Reserved.



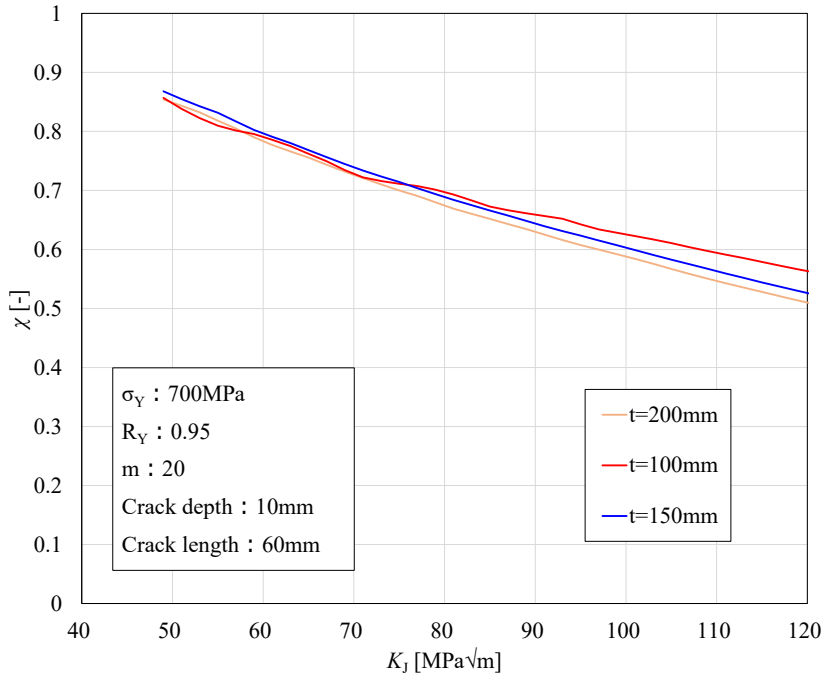
(a) Flaw depth: 10mm, flaw length: 60mm



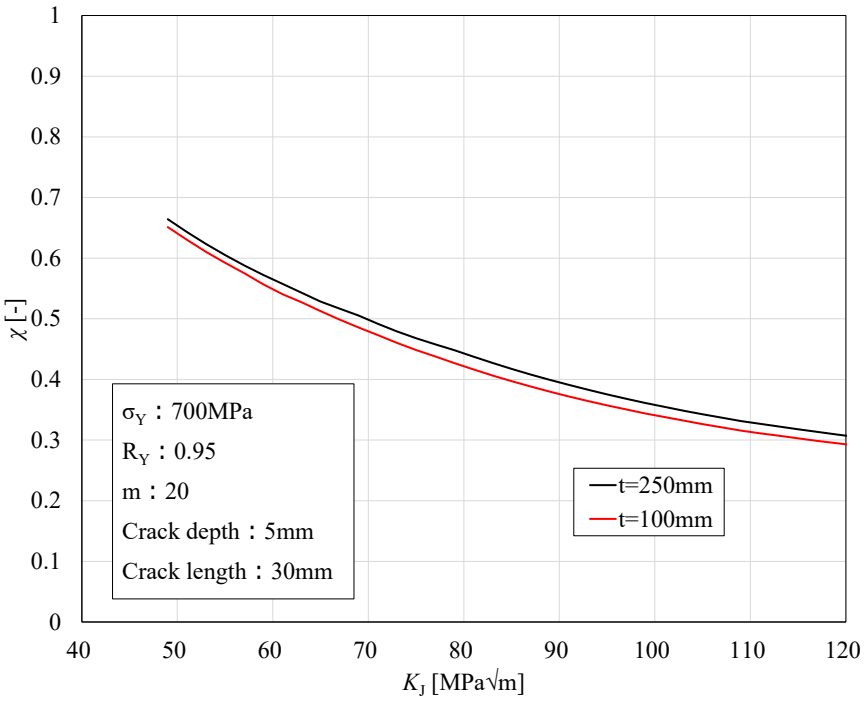
(b) Flaw depth: 5mm, flaw length: 30mm

Fig. 5.2.2-3 Relationship between σ_w and K_J (thickness effect)

Copyright © 2026 The Japan Welding Engineering Society, All Rights Reserved.



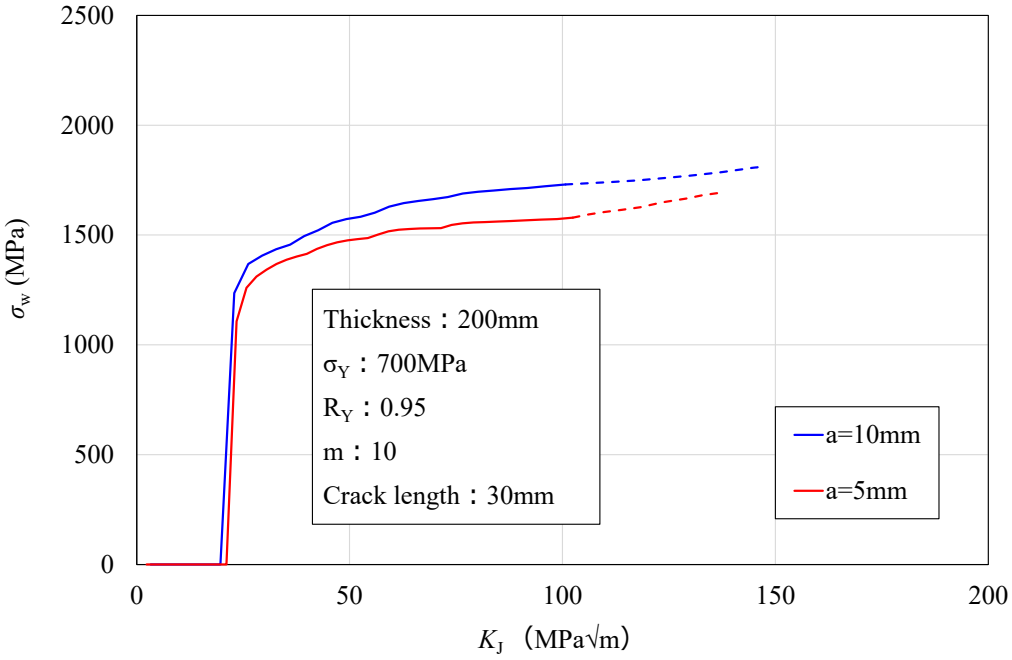
(a) Flaw depth: 10mm, flaw length: 60mm



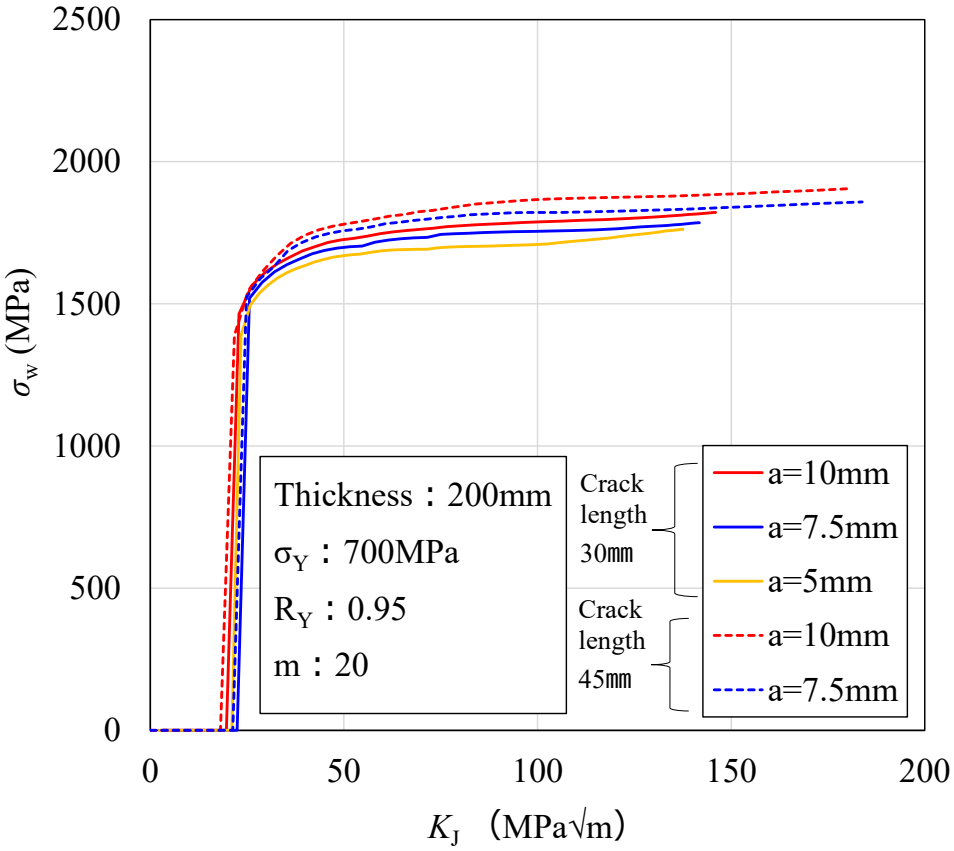
(b) Flaw depth: 5mm, flaw length: 30mm

Fig. 5.2.2-4 Relationship between K_J and χ (thickness effect)

Copyright © 2026 The Japan Welding Engineering Society, All Rights Reserved.



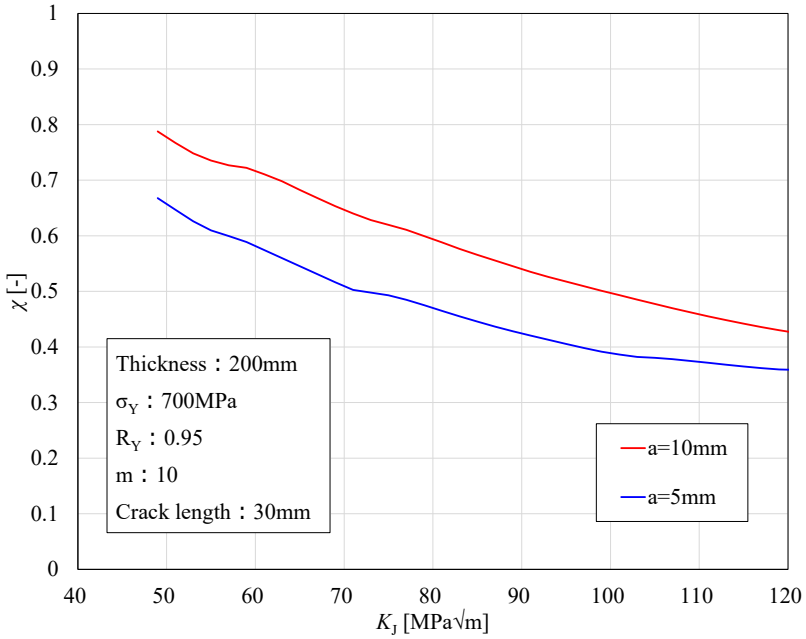
(a) *m*=10



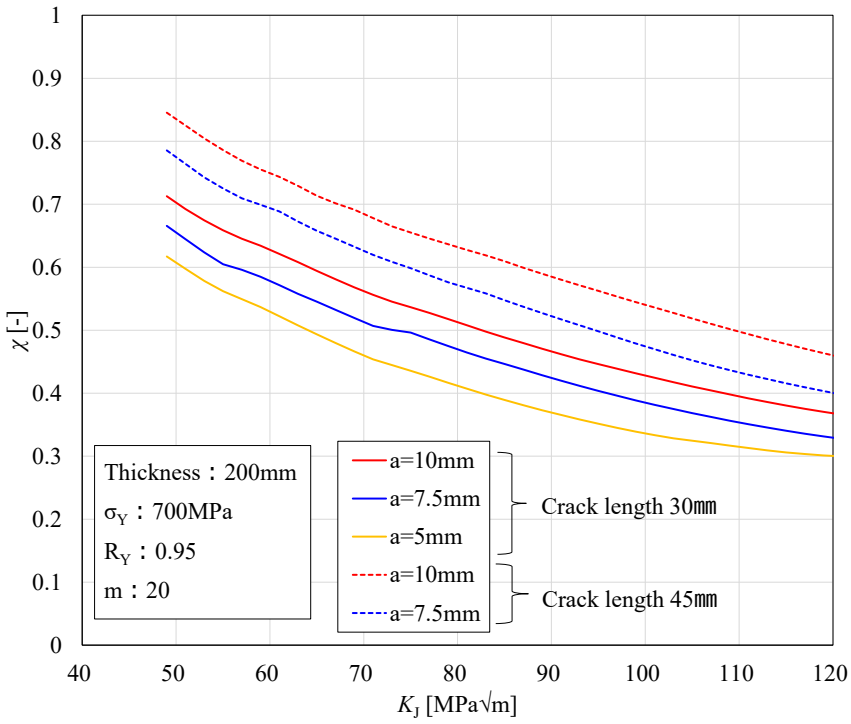
(b) *m*=20

Fig. 5.2.2-5 Relationship between σ_w and K_J (flaw depth effect)

Copyright © 2026 The Japan Welding Engineering Society, All Rights Reserved.



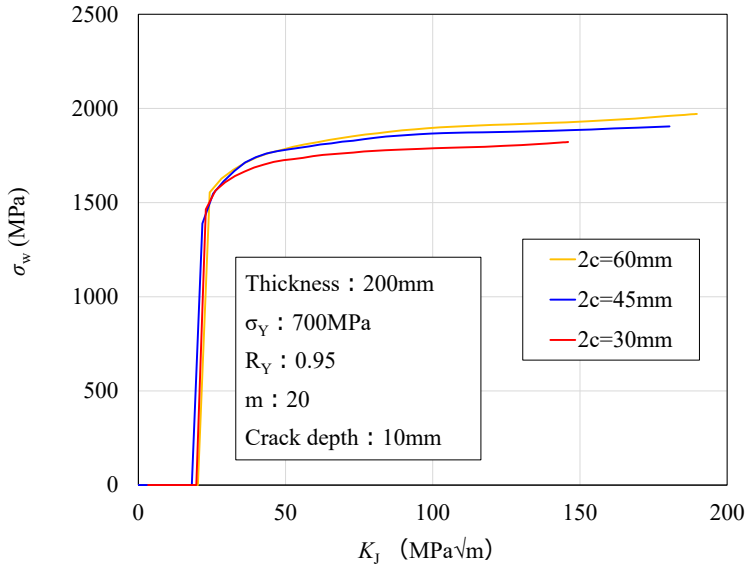
(a) m=10



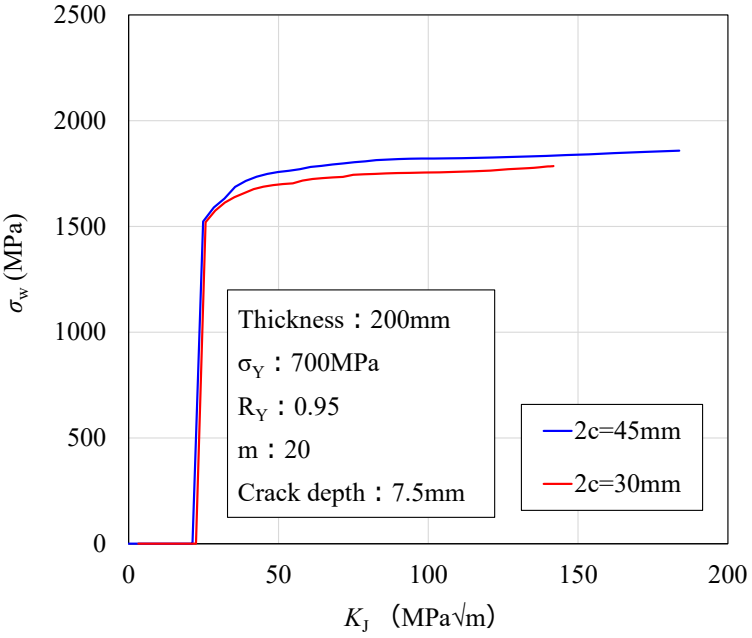
(b) m=20

Fig. 5.2.2-6 Relationship between K_J and χ (flaw depth effect)

Copyright © 2026 The Japan Welding Engineering Society, All Rights Reserved.



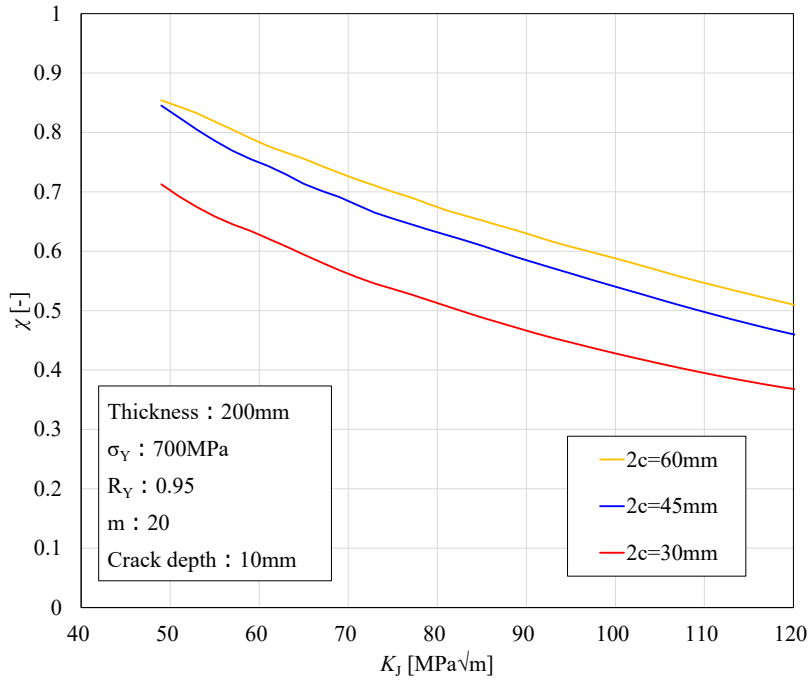
(a) Flaw depth: 10mm



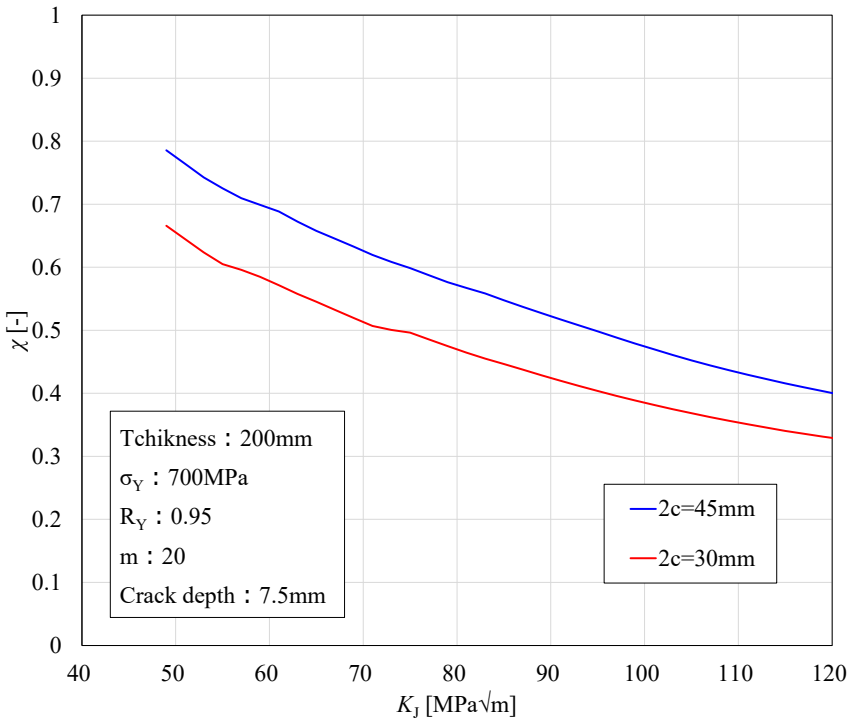
(b) Flaw depth: 7.5mm

Fig. 5.2.2-7 Relationship between σ_w and K_J (flaw length effect)

Copyright © 2026 The Japan Welding Engineering Society, All Rights Reserved.



(a) Flaw depth 10mm



(b) Flaw depth: 7.5mm

Fig. 5.2.2-8 Relationship between K_J and χ (flaw length effect)

Copyright © 2026 The Japan Welding Engineering Society, All Rights Reserved.

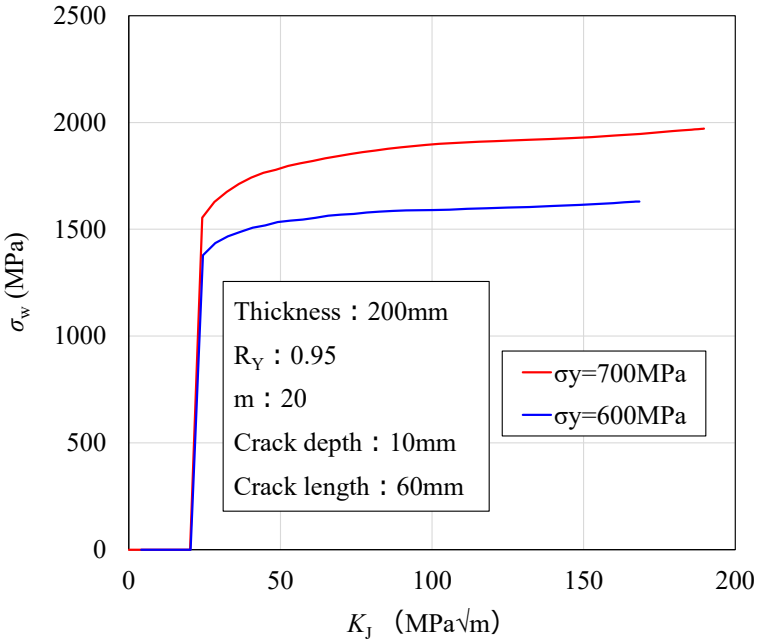


Fig. 5.2.2-9 Relationship between σ_w and K_J (yield strength effect)

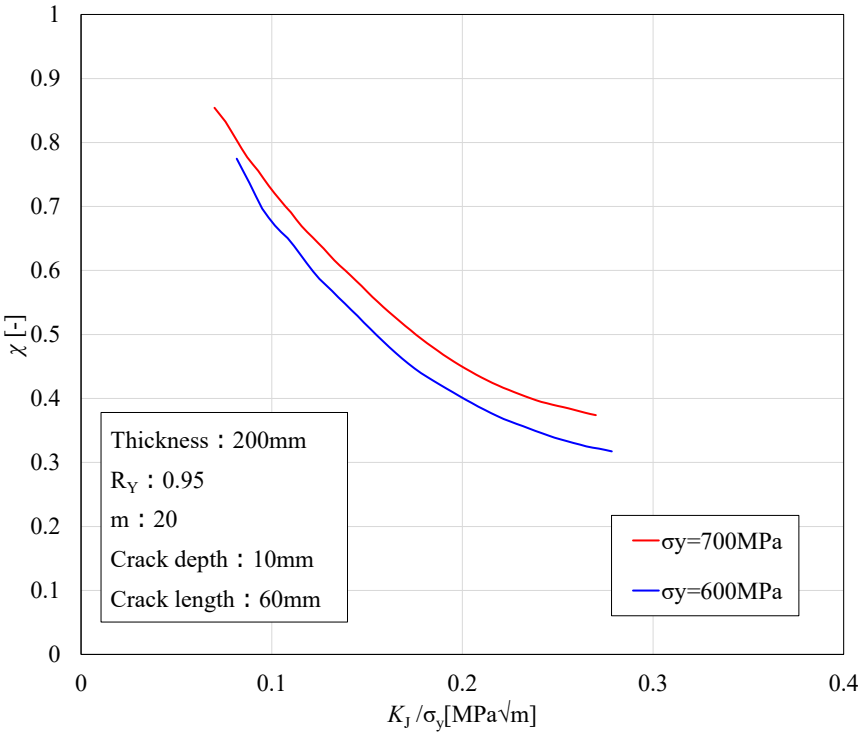


Fig. 5.2.2-10 Relationship between K_J and χ (yield strength effect)

Copyright © 2026 The Japan Welding Engineering Society, All Rights Reserved.

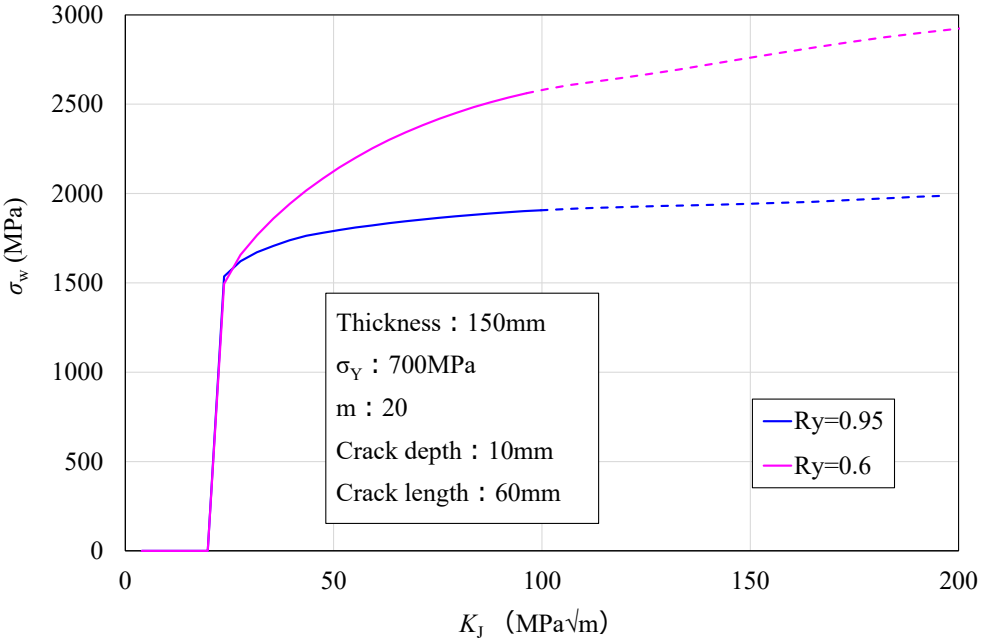


Fig. 5.2.2-11 Relationship between σ_w and K_J (effect of yield ratio R_Y)

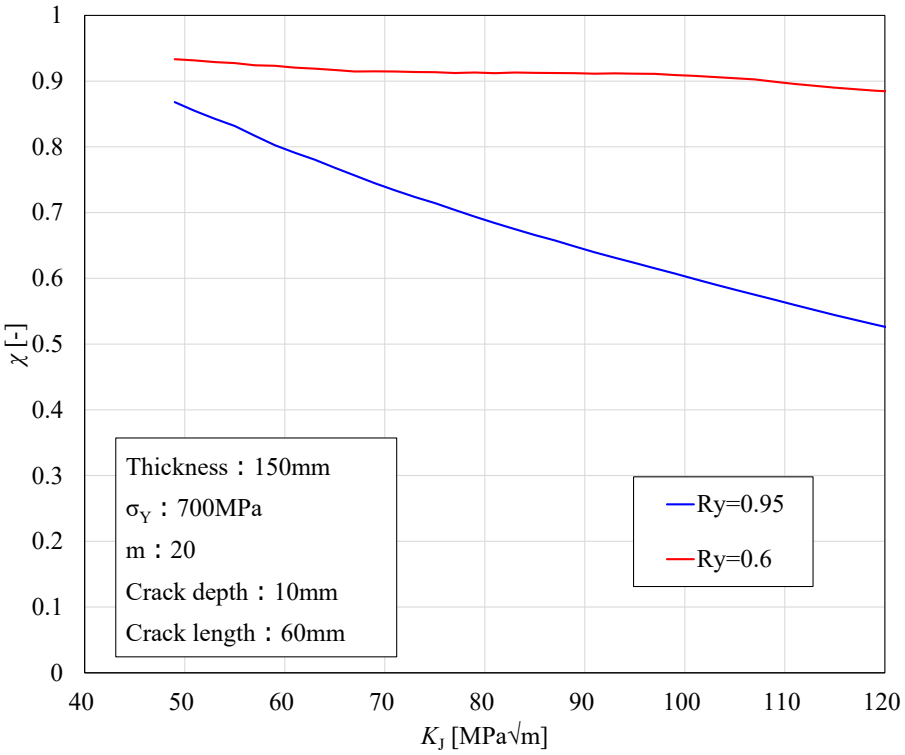
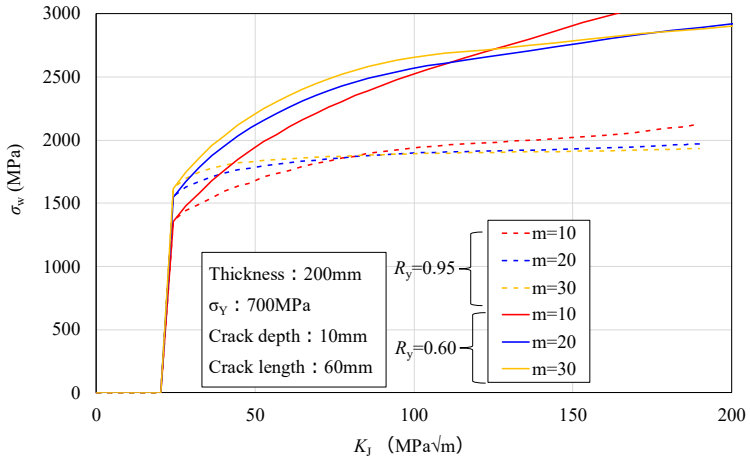
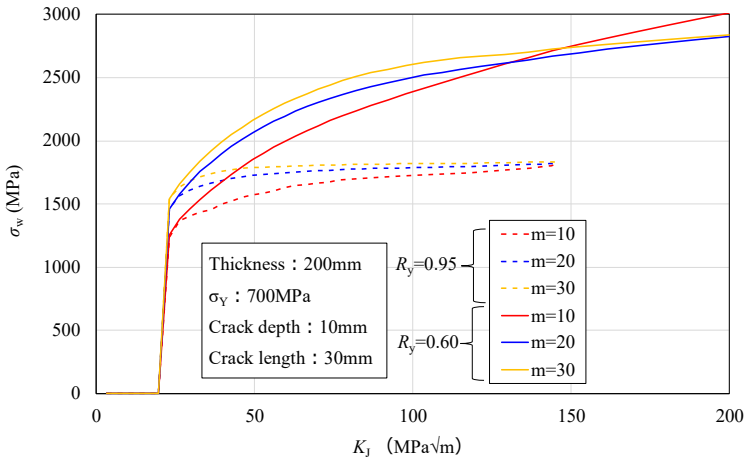


Fig. 5.2.2-12 Relationship between K_J and χ (effect of yield ratio R_Y)

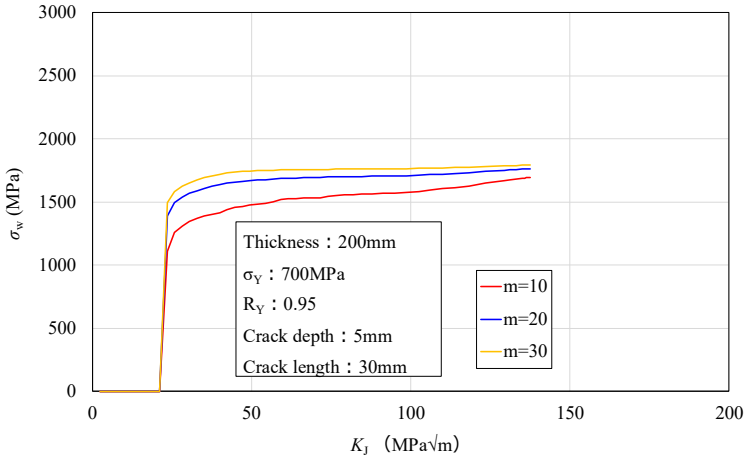
Copyright © 2026 The Japan Welding Engineering Society, All Rights Reserved.



(a) Case A-1 and A-5



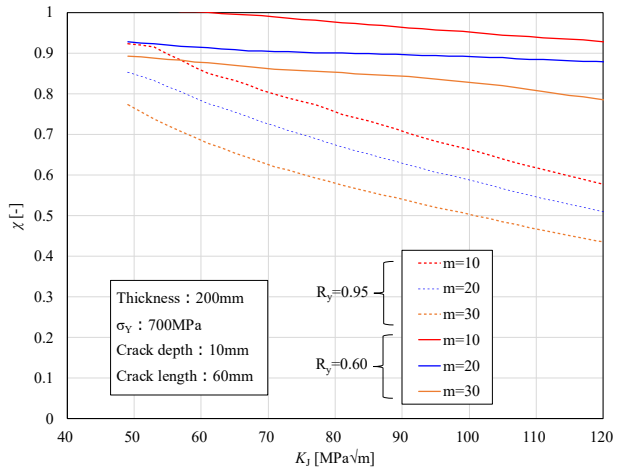
(b) Case B-1 and B-2



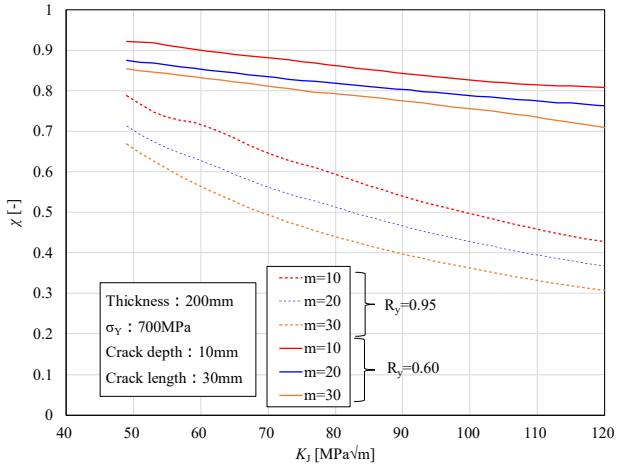
(c) Case C-1

Fig. 5.2.2-13 Relationship between σ_w and K_J (effect of Weibull parameter m)

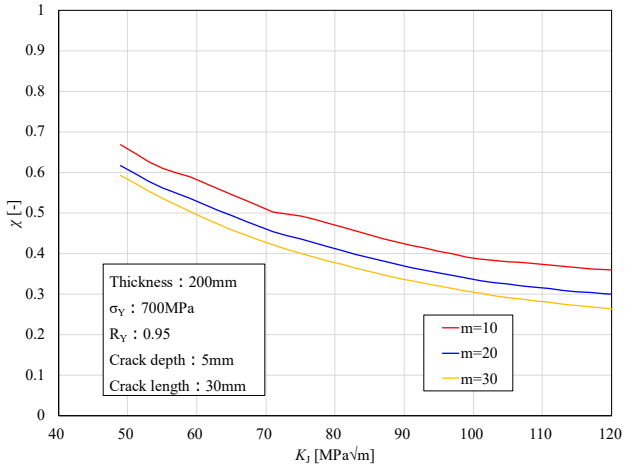
Copyright © 2026 The Japan Welding Engineering Society, All Rights Reserved.



(a) Case A-1 and A-5



(b) Case B-1 and B-2



(c) Case C-1

Fig. 5.2.2-14 Relationship between K_J and χ (effect of Weibull parameter m)

Copyright © 2026 The Japan Welding Engineering Society, All Rights Reserved.

5.2.3 Formulation of χ

5.2.3.1 Formulation approach

Figure 5.2.3-1 shows the calculation conditions of flaw depth a and flaw length c targeted for FE analysis to formulate χ. Four flaw geometries cases —(a=10, c=30) (Model A), (a=10, c=15) (Model B), (a=5, c=15) (Model C), and (a=5, c=7.5) (Model L)—were selected for formulation. χ for arbitrary flaw shapes was obtained by interpolation and extrapolation of χ of these four models.

For the Weibull stress calculation for formulation, χ was determined considering the influence of R_Y and Weibull parameter m. For R_Y, five levels of 0.6, 0.7, 0.8, 0.85, and 0.95 were set for the reference case (a=10, c=30), and two levels of 0.6 and 0.95 for other models. Weibull parameter m was calculated for three levels: 10, 20, and 30.

5.2.3.2 Approximation of FE analysis results

Since the case of large R_Y conditions such as irradiated materials tends to show significant constraint relaxation, this effect should be appropriately incorporated for the χ formulation. To reflect this constraint relaxation behavior, an evaluation diagram combining three liner segments was constructed, with two linear approximations followed by a constant value.

Figure 5.2.3-2 shows a schematic diagram of the formulation. The formulation was designed to fit the curves output by FEA as closely as possible. Since it is difficult to theoretically determine the inflection points, the transition from small-scale yielding (SSY) to large-scale yielding (LSY) at the crack tip stress field, represented by $K_{SSYlimit}$, was used as a reference. Inflection points were set at twice and three times $K_{SSYlimit}/\sigma_Y$. Equation (5.2.3-1) shows the calculation formula for $K_{SSYlimit}$.

$$K_{SSYlimit} = \left(\frac{a_0\sigma_Y^2}{2.5}\right)^{1/2} \qquad (5.2.3\text{-}1)$$

Here, a_0 is the initial flaw depth and σ_Y is the yield stress. Although the applicability of this equation to the flat plate model with semi-elliptical flaws is uncertain, it was used as a guideline.

Also, χ tends to approach 1.0 at low K_J because the effect of plastic constraint is negligible. Figure 5.2.3-3 shows the relationship between Weibull stress σ_w and K_J. Even for highly constrained C(T) specimens, there is no possibility of brittle fracture below K_J = 20 MPa√m. Where σ_1 at the crack tip of the plate model remains below the σ_1 value at crack tip of the center of thickness of the C(T) specimen at K_J = 20 MPa√m, the Weibull stress was set to zero in this region. Consequently, the region where the Weibull stress is zero corresponds to χ of 1.0. However, for the case of a=10, c=30 with

Copyright © 2026 The Japan Welding Engineering Society, All Rights Reserved.

m=10 and 20, this approach could not represent the curve trend. Therefore, for the case of a=10, c=30 with m=10, χ was set to 1.0 up to K_J/σ_Y=0.06, and for m=20, χ was set to 1.0 up to K_J/σ_Y=0.04.

Figure 5.2.3-4 shows fitting results for the standard (a=10, c=30) curves, and Figure 5.2.3-5 shows fitting results for flaw shapes with varying flaw depths and lengths: (a=10, c=15), (a=5, c=15), and (a=5, c=7.5). The formulation was based on these fitting results.

The K_J level of the constant χ is approximately 130 MPa√m at σ_Y of 700 MPa, covering the load levels assumed in PTS events.

5.2.3.3 Formulation of approximate lines

An equation to estimate the plastic constraint correction factor χ was developed with parameters of R_Y, m, and flaw geometry (a, c).

χ was expressed by the following equation:

$$\chi = \mathrm{MAX}[Ax+B, Cx+D, E], \quad x = K_J / \sigma_Y \quad (\chi \text{ is less than or equal to 1}) \qquad (5.2.3\text{-}2)$$

Here, A, B, C, D, and E are coefficients determined from R_Y and m.

Using R_Y and m as parameters, χ was formulated for four flaw types as shown in Equations (5.2.3-3) through (5.2.3-6). Figure 5.2.3-6 outlines the interpolation of flaw dimensions. First, linear interpolation of χ values was performed with respect to crack length c at crack depths of 5 mm and 10 mm, respectively. Subsequently, interpolation with respect to crack depth a was conducted for χ values at the same crack length.

The specific calculation formula for χ (a, c) at a and c is shown in Equation (5.2.3-7).

In the case of a_0=10mm, 2c=60mm

$$A = -0.0605m - 9.65R_Y + 5.94$$
$$B = -0.000814\,m + 0.439\,R_Y + 0.795$$
$$C = 0.0150m - 5.46R_Y + 2.35$$
$$D = -0.0103m - 0.0896\,R_Y + 1.25$$
$$E = -0.00747m - 1.13\,R_Y + 1.69 \qquad (5.2.3\text{-}3)$$

In the case of a_0=10mm, 2c=30mm

Copyright © 2026 The Japan Welding Engineering Society, All Rights Reserved.

$$A = -0.0570m - 10.3R_Y + 5.26$$

$$B = 0.00187\,m + 0.337\,R_Y + 0.827$$

$$C = -0.00851m - 3.26R_Y + 1.16$$

$$D = -0.00423m - 0.545\,R_Y + 1.34$$

$$E = -0.00585m - 1.16\,R_Y + 1.56 \qquad (5.2.3\text{-}4)$$

In the case of a_0=5mm, $2c$=30mm

$$A = -0.0460m - 9.41R_Y + 1.29$$

$$B = 0.00157\,m + 0.201\,R_Y + 1.06$$

$$C = -0.0162m - 6.89R_Y + 3.41$$

$$D = -0.00109m - 0.0228\,R_Y + 0.870$$

$$E = -0.00325m - 0.946\,R_Y + 1.33 \qquad (5.2.3\text{-}5)$$

In the case of a_0=5mm, $2c$=15mm

$$A = 0.0179m - 22.5R_Y + 6.63$$

$$B = -0.000781\,m + 1.17\,R_Y + 0.581$$

$$C = -0.0114m - 6.12R_Y + 3.08$$

$$D = 0.00183m - 0.288\,R_Y + 0.897$$

$$E = 0.000301m - 1.11\,R_Y + 1.31 \qquad (5.2.3\text{-}6)$$

$$\chi(10,c) = \frac{\left(\chi(10,30) - \chi(10,15)\right)}{(30 - 15)} \times (c - 15) + \chi(10,15)$$

$$\chi(5,c) = \frac{\left(\chi(5,15) - \quad (5,7.5)\right)}{(15 - 7.5)} \times (c - 7.5) + \chi(5,7.5)$$

$$\chi(a,c) = \frac{\left(\chi(10,c) - \chi(5,c)\right)}{(10-5)} \times (a - 5) + \chi(5,c) \qquad (5.2.3\text{-}7)$$

5.2.3.4 Verification of formulation

Verification was conducted regarding the interpolation of flaw depth and flaw length. As shown in Figure 5.2.3-7, the formulation accurately interpolates the calculated results for cases not used in the original formulation, such as a crack depth of 7.5 mm and a crack geometry of a = 10 mm, c = 22.5 mm.

Copyright © 2026 The Japan Welding Engineering Society, All Rights Reserved.

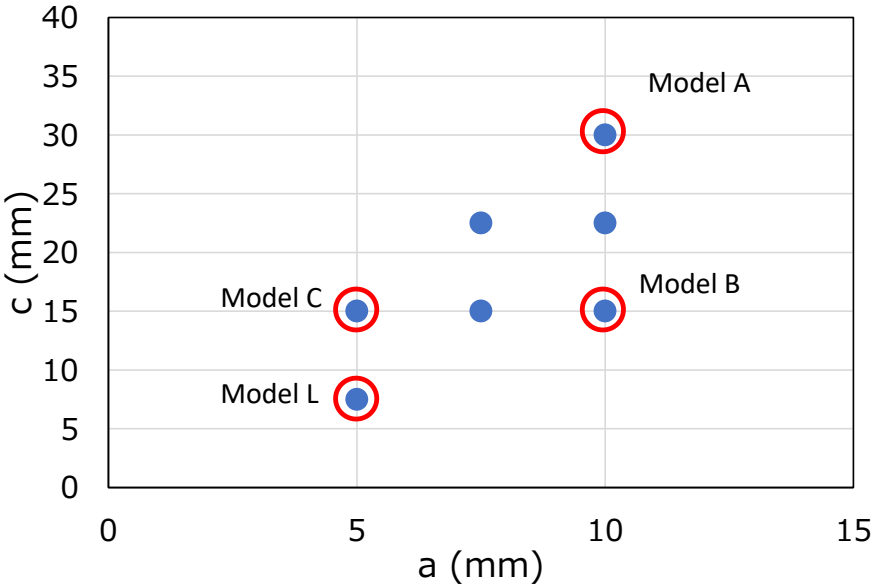


Fig.5.2.3-1 Flaw shapes of FE models and those used for formulation

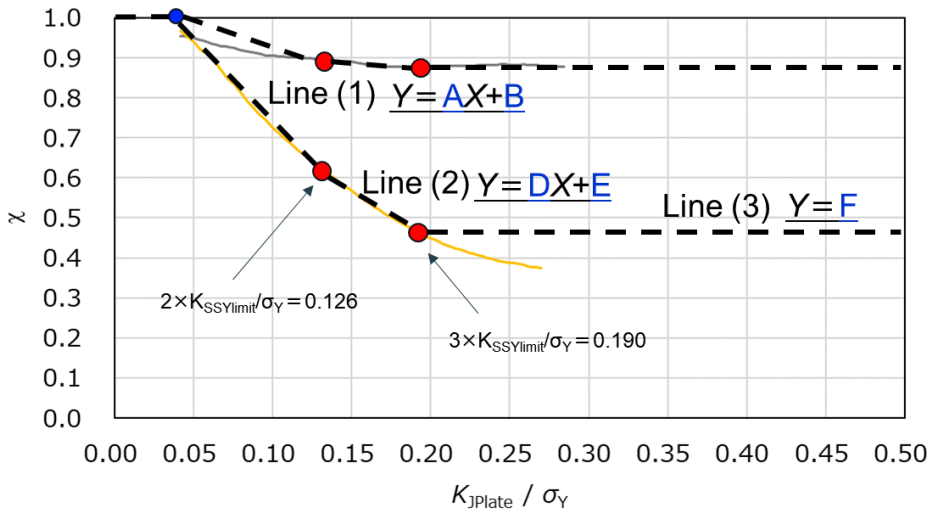
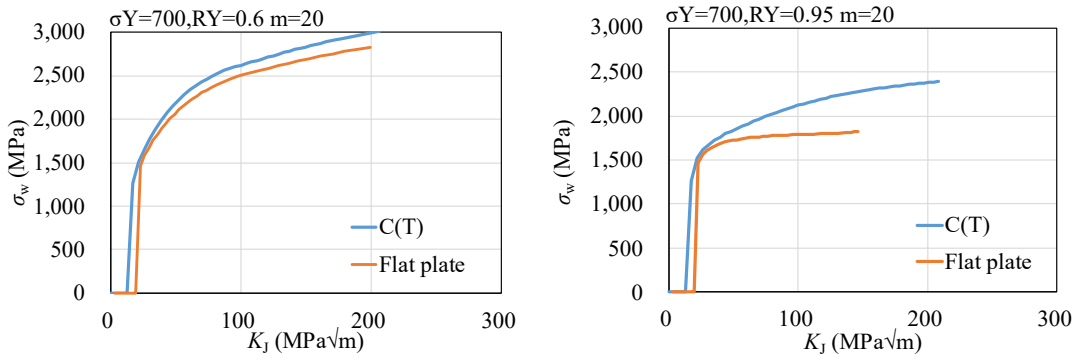
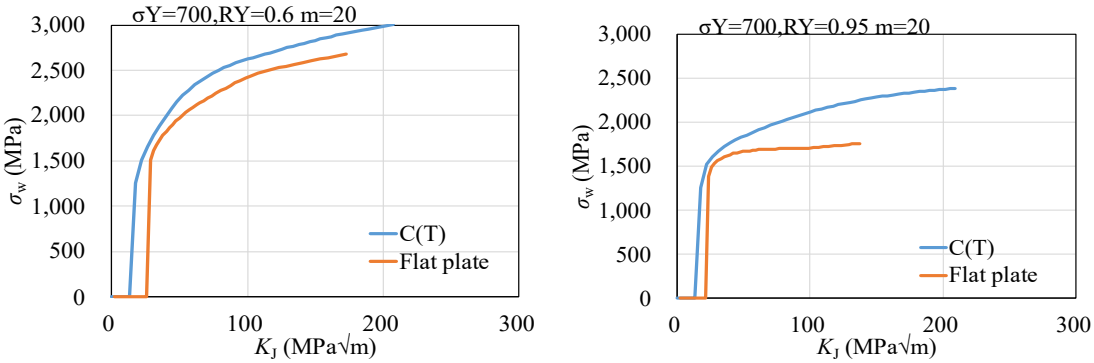


Fig. 5.2.3-2 Schematic diagram for formulation of χ

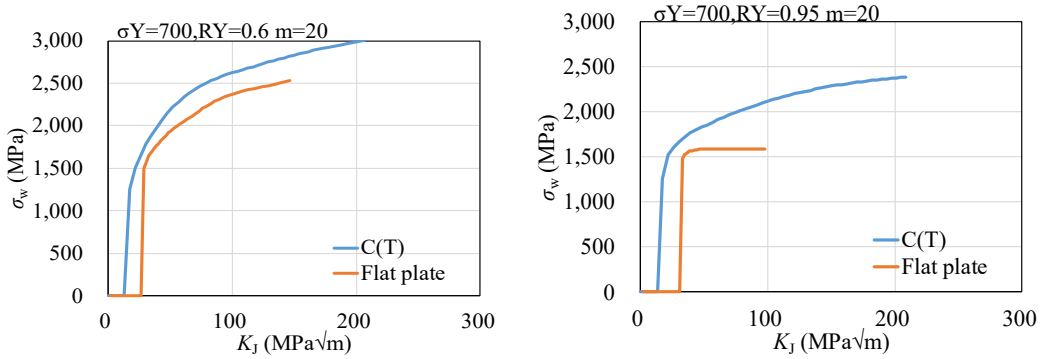
Copyright © 2026 The Japan Welding Engineering Society, All Rights Reserved.



(a) a=10mm, c=15mm



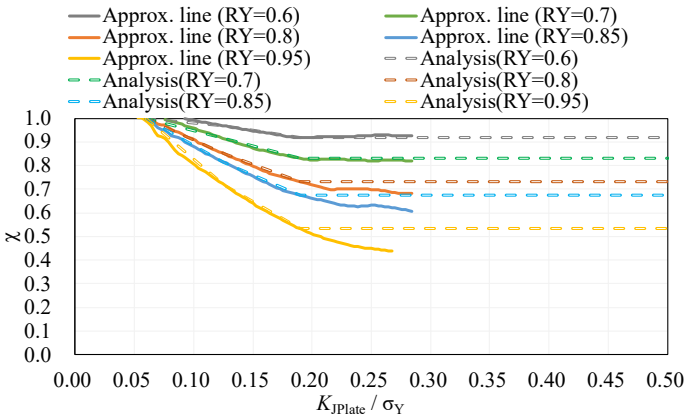
(b) a=5mm, c=15mm



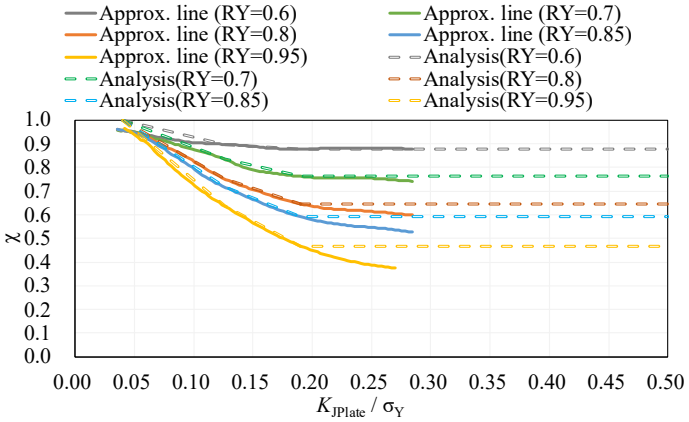
(c) a=5mm, c=7.5mm

Fig. 5.2.3-3 The onset of Weibull stress for each flaw shape

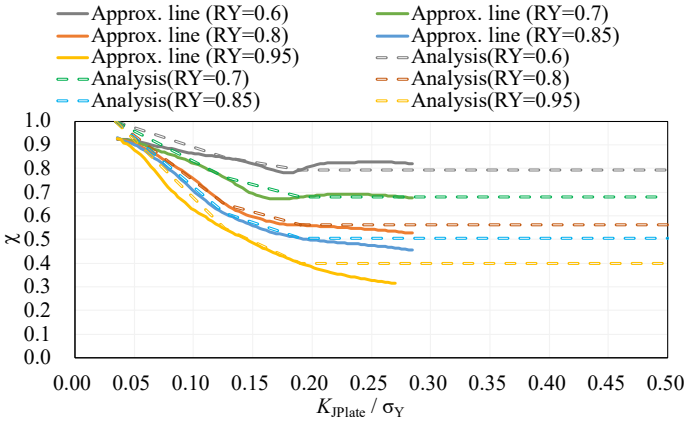
Copyright © 2026 The Japan Welding Engineering Society, All Rights Reserved.



(a) m=10



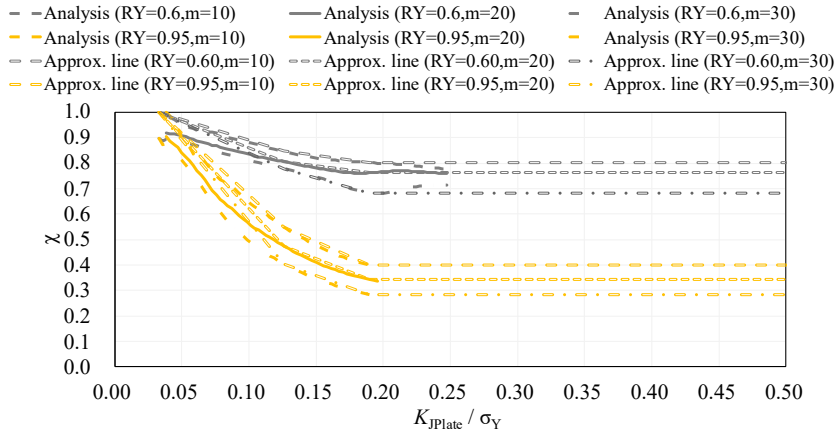
(b) m=20



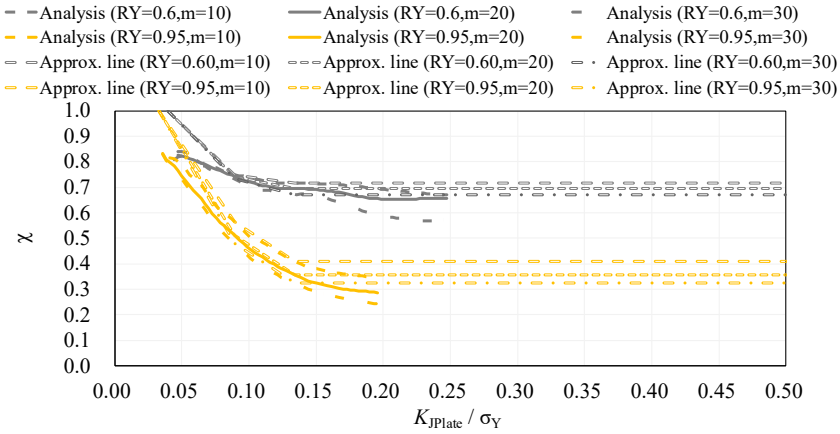
(c) m=30

Fig. 5.2.3-4　Curve fitting for formulation with parameter of m (a=10mm, c=30mm)

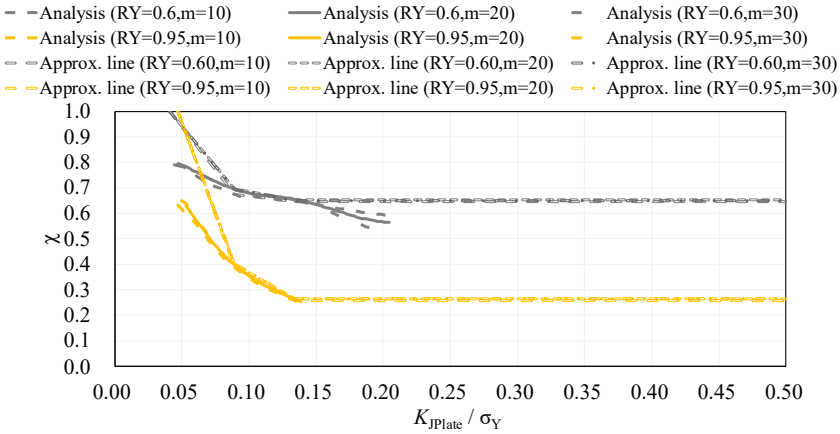
Copyright © 2026 The Japan Welding Engineering Society, All Rights Reserved.



(a) a=10mm, c=15mm



(b) a=5mm, c=15mm



(c) a=10mm, c=7.5mm

Fig. 5.2.3-5 Curve fitting for formulation with parameter of flaw shape

Copyright © 2026 The Japan Welding Engineering Society, All Rights Reserved.

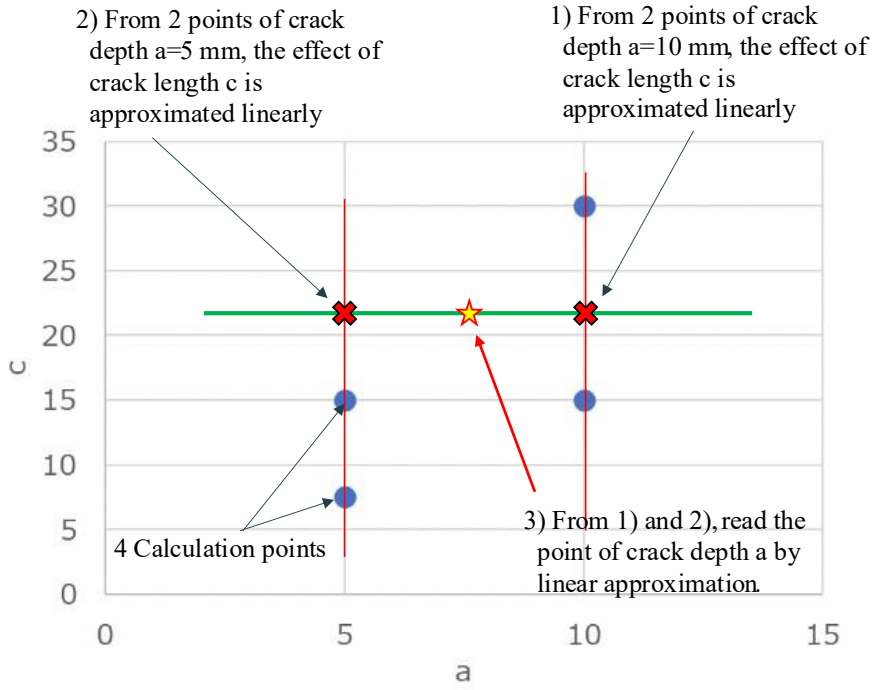


Fig. 5.2.3-6 Interpolation procedure for flaw depth and flaw length

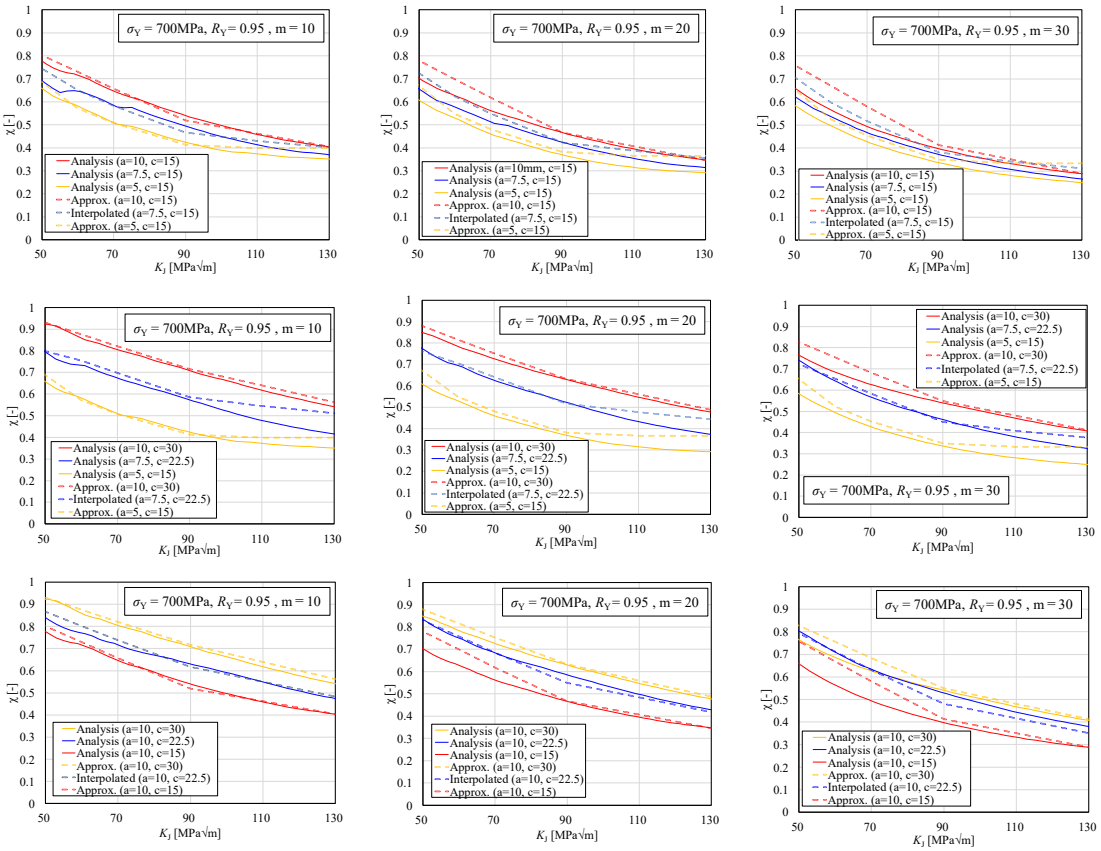


Fig. 5.2.3-7 Interpolation results for flaw depth and flaw length

Copyright © 2026 The Japan Welding Engineering Society, All Rights Reserved.

5.2.4 Setting method for material properties used in χ calculation

5.2.4.1 Procedure

To calculate χ for the RPV in service, it is necessary to know the post-irradiation σ_Y and R_Y for the corresponding period. Since χ depends on these values and tends to decrease due to neutron irradiation, reasonably accurate evaluation can be achieved by appropriately predicting σ_Y and R_Y after irradiation.

For the investigation, tensile test results before and after irradiation (at room temperature) of rolled materials, forged products, and weld metals obtained from surveillance tests of PWRs in Japan were used. The study flow is shown in Fig. 5.2.4-1.

First, to select appropriate parameters for the prediction formula, correlations with test data were compared. Since surveillance tests have focused on T_{41J}, the temperature corresponding to 41 J on the Charpy impact energy transition curve, correlation between tensile properties and measured T_{41J}, measured ΔRT_{NDT} (shift in T_{41J} from unirradiated state), and calculated ΔRT_{NDT} from the embrittlement prediction method JEAC4201[5-9] was confirmed. Correlation with tensile properties indicated that the measured ΔRT_{NDT} was the most suitable parameter.

Next, it was examined whether to treat material categories (rolled materials, forged steels, weld metals) separately, group base metals (rolled and forged steels) together and weld metals separately, or treat all materials collectively. Because the distributions of measured ΔRT_{NDT} versus tensile properties differed among material categories, it was decided to establish separate correlation formulas for each category.

Finally, the approach to predicting tensile properties was considered: whether to predict absolute values or changes from the unirradiated state. Generally, a linear relationship is accepted between the irradiation-induced change in yield stress ($\Delta\sigma_Y$) and the shift in Charpy transition temperature (ΔRT_{NDT}). Surveillance test data for rolled materials, forged steels, and weld metals show a positive correlation between $\Delta\sigma_Y$ and measured ΔRT_{NDT} [5-10]. As shown in Figure 5.2.4-2, an approximately proportional relationship was observed on average, leading to the decision to predict changes rather than absolute values.

5.2.4.2 Prediction formulas for σ_Y, σ_B, and R_Y

For χ calculation, it is sufficient to estimate σ_Y and R_Y, but since R_Y is defined as the ratio σ_Y/σ_B, σ_B was also considered for estimation. The study cases are shown in Fig. 5.2.4-3. While only σ_Y and

Copyright © 2026 The Japan Welding Engineering Society, All Rights Reserved.

R_Y are needed to calculate χ, since R_Y is defined as the ratio σ_Y/σ_B, the prediction of tensile strength σ_B was also considered. The cases examined are summarized in Figure 5.2.4-3. To predict σ_Y from ΔRT_{NDT}, a linear relationship between the irradiation-induced shift $\Delta\sigma_Y$ and ΔRT_{NDT} was established from test data, which was then added to the unirradiated σ_{Y0} (Case No.1 in Figure 5.2.4-3). σ_B was predicted similarly (Case No.2), but other approaches were also considered: focusing on the linear relationship between $\Delta\sigma_Y$ and $\Delta\sigma_B$ (No.3) and on the linear relationship between absolute values of σ_Y and σ_B (No.4).

For R_Y, three cases corresponding to the three σ_B prediction methods were examined (No.5 to No.7). Additionally, methods using directly measured σ_Y and σ_B to derive R_Y and establishing a linear relationship between measured R_Y and ΔRT_{NDT} (No.8), and a method based on a linear relationship between measured σ_Y and R_Y (No.9) were investigated.

Prediction targets were room temperature values, and temperature dependence was examined as ratios relative to room temperature values (see Section 5.2.4.3). For the cases No. 1, No. 2, and No. 8, measured ΔRT_{NDT} was used to establish linear relations. The number of irradiated material data evaluated was 108 for rolled material, 60 for forged steel, and 70 for weld metal.

Table 5.2.4-1 summarizes the prediction formulas for tensile properties for rolled material, forged product, and weld metal. The standard deviation of prediction residuals represents the standard deviation of differences between predicted values and measured values. The mean residual is the average of these differences.

Predicted σ_Y and R_Y (five cases from R_Y1 to R_Y5) for rolled material, forged product, and weld metal are shown in Fig. 5.2.4-4. Although slight differences in predictability exist among cases for R_Y, no clear differences were recognized among the five cases. The optimal case was determined based on χ predictability in the next section.

5.2.4.3 Consideration of Conservatism in χ

χ set from predicted σ_Y and R_Y values should be conservative (larger χ) compared to χ obtained from measured σ_Y and R_Y . Therefore, a margin of 2σ (σ being the standard deviation of prediction residuals) was applied in the conservative direction for both σ_Y and R_Y predictions. Here, larger σ_Y is conservative for χ, and smaller R_Y is conservative for χ. Examples of results considering these margins for rolled material are shown in Figs. 5.2.4-5 and 5.2.4-6.

Considering variability, predicted σ_Y and R_Y values were obtained using ΔRT_{NDT} calculation

Copyright © 2026 The Japan Welding Engineering Society, All Rights Reserved.

values from JEAC4201 embrittlement prediction method as input, and χ was calculated and compared with χ obtained from measured σ_Y and R_Y for rolled material, as shown in Fig. 5.2.4-7. Parameters m = 10 and K_I = 70 MPa√m were used for χ calculation. All cases predicted values conservatively above the 1:1 line, with the R_{Y4} case showing the closest trend and highest prediction accuracy. Thus, R_{Y4} was selected as the prediction equation.

The above Fig. 5.2.4-7 compares χ from measured σ_Y and R_Y (horizontal axis) with χ from predicted σ_Y and R_Y (vertical axis). Since 2σ conservative margin was applied, the prediction may be overly conservative. To address this, a correction method incorporating measured surveillance test values was investigated. By adjusting to include measured surveillance values as in Fig. 5.2.4-8, margins between measured and predicted values can be reduced compared to applying 2σ standard deviation for all plants, as shown in Fig. 5.2.4-9. Here, the horizontal axis ΔRT_{NDT} in Fig. 5.2.4-9 uses the calculated values according to JEAC 4201. In section 5.2.4.2, the relationship between σ_Y, R_Y and ΔRT_{NDT} was examined using measured values of ΔRT_{NDT}. However, for evaluation purposes, σ_Y and R_Y are estimated using the ΔRT_{NDT} calculated by JEAC4201. Therefore, it is appropriate to use these calculated values for margin settings.

Figure 5.2.4-10 compares χ predicted from σ_Y and R_Y values adjusted with the recalculated margin against χ from measured values. This adjustment alleviated excessive conservatism while maintaining conservative χ predictions..

5.2.4.4 Temperature Dependence Formulas for σ_Y and σ_B

To consider temperature dependence of σ_Y and σ_B, formulas applicable beyond room temperature were extracted from standards and literature as follows.

[Temperature dependence of σ_Y]

WES1108-1995[5-11] (JEAC4216-2015[5-12])

$$\sigma_{YS(T)} = \sigma_{YS(RT)} \exp\left[\left\{481.4 - 66.5 \ln\left(\sigma_{YS(RT)}\right)\right\}\left(\frac{1}{T+273} - \frac{1}{293}\right)\right] \quad (5.2.4\text{-}1)$$

ASTM E1921-19[5-13]

$$\sigma_{YS(T)} = \sigma_{YS(RT)} + 10^5 / (491 + 1.8T) - 189 \quad (5.2.4\text{-}2)$$

Zerilli - Armstrong[5-14]

Copyright © 2026 The Japan Welding Engineering Society, All Rights Reserved.

$$\sigma_{YS(T)} = \sigma_{YS(RT)} + [1200 \exp\{-(T + 273.15) / 97.8\} - 55.8] \quad (5.2.4\text{-}3)$$

Here, $\sigma_{YS(T)}$ is the yield stress at temperature T (MPa), $\sigma_{YS(RT)}$ is the yield stress at room temperature (MPa), and T is the temperature (°C).

[Temperature dependence of σ_B]

BS7910: 2019

It provides equations for σ_B from -196°C to room temperature; for room temperature to 200°C, the correction values read from the graphs are subtracted from the room temperature values, resulting in:

$$\sigma_{B(T)} = \sigma_{B(RT)} - f(T) \quad (5.2.4\text{-}4)$$

$$f(T) = \begin{cases} 0, & \mathrm{RT} < T \leqq 50 \\ 0.6T - 30 & 50 < T \leqq 100 \\ 0.4T - 10 & 100 < T \leqq 200 \end{cases}$$

Here, $\sigma_{B(T)}$ is the tensile strength at temperature T (MPa), $\sigma_{B(RT)}$ is the tensile strength at room temperature (MPa), and T is the temperature (°C).

WES2808: 2017[5-15]

(400～590MPa Grade)

$$\sigma_{B(\dot{e},T)} = \sigma_{B(RT)} \exp\left[8 \times 10^{-4} RT \left(\frac{\sigma_{B(RT)}}{E}\right)^{-1.5} \left\{\frac{1}{T \cdot \ln\left(\frac{10^9}{\dot{e}}\right)} - \frac{1}{RT \cdot \ln\left(\frac{10^9}{\dot{e}_0}\right)}\right\}\right] \quad (5.2.4\text{-}5)$$

(780MPa Grade)

$$\sigma_{B(\dot{e},T)} = \sigma_{B(RT)} \exp\left[1 \times 10^{-2} RT \left(\frac{\sigma_{B(RT)}}{E}\right)^{-1.1} \left\{\frac{1}{T \cdot \ln\left(\frac{10^9}{\dot{e}}\right)} - \frac{1}{RT \cdot \ln\left(\frac{10^9}{\dot{e}_0}\right)}\right\}\right] \quad (5.2.4\text{-}6)$$

Here, $\sigma_{B(RT)}$ is the tensile strength at static strain rate $\dot{e}_0$ (=10^{-4}/s) and room temperature RT (K), $\sigma_{B(\dot{e},T)}$ is the tensile strength at arbitrary strain rate $\dot{e}$ and temperature T (K), and E is Young's modulus (constant at 206,000 MPa). Setting $\dot{e} = \dot{e}_0$ enables estimation of temperature dependence at static strain rate.

In addition to these equations, values extracted from the temperature dependence table of the JSME material standard[5-16] were used and compared with measured data from surveillance tests,

Copyright © 2026 The Japan Welding Engineering Society, All Rights Reserved.

shown in Figs. 5.2.4-11 and 5.2.4-12. These results indicate that the WES1108:1995 (JEAC4216-2015) formula for σ_Y is conservative and consistent with trends of measured data from surveillance tests, and the WES2808:2017 formula for σ_B is conservative and consistent with surveillance data trends.

Therefore, even without high-temperature measured data for σ_Y and σ_B, these formulas can estimate high-temperature σ_Y and σ_B from room temperature data.

5.2.4.5 Options for RY setting for standardization

As described above, methods to predict R_Y as a function of ΔRT_{NDT} were investigated. In standardization, a simpler method is to be define R_Y as a step function enveloping measured R_Y values. Figure 5.2.4-13 shows such as a step function for R_Y enveloping measured R_Y values of all steel grades. Corresponding χ values calculated from this step function are shown in Figure 5.2.4-14, using predicted σ_Y adjusted by measured corrections, m = 10, and K_I = 70 MPa√m. Because R_Y is a two-level step function of ΔRT_{NDT}, the resulting χ values also split into two groups, causing overly conservative evaluation for the low ΔRT_{NDT} group.

Figure 5.2.4-15 illustrates R_Y step functions for rolled materials (irradiated and unirradiated) with varying enveloping ratios. Corresponding χ values calculated using these step functions are shown in Figure 5.2.4-16. Using enveloping ratios of 95% or 90% eliminates excessive conservatism.

5.2.4.6 Summary

To determine the plastic constraint correction factor χ for irradiated materials, formulas predicting σ_Y and R_Y from ΔRT_{NDT} were investigated. As a result, separate predictions for $\Delta\sigma_Y$ and R_Y were established for each material category, incorporating conservative margins ($M_{\sigma Y}$, M_{RY}) as 2σ (σ : standard deviation of prediction residuals). Corrections to envelop measured data enabled appropriate prediction of χ. The final prediction formulas are shown in Equations (5.2.4-7) through (5.2.4-13).

$$\sigma_Y = \Delta\sigma_Y + \sigma_{Y0} + M\sigma_Y \quad (5.2.4\text{-}7)$$

$$\Delta\sigma_Y = 1.66\,\Delta RT_{NDT},\ M\sigma_Y = 60.6 \text{ (Plate)} \quad (5.2.4\text{-}8)$$

$$\Delta\sigma_Y = 2.19\,\Delta RT_{NDT},\ M\sigma_Y = 42.4 \text{ (Forging)} \quad (5.2.4\text{-}9)$$

$$\Delta\sigma_Y = 1.83\,\Delta RT_{NDT},\ M\sigma_Y = 86.0 \text{ (Weld)} \quad (5.2.4\text{-}10)$$

Copyright © 2026 The Japan Welding Engineering Society, All Rights Reserved.

$$R_Y = 0.000858\ \Delta RT_{NDT} + 0.761 - M_{RY},\ M_{RY} = 0.0494 \text{ (Plate)} \quad (5.2.4\text{-}11)$$

$$R_Y = 0.00102\ \Delta RT_{NDT} + 0.775 - M_{RY},\ M_{RY} = 0.0200 \text{ (Forging)} \quad (5.2.4\text{-}12)$$

$$R_Y = 0.000390\ \Delta RT_{NDT} + 0.870 - M_{RY},\ M_{RY} = 0.0620 \text{ (Weld)} \quad (5.2.4\text{-}13)$$

Moreover, temperature dependence formulas from standards and literature were confirmed to be applicable and consistent with trends of measured surveillance test data.

In addition to the method of predicting R_Y by formulas, a method of setting R_Y as a step function enveloping measured values was examined. It was found that in regions with low ΔRT_{NDT}, χ values calculated using the step-function-based R_Y tended to be excessively conservative. By adopting an enveloping ratio of, for example, 95% instead of full coverage, this excessive conservatism can be mitigated.

Copyright © 2026 The Japan Welding Engineering Society, All Rights Reserved.

Copyright © 2026 The Japan Welding Engineering Society, All Rights Reserved.

Table 5.2.4-1 (1/3) Prediction model for tensile properties of plates

No.	Prediction target	Method	Standard deviation of prediction residuals	Mean value of prediction residuals	Formula
1	σ_Y	$\Delta\sigma_Y$ is predicted from ΔRT_{NDT} and added to the initial σ_Y value.	30.3	3.34	$\sigma_Y = \Delta\sigma_Y + \sigma_{Y0}$ $\Delta\sigma_Y = 1.66*\Delta RT_{NDT}$
2	σ_{B1}	$\Delta\sigma_B$ is predicted from ΔRT_{NDT} and added to the initial value of σ_B	27.5	2.64	$\sigma_{B1} = \Delta\sigma_{B1} + \sigma_{B0}$ $\Delta\sigma_{B1} = 1.35*\Delta RT_{NDT}$
3	σ_{B2}	$\Delta\sigma_B$ is predicted from the predicted $\Delta\sigma_Y$ value based on the relationship between $\Delta\sigma_Y$ and $\Delta\sigma_B$ and add it to the initial σ_B value.	27.4	3.58	$\sigma_{B2} = \Delta\sigma_{B2} + \sigma_{B0}$ $\Delta\sigma_{B2} = 0.806*\Delta\sigma_Y$
4	σ_{B3}	σ_B is predicted from σ_Y obtained by adding the initial value of σ_Y to the predicted $\Delta\sigma_Y$ value based on the relationship between σ_Y and σ_B.	25.3	2.71	$\sigma_{B3} = 0.809*\sigma_Y + 239$
5	R_{Y1}	Ratio of σ_Y to σ_{B1} (Ratio between No. 1 and No. 2)	0.0334	0.00240	$R_{Y1} = \sigma_Y/\sigma_{B1}$
6	R_{Y2}	Ratio of σ_Y to σ_{B2} (Ratio between No. 1 and No. 3)	0.0334	0.00130	$R_{Y2} = \sigma_Y/\sigma_{B2}$
7	R_{Y3}	Ratio of σ_Y to σ_{B3} (Ratio of No. 1 to No. 4)	0.0291	0.00238	$R_{Y3} = \sigma_Y/\sigma_{B3}$
8	R_{Y4}	σ_Y/σ_B is predicted directly from ΔRT_{NDT}.	0.0247	3.39E-17	$R_{Y4} = 0.000858*\Delta RT_{NDT} + 0.761$
9	R_{Y5}	R_Y is predicted from the relationship between σ_Y and R_Y	0.0286	0.00150	$R_{Y5} = 0.000503*\sigma_Y + 0.526$

Copyright © 2026 The Japan Welding Engineering Society, All Rights Reserved.

Table 5.2.4-1 (2/3) Prediction model for tensile properties of plates

No.	Prediction target	Method	Standard deviation of prediction residuals	Mean value of prediction residuals	Formula
1	σ_Y	$\Delta\sigma_Y$ is predicted from ΔRT_{NDT} and added to the initial σ_Y value.	21.2	7.22	$\sigma_Y = \Delta\sigma_Y + \sigma_{Y0}$ $\Delta\sigma_Y = 2.19*\Delta RT_{NDT}$
2	σ_{B1}	$\Delta\sigma_B$ is predicted from ΔRT_{NDT} and added to the initial value of σ_B	17.5	4.63	$\sigma_{B1} = \Delta\sigma_{B1} + \sigma_{B0}$ $\Delta\sigma_{B1} = 1.62*\Delta RT_{NDT}$
3	σ_{B2}	$\Delta\sigma_B$ is predicted from the predicted $\Delta\sigma_Y$ value based on the relationship between $\Delta\sigma_Y$ and $\Delta\sigma_B$ and add it to the initial σ_B value.	17.8	3.97	$\sigma_{B2} = \Delta\sigma_{B2} + \sigma_{B0}$ $\Delta\sigma_{B2} = 0.755*\Delta\sigma_Y$
4	σ_{B3}	σ_B is predicted from σ_Y obtained by adding the initial value of σ_Y to the predicted $\Delta\sigma_Y$ value based on the relationship between σ_Y and σ_B.	17.7	5.51	$\sigma_{B3} = 0.771*\sigma_Y + 238$
5	R_{Y1}	Ratio of σ_Y to σ_{B1} (Ratio between No. 1 and No. 2)	0.0167	0.00626	$R_{Y1} = \sigma_Y/\sigma_{B1}$
6	R_{Y2}	Ratio of σ_Y to σ_{B2} (Ratio between No. 1 and No. 3)	0.0164	0.00712	$R_{Y2} = \sigma_Y/\sigma_{B2}$
7	R_{Y3}	Ratio of σ_Y to σ_{B3} (Ratio of No. 1 to No. 4)	0.0146	0.00520	$R_{Y3} = \sigma_y/\sigma_B\_3$
8	R_{Y4}	σ_Y/σ_B is predicted directly from ΔRT_{NDT}.	0.00993	5.92E-17	$R_{Y4} = 0.00102*\Delta RT_{NDT} + 0.775$
9	R_{Y5}	R_Y is predicted from the relationship between σ_Y and R_Y	0.0146	0.00424	$R_{Y5} = 0.000619*\sigma_Y + 0.492$

Copyright © 2026 The Japan Welding Engineering Society, All Rights Reserved.

Table 5.2.4-1 (3/3) Prediction model for tensile properties of plates

No.	Prediction target	Method	Standard deviation of predicted residuals	Mean value of predicted residuals	Formula
1	σ_Y	$\Delta\sigma_Y$ is predicted from ΔRT_{NDT} and added to the initial σ_Y value.	43.0	6.78	$\sigma_Y = \Delta\sigma_Y + \sigma_{Y0}$ $\Delta\sigma_Y = 1.83*\Delta RT_{NDT}$
2	σ_{B1}	$\Delta\sigma_B$ is predicted from ΔRT_{NDT} and added to the initial value of σ_B	24.0	3.81	$\sigma_{B1} = \Delta\sigma_{B1} + \sigma_{B0}$ $\Delta\sigma_{B1} = 1.47*\Delta RT_{NDT}$
3	σ_{B2}	$\Delta\sigma_B$ is predicted from the predicted $\Delta\sigma_Y$ value based on the relationship between $\Delta\sigma_Y$ and $\Delta\sigma_B$ and add it to the initial σ_B value.	23.4	8.81	$\sigma_{B2} = \Delta\sigma_{B2} + \sigma_{B0}$ $\Delta\sigma_{B2} = 0.746*\Delta\sigma_Y$
4	σ_{B3}	σ_B is predicted from σ_Y obtained by adding the initial value of σ_Y to the predicted $\Delta\sigma_Y$ value based on the relationship between σ_Y and σ_B.	29.4	5.05	$\sigma_{B3} = 0.752*\sigma_Y + 233$
5	R_{Y1}	Ratio of σ_Y to σ_{B1} (Ratio between No. 1 and No. 2)	0.0425	0.00472	$R_{Y1} = \sigma_Y/\sigma_{B1}$
6	R_{Y2}	Ratio of σ_Y to σ_{B2} (Ratio between No. 1 and No. 3)	0.0435	-0.00152	$R_{Y2} = \sigma_Y/\sigma_{B2}$
7	R_{Y3}	Ratio of σ_Y to σ_{B3} (Ratio of No. 1 to No. 4)	0.0337	0.00370	$R_{Y3} = \sigma_Y/\sigma_{B3}$
8	R_{Y4}	σ_Y/σ_B is predicted directly from ΔRT_{NDT}.	0.0310	-3.38E-16	$R_{y4} = 0.000390*\Delta RT_{NDT} + 0.870$
9	R_{Y5}	R_Y is predicted from the relationship between σ_Y and R_Y	0.0330	0.00289	$R_{Y5} = 0.000458*\sigma_Y + 0.602$

Copyright © 2026 The Japan Welding Engineering Society, All Rights Reserved.

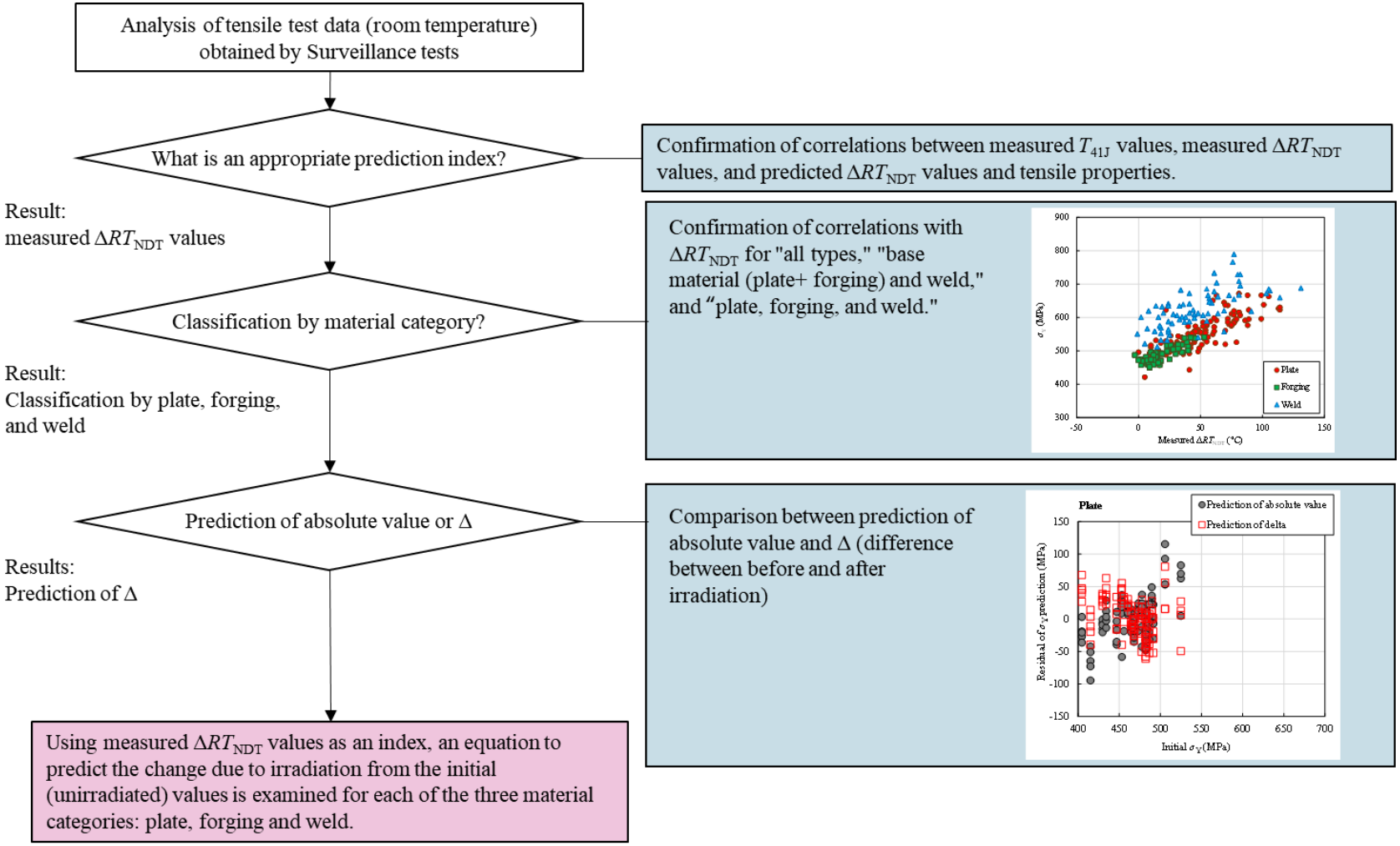
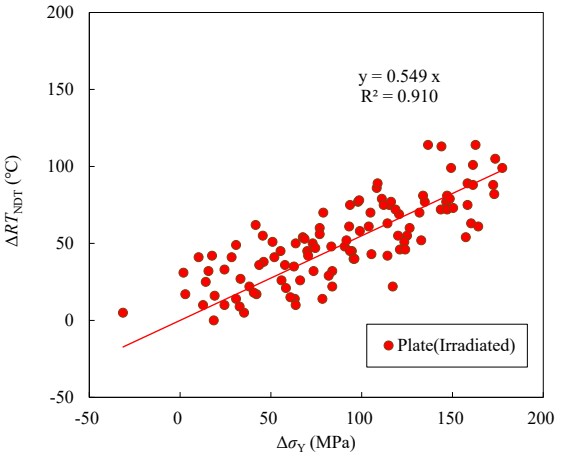
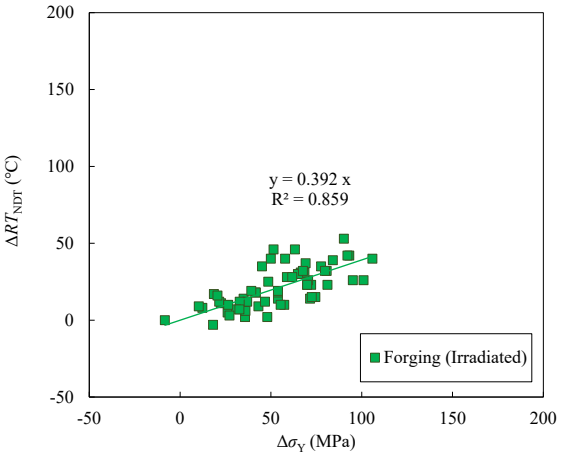


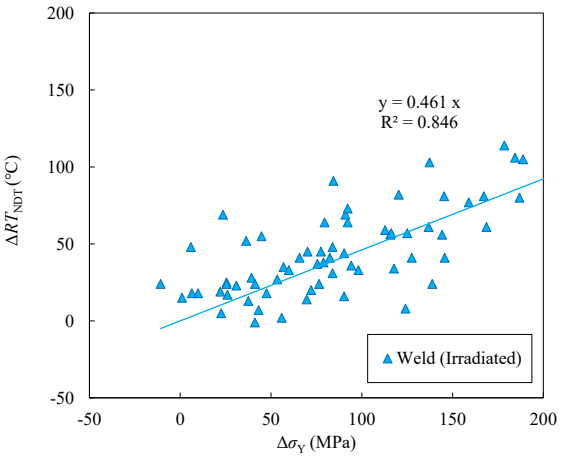
Fig. 5.2.4-1 Flow for development of prediction formula of tensile properties of irradiated materials



(a) Plate



(b) Forging



(c) Weld

Fig. 5.2.4-2 Correlation between $\Delta\sigma_Y$ and ΔRT_{NDT} obtained from surveillance tests

Copyright © 2026 The Japan Welding Engineering Society, All Rights Reserved.

No.	Prediction target	Method
1	σ_Y	$\Delta\sigma_Y$ is predicted from ΔRT_{NDT} and added to the initial σ_Y value.
2	σ_{B1}	$\Delta\sigma_B$ is predicted from ΔRT_{NDT} and added to the initial value of σ_B
3	σ_{B2}	$\Delta\sigma_B$ is predicted from the predicted $\Delta\sigma_Y$ value based on the relationship between $\Delta\sigma_Y$ and $\Delta\sigma_B$ and add it to the initial σ_B value.
4	σ_{B3}	σ_B is predicted from σ_Y obtained by adding the initial value of σ_Y to the predicted $\Delta\sigma_Y$ value based on the relationship between σ_Y and σ_B.
5	R_{Y1}	Ratio of σ_Y to σ_{B1} (Ratio between No. 1 and No. 2)
6	R_{Y2}	Ratio of σ_Y to σ_{B2} (Ratio between No. 1 and No. 3)
7	R_{Y3}	Ratio of σ_Y to σ_{B3} (Ratio of No. 1 to No. 4)
8	R_{Y4}	σ_Y/σ_B is predicted directly from ΔRT_{NDT}.
9	R_{Y5}	R_Y is predicted from the relationship between σ_Y and R_Y

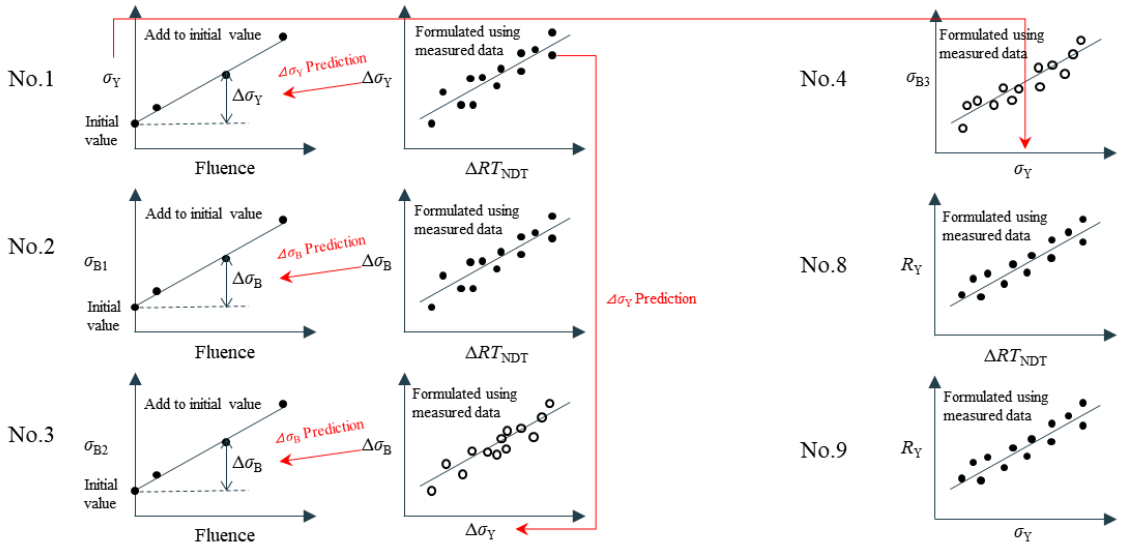
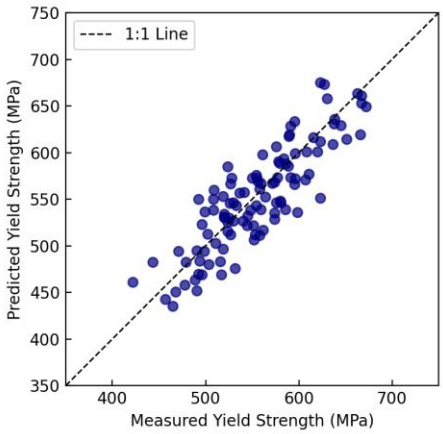
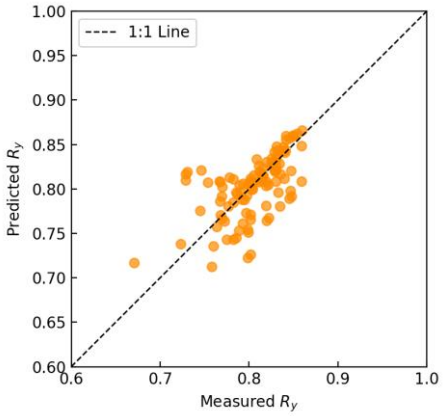


Fig. 5.2.4-3 Analysis cases of prediction model of tensile properties

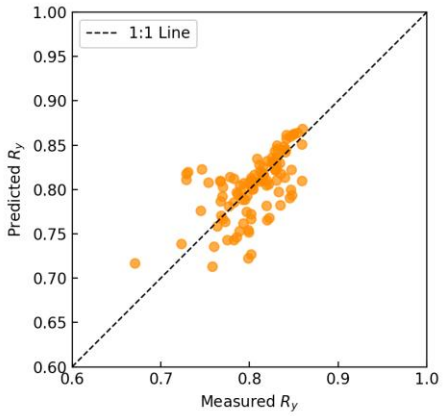
Copyright © 2026 The Japan Welding Engineering Society, All Rights Reserved.



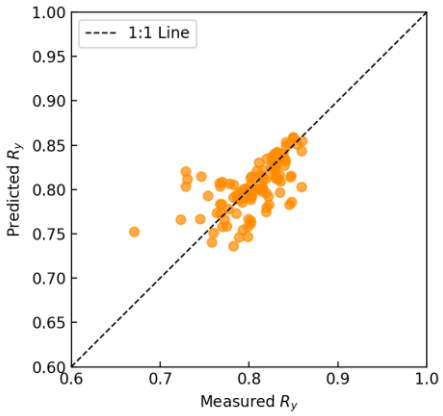
(a) σ_{Y}



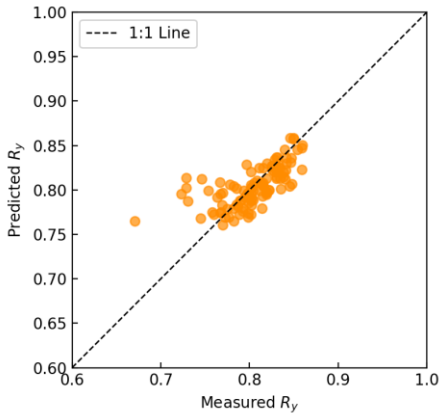
(b) R_{Y1}



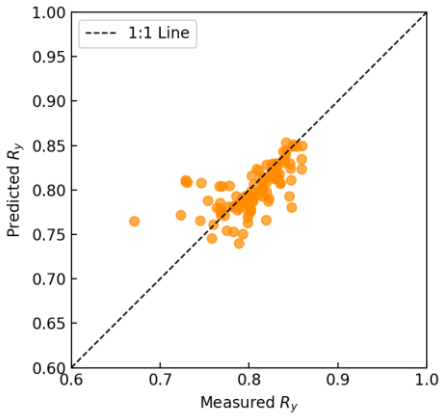
(c) R_{Y2}



(d) R_{Y3}



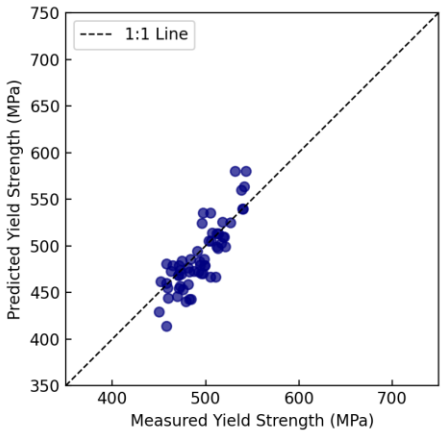
(e) R_{Y4}



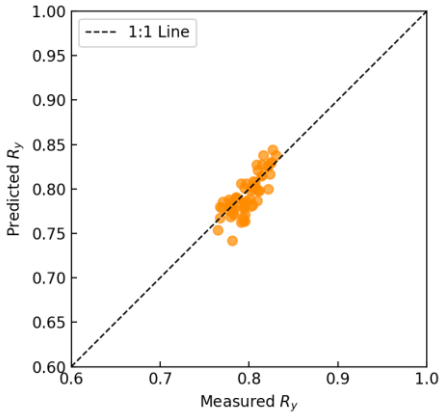
(f) R_{Y5}

Fig. 5.2.4-4 (1/3)　Prediction results for σ_{Y} and R_{Y} (plates)

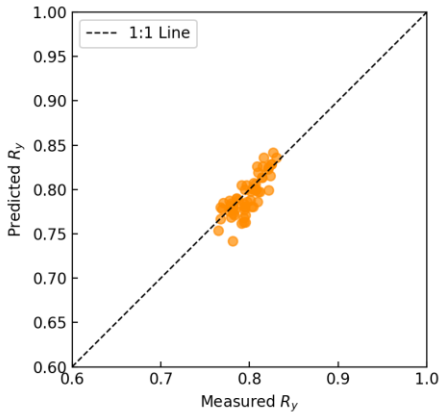
Copyright © 2026 The Japan Welding Engineering Society, All Rights Reserved.



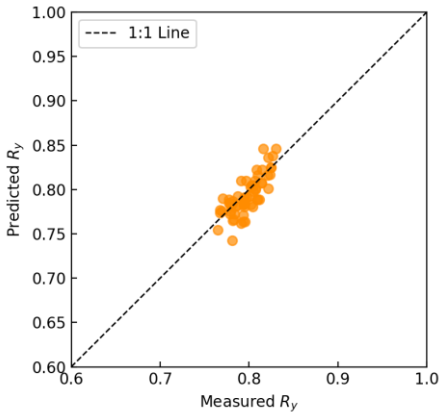
(a) σ_{Y}



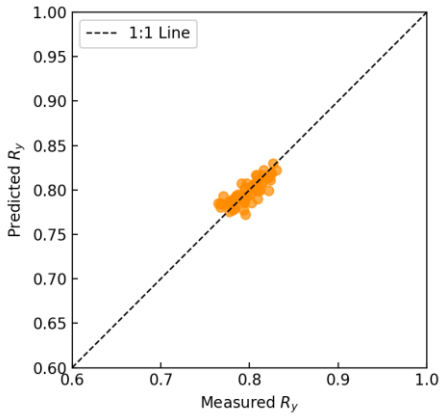
(b) R_{Y1}



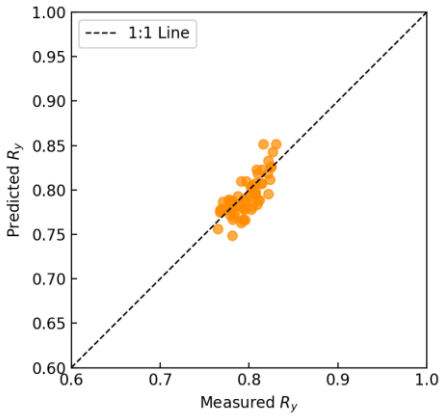
(c) R_{Y2}



(d) R_{Y3}



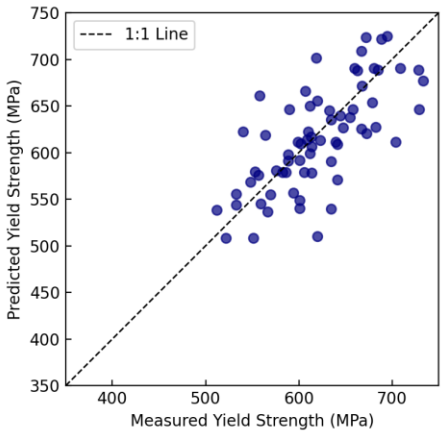
(e) R_{Y4}



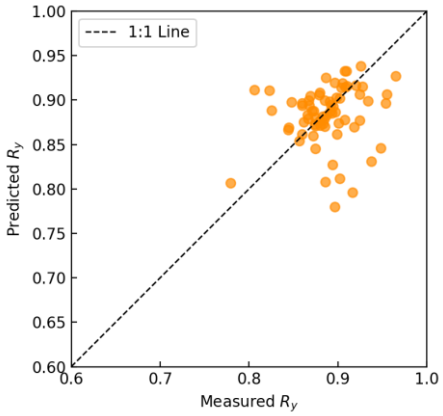
(f) R_{Y5}

Fig. 5.2.4-4 (2/3)　Prediction results for σ_{Y} and R_{Y} (forgings)

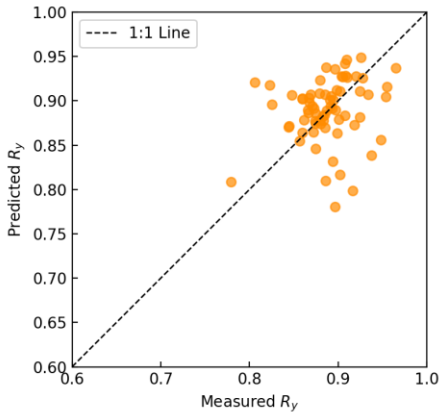
Copyright © 2026 The Japan Welding Engineering Society, All Rights Reserved.



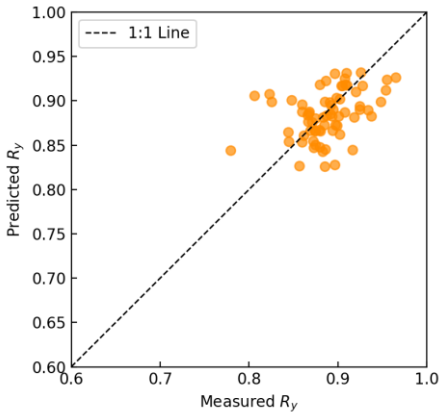
(a) σ_{Y}



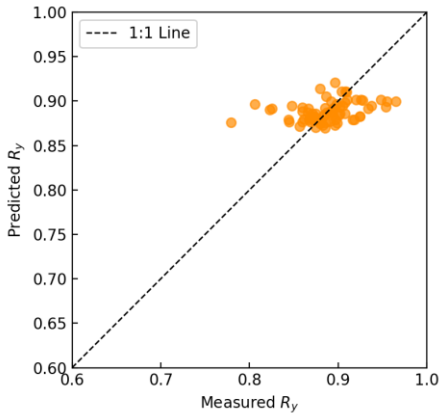
(b) R_{Y1}



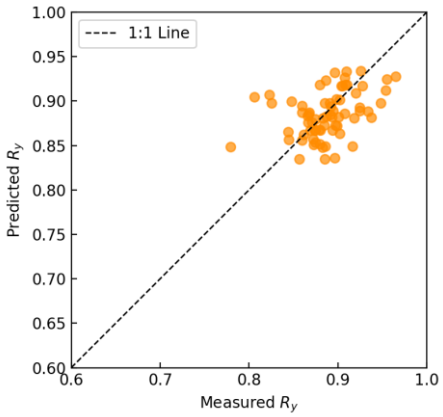
(c) R_{Y2}



(d) R_{Y3}



(e) R_{Y4}



(f) R_{Y5}

Fig. 5.2.4-4 (3/3) Prediction results for σ_{Y} and R_{Y} (weld metals)

Copyright © 2026 The Japan Welding Engineering Society, All Rights Reserved.

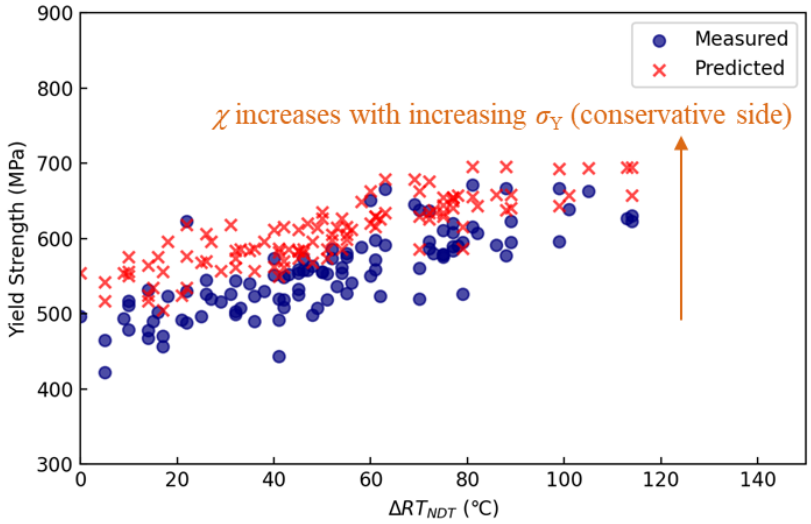


Fig. 5.2.4-5 Method for considering variability in σ_Y (example of plates)

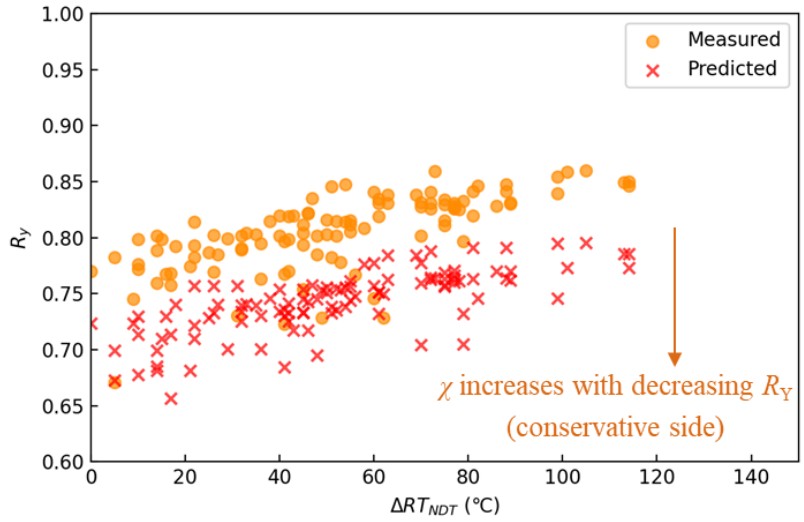
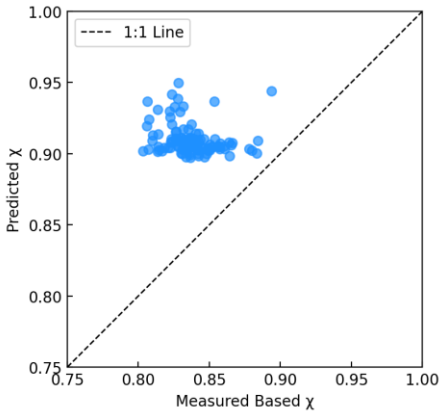
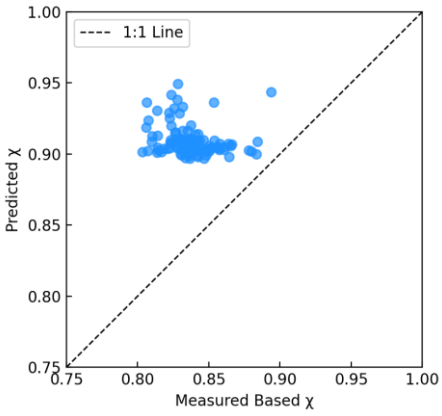


Fig. 5.2.4-6 Method for considering variability in R_Y(example of plates)

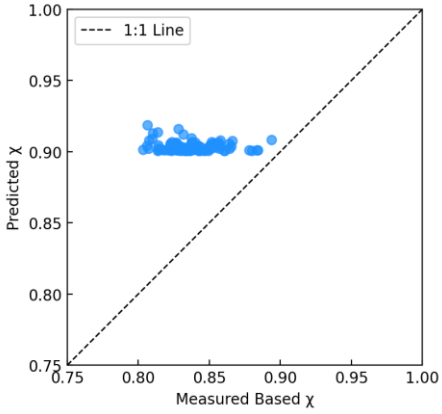
Copyright © 2026 The Japan Welding Engineering Society, All Rights Reserved.



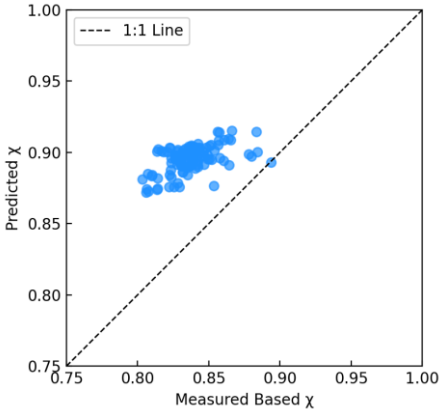
(a) R_{Y1}



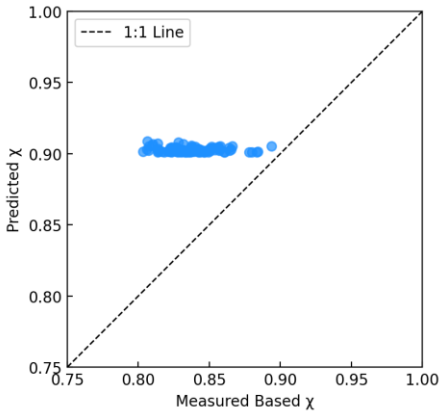
(b) R_{Y2}



(c) R_{Y3}



(d) R_{Y4}



(e) R_{Y5}

Fig. 5.2.4-7 Comparison between measured based χ and predicted χ. (plates)

(χ was calculated with m = 10 and K_I = 70 MPa√m.)

Copyright © 2026 The Japan Welding Engineering Society, All Rights Reserved.

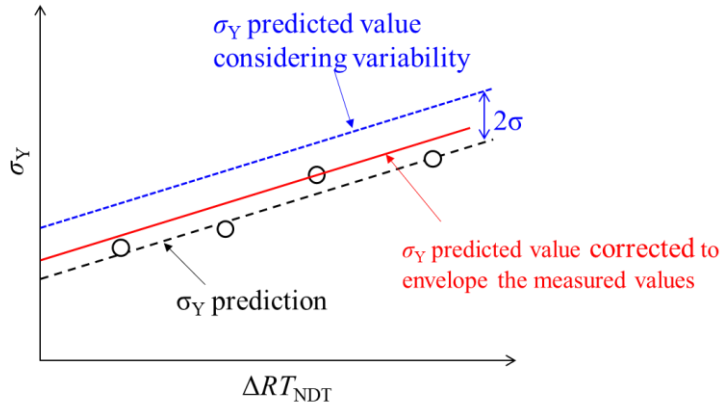
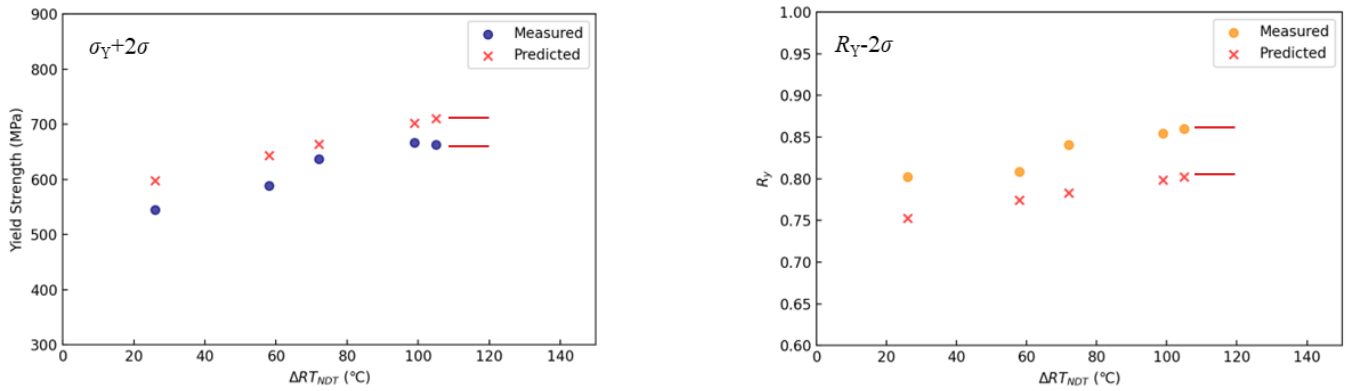


Fig. 5.2.4-8 Correction method based on measured values from surveillance tests



↓ adjust to include measured surveillance values

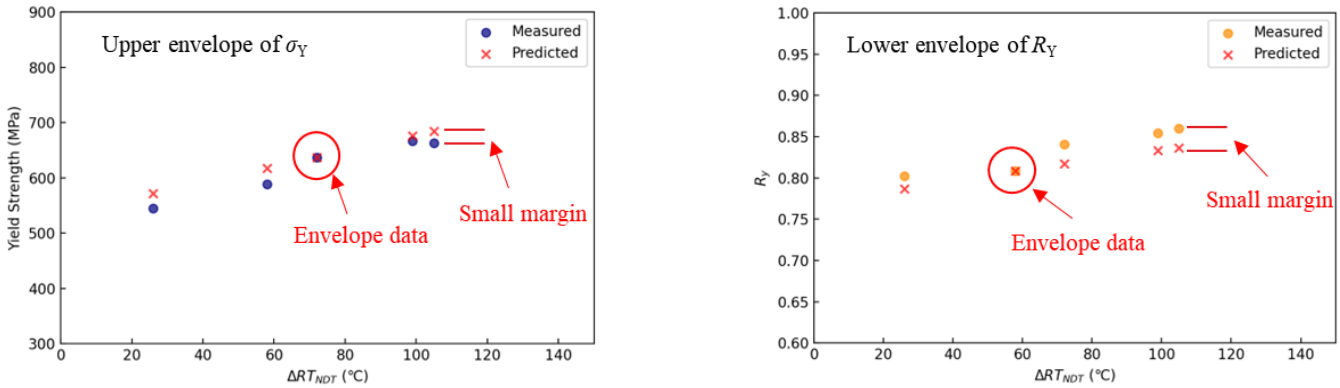
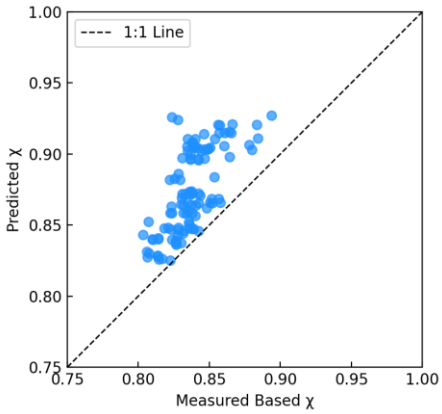
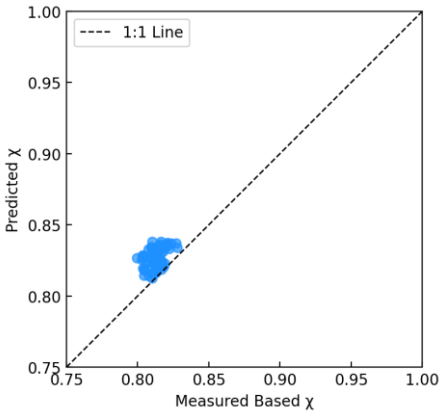


Fig. 5.2.4-9 Example of correction results based on measured values from surveillance tests

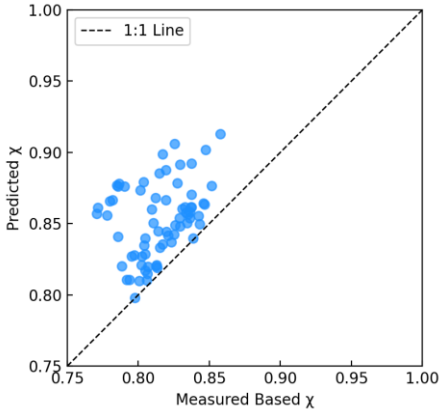
Copyright © 2026 The Japan Welding Engineering Society, All Rights Reserved.



(a) Plate



(b) Forging



(c) Weld

Fig. 5.2.4-10 Comparison between measured based χ and predicted χ

(χ was calculated with m = 10 and K_I = 70 MPa$\sqrt{m}$ after correction based on measured values)

Copyright © 2026 The Japan Welding Engineering Society, All Rights Reserved.

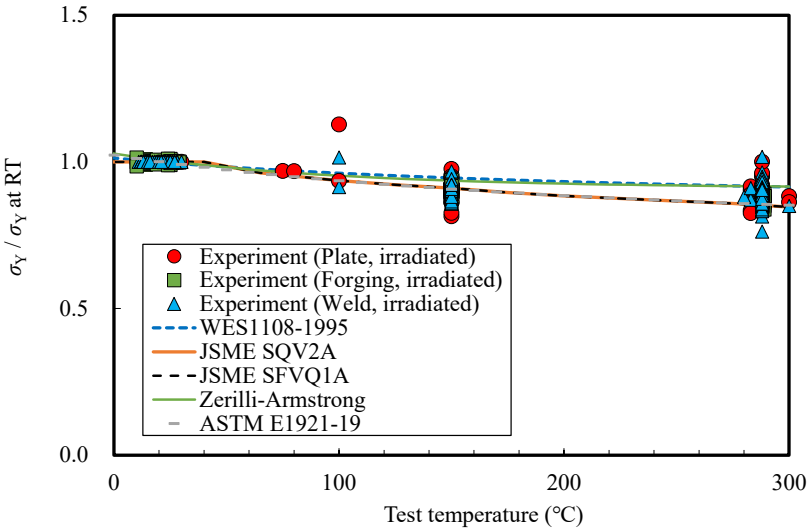


Fig. 5.2.4-11　Comparison between temperature dependence of σ_Y from models and experiments

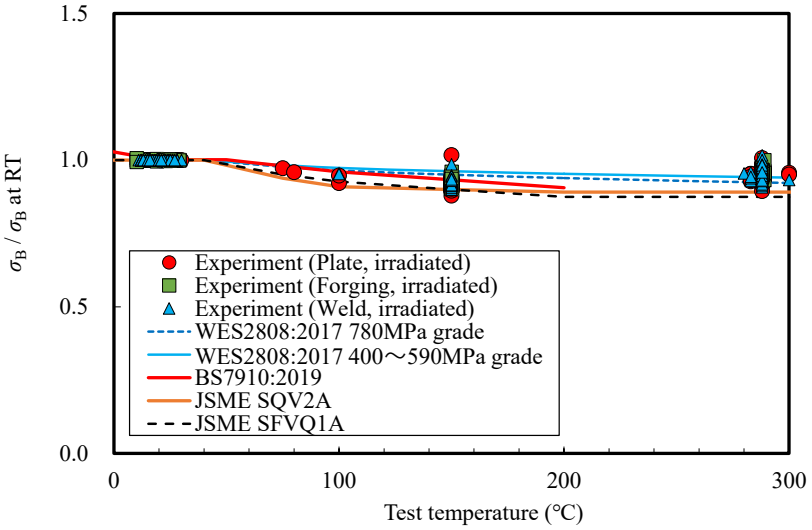


Fig. 5.2.4-12　Comparison between temperature dependence of σ_B from models and experiments

Copyright © 2026 The Japan Welding Engineering Society, All Rights Reserved.

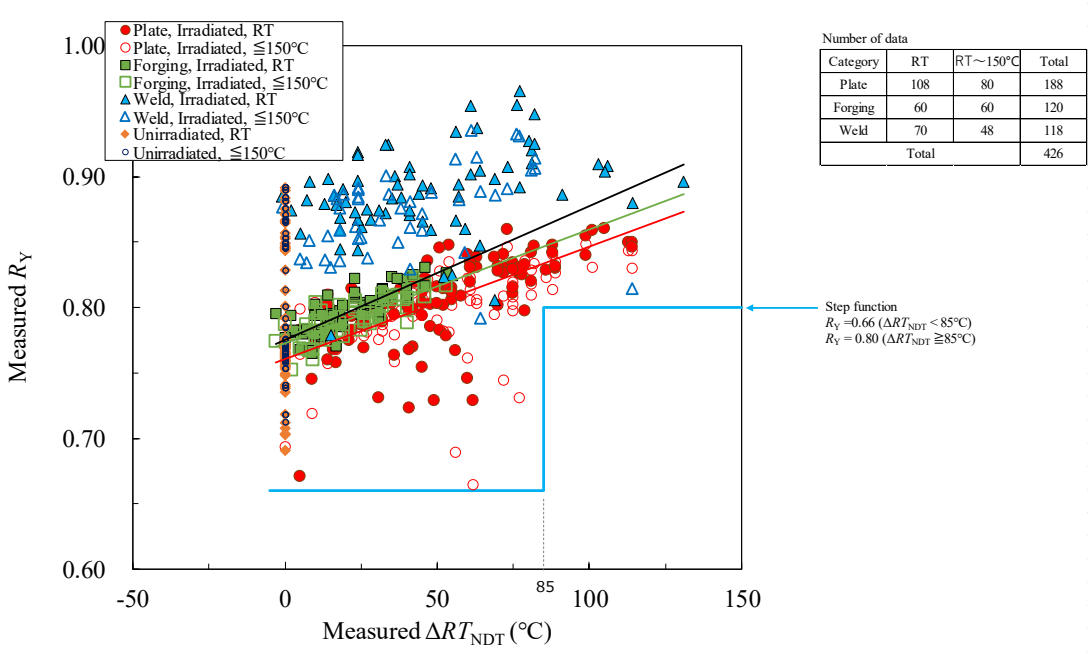
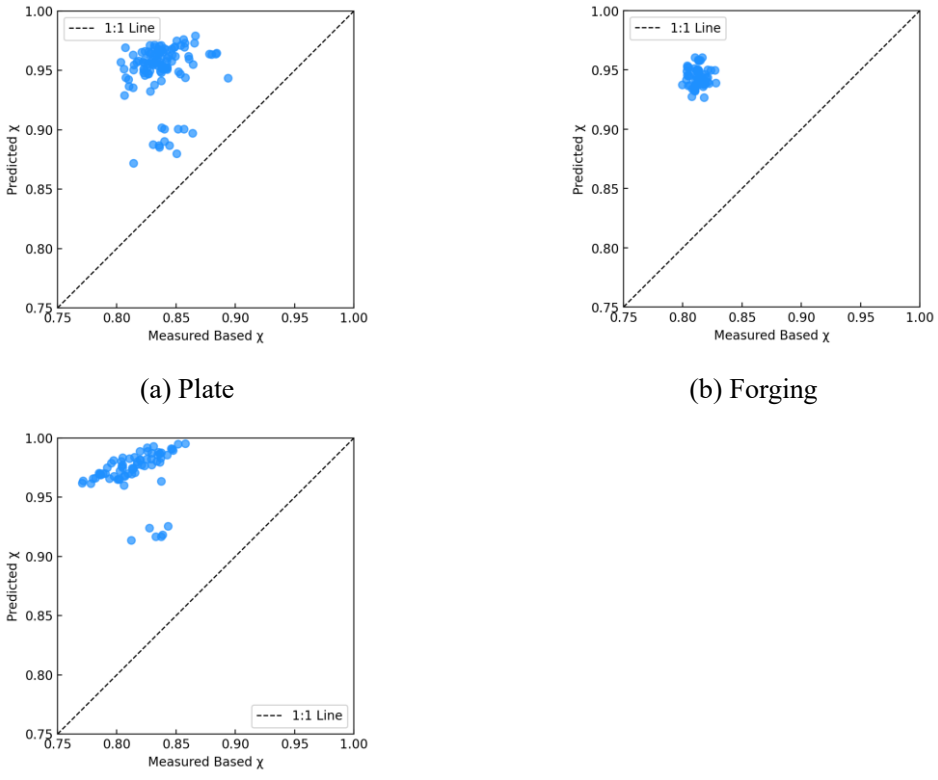


Fig. 5.2.4-13 R_Y enveloped by step function



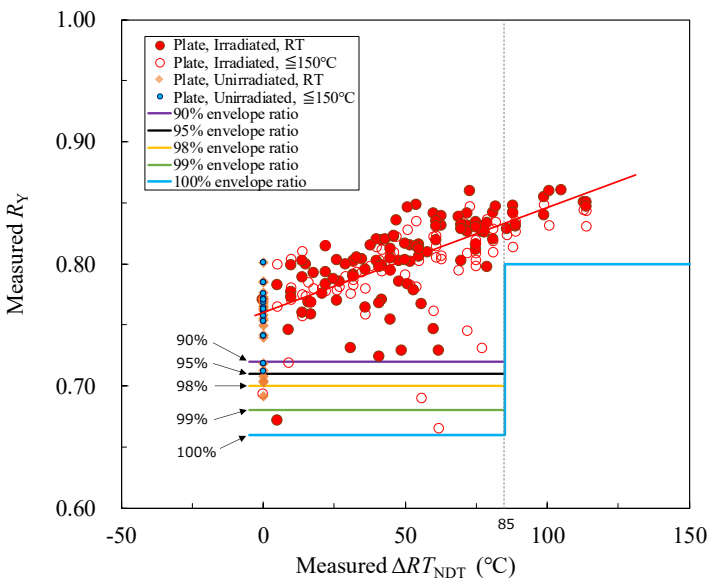
(a) Plate

(b) Forging

(c) Weld

Fig. 5.2.4-14 Calculated χ using R_Y by step function

Copyright © 2026 The Japan Welding Engineering Society, All Rights Reserved.



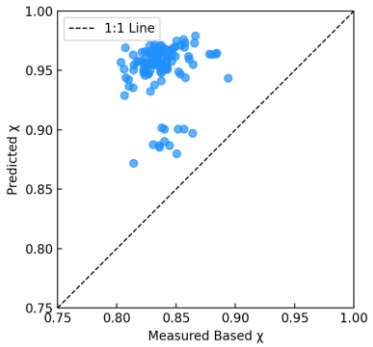
Number of data (ΔRT_{NDT}≦85℃)

Item	RT	RT～150℃	Total
Unirradiated	60	42	102
Irradiated	96	70	166
Total			268

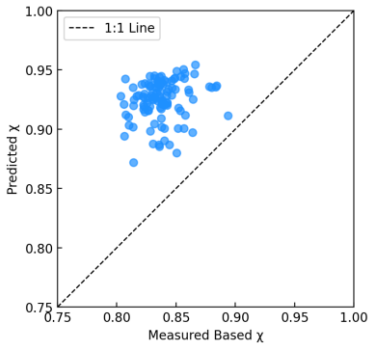
R_Y for each envelope ratio

Enveope ratio (%)	No. of data	No. of not enveloped data	R_Y
99	266	2	0.68
98	263	5	0.70
95	255	13	0.71
90	242	26	0.72

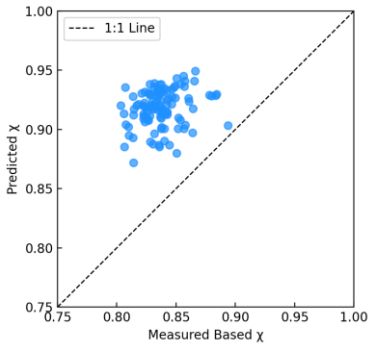
Fig. 5.2.4-15 R_Y by step function with different enveloping ratio (plates)



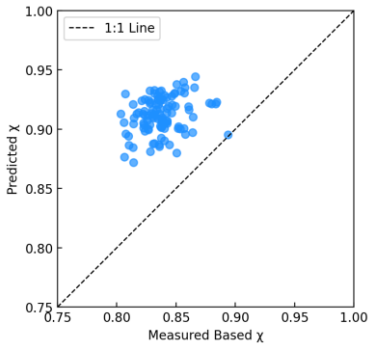
(a) Envelope probability: 100%



(b) Envelope probability: 98%



(c) Envelope probability: 95%



(d) Envelope probability: 90%

Fig. 5.2.4-16 Calculated χ using the R_Y by step function with different enveloping ratio (plate)

(χ was calculated with m = 10 and K_I = 70 MPa√m)

Copyright © 2026 The Japan Welding Engineering Society, All Rights Reserved.

5.2.5 Application examples of plastic constraint correction

Using the predicted tensile properties of a representative plant estimated by the post-irradiation tensile property prediction formula studied in Section 5.2.4 (which considers corrections based on measured values obtained from surveillance tests), a comparison was made. This comparison was between χ formulated in Section 5.2.3 and χ directly obtained from the RPV model. The results studied in Sections 5.2.3 and 5.2.4 have been published in reference[5-17]. The estimated post-irradiation tensile properties had a yield stress of 674 MPa and a yield ratio R_Y of 0.83. The Weibull parameter m was set to two values: 20 (conservative) and 10.

Figure 5.2.5-1 shows a comparison of χ directly obtained from the RPV model and the normalized K_J relationship and formulated χ–K_J relationship. It can be seen that the formulated χ is larger, thus providing a more conservative estimate compared to the plastic constraint correction factor χ from the RPV model.

Figure 5.2.5-2 presents the results of K_J correction for the RPV using each χ. The horizontal axis corresponds to the temperature at the deepest point of the flaw; however, the temperature varies within the flaw. Since the Weibull stress was calculated for the entire flaw and used for K_J correction, a conservative approach regarding temperature is to evaluate at the temperature at the clad/base metal interface, which is the lowest temperature within the flaw region. Therefore, in Figure 5.2.5-2, results using the temperature at the clad/base metal interface instead of the crack deepest point temperature are also shown as dashed lines.

When using the formulated χ, the corrected K_J ($K_{J\,Corr}$) of the RPV decreases less than when using χ from the RPV model, indicating a more conservative evaluation. Also, the effect of plastic constraint correction using χ was evaluated using the fracture toughness transition curve of JEAC4206-2007 shown in Equation (5.2.5-1). Here, the final term 125 is the reference temperature (°C), denoted as T_p, and the T_p where the maximum K_J history of the LBCOCA intersects the K_{Ic} curve was determined. The T_p values obtained for each evaluation are shown in Table 5.2.5-1. From Table 5.2.5-1, when using formulated χ, T_p is 18°C for m=20 and 10°C for conservative m=10, and when evaluated in detail by the RPV model, T_p is 54°C for m=20 and 38°C for conservative m=10, showing reasonable evaluation.

Furthermore, even when conservatively using the cladding-base metal boundary temperature in the correction by the RPV model, reasonable evaluation is possible, and it is confirmed that formulated χ can provide even more conservative evaluation.

Copyright © 2026 The Japan Welding Engineering Society, All Rights Reserved.

$$(K_{Ic} \text{ at evaluation period}) \ > 20.16 + 129.9\exp[0.0161(T - 125)] \qquad (5.2.5\text{-}1)$$

Copyright © 2026 The Japan Welding Engineering Society, All Rights Reserved.

Table 5.2.5-1 Values of T_p for K_J correction result using plastic constraint correction

Item	T_p (°C)*1	
m	10	20
Without correction	199	
RPV model	237 (+38)	253 (+54)
RPV model (using temperature at the interface of cladding and base metal)	217 (+18)	232 (+33)
Formulation	209 (+10)	217 (+18)

*1: The values in parentheses indicate the difference in T_p from the uncorrected case (relaxation effect).

Copyright © 2026 The Japan Welding Engineering Society, All Rights Reserved.

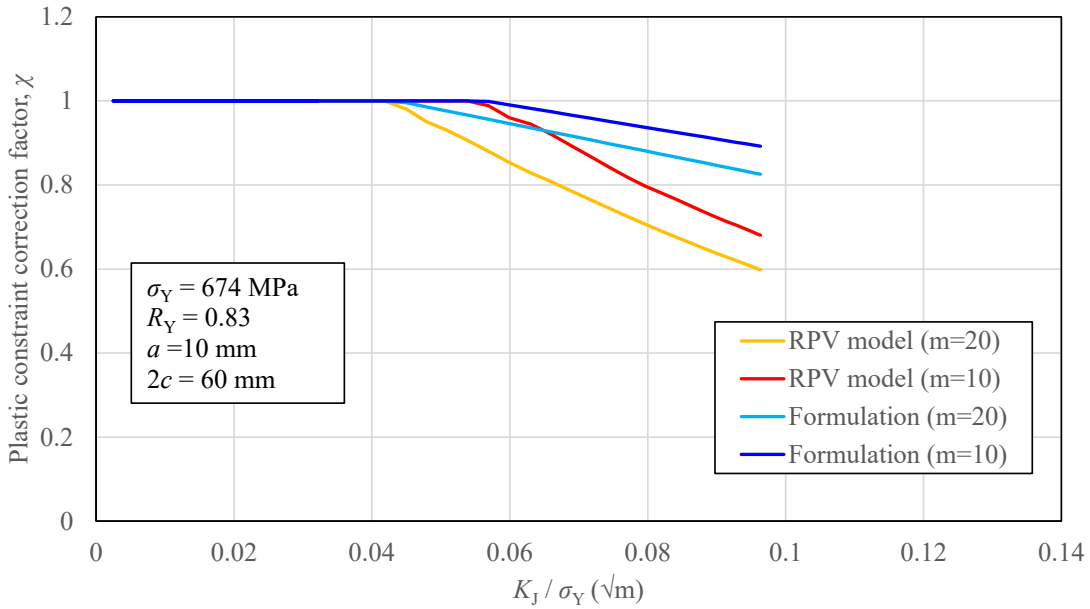


Fig. 5.2.5-1 Comparison of plastic constraint correction factor χ between RPV model and formulated equation

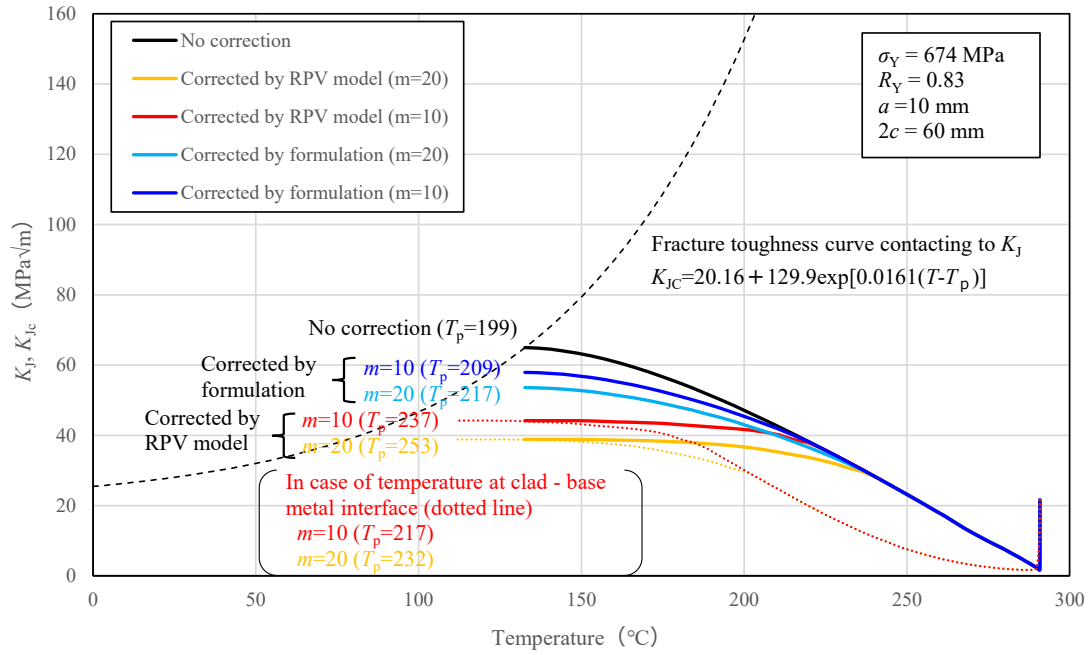


Fig. 5.2.5-2 K_J correction result using plastic constraint correction factor χ

Copyright © 2026 The Japan Welding Engineering Society, All Rights Reserved.

Reference

[5-1] ISO 27306:2009, 2016, “Metallic materials - Method of constraint loss correction of CTOD fracture toughness for fracture assessment of steel components”.

[5-2] BS 7910:2019, “Guide to methods for assessing the acceptability of flaws in metallic structures”, BSI Standards Publication.

[5-3] Japan Electric Association code, “Verification Method of Fracture Toughness for In-service Reactor Pressure Vessel”, JEAC4206-2016, (2016).

[5-4] T. Tobita, et al., “Effect of neutron irradiation on the mechanical properties of weld overlay cladding for reactor pressure vessel”, Journal of Nuclear Materials, 452 (2014) 61-68.

[5-5] Welding research council bulletin series, no.413, “Development of criteria for assessment of reactor vessels with low upper shelf fracture toughness”, (1996).

[5-6] ASME Boiler and Pressure Vessel Code Section VIII, “Rules for Construction of Pressure Vessels”, Division 2, “Alternative Rules”, (2019).

[5-7] T. Hirota, N. Ogawa and H Sakamoto, “Investigation of calculation procedure of stress intensity factor for fully circumferential flaw beneath reactor pressure vessel cladding”, Transactions of the JSME (in Japanese), Vol.86, No.882 (2020).

[5-8] F. Minami, et al., "Flaw Geometry Effect on Stress-Strain Fields for Flaw Under Biaxial Loading", Journal of Pressure Vessel Technology, Vol. 132, (2010).

[5-9] Japan Electric Association code, “Method of Surveillance Tests for Structural Materials of Nuclear Reactors”, JEAC4201-2007 [2013 addenda], (2013).

[5-10] J. F. Perrin, et al., “Physically Based Regression Correlations of Embrittlement Data From Reactor Pressure Vessel Surveillance Program”, EPRI NP-3319, Project 1240-1, Final Report, (1984).

[5-11] The Japan Welding Engineering Society, “Standard test method for Crack tip Opening Displacement (CTOD) fracture toughness measurement”, WES1108:1995, (1995).

[5-12] Japan Electric Association code, “Test Method for Determination of Reference Temperature, T_0, o Ferritic Steels”, JEAC4216-2015, (2015).

[5-13] ASTM E1921-19, “Standard Test Method for Determination of Reference Temperature, T_0, for Ferritic Steels in the Transition Range”, ASTM International, West Conshohocken, PA, 2019, www.astm.org.

Copyright © 2026 The Japan Welding Engineering Society, All Rights Reserved.

[5-14] Zerilli, F.J., and Armstrong, R.W., “Dislocation-Mechanics-Based Constitutive Relations for Material Dynamics Calculations”, J. Appl. Phys., Vol.65, No. 5, March 1987, pp.1816-1825.

[5-15] The Japan Welding Engineering Society, “Method of Assessing Brittle Fracture in Steel Weldments Subjected to Large Cyclic and Dynamic Strain”, WES2208: 2017, (2017).

[5-16] The Japan Society of Mechanical Engineers, “Codes for nuclear power generation facilities, rules on materials for nuclear facilities”, JSME S NJ1-2012 (2012) (in Japanese).

[5-17] Nagoshi. Y., Hirota, T., Fukahori, T., Sakima, K., Hojo, K., Ohata, M., and Minami, F., “Plastic Constraint Correction Factor on Brittle Fracture in Ductile-Brittle Transition Temperature Region (Report 2)”, Proceedings of ASME 2025 Pressure Vessels and Piping Conference, PVP2025-152875, 2025.

Copyright © 2026 The Japan Welding Engineering Society, All Rights Reserved.

6. Study toward standardization

In Chapter 4, fracture tests were conducted using standard fracture toughness specimens such as C(T) and SE(B) specimens with high plastic constraint, made from RPV materials, and surface-flawed plate specimens with low plastic constraint. It was verified that the critical Weibull stress can be applied as the fracture criterion in the DBTT region for specimens with different plastic constraint levels.

Based on this knowledge, Chapter 5 formulated a method to convert the K_J of structures to an equivalent K_J with plastic constraint corresponding to standard fracture toughness specimens with high plastic constraint by introducing the plastic constraint correction factor χ. χ is defined as the ratio of the K_J values of fracture toughness specimens and structures (K_{JCT} and K_{JRV}, respectively) corresponding to the same σ_w value. Namely,

$$\chi = K_{JCT} / K_{JRV} \tag{6-1}$$

If χ is prepared in advance by Equation (6-1), the K_J of structures (K_{JRV}) calculated by conventional fracture mechanics analysis methods can be converted to the K_J equivalent to standard fracture toughness specimens under large plastic constraint conditions. This enables a more accurate fracture evaluation through comparison with the fracture toughness criterion K_{Jc}. Furthermore, if the σ_w-K_J relationships for both structures and standard fracture toughness specimens are available, the K_J of structures can be translated to a value corresponding to the constraint level of standard fracture toughness specimens via σ_w.

The CAF Subcommittee initially formulated χ under limited conditions assuming a representative PWR vessel thickness of 200 mm and a semi-elliptical surface flaw with a depth of 10 mm and a total length of 60 mm. The subcommittee reconsidered the formulation of χ to include a broader thickness range of 100 mm to 250 mm to accommodate BWR applications and to cover smaller flaws based on flaw detectability by nondestructive inspection. Moreover, for χ formulated by the subcommittee targeting RPVs, a draft standard was examined which stipulates a simplified evaluation method to convert the K_J of RPVs to K_J under conditions of large plastic constraint using χ (Appendix 2). In addition to the simplified evaluation method, a guideline was developed (Appendix 3) that stipulates two methods: a detailed evaluation method that converts the K_J of RPV by obtaining the σ_w-K_J relationships of standard fracture specimens and RPV through numerical analysis.

Copyright © 2026 The Japan Welding Engineering Society, All Rights Reserved.

7. Summary

The CAF Subcommittee and CAF-II Subcommittee were established under the Nuclear Research Committee of the Japan Welding Engineering Society to develop a fracture safety evaluation methodology assuming brittle fracture or brittle fracture accompanied by ductile crack growth. This initiative aimed to enable rational safety evaluations ensuring the secure and reliable operation of nuclear power plants, which tend to experience significant aging. Research activities have been conducted over seven years since 2018. The evaluation targeted pressurized water reactor (PWR) plants, assuming fracture scenarios under pressurized thermal shock (PTS) conditions where internal pressure stresses and thermal transient stresses are superimposed.

The evaluation methods incorporated recent advances in fracture mechanics by accounting for the differences in plastic constraint between fracture toughness specimens and actual structural components. For brittle fracture, the Beremin model using Weibull stress as the fracture driving force was employed. For brittle fracture accompanied by ductile crack growth, a combined model of a ductile damage model and the Beremin model was applied.

The main outcomes are summarized as follows and have been published in references [7-1] through [7-10]. These results are expected to contribute to the standardization of fracture evaluation criteria considering plastic constraint effects in the nuclear field.

(1) Literature survey

As fracture evaluation methods capable of considering plastic constraint effect, the application of the Beremin model for brittle fracture and the GTN model for ductile fracture has been relatively widely advanced. Since these are considered the most effective methods currently for brittle fracture and brittle fracture after ductile crack growth, they were proposed as fracture evaluation models handled by this committee.

(2) Verification of fracture prediction models

To validate fracture prediction models, fracture test data were obtained through fracture toughness tests using C(T) and SE(B) specimens, and fracture tests using surface-flawed flat plates subjected to bending and tensile loads on RPV steel. Using the proposed fracture prediction models, fracture predictions were performed for surface-flawed plate specimens subjected to tensile and bending loads with low plastic constraint levels. The experimentally obtained K_{Jc} values were within

Copyright © 2026 The Japan Welding Engineering Society, All Rights Reserved.

the predicted range, confirming that fracture can be appropriately predicted by the proposed methods.

(3) Benchmark analysis of numerical analysis methods

Benchmark analyses by multiple organizations were conducted on low-alloy steel C(T) specimens, SE(B) specimens, surface-flawed plate bending specimens, and surface-flawed tensile specimens. The results for σ_w and fracture predictions for each specimen were generally consistent across all organizations. Although some differences appeared in GTN analyses, load-opening displacement relationships and ductile crack growth-J integral relationships were generally in agreement.

(4) Derivation of plastic constraint correction factor formula

For establishing fracture evaluation methods applicable to RPVs, the plastic constraint correction factor χ was calculated using surface-flawed flat plate models. Factors affecting χ (flaw depth, flaw length, yield ratio, yield stress, and Weibull parameter m) were considered. A simplified approach approximating the χ–K_J relationship by three linear segments was applied, resulting in a practical formula for χ. Comparison of χ values derived by this method with those obtained from plate and reactor pressure vessel models showed that the formulated χ values are conservative, enabling a conservative evaluation of constraint effects in RPVs.

(5) Estimation method of post-irradiation tensile properties used for calculation of plastic constraint correction factor

Based on surveillance test results of PWR plants in Japan, estimation methods for post-neutron irradiation yield stress σ_Y and yield ratio R_Y used in the χ calculation formula were established. Additionally, a literature review on the temperature dependence formulas of σ_Y and R_Y (σ_B) was conducted, and temperature dependence formulas capable of appropriately predicting surveillance test results were proposed.

(6) Standardization of plastic constraint correction method

Based on the results, a draft guideline for fracture evaluation methods considering plastic constraint effect was prepared targeting neutron-irradiated RPVs. In addition, with the incorporation into existing standards, a draft annex was developed specifying procedures to correct stress intensity factors accounting for plastic constraint effects.

Copyright © 2026 The Japan Welding Engineering Society, All Rights Reserved.

Reference

[7-1] K. Hojo, T. Hirota, Y. Nagoshi, T. Fukahori, K. Sakima, M. Ohata, and F. Minami, “Constraint effect on fracture in ductile-brittle transition temperature region”, PVP2021-61318, Pressure Vessels & Piping Conference PVP2021, July 12-16, 2021, Virtual, Online.

[7-2] T. Hirota, Y. Nagoshi, K. Hojo, H. Okada, A. Takahashi, T. J. Katsuyama, T. Ueda, T. Okada, K. Yashirodai, M. Ohata, and F. Minami, “Benchmark analysis of Beremin model and GTN model by CAF subcommittee”, PVP2021-61668, Pressure Vessels & Piping Conference PVP2021, July 12-16, 2021, Virtual, Online.

[7-3] K. Yashirodai and M. Nakane, ”Analysis for the effect of flaw front element on the brittle fracture evaluation results based on Weibull stress”, The Japan Society of Mechanical Engineers, The Proceedings of the Materials and Mechanics Conference -2021: OS1908, (2021).

[7-4] K. Hojo, T. Hirota, Y. Nagoshi, T. Fukahori, K. Sakima, M. Ohata, and F. Minami, “Constraint effect on fracture in ductile-brittle transition temperature region (Report 2)”, PVP2022-84186, Pressure Vessels & Piping Conference PVP2022, July 17-22, 2022, Las Vegas, NV, USA.

[7-5] K. Hojo, T. Hirota, Y. Nagoshi, T. Fukahori, K. Sakima, M. Ohata, and F. Minami, “Constraint effect on fracture in ductile-brittle transition temperature region (Report 3)”, PVP2023-105965, Pressure Vessels & Piping Conference PVP2023, July 16-21, 2023, Atlanta, GA, USA.

[7-6] Y. Nagoshi, T. Fukahori, H. Okada, A. Takahashi, M. Shimodaira, T. Ueda, T. Ogawa, K. Yashirodai, Y. Takahashi, and M. Ohata, “Benchmark analysis by Bermin model and GTN model in CAF Subcommittee”, Transactions of the SMiRT 27 Yokohama, Japan, March 3-8, 2024.

[7-7] K. Hojo, T. Hirota, Y. Nagoshi, T. Fukahori, K. Shimizu, M. Shimodaira, T. Ogawa, K. Yashirodai, M. Ohata, and F. Minami, “Plastic constraint correction factor χ for WES standard on brittle fracture in ductile - brittle transition temperature region”, PVP2024-123140, Pressure Vessels & Piping Conference PVP2024, July 29 – August 2, 2024, Bellevue, WA, USA.

[7-8] K. Shimizu, H. Yago, H. Shoji, M. Ohata, Y. Nagoshi, T. Hirota, K. Hojo and F. Minami, “Temperature Dependence of Critical Weibull Stress Distribution in Ductile-to Brittle Transition Temperature Region”, Quarterly Journal of the Japan Welding Society, Vol. 43, No. 2, pp. 260–271 (2025).

[7-9] Y. Nagoshi, T. Hirota, T. Fukahori, K. Sakima, K. Hojo, M. Ohata, and F. Minami, “Plastic

Copyright © 2026 The Japan Welding Engineering Society, All Rights Reserved.

constraint correction factor on brittle fracture in ductile - brittle transition temperature region (Report 2)", PVP2025-152875, Pressure Vessels & Piping Conference PVP2025, July 20-24, 2025, Montreal, Quebec, Canada.

[7-10] K. Hojo, T. Hirota, Y. Nagoshi, T. Fukahori, K. Sakima, M. Ohata, and F. Minami, "Application of fracture assessment method considering constraint effect to ductile – brittle transition temperature region", ASME Journal of Pressure Vessel Technology, PVT-24-1192, October 2025, Vol. 147/ 051501.

Copyright © 2026 The Japan Welding Engineering Society, All Rights Reserved.

Appendix 1

Committee Member List

Copyright © 2026 The Japan Welding Engineering Society, All Rights Reserved.

CAF subcommittee member list as of March 2023

No.	Title	Name	Affiliation
1	Chair	Fumiyoshi Minami	The University of Osaka
2	Vice chair	Mitsuru Ohata	The University of Osaka
3	Secretary	Kiminobu Hojo	Mitsubishi Heavy Industries, Ltd.
4	Secretary	Takatoshi Hirota	Mitsubishi Heavy Industries, Ltd.
5	Secretary	Takashi Hojo	The Kansai Electric Power Co., Inc.
6	Secretary	Ryo Nakazaki	The Kansai Electric Power Co., Inc.
7	Secretary	Teruyoshi Sato	IHI Corporation
8	Secretary	Toshiyuki Saito	Toshiba Energy Systems & Solutions Corporation
9	Secretary	Motoki Nakane	Hitachi GE Nuclear Energy, Ltd.
10	Neutral Member	Hiroshi Okada	Tokyo University of Science
11	Neutral Member	Akiyuki Takahashi	Tokyo University of Science
12	Neutral Member	Yukio Takahashi	Central Research Institute of Electric Power Industry
13	Neutral Member	Naoki Miura	Central Research Institute of Electric Power Industry
14	Neutral Member	Kazuma Suzuki	Central Research Institute of Electric Power Industry
15	Neutral Member	Masaki Shimodaira	Japan Atomic Energy Agency
16	Neutral Member	Kazuma Shimizu	The University of Osaka
17	Member	Kensuke Watanabe	Hokkaido Electric Power Co., Inc.
18	Member	Hiroaki Nishikatsu	Tokyo Electric Power Company Holdings, Inc.
19	Member	Akihiro Tomioka	Shikoku Electric Power Co., Inc.
20	Member	Yuta Nakayama	Kyushu Electric Power Co., Inc.
21	Member	Shuntaro Souma	Electric Power Development Co., Ltd.
22	Member	Katsuhiko Hayasaka	The Japan Atomic Power Company
23	Member	Yoichi Yamashita	IHI Corporation
24	Member	Takashi Ueda	IHI Corporation
25	Member	Tetsuya Tagawa	JFE Steel Corporation
26	Member	Shunsuke Sasaki	Toshiba Energy Systems & Solutions Corporation

Copyright © 2026 The Japan Welding Engineering Society, All Rights Reserved.

No.	Title	Name	Affiliation
27	Member	Takuya Ogawa	Toshiba Energy Systems & Solutions Corporation
28	Member	Fumihito Hirokawa	Hitachi GE Nuclear Energy, Ltd.
29	Member	Kenji Yashirodai	Hitachi, Ltd.
30	Member	Kimihisa Sakima	Mitsubishi Heavy Industries, Ltd.
31	Member	Yasuto Nagoshi	Mitsubishi Heavy Industries, Ltd.
32	Member	Takuya Fukahori	Mitsubishi Heavy Industries, Ltd.
33	Member	Akihiro Kiguchi	The Japan Welding Engineering Society
34	Member	Tomoko Sasaki	The Japan Welding Engineering Society

Former Member

No.	Title	Name	Affiliation	Participation Period
1	Secretary	Yasukazu Takada	The Kansai Electric Power Co., Inc.	April 2018 - May 2022
2	Secretary	Toru Oumaya	The Kansai Electric Power Co., Inc.	April 2018 – February 2022
3	Secretary	Takashi Hirano	IHI Corporation	April 2018 - February 2021
4	Neutral Member	Yasunori Yusa	Tokyo University of Science	April 2018 - February 2019
5	Neutral Member	Jinya Katsuyama	Japan Atomic Energy Agency	April 2018 – May 2022
6	Member	Masayoshi Nishino	Hokkaido Electric Power Co., Inc.	April 2018 – May 2021
7	Member	Atsushi Taniguchi	Tokyo Electric Power Company Holdings, Inc.	April 2018 – May 2018
8	Member	Takayuki Toida	Tokyo Electric Power Company Holdings, Inc.	November 2019 – July 2020
9	Member	Kazushige Nakagawa	Shikoku Electric Power CO., Inc.	April 2018 - February 2022
10	Member	Satoshi Yamamoto	Kyushu Electric Power Co., Inc.	April 2018 – July 2020
11	Member	Hiroyuki Hasunuma	Electric Power Development Co., Ltd.	April 2018 – November 2021
12	Member	Ryo Takagi	The Japan Atomic Power Company	April 2018 – May 2021
13	Member	Koji Iwata	Kobe Steel, Ltd.	April 2018 – May 2019
14	Member	Masatoshi Ishida	Kobe Steel, Ltd.	November 2019 – May 2021
15	Member	Atsushi Mori	Toshiba Energy Systems & Solutions Corporation	April 2018 – July 2020

Copyright © 2026 The Japan Welding Engineering Society, All Rights Reserved.

CAF-II subcommittee member list as of March 2025

No.	Title	Name	Affiliation
1	Chair	Fumiyoshi Minami	The University of Osaka
2	Vice chair	Mitsuru Ohata	The University of Osaka
3	Secretary	Kiminobu Hojo	Mitsubishi Heavy Industries, Ltd.
4	Secretary	Takatoshi Hirota	Mitsubishi Heavy Industries, Ltd.
5	Secretary	Takashi Hojo	The Kansai Electric Power Co., Inc.
6	Secretary	Ryo Nakazaki	The Kansai Electric Power Co., Inc.
7	Secretary	Takashi Ueda	IHI Corporation
8	Secretary	Toshiyuki Saito	Toshiba Energy Systems & Solutions Corporation
9	Secretary	Motoki Nakane	Hitachi GE Nuclear Energy, Ltd.
10	Neutral Member	Yukio Takahashi	Tokyo University of Science
11	Neutral Member	Naoki Miura	Central Research Institute of Electric Power Industry
12	Neutral Member	Kazuma Suzuki	Central Research Institute of Electric Power Industry
13	Neutral Member	Tomoki Shinko	Central Research Institute of Electric Power Industry
14	Neutral Member	Jinya Katsuyama	Japan Atomic Energy Agency
15	Neutral Member	Masaki Shimodaira	Japan Atomic Energy Agency
16	Neutral Member	Kazuma Shimizu	The University of Osaka
17	Member	Syunsuke Aoki	Hokkaido Electric Power Co., Inc.
18	Member	Hiroaki Nishikatsu	Tokyo Electric Power Company Holdings, Inc.
19	Member	Kazushige Nakagawa	Shikoku Electric Power CO.,Inc.
20	Member	Naoki Nakamura	Kyushu Electric Power Co., Inc.
21	Member	Takushi Fujino	The Japan Atomic Power Company
22	Member	Toshiaki Kawano	IHI Corporation
23	Member	Yoichi Yamashita	IHI Corporation
24	Member	Takuya Ogawa	Toshiba Energy Systems & Solutions Corporation
25	Member	Syunsuke Sasaki	Toshiba Energy Systems & Solutions Corporation
26	Member	Ryota Muranaka	Hitachi GE Nuclear Energy, Ltd.

Copyright © 2026 The Japan Welding Engineering Society, All Rights Reserved.

No.	Title	Name	Affiliation
27	Member	Kenji Yashirodai	Hitachi, Ltd.
28	Member	Yasuto Nagoshi	Mitsubishi Heavy Industries, Ltd.
29	Member	Takuya Fukahori	Mitsubishi Heavy Industries, Ltd.
30	Secretary	Tomoko Sasaki	The Japan Welding Engineering Society

Former Member

No.	Title	Name	Affiliation	Participation Period
1	Member	Akihiro Tomioka	Shikoku Electric Power Co., Inc.	April 2023 – February 2024
2	Member	Yuta Nakayama	Kyushu Electric Power Co., Inc.	April 2023 – February 2024
3	Member	Jun Kusaka	The Japan Atomic Power Company	April 2023 – June 2024
4	Member	Nannichi Takashi	IHI Corporation	April 2023 – February 2024
5	Member	Fumihito Hirokawa	Hitachi GE Nuclear Energy, Ltd.	April 2023 – February 2024

Copyright © 2026 The Japan Welding Engineering Society, All Rights Reserved.

Appendix 2

Draft Code for Simplified Evaluation Method: "Correction Method for PTS Transient Curve Considering Plastic Constraint Effects"

Copyright © 2026 The Japan Welding Engineering Society, All Rights Reserved.

Correction Method for PTS Transient Curve Considering Plastic Constraint Effect

1000 Application

This standard specifies the method for correcting the plastic constraint effect on PTS transient curves. However, the correction of the stress intensity factor prescribed herein shall not be applied to the acceptance criteria for the arrest of the propagating flaws. (Commentary-1000-1)

2000 Definition of Symbols

(1) A, B, C_1, C_2, C_3, D, E : constants for calculating plastic constraint correction factor (-)
(2) a : maximum postulated flaw depth (mm)
(3) c : maximum postulated flaw half-length (mm)
(4) K_I : stress intensity factor of the PTS transient curve (MPa√m)
(5) m : Weibull parameter of the Beremin model used for plastic constraint correction factor χ formulation shown in 3200 (-)
(6) $M_{\sigma Y}$: margin set conservatively for uncertainty of σ_Y
(7) M_{RY} : margin set conservatively for uncertainty of R_Y
(8) R_Y : yield ratio (-), ratio of yield stress or 0.2% proof stress σ_Y to tensile strength σ_B
(9) t : thickness of base metal or weld joint including weld metal of reactor pressure vessel shell (mm)
(10) χ : plastic constraint correction factor (-)
(11) ΔRT_{NDT} : embrittlement amount (°C) calculated by domestic embrittlement prediction method of JEAC4201-2007 [2013 supplement]
(12) σ_B : tensile strength (MPa)
(13) σ_{B_ini} : tensile strength before irradiation (MPa)
(14) $\Delta\sigma_B$: increase in tensile strength due to irradiation (MPa)
(15) σ_Y : yield stress or 0.2% proof stress (MPa)
(16) σ_{Y_ini} : yield stress or 0.2% proof stress before irradiation (MPa)
(17) $\Delta\sigma_Y$: increase in yield stress or 0.2% proof stress due to irradiation (MPa)

3000 Correction Method for PTS Transient Curve

Within the application range specified in 3100, the plastic constraint correction factor χ shall be determined in accordance with 3200. The PTS transient curve shall be adjusted to account for the plastic constraint effect as prescribed in 3300.

Copyright © 2026 The Japan Welding Engineering Society, All Rights Reserved.

3100 Application Range

The application range is shown in Table-3100-1. (Commentary-3100-1)

Table-3100-1 Application range

Parameters	Range
R_Y[1)]	0.6 to 0.95
σ_Y	450MPa to 900MPa
a	5mm to 10mm
$2c$	15mm to 60mm
t	100mm to 250mm
K_I	Equal or less than 120MPa√m
m	10 to 30

1) When R_Y exceeds 0.95, conservatively set R_Y to 0.95.

3200 Calculation of Plastic Constraint Correction Factor χ

The plastic constraint correction factor χ for K_I at each time history of the PTS transient curve shall be calculated using the following equations (see Fig.-3200-1). The value of χ shall be limited to a maximum of 1. For conservative evaluation, a value of m=10 shall be used. When the parameter m of the Beremin model is available for the material, the value of m within the application range specified in Table-3100-1 may be applied. (Refer to Commentary-3200-1)

$$\chi = \mathrm{MAX}\,[Ax + B,\ Cx + D,\ E] \tag{1}$$

$$x = K_I / \sigma_Y \tag{2}$$

In Equation (1), the coefficients A, B, C, D, and E are calculated as $F_1 m + F_2 R_Y + F_3$, where F_1, F_2, and F_3 are taken from Table-3200-1 for parameters a and c. Values corresponding to intermediated a and c shall be obtained by linear interpolation.

Also, σ_Y and R_Y are obtained considering increases due to neutron irradiation by Equations (3) to (9). Conservatively, non-irradiated values may be used instead of Equations (3) to (9). If two or more measured values of $\Delta\sigma_Y$ and R_Y from surveillance tests exist for the material, $M_{\sigma Y}$ and M_{RY} may be set to encompass all measured values instead of values from Equations (3) to (9). σ_Y and R_Y are conservatively used as room temperature values. However, σ_Y may be calculated using temperature at the virtual flaw position by the temperature dependence formula specified in WES1108: 1995. (Commentary-3200-2)

Copyright © 2026 The Japan Welding Engineering Society, All Rights Reserved.

$$\sigma_Y = \sigma_{Y\_ini} + \Delta\sigma_Y + M_{\sigma Y} \quad (3)$$

(Plate) $\Delta\sigma_Y = 1.66\ \Delta RT_{NDT}$, $M_{\sigma Y} = 60.6$ (4)

(Forging) $\Delta\sigma_Y = 2.19\ \Delta RT_{NDT}$, $M_{\sigma Y} = 42.4$ (5)

(Weld) $\Delta\sigma_Y = 1.83\ \Delta RT_{NDT}$, $M_{\sigma Y} = 86.0$ (6)

(Plate) $R_Y = 0.000858\ \Delta RT_{NDT} + 0.761 - M_{RY}$, $M_{RY} = 0.049$ (7)

(Forging) $R_Y = 0.001020\ \Delta RT_{NDT} + 0.775 - M_{RY}$, $M_{RY} = 0.020$ (8)

(Weld) $R_Y = 0.000390\ \Delta RT_{NDT} + 0.870 - M_{RY}$, $M_{RY} = 0.062$ (9)

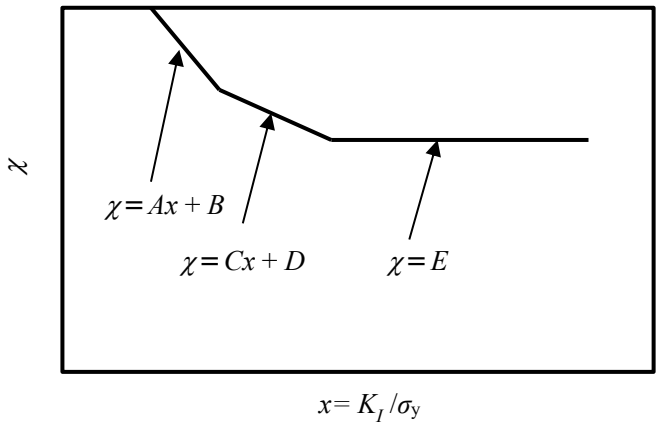


Figure-3200-1 Plastic constraint correction factor, χ

Copyright © 2026 The Japan Welding Engineering Society, All Rights Reserved.

Table-3200-1 Factors for plastic constraint correction factor

a (mm)	c (mm)	Coefficient	F_1	F_2	F_3
10	30	*A*	-0.0605	-9.65	5.94
		B	-0.000814	0.439	0.795
		C	0.015	-5.46	2.35
		D	-0.0103	-0.0896	1.25
		E	-0.00747	-1.13	1.69
	15	*A*	-0.057	-10.3	5.26
		B	0.00187	0.337	0.827
		C	-0.00851	-3.26	1.16
		D	-0.00423	-0.545	1.34
		E	-0.00585	-1.16	1.56
5	15	*A*	-0.046	-9.41	1.29
		B	0.00157	0.201	1.06
		C	-0.0162	-6.89	3.41
		D	-0.00109	-0.0228	0.87
		E	-0.00325	-0.946	1.33
	7.5	*A*	0.0179	-22.5	6.63
		B	-0.000781	1.17	0.581
		C	-0.0114	-6.12	3.08
		D	0.00183	-0.288	0.897
		E	0.000301	-1.11	1.31

3300 Correction of PTS Transient Curve

The PTS transient curve may be adjusted by multiplying the stress intensity factor K_I by the plastic constraint correction factor χ, as determined in Section 3200.

Copyright © 2026 The Japan Welding Engineering Society, All Rights Reserved.

(Commentary-1000-1) Method for Correcting PTS Transient Curves Considering Plastic Constraint Effect

(1) Background

Conventional structural integrity evaluation methods based on fracture mechanics evaluate the fracture safety of structures using fracture toughness values derived from standard fracture toughness specimens characterized by high plastic constraint conditions as material properties. However, in practical applications, cracks occurring in structures are often small surface flaws, where the surrounding stress field seldom exhibit the high constraint state (i.e., high multiaxial stress state) observed in standard fracture toughness specimens. Consequently, conventional fracture mechanics approaches tend to yield overly conservative evaluations of structural fracture safety, particularly in the case of high-strength steels.

In response to this issue, ISO 27306 - the world's first standard addressing brittle fracture evaluation with consideration of plastic constraint effects - was established in 2009. Its second edition, published in 2016, improved evaluation accuracy and expanded the scope of applicability [1,2]. The principles of ISO 27306 have also been incorporated into WES 2808, a brittle fracture evaluation standard for large earthquake scenarios [3,4], thereby enabling more rational and less conservative evaluations of brittle fracture behavior of building structures. Additionally, BS 7910 [5], the British standard for flaw assessment of steel structures, includes a correction method that accounts for plastic constraint effect.

The CAF Subcommittee under the Atomic Energy Research Committee of the Japan Welding Engineering Society (April 2018 to March 2023) has conducted extensive research and development on fracture evaluation methods that incorporate plastic constraint effects for brittle fracture accompanied by ductile crack growth in the ductile-brittle transition temperature (DBTT) region of reactor pressure vessels [6–16]. In particular, a combined model integrating the Beremin model for brittle fracture and the Gurson model for ductile fracture was applied, demonstrating that fracture limits in the DBTT region for surface-flawed plate specimens can be predicted based on data from standard fracture toughness specimens. Based on these findings, a fracture evaluation guideline considering plastic constraint effects in the DBTT region was formulated.

The succeeding CAF-II Subcommittee (April 2023 to March 2025) is focused on the practical implementation of the guideline and has been developing a draft standard for fracture evaluation methods specifically addressing pressurized thermal shock (PTS) events in reactor pressure vessels within the nuclear industry. This effort aims to eliminate the excessive conservatism inherent in conventional evaluation methods and to enable realistic evaluation of safety margins.

Accordingly, for integrity evaluations under service levels C and D, i.e., for PTS events, this standard incorporates the results of the CAF and CAF-II Subcommittees and specifies a method to correct PTS transient curves of stress intensity factors by considering the effects of plastic constraint.

Copyright © 2026 The Japan Welding Engineering Society, All Rights Reserved.

(2) Overview of the Beremin Model

The Weibull stress σ_w, introduced by the French research group, Beremin, is defined as a stochastic fracture driving force parameter that accounts for the weighted contribution of stresses at each point within the vicinity of crack tip under conditions leading to unstable fracture. It expressed as follows:

$$\sigma_w = \left(\frac{1}{V_0} \int_{V_f} {\sigma_1}^m dV \right)^{\frac{1}{m}}$$

Here, V_0 is the reference volume associated with fracture, V_f is the total volume of the fracture process zone, σ_1 is the maximum principal stress, and m is the shape parameter of the Weibull distribution.

The model is based on the premise that brittle microcracks originated at hard inclusions such as carbides or regions of dislocation accumulation. Employing the weakest link theory, it assumes that the initiation of unstable crack propagation is governed by the most vulnerable microcrack, which in turn controls the overall brittle fracture strength of the material.

The cumulative fracture probability, P_f, is defined as:

$$P_f = 1 - exp\left(-\left(\frac{\sigma_w}{\sigma_u} \right)^m \right)$$

where σ_u represents the scale parameter of the Weibull distribution.

Compared to conventional fracture mechanics approaches, the Beremin model offers enhanced predictive capability by explicitly incorporating the effects of plastic constraint near the crack tip. Its validity and applicability are currently under extensive international evaluation [15].

(3) Overview of CAF Subcommittee Achievements

The CAF Subcommittee undertook comprehensive investigations into state-of-the-art evaluation methods that incorporate the plastic constraint effect. Validation of fracture prediction methodologies was performed using divers fracture test data obtained from specimens with varying geometries. Additionally, benchmark analyses involving multiple organizations were conducted. The principal achievements are summarized as follows:

1) Through the investigation of evaluation methods capable of accounting for plastic constraint effects, it was confirmed that the Beremin model is extensively applied for brittle fracture evaluation, while the GTN model is predominantly used for ductile fracture evaluation. These models represent the most effective approaches for predicting brittle fracture and brittle fracture following ductile crack growth, respectively.

Copyright © 2026 The Japan Welding Engineering Society, All Rights Reserved.

2) Utilizing the fracture evaluation methods identified in item 1), and employing model parameters derived from test results of C(T) and SE(B) specimens, fracture behavior of surface-flawed plate tensile and bending specimens characterized by low plastic constraint was predicted. The fracture toughness values K_{Jc} obtained from experimental tests fell within the predicted ranges, thereby validating the accuracy of the fracture prediction.
3) Benchmark analyses were conducted for C(T) specimens, SE(B) specimens, surface-flawed plate bending specimens, and surface-flawed plate tensile specimens. The Weibull stress σ_w computed for each specimen type exhibited general consistency across all participating organizations.
4) For development of fracture evaluation methods incorporating plastic constraint effects applicable to reactor pressure vessels, analyses were conducted on surface-flawed plate models subjected to bending load. These analyses varied the yield ratio R_Y and Weibull parameter m to determine the plastic constraint correction factor χ. The analytical model and boundary conditions were established following confirmation of the influence of load type (membrane versus bending stress), multiaxial loading, residual stresses, and cladding effects. It was further demonstrated that χ can be expressed as a function of the normalized stress intensity factor K_J/σ_Y, and the χ–K_J/σ_Y relationship was approximated to derive simplified calculation formulas parameterized by R_Y and m. Comparison of χ obtained by this approach with those derived from plate and reactor pressure vessel models under PTS events indicated that the method provides conservative estimates, thus conservative evaluation of constraint effects in reactor vessel evaluation.
5) Assuming an upper shelf absorbed energy of 60 J in Charpy impact tests – representative of values achievable during long-term operation of the plants in Japan, and employing the conversion formula from upper shelf energy to J-R curves specified in JEAC4206, an average -2σ equivalent J-R curve was established. Ductile crack growth analyses conducted at rated operation conditions and under PTS events using the GTN model confirmed that no ductile crack growth initiates from the maximum assumed postulated flaw in the PTS evaluation.

(3) Conservatism in PTS Evaluation

In the context PTS evaluations, considering the implementation status of nondestructive inspections within the reactor pressure vessel core region during both construction and service, sufficiently large flaw sizes are conservatively assumed. Evaluations employ lower-bound fracture toughness data, and factors influencing fracture are treated deterministically and conservatively on an individual basis. Consequently, even when incorporating fracture evaluation methods that account for plastic constraint effects in accordance with this standard, an adequate level of conservatism is maintained.

Reference

(1) “Metallic materials – Method of constraint loss correction of CTOD fracture toughness for fracture assessment of steel components”, ISO27306: 2016.

Copyright © 2026 The Japan Welding Engineering Society, All Rights Reserved.

(2) F. Minami, M. Ohata, H. Shimanuki, T. Handa, S. Igi, M. Kurihara, T. Kawabata, Y. Yamashita, T. Tagawa, Y. Hagihara, “Method of Constraint Loss Correction of CTOD Fracture Toughness for Fracture Assessment of Steel Components”, Engineering Fracture Mechanics, 2006, Vol. 73, P1996–2020.

(3) The Japan Welding Engineering Society, “Method of Assessing Brittle Fracture in Steel Weldments Subjected to Large Cyclic and Dynamic Strain”, WES2208: 2017, (2017).

(4) F. Minami, Y. Takashima, M. Ohata, Y. Shimada, T. Suzuki, H. Shimannuki, S. Igi, T. Ishii, M. Kinefuchi, T. Yamaguchi, Y. Hagihara, “Fracture assessment procedure developed in Japan for steel structures under seismic conditions”, Engineering Fracture Mechanics, Vol. 187, 2018, P142-164.

(5) British Standard, “Guide to methods for assessing the acceptability of flaws in metallic structures”, BS7910: 2019.

(6) K. Hojo, T. Hirota, Y. Nagoshi, T. Fukahori, K. Sakima, M. Ohata, and F. Minami, “Constraint effect on fracture in ductile-brittle transition temperature region”, PVP2021-61318, Pressure Vessels & Piping Conference PVP2021, July 12-16, 2021, Virtual, Online.

(7) T. Hirota, Y. Nagoshi, K. Hojo, H. Okada, A. Takahashi, T. J. Katsuyama, T. Ueda, T. Okada, K. Yashirodai, M. Ohata, and F. Minami, “Benchmark analysis of Beremin model and GTN model by CAF subcommittee”, PVP2021-61668, Pressure Vessels & Piping Conference PVP2021, July 12-16, 2021, Virtual, Online.

(8) K. Yashirodai and M. Nakane, ”Analysis for the effect of crack front element on the brittle fracture evaluation results based on Weibull stress”, The Japan Society of Mechanical Engineers, The Proceedings of the Materials and Mechanics Conference -2021: OS1908, (2021).

(9) K. Hojo, T. Hirota, Y. Nagoshi, T. Fukahori, K. Sakima, M. Ohata, and F. Minami, “Constraint effect on fracture in ductile-brittle transition temperature region (Report 2)”, PVP2022-84186, Pressure Vessels & Piping Conference PVP2022, July 17-22, 2022, Las Vegas, NV, USA.

(10) K. Hojo, T. Hirota, Y. Nagoshi, T. Fukahori, K. Sakima, M. Ohata, and F. Minami, “Constraint effect on fracture in ductile-brittle transition temperature region (Report 3)”, PVP2023-105965, Pressure Vessels & Piping Conference PVP2023, July 16-21, 2023, Atlanta, GA, USA.

(11) Y. Nagoshi, T. Fukahori, H. Okada, A. Takahashi, M. Shimodaira, T. Ueda, T. Ogawa, K. Yashirodai, Y. Takahashi, and M. Ohata, “Benchmark analysis by Bermin model and GTN model in CAF Subcommittee”, Transactions of the SMiRT 27 Yokohama, Japan, March 3-8, 2024.

(12) K. Hojo, T. Hirota, Y. Nagoshi, T. Fukahori, K. Shimizu, M. Shimodaira, T. Ogawa, K. Yashirodai, M. Ohata, and F. Minami, “Plastic constraint correction factor χ for WES standard on brittle fracture in ductile - brittle transition temperature region”, PVP2024-123140, Pressure Vessels & Piping Conference PVP2024, July 29 – August 2, 2024, Bellevue, WA, USA.

(13) K. Shimizu, H. Yago, H. Shoji, M. Ohata, Y. Nagoshi, T. Hirota, K. Hojo and F. Minami, “Temperature Dependence of Critical Weibull Stress Distribution in Ductile-to Brittle Transition

Copyright © 2026 The Japan Welding Engineering Society, All Rights Reserved.

Temperature Region", Quarterly Journal of the Japan Welding Society, Vol. 43, No. 2, pp. 260–271 (2025).

(14) Y. Nagoshi, T. Hirota, T. Fukahori, K. Sakima, K. Hojo, M. Ohata, and F. Minami, "Plastic constraint correction factor on brittle fracture in ductile - brittle transition temperature region (Report 2)", PVP2025-152875, Pressure Vessels & Piping Conference PVP2025, July 20-24, 2025, Montreal, Quebec, Canada.

(15) The Japan Welding Engineering Society, Atomic Energy Research Committee, "Activity Report Subcommittee on Constraint based Assessment on Fracture in ductile-brittle transition temperature region", (2026).

(16) K. Hojo, T. Hirota, Y. Nagoshi, T. Fukahori, K. Sakima, M. Ohata, and F. Minami, "Application of fracture assessment method considering constraint effect to ductile – brittle transition temperature region", ASME Journal of Pressure Vessel Technology, PVT-24-1192, October 2025, Vol. 147/ 051501.

(Commentary-3100-1) Application Range

The application scope presented in Table-3100-1 has been established based on the analytical conditions employed in the study that developed the formulation of the plastic constraint correction factor, χ. While grain boundary embrittlement caused by neutron irradiation may arise in steels with elevated phosphorus content, it is recognized that such embrittlement is not expected to occur in operating reactor pressure vessels due to the controlled low phosphorus levels (1). Consequently, grain boundary fracture is explicitly excluded from the scope of this Standard.

Reference

(1) K. Hata, H. Takamizawa, T. Hojo, K. Ebihara, Y. Nishiyama, Y. Nagai, "Grain-boundary phosphorus segregation in highly neutron-irradiated reactor pressure vessel steels and its effect on irradiation embrittlement", Journal of Nuclear Materials, Volume 543, 2021.

(Commentary-3200-1) Weibull Parameter *m*

The Weibull parameter *m* of the Beremin model represents the degree of scatter in material fracture toughness. Determination of an appropriate *m* value for specific materials requires a substantial amount of fracture toughness test data. Annex A of ISO27306 provides the correlation between *m* values and crack tip opening displacement, *CTOD*, for various steels across different strength levels. When the average *CTOD* is 0.05 mm or less, the lower bound of *m* values for these steels is 10, for average *CTOD* values exceeding 0.05mm, a conservative value of 20 may be applied. A *CTOD* of 0.05 mm roughly corresponds to K_J of 70 MPa√m. However, since K_J values encountered in PTS evaluation may surpass 70 MPa√m, adopting m=10 is considered a conservative approach.

Copyright © 2026 The Japan Welding Engineering Society, All Rights Reserved.

The applicability of the master curve method, which characterizes the scatter of fracture toughness, has been validated for reactor vessel materials both before and after neutron irradiation by many studies. Although neutron irradiation embrittlement results in an increase in the reference temperature of the master curve, the scatter in fracture toughness remains essentially unchanged and can be adequately described by the master curve. Therefore, the impact of irradiation on the Weibull parameter m is regarded as minimal, and the use of m=10 in the calculation of χ is considered conservative.

(Commentary-3200-2) Tensile Properties of Irradiated Materials

Reactor pressure vessel steels are known to exhibit increased strength and decreased toughness as a result of neutron irradiation during operation. For the purpose of calculating the plastic constraint correction factor χ for reactor pressure vessels in operation, it is necessary to obtain post-irradiation tensile properties, specifically σ_Y and σ_B. Reference (1) investigated correlation equations relating the embrittlement shift ΔRT_{NDT} caused by neutron irradiation to the increases in tensile properties $\Delta\sigma_Y$ and $\Delta\sigma_B$, based on tensile test data acquired from surveillance specimens of PWR reactor pressure vessels in Japan. Conservative approaches were applied to account for uncertainties in these correlation equations when estimating $\Delta\sigma_Y$, $\Delta\sigma_B$, and R_Y. Furthermore, the validity of the temperature dependence expressed in correlation formulas for $\Delta\sigma_Y$ and $\Delta\sigma_B$ was confirmed through tensile test data from surveillance tests. Accordingly, this Standard incorporates these correlation formulas for estimating the tensile properties of irradiated materials.

Reference

(1) Y. Nagoshi, T. Hirota, T. Fukahori, K. Sakima, K. Hojo, M. Ohata, and F. Minami, “Plastic constraint correction factor on brittle fracture in ductile - brittle transition temperature region (Report 2)”, PVP2025-152875, Pressure Vessels & Piping Conference PVP2025, July 20-24, 2025, Montreal, Quebec, Canada.

Copyright © 2026 The Japan Welding Engineering Society, All Rights Reserved.

Appendix 3

Draft Standard for Simplified and Detailed Evaluation Methods: "Method of Constraint Loss Correction for Fracture Driving Force in PTS Transient of Reactor Pressure Vessel"

Copyright © 2026 The Japan Welding Engineering Society, All Rights Reserved.

Method of constraint loss correction for fracture driving force in PTS transient of reactor pressure vessel

Copyright © 2026 The Japan Welding Engineering Society, All Rights Reserved.

Table of Contents

Page

Introduction 1
1. Scope of Application 1
2. Referenced Standards 1
3. Terms and Definitions 1
4. Symbols and Their Meanings 2
5. Plastic Constraint Correction Factor χ 3
6. Evaluation of χ 4
6.1 Overview 4
6.2 Level I Evaluation of χ (Simple Evaluation) 4
6.3 Level II Evaluation of χ (Detailed Evaluation) 5
7. Setting of m 10
7.1 Overview 10
7.2 Setting of m in Level I Evaluation 10
7.3 Setting of m in Level II Evaluation 11
8. Plastic Constraint Correction in Fracture Assessment 11

Appendix A (Prescriptive) Method for Calculating Weibull Parameter m 13
Appendix B (Reference) Example Calculations of Plastic Constraint Correction Factor χ 15
Appendix C (Reference) Considerations in FE Analysis 17

Copyright © 2026 The Japan Welding Engineering Society, All Rights Reserved.

Method of constraint loss correction for fracture driving force in PTS transient of reactor pressure vessel

Introduction

This standard specifies a method for evaluating the fracture driving force of assumed or detected flaws in a reactor pressure vessel (hereinafter referred to as the pressure vessel) in service, by applying a correction to the plastic constraint of the pressure vessel.

1. Scope of Application

This standard applies to cleavage-type brittle fracture of light water reactor pressure vessels subjected to pressurized thermal shock (PTS) events. It prescribes a method to evaluate the fracture driving force, taking into account the reduction of plastic constraint in the pressure vessel. The evaluation is conducted at the reactor core region base metal, where the base metal consists of low alloy steel, and the assumed flaw is an inner surface flaw. Ductile fracture and plastic collapse in the upper shelf temperature region are excluded from the scope of this standard. Although embrittlement in light water reactors arises due to neutron irradiation and its severity depends on the irradiation dose, the prediction of embrittlement is also excluded from the scope of this standard.

2. Referenced Standards

The following standards are incorporated by reference in this standard and constitute an integral part thereof. The latest editions of these standards, including any amendments, shall be applied.

ASTM E1820 Standard Test Method for Measurement of Fracture Toughness

ISO 12135 Metallic Materials -- Unified Method of Test for the Determination of Quasi-Static Fracture Toughness

ISO 27306 Metallic Materials--Method of Constraint Loss Correction of CTOD Fracture Toughness for Fracture Assessment of Steel Components

3. Terms and Definitions

The main terms used in this standard are defined as follows, in addition to those specified in ISO 12135 and ASTM E1820.

PTS	Pressurized Thermal Shock (PTS). An event occurring during a loss-of-coolant accident or main steam pipe break accident, wherein the emergency core cooling system operates to cool the inner surface of the reactor vessel (RV). This results in high thermal stress on the inner surface due to the temperature difference between the inner and outer

Copyright © 2026 The Japan Welding Engineering Society, All Rights Reserved.

	surfaces, which superimposes on the membrane stress caused by internal pressure, thereby generating a high tensile stress on the inner surface.
RV	Reactor Pressure Vessel (RPV), Reactor Vessel.
WPS	Warm Prestressing (WPS) effect. A phenomenon in which the apparent fracture toughness of ferritic steel structures or equipment containing flaws increases when subjected to a tensile load at elevated temperature prior to fracture.
Plastic Constraint	A state characterized by multiaxial stress fields occurring at stress concentration points such as notch roots or crack tips, which restricts the extent of the plastic zone.
Weibull Stress	A stochastic fracture-driving parameter defined by considering the stress distribution near the crack tip and weighting the stresses at each point according to their contribution to unstable fracture.
Weibull Parameters	Parameters defining the Weibull distribution. When representing the distribution of critical Weibull stress, the shape parameter m and scale parameter σ_u are used.

4. Symbols and Their Meanings

The symbols used in this code and their meanings are as follows.

A, B, C, D, E, F_1, F_2, F_3	constants used to calculate the plastic constraint correction factor χ
a (mm)	depth of semi-elliptical surface flaw
c (mm)	half-length of semi-elliptical surface flaw
B (mm)	thickness of standard fracture toughness specimen used in the test
$CTOD$ (mm)	crack tip opening displacement
E (MPa)	Young's modulus
K_J (MPa√m)	J converted to K using the relation between J and K under small-scale yielding conditions
K_{Jc} (MPa√m)	K_J at brittle fracture initiation
$K_{Jc(25)}$ (MPa√m)	K_{Jc} for a specimen thickness of 25 mm
$K_{Jc(B)}$ (MPa√m)	K_{Jc} for a specimen thickness B
K_{JRV} (MPa√m)	K_J of the pressure vessel before plastic constraint correction
$K_{JRV,corr}$ (MPa√m)	K_J of the pressure vessel after plastic constraint correction
K_{JCT} (MPa√m)	K_J of the standard fracture toughness specimen
m (-)	Weibull shape parameter of the critical Weibull stress distribution
R_Y(-)	yield ratio, the ratio of yield stress or 0.2% proof stress σ_Y to tensile strength σ_U
χ(-)	plastic constraint correction factor for K_J, which is defined as the ratio of K_{JCT} to K_{JRV} that yields the same level of σ_w in the σ_w-K_J relationship for standard fracture toughness specimens such as C(T) and SE(B) and for structures such as pressure vessels
t (mm)	thickness of the core region of the pressure vessel
T (°C)	temperature
σ_w (MPa)	Weibull stress
σ_Y (MPa)	yield stress or 0.2% proof stress

Copyright © 2026 The Japan Welding Engineering Society, All Rights Reserved.

σ_U (MPa) tensile strength

σ_u (MPa) Weibull scale parameter of the critical Weibull stress distribution

5. Plastic Constraint Correction Factor χ

The σ_w-K_J relationships for the RV and C(T) specimens differ due to variations in plastic constraint at the crack tip, as shown in Figure 5.1. The ratio of K_J for the RV ((K_{JRV})) to that for the C(T) specimen (K_{JCT}) at the same σ_w is defined as χ, given by the following equation.

$$\chi = K_{JCT} / K_{JRV} \tag{5.1}$$

This standard defines two evaluation levels for χ in the context of the RV's PTS event:

Level I (Simplified Evaluation)

χ is formulated as a function of the material parameters m, R_Y, and the load level K_{JRV}/σ_Y. m is selected as either 10 or 20, as specified in Appendix A.

Level II (Detailed Evaluation)

Using m and R_Y as parameters, finite element (FE) analyses are conducted separately for the RV and C(T) specimens (standard fracture toughness specimens) to calculate the σ_w- K_J relationships. The relation between K_{JRV} and K_{JCT} that yields equivalent σ_w values is obtained by equation (5.1). m is selected as 10 or 20 as specified in Appendix A, or alternatively determined by fracture toughness testing at representative temperatures where brittle fracture occurs, combined with Weibull stress analysis.

The evaluation flow of χ for Levels I and II is shown in Figure 5.2.

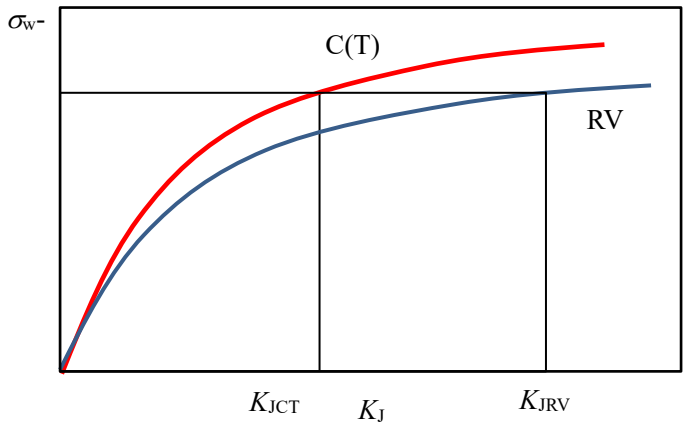


Fig. 5.1 σ_w- K_J relation of C(T) specimen and RV

Copyright © 2026 The Japan Welding Engineering Society, All Rights Reserved.

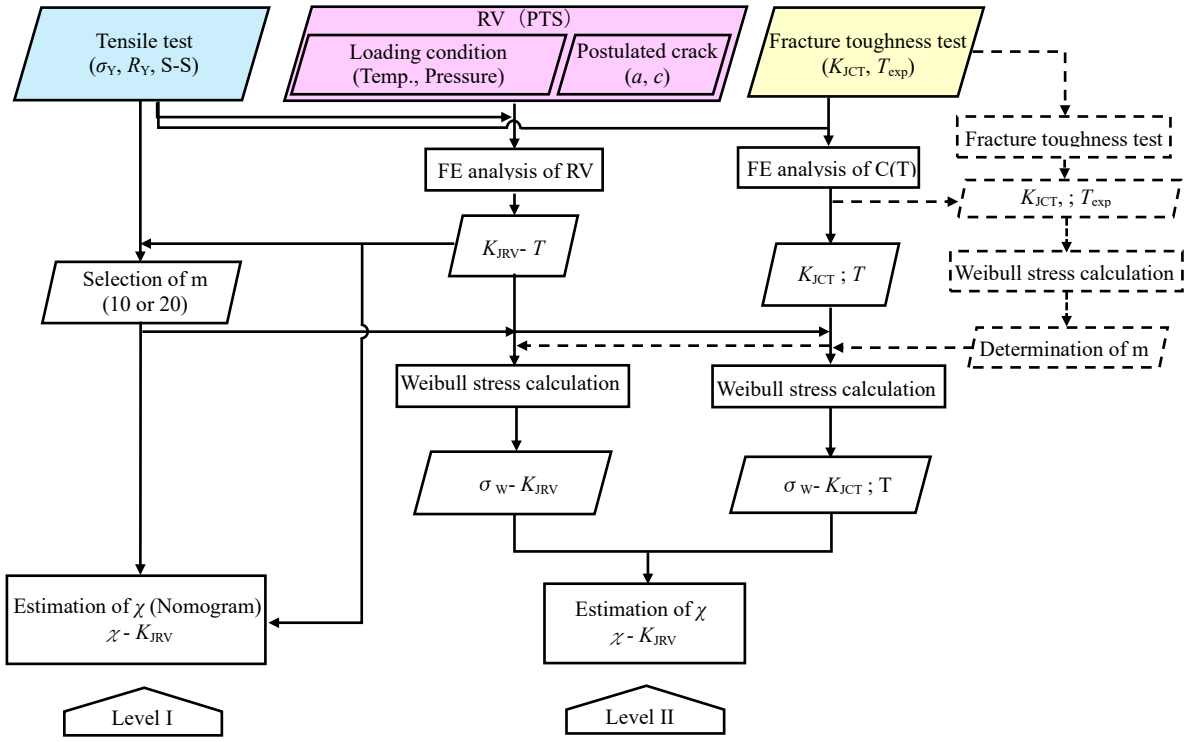


Fig. 5.2 Evaluation flow χ of for level I and level II

6. Evaluation of χ

6.1 Overview

This section specifies the method for determining the correction factor χ used to adjust K_J of the RV. Two calculation methods are provided, Level I and Level II. Level I calculates χ using the material properties σ_Y, R_Y, and m with a prescribed formula. Level II calculates χ from the σ_w-K_J relationships obtained from FE analyses of standard specimens and the RV.

6.2 Level I Evaluation of χ (Simplified Evaluation)

In the Level I evaluation, χ is calculated through the following steps, as illustrated in Figure 5.2:

Step 1: Perform transient heat conduction and stress analyses under the specified loading conditions, and calculate the time-dependent temperature at the deepest point of the flaw of the RV (see Figure 6.1), as well as the time-dependent stress-strain field.

Step 2: Using the time-dependent stress-strain field obtained in Step 1, determine the relationship between the temperature T at the deepest point of the flaw and K_{JRV}, i.e., the K_{JRV}-T curve (Figure 6.2).

Copyright © 2026 The Japan Welding Engineering Society, All Rights Reserved.

Step 3: Calculate χ using the following equation. Note that χ is limited to a maximum value of 1. To capture the maximum χ within the range of K_{JRV} obtained in Step 2, calculate χ at multiple K_{JRV} points (or corresponding crack tip temperatures T) (see Figure 6.4).

$$\chi = \text{Max}\,[Ax+B,\ Cx+D,\ E] \tag{6.1}$$

where the coefficients A, B, C, D, and E are determined by $F_1\ m + F_2\ R_Y + F_3$ using the values of F_1, F_2, and F_3 corresponding to a and c given in Table 6.1.

For values for a and c not listed, linear interpolation shall be applied.

The variable x is defined as:

$$x = K_{JRV} / \sigma_Y \tag{6.2}$$

The Weibull shape parameter m is taken as 10 or 20, or alternatively values from relevant literature may be used.

The applicable range of the formulated χ is as follows.

$10 \leqq m \leqq 30$
$0.6 \leqq R_Y \leqq 0.95$
$450\text{MPa} \leqq \sigma_Y \leqq 900\text{MPa}$
$5\text{mm} \leqq a \leqq 10\text{mm}$
$15\text{mm} \leqq 2c \leqq 60\text{mm}$
$100\text{mm} \leqq t \leqq 250\text{mm}$
$K_J \leqq 120\ \text{MPa}\sqrt{\text{m}}$

Examples of the χ - K_{JRV} / σ_Y relationship based on equations (6.1) and (6.2) for m=10 are shown as three straight lines in Figure 6.5.

6.3 Level II Evaluation of χ (Detailed Evaluation)

As illustrated in Figure 5.2, the Level II evaluation may utilize m from Level I or determine m through Weibull stress analysis of fracture toughness data and specimen models for the material's standard specimens. The calculation steps for χ in Level II are as follows:

Step 1: Perform transient heat conduction and stress analyses under the loading conditions, and calculate the time-dependent temperature at the deepest point of the flaw of the RV (see Figure 6.1), as well as the time-dependent stress-strain field.

Step 2: Using the time-dependent stress-strain field obtained in Step 1, establish the relationship between

Copyright © 2026 The Japan Welding Engineering Society, All Rights Reserved.

the temperature T at the deepest point of the flaw and K_{JRV}, i.e., the K_{JRV}-T curve (see Figure 6.2).

Step 3: Calculate the Weibull stress based on the time-dependent stress-strain field from Step 1 in accordance with ISO 27306:2016 and determine the σ_w-K_{JRV} relationship.

Step 4: For the standard specimen, perform Weibull stress analyses at temperature conditions corresponding to the temperatures T_i at the deepest point of the flaw at transient time points i=1 ～n (with n = 3 points recommended) and obtain the σ_w-K_{JCT} curve (see Figure 6.3). In cases where ductile crack growth occurs, perform FE analyses incorporating damage models prior to Weibull stress analysis as described in ISO 27306:2016.

Step 5: For each temperature point, determine σ_{wi} corresponding to K_{Ji} of the RV from the σ_w-K_{JRV} curve. Then, find the corresponding K_J of the C(T) specimen from the σ_w-K_{JCT} curve with the same σ_{wi} (see Figure 6.3). Using these values of K_{JRV} and K_{JCT}, calculate χ according to equation (5.1).

Since K_{JRV} varies with temperature, calculate χ at multiple transient temperature points as performed in Level I (see Figure 6.4).

Table 6.2 summarizes the evaluation levels of χ and the required information for each level.

Copyright © 2026 The Japan Welding Engineering Society, All Rights Reserved.

Table 6.1 Coefficients for calculating plastic constraint correction factors

a (mm)	c (mm)	Coefficient	F_1	F_2	F_3
10	30	*A*	-0.0605	-9.65	5.94
		B	-0.000814	0.439	0.795
		C	0.015	-5.46	2.35
		D	-0.0103	-0.0896	1.25
		E	-0.00747	-1.13	1.69
	15	*A*	-0.057	-10.3	5.26
		B	0.00187	0.337	0.827
		C	-0.00851	-3.26	1.16
		D	-0.00423	-0.545	1.34
		E	-0.00585	-1.16	1.56
5	15	*A*	-0.046	-9.41	1.29
		B	0.00157	0.201	1.06
		C	-0.0162	-6.89	3.41
		D	-0.00109	-0.0228	0.87
		E	-0.00325	-0.946	1.33
	7.5	*A*	0.0179	-22.5	6.63
		B	-0.000781	1.17	0.581
		C	-0.0114	-6.12	3.08
		D	0.00183	-0.288	0.897
		E	0.000301	-1.11	1.31

Copyright © 2026 The Japan Welding Engineering Society, All Rights Reserved.

Table 6.2 Required information for evaluation of χ for level I and level II

	Level I Evaluation (Simplified Evaluation))	Level II Evaluation (Detailed Evaluation)
Required Information	- m=10 or 20 - σ_Y - R_Y	- m in Level I, or m determined by fracture toughness tests - σ_Y - R_Y - Flaw shape and dimension - Stress-strain curve for FE analysis (temperature dependent)
Plastic constraint correction factor, χ	χ = Max [$Ax+B$, $Cx+D$, E] A, B, C, D, and E are determined by F_1 m + F_2 R_y + F_3 using F_1, F_2, and F_3 for a and c given in Table 6.1.	It is calculated using the following equation by employing the K_J of the standard test specimen (K_{JCT}) and the K_J of the structure (K_{JRV}) corresponding to the same σ_w. $\chi=K_{JCT}/K_{JRV}$
Applicable range	Cleavage-type brittle fracture $10 \leqq m \leqq 30$ $0.6 \leqq R_Y \leqq 0.95$ $450\text{MPa} \leqq \sigma_Y \leqq 900\text{MPa}$ $5\text{mm} \leqq a \leqq 10\text{mm}$ $15\text{mm} \leqq 2c \leqq 60\text{mm}$ $100\text{mm} \leqq t \leqq 250\text{mm}$ $K_J \leqq 120\ \text{MPa}\sqrt{\text{m}}$	Cleavage-type brittle fracture and cleavage-type brittle fracture after small ductile crack growth

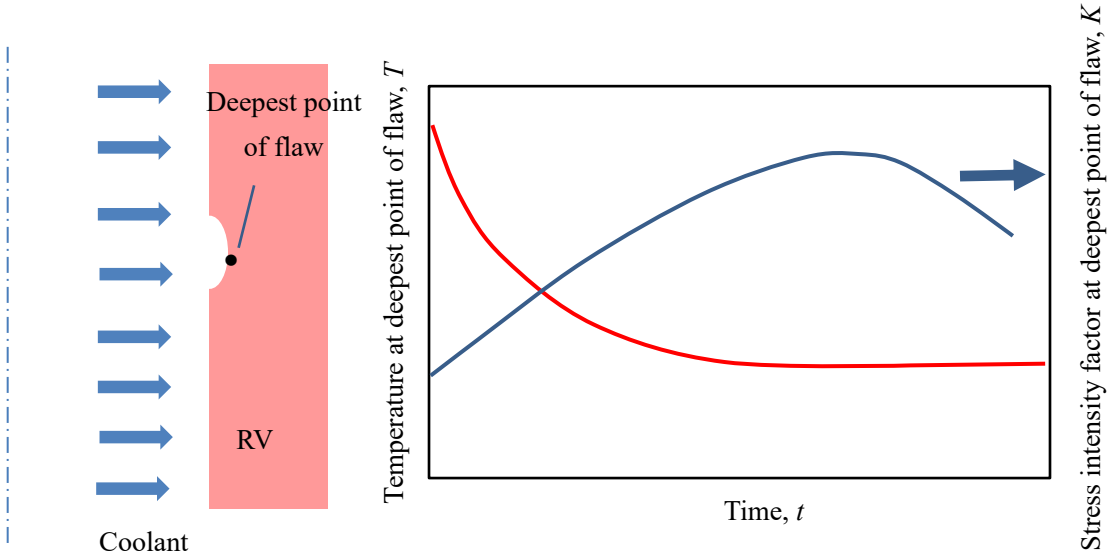


Fig. 6.1 Time-dependent temperature and stress intensity factor at deepest point of flaw by PTS event

Copyright © 2026 The Japan Welding Engineering Society, All Rights Reserved.

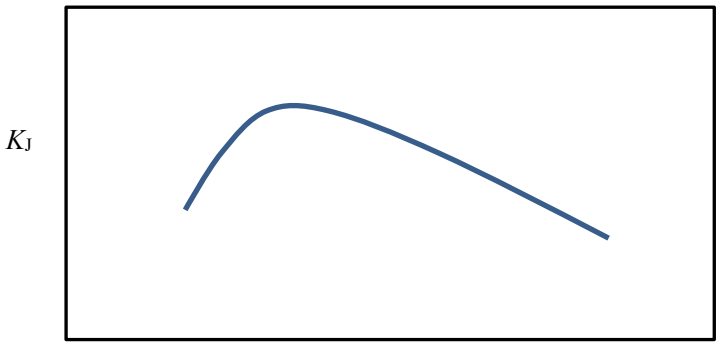


Fig. 6.2 K_J-T relation of RV

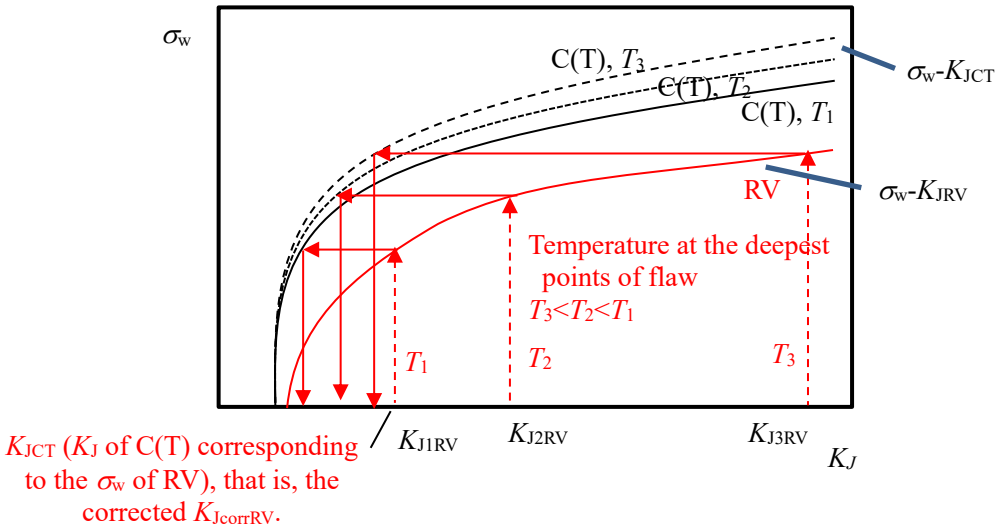


Fig. 6.3 Derivation of χ from stress intensity factor of RV

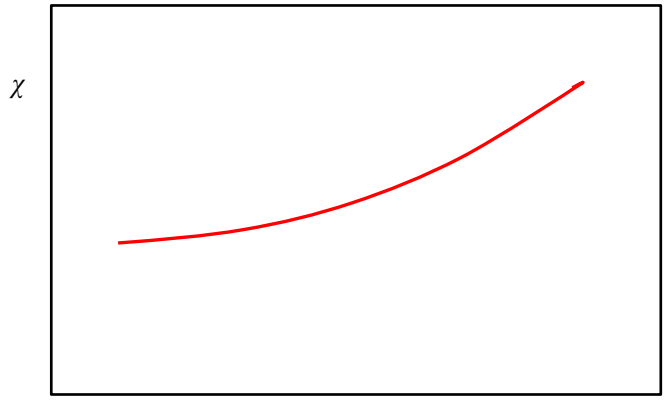


Fig. 6.4 χ -T relation

Copyright © 2026 The Japan Welding Engineering Society, All Rights Reserved.

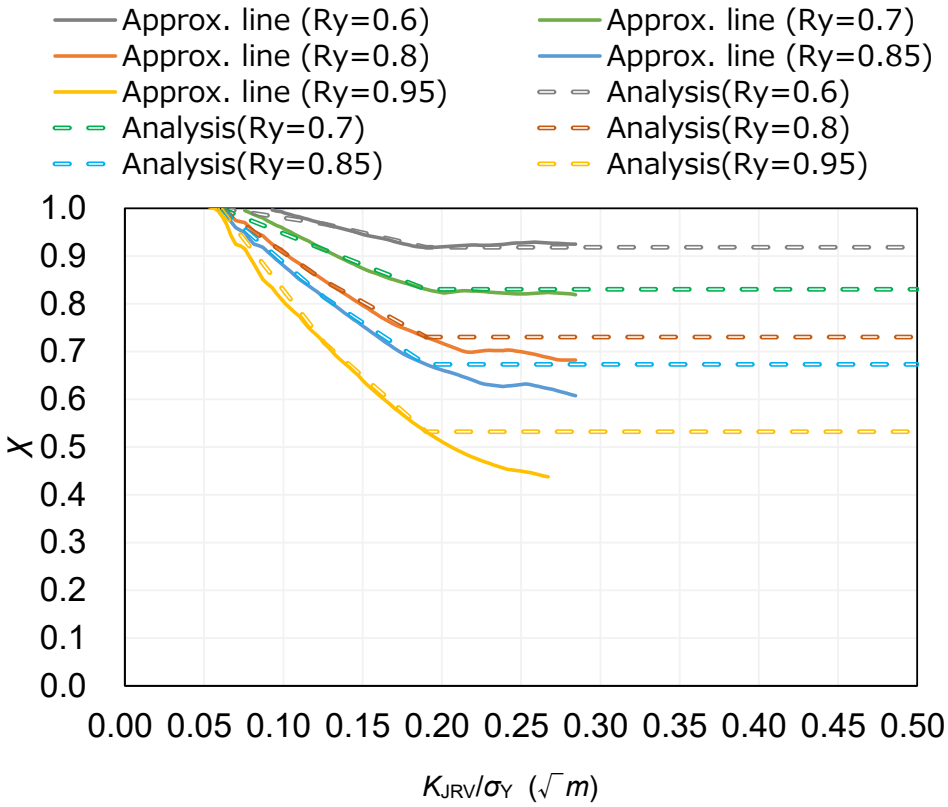


Fig. 6.5 Relationship between formulated χ and K_J for plate model (m=10)

7. Setting of *m*

7.1 Overview

The *m* value of the target material shall be determined according to the evaluation level described below.

7.2 Setting of *m* for Level I Evaluation

The value *m* shall be estimated from the material's fracture toughness data in accordance with Appendix A.1. If other reliable information is available, the corresponding *m* may be used. In cases where fracture toughness data are not available, fracture toughness tests shall be conducted using three standard specimens according to ASTM 1820 or ISO 12135, and the average value shall be used. The fracture toughness test shall be performed at the temperature at which the material undergoes brittle fracture, employing a 25 mm thick standard specimen. For specimens of thicknesses other than 25 mm, the fracture toughness corrected to 25 mm thickness shall be calculated using the following equation.

$$K_{Jc(25)} = 20 + (K_{Jc(B)} - 20)\,(B/25)^{1/4} \tag{7.1}$$

Copyright © 2026 The Japan Welding Engineering Society, All Rights Reserved.

7.3 Setting of *m* for Level II Evaluation

The *m* used in Level II evaluation is based on the *m* determined in Level I evaluation as described in Section 7.2. Alternatively, *m* may be directly determined for the material by performing fracture toughness tests at brittle fracture temperatures on standard specimens in accordance with ASTM 1820 or ISO 12135. The Weibull distribution parameters of the two-parameter Beremin model shall be determined as described in Annex B of ISO 27306:2016. Although ISO 27306:2016 recommends using 30 specimens for a single test method, fracture tests with fewer specimens may be acceptable if validity is demonstrated. Since *m* may not be uniquely determined by the single test method, it may also be calculated using a two-shape test method employing two specimen geometries: a standard fracture toughness specimen with high constraint and a shallow-flaw specimen with low constraint.

8. Plastic Constraint Correction in Fracture Assessment

Using the χ-T relationship obtained in Chapter 7, the K_{JRV}-T curve shall be corrected as illustrated in Figure 8.1.

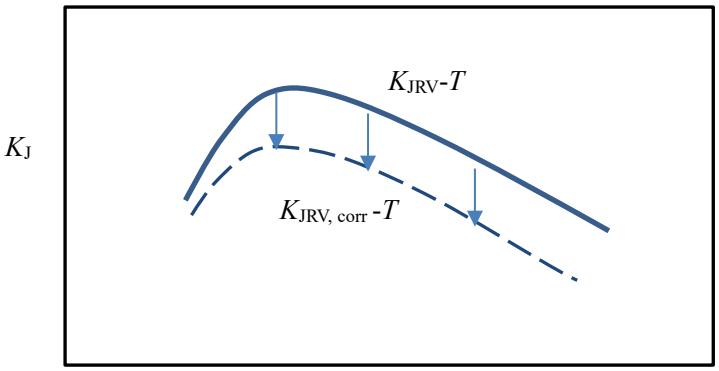


Fig. 8.1 K_{JRV}-T relation before and after correction

Fracture evaluation shall be conducted by comparing the plastic constraint-corrected K_{JRV}-T relationship ($K_{JRV,\ corr}$ -T) of the RV with the K_{Jc} - T relationship. The flow of the RV integrity evaluation using χ is shown in Figure 8.2. As demonstrated in Figure 8.3, it is confirmed that the $K_{JRV,corr}$ -T curve of the RV does not intersect with the K_{JcCT} - T curve of the C(T) specimen, indicating an increased safety margin compared to conventional methods.

Note that when considering WPS, the decreasing trends of K_{JRV} -T and $K_{JRV,corr}$ -T curves with decreasing temperature shall not be used for fracture evaluation.

Copyright © 2026 The Japan Welding Engineering Society, All Rights Reserved.

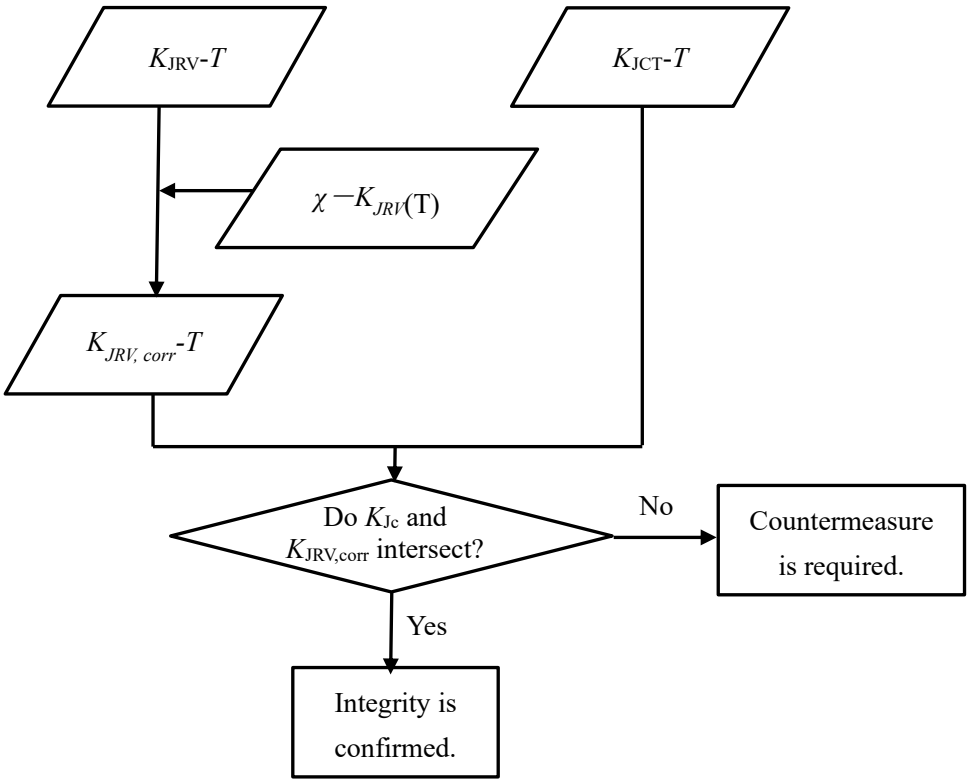


Fig. 8.2 Integrity evaluation flow of RV using χ

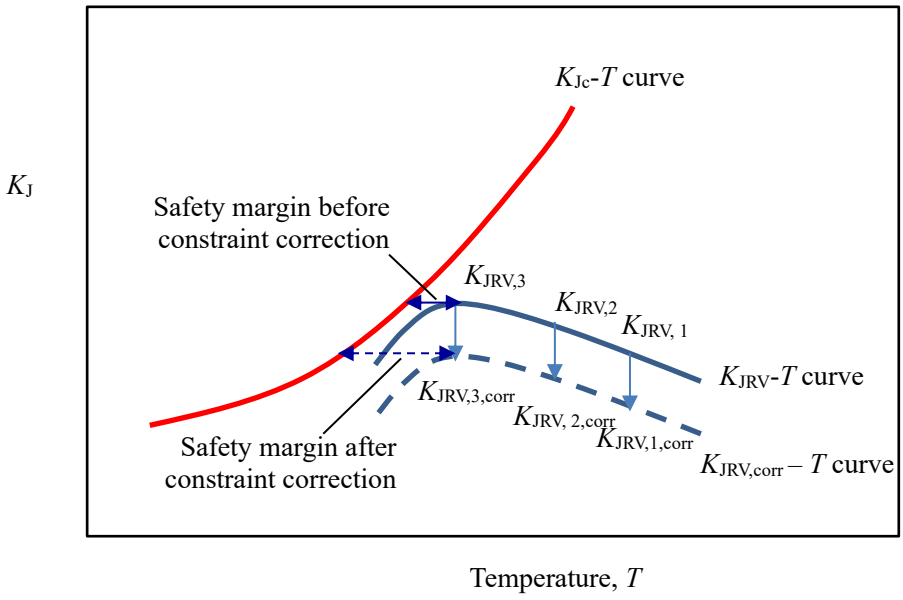


Fig. 8.3 K_J-T relation of RV and fracture toughness specimen

Copyright © 2026 The Japan Welding Engineering Society, All Rights Reserved.

Appendix A (Mandatory) Method for Calculating Weibull Parameter *m*

Introduction

This appendix presents the calculation method for the Weibull parameters m and σ_u, which define the Weibull distribution of the Weibull stress used to evaluate the fracture probability due to cleavage fracture based on the Beremin model. This appendix forms an integral part of the prescriptive provisions of this standard.

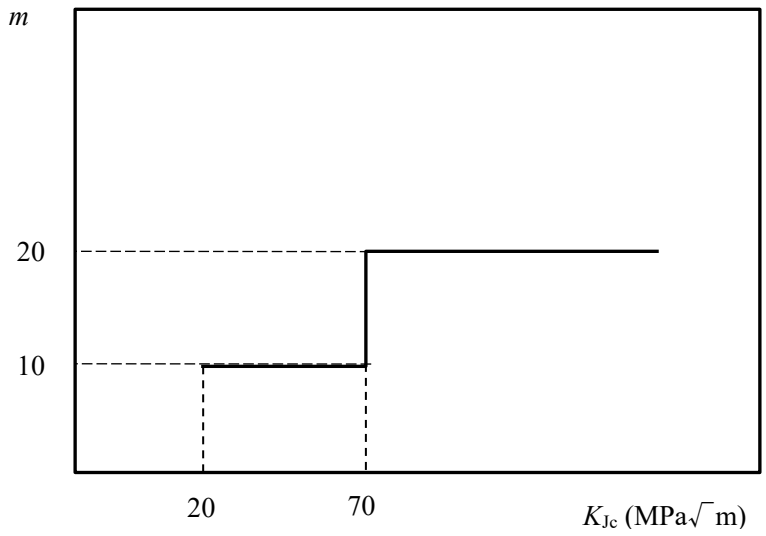
1. Determination of *m* in Level I

The Weibull parameter m used in Level I evaluation shall be determined based on the fracture toughness K_{Jc} obtained from standard specimens according to following equations.

$$\left.\begin{array}{lll} m=10 & K_{Jc} \leqq 70 & (\mathrm{MPa}\sqrt{\mathrm{m}}) \\ m=20 & K_{Jc} > 70 & (\mathrm{MPa}\sqrt{\mathrm{m}}) \end{array}\right\} \quad \text{(A1.1)}$$

Equation (A1-1) is based on Appendix Figure A1.1, which correlates m with $\delta_{cr,\ ave\text{-}25}$ by converting $\delta_{cr,\ ave\text{-}25}$ to K_{Jc} based on the relationship shown in between shown in Figure A.1 of Annex A in ISO 27306:2016.

It should be noted that K_{Jc} typically represents the average fracture toughness obtained from three standard fracture toughness specimens. The fracture toughness tests shall be conducted in accordance with ASTM 1820 or ISO 12135 at the temperature at which the material exhibits brittle fracture.



Appendix Fig. A1.1 Relation between Weibull parameter *m* and fracture toughness K_{Jc}

Copyright © 2026 The Japan Welding Engineering Society, All Rights Reserved.

If fracture toughness test data for fracture assessment are not available, three fracture toughness tests shall be conducted using standard specimens.

2. Determination of *m* in Evaluation Level II

2.1 Using Single Geometry Specimens

In Level II evaluation, fracture toughness tests shall be conducted on the target material using standard specimens to determine the Weibull parameter *m*. The calculation method is specified in Annex B of ISO 27306:2016. The fracture toughness tests shall be performed in accordance with ASTM 1820 or ISO 12135 at the temperature at which the material undergoes brittle fracture.

2.2 Using Two Specimen Geometries with Different Constraint Levels

When fracture toughness specimens fracture under small-scale yielding conditions, *m* may not be uniquely determined using single-geometry specimens. In such cases, *m* and σ_u may be calculated using the two-geometry test method, which employs two types of specimens: a standard fracture toughness specimen with high constraint and a toughness specimen with a shallow flaw exhibiting low constraint.

Copyright © 2026 The Japan Welding Engineering Society, All Rights Reserved.

Appendix B (Nonmandatory)

Example Calculation of Plastic Constraint Correction Factor χ

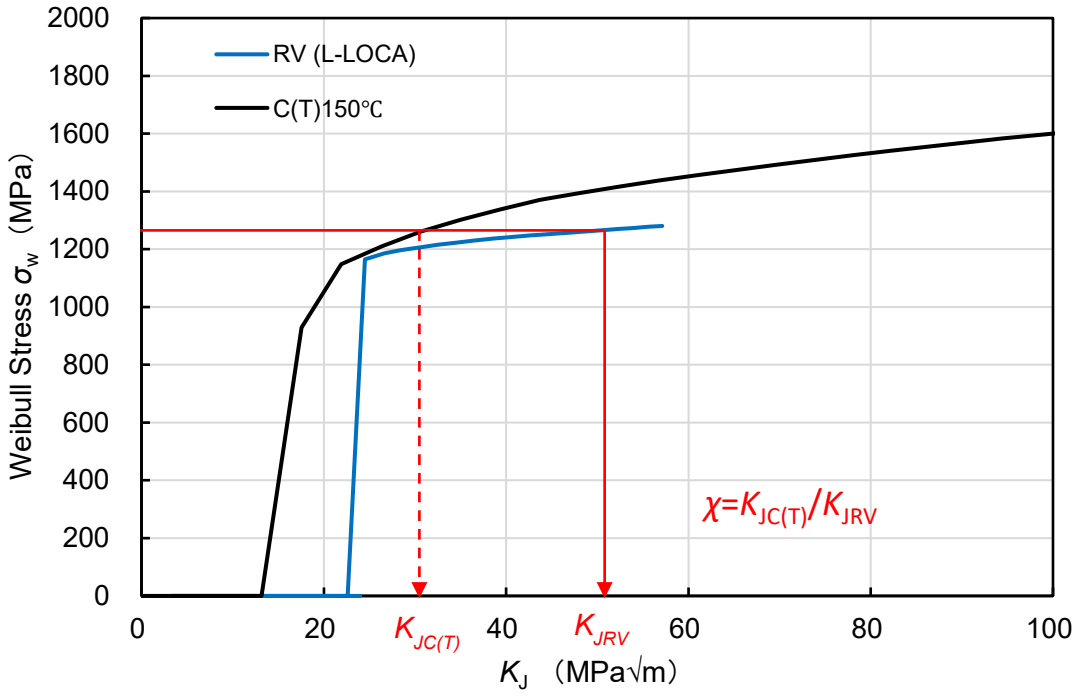
Introduction

This appendix provides an example calculation of the Level I plastic constraint correction factor χ. Note that this appendix is not part of the mandatory standard.

The plastic constraint correction factor χ is a coefficient used to convert the K_J of a structure exhibiting low plastic constraint into an equivalent K_J corresponding to the constraint effect of standard specimens with high plastic constraint, such as C(T) specimens and SE(B) specimens with $a/W = 0.5$.

As an example of determining χ, Appendix Figure B1.1 illustrates the σ_w-K_J relationships for the reactor pressure vessel under the most severe large LOCA condition during the PTS transient, alongside the σ_w-K_J relationship of the C(T) specimen[1]. The plastic constraint correction factor χ is obtained by calculating the respective K_{JRV} and K_{JCT} values corresponding to the same Weibull stress using the σ_w-K_J relationships of the structure and fracture toughness specimen, according to the following equation:

$$\chi = K_{JCT} / K_{JRV} \tag{B.1}$$



Appendix Fig. B1.1 Example of determination procedure of correction coefficient χ (RV(Large LOCA))

Copyright © 2026 The Japan Welding Engineering Society, All Rights Reserved.

1. Example Calculation of Formulated Plastic Constraint Correction Factor χ

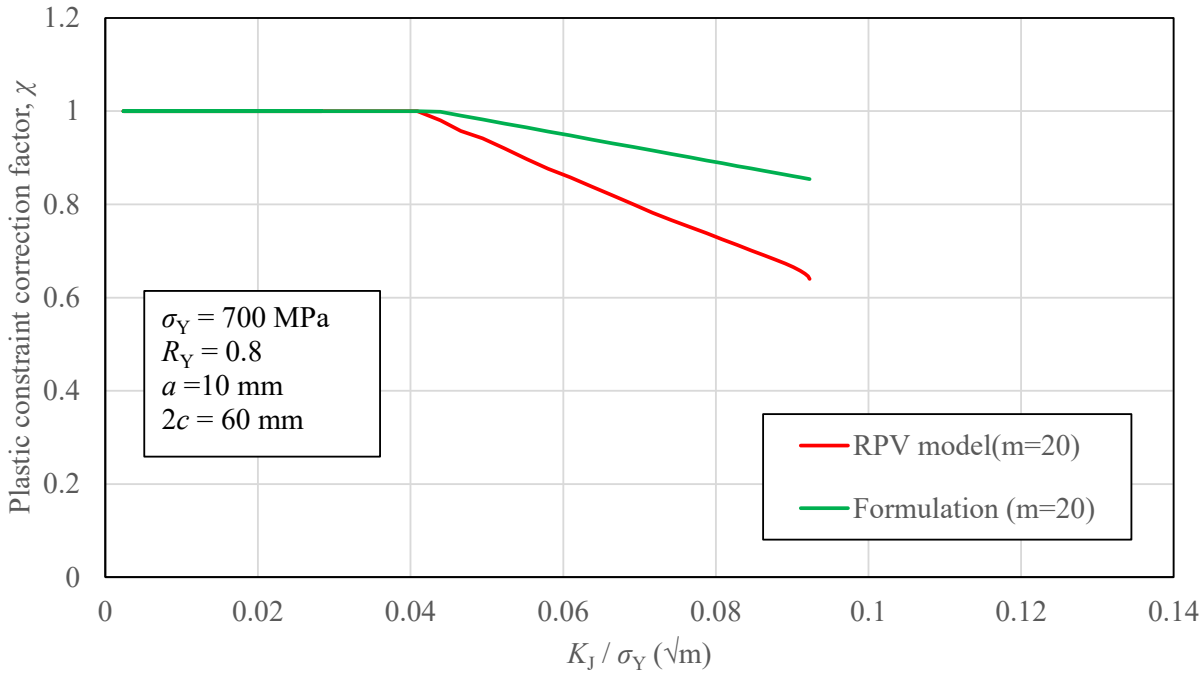
For a material with Weibull parameter m = 20 and R_Y, the K_J -temperature relationship from conventional fracture mechanics analysis and the calculation result of the formulated χ are presented for a pressure vessel containing an assumed semi-elliptical inner surface flaw with a flaw depth of 10 mm and flaw length of 60 mm subjected to a large LOCA.

For m = 20 and R_Y = 0.8, the coefficients (A, B, C, D and E) in the χ calculation formula (Equation B.2) are as follows:

$$\chi = \text{Max}\,[Ax+B,\ Cx+D,\ E] \qquad \text{(B.2)}$$

A = -2.99
B = 0.983
C = -1.72
D = 0.972
E = 0.637

Assuming σ_Y = 700 MPa, the formulated χ-K_{JRV}/σ_Y relationship is illustrated in Appendix Figure B1.2.



Appendix Fig. B1.2 Formulated χ-K_{JRV}/σ_Y relation for large LOCA(m=20, R_Y =0.8)

Copyright © 2026 The Japan Welding Engineering Society, All Rights Reserved.

Appendix C (Reference) Considerations in FE Analysis

Introduction

This appendix describes considerations in the FE analyses conducted to calculate the plastic constraint correction factor χ, as well as for FE analyses incorporating the constraint effect using χ in fracture evaluation. Note that this appendix is not part of the mandatory standard.

1. Stress-Strain Curve

(1) Test Standards

The stress-strain curves used for analysis shall be obtained in accordance with appropriate test standards, such as ASTM E8/E8M-21.

(2) Stress-Strain Curves Used in Analysis

The stress-strain curves employed in the analysis shall be true stress-true strain curves, determined with consideration of the temperature conditions of the transient event under consideration. Accordingly, multiple stress-strain curves at different temperatures should be prepared. However, the stress-strain curve at the representative temperature - defined as the average of the highest and lowest temperatures during the transient event- may be used.

When a Lüders band appears in the stress-strain curve, the curve must be defined with sufficiently fine data points to accurately reproduce this behavior. This is particularly important when an explicit integration method in the analysis code, as the spacing of data points can significantly influence the results and may differ from those obtained by implicit methods. Therefore, careful attention must be given to the selection and distribution of data points. For example, in a commercial-based FEM code Abaqus, if data points are finely spaced in regions exhibiting large changes in stress-strain characteristics such as Lüders bands but coarsely spaced elsewhere, the FE code may interpret the overall data spacing as coarse, potentially neglecting the Lüders band behavior. Hence, the entire stress-strain characteristic must be input with uniformly fine data spacing.

For strain values exceeding those obtained from tests, linear extrapolation of the true stress-true strain relationship shall be applied.

If only the yield point and tensile strength are available as stress-strain characteristics, methods described in WRC Bulletin No.413 or ASME Sec. VIII, Division 2 may be used to specify the true stress-true strain curve.

2 Fracture Toughness

(1) Test Standards

Fracture toughness data used for fracture evaluation shall be obtained in accordance with appropriate test

Copyright © 2026 The Japan Welding Engineering Society, All Rights Reserved.

standards such as ASTM E1921-21 and ASTM E1820-21. For reference, the master curve method may be used to calculate the reference temperature T_0.

(2) Fracture Toughness Required for Analysis

a. Beremin Model Analysis

The Beremin model analysis, which addresses cleavage fracture, requires fracture toughness specimens such as C(T) and SE(B) specimens that satisfy small-scale yielding conditions. Weibull parameters m and σ_u shall be obtained from fracture test data using at least six specimens of the same geometry. Since a single specimen geometry may not yield appropriate Weibull parameters, the two-geometry test method may be employed to determine m, using specimens with different plastic constraint levels -for example, two types of SE(B) specimens with different flaw length/thickness ratios.

b. GTN Model

For GTN model analysis, which deals with ductile crack growth in the ductile-brittle transition temperature region (DBTT Region), fracture toughness tests shall be conducted using two C(T) or SE(B) specimens at temperatures where ductile crack growth on the order of 1 mm occurs. Due to the large number of parameters in the GTN model, verification analyses using specimens with different constraint levels are necessary to ensure the validity of the obtained results.

Copyright © 2026 The Japan Welding Engineering Society, All Rights Reserved.

Appendix 4

Fundamental Study of Fracture Analysis by Benchmark Analysis

Copyright © 2026 The Japan Welding Engineering Society, All Rights Reserved.

Fundamental Study of Fracture Analysis by Benchmark Analysis

A benchmark analysis was conducted using a material designated Low Alloy Steel A, for which existing fracture test data are available, to verify the applicability and evaluation accuracy of brittle fracture analyses, including the Beremin model and damage mechanics model analyses. The benchmark analysis was conducted in three sequential steps, designated as STEP0 through STEP2. The objectives of each STEP are summarized as follows.

The benchmark analyses from STEP0 through STEP2 were performed on the specimens described in Sections 1.1 and 1.2. Seven organizations participated in the benchmark analysis: The University of Osaka (UO), Tokyo University of Science (TUS), Japan Atomic Energy Agency (JAEA), Toshiba Energy Systems & Solutions Corporation (Toshiba), IHI Corporation (IHI), Hitachi and Hitachi-GE Nuclear Energy, Ltd. (Hitachi), and Mitsubishi Heavy Industries, Ltd (MHI).

(STEP0)

Verify the consistency of the FE analysis outputs among the participating organizations. This step aims to confirm that no significant discrepancies arise in the FE analysis results under the prescribed analysis conditions.

(STEP1)

Assess the consistency of Weibull stress and Weibull parameter values obtained by the participants using the Beremin model. For the GTN model, verify the consistency of analysis results when identical parameter values are employed.

(STEP2)

Conduct sensitivity analyses on factors potentially influencing the analysis outcomes, such as element size effects and convergence criteria. For the GTN model, each participant fits the test results and determines their respective parameter values.

Copyright © 2026 The Japan Welding Engineering Society, All Rights Reserved.

1. Benchmark Analysis Conditions

1.1 C(T) Specimen

(1) Material Properties

The material properties used for the analysis are shown below.

・Young's modulus E= 218,409 MPa※1 (-125 ºC)

213,714 MPa (-50 ºC)

※1 After revision of Young's modulus, analyses are conducted with 205,304 MPa.

・Poisson's ratio ν=0.3

・Stress-strain (S-S) characteristics : Measured values at -125 °C and -50 °C are shown in Figures 1.1-1 to 1.1-3.

・For FE analysis, the stress-strain curve shown in Figure 1.1-4 is used.

The nominal stress σ and nominal strain ε were calculated from the load P measured by the load cell and the elongation $\Delta\ell$ measured over the gauge length (ℓ_0 = 50 mm) of the specimen in the tensile test, using the following equations (the tensile specimen geometry is shown in Figure 1.1-5).

Nominal stress: $\sigma = P/A_0$ (1-1)

Nominal strain: $\varepsilon = \Delta\ell/\ell_0$ (1-2)

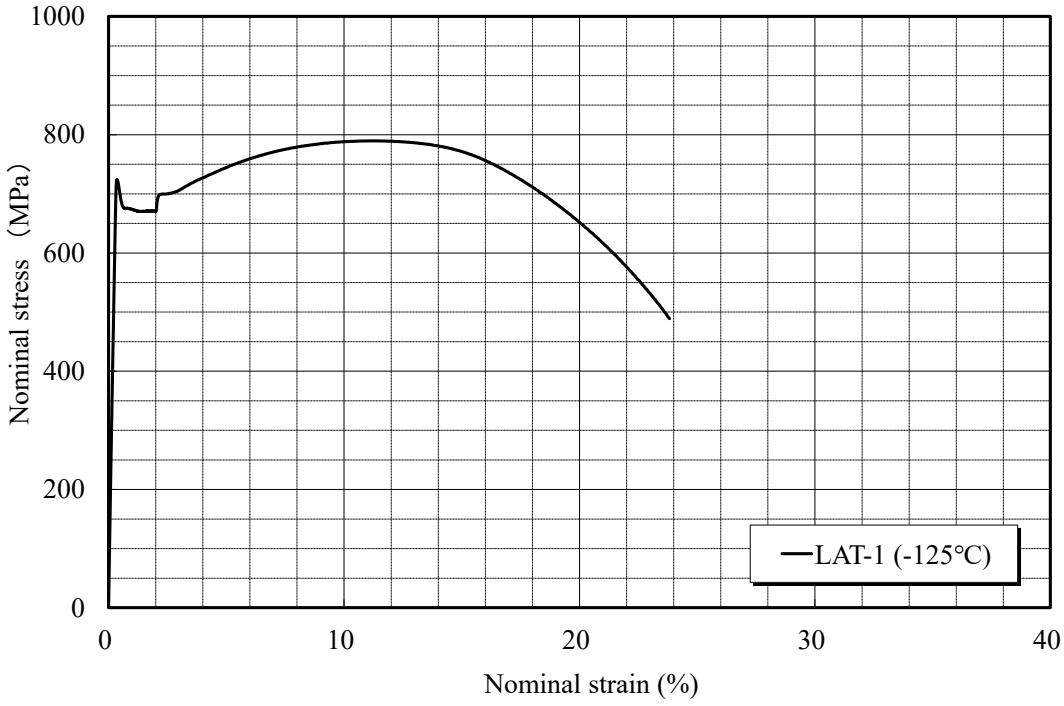
Here, A_0 is the initial cross-sectional area of the test section.

Also, the true stress σ_t and true strain ε_t up to the point of maximum load (onset of necking in the specimen) were calculated from the nominal stress σ and nominal strain ε as follows.

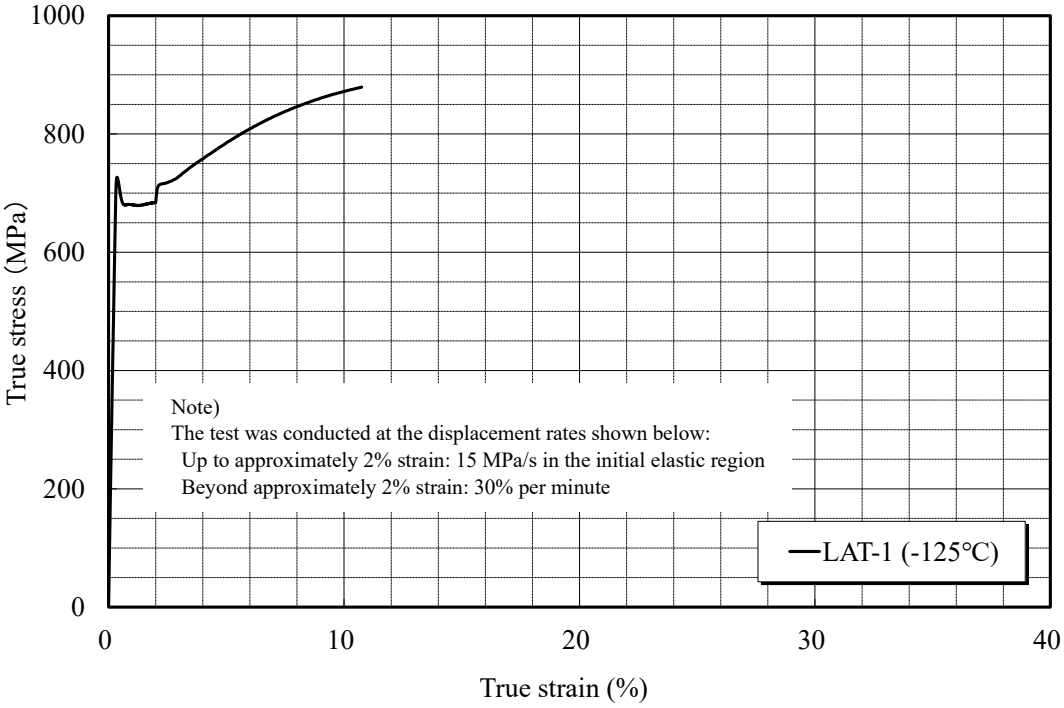
True stress: $\sigma_t = \sigma(1+\varepsilon)$ (1-3)

True strain: $\varepsilon_t = \ln(1+\varepsilon)$ (1-4)

Copyright © 2026 The Japan Welding Engineering Society, All Rights Reserved.



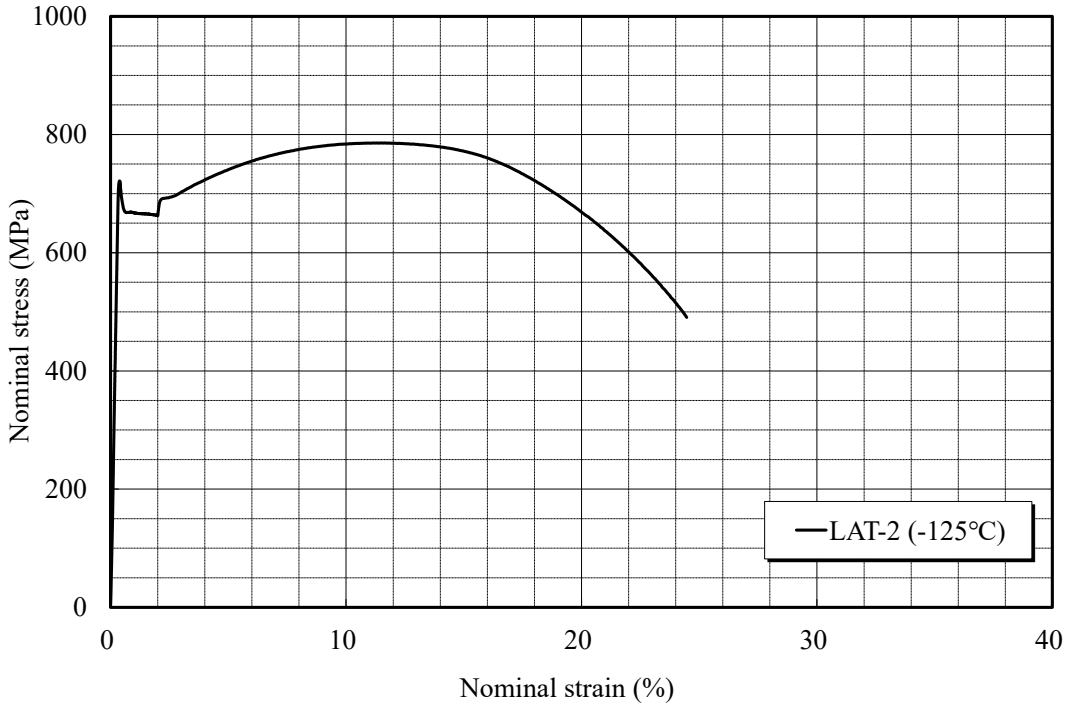
(a) Nominal stress – Nominal strain



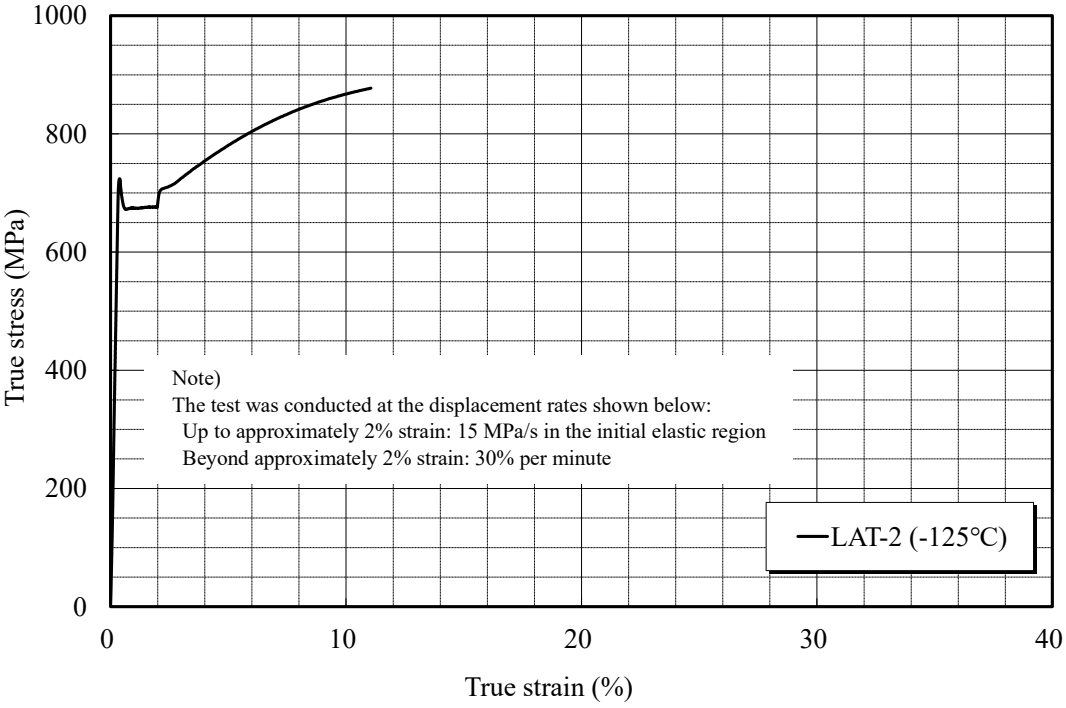
(b) True stress – True strain

Fig. 1.1-1　Stress-strain curve of low alloy steel A (temperature: -125° C, specimen: LAT-1)

Copyright © 2026 The Japan Welding Engineering Society, All Rights Reserved.



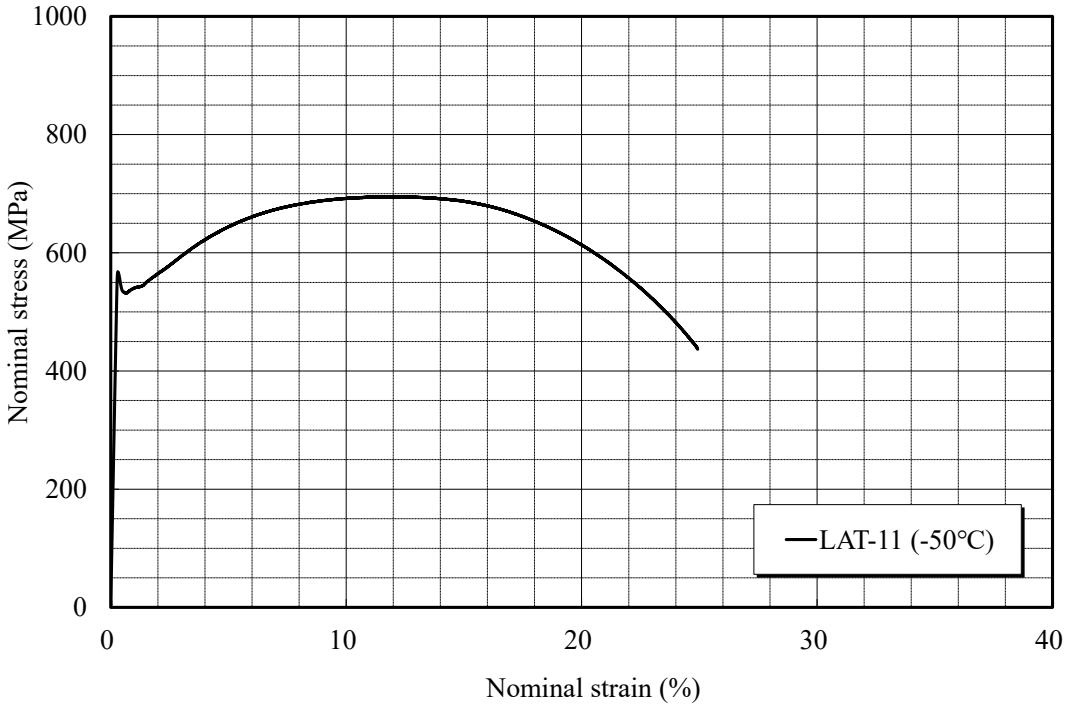
(a) Nominal stress – Nominal strain



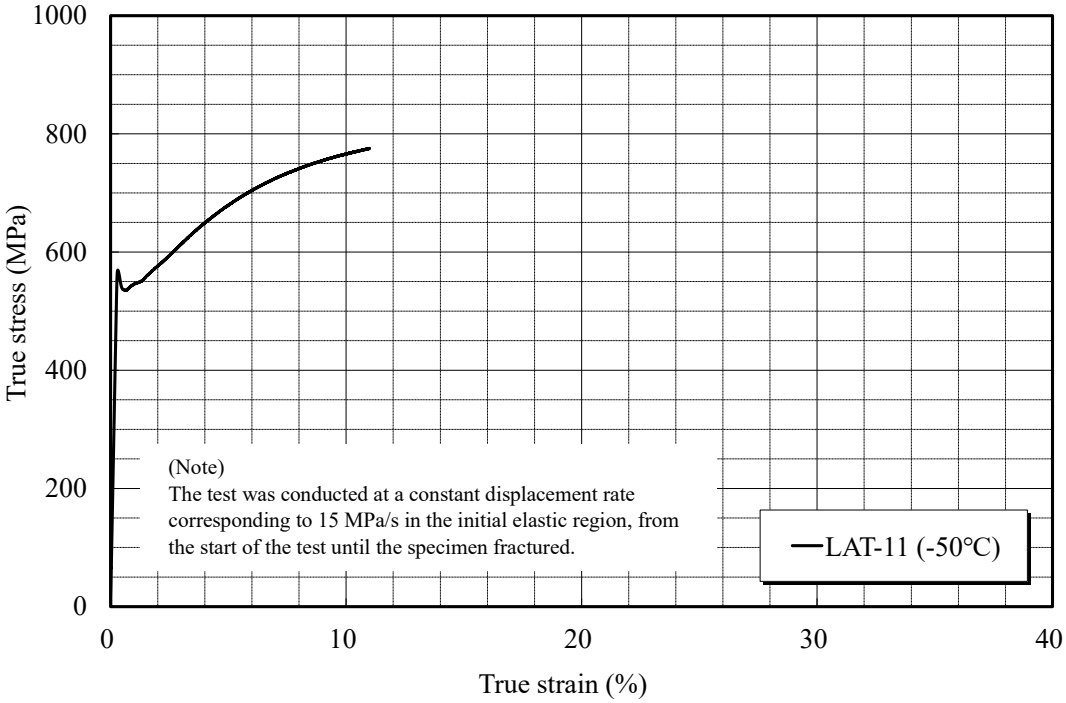
(b) True stress – True strain

Fig. 1.1-2 Stress-strain curve of low alloy steel A (temperature: -125°C, specimen: LAT-2)

Copyright © 2026 The Japan Welding Engineering Society, All Rights Reserved.



(a) Nominal stress – Nominal strain



(b) True stress – True strain

Fig. 1.1-3 Stress-strain curve of low alloy steel A (temperature: -50°C, specimen: LAT-11)

Copyright © 2026 The Japan Welding Engineering Society, All Rights Reserved.

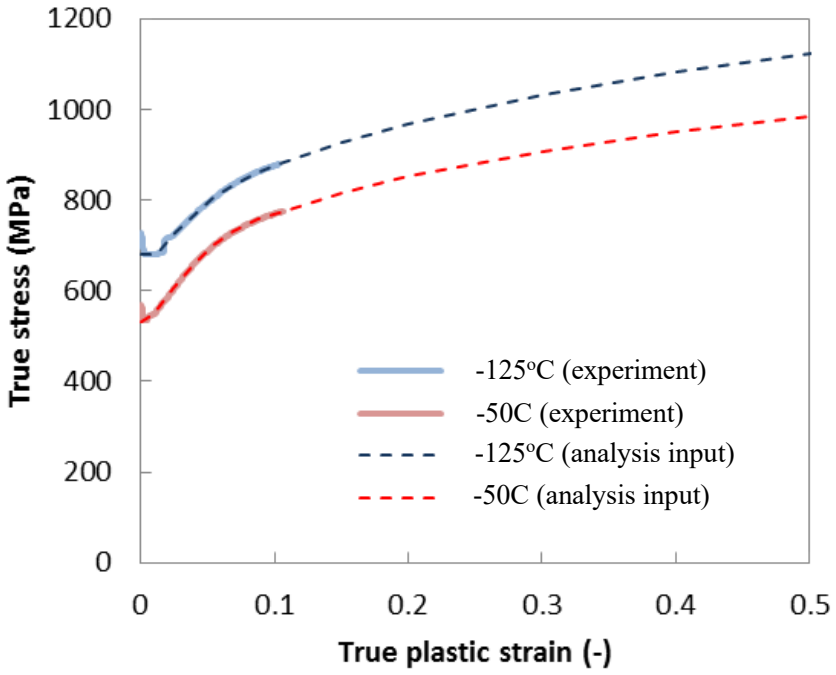
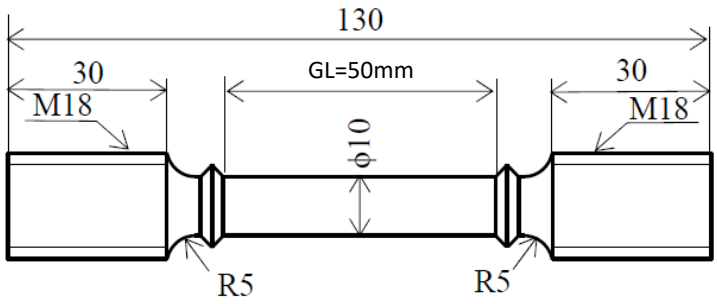


Fig. 1.1-4 True stress- true plastic strain relationship of measurement and FEA input



Unit : mm

Fig. 1.1-5 Geometry of round bar tensile specimen

Copyright © 2026 The Japan Welding Engineering Society, All Rights Reserved.

(2) Specimen Geometry

Key specimen dimensions: The dimensions of the specimen used for testing at -125°C are shown in Figure 1.1-6.

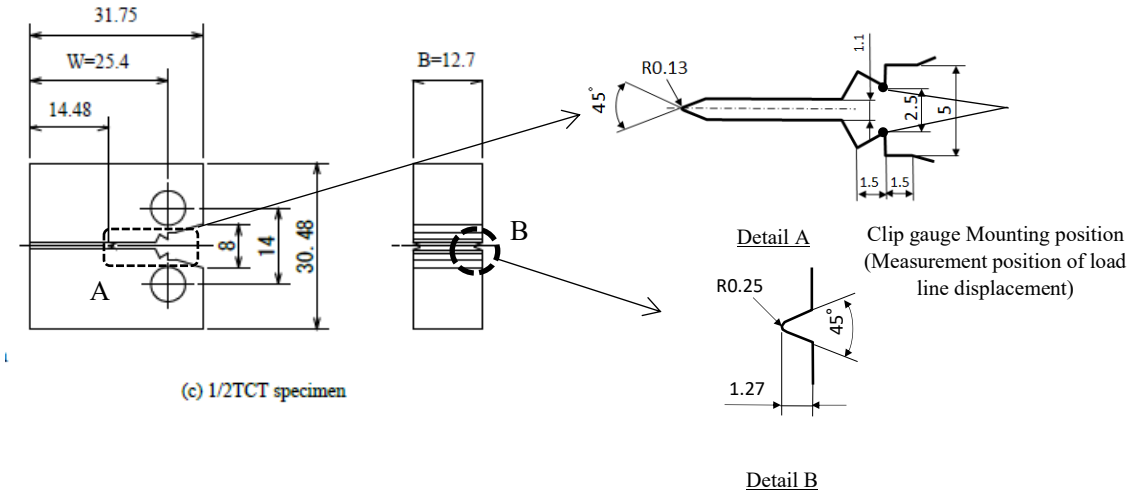


Fig. 1.1-6 Geometry of 1/2TC(T) specimen

Copyright © 2026 The Japan Welding Engineering Society, All Rights Reserved.

(3) Analysis Model

The analysis model is as follows.

Symmetry condition: 1/4 symmetry condition

Element type: 8-node brick elements

FEM model: Crack tip element size: 0.03 mm (see Figure 1.1-7).

In this model, only a 45° sector of the pin part is modeled, and the pin-specimen contact area is integrated. A prescribed displacement is applied to the central node of the pin. The elements of the pin part are assumed rigid compared to the specimen.

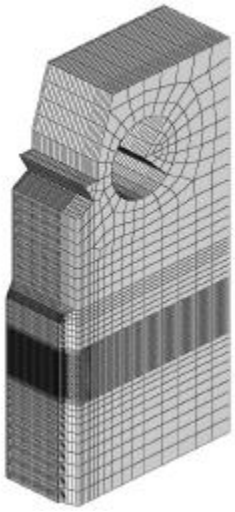


Fig. 1.1-7 FE model of 1/2TC(T) specimen

(4) Initial Crack Length

The initial crack length is as shown in Table 1.1-1.

Following JEAC4216-2011 “Test Method for Determination of Reference Temperature T_o of Fracture Toughness for Ferritic Steel,” MCT-4320 (Measurement of crack size after test completion), the average value in the thickness direction was used.

Copyright © 2026 The Japan Welding Engineering Society, All Rights Reserved.

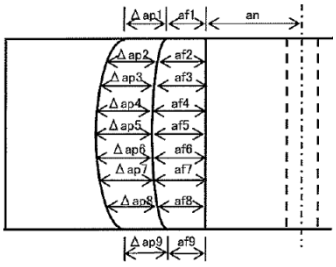
Table. 1.1-1 Fracture toughness test results of 1/2T C(T) (-125°C and -50°C, low alloy steel A)

Specimen ID	Temperature T (°C)	Width W (mm)	Thickness B (mm)	Net thickness B_N (mm)	Initial crack size*1 a_0 (mm)	Fracture Toughness		Ductile crack growth*1 Δa_p (mm)
						J_c (kJ/m^2)	K_{Jc} (MPa√m)	
LAF-2	-125	25.45	12.73	10.20	13.81	22.9	71.5	0.00
LAF-4	-125	25.45	12.73	10.19	13.62	14.2	56.4	0.00
LAF-5	-125	25.46	12.73	10.20	13.74	19.6	66.2	0.00
LAF-6	-125	25.46	12.73	10.20	13.54	24.5	74.0	0.00
LAF-7	-125	25.45	12.73	10.21	13.67	75.0	129	0.00
LAF-8	-125	25.45	12.73	10.21	13.77	45.4	101	0.00
LAF-9	-125	25.46	12.73	10.21	13.60	52.3	108	0.00
LAF-10	-125	25.45	12.73	10.21	13.78	14.8	57.5	0.00
LAF-11	-125	25.45	12.73	10.20	13.85	32.3	84.9	0.00
LAF-12	-125	25.45	12.73	10.21	13.58	62.2	118	0.00
LAF-13	-125	25.40	12.74	10.22	13.31	54.9	111	0.00
LAF-14	-125	25.39	12.74	10.22	13.48	29.6	81.2	0.00
LAF-15	-125	25.37	12.74	10.24	13.49	39.5	93.9	0.00
LAF-16	-125	25.39	12.73	10.21	13.58	27.9	78.9	0.00
LAF-17	-125	25.42	12.73	10.23	13.43	44.8	100	0.00
CT-44	-50	25.43	12.71	10.23	13.53	313	264	0.40
CT-45	-50	25.42	12.71	10.20	13.55	1157	508	2.45
CT-46	-50	25.43	12.72	10.23	13.48	842	433	1.50
CT-51	-50	25.41	12.72	10.22	13.51	502	335	0.75
CT-52	-50	25.42	12.72	10.22	13.76	595	364	0.71
CT-53	-50	25.42	12.72	10.22	13.53	232	228	0.20
CT-54	-50	25.42	12.72	10.22	13.54	220	222	0.15

*1: The crack length was measured at nine locations on the fracture surface of the specimen after testing using a stereomicroscope, as shown below and calculated using the following equation based on JEAC4216-2011. Note that the measured value of the ductile crack growth includes the length of the stretch zone.

Initial crack size: $a_0 = a_n + \{a_{f2}+a_{f3}+a_{f4}+a_{f5}+a_{f6}+a_{f7}+a_{f8}+((a_{f1}+a_{f9})/2)\}/8$

Ductile crack growth: $\Delta a_p = \{\Delta a_{p2}+\Delta a_{p3}+\Delta a_{p4}+\Delta a_{p5}+\Delta a_{p6}+\Delta a_{p7}+\Delta a_{p8}+((\Delta a_{p1}+\Delta a_{p9})/2)\}/8$



Copyright © 2026 The Japan Welding Engineering Society, All Rights Reserved.

(5) Data Obtained from Experiments

The load versus load-line displacement during the test at -125°C is shown in Figure 1.1-8.

The load was measured by a load cell installed in the testing apparatus, and the displacement was measured using a clip gauge attached to the load line of the specimen. The alignment of the test jig and the specimen axis during the test was confirmed by the following procedure:

1) A load rod and U-links were attached to the testing apparatus (the load rod and U-link were connected by screws, and no universal joints or the like were used).

2) The gap occurring when the upper and lower U-links were brought close together was measured with a gap gauge, confirming it was 0.8 mm or less* (see Figure 1.1-9).

3) After attaching the C(T) specimen to the U-links, it was visually confirmed that the gaps between the U-links and the specimen on the left and right sides were approximately equal.

*Note: According to ASTM E399-12 Section A2.2.3, the misalignment of the axes of the upper and lower load rods shall be within +/- 0.8 mm.

Figures 1.1-10 and 1.1-11 show the distribution of ductile crack growth at fracture at -50°C and room temperature, respectively.

The distribution of ductile crack growth within the specimen thickness was measured at nine locations, equally dividing the thickness direction into eight segments on the fracture surface after the test. The measured ductile crack growth length also includes the stretch zone length.

Copyright © 2026 The Japan Welding Engineering Society, All Rights Reserved.

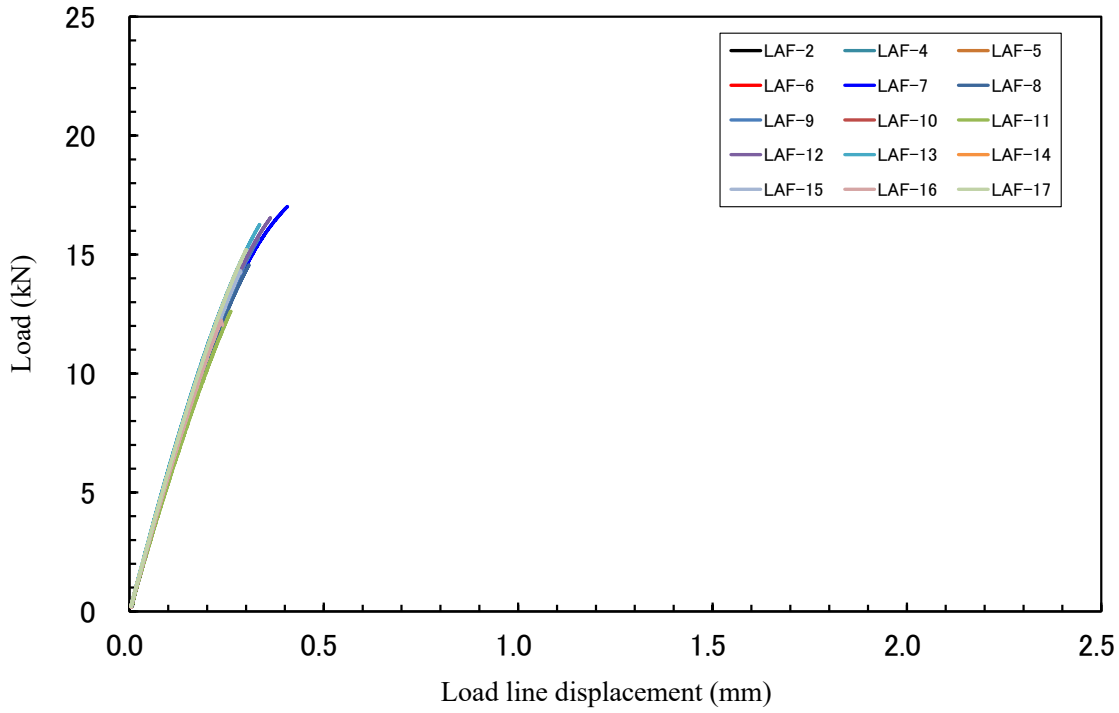
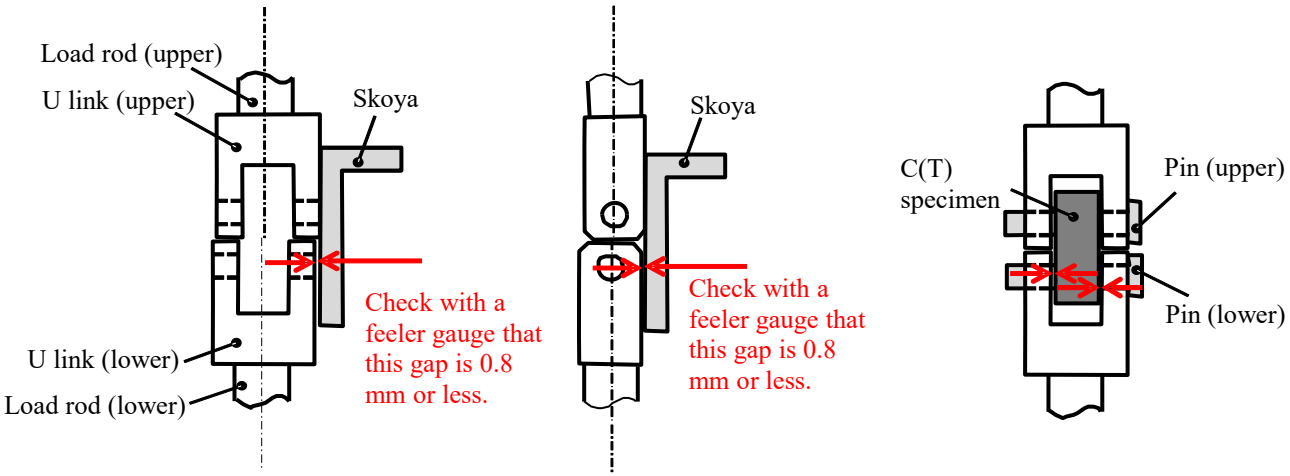


Fig. 1.1-8 Load-load line displacement (1/2TC(T), -125°C, low alloy steel A)



Before mounting the specimen

After mounting the specimen

Fig. 1.1-9 Geometry of attachment of specimen

Copyright © 2026 The Japan Welding Engineering Society, All Rights Reserved.

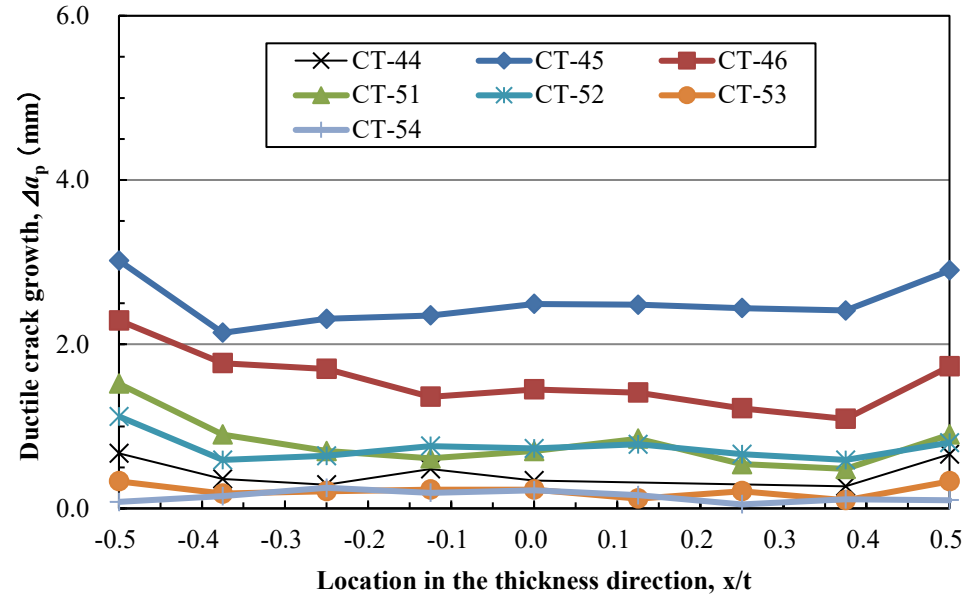


Fig. 1.1-10 Ductile crack growth distribution along thickness (1/2TC(T), -50°C, low alloy steel A)

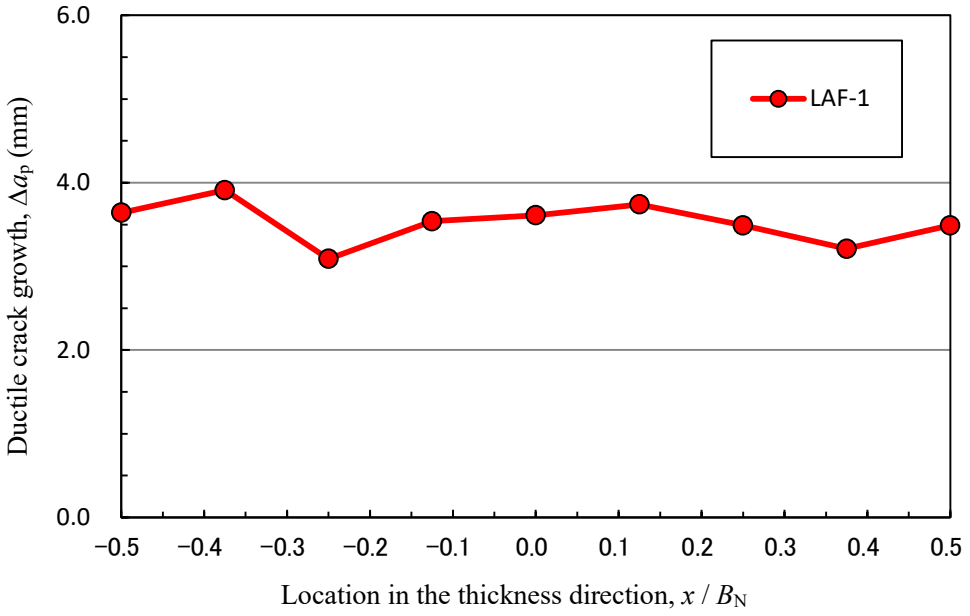


Fig. 1.1-11 Ductile crack growth distribution along thickness (1/2TC(T), RT, low alloy steel A)

Copyright © 2026 The Japan Welding Engineering Society, All Rights Reserved.

(6) Analysis Method

-125ºC：Original Beremin model, two-parameter type

$$P_f = 1 - \exp\left(-\left(\frac{\sigma_w}{\sigma_u}\right)^m\right) \tag{1-5}$$

Here

$$\sigma_w = \left(\frac{1}{V_0}\int_V (\sigma_1)^m dV\right)^{\frac{1}{m}} \tag{1-6}$$

-50ºC：GTN model

$$\Phi = \left(\frac{\sigma_{eq}}{\sigma_0}\right)^2 + 2fq_1\cosh\left(\frac{3}{2}\frac{q_2\sigma_m}{\sigma_0}\right) - \left(1 + q_3 f^2\right) = 0 \tag{1-7}$$

Here

$$f^* = \begin{matrix} f & \text{for} & f \le f_c \\ f_c + K(f - f_c) & \text{for} & f > f_c \end{matrix} \tag{1-8}$$

$$K = \frac{1/q_1 - f_c}{f_F - f_c} \tag{1-9}$$

The GTN model is applied under the condition considering only primary voids, using the GTN model parameters shown in Table 1.1-2.

Table. 1.1-2　GTN model parameters (consideration of initial voids only)

f_F	f_c	ε_N	S_N	f_0	q_1	q_2	f_N
2.50×10^{-2}	4.00×10^{-3}	—	—	3.00×10^{-5}	1.25	1.00	—

Copyright © 2026 The Japan Welding Engineering Society, All Rights Reserved.

1.2 Tensile Specimen with Surface Crack on Flat Plate

(1) Material Properties

The same conditions as for the C(T) specimen shown in Section 1.1 are used.

(2) Specimen Geometry

The specimen geometry is as shown in Figure 1.2-1.

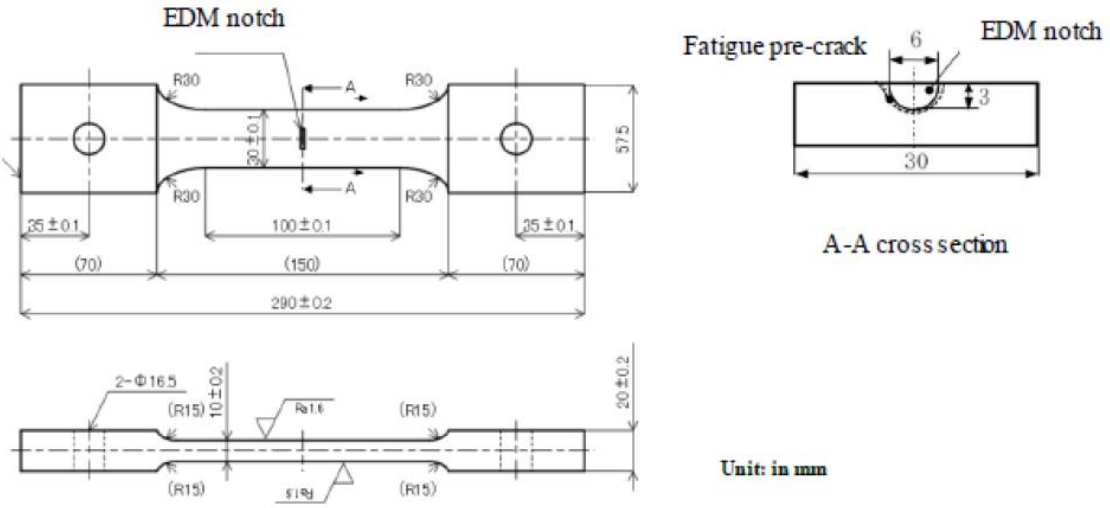


Fig. 1 Geometry of Flat Plate Specimen

Fig. 1.2-1 Geometry of flat plate tensile specimen with surface flaw

(3) Analysis Model

The symmetry condition, element type, and element size are the same as those of the C(T) specimen.

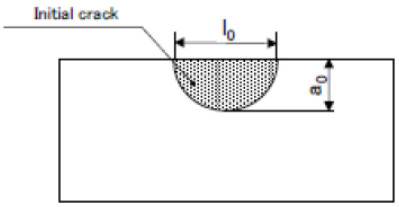
Copyright © 2026 The Japan Welding Engineering Society, All Rights Reserved.

(4) Initial Crack Shape

The initial crack shape is as shown in Table 1.2-1.

Table 1.2-1 Initial flaw shape

Type of specimen	Initial crack size (mm)		Failure load (kN)
	Depth a_0	Length l_0	
Flat Plate	4.59	9.41	192.8
	4.69	9.25	192.2
	5.07	10.80	183.7
	4.90	10.71	186.4
	5.20	10.90	184.7



(5) Data Obtained from Experiments

The load-displacement relationship is shown in Figure 1.2-2.

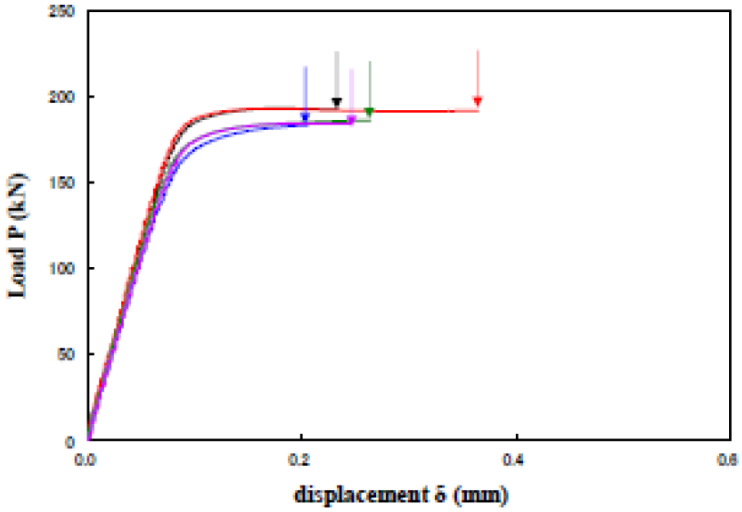


Fig.1.2-2 Load displacement curve of flat plate fracture tests

Copyright © 2026 The Japan Welding Engineering Society, All Rights Reserved.

(6) Analysis Method

As fracture assessment methods considering the plastic constraint effect, the original Beremin model targeting brittle fracture and the GTN model targeting ductile fracture are applied.

$$\sigma_W = \left[\frac{1}{V_0}\int_{V_f}\left(\sigma_{eff}\right)^m dV_f\right]^{1/m} \tag{1-10}$$

Copyright © 2026 The Japan Welding Engineering Society, All Rights Reserved.

2. Benchmark Analysis Results

2.1 Comparison of FE Analysis Outputs

(STEP 0)

FE analyses were conducted on C(T) specimens tested at -125°C, and it was confirmed that no significant differences occurred in the analysis results. The analysis codes, solution methods, and element types used by each organization are shown in Table 2.1-1.

As analysis results, the load versus load-line displacement, the Mises equivalent stress versus equivalent plastic strain at the crack-tip-nearest element in the mid-thickness, and the distributions of crack face normal stress and equivalent plastic strain at the crack-tip-nearest element in the mid-thickness cross-section were compared. The analysis results are shown in Figures 2.1-1 through 2.1-7.

As illustrated, the load versus load-line displacement and equivalent stress versus equivalent plastic strain agreed closely among all organizations.

Regarding the crack face normal stress and equivalent plastic strain, the results from Tokyo University of Science (A, B) differed from those of other organizations, which may be attributed to differences in analysis codes and element types.

Table 2.1-1 FE analysis method

Item	UO	TUS		JAEA	Toshiba	IHI	Hitachi	MHI
		A	B					
Analysis Code	ABAQUS 6.12	Original code	MSC.Marc 2016	ABAQUS 2018	ABAQUS 2017 hf13	ABAQUS 6.13-4	ABAQUS 2018	ABAQUS 6.12
Element Type	Selective Reduced Integration	Selective Reduced Integration	Selective Reduced Integration	Reduced Integration	Reduced Integration	Reduced Integration	Reduced Integration	Reduced Integration
Analysis method	Implicit	Implicit	Implicit	Implicit	Implicit	Implicit	Implicit	Explicit

Copyright © 2026 The Japan Welding Engineering Society, All Rights Reserved.

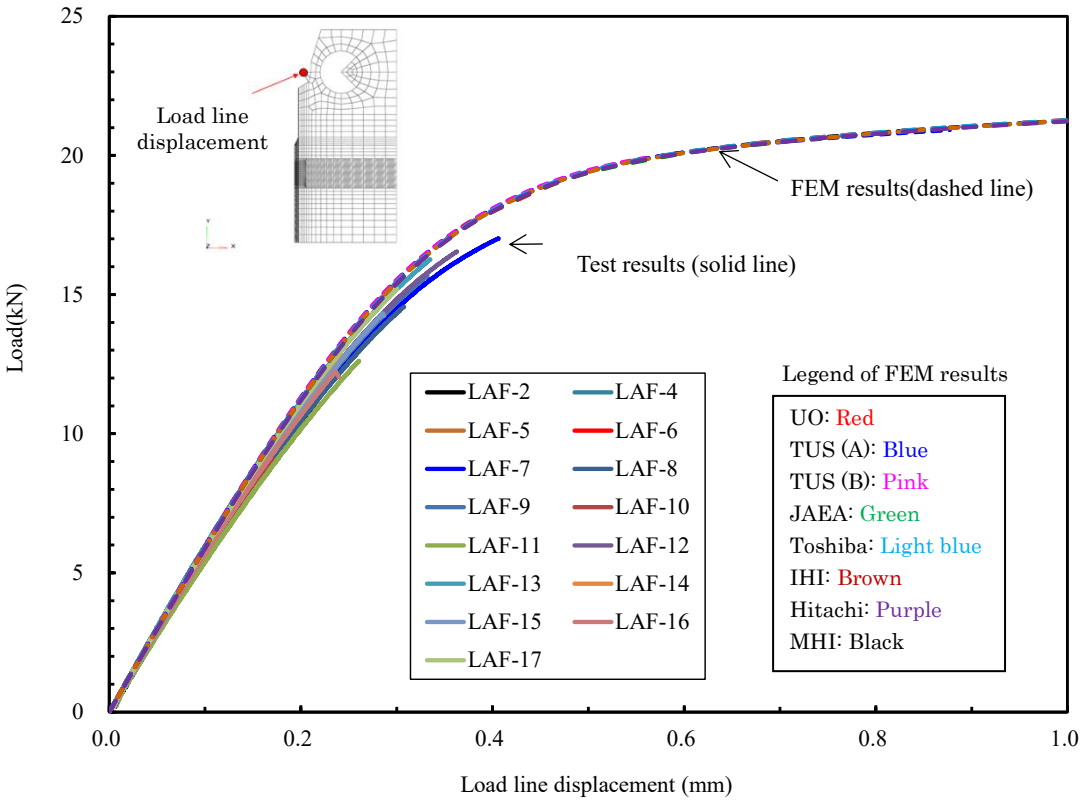


Fig. 2.1-1 Load – load line displacement curve

Copyright © 2026 The Japan Welding Engineering Society, All Rights Reserved.

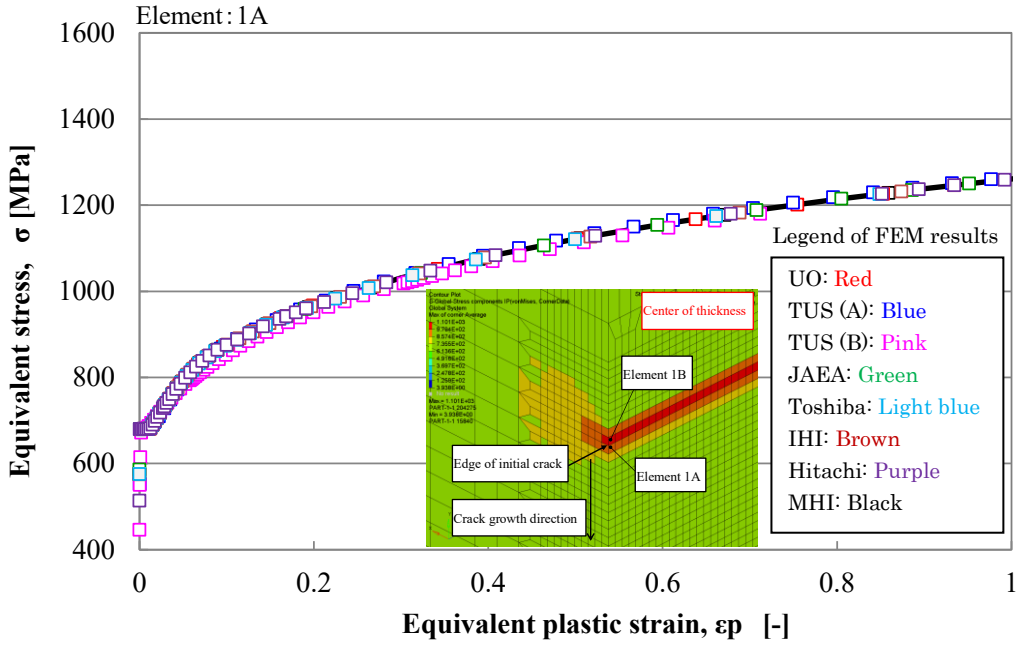


Fig. 2.1-2 Mises equivalent stress – equivalent plastic strain near crack tip (1A)

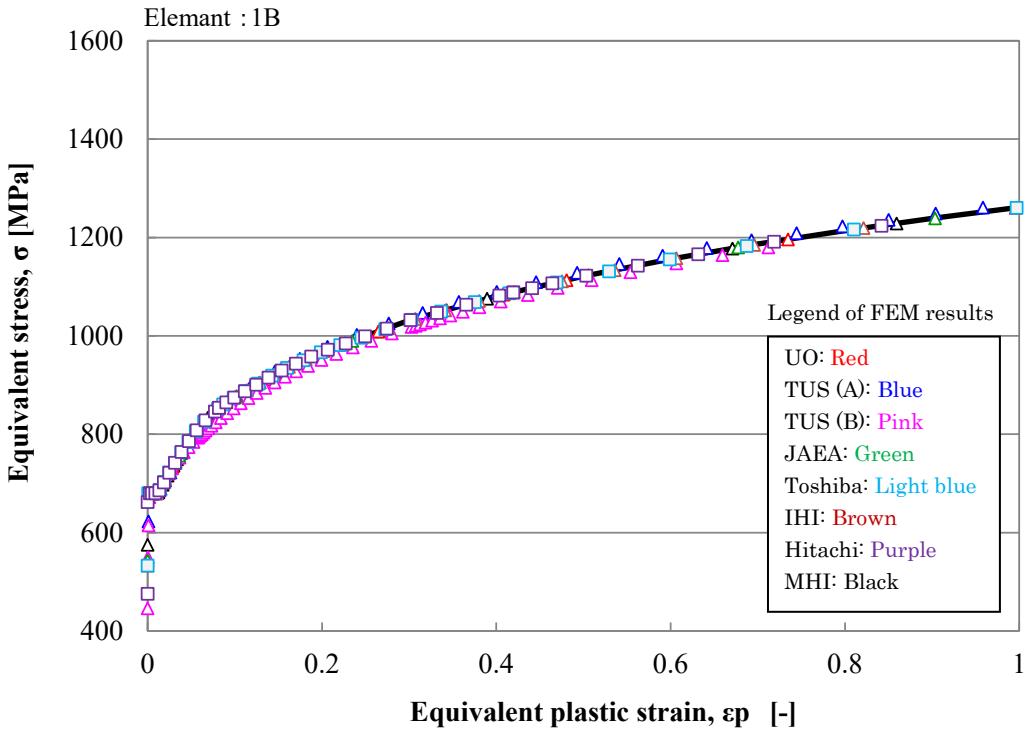


Fig. 2.1-3 Mises equivalent stress – equivalent plastic strain near crack tip (1B)

Copyright © 2026 The Japan Welding Engineering Society, All Rights Reserved.

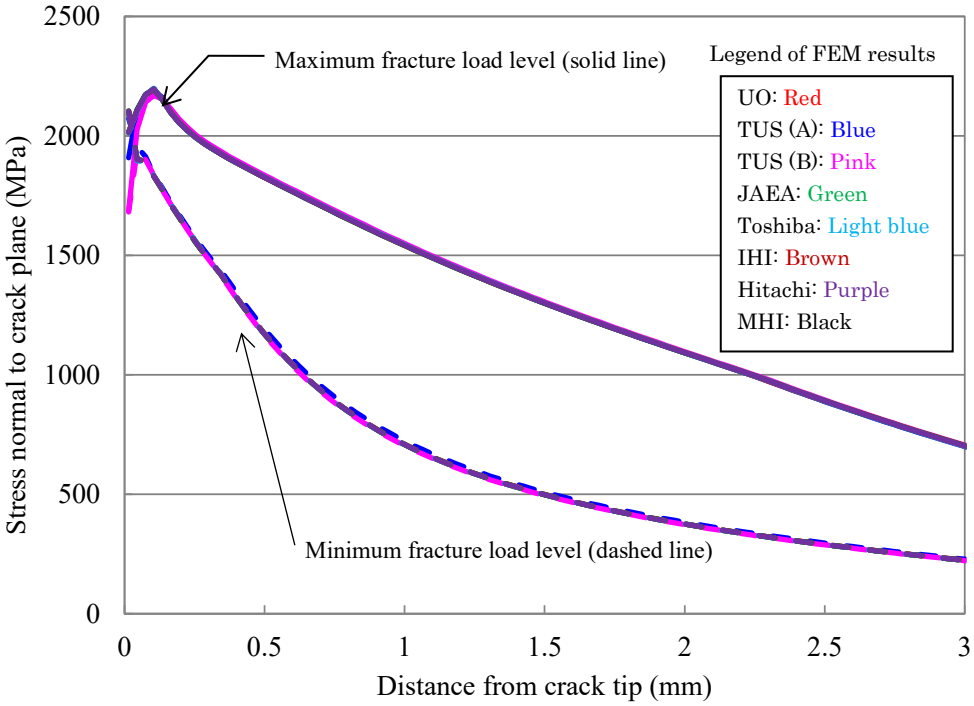


Fig. 2.1-4 Vertical stress for crack surface near crack tip (overall)

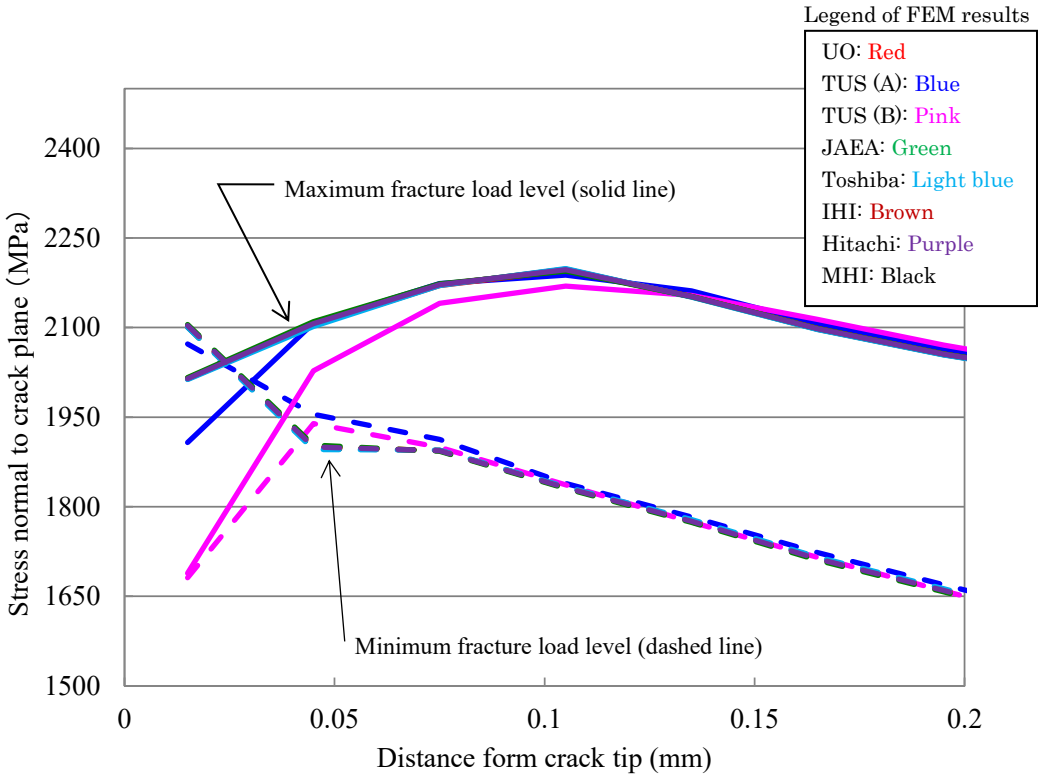


Fig. 2.1-5 Vertical stress for crack surface near crack tip (expanded)

Copyright © 2026 The Japan Welding Engineering Society, All Rights Reserved.

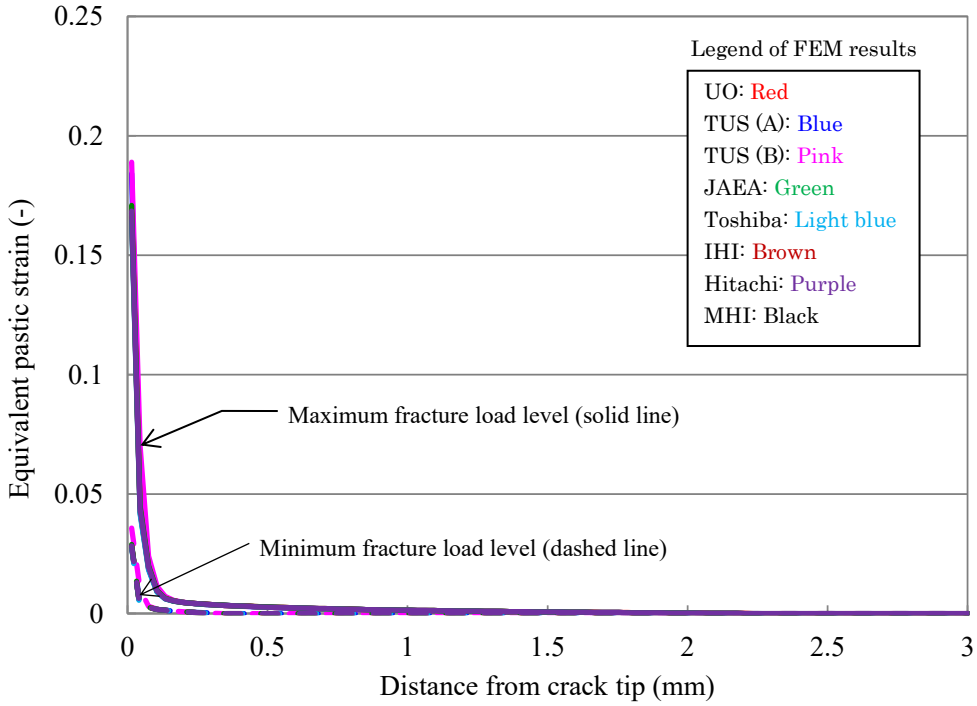


Fig. 2.1-6 Equivalent plastic strain for crack surface near crack tip (overall)

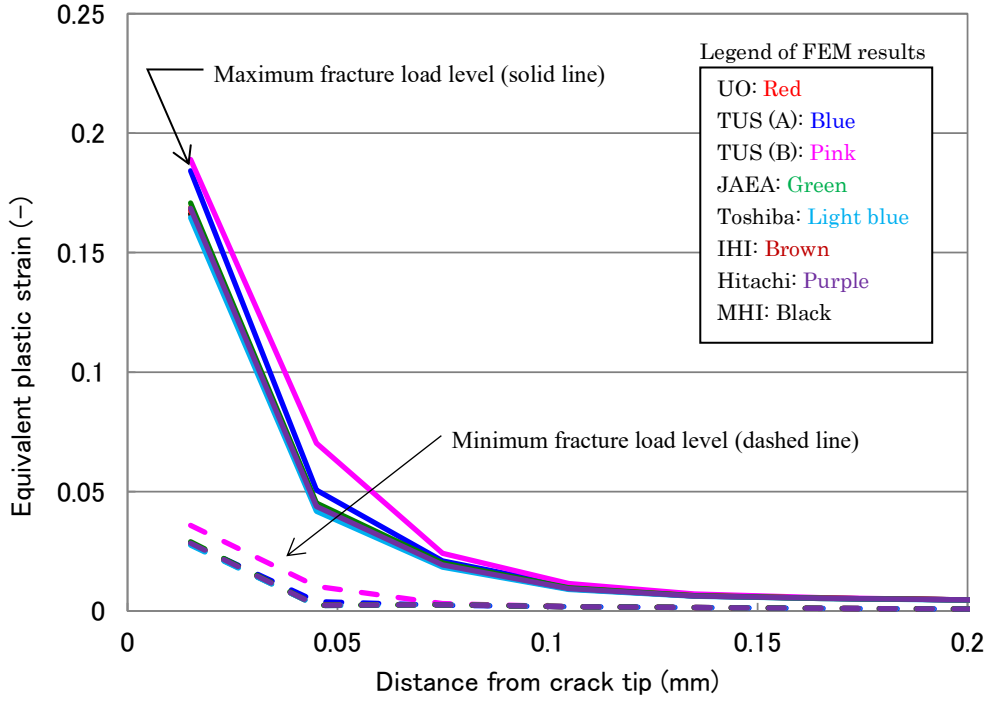


Fig. 2.1-7 Equivalent plastic strain for crack surface near crack tip (expanded)

Copyright © 2026 The Japan Welding Engineering Society, All Rights Reserved.

2.2 Comparison of Weibull Stress Analyses

(STEP 1)

Based on the stress-strain information obtained from FE analyses, Weibull stress analyses using the Beremin model were conducted to verify whether the Weibull stress analysis programs owned by the participating organizations have equivalent functionality. The analysis target was the fracture toughness test of the C(T) specimen at -125°C, and the FE analysis method was the same as that shown in Table 2.1-1.

The σ_w-K_J relationships and Weibull plots of Weibull stress for the case where m was fixed between 5 and 60 are shown in Figures 2.2-1 through 2.2-6.

Furthermore, Figure 2.2-7 shows the analysis results when using the Weibull parameters obtained by convergence calculations based on the fracture test results at each organization.

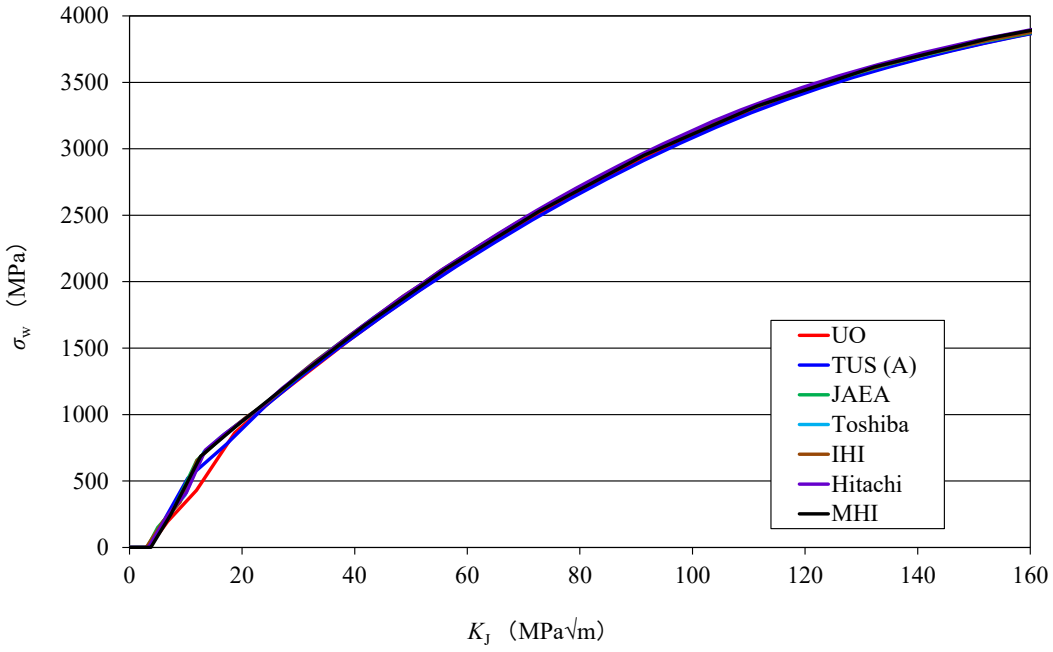
When m was fixed between 5 and 60, the analysis results of each organization appear to be almost consistent; however, as will be described later in STEP2, a detailed examination reveals slight differences between MHI and the other organizations.

The m values obtained by the convergence calculations, as shown in Table 2.2-1, differ among the participating organizations and can be broadly divided into three groups: (i) Toshiba, IHI, Hitachi, (ii) UO, and (iii) MHI.

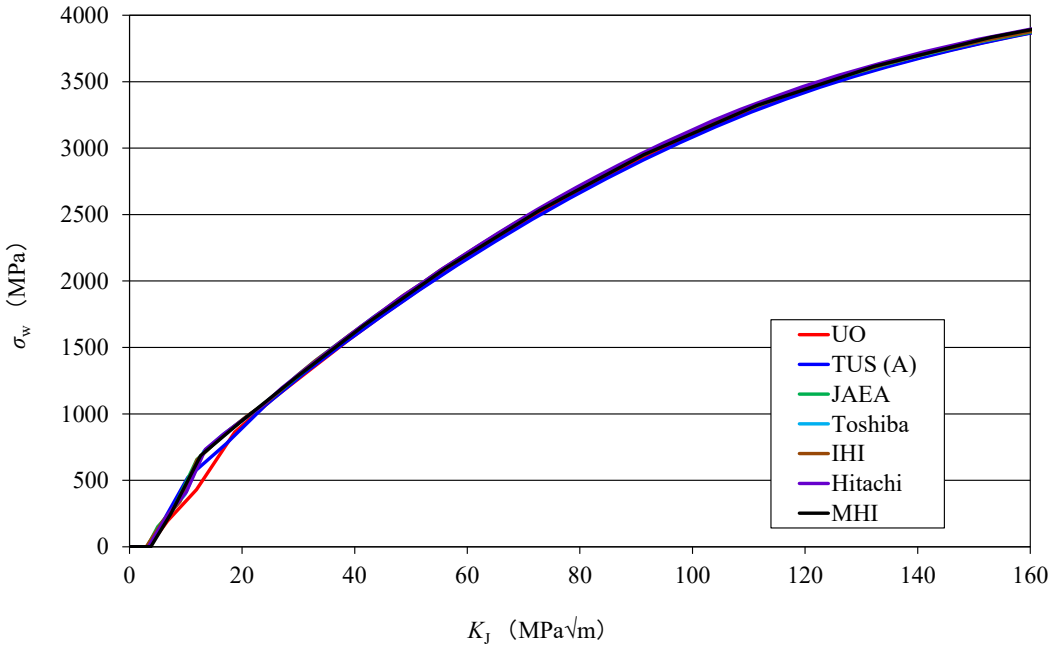
Table 2.2-1 Convergence results of Weibull parameter, m

Organization	UO	TUS (A)	JAEA	Toshiba	IHI	Hitachi	MHI
m	59.2	Not converged	Not converged	101.4	111	107.0	36.5
Analysis method	Implicit	Implicit	Implicit	Implicit	Implicit	Implicit	Explicit
Bias correction	No	No	No	No	No	No	Yes

Copyright © 2026 The Japan Welding Engineering Society, All Rights Reserved.



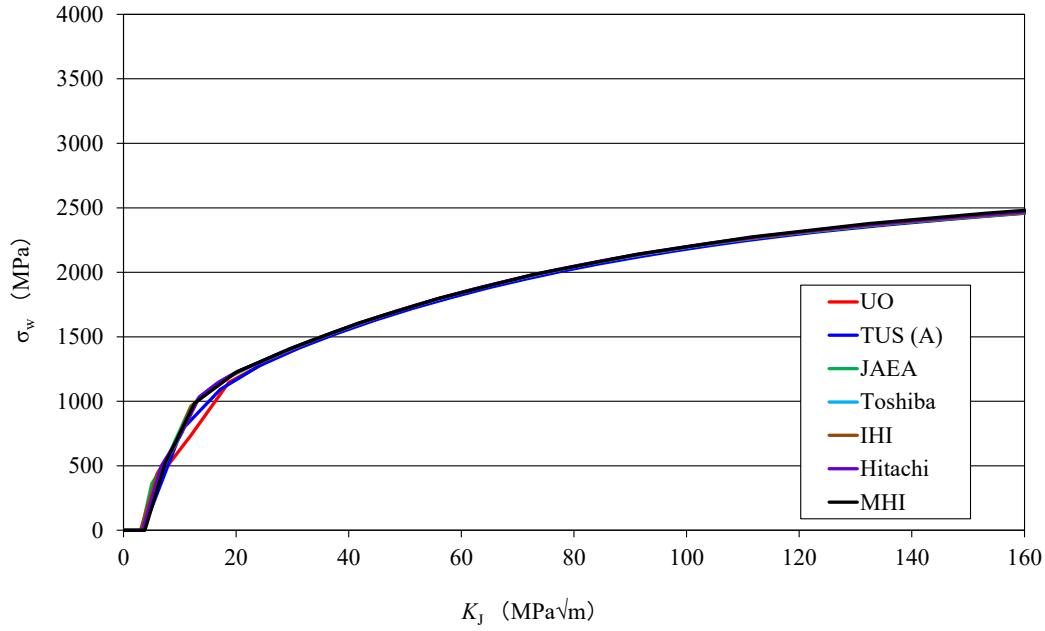
(a) $\sigma_w - K_J$



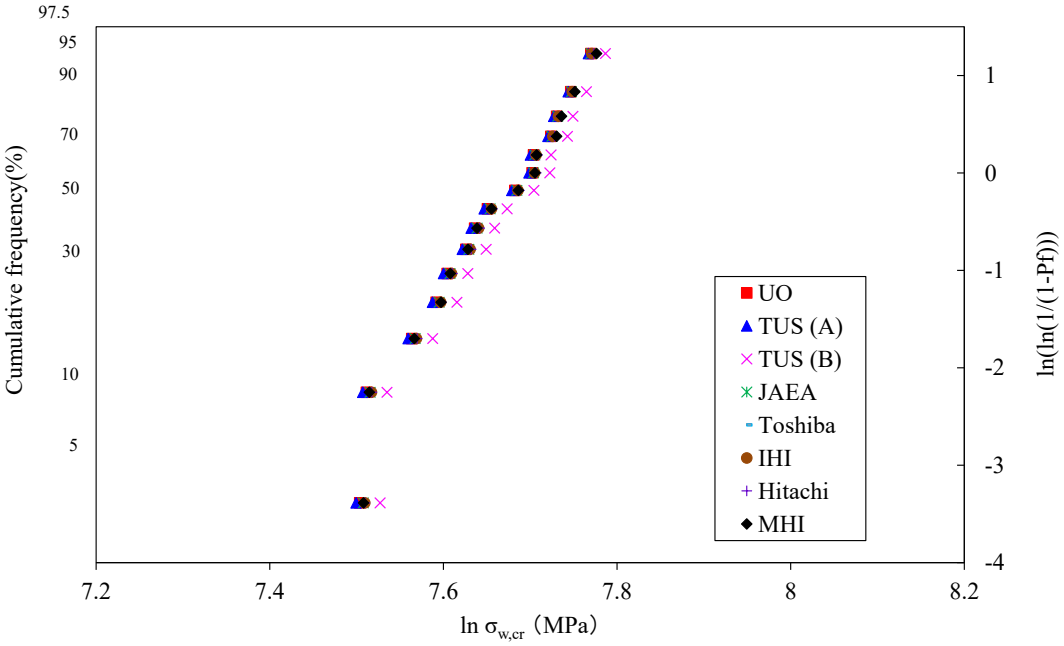
(b) Weibull plot of $\sigma_{w,cr}$

Fig. 2.2-1 Weibull stress evaluation results in case of m=5

Copyright © 2026 The Japan Welding Engineering Society, All Rights Reserved.



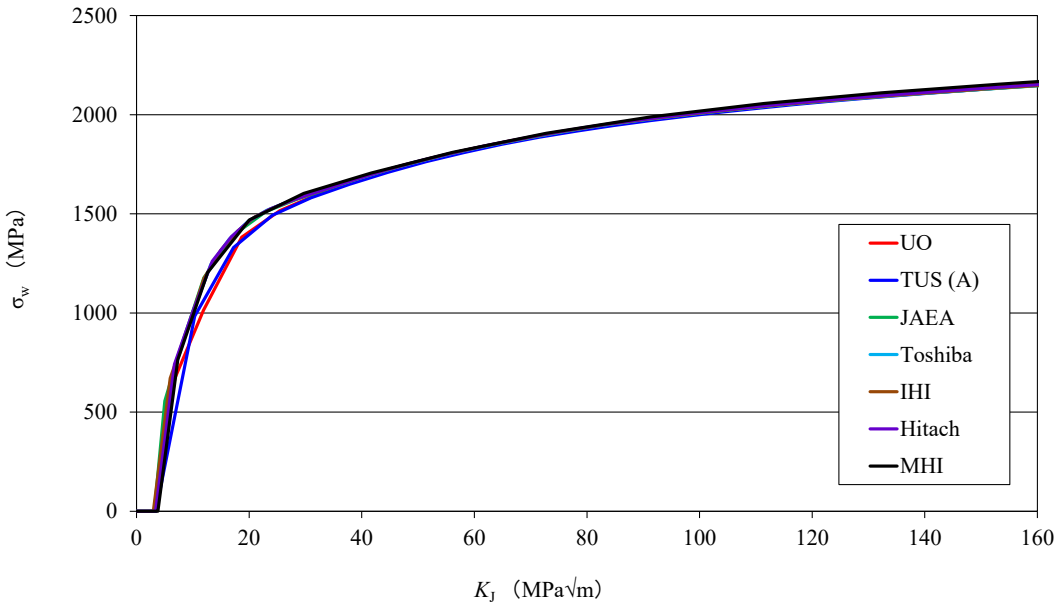
(a) $\sigma_w - K_J$



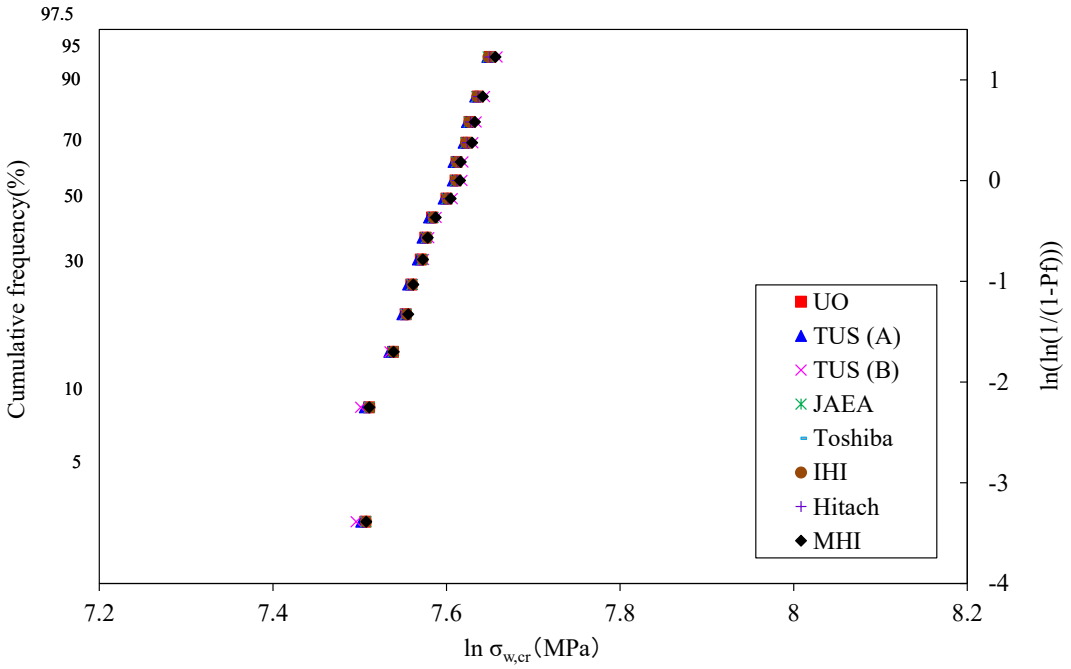
(b) Weibull plot of $\sigma_{w,cr}$

Fig. 2.2-2 Weibull stress evaluation results in case of m =10

Copyright © 2026 The Japan Welding Engineering Society, All Rights Reserved.



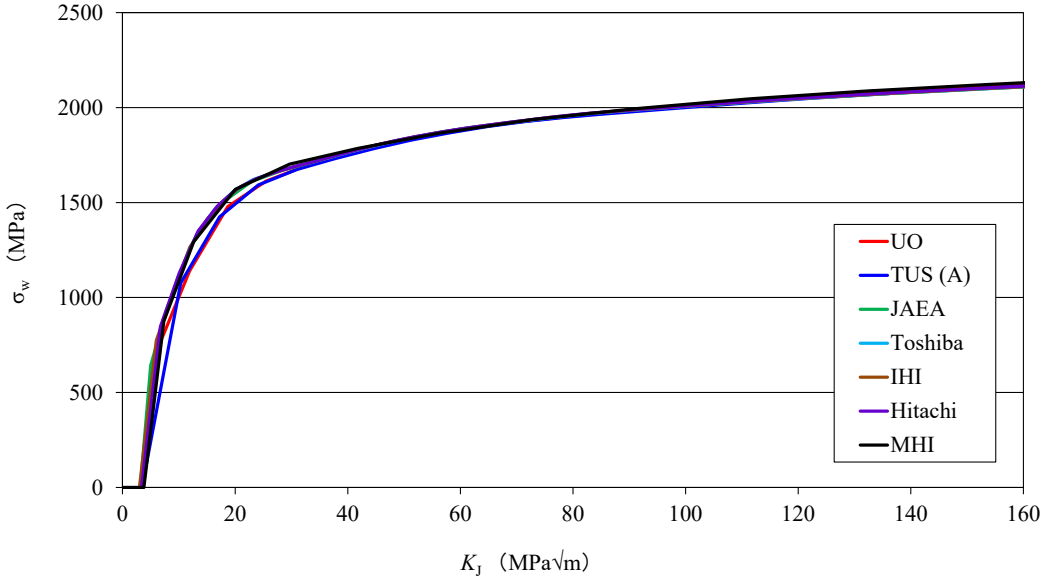
(a) $\sigma_w - K_J$



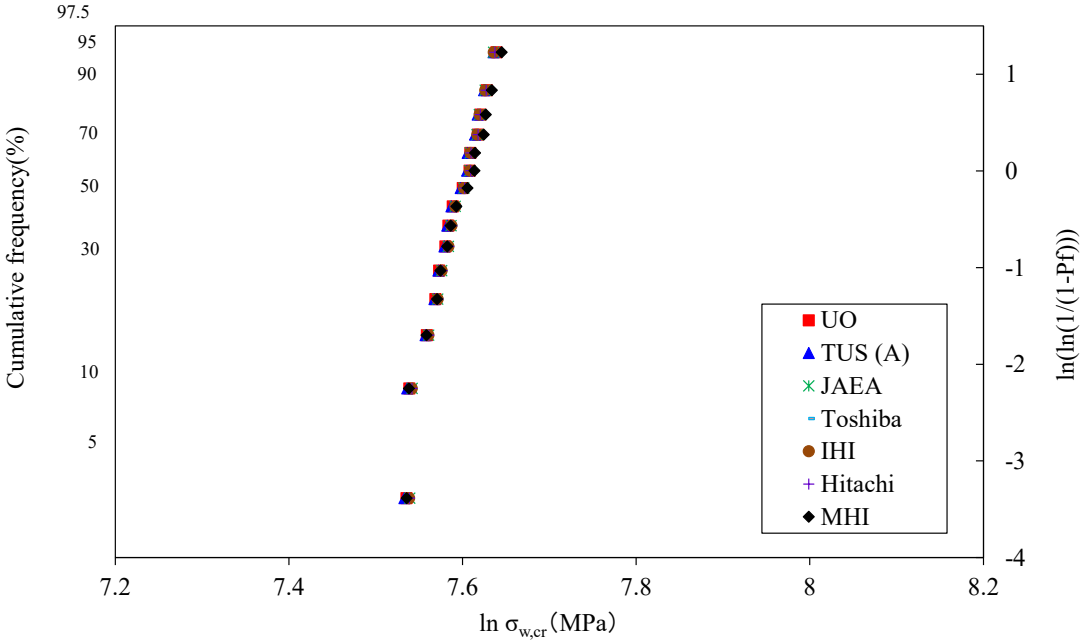
(b) Weibull plot of $\sigma_{w,cr}$

Fig. 2.2-3 Weibull stress evaluation results in case of m=20

Copyright © 2026 The Japan Welding Engineering Society, All Rights Reserved.



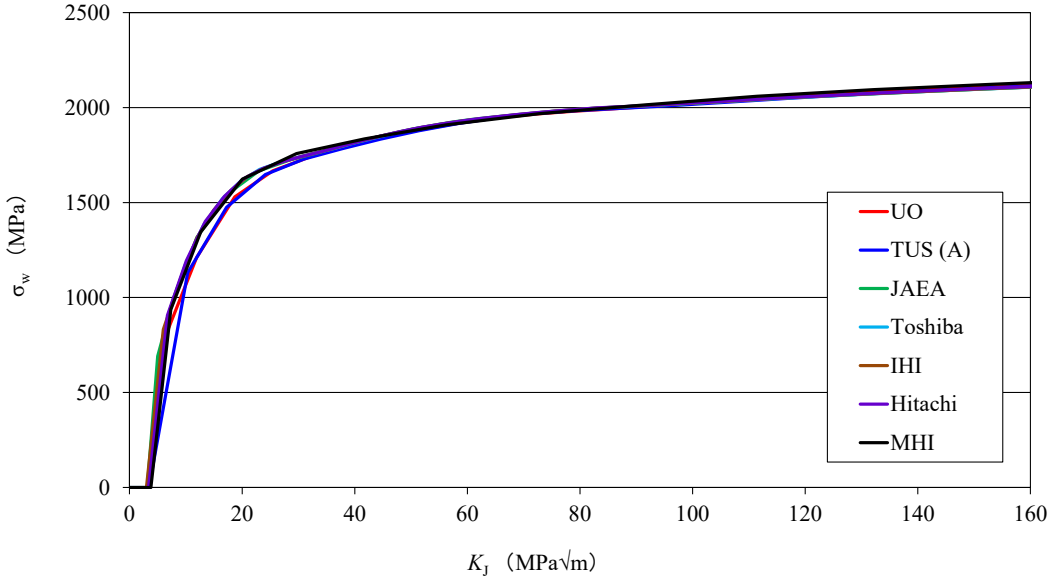
(a) $\sigma_w - K_J$



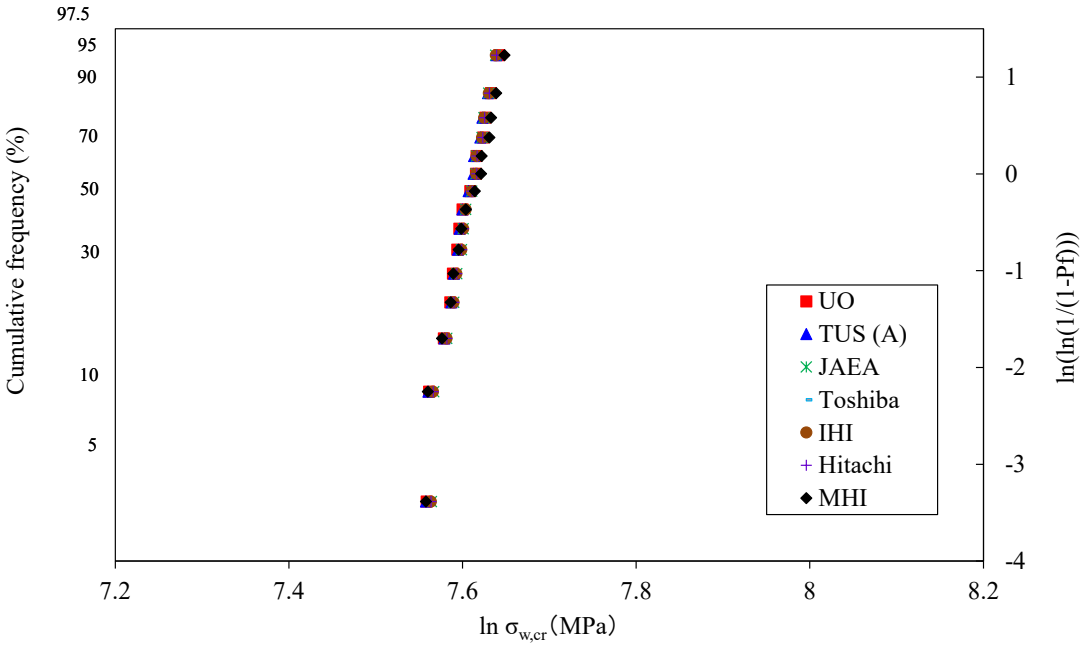
(b) Weibull plot of $\sigma_{w,cr}$

Fig. 2.2-4 Weibull stress evaluation results in case of m=30

Copyright © 2026 The Japan Welding Engineering Society, All Rights Reserved.



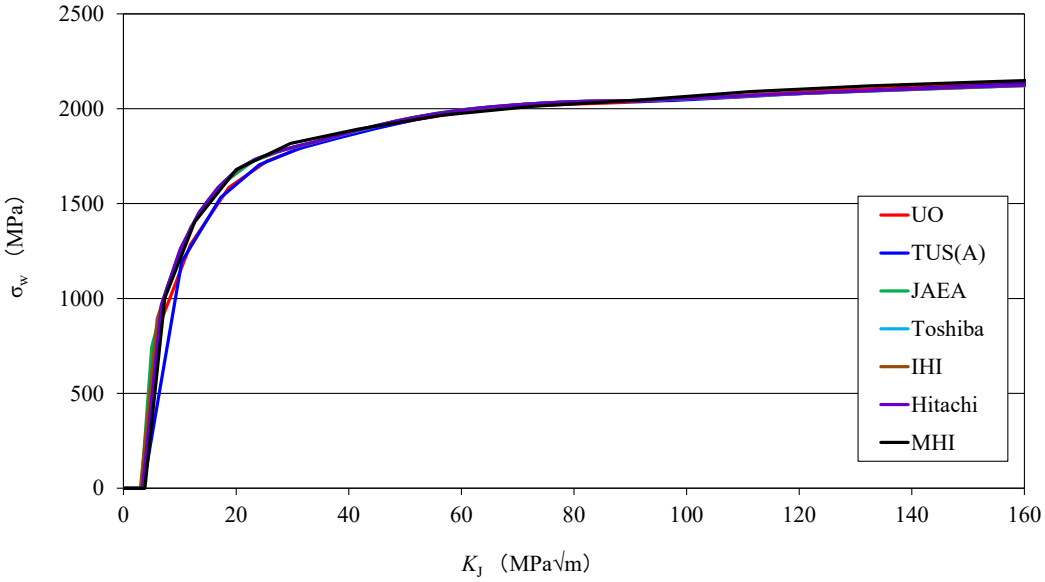
(a) $\sigma_w - K_J$



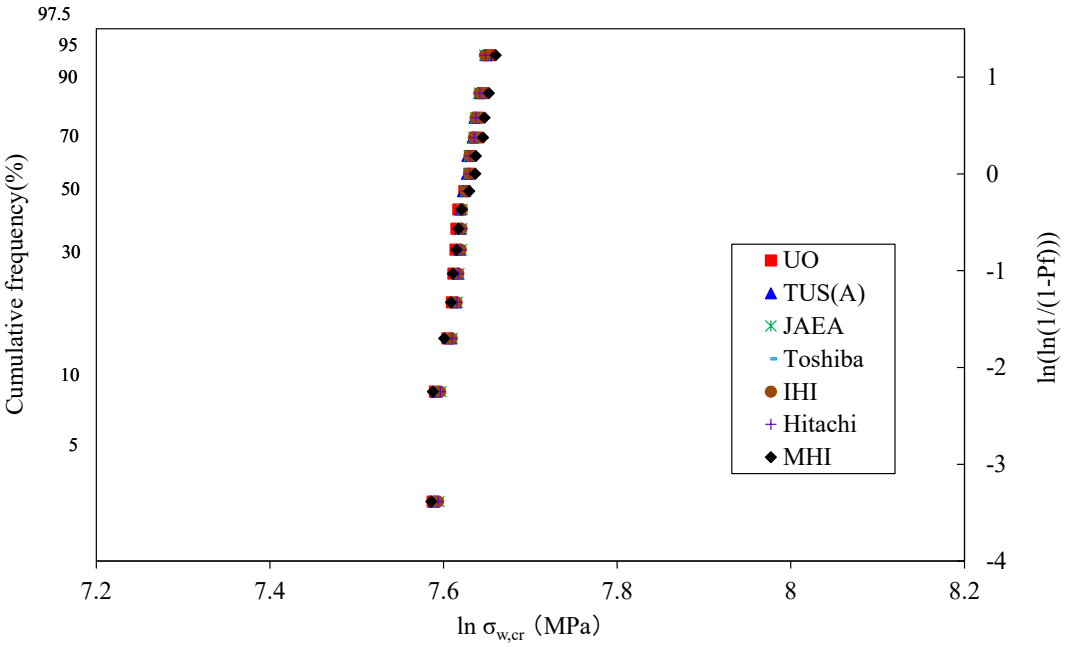
(b) Weibull plot of $\sigma_{w,cr}$

Fig. 2.2-5 Weibull stress evaluation results in case of m=40

Copyright © 2026 The Japan Welding Engineering Society, All Rights Reserved.



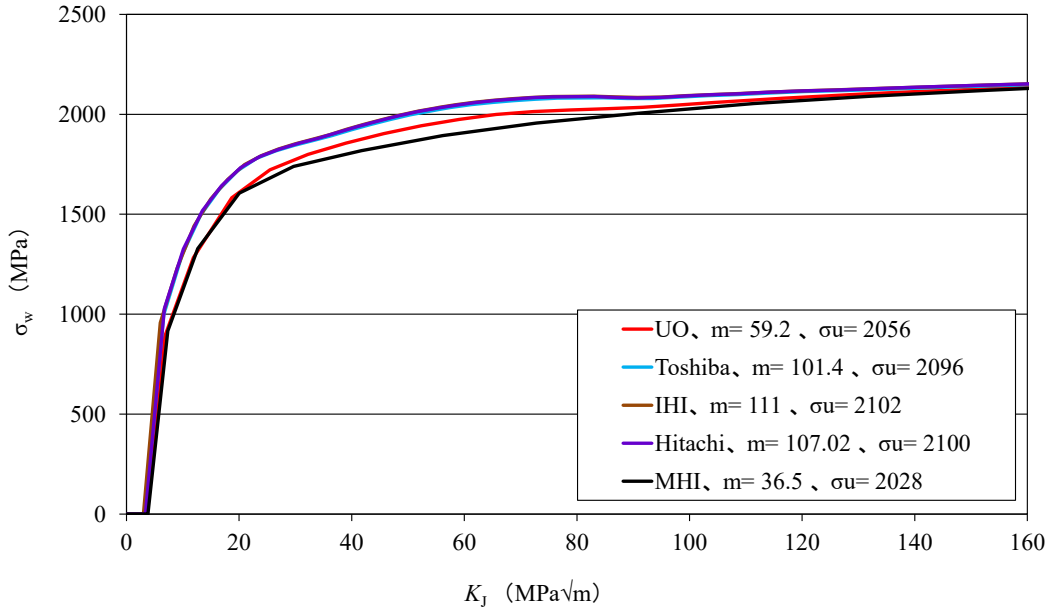
(a) $\sigma_w - K_J$



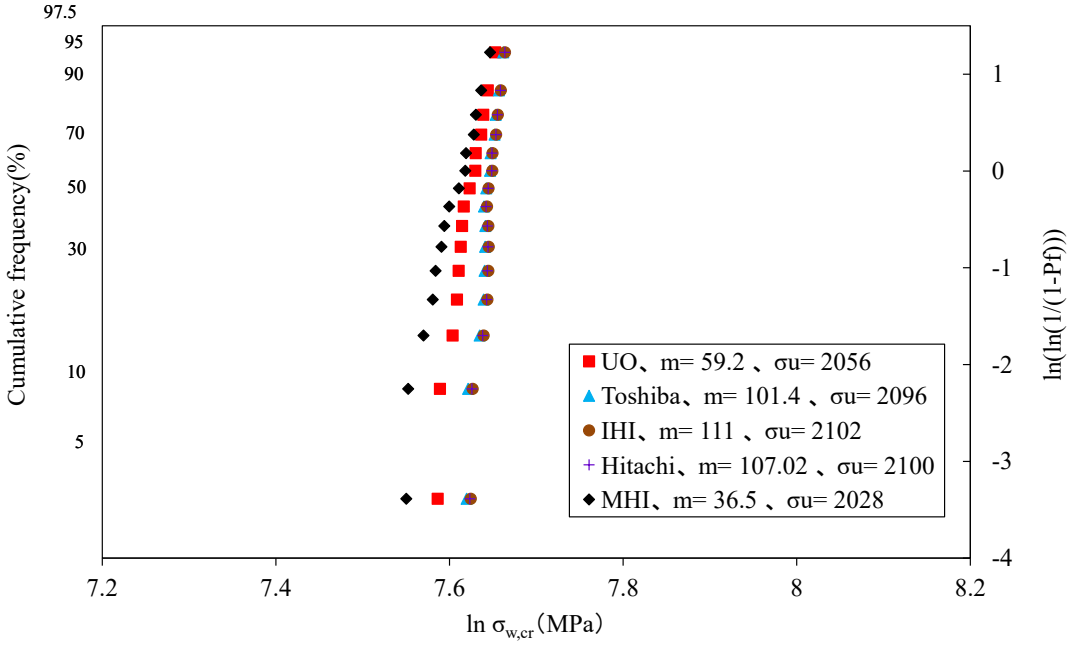
(b) Weibull plot of $\sigma_{w,cr}$

Fig. 2.2-6 Weibull stress evaluation results in case of m=60

Copyright © 2026 The Japan Welding Engineering Society, All Rights Reserved.



(a) $\sigma_w - K_J$



(b) Weibull plot of $\sigma_{w,cr}$

Fig. 2.2-7 Weibull stress evaluation results using obtained Weibull parameter

Copyright © 2026 The Japan Welding Engineering Society, All Rights Reserved.

(STEP 2)

As described above, while the σ_w-K_J relationships calculated by Weibull stress analysis with fixed m showed good agreement among the participating organizations, the values of m obtained by convergence calculations varied widely between organizations. To investigate the cause of this, a detailed examination of the Weibull stress analysis results was conducted.

Figures 2.2-8 through 2.2-13 show the relative differences between the calculation results of MHI and those of the other participating organizations for $\sigma_{w,cr}$ at fixed m, normalized by MHI's results. Overall, when m was small, the differences (variation in results) among organizations were large, whereas when m was large, the differences tended to be smaller.

At m = 5, the results split into two groups: one with $\sigma_{w,cr}$ larger than MHI (JAEA, Toshiba, Hitachi, IHI) and one with smaller values (UO, TUS). At m = 10, the results generally matched or were smaller than MHI's values, and for m >20, especially in the region of large K_J, the values tended to be smaller than those of MHI.

For m >30, the trends among JAEA, TUS, Hitachi, Toshiba, and IHI were very similar; for K_J < 80 $\mathrm{MPa}\sqrt{\mathrm{m}}$ their values were larger than MHI's, but for K_J above this, they became smaller than MHI's.

Figure 2.2-14 shows the σ_w-K_J relationships for m = 60 and m = 30 (the fracture toughness K_{Jc} of the C(T) specimens ranged approximately from 58 to 134 $\mathrm{MPa}\sqrt{\mathrm{m}}$, so the target region was expanded). The curves of JAEA, TUS, Hitachi, Toshiba, and IHI almost coincide; however, for m = 60, an inflection point occurs near $K_J = 90$ $\mathrm{MPa}\sqrt{\mathrm{m}}$, around which the relative magnitude between MHI and the others reverses.

Using the σ_w calculation results with fixed m corresponding to the K_{Jc} obtained from fracture toughness tests of the C(T) specimens, maximum likelihood estimation was performed to determine m. Figure 2.2-15 shows the relationship between the two m values: m_0 is the input value, and m_1 is the m obtained by maximum likelihood estimation using σ_w. UO's results plot the convergence process of m (○). Points lying on the line m_0=m_1 indicate convergence of the Weibull stress calculation.

UO's results converge near m = 60, whereas MHI's results converge near m = 40 (without bias correction). MHI's calculations align closely with UO's trajectory when m is less than 30 but diverge for larger m. Other organizations deviate above UO's trajectory. This suggests that as m and K_J

Copyright © 2026 The Japan Welding Engineering Society, All Rights Reserved.

increase, the differences between MHI and the other groups widen.

As shown in Table 2.1-1, differences in analysis codes, element types, solution methods, and other factors among the organizations are believed to influence the converged values of m.

Copyright © 2026 The Japan Welding Engineering Society, All Rights Reserved.

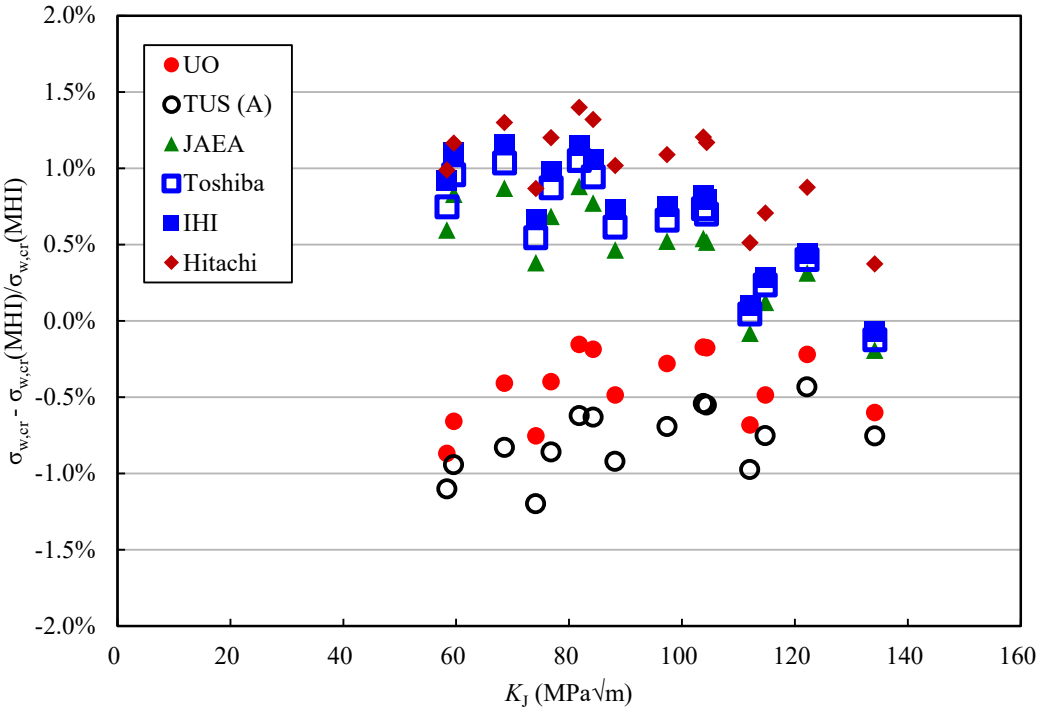


Fig. 2.2-8 Difference of $\sigma_{w,r}$ between MHI and other organizations (m=5)

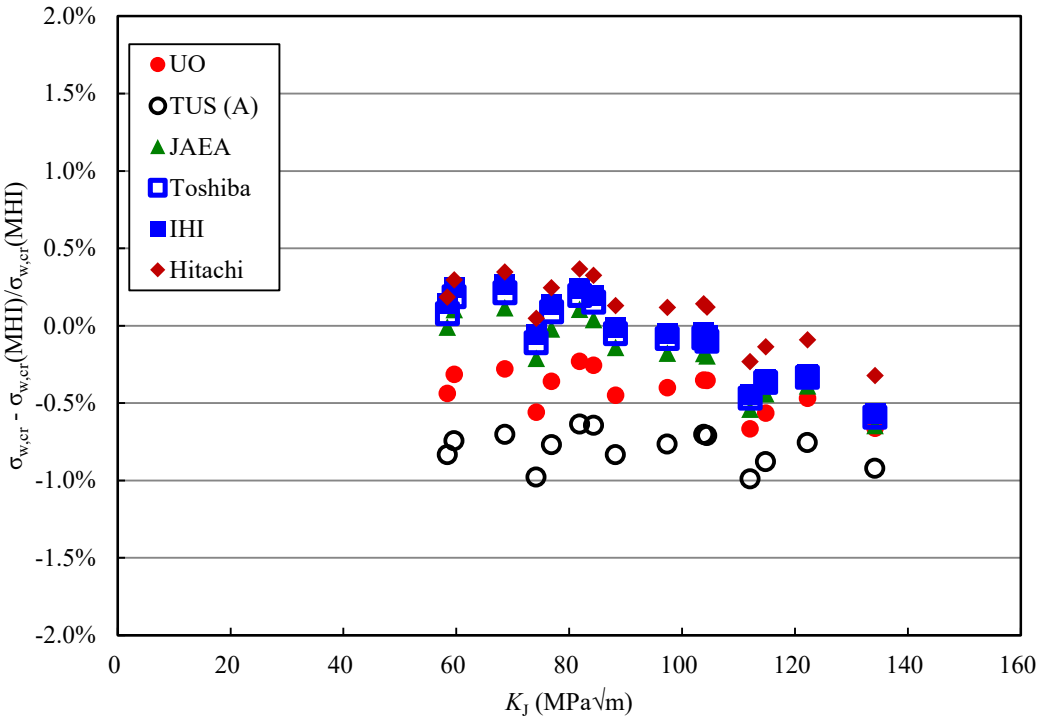


Fig. 2.2-9 Difference of $\sigma_{w,cr}$ between MHI and other organizations (m=10)

Copyright © 2026 The Japan Welding Engineering Society, All Rights Reserved.

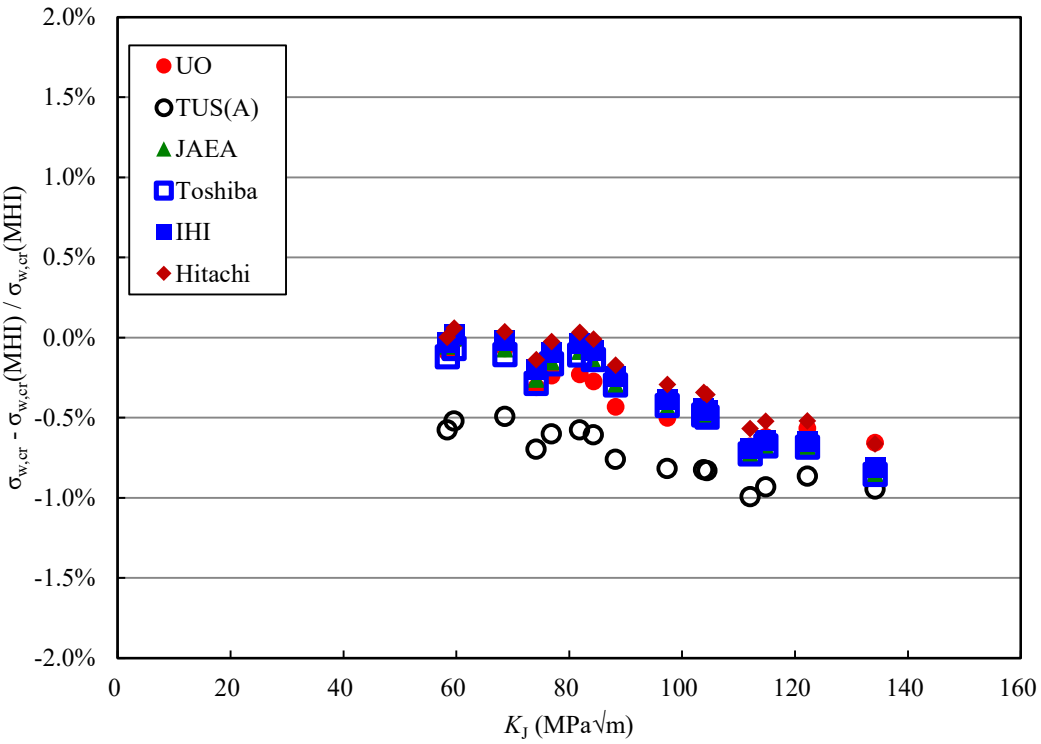


Fig. 2.2-10 Difference of $\sigma_{w,cr}$ between MHI and other organizations (m=20)

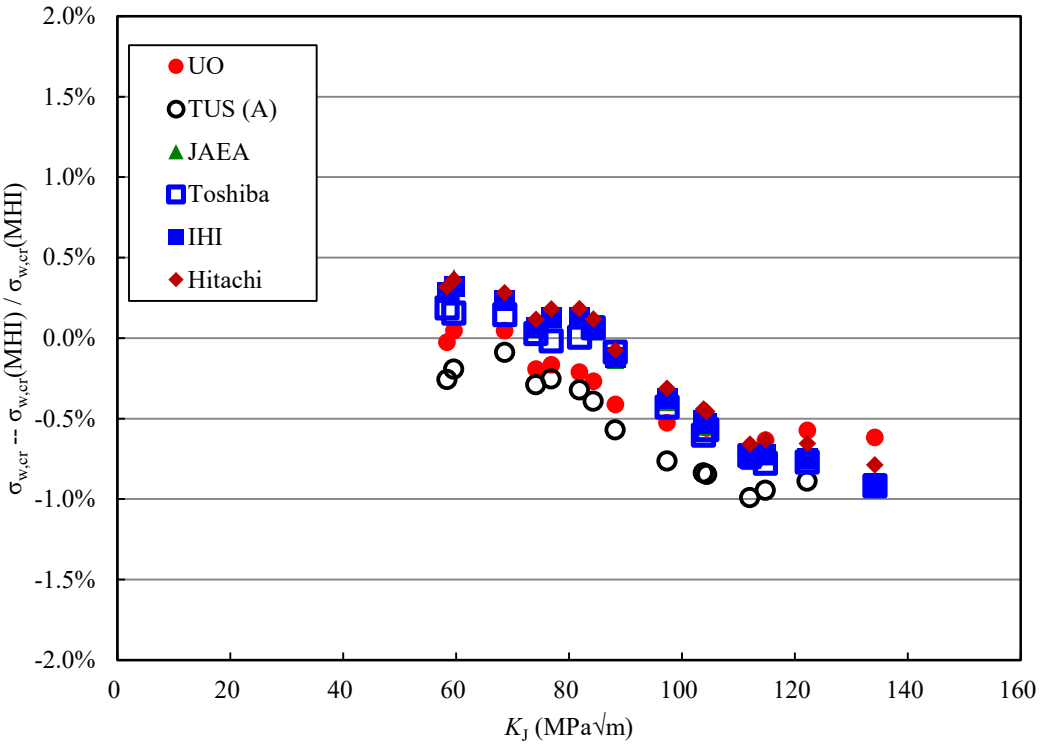


Fig. 2.2-11 Difference of $\sigma_{w,cr}$ between MHI and other organizations (m=30)

Copyright © 2026 The Japan Welding Engineering Society, All Rights Reserved.

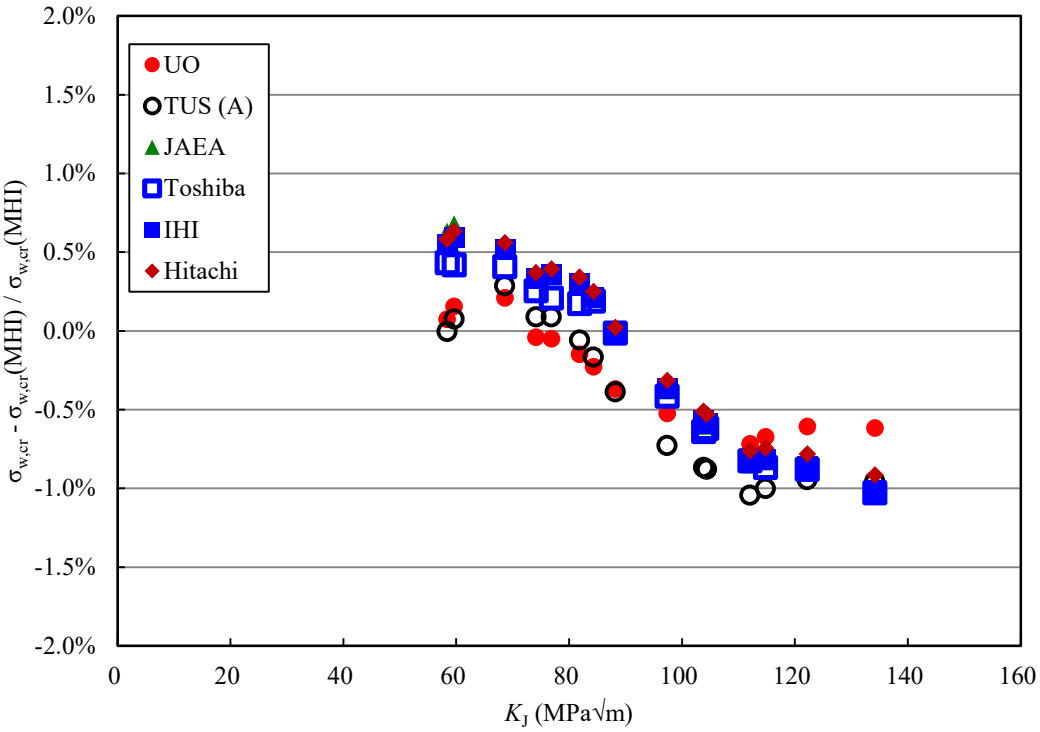


Fig. 2.2-12 Difference of $\sigma_{w,cr}$ between MHI and other organizations (m =40)

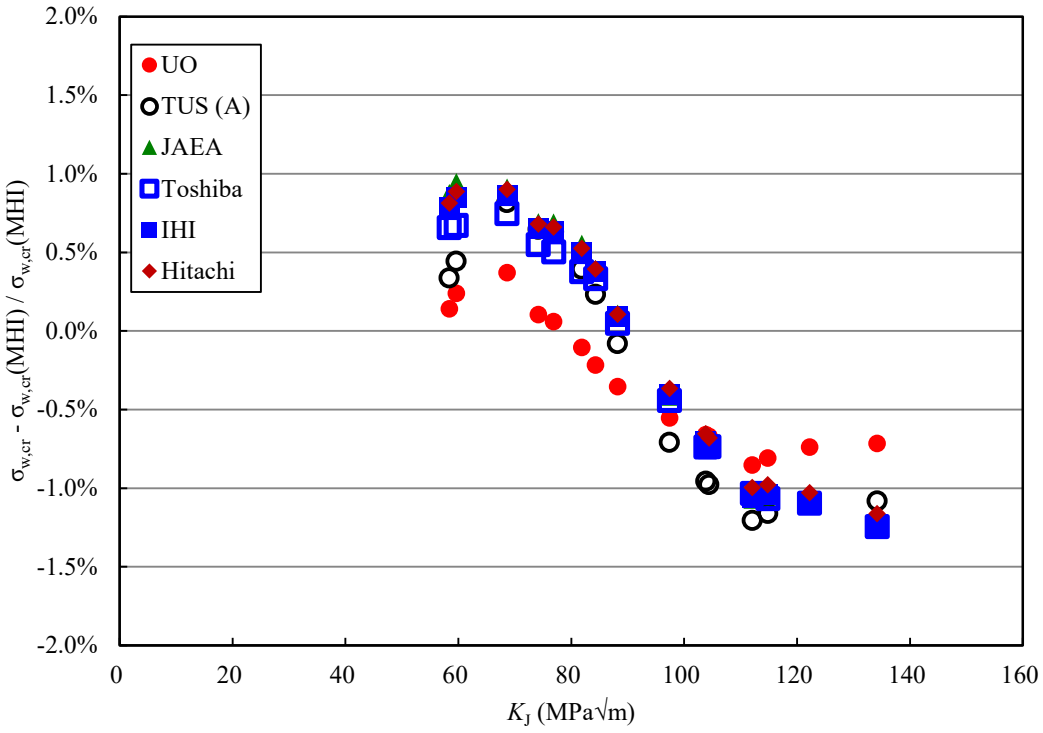
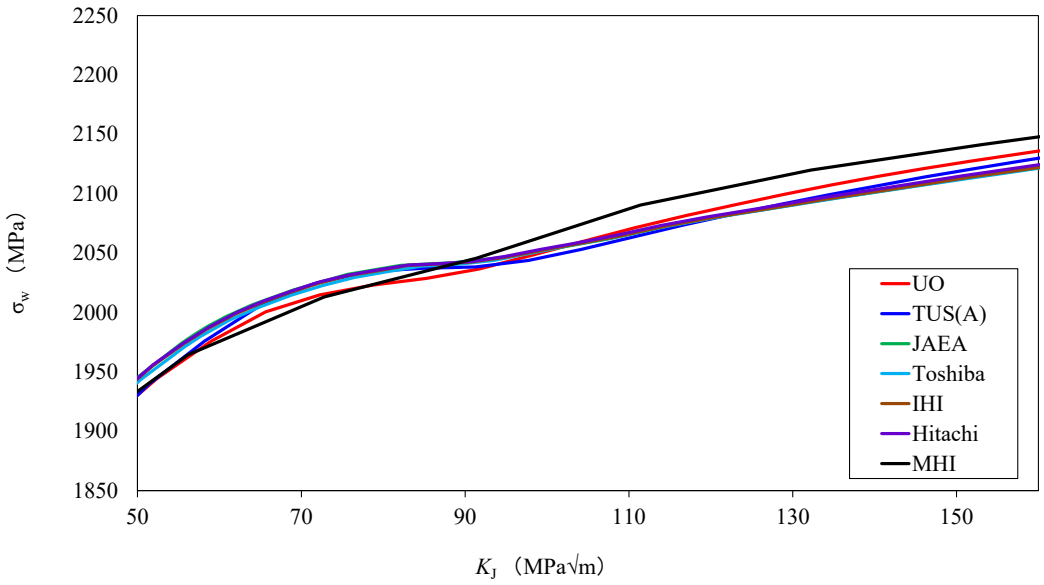
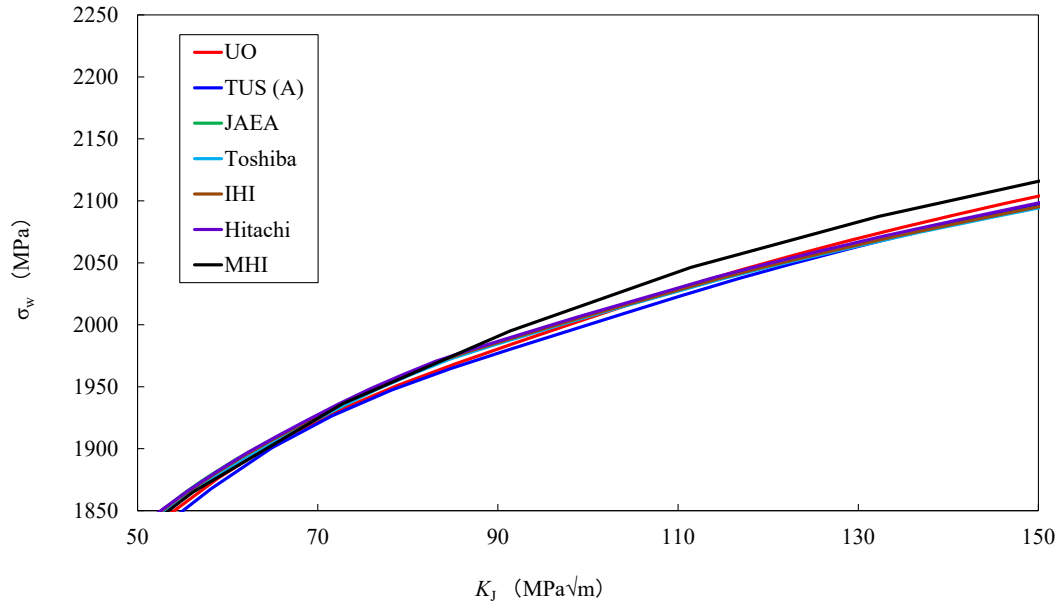


Fig. 2.2-13 Difference of $\sigma_{w,cr}$ between MHI and other organizations (m =60)

Copyright © 2026 The Japan Welding Engineering Society, All Rights Reserved.



(a) m =60



(b) m =30

Fig. 2.2-14 Relationship between σ_w and K_J

Copyright © 2026 The Japan Welding Engineering Society, All Rights Reserved.

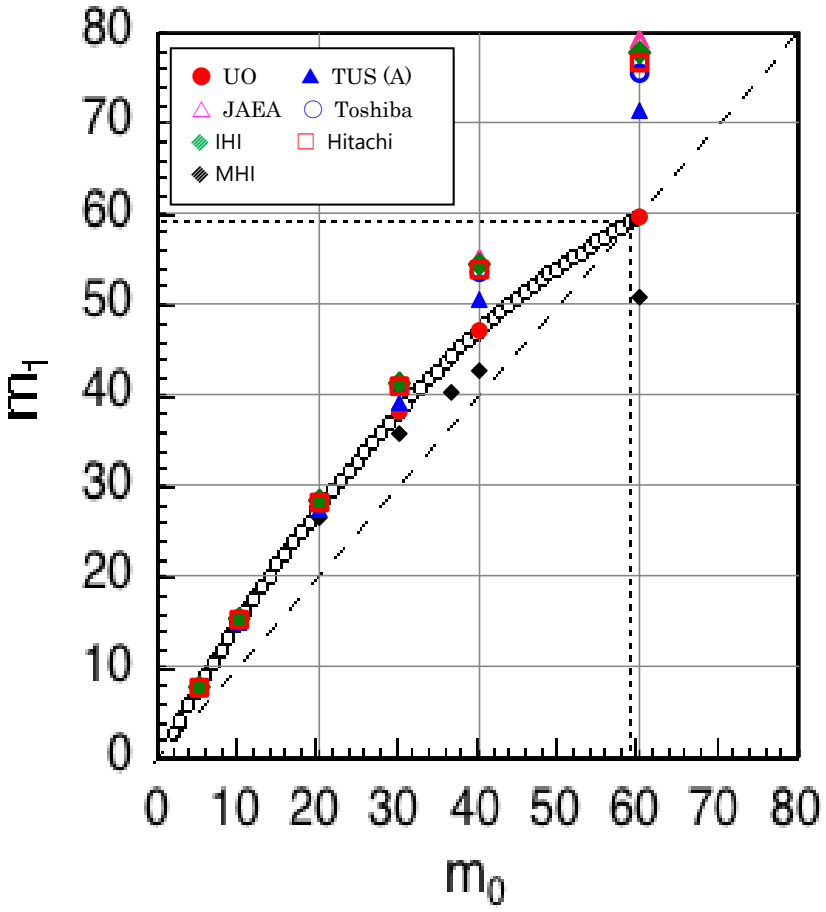


Fig. 2.2-15 Comparison of m (m_0) with m_1 obtained by maximum likelihood method

Copyright © 2026 The Japan Welding Engineering Society, All Rights Reserved.

2.3 Factors Affecting Weibull Stress Analysis Results

(1) Influence of Differences between Implicit and Explicit Methods

As shown in Table 2.1-1, only MHI used the explicit method for Weibull stress analysis. This is because MHI plans to apply a coupling model that combines the Beremin model and the GTN model in the future, and therefore used the explicit method also for Weibull stress analysis.

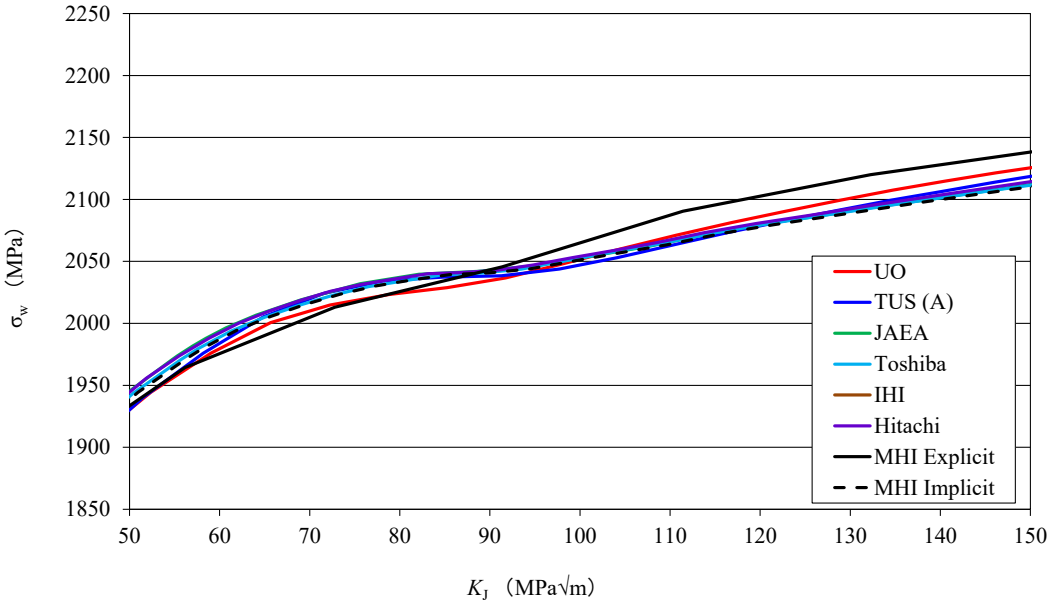
To understand the differences in FE analysis and Weibull stress analysis results between the explicit and implicit methods, MHI performed reanalysis using the implicit method. Since the differences between MHI and other organizations became larger in the region of large m, the reanalysis was conducted under the condition of $m = 60$, as shown in Figures 2.2-8 through 2.2-13.

Figure 2.3-1 shows the analysis results of the explicit and implicit methods. The implicit method results from MHI almost matched those of the other organizations. When convergence calculations of Weibull stress analysis were performed using stress-strain data from the implicit method, $m = 91.9$ (without bias correction) was obtained, which is close to the values obtained by IHI and Hitachi that also achieved convergence. However, Figure 2.3-1(a) shows an enlarged scale of σ_w, and when σ_w is displayed from zero as in Figure 2.3-1(b), differences among the research organizations and between the explicit and implicit methods are hardly discernible.

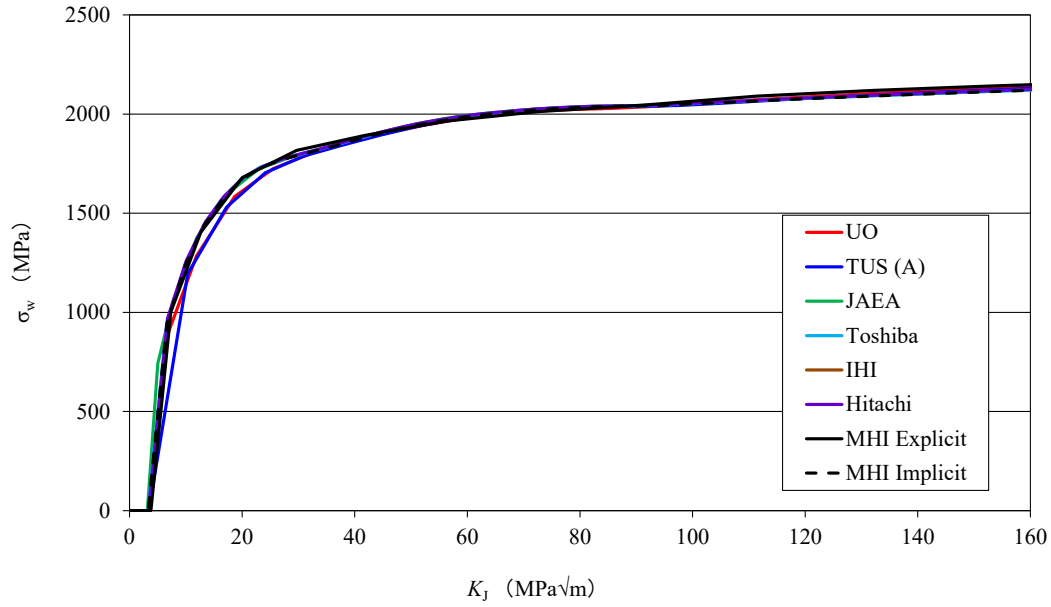
These results suggest that slight differences in the slope of the σ_w-K_J relationship curve may have a large impact on the converged value of m.

Figure 2.3-2 shows a comparison of the maximum principal stress distribution near the crack tip between the implicit and explicit methods. The increase in the peak of the maximum principal stress near the crack tip with increasing K_J is more distinct in the explicit method than in the implicit method. This difference is considered to have affected the variation in Weibull stress increase due to increasing K_J.

Copyright © 2026 The Japan Welding Engineering Society, All Rights Reserved.



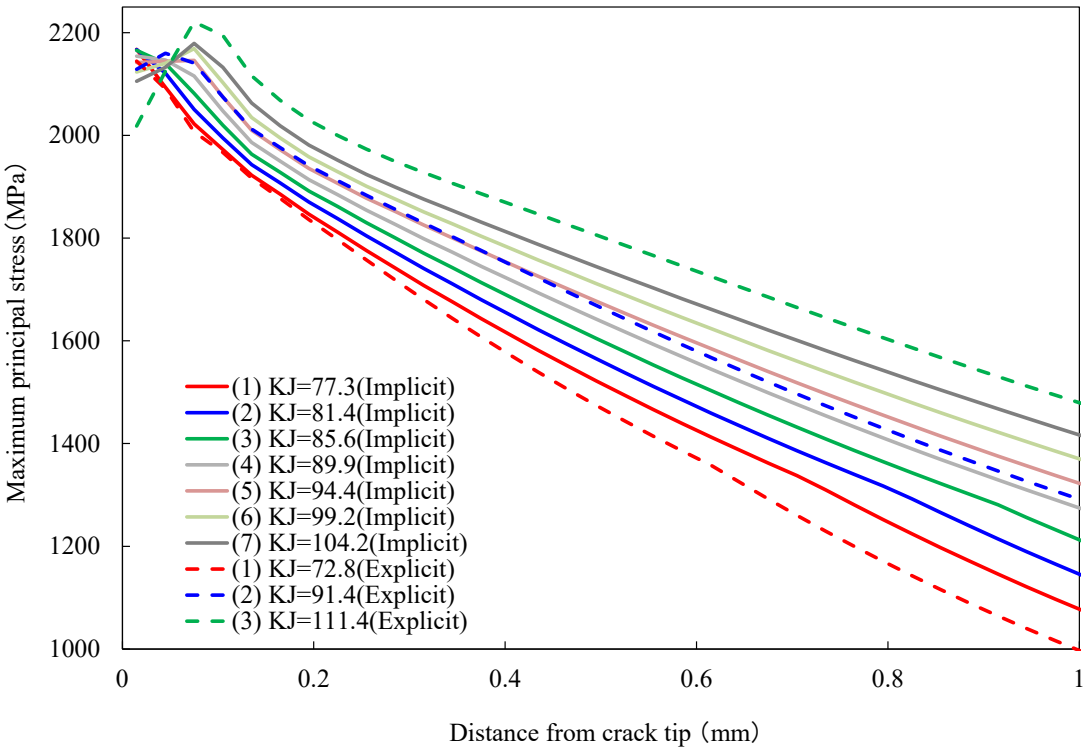
(a) Enlarged view



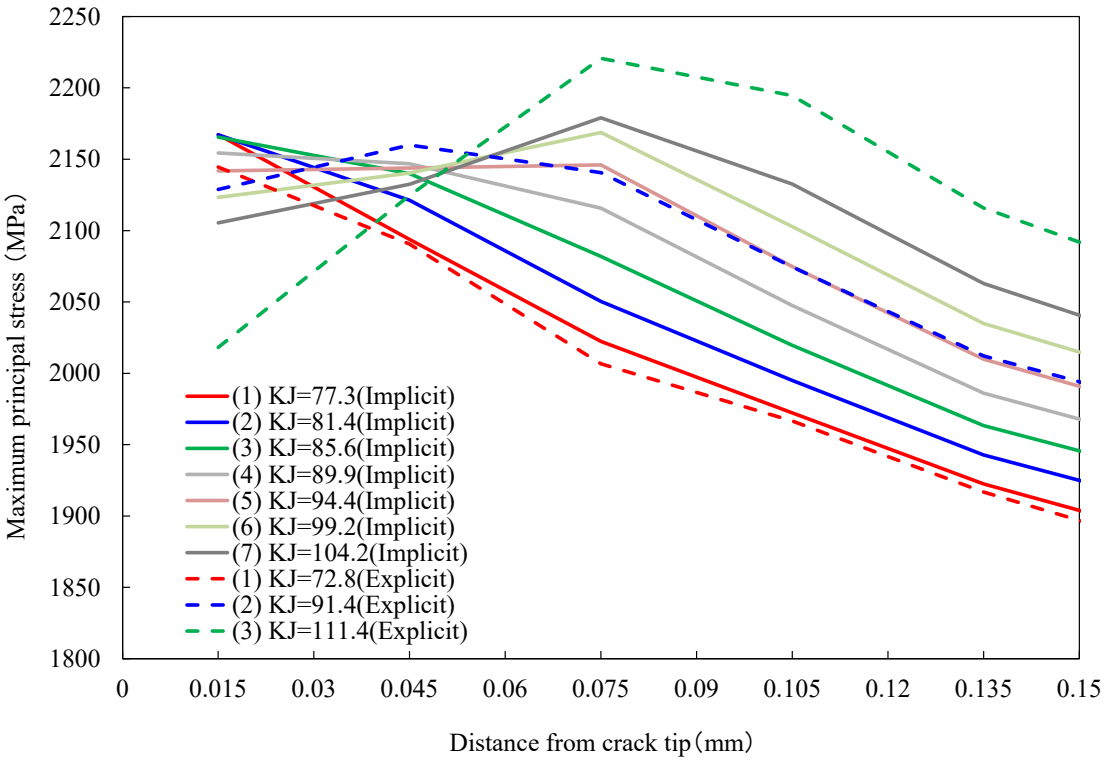
(b) Overall view

Fig. 2.3-1 Relationship between σ_w and K_J (m=60) (Implicit vs Explicit)

Copyright © 2026 The Japan Welding Engineering Society, All Rights Reserved.



(a) Overall view



(b) Enlarged view

Fig. 2.3-2 Comparison of maximum principal stress by explicit method and implicit method

Copyright © 2026 The Japan Welding Engineering Society, All Rights Reserved.

(2) Influence of the Young's Modulus Setting Value

In the analysis of STEP 0, when comparing the load versus load-line displacement analysis results of the C(T) specimen with the test results, the analysis results were slightly above the test results as shown in Figure 2.1-1. The fracture toughness K_{Jc} at specimen failure is calculated using the experimentally measured load-displacement curve and the equation from ASTM E-1921-10. On the other hand, in the Weibull stress calculation, since the stress-strain distribution corresponding to the K_J calculated to be equal to this K_{Jc} is used, the mismatch between the load-displacement curves and the experimental results may indicate that the stress-strain state at fracture occurrence is not accurately represented.

Therefore, as shown in Figure 2.3-3, the Young's modulus was revised to match the average value from the test results, and the Weibull stress was recalculated. The revised Young's modulus was set to 205.304 GPa (approximately 6% lower than in STEP 0). Table 2.3-1 shows the comparison of the Weibull parameter *m* obtained before and after the revision of Young's modulus. Figures 2.3-4 through 2.3-9 show the Weibull stress evaluation results after the revision of Young's modulus. From these figures, the influence on Weibull stress before and after the Young's modulus revision was minor, and there was no significant difference in the *m* obtained by convergence calculations before and after the Young's modulus change.

Note that IHI changed from load control (before Young's modulus adjustment) to displacement control (after Young's modulus adjustment), but this had only a minor effect.

Table 2.3-1 Comparison of obtained Weibull parameter, *m*

Item	JAEA	Toshiba	IHI	Hitachi	MHI (Implicit)
Before Young's modulus adjustment	—	101.4	111	107.0	91.9
After Young's modulus adjustment	102.6	95.4	99.9	101.3	96.3

Copyright © 2026 The Japan Welding Engineering Society, All Rights Reserved.

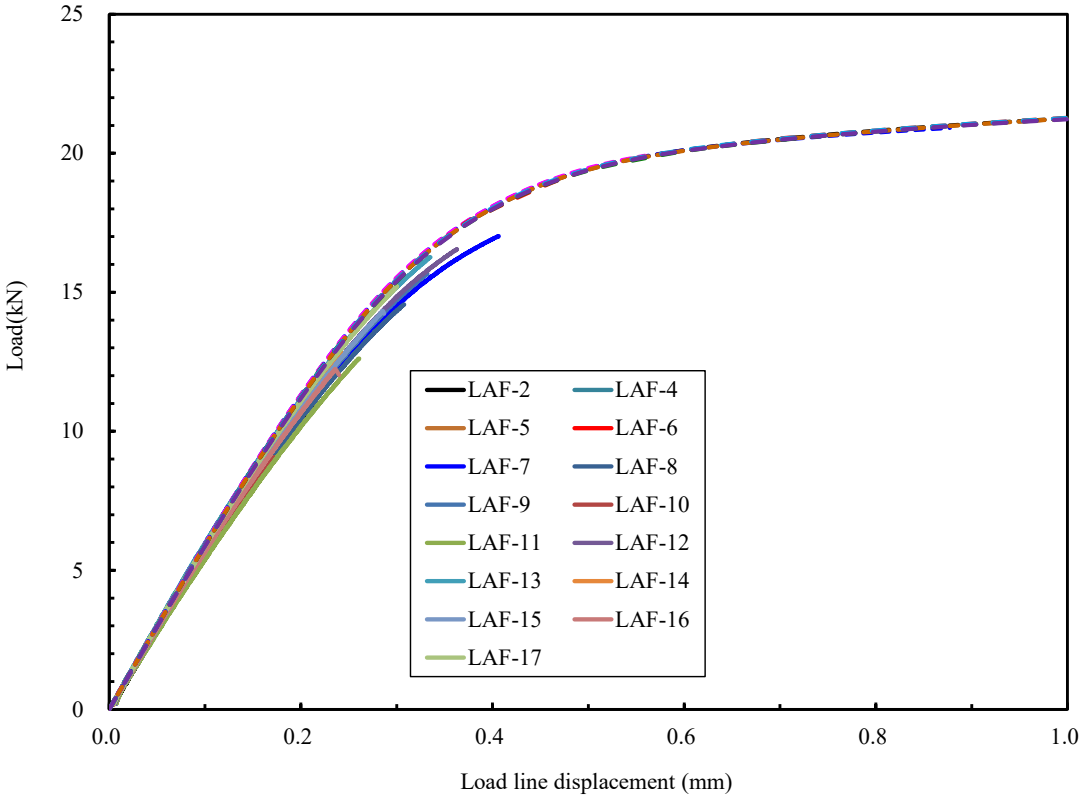
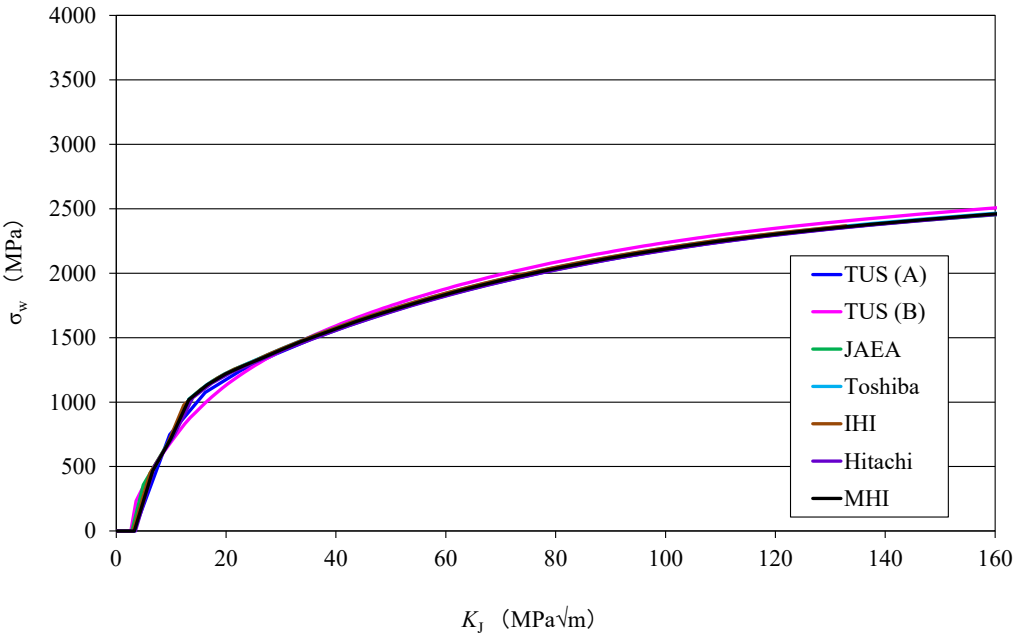
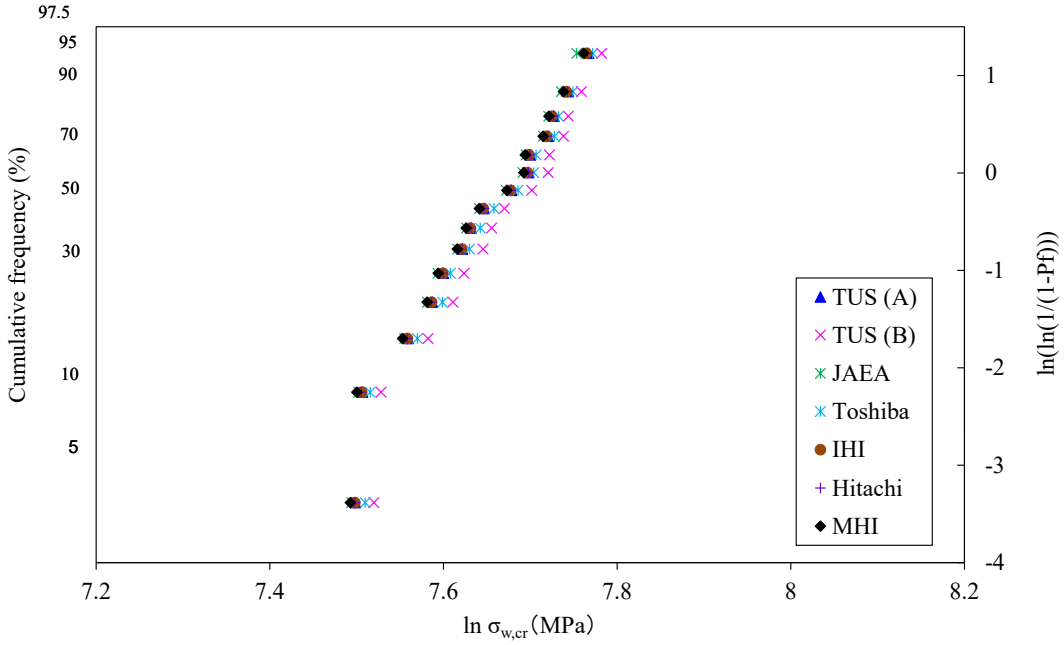


Fig. 2.3-3 Load – load line displacement curve

Copyright © 2026 The Japan Welding Engineering Society, All Rights Reserved.



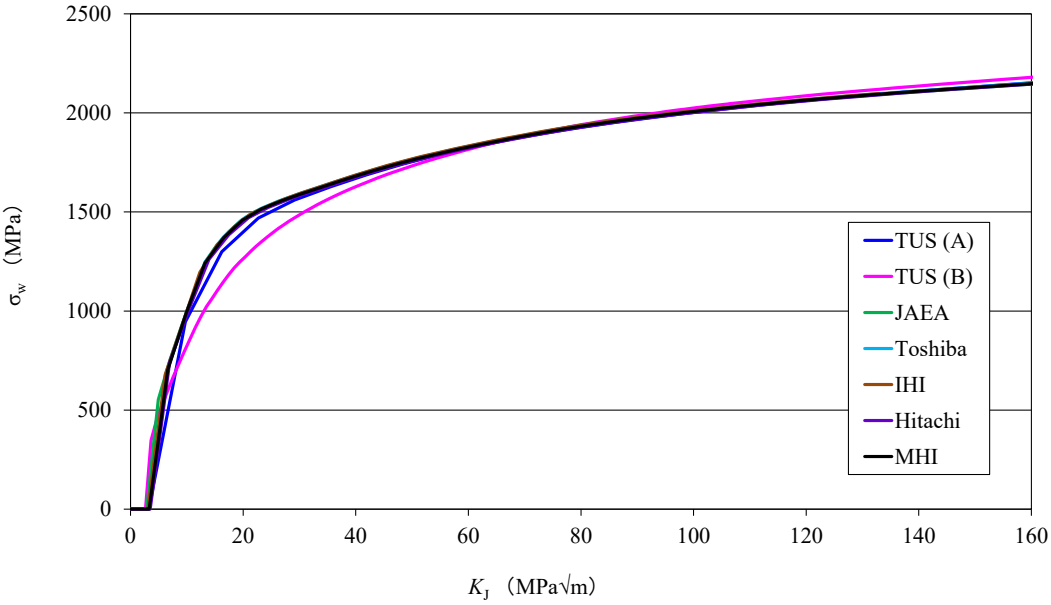
(a) $\sigma_w - K_J$



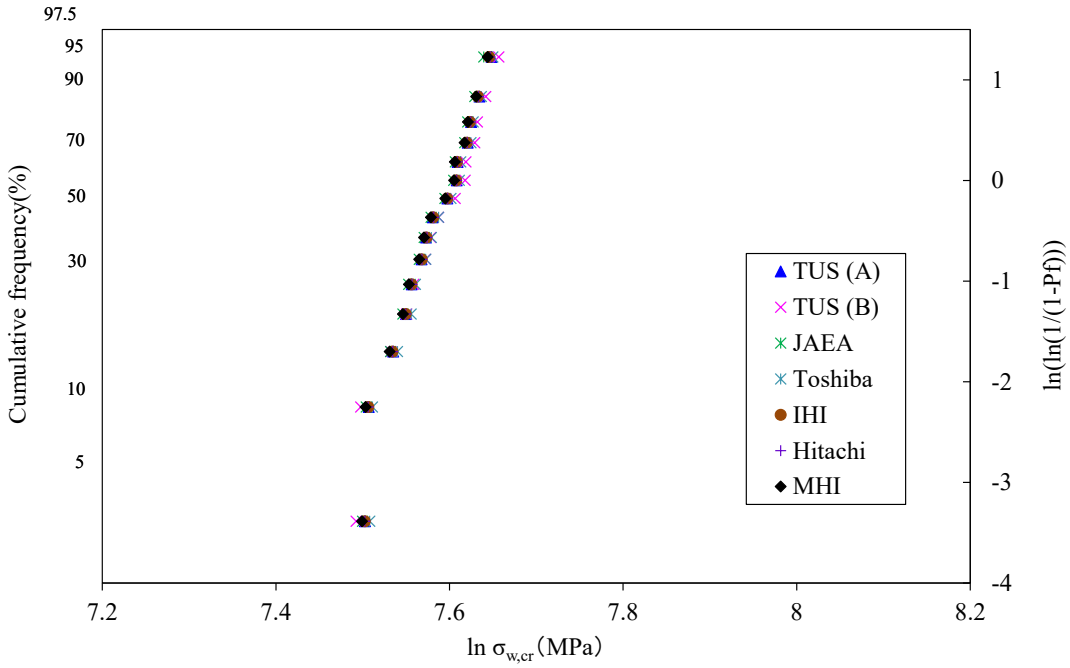
(b) Weibull plot of $\sigma_{w,cr}$

Fig. 2.3-4 Weibull stress evaluation results in case of m =10

Copyright © 2026 The Japan Welding Engineering Society, All Rights Reserved.



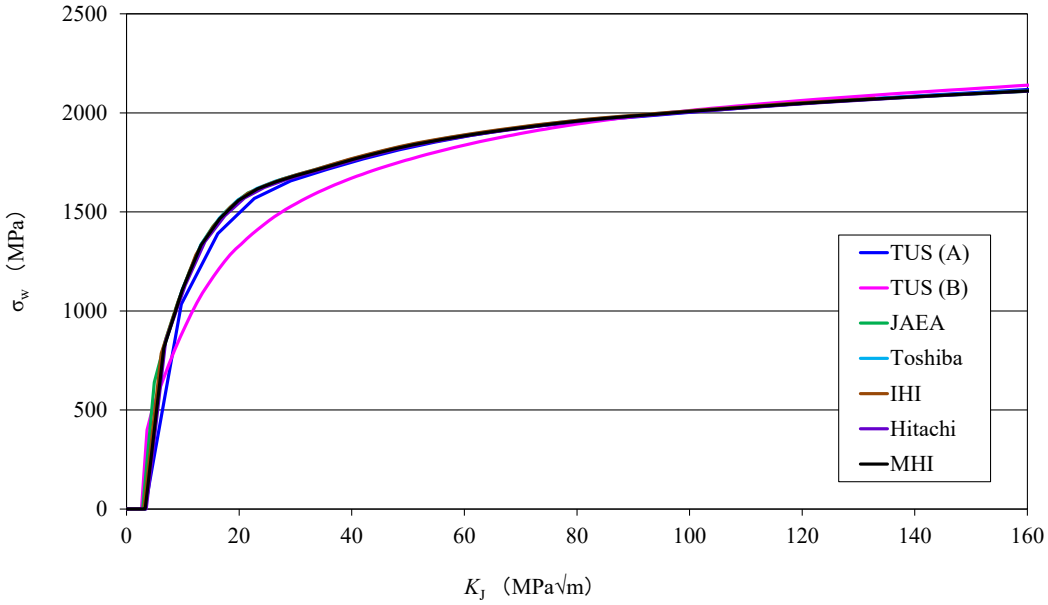
(a) $\sigma_w - K_J$



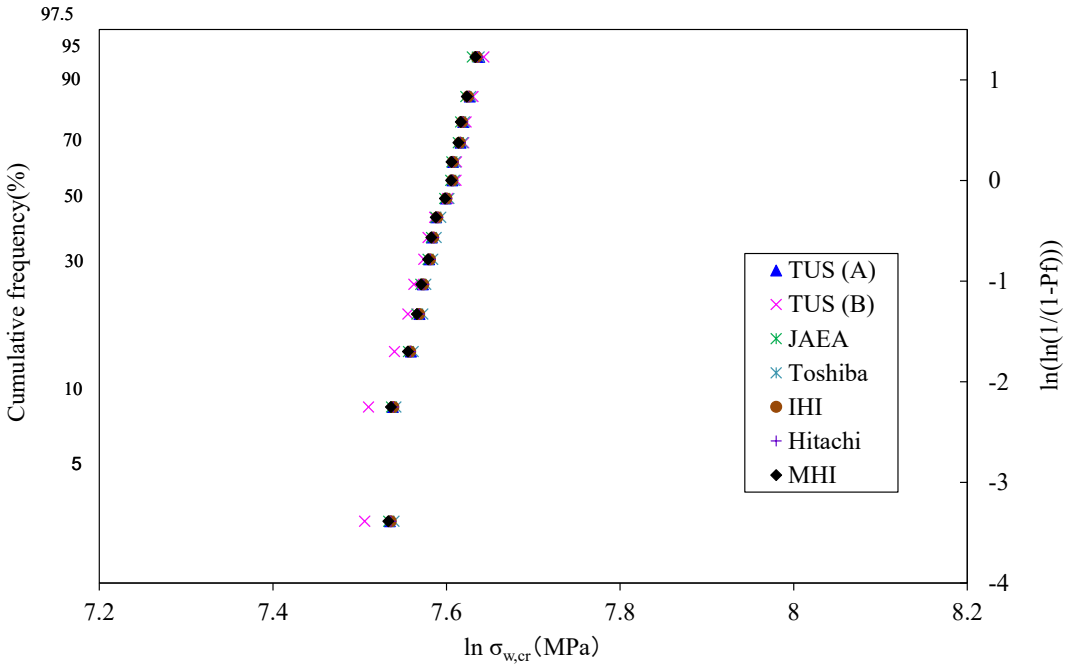
(b) Weibull plot of $\sigma_{w,cr}$

Fig. 2.3-5 Weibull stress evaluation results in case of m =20

Copyright © 2026 The Japan Welding Engineering Society, All Rights Reserved.



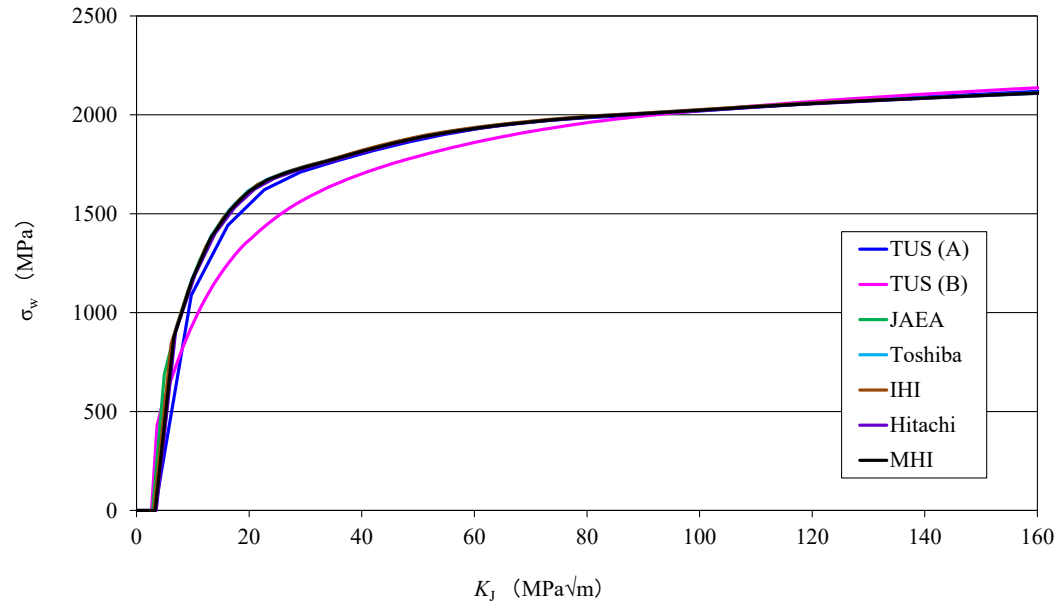
(a) $\sigma_w - K_J$



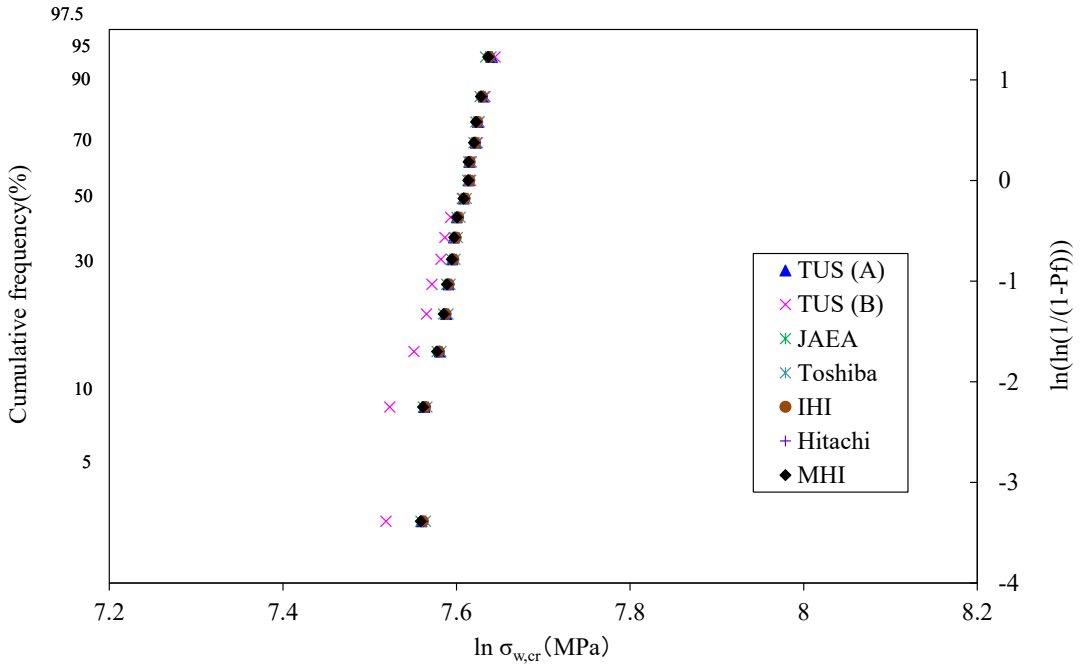
(b) Weibull plot of $\sigma_{w,cr}$

Fig. 2.3-6 Weibull stress evaluation results in case of m =30

Copyright © 2026 The Japan Welding Engineering Society, All Rights Reserved.



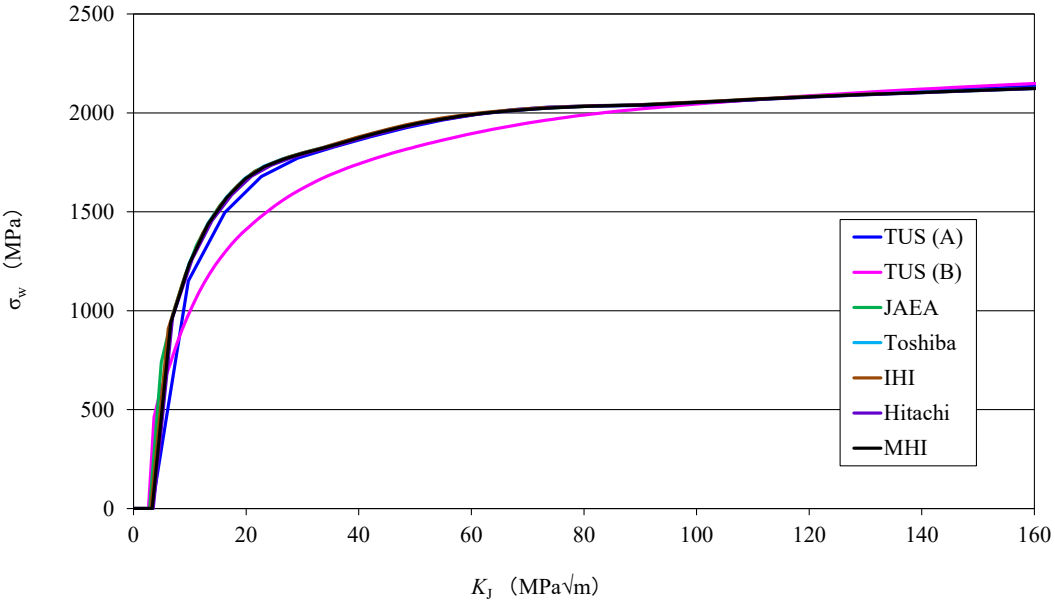
(a) $\sigma_w - K_J$



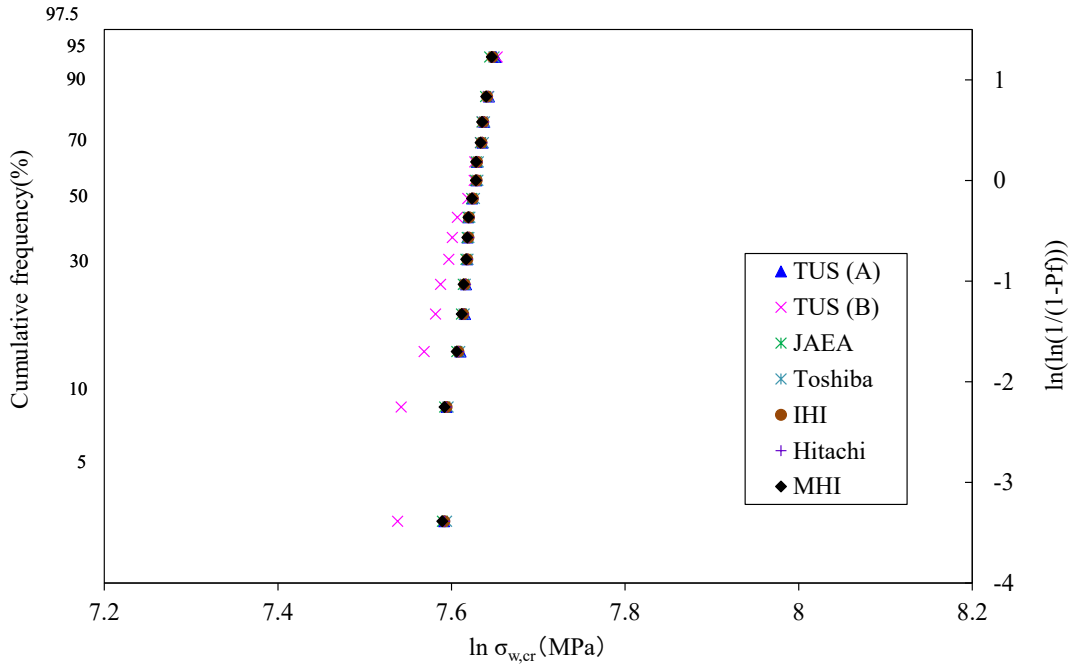
(b) Weibull plot of $\sigma_{w,cr}$

Fig. 2.3-7 Weibull stress evaluation results in case of m=40

Copyright © 2026 The Japan Welding Engineering Society, All Rights Reserved.



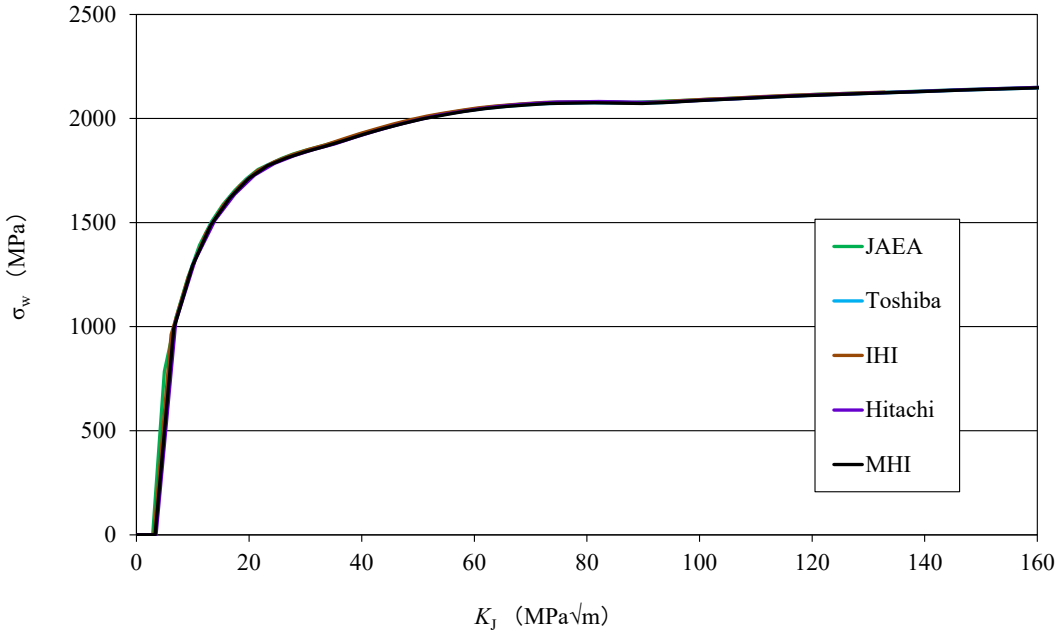
(a) $\sigma_w - K_J$



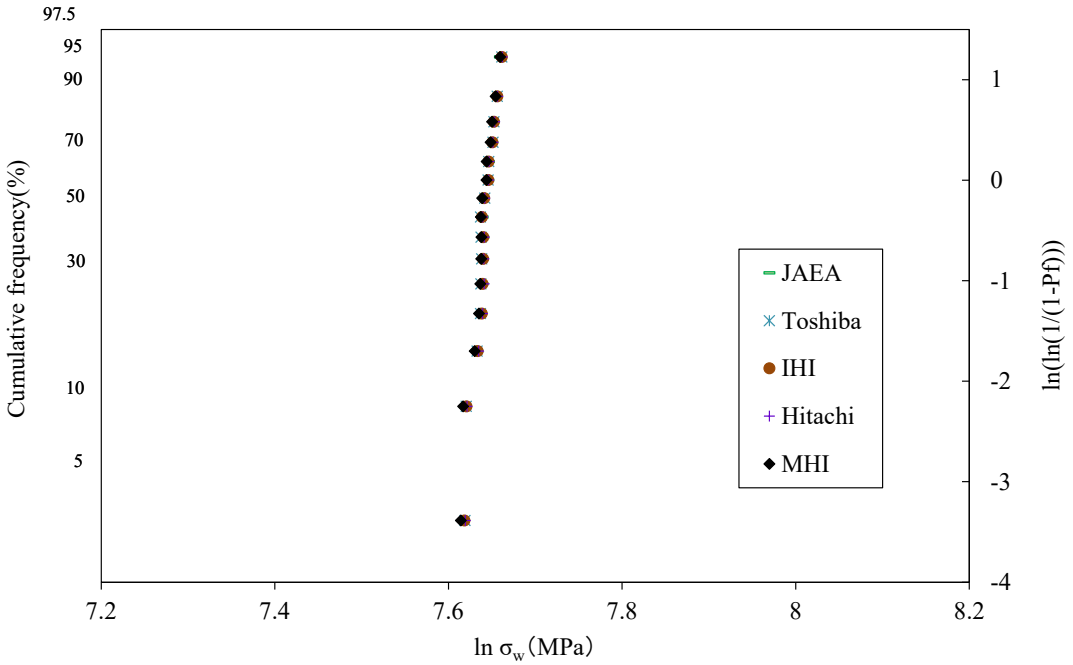
(b) Weibull plot of $\sigma_{w,cr}$

Fig. 2.3-8 Weibull stress evaluation results in case of m =60

Copyright © 2026 The Japan Welding Engineering Society, All Rights Reserved.



(a) $\sigma_w - K_J$



(b) Weibull plot of $\sigma_{w,cr}$

Fig. 2.3-9 Weibull stress evaluation results in case using obtained Weibull parameter, *m*

Copyright © 2026 The Japan Welding Engineering Society, All Rights Reserved.

(3) **Element Type**

(i) Influence of Element Type and Small Deformation / Large Deformation Theories on Deformation Behavior and Stress-Strain Fields

Elastic-plastic FE analyses were conducted assuming the element types shown in Table 2.3-2. Figure 2.3-10 compares the macroscopic deformation behavior (load versus load-line displacement relationship) obtained from the analyses with the experimental results. At low deformation levels, all behaviors match the experimental results; however, at large deformation levels, the small deformation theory shows slightly higher load than the large deformation theory. No difference was observed between reduced integration elements and selectively reduced integration elements.

Figure 2.3-11 shows the deformation near the crack tip at the maximum load level in the experiment. Although no influence was observed on macroscopic deformation behavior at low deformation levels, the analysis results using the small deformation theory show that the elements are severely distorted near the crack tip, indicating that the stress and strain fields near the crack tip cannot be accurately captured.

Therefore, focusing only on the analysis results using the large deformation theory, the influence of the integration element type on the crack opening direction stress and plastic strain distribution near the crack tip was examined.

As shown in Figure 2.3-12, only slight differences were observed at the very tip of the crack in both the crack opening direction stress and plastic strain. Both values tend to be lower for reduced integration elements compared to selectively reduced integration elements. However, the differences between the two are not considered significant.

Table 2.3-2 Element type used for FE-analysis.

		Deformation theory	
		Small deformation	Large deformation
Element type	Reduced Integration 1) C3D8R	(S-1)	(L-1)
	Selective Reduced Integration 2) C3D8	-	(L-2)

Copyright © 2026 The Japan Welding Engineering Society, All Rights Reserved.

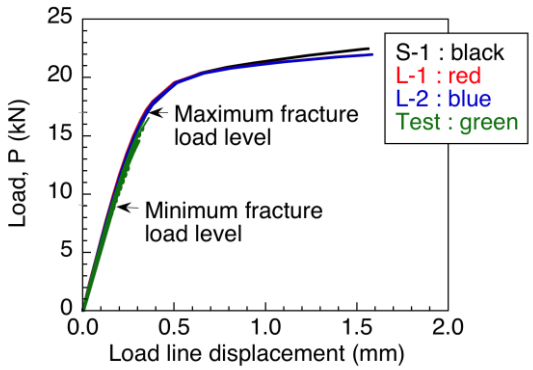


Fig. 2.3-10 Effect of deformation theory and element type on load-load line displacement curve.

Load level : P =17kN (@mid-thickness cross section)

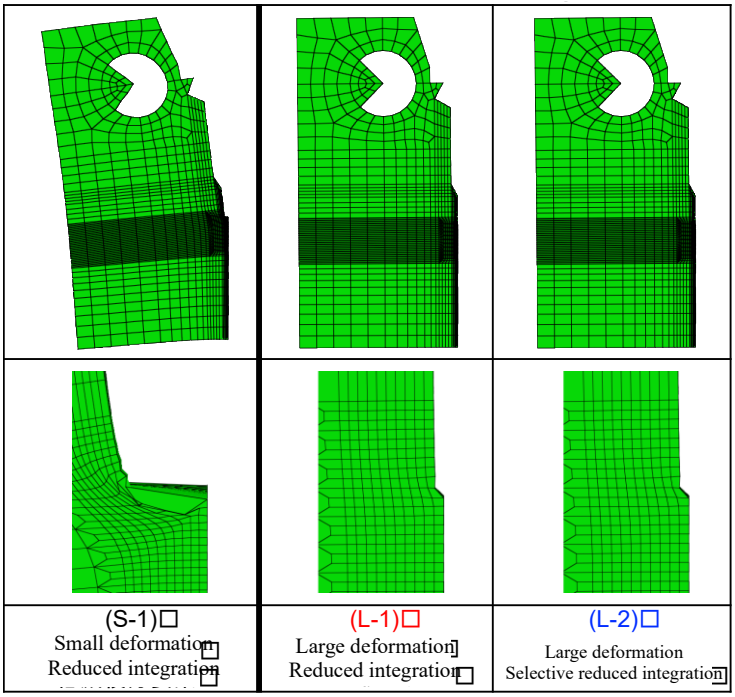
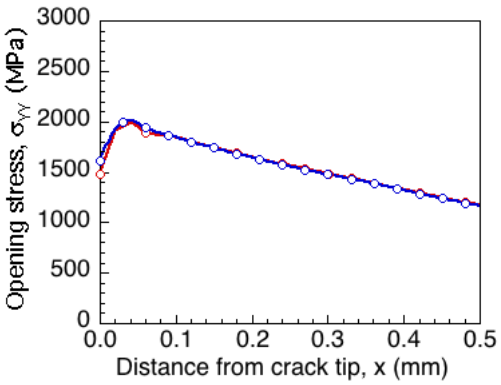


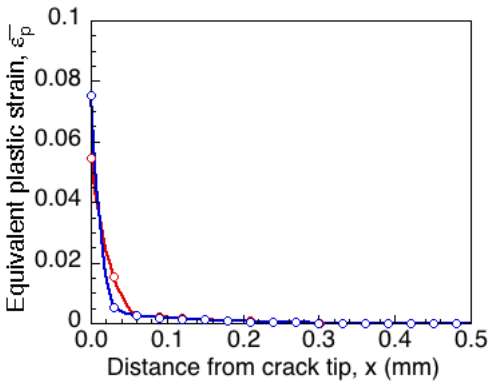
Fig. 2.3-11 Comparison of crack opening behaviors obtained by FE-analyses based on small deformation theory and large deformation theory.

Copyright © 2026 The Japan Welding Engineering Society, All Rights Reserved.



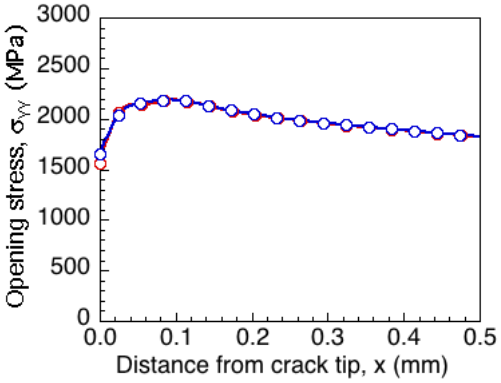
(a-1) Crack opening direction stress

(at P=9.1 kN)



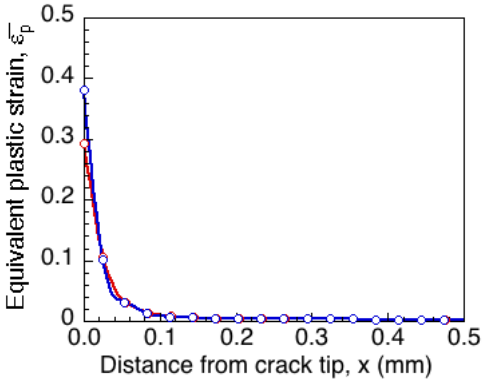
(b-1) Equivalent plastic strain

(at P=9.1 kN)



(a-2) Crack opening direction stress

(at P=17.0 kN)



(b-2) Equivalent plastic strain

(at P=17.0 kN)

Fig. 2.3-12 Effect of element type on crack-tip stress and strain behaviors (Large deformation theory).

Copyright © 2026 The Japan Welding Engineering Society, All Rights Reserved.

(ii) Influence of Volume Integration Method on Weibull Stress

Based on the results of (i), the influence of the volume integration method on Weibull stress and the critical Weibull stress distribution was examined using the results of elastic-plastic FE analyses with large deformation theory employing selectively reduced integration elements. Two types of volume integration methods were selected:

(1) The product of the average of the maximum principal stresses at eight Gauss integration points within the element and the element volume.
(2) Gaussian integration using the maximum principal stresses at the eight Gauss integration points within the element.

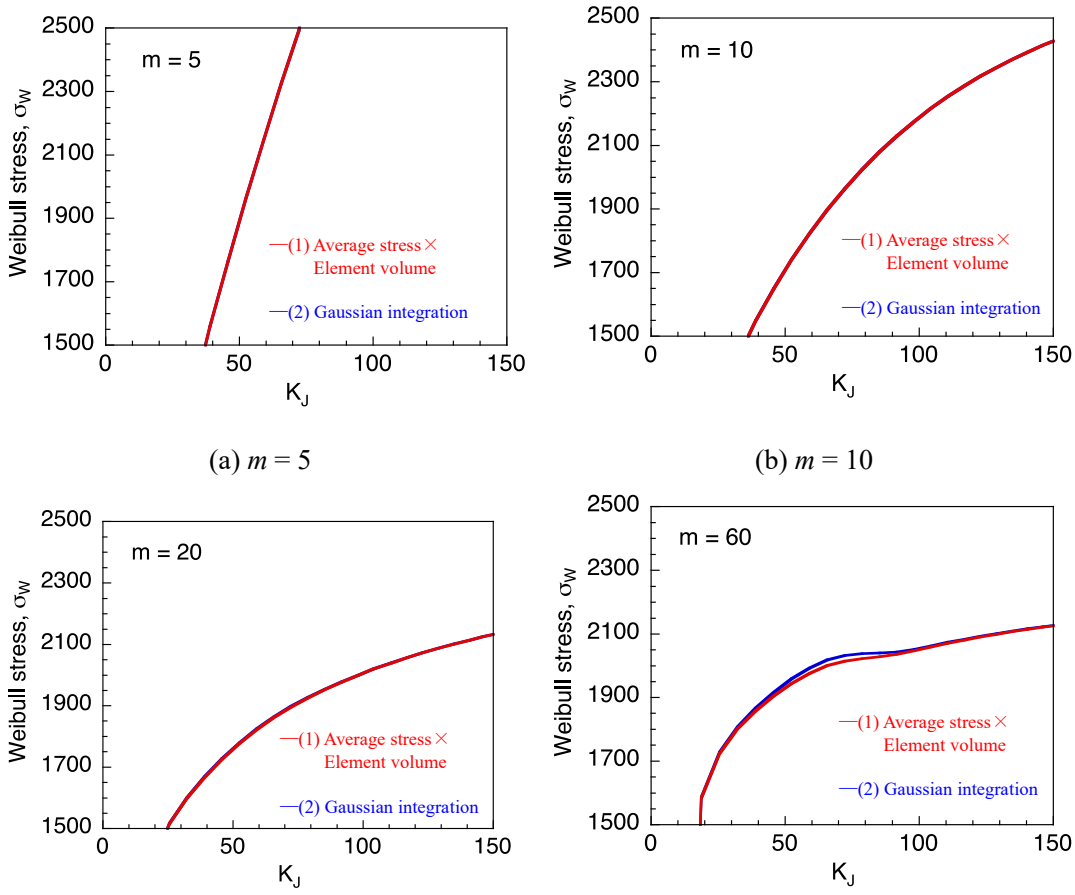
First, the influence of differences in the volume integration method on Weibull stress obtained by assuming a Weibull shape parameter *m* was examined. As shown in Figure 2.3.2-13, a difference between the two methods appears when *m* becomes considerably large, and the Weibull stress calculated using Gaussian integration (method (2)) tends to be higher at certain K_J levels. However, when *m* is small, almost no difference is observed between the two methods, indicating that the influence of the volume integration method on Weibull stress calculation is minimal.

Next, referring to the Weibull stresses calculated by both volume integration methods, the critical Weibull stress distribution was determined from experimental results, and the influence of the volume integration method on the Weibull shape parameter *m* was examined.

The obtained Weibull shape parameters *m* are summarized in Table 2.3-3. Appropriate *m* values were obtained only when the volume integration method (1) (average stress × element volume) was used.

This is considered to be because the *m* values of the target material in this study were relatively large, and thus the results shown in Figure 2.3-13 became apparent.

Copyright © 2026 The Japan Welding Engineering Society, All Rights Reserved.



(a) m = 5　　(b) m = 10

(c) m = 15　　(d) m = 20

Fig. 2.3-13　Effect of method for integrating maximum principal stress on Weibull stress.

Table 2.3-3　Effect of methods for volume integral of maximum principal stress over fracture process zone on Weibull shape parameter m of material constant

Methods for volume integral	Weibull shape parameter m
(1) product of the average of the maximum principal stresses and the element volume	56.5
(2) Gaussian integration	83.6 (However, an inversion phenomenon occurs in the Weibull stress.)

Copyright © 2026 The Japan Welding Engineering Society, All Rights Reserved.

(4) Influence of Differences in K_J Calculation Methods

Generally, K_J is calculated based on the relationship between load and load-line displacement according to ASTM E1921. On the other hand, the general-purpose analysis code Abaqus has a function to directly output the J-integral, from which K_J can also be calculated. To confirm the influence of differences in K_J calculation methods, K_J and the Weibull parameter m were calculated by each method and compared.

(i) Calculation Method of K_J Based on ASTM E1921

In ASTM E1921, K_J is calculated using the load versus load-line displacement curve. The analysis conditions are shown in Table 2.3-4, and the load versus load-line displacement relationship obtained from the analysis is shown in Figure 2.3-14.

The J-integral is calculated as the sum of the elastic component J_e and the plastic component J_p as shown in equation (2-1).

$$J = J_e + J_p \tag{2-1}$$

The elastic component J_e of the J-integral is expressed as follows:

$$J_e = [(1-\nu^2)K_e^2]/E \tag{2-2}$$

Where

$$K_e = [P/(BB_N W)^{1/2}]\, f(a_o/W) \tag{2-3}$$

$$f(a_o/W) = (2+a_o/W)/(1-a_o/W)^{3/2} \cdot [0.886+4.64(a_o/\mathrm{W})-13.32(a_o/W)^2+14.72(a_o/W)^3-5.6(a_o/W)^4] \tag{2-4}$$

The plastic component J_p of the J-integral is expressed as:

$$J_p = \eta A_p/B_N b_0 \tag{2-5}$$

Copyright © 2026 The Japan Welding Engineering Society, All Rights Reserved.

where

$A_p = A - 1/2C_0P^2$ (Refer to Fig. 2.3-14) (2-6)

$A = A_e + A_p$ (Refer to Fig. 2.3-14) (2-7)

C_0 : Initial elastic compliance

b_0 : Initial ligament length (= W-a_0)

$\eta = 2+0.522b_0/W$ (2-8)

The area A was calculated by integration from Figure 2.3-14. Also, when $J_p < 0$ from equation (2-6), J_p was set to zero.

The initial elastic compliance C_0 was calculated by: (i) determining the range from zero load to an appropriate range for drawing a regression line from Figure 2.3-14, (ii) calculating the slope and determination coefficient (R^2) by least squares using Excel's LINEST function, and (iii) extending the range in (i) to find the maximum range where $R^2 \geqq 0.9999$. The reciprocal of the slope at this point was taken as C_0.

From these results, (K_J) is calculated by the following equation:

$K_J = \sqrt{JE/(1-\nu^2)}$ (2-9)

(ii) Calculation Method of K_J Using Abaqus Output Values

The J-integral was obtained at the mid-thickness location, using the value of integration path 10. The obtained J-integral was converted to K_J using equation (2-9).

(iii) Comparison Results of K_J Values and m

Figure 2.3-15 shows the comparison between K_J calculated based on ASTM E1921 and K_J calculated from Abaqus output values. Within the load range used for Weibull stress evaluation, the difference between the two was about 3.5% at most.

Moreover, the converged value of m using K_J calculated based on ASTM E1921 was 99.87, whereas that using K_J calculated from Abaqus output values was 88.80, indicating that the difference did not significantly affect the convergence results.

Copyright © 2026 The Japan Welding Engineering Society, All Rights Reserved.

Table 2.3-4 Analysis condition

Analysis code	Abaqus 6.13-4
Specimen thickness: B	12.7 [mm]
Net specimen thickness: B_N	10.16 [mm]
Specimen width: W	25.4 [mm]
Initial crack size: a_o	13.62 [mm]
Young's modulus: E	205304 [MPa]
Poisson's ratio: ν	0.3

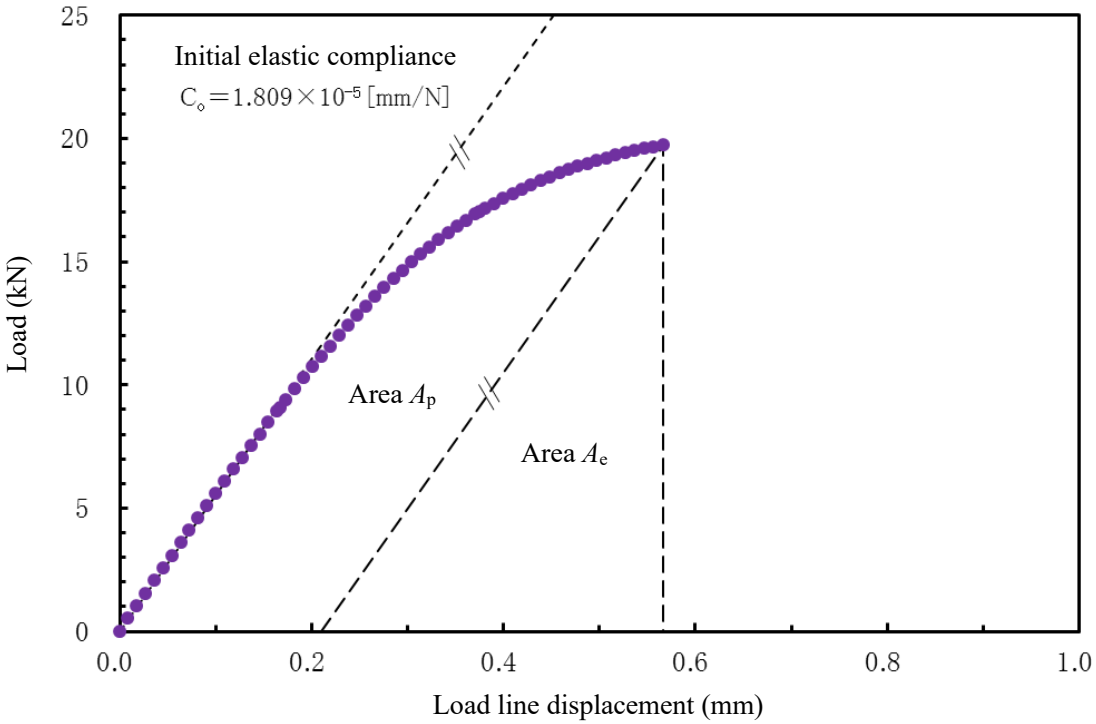


Fig. 2.3-14 Load – load line displacement curve

Copyright © 2026 The Japan Welding Engineering Society, All Rights Reserved.

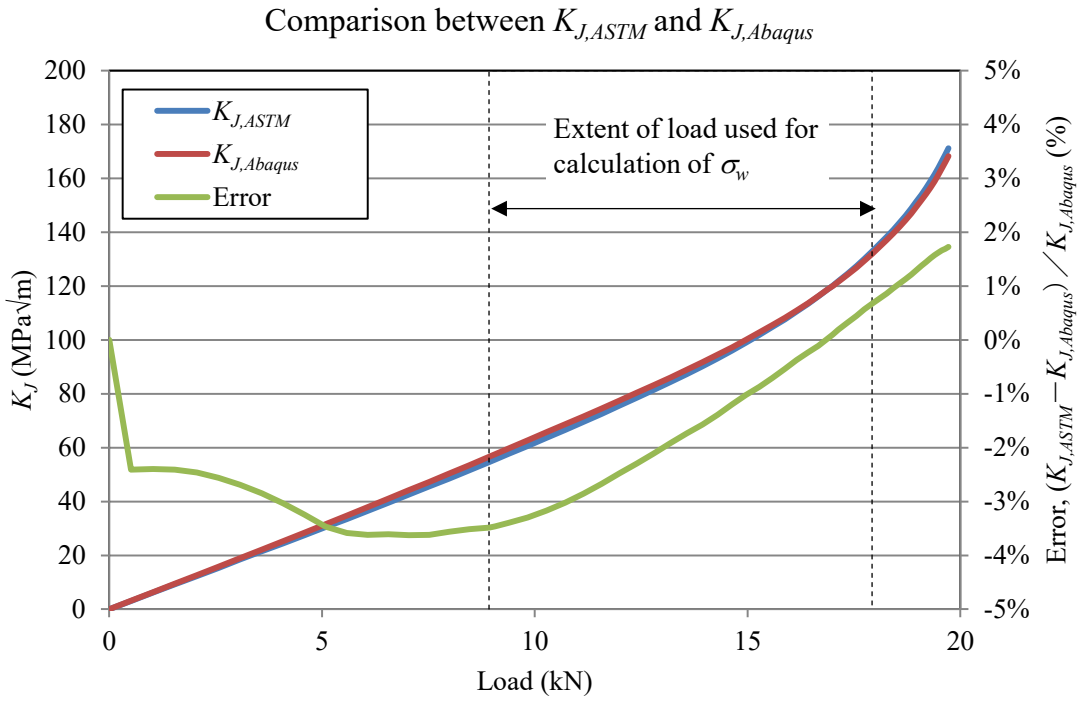


Fig. 2.3-15 Comparison of K_J between ASTM and Abaqus

(5) **Influence of Considering Volume Change**

This section examines the influence of considering or not considering volume change on Weibull stress evaluation.

Figure 2.3-16 shows, as an example, the relationship between the volume ratio V/V_0 and K_J at the crack tip element at the mid-thickness of the C(T) specimen. The volume ratio V/V_0 at the crack tip element in the mid-thickness reaches a maximum at approximately K_J = 70 MPa$\sqrt{\text{m}}$, corresponding to about a 1% increase in volume from the initial state.

To confirm the influence of considering this volume change on the Weibull stress σ_w, the relationship between Weibull stress σ_w and K_J was compared under two conditions: with and without consideration of volume change. The comparison results are shown in Figure 2.3-17.

For Weibull shape parameters m of 5 and 80 shown in Figure 2.3-17, no difference was observed between the conditions with and without volume change consideration.

For detailed confirmation, Figure 2.3-18 shows the ratio of Weibull stress σ_w (Weibull stress considering volume change σ_w divided by Weibull stress not considering volume change $\sigma_{w(V0)}$) and the shape parameter m at conditions of K_J approximately 21, 50, and 98 MPa$\sqrt{\text{m}}$.

Copyright © 2026 The Japan Welding Engineering Society, All Rights Reserved.

The ratio $\sigma_w/\sigma_{w(V0)}$ tends to decrease with increasing Weibull shape parameter m. For the typical range of shape parameter m from 10 to 50, which is often used for structural steels, the difference in Weibull stress σ_w due to consideration or non-consideration of volume change is less than 0.1%, which can be sufficiently neglected.

The reason why the influence of volume change decreases with increasing shape parameter m is because, as shown in the Weibull stress evaluation formula (equation (2-10)), the effective stress σ_{eff} is raised to the power of m inside the brackets, so the influence of stress becomes larger as m increases.

$$\sigma_W = \left[\frac{1}{V_0}\int_{V_f}\left(\sigma_{eff}\right)^m dV_f\right]^{1/m} \tag{2-10}$$

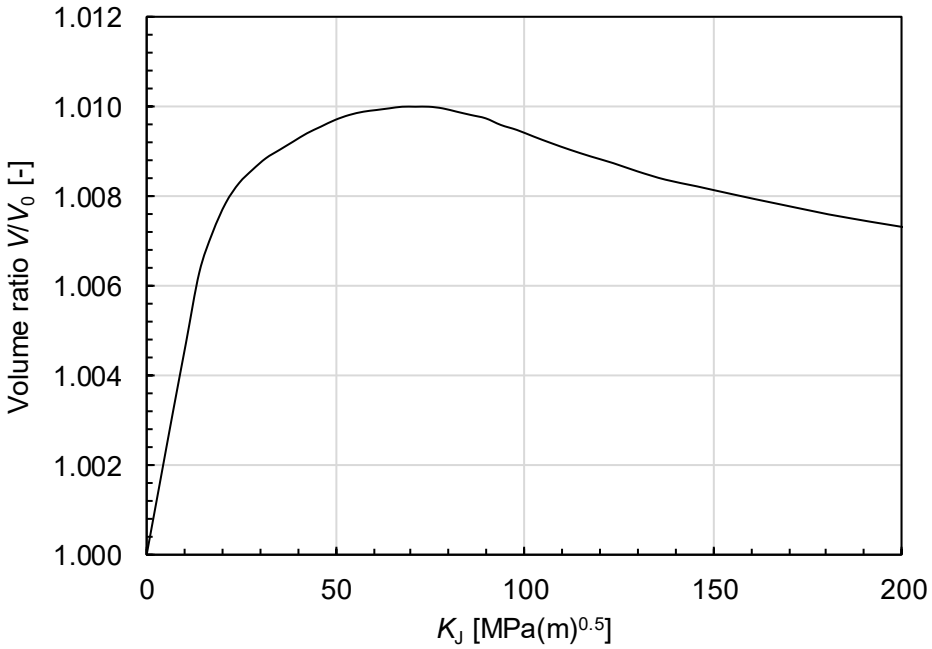
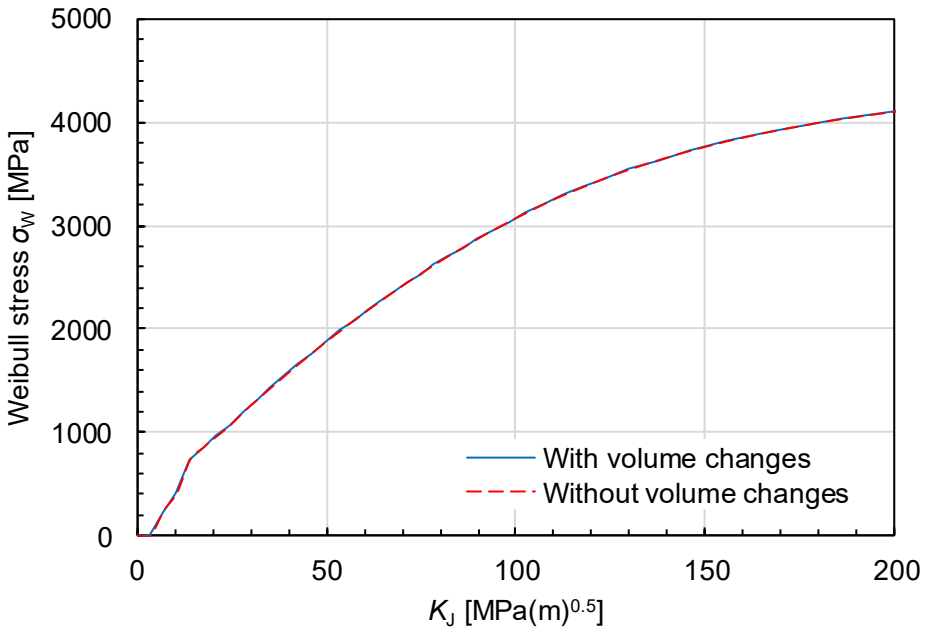
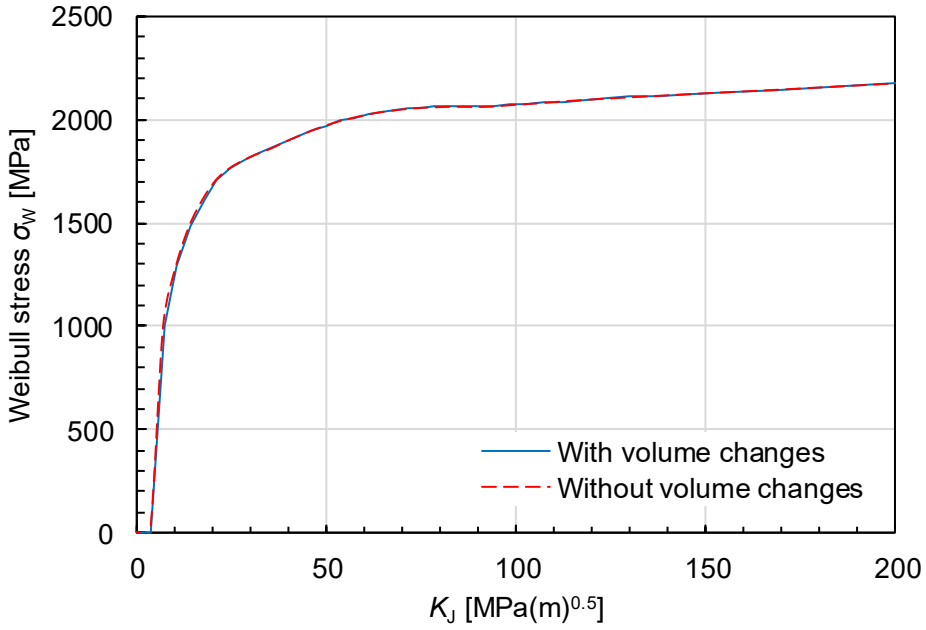


Fig. 2.3-16 Relationship between volume ratio V/V_0 and K_J.

Copyright © 2026 The Japan Welding Engineering Society, All Rights Reserved.



(a) Shape parameter m = 5



(b) Shape parameter m = 80

Fig. 2.3-17 Relationship between Weibull stress σ_w and K_J with and without volume change.

Copyright © 2026 The Japan Welding Engineering Society, All Rights Reserved.

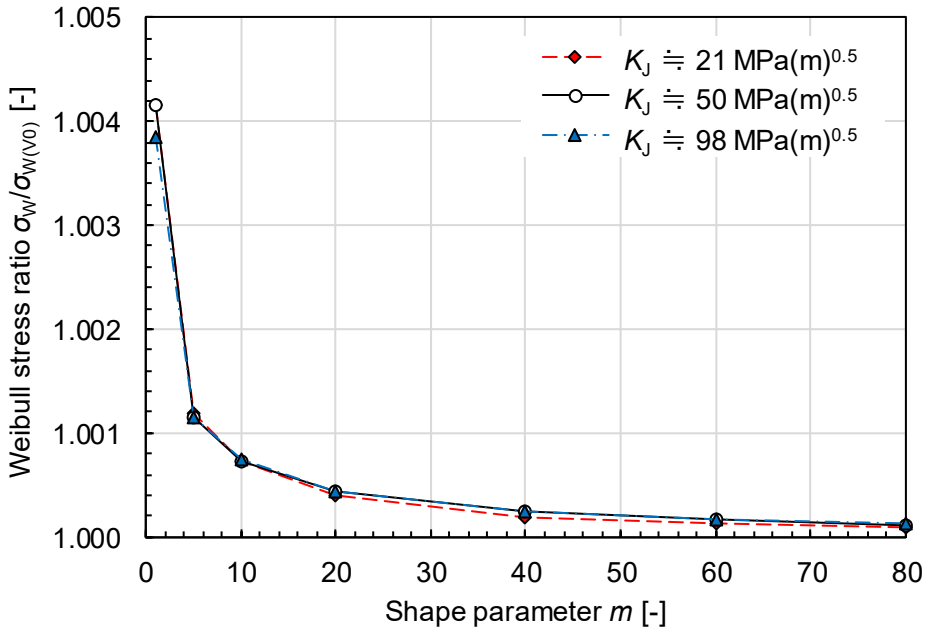


Fig. 2.3-18 Relationship between Weibull stress ratio $\sigma_w/\sigma_{w(V0)}$ and shape parameter m

Copyright © 2026 The Japan Welding Engineering Society, All Rights Reserved.

(6) Influence of Bias Correction

JIS R 1625:2010[1] specifies the estimation method of the shape parameter m of the two-parameter Weibull distribution by the maximum likelihood method. The estimation of the shape parameter m in JIS R 1625:2010 involves applying a statistical bias correction using the following equation:

$$m = B_n \times m_t \tag{2-11}$$

Here, B_n is the bias correction factor, and m_t is the shape parameter m estimated by the maximum likelihood method. The bias correction factor B_n is a function of the number of specimens n and is given by the following equations:

$$B_n = \left(2.04 \times n^{-1.1} + 1\right)^{-1} \qquad (n \leqq 120) \tag{2-12}$$

$$B_n = 1 \qquad (n > 120) \tag{2-13}$$

In the benchmark analysis targeting the Beremin model (specimens: C(T) specimens, test temperature: -125°C), the influence of the presence or absence of bias correction on the converged value of the shape parameter m was evaluated. The evaluation conditions are as follows. Since the number of specimens in the benchmark analysis is (n = 15), the correction factor for bias correction is B_n = 0.906.

- Numerical analysis : Implicit method
- Young's modulus : E = 205304 MPa
- Element type : C3D8R
  (8-node, linear, brick type, reduced integration, hourglass control)
- Method of calculating K_J value: Calculated from the area under the load versus load-line displacement curve

Convergence calculations of the shape parameter m were performed both with and without bias correction. Figure 2.3-19 shows the relationship between the assumed shape parameter m_0 (initial

Copyright © 2026 The Japan Welding Engineering Society, All Rights Reserved.

value) used in the Weibull stress calculation and the estimated shape parameter m_1 obtained by the maximum likelihood method. The dashed line indicates $m_0 = m_1$, and when the plotted points of m_0 and m_1 lie on this line, the shape parameter m is judged to have converged.

In the convergence calculation, m_1 was first calculated in increments of 10 for m_0 ranging from 10 to 100 to approximate the converged value. Then, m_0 was varied in increments of 0.1 to find the value minimizing the difference between m_0 and m_1.

Without bias correction, the converged value of the shape parameter m was 95.4. On the other hand, with bias correction, the converged value of m was 79.7. Since bias correction reduces m_1, convergence is judged at a smaller value. Under the conditions of this benchmark analysis, bias correction caused a difference of 15.7 in the converged value of the shape parameter m.

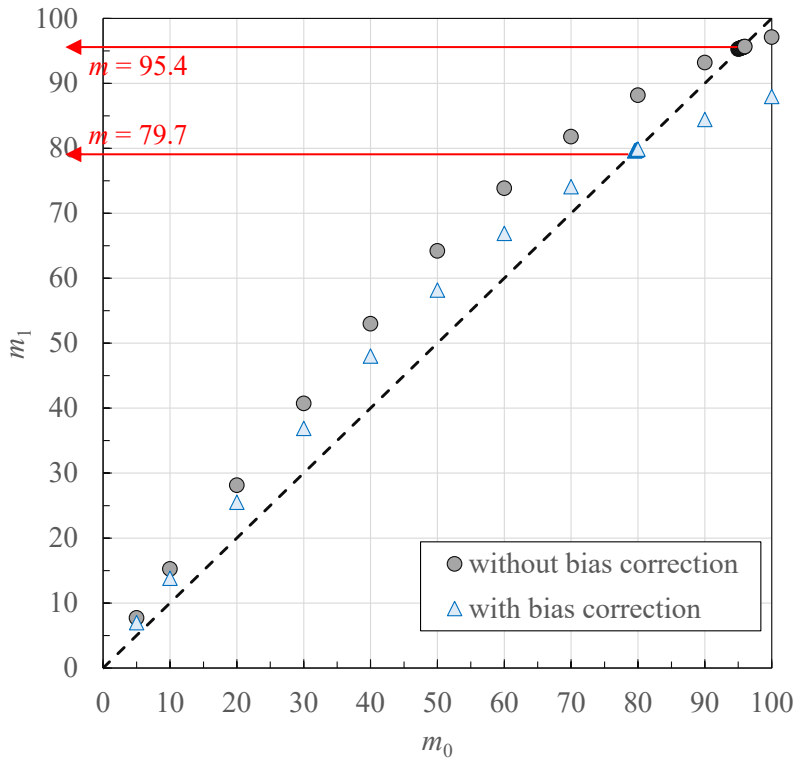


Fig. 2.3-19 Effect of bias correction on converged shape parameter m

[1] Japanese Industrial Standard, ”Weibull statistics of strength data for fine ceramics”, JIS R 1625 : 2010, (2010).

Copyright © 2026 The Japan Welding Engineering Society, All Rights Reserved.

2.4 Comparison of GTN Model Analyses

To verify the consistency of analysis results for the same parameter values using the damage mechanics model (GTN model), evaluations using the GTN model were conducted on C(T) specimens at -50°C. The benchmark analysis results of load versus load-line displacement and ductile crack growth amount are shown in Figures 2.4-1 and 2.4-2.

The analysis confirmed that the load versus load-line displacement and ductile crack growth amount were almost consistent among all participating organizations: Toshiba, IHI, Hitachi, and MHI.

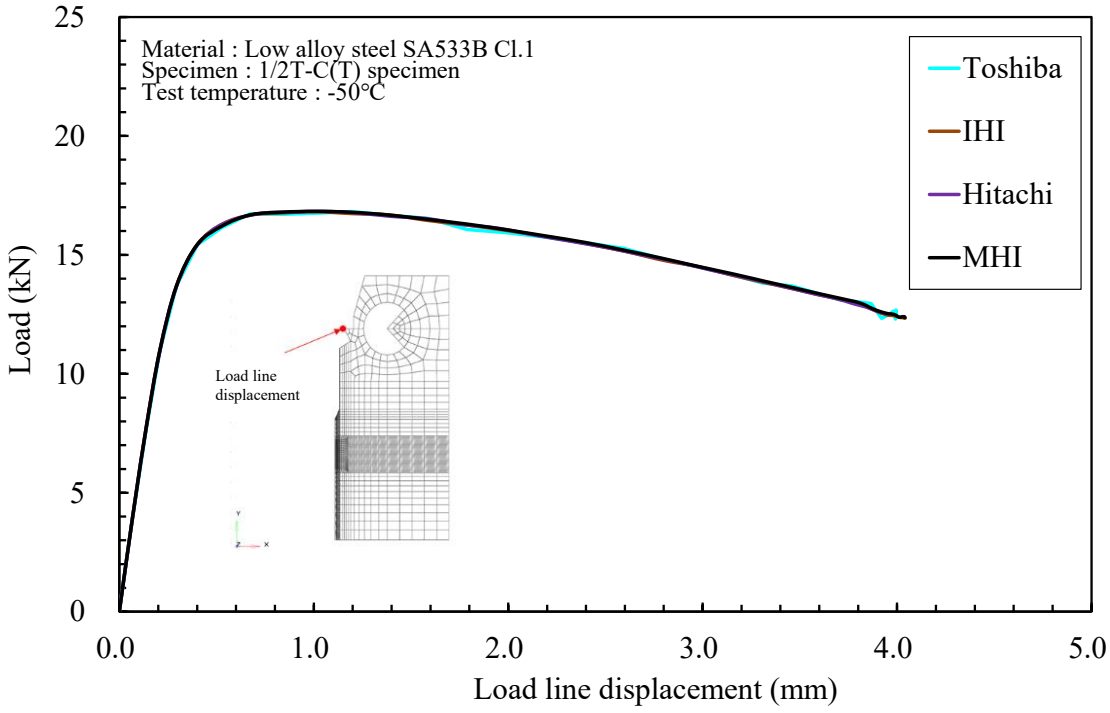


Fig. 2.4-1 Load – load line displacement curve

Copyright © 2026 The Japan Welding Engineering Society, All Rights Reserved.

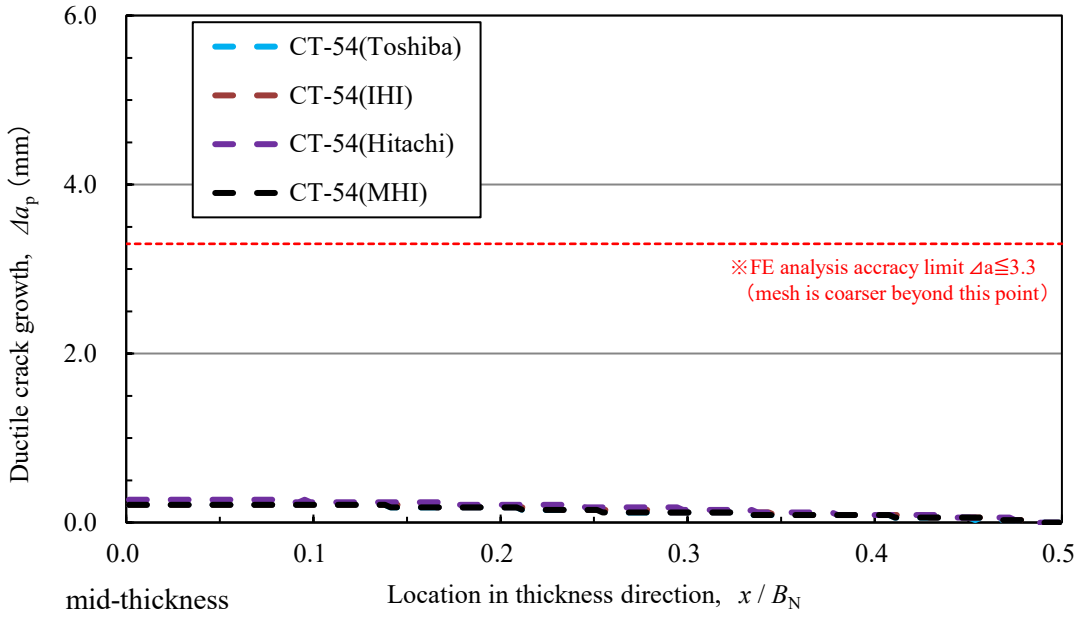


Fig. 2.4-2 Ductile crack growth in the thickness direction (1/7)

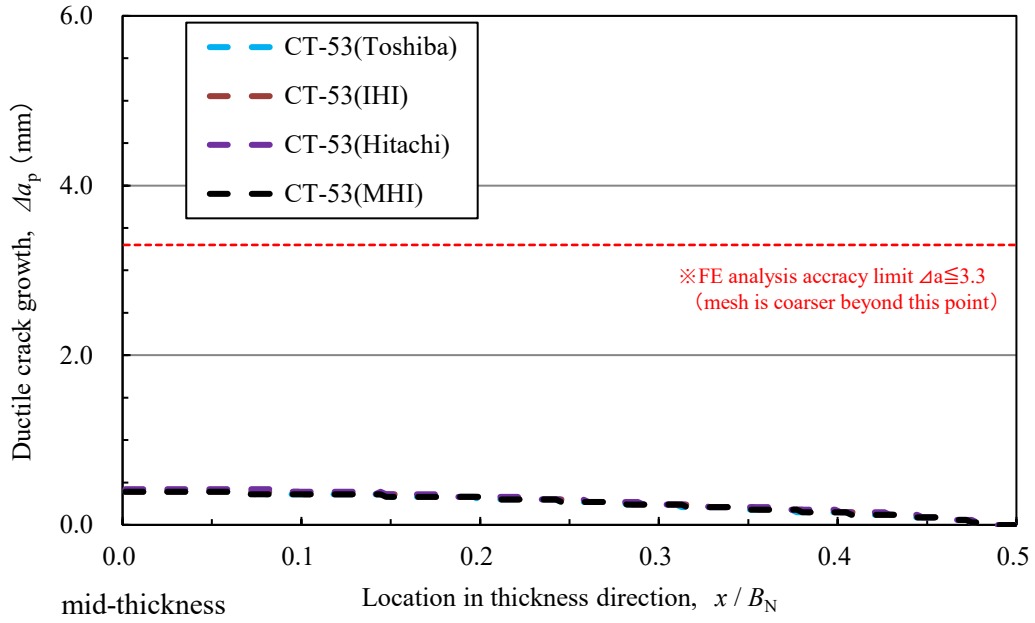


Fig. 2.4-2 Ductile crack growth in the thickness direction (2/7)

Copyright © 2026 The Japan Welding Engineering Society, All Rights Reserved.

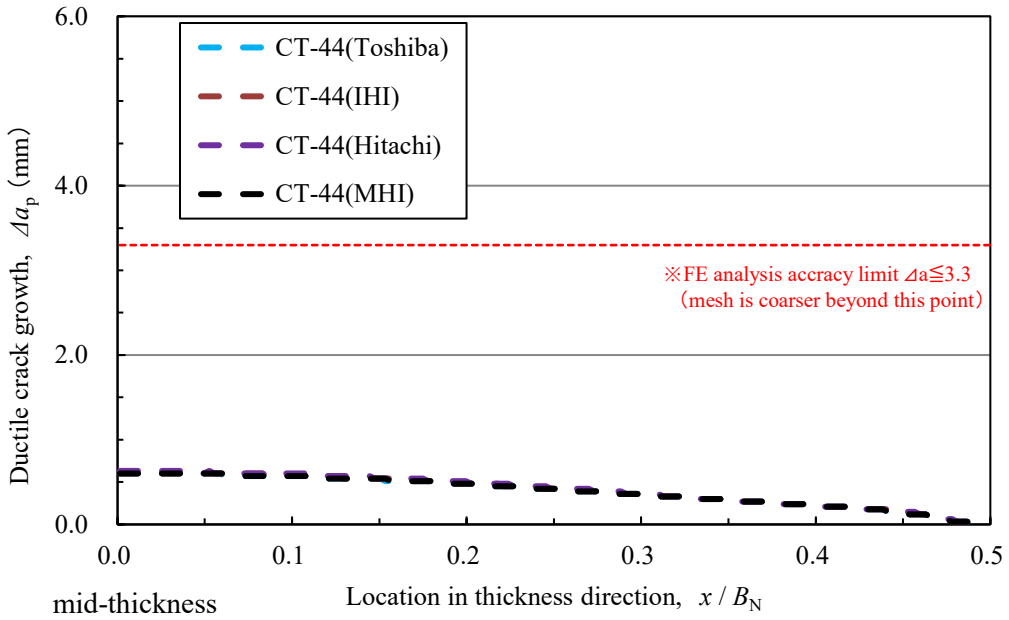


Fig. 2.4-2 Ductile crack growth in the thickness direction (3/7)

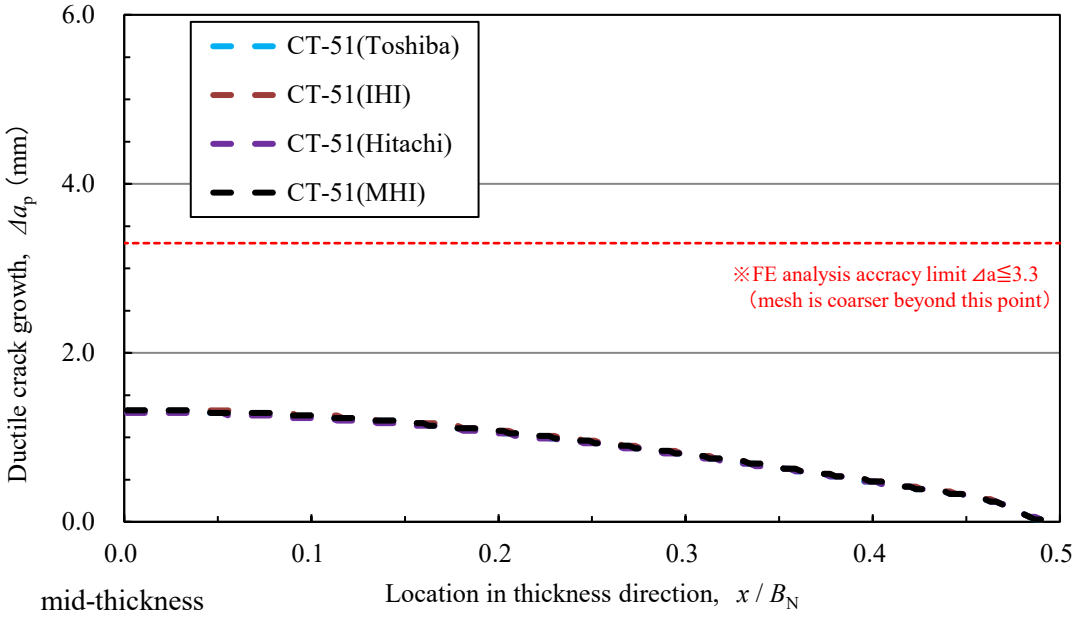


Fig. 2.4-2 Ductile crack growth in the thickness direction (4/7)

Copyright © 2026 The Japan Welding Engineering Society, All Rights Reserved.

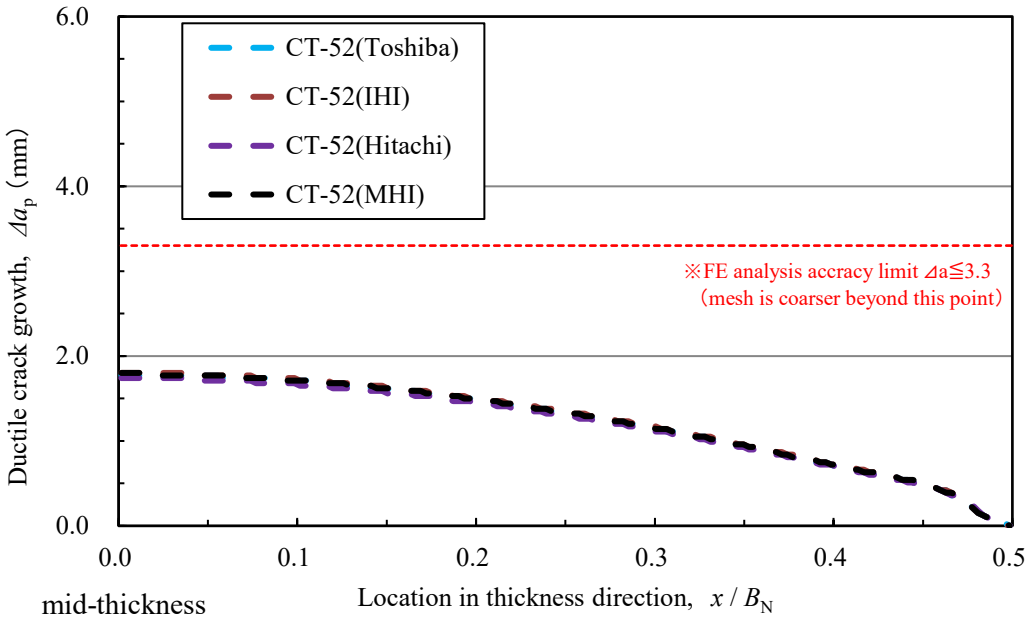


Fig. 2.4-2 Ductile crack growth in the thickness direction (5/7)

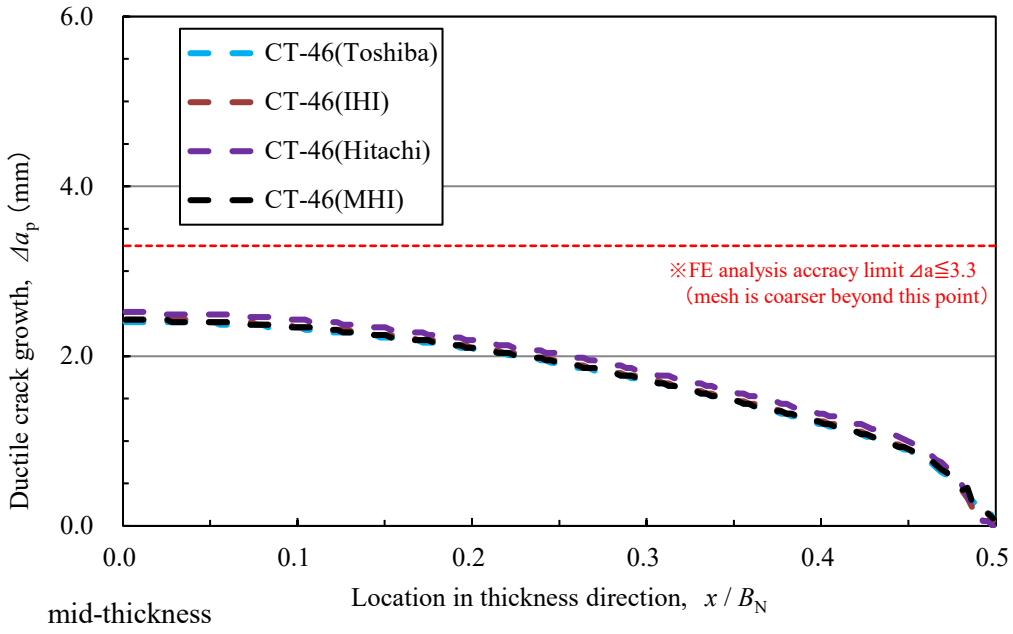


Fig. 2.4-2 Ductile crack growth in the thickness direction (6/7)

Copyright © 2026 The Japan Welding Engineering Society, All Rights Reserved.

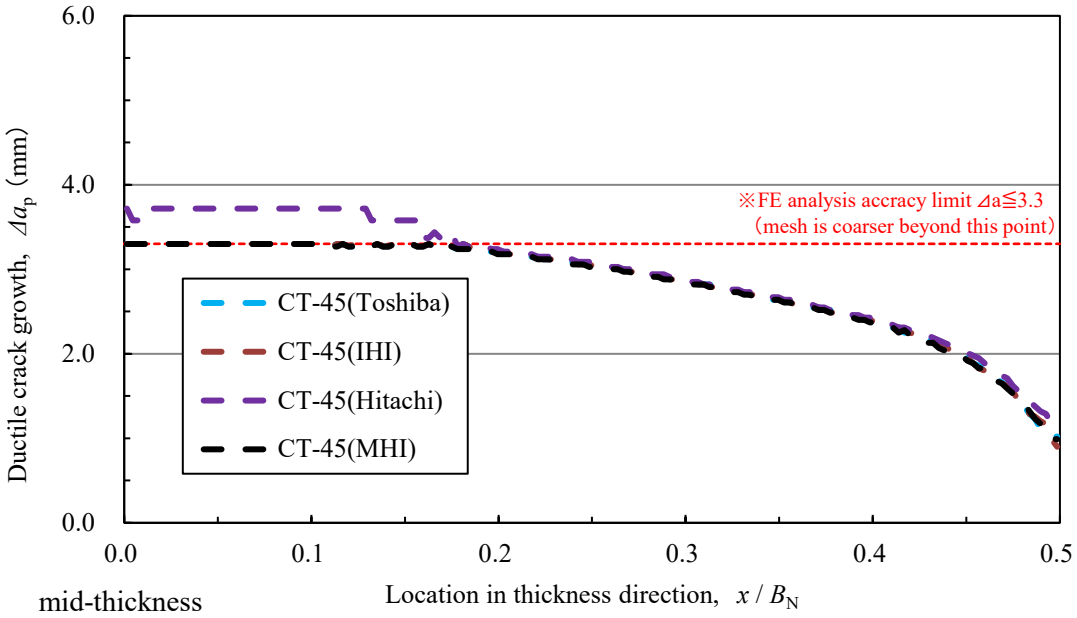


Fig. 2.4-2 Ductile crack growth in the thickness direction (7/7)

Copyright © 2026 The Japan Welding Engineering Society, All Rights Reserved.